Copyright

by

Athreya Suresh Babu

2023

The Dissertation Committee for Athreya Suresh Babu Certifies that this is the approved version of the following Dissertation:

MODELING ADVANCED STRIPPERS FOR CO_2 CAPTURE FROM GAS-FIRED POWER PLANTS BY AQUEOUS PIPERAZINE

Committee:

Gary T. Rochelle, Supervisor

Michael Baldea

Roger Bonnecaze

Robert Tsai

Yu-Jeng Lin

Modeling Advanced Strippers for CO_2 Capture from Gas-Fired Power Plants using Aqueous Piperazine

by

Athreya Suresh Babu

Dissertation

Presented to the Faculty of the Graduate School of

The University of Texas at Austin

in Partial Fulfillment

of the Requirements

for the Degree of

Doctor of Philosophy in Chemical Engineering

The University of Texas at Austin

August 2023

Dedicated to

The giants whose shoulders I stand on,

&

The giants who will stand on mine.

Acknowledgements

First, I want to thank Dr. Rochelle for giving me the opportunity to pursue graduate school research. He has taught me to take simple, elegant approaches to solve complicated engineering problems, while also allowing me to wander off into the unknown. I will carry this learning far beyond graduate school. Dr. Rochelle has been a great mentor at life, a humorous friend, and has always treated his students as family. I thoroughly enjoyed our discussions and always looked forward to the weekly meetings. Travelling to conferences in different countries and backpacking with him are some memories that I will cherish. I will certainly miss working with him.

No PhD is possible without collaboration. I have become better at teamwork, exchanging ideas, and giving/accepting criticism by working with the Texas Carbon Engineers. I enjoyed TA'ing with Dr. Yuying Wu, Dr. Ching-Ting Liu, Dr. Korede Akinpelumi, and Dr. Tianyu Gao, as much as I enjoyed collaborating on the FEED project with Miguel Abreu, Benjamin Drewry, and Dr. Fred Closmann. I also want to thank Ariel Plantz, Chih-I Chen, and James Obute for discussions on and off the research lab. Many undergraduate students contributed to data collection, for which I am thankful.

As every graduate student, I spent a good amount of time writing papers and quarterly reports. The quarterly reports, despite being demanding at times, certainly helped me keep track of progress in my PhD and made writing this dissertation a little bit easier. I want to thank Maeve Cooney for patiently editing these reports despite me not formatting the references correctly every single time. The research group is a well-oiled machine due to her relentless help with administrative affairs, and I am very thankful for that.

I also want to thank all pilot plant support personnel for their invaluable help. Laura Uhrig and Jason Arriazola graciously extended their support during heat loss and heat duty measurements at NCCC. At UT-SRP, Dr. Frank Seibert and Jared Spinhirne helped plan and conduct heat loss measurements. Interacting with pilot plant engineers has allowed me to think broadly about the practical implications of my research.

This PhD wouldn't have been possible without the generous funding from several agencies like the US-DOE, $CCSI^2$, FEED sponsors, Texas Carbon Management Program, and Carbon Capture Project 4 (CCP4). I am thankful for their unending financial support.

Moving 10,000 miles from home to pursue graduate studies is no easy feat, and I want to thank my friends in Austin for making this transition a little bit easier. Having a support system that could relate to the ups and downs of a typical PhD helped me maintain my sanity through the past 6 years. Unrelenting support from my parents and brother helped me feel a bit more secure during trying times in this PhD. Lastly, I will deeply miss the comforts of living in downtown Austin, by the lake, and I hope to someday be back in this beautiful city.

Abstract

Modeling Advanced Strippers for CO_2 Capture from Gas-Fired Power Plants using Aqueous Piperazine

Athreya Suresh Babu, M.S.E, PhD

The University of Texas at Austin, 2023

Supervisor: Gary T. Rochelle

Energy performance of 5 m piperazine was evaluated with an advanced stripper at the pilot scale, accounting for heat loss. Modeling studies indicated that heat loss at locations other than the heat source impacted the heat duty. For strippers with excess packing, the column was the most important source of heat loss, and values as low as 0.03 GJ/hr can cause pinch and reabsorption of CO_2. Solvents like 5 m PZ are more affected by heat loss in the column due to a top-side temperature pinch at high lean loading. Heat loss impacts NGCC CO_2 capture more than coal-based CO_2 capture.

Surface temperature measurements pilot plants showed that heat loss was 50-75% controlled by natural convection. Measured heat loss was correlated with steam flowrate and wind speed and ranged from 8126 to 219668 Btu/hr, representing 35% of the measured heat rate on average. Net heat duty linearly varied with CO_2 removal at low lean loading and was similar for coal and NGCC conditions at fixed removal. At 90% removal, net heat duty was about 2.5 GJ/t with 4 and 12% CO_2 in the flue gas.

At NGCC conditions, strippers with finite packing can benefit from a flashing feed to the top of the column by using a hot bypass. A flashing feed was linked to a reduction in irreversibility of the stripper from temperature driving forces. It also reduces heat duty by up to 6% at fixed packing height and reduces packing requirement for a fixed steam heater size compared to a warm bypass. Lean loading and lean solvent rate were effective handles to maximize profitability of a fixed stripper design at low gas price. High ambient temperature operation can benefit from low pressure stripping to about 0.18 lean loading at 150 °C to maintain the cyclic capacity at reduced rich loading. At low gas price, the capture plant was able to maximize profitability even with a high heat duty of 2.7-3.1 GJ/t at a lean loading of 0.2-0.22 mol/mol.

Heat recovery by partial water vapor condensation in a gas-liquid exchanger can be replaced by a direct contact condenser (DCC). The DCC improved gas cooling and reduced heat duty compared to the CO_2 exchanger at 0.2 lean loading. The DCC when used with a 150 °C/5.5 bar stripper can reduce the cost of capture compared to the base case by $3-4/tonne at 15 ft of packing (optimum) but increases cost of capture by $6/tonne with a 120 °C/2 bar stripper and 10 ft of packing (optimum). The DCC can work effectively with a solvent with a high heat of absorption and thermal stability.

Table of Contents

List of Tables 17

List of Figures 18

Chapter 1: Introduction 33

1.1 EMISSIONS FROM ELECTRICITY GENERATION 33

1.2 CO_2 CAPTURE BY AMINE SCRUBBING 34

1.3 ENERGY USE IN AMINE SCRUBBING 35

1.4 PRIOR WORK IN STRIPPERS FOR CO_2 CAPTURE 37

1.4.1 Piperazine with the Advanced Stripper (Advanced Flash Stripper / PZAS™) 40

1.5 OBJECTIVES OF THIS RESEARCH 41

Chapter 2: Heat Loss in Amine Scrubbing Pilot Plants 47

2.1 INTRODUCTION 47

2.2 OBJECTIVES 50

2.3 PILOT PLANT OVERVIEW 50

2.3.1 PZAS at PSTU, NCCC 51

2.3.2 PZAS at UT-SRP Pilot Plant 52

2.3.3 Simple Stripper Process at PSTU, NCCC 53

2.4 HEAT TRANSFER STUDIES FOR HEAT LOSS 54

2.4.1 Surface Temperature Measurements at Pilot Plant 54

2.4.2 Heat Transfer Characteristics of Heat Loss at UT-SRP Pilot Plant (2021-22 campaign) 56

2.4.3 Heat Transfer Characteristics of Heat Loss at NCCC (2023 campaign) 57

2.5 HEAT LOSS MODELING.....60

2.5.1 Modeling Methodology 60

2.5.2 Effect of Heat Loss in Different Locations in PZAS.....63

2.5.3 Effect of Heat Loss on Stripper Performance in PZAS 64

2.5.4 Effect of Heat Loss in Different Locations of Simple Stripper with 5 m PZ.....65

2.5.5 Effect of Heat Loss on Simple Stripper Performance.....66

2.5.6 Effect of Lean Loading on Heat Loss: 5 m PZ vs 7 m MEA.....68

2.5.7 Implications of Heat Loss in Coal vs NGCC CO_2 Capture Using PZAS 69

2.6 STEAM FLOW MEASUREMENT 70

2.6.1 Steam Flowrate Correction for Temperature and Pressure in the Coal 2018 and NGCC 2019 Campaigns 70

2.6.2 Steam Flowmeter Calibration in the NGCC 2023 Campaign at NCCC.....72

2.7 HEAT LOSS MEASUREMENT.....74

2.7.1 NCCC Coal 2018 and NGCC 2019 Campaigns 74

2.7.2 UT-SRP NGCC Campaign 2021-22 76

2.7.3 NCCC NGCC Campaign 2023 78

2.7.4 Consolidated Heat Loss Data from all Pilot Campaigns 82

2.8 CONCLUSIONS 88

RECOMMENDATIONS FOR FUTURE WORK 90

ACKNOWLEDGEMENTS.....91

Chapter 3: Pilot Plant Data Reconciliation and Stripper Model Validation 92

3.1 INTRODUCTION 92

3.1.1. Modeling and Data Reconciliation Approaches for Strippers 93
3.2 PILOT PLANT AND CAMPAIGN OVERVIEW 95
3.2.1. NCCC 2018 Coal and NGCC 2019 95
3.2.2 UT-SRP 2021-22 NGCC Campaign 97
3.2.3 NCCC 2023 NGCC Campaign 98
3.3 ANALYTICAL METHODS AND PILOT PLANT MEASUREMENTS 99
3.3.1 NCCC 2018 Coal and 2019 NGCC Campaigns 99
3.3.2 UT-SRP 2021-22 NGCC Campaign 102
3.3.3 NCCC 2023 NGCC Campaign 103
3.4 MODELING METHOD 105
3.4.1 Coal 2018 and NGCC 2019 Campaigns at NCCC 105
3.4.2 UT-SRP NGCC 2021-22 Campaign 106
3.4.3 NCCC 2023 NGCC Campaign 108
3.5 PILOT PLANT EXPERIMENTAL RESULTS 108
3.5.1 Reconciliation of Solvent Composition 108
3.5.1.1 NCCC 2018 Coal and 2019 NGCC Campaigns 108
3.5.1.2 UT-SRP 2021-22 NGCC Campaign 111
3.5.1.3 NCCC 2023 NGCC Campaign 115
3.5.2 Energy Performance of Stripper at Pilot Plants 118
3.5.2.1 NCCC 2018 Coal and 2019 NGCC Campaigns 118
3.5.2.2 UT-SRP 2021-22 NGCC Campaign 122
3.5.2.3 NCCC 2023 NGCC Campaign 125
3.6 MODEL VALIDATION 133

3.6.1 NCCC 2018 Coal and 2019 NGCC Campaign.....133
3.6.2 NGCC NCCC 2023 Campaign.....138
3.7 OVERALL MODEL ERROR ANALYSIS 143
3.8 MODEL RECONCILIATION 148
3.9 CONCLUSIONS 150
RECOMMENDATIONS FOR FUTURE WORK 152
ACKNOWLEDGMENTS 154
Chapter 4: Commercial Stripper Design for a FEED on a 460 MW NGCC 155
4.1 DESIGN METHODOLOGY.....156
4.1.1 Simulation Method 156
4.1.2 Process Description and Design Rationale 156
4.1.3 Bypass Optimization Procedure.....158
4.1.4 Design of Heat Exchangers.....159
4.1.5 Column Design 160
4.1.6 Water Balance in PZAS.....160
4.2 SUMMARY OF BASE CASE DESIGN 161
4.3 SELECTION OF PACKING TYPE.....162
4.4 SELECTION OF PACKING HEIGHT.....164
4.5 ESTIMATION OF MINIMUM HEAT RATE.....166
4.6 IMPACT OF SUMP TEMPERATURE ON COLUMN DIAMETER 166
4.7 SELECTION OF HEAT EXCHANGER NTU.....168
4.8 ALTERNATIVE PROCESS CONFIGURATIONS 170
4.8.1 Distribution of Heat Exchanger NTU.....170

4.8.2 Use of a Hot Rich Bypass Flow 171

4.8.3 Benefits of Using a Hot Rich Bypass 173

4.8.4 Benefits of Flashing Total Rich Bypass 174

4.9 EQUIVALENT WORK OF STRIPPING AND COMPARISONS WITH OTHER PROCESS CONFIGURATIONS 175

4.10 EFFECT OF AMBIENT TEMPERATURE ON ENERGY REQUIREMENT 178

4.11 OPERATIONAL BOUNDS OF PZAS WITH HOT RICH BYPASS 180

4.12 OPERATIONAL CHALLENGES WITH PZAS WITH HOT RICH BYPASS 182

4.13 CONCLUSIONS 186

RECOMMENDATIONS FOR FUTURE WORK 187

Chapter 5: Off-Design Performance of Commercial Stripper Design 189

5.1 MODELING METHODS 190

5.2 SUMMARY OF BASE CASE STRIPPER DESIGN 191

5.3 DEVELOPMENT OF OFF-DESIGN (RATING) MODELS 192

5.3.1 Operational Limit of Rich Pump 197

5.4 OFF-DESIGN PERFORMANCE OF CO_2 COMPRESSOR 199

5.5 DEVELOPMENT OF SURROGATE MODELS FOR PZAS 200

5.6 PROCESS SURROGATE MODEL 202

5.6.1 Convergence of Process Surrogate Model 203

5.6.2 Operational Constraints in Process Surrogate Model 208

5.6.3 Modified Bypass Extraction Strategy for FEED of PZAS 212

5.6.3.1 Simulation of Modified Configuration 214

5.6.3.2 Scenario 1: Fluid Density in Total Rich Bypass Line Determines Elevation Head 215

5.6.3.3 Scenario 2: Liquid Density in Total Rich Bypass Line Determines Elevation Head 217

5.6.3.4 Control Valve Operation.....218

5.6.3.5 Vapor Content in Solvent Lines.....219

5.7 CONCLUSIONS 220

RECOMMENDATIONS FOR FUTURE WORK 222

ACKNOWLEDGMENTS 223

Chapter 6: Optimization of Off-Design Performance of PZAS.....224

6.1 FLUE GAS CASES INVESTIGATED.....224

6.2 OPTIMIZATION OF VARIABLE PROFIT.....225

6.3 EFFECT OF PROCESS CONSTRAINTS ON MAXIMUM ACHIEVABLE PROFIT.....227

6.4 DEPENDENCE OF OPTIMAL HEAT DUTY ON GAS PRICE 231

6.5 SUMMARY TABLE OF OPTIMIZATION RESULTS WITH VARIABLE LEAN LOADING (STRIPPER PRESSURE).....233

6.6 DISCUSSION OF OPTIMIZATION RESULTS.....236

6.6.1 Air Cooler Operation for Rich Loading Maximization 236

6.6.2 Stripper Flooding 237

6.6.3 Approach to Maximum Boiler Heat Rate 238

6.6.4 Approach to Maximum Boiler Fan Speed 238

6.6.5 Approach to Maximum Compressor Capacity 239

6.6.6 Maximum Variable Profit and Optimum Variables 239

6.7 SOLVENT PRECIPITATION 248

6.8 AMINE VOLATILITY 249

6.9 CONCLUSIONS 250

RECOMMENDATIONS FOR FUTURE WORK 251

ACKNOWLEDGEMENTS.....253

Chapter 7: Alternative Stripper Designs for FEED of PZAS 254

7.1 ADVANCED SCENARIOS CONSIDERED 255

7.2 LITERATURE REVIEW ON ADVANCED STRIPPER CONFIGURATIONS 256

7.3 SUMMARY OF BASE CASE DESIGN 259

7.4 STRIPPER MODELING METHOD AND TOOLS 260

7.5 MODELING THE DIRECT CONTACT CONDENSER.....262

7.6 DISCUSSION OF THE MODELING METHODS 263

7.6.1 Reaction Kinetics.....263

7.6.2 Mass Transfer 263

7.6.3 Diffusivity of PZ.....264

7.6.4 Cases Studied.....266

7.6.5 Impact of Modeling Method Choice on Heat Duty 267

7.6.6 Impact of Modeling Method Choice on Temperature Profile 269

7.6.7 Differences in Kinetics Method.....271

7.7 PZAS WITH DOUBLE THE NUMBER OF SOLVENT CROSS EXCHANGERS.....273

7.8 PZAS WITH A DIRECT CONTACT CONDENSER.....275

7.8.1 Impact of Direct Contact Condenser on Steam Heater Duty.....277

7.8.2 Temperature and Flux Profile in Direct Contact Condenser 278

7.8.3 Effect of Direct Contact Condenser on Rich Loading.....280

7.8.4 Impact of Direct Contact Condenser on Gas Cooling and Condenser Duty 282

7.9 PZAS WITH A DIRECT CONTACT CONDENSER AND DOUBLE THE NUMBER OF SOLVENT CROSS EXCHANGERS 284

7.9.1 Impact of Direct Contact Condenser on Steam Heater Duty.....285

7.9.2 Temperature and Flux Profile in Direct Contact Condenser 286

7.9.3 Impact of Direct Contact Condenser on Rich Loading.....287

7.9.4 Impact of Direct Contact Condenser on Gas Cooling and Residual Condenser Duty 288

7.10 EFFECT OF BYPASS FLOWRATE ON PERFORMANCE OF DIRECT CONTACT CONDENSER 290

7.11 LOW PRESSURE STRIPPING WITH PZAS 292

7.11.1 Impact on Process Equipment.....292

7.11.2 Impact on Stripper Performance 294

7.12 PZAS WITH LOW PRESSURE/LOW TEMPERATURE STRIPPER AND DIRECT CONTACT CONDENSER 296

7.12.1 Impact of Direct Contact Condenser on Steam Heater Duty.....298

7.12.2 Temperature and Flux Profile in Direct Contact Condenser 299

7.12.3 Impact of Direct Contact Condenser on Rich Loading.....300

7.12.4 Impact of Direct Contact Condenser on Gas Cooling and Residual Condenser Duty 302

7.13 SUBOPTIMIZATION OF FEED POINT FOR WARM RICH BYPASS.....302

7.14 CONCLUSIONS 307

RECOMMENDATIONS FOR FUTURE WORK 310

Chapter 8: Process Economics with Alternative Stripper Designs 311

8.1 COST SCALING METHODOLOGY 311

8.2 PROCESS ECONOMICS 313

8.3 REDUCTION IN DIRECT FIELD COST 315

8.4 ADDED COST OF STRIPPER COLUMN 319

8.5 MISCELLANEOUS COSTS 320

8.6 BREAKDOWN OF DIRECT FIELD COSTS BY DESIGN 321

8.7 ANNUALIZED TOTAL CAPITAL INVESTMENT AND ANNUAL OPERATING COST 322

8.8 TOTAL COST OF CAPTURE 325

8.9 CONCLUSIONS 327

RECOMMENDATIONS FOR FUTURE WORK 329

Chapter 9: Summary of Conclusions and Recommendations for Future Work 330

9.1 PILOT PLANT TESTING 330

9.2 STRIPPER MODELING 333

9.3 STRIPPER DESIGN AND OPTIMIZATION 334

Appendices 339

References 463

Vita 472

List of Tables

Table 1.1: Comparison of past and current work in strippers for CO_2 capture.....37

Table 2.1: Process specifications of cases investigated for heat loss modeling 61

Table 4.1: Packing height per section and column diameter for 3 different sets of packing.....162

Table 5.1: Scaling of pressure drop in heat exchangers.....194

Table 5.2: Feasibility flags incorporated in optimization model 209

Table 5.3: Vapor content in solvent lines after control valves for two design scenarios with modified bypass extraction 220

Table 6.1: Flue gas conditions considered for process optimization.....225

Table 6.2: Flue gas cases with gas and power price considered.....227

Table 6.3: Summary table of results from optimization of variable profit for 5 different flue gas cases; gas price = $3/MMBtu; all numbers except profit and electric power are for one process train; CO_2 value: $80/tonne.234

Table 7.1: Cases studied to analyze the impact of mass transfer, kinetics, and diffusivity method on stripper modeling.....267

Table 8.1: Base case direct field cost (DFC) and scaling variable chosen for some equipment.....311

Table 8.2: Direct field cost (DFC) of equipment for 6 design scenarios.....321

List of Figures

Figure 1.1: Electricity generation and CO_2 emissions by fuel source (2005-2019) (EIA, 2021) 33

Figure 1.2: Flowsheet of a simple amine scrubbing process configuration for CO_2 capture.....34

Figure 1.3: Schematic of a typical NGCC with a CCS unit retrofitted onto it 36

Figure 1.4: Flowsheet of Piperazine with the Advanced Stripper (PZAS).....40

Figure 2.1: PZAS flowsheet with important heat loss locations.....52

Figure 2.2: PZAS process at the UT-SRP pilot plant with the heat loss measurement boundary 53

Figure 2.3: Flowsheet of the simple stripper process at NCCC.....54

Figure 2.4: Schematic for surface temperature measurements at pilot plant.....55

Figure 2.5: Maximum temperature driving force for heat loss through natural convection for 3 locations at variable ambient temperature 56

Figure 2.6: Heat transfer in heat loss is primarily controlled by natural convection for the UT-SRP pilot plant between 51 and 84 °F ambient temperature.....57

Figure 2.7: Temperature driving force to ambient for heat loss for Run 4.....58

Figure 2.8: Ratio of ambient-side to fluid-side temperature driving force for heat loss for Run 4 across several locations 60

Figure 2.9: Sensitivity of heat duty to heat loss in different locations in PZAS.....63

Figure 2.10: Sensitivity of CO_2 flux in the PZAS stripper to heat loss in different locations; negative flux indicates reabsorption of CO_2.....65

Figure 2.11: Sensitivity of heat duty to heat loss in different locations of the simple stripper with 5 m PZ 66

Figure 2.12: Reabsorption in simple stripper with 5 m PZ occurs at low heat loss value; heat loss was added to the column 67
Figure 2.13: Effect of heat loss is less pronounced in 7 m MEA compared to 5 m PZ with the simple stripper.....69
Figure 2.14: Effect of heat loss on heat duty with PZAS applied for NGCC and coal flue gas conditions 70
Figure 2.15: Steam flow arrangement with condensate measurement at NCCC.....71
Figure 2.16: Back-calculated value of standard density of the flowmeter deviated significantly from the factory-setting value at high steam flow 72
Figure 2.17: Steam flowrate and condensate flowrate measurements compared to the tote measurements.....74
Figure 2.18: Measured heat loss showed no dependence on steam rate.....77
Figure 2.19: Heat loss in equipment in PZAS as fraction of total heat loss 78
Figure 2.20: Change in water level in tank S-602 for heat loss runs 4 and 5 79
Figure 2.21: Mass balance closed within 0.5% for heat loss runs 80
Figure 2.22: Stripper sump and overhead gas temperature as a function of steam flow rate for water testing at NCCC across all campaigns between 2018 and 2023.....81
Figure 2.23: Stripper sump and overhead gas temperature as a function of steam flow rate for water testing at UT-SRP pilot plant across all campaigns between 2015 and 2013 (except for the MTR and Osaka Gas campaigns)..82
Figure 2.24: Measured heat loss as a function of temperature driving force from the stripper sump to ambient from 5 different pilot plant campaigns; SRP 2015 data taken from Lin (2016) 85

Figure 2.25: Heat loss normalized by steam heat rate removes its dependence on sump temperature; heat loss per unit steam flow depends inversely on ambient temperature....86
Figure 2.26: Heat loss shows a weak dependence on local wind speed 87
Figure 3.1: Simplified process flow diagram of PZAS at NCCC....96
Figure 3.2: Simplified process flow diagram of PZAS at UT-SRP pilot plant....98
Figure 3.3: Stripper-side pilot measurements showing key model inputs and outputs for PZAS at NCCC 100
Figure 3.4: On-line measurements for rich and lean samples around the absorber (Gao, 2021) 101
Figure 3.5: Flowsheet of PZAS at UT-SRP showing measurements and variables manipulated and not manipulated by Aspen Plus® Data Fit™ 103
Figure 3.6: Flowsheet of PZAS at NCCC in the 2023 campaign showing key model inputs and outputs 104
Figure 3.7: Density-viscosity based lean loading agreed within 10% of the model-predicted lean loading 110
Figure 3.8: Density-viscosity based lean loading agrees better with modeled lean loading with the use of a carbon bed 111
Figure 3.9: Relative error in PZ concentration from ion chromatography, auto-titrated PZ, and manually titrated PZ 112
Figure 3.10: Relative error of CO_2 by density and manual titration PZ compared to TIC and manual titration of CO_2, orange points are lean samples, blue points are rich samples....113

Figure 3.11: Relative error of CO_2 by density and auto titration PZ compared to TIC and manual titration of CO_2, orange points are lean samples, blue points are rich samples.....114
Figure 3.12: Loading measurements done 6 different ways in the SRP campaign
Figure 3.13: Comparison of PZ concentration using 3 different methods with online titration; IC PZ data after recalibration of instrument in April 2023.....115
Figure 3.14: Comparison of CO_2 concentration using 2 different methods with online titration; CO_2 concentration from online titration was adjusted by +15% per Gao (2021) to match density-viscosity based CO_2 concentration 116
Figure 3.15: Net heat duty increased with CO_2 removal in the coal and NGCC campaigns at NCCC.....117
Figure 3.16: Net heat duty decreased with increasing rich loading.....121
Figure 3.17: Carbon treating improved heat exchanger performance 122
Figure 3.18: Measured heat duty depends on measured lean loading and cold rich bypass flowrate 124
Figure 3.19: Measured lean loading is correlated with stripper sump temperature at constant pressure.....125
Figure 3.20: Measured heat duty during evolutionary optimization of bypass flowrates for I/O IC.....126
Figure 3.21: Measured heat duty during the evolutionary optimization of bypass flowrates for PA IC.....127
Figure 3.22: Measured heat duty as a function of solvent loading from online titration 128

Figure 3.23: Effect of total rich bypass split fraction on measured heat duty and stripper overhead temperature difference 128
Figure 3.24: Effect of total rich bypass split fraction on estimated vapor fraction in the total rich bypass; pink triangles represent total rich bypass at bubble point with suboptimal cold rich bypass 129
Figure 3.25: Temperatures around the CO_2 exchanger as a function of cold rich bypass split at NCCC 132
Figure 3.26: Model underpredicts net heat measured heat duty at NCCC with a 9% average error 134
Figure 3.27: Error comparison in steam heat rate between two mass transfer models for NGCC and coal campaigns 135
Figure 3.28: Comparing error in heat duty for NGCC and coal campaigns with two mass transfer models.....135
Figure 3.29: Validating stripper temperature profile in the NGCC campaign using the rate-based model, run 72, wetted area correction factor = 0.16, stage 1 is the top, stage 35 is the bottom; stages represent computational segments .137
Figure 3.30: Validating stripper temperature profile in the coal campaign using the rate-based model, run 52, wetted area correction factor = 0.16, stage 1 is the top, stage 35 is the bottom; stages represent computational segments .138
Figure 3.31: Model predicted heat duty and measured net heat duty versus time for NCCC 2023 campaign; blue points represent measured values; orange points represent model-predicted values.....139
Figure 3.32: Ratio of model-predicted to measured heat rate (blue) and CO_2 flowrate (orange) 140

Figure 3.33: Loading comparison from different methods used in the NGCC NCCC 2023 campaign 141
Figure 3.34: Validation of stripper temperature profile for a long-term pump-around intercooling case (Run 58); stages represent computational segments.....143
Figure 3.35: Model error across all pilot plant campaigns with PZAS as a function of liquid load in the stripper; measured heat duty corrected for heat loss 144
Figure 3.36: Model error across all pilot plant campaigns with PZAS as a function of flooding in the stripper; flooding estimated from the model; measured heat duty corrected for heat loss 146
Figure 3.37: Liquid load and flooding in the stripper are well correlated; smaller stripper column resulted in higher liquid loading, flooding and better model performance 147
Figure 3.38: Adjusted heat loss for perfect model reconciliation of heat duty for SRP and NCCC data 149
Figure 4.1: Base case design specification of PZAS (1 of 2 parallel trains)……...158
Figure 4.2: Packing area and heat duty comparison for 3 different sets of packing.....163
Figure 4.3: Trade-off of heat duty and packing height 165
Figure 4.4: Higher stripper temperature (and pressure) would reduce column diameter 168
Figure 4.5: Effect of heat exchanger NTU on steam heater duty 169
Figure 4.6: Effect of relative size of cold and hot cross exchanger on steam heater duty 171
Figure 4.7: Use of hot rich bypass with base case design of stripper for FEED 173

Figure 4.8: Reduction in stripper LMTD associated with higher total rich bypass temperature 174
Figure 4.9: Hot rich bypass produces more vapor in total rich bypass line than warm rich bypass 175
Figure 4.10: Equivalent work comparison between different stripper configurations 177
Figure 4.11: Effect of rich loading on energy performance at different ambient temperatures.....179
Figure 4.12: PZAS with hot rich bypass outperforms PZAS only at packing height less than 15 m.....181
Figure 4.13: Stripper LMTD comparison of PZAS and PZAS with hot rich bypass as a function of packing height 182
Figure 4.14: Optimizing heat duty for hot rich bypass results in high quality steam requirement 183
Figure 4.15: Optimizing equivalent work for hot rich bypass results in lower quality steam requirement.....184
Figure 4.16: Steam inlet temperature and rich solvent temperature exiting steam heater when heat duty is optimized using warm rich bypass for PZAS 185
Figure 4.17: Optimizing equivalent work for warm rich bypass with representative steam temperature 186
Figure 5.1: Final base case design of PZAS for FEED.....192
Figure 5.2: Extrapolated pump head from design curve for the lean pump 195
Figure 5.3: Extrapolated lean pump power from design curve.....195
Figure 5.4: Limits of rich pump for a 150 °C and 5.5 bar stripper; feasible cases are above the zero line; infeasible cases are below the zero line.....198

Figure 5.5: Compressor power as a function of CO_2 flow and ambient temperature.....199
Figure 5.6: Interaction between different models and their data in the working of the process surrogate model.....203
Figure 5.7: Convergence scheme to attain steady state using PZAS process surrogate model.....204
Figure 5.8: Process surrogate model reaches steady state in about 8 iterations 205
Figure 5.9: Effect if rich solvent temperature and cold rich bypass flow on lean solvent temperature.....211
Figure 5.10: Design specifications at base case conditions 213
Figure 5.11: Modified bypass extraction for PZAS to avoid flashing in solvent lines entering control valves.....214
Figure 5.12: Design specifications of scenario 1 with the modified bypass extraction...216
Figure 5.13: Design specifications of scenario 2 with the modified bypass extraction...218
Figure 5.14: Valve operation as a function of total rich bypass 219
Figure 6.1: Effect of removing different process constraints on profitability at 40 °F with 95% HRSG flue gas; vertical bars to the left of the constraint removed represent the respective change in maximum variable profit; figure is read right to left, going from the most constrained to the least constrained case 229
Figure 6.2: Variation of optimum specific heat duty with gas price as a function of lean loading and ambient temperature, where α_{lean} denotes the lean solvent CO_2 loading. 233
Figure 6.3: Relation between stripper flooding, ambient temperature, solvent rate, and CO_2 flowrate; gas price = $3-5/MMBtu 237

Figure 6.4: Relation between approach to maximum capacity of boiler equipment, ambient temperature, and boiler heat rate 239
Figure 6.5: Optimum variable profit for the different scenarios is driven by lean solvent rate, 150 °C stripper, CO_2 value: $80/tonne 240
Figure 6.6: Lean solvent rate drives optimum operation but is limited by compressor operation, 150 °C stripper, CO_2 value: $80/tonne, gas price = $3–5/MMBtu.....241
Figure 6.7: Optimum CO_2 flowrate for a single process train and removal indicate that high removal is important for optimization of operation, 150 °C stripper, CO_2 value: $80/tonne, gas price = $3–5/MMBtu 242
Figure 6.8: Optimum rich and lean loading for different scenarios; rich loading is maximized at high ambient temperature by using more air cooler bays for intercooling; optimum profit requires low lean loading at high ambient temperature, 150 °C stripper, CO_2 value: $80/tonne, gas price = $3–5/MMBtu.....244
Figure 6.9: Stripper operated at low heat duty even at high ambient temperature by manipulating lean loading and solvent rate, 150 °C stripper, CO_2 value: $80/tonne, gas price = $3–5/MMBtu; numbers inside the bars represent rich loading 245
Figure 6.10: Total electric power requirement was highest at low ambient temperature due to maximization of lean solvent rate and CO_2 flowrate, 150 °C stripper, CO_2 value: $80/tonne, gas price = $3–5/MMBtu, total air cooler bays for intercooling = 20, total air cooler bays for water wash = 18, design lean solvent rate = 450 kg/s 247

Figure 6.11: Profitable operation of PZAS at different ambient temperatures is possible while avoiding solvent precipitation 249
Figure 7.1: Fraction of the total direct field cost of the FEED likely to be affected by the direct contact condenser 255
Figure 7.2: Simplified absorber and advanced stripper with PZ and the direct contact condenser (DCC) for the FEED 258
Figure 7.3: Flowsheet of the base case design of PZAS (Rochelle et al. (2022) 260
Figure 7.4: Diffusivity of PZ at high temperature is overpredicted by the model; 15 ft of packing in direct contact condenser and 24 ft of packing in the stripper 265
Figure 7.5: Effect of correcting diffusivity model for PZ 266
Figure 7.6: Effect of different modeling methods on liquid temperature profile; stages represent computational segments in the stripper 269
Figure 7.7: Effect of different modeling methods on vapor temperature profile; stages represent computational segments in the stripper 270
Figure 7.8: Differences between equilibrium constant from speciation and rate-based kinetics between 40 and 150 °C; 0.2 to 0.4 loading 273
Figure 7.9: Design specifications of PZAS with double the solvent cross exchanger area 274
Figure 7.10: Design specifications of PZAS with the direct contact condenser with base case heat exchanger sizes 277
Figure 7.11: Sensitivity of heat duty to packing height in direct contact condenser; base case heat exchanger size 278

Figure 7.12: Temperature and flux profiles in the direct contact condenser; stage 1 is the top of the column; stage 35 is the bottom of the column; base case heat exchanger size; packed height = 12.3 ft; stages represent computational segments 279
Figure 7.13: Rich loading profile in direct contact condenser for a symmetric stripper; 12.3 ft of packing in direct contact condenser; base case heat exchanger size; theoretical stage represents computational segments 280
Figure 7.14: Rich loading in cold rich bypass leaving direct contact condenser as a function of packing height in the direct contact condenser; base case heat exchanger size 281
Figure 7.15: Gas cooling as a function of packed height in direct contact condenser; base case heat exchanger size 282
Figure 7.16: Downstream condenser duty as a function of packed height in direct contact condenser; base case heat exchanger size 283
Figure 7.17: Design specifications of PZAS with a direct contact condenser and double the solvent cross exchanger area 284
Figure 7.18: Sensitivity of heat duty to packing height in direct contact condenser; double the solvent cross exchanger area 285
Figure 7.19: Temperature and flux profiles in the direct contact condenser; stage 1 is the top of the column; stage 40 is the bottom of the column; double the solvent cross exchanger area; packed height = 12.3 ft; stages represent computational segments 286

Figure 7.20: Rich loading profile in direct contact condenser for a symmetric stripper; 12.3 ft of packing in direct contact condenser; double the solvent cross exchanger area; theoretical stage represents computational segment.....287
Figure 7.21: Rich loading in cold rich bypass leaving direct contact condenser as a function of packing height in the direct contact condenser; double the solvent cross exchanger area.....288
Figure 7.22: Gas cooling as a function of packed height in direct contact condenser; double the solvent cross exchanger area.....289
Figure 7.23: Downstream condenser duty as a function of packed height in direct contact condenser; double the solvent cross exchanger area.....290
Figure 7.24: Sensitivity of heat duty and condenser duty to total rich bypass split fraction; base case heat exchanger size.....291
Figure 7.25: Sensitivity of heat duty and condenser duty to total rich bypass split fraction; double the solvent cross exchanger area 292
Figure 7.26: Design specifications of PZAS with a low temperature and low pressure stripper 293
Figure 7.27: Comparison of mass flow and partial pressure ratio of CO_2 to water at two different pressure and temperature levels in stripper.....295
Figure 7.28: PZAS with a low pressure stripper and direct contact condenser; base case heat exchanger sizes.....297
Figure 7.29: Heat duty as a function of packing height in direct contact condenser; low pressure stripper and base case heat exchanger sizes 298

Figure 7.30: Temperature and flux profile in direct contact condenser for a symmetrical stripper; stage 1 is the top of the column; stage 35 is the bottom of the column; low pressure stripper with base case heat exchanger sizes; theoretical stages represent computational segments 299
Figure 7.31: Rich loading profile in the direct contact condenser for a symmetrical stripper; low pressure stripper with base case heat exchanger sizes; theoretical stages represent computational segments 300
Figure 7.32: Rich loading in the cold rich bypass leaving the direct contact condenser as a function of packing height in the direct contact condenser; low pressure stripper with base case heat exchanger sizes 301
Figure 7.33: Gas temperature and condenser duty as a function of packing height in direct contact condenser; low pressure stripper with base case heat exchanger sizes 302
Figure 7.34: Liquid temperature and loading profile in the direct contact condenser and stripper for PZAS with the base case design and direct contact condenser; packed height = 15 ft (optimum); theoretical stages represent computational segments.....303
Figure 7.35: Liquid temperature and loading profile in the direct contact condenser and stripper for PZAS with the base case design and double the number of solvent cross exchangers and direct contact condenser; packed height = 15 ft (optimum); theoretical stages represent computational segments...304

Figure 7.36: Liquid temperature and loading profile in the direct contact condenser and stripper for PZAS with the low pressure stripper and direct contact condenser; packed height = 10 ft (optimum); theoretical stages represent computational segments 304
Figure 7.37: Suboptimization of feed point of warm rich bypass for PZAS with the direct contact condenser in 3 design scenarios; black points represent optimal feed point for warm rich bypass 306
Figure 8.1: Mechanical and actual availability of flue gas from steam turbine generator (STG) for capture plant at Mustang Station.....314
Figure 8.2: Effect of packing height in direct contact condenser on DFC of condenser and KO drums 316
Figure 8.3: Effect of packing height in direct contact condenser on DFC natural gas boilers.....317
Figure 8.4: Effect of packing height in direct contact condenser on steam heaters 318
Figure 8.5: Effect of packing height in direct contact condenser on water wash air coolers 319
Figure 8.6: Comparison of direct field cost for stripper column between a high pressure and low pressure stripper 320
Figure 8.7: Optimum packing height for PZAS with the direct contact condenser…….323
Figure 8.8: Optimum packing height for PZAS with the direct contact condenser and double the number solvent cross exchangers 324
Figure 8.9: Optimum packing height of PZAS with the direct contact condenser and a low pressure stripper 325

Figure 8.10: Comparison of total cost of capture; cases with direct contact condenser have been optimized for packing height in the direct contact condenser; stripper packing height constant = 24.4 ft (for all cases 326

Chapter 1: Introduction

1.1 EMISSIONS FROM ELECTRICITY GENERATION

Over the past 15 years, the U.S. electricity generation mix has shifted away from coal and towards natural gas and renewables resulting in lower CO_2 emissions. Natural gas-based technologies for electricity generation are favorable due to the lower carbon and particulate content in natural gas, higher combined cycle efficiencies, lower price, and higher availability of natural gas compared to coal. In 2019, coal-fired generation produced 2257 lb CO_2/MWh of electricity compared to about 976 lb CO_2/MWh from natural gas-fired generation, less than half the value of coal. The gradual phasing-out of coal-fired power plants is shown by Figure 1.1. This is seen to be accompanied by a gradual increase in emissions from natural gas-based electricity generation facilities.

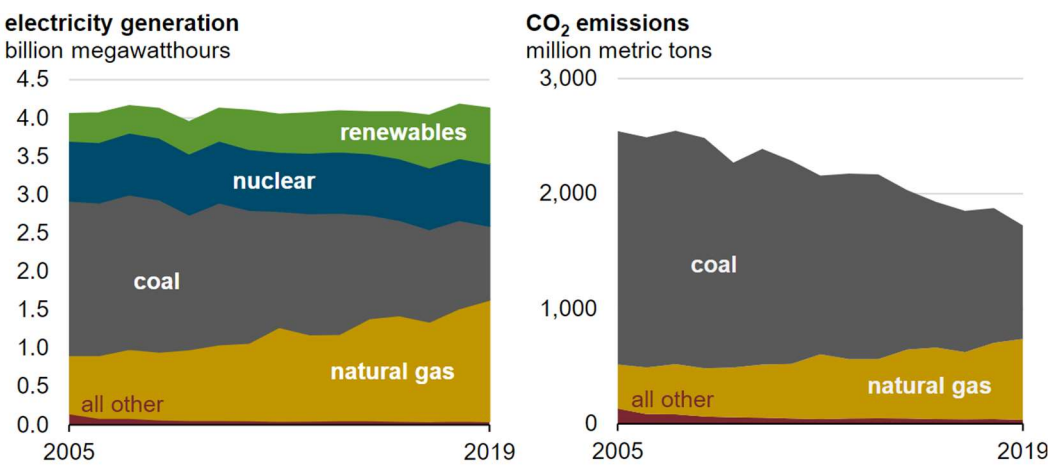

Figure 1.1: Electricity generation and CO_2 emissions by fuel source (2005-2019) (EIA, 2021)

The typical flue gas composition from a NG combined cycle power plant looks as follows: 4.1% CO_2 v/v, 8% H_2O v/v, 12% O_2 v/v, and 76% N_2 v/v at about 106 °C.

Compared to coal flue gas, the CO_2 content is much lower, the oxygen content, and flue gas temperature are much higher. Despite the low CO_2 content, the emissions from NGCC power plants are still significant and need to be abated.

1.2 CO_2 CAPTURE BY AMINE SCRUBBING

Amine scrubbing has been a long-studied, useful chemical process that has been demonstrated to be robust and reliable at both the pilot and commercial scale to capture CO_2 in flue gas with various compositions (Rochelle GT, 2009). The simplest process flowsheet for amine scrubbing is shown in Figure 1.2.

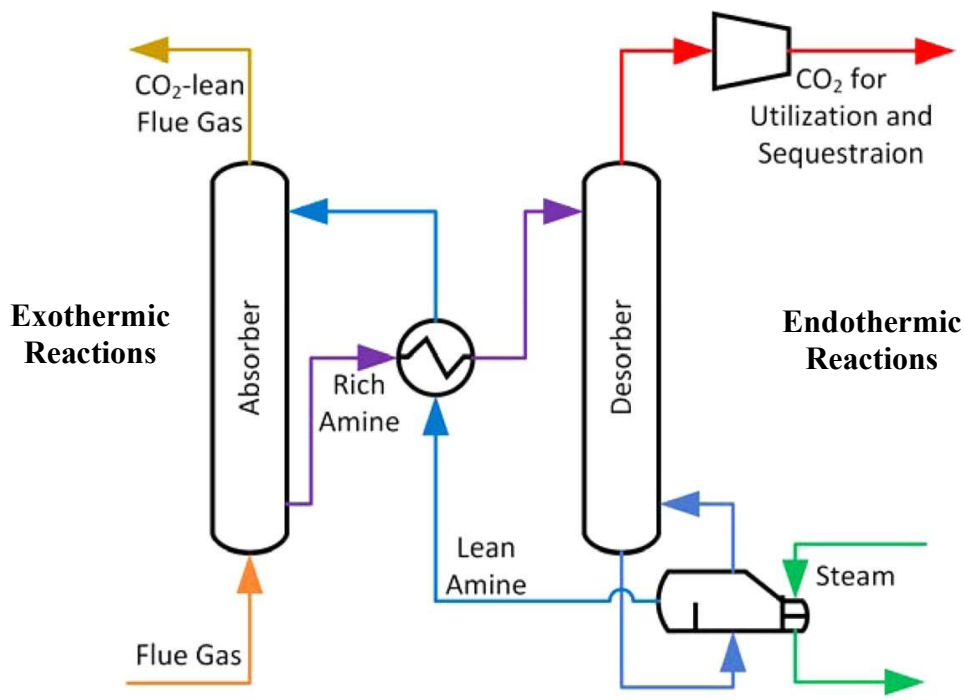

Figure 1.2: Flowsheet of a simple amine scrubbing process configuration for CO_2 capture

The process consists of an absorber column, a cross exchanger, and a stripper column. An amine such as monoethanolamine (MEA) or piperazine (PZ) is used to

counter-currently contact flue gas entering the bottom of the absorber in one or more sections of structured packing or other contactor types. Exothermic reactions occur in the absorber that results in the binding of CO_2 to the amine molecule, which also results in a rise in temperature through this column.

The solvent containing CO_2 (rich solvent) is pumped from the absorber to a cross exchanger which exchanges some sensible and latent heat with the lean solvent (CO_2 deprived) coming from the bottom of the stripper column. This preheats the rich solvent solution as it is sent to the top of the stripper column. The CO_2 is removed from the solvent in the stripper column using a stripping agent, typically medium to high pressure steam. The stripper reactions are endothermic, which require the input of heat through steam.

Ultimately the CO_2 and water vapor that leave the stripper are sent to a condenser where most of the water is removed, and the CO_2 is compressed in a compressor downstream to about 150 bar for commercial use such as EOR (Enhanced Oil Recovery) or for permanent geological storage.

While much of the previous work in amine scrubbing was focused on coal-fired flue gas, the attention needs to shift to natural gas conditions with changes in the electricity generation mix of the United States. The flue gas composition affects several design parameters such as packing height, heat exchanger size, column diameter, and temperature profiles in contactors, and must be studied in detail for NGCC flue gas both at the pilot and commercial scale.

1.3 ENERGY USE IN AMINE SCRUBBING

Amine scrubbing is an energy intensive process and typically relies on the steam cycle of the power plant for steam for stripping and electricity for pump and compressor

work. The extraction of steam from a power plant is said to reduce electricity output by 20-30%. A typical power plant with steam extraction is shown in Figure 1.3.

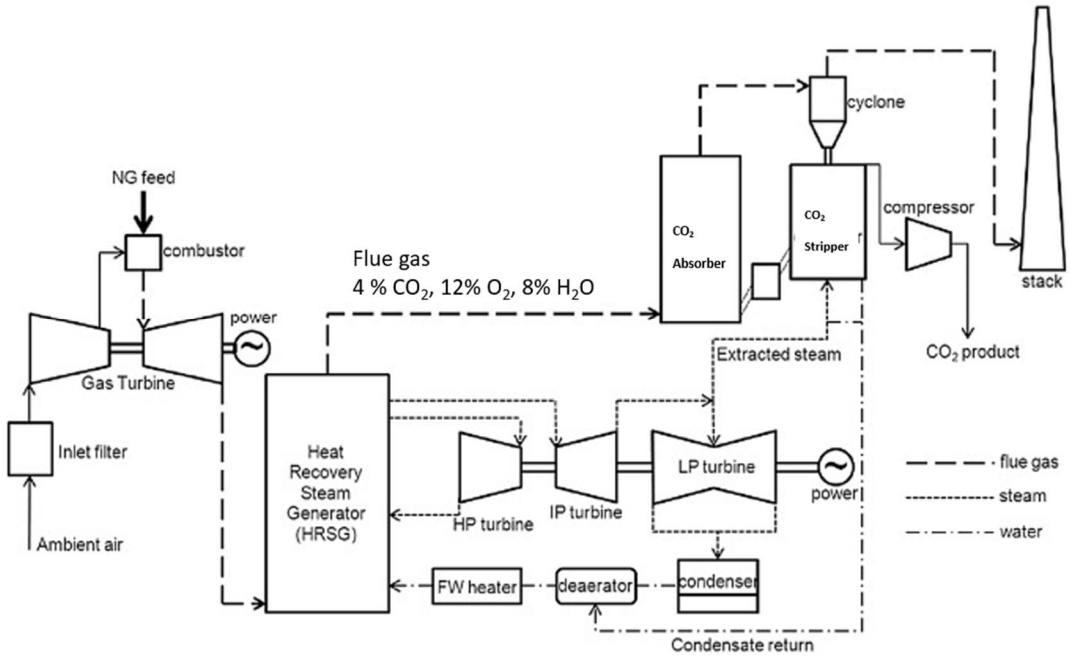

Figure 1.3: Schematic of a typical NGCC with a CCS unit retrofitted onto it

The steam use is heavily dependent on the temperature and pressure level of the stripper, solvent composition, capacity, and viscosity, heat exchanger performance, and absorber performance to name a few. The key elements that govern heat duty of stripping are sensible heat, latent heat of vaporization of water in the stripper, and heat of desorption of CO_2. The total heat of stripping is a sum of these three elements. By optimally tuning process parameters and optimal stripper design, the three elements to heat duty can be minimized, ultimately resulting in a lower overall heat duty for stripping, lower steam consumption, and lesser reduction in the electricity output of a power plant.

1.4 PRIOR WORK IN STRIPPERS FOR CO_2 CAPTURE

A summary of some prior work on strippers for CO_2 capture has been shown in Table 1.1 and is compared to this work.

Table 1.1: Comparison of past and current work in strippers for CO_2 capture

Author	Flue Gas / Solvent	Experiment	Modeling method	Economics
Oh et al. (2020)	Coal / MEA	None	Aspen Plus®, rate-based	Yes
Jiang et al. (2017)	Coal / Ammonia	None	Aspen Plus®, rate-based	Yes
Liu et al. (2020)	Coal / Ammonia	None	Aspen Plus®, rate-based	None
Frimpong et al. (2021)	14-16% CO_2 / APBS-CDRMax®	Pilot scale, 0.7 MWe	None	None
Zhao et al. (2017)	Coal /MDEA-PZ	None	Aspen Plus®, Equilibrium	None
Jiang et al. (2018)	Coal/PZ-NH_3	None	Aspen Plus®, rate-based	None
Nguyen et al. (2021)	Coal/Ammonia	None	Aspen Plus®, rate-based	Yes
Adu et al. (2020)	Coal and NGCC/MEA	Pilot scale	NA	Yes

Akula et al. (2021)	Coal and NGCC/MEA	None	IDAES	None
Bravo et al. (2021)	Coal/MEA	None	Aspen Plus®, Equilibrium	None
Jin et al. (2018)	Coal/MEA	None	Aspen Plus®, rate-based	None
Du et al. (2021)	Coal and NGCC/MEA	None	Aspen Plus®, rate-based	Yes
Putta et al. (2022)	NGCC/MEA	None	Aspen Plus®, rate-based	Yes
Fine et al. (2022)	Coal and NGCC/ICE-31	Pilot, 0.6 MWe	Pro-Treat®	None
Seo et al. (2020)	Prototypical plant/Ionic Liquid	None	Pseudo-Transient Modeling	Yes
Aburime et al. (2022)	NGCC/AMP	None	Aspen Plus®, rate-based	Yes
This work	**NGCC and Coal/5 m PZ**	**Pilot, 0.2-0.5 MW_e**	**Aspen Plus®, rate-based Off-design rating models Surrogate models**	**FEED Economics Variable Cost Optimization Model**

As seen from Table 1.1, much of the previous work was related to screening different solvents such as MEA and PZ-ammonia, and process configurations for strippers to minimize heat duty, but primarily for coal flue gas. While some of the research conducted economic evaluation of the process, they were based on textbook evaluation methods or evaluation using Aspen Economic Analyzer. Moreover, the operation and optimization of the amine scrubbing system retrofitted to a real power plant was not studied in detail.

The Texas Carbon Engineers (researchers at the Texas Carbon Management Program) have successfully modeled and demonstrated the application of 5 molal Piperazine (PZ), a second-generation solvent superior to the conventional alternative MEA, with many different process configurations and process conditions for coal flue gas. The best configuration has been found to be the Piperazine with the Advanced Stripper (Advanced Flash Stripper/PZAS) by Lin (2016).

This work will extend the application of PZ with an advanced stripper configuration (PZAS) for an NGCC power plant. This will be done through pilot plant tests at NGCC flue gas conditions, rate-based modeling for model validation, optimal process design and scale up to a 460 MW scale and optimizing operation of the plant subject to gas and power price, value for CO_2, and ambient temperature. The FEED (Front-End Engineering Design) for a 460 MW NGCC located in west Texas (GSEC Mustang Station) will be used as the case study in this research. The economic analysis will be based on equipment cost obtained directly from vendors rather than using a conventional textbook method.

1.4.1 Piperazine with the Advanced Stripper (Advanced Flash Stripper / PZAS™)

A high-level process flowsheet of the PZAS process is shown in Figure 1.4. This process reduces the process irreversibility compared to the simple stripper configuration through efficient heat integration and water condensation. The thermodynamic efficiency of this process is about 74% (Lin, 2016). This stripper configuration will be used to study the application of 5 molal PZ to NGCC power plants through pilot plant campaigns, and optimized stripper design for scale-up, optimal stripper operation, advanced stripper designs, and stripper economics for a 460 MW NGCC.

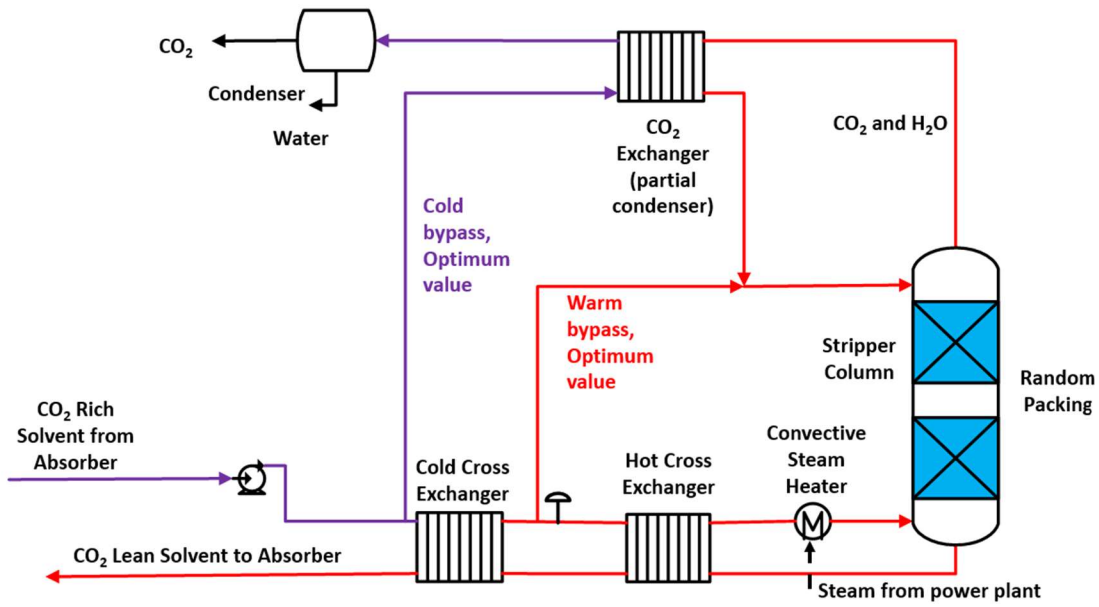

Figure 1.4: Flowsheet of Piperazine with the Advanced Stripper (PZAS)

The stripper section is only shown in Figure 1.4. The CO_2 rich solvent from the absorber is pumped to high pressure to accommodate for pressure drop in solvent lines and in heat exchangers. Two bypass streams are drawn, the cold rich bypass and the warm rich bypass. The bypasses serve to manipulate temperature pinch in the heat exchangers, temperature pinch in the stripper column, direct contact water condensation in the stripper

column, and to condense some of the water vapor leaving the stripper in the CO_2 exchanger. The cold and hot cross exchangers exchange sensible and some latent heat between the rich and the lean solvent that exits the stripper. The stripper is typically operated at high pressure and temperature (150 °C), at a lean loading of 0.2 mol/mol. The stripper contains one or more sections of random packing for mass transfer. The gas leaving the stripper is partially cooled by the condensation of water vapor in the CO_2 exchanger using the cold rich bypass. This also preheats the cold rich bypass to the bubble point temperature at the stripper pressure.

It is this combination of bypasses and their unique functions that allows the advanced stripper to perform far better compared to the simple stripper shown in Figure 1.2. The process irreversibility mainly comes from the uncondensed water vapor in the simple stripper, which is eliminated to a large extent in this design.

1.5 OBJECTIVES OF THIS RESEARCH

This research work will deal with the stripper configuration only. The absorber is out of scope. The solvent used will be 5 m PZ. The objectives of this research work are divided into sections given below:

The first two objectives are related to pilot plant activities. Rigorous testing of the PZAS process at the pilot scale at NGCC conditions is necessary to demonstrate operability over a wide range of process conditions. This involves design of experiments to measure heat loss and net energy requirement. Heat loss has been poorly understood at the pilot scale but have been shown to affect stripper performance in many ways and confound the measured value of energy requirement for stripping. These effects will be studied through

modeling and measurements at the plant, and heat duty will be appropriately measured after applying a correction for heat loss.

The pilot plant test plan is divided into parametric tests which are used to demonstrate the operation at different process conditions and long-term tests that demonstrate stability and process performance as a function of solvent degradation. Lab analysis data and pilot data are then reconciled with model-predicted data by minimizing the error between the different performance indicators that are considered. This is especially useful to identify errors in the model, explore opportunities to improve the model using adjustable parameters.

1. Pre-campaign Pilot Plant Activities
    a. Model the effect of heat loss on stripper heat duty and performance for PZ and MEA with different stripper configurations and flue gas composition
    b. Conduct pilot tests to measure heat loss of PZAS at different process conditions, flue gas compositions, and pilot plants at different ambient conditions
    c. Study mechanisms for convective heat loss through surface temperature measurements and thermal imaging at different process conditions, flue gas compositions, and pilot plants
2. In-campaign Pilot Plant Activities
    a. Measure heat duty of PZAS at different pilot plants, flue gas compositions, and process conditions by appropriately correcting for heat loss
    b. Compare different laboratory analysis methods to estimate piperazine and CO_2 content in solvent
    c. Validate a rate-based model in Aspen Plus® by comparing model predictions of heat duty and loading compared to measurements through a rigorous data

reconciliation method and identify flaws and opportunities for improvement in model

Objectives 3 and 4 deal with the scale-up and design of strippers for large scale NGCC from pilot plant data. The design of strippers includes multiple variables that dictate capital costs such as heat exchanger area, stripper packing type and height, and operating costs such as stripper pressure/temperature, steam availability and flowrate, cooling sources, ambient temperature, location of plant, gas and power price, and the value of CO_2. These factors not only affect the design choices but also the operation of strippers and the operating profit of the process.

Off-design performance of stripper will be estimated using rating models that will be built from the design models in Aspen Plus®. The rating models will be used to study process constraints and construct surrogate models that will be used to optimize process variables to maximize variable profit through the year.

3. Stripper Design and Scale-Up
    a. Propose a stripper design to minimize capital cost for locations with low gas and power price by considering tradeoffs between energy requirement and heat exchanger sizes, packing height and type, stripper diameter and stripper pressure, and seasonal variations in ambient temperature.
    b. Utilize alternate bypass extraction strategies that increase vapor fraction in stripper solvent feed to lower energy requirement. Identify the benefits of a flashing feed on stripper performance and process irreversibility by conducting an equivalent work (W_{eq}) analysis and comparing it to other existing stripper configurations at different heat exchanger sizes.

c. Understand and quantify the advantages and operational limitations of the flashing feed by comparing its performance to the regular PZAS at different stripper packing heights and ambient temperature.

4. Off-Design Performance and Optimization of Stripper

a. Expand existing design models in Aspen Plus® to off-design or rating models by incorporating real equipment performance obtained from vendors for pumps, compressor, heat exchangers, and boilers, and by incorporating variable pressure drop in heat exchangers and solvent lines, and elevation heads in the solvent lines as a function of solvent flow rate.

b. Identify operational bounds of stripper as a function of equipment performance, process variables, and practical issues such as solvent precipitation.

c. Use the rating models to identify and demonstrate strategies to minimize practical challenges such as flashing upstream of control valves and to estimate the performance of PZAS with low and high pressure/temperature stripper, different elevations and pressure drop in solvent lines and advanced stripper configurations.

d. Expand the applicability of the process model by obtaining data from the rating models for variables such as heat rate, heat duty, CO_2 flow etc. to create surrogate models within the bounds of the operational limits. Create an overall process surrogate model in MATLAB by combining absorber, stripper, air coolers, and compressor surrogate models to create a "process surrogate model" that provides faster convergence times compared to Aspen Plus® and ease of convergence and process optimization.

e. Overlay process surrogate model into an optimization framework in MATLAB. Optimize process variables by minimizing variable operating cost as a function of gas price, power price, CO_2 value, and ambient temperature for different flue gas loads using the steady state values from the process surrogate model.

f. Identify process equipment that limit maximization of variable profit and the dependence between heat duty and gas price (or source of flue gas – HRSG vs Boiler) for different lean loadings.

Objective 5 deals with cost effective stripper design strategies. A different method of water condensation in the stripper column using a direct contact condenser instead of a CO_2 exchanger will be studied for its impacts on process performance and economic viability for NGCC applications. This design is compared to other designs that double the number of solvent cross exchangers to reduce the heat duty. A technoeconomic analysis will be conducted to identify cost improvements between the direct contact condensation method and using a gas-liquid condensing exchanger for PZAS and compare the costs to other advanced designs considered.

5. Cost-Effective Stripper Design

a. Utilize existing absorber modeling methods to model a direct contact condenser atop the stripper at lower temperatures compared to the main stripper column. Compare and contrast different representations of kinetics, mass transfer and thermodynamics in the direct contact condenser and derive conclusions on mechanisms governing stripper operation.

b. Utilize the rating model to evaluate the performance of PZAS with double the number of solvent cross exchangers as the base case design.

c. Utilize the rating model to evaluate the performance of PZAS with a low pressure and low temperature stripper. Understand the process impacts of using a low pressure stripper with PZ.
d. Utilize the rating model to understand process impacts of using a direct contact condenser with PZAS. Study the impact of direct contact condenser at different packing heights on steam heater duty, condenser duty, gas cooling, and solvent preheating.
e. Utilize the rating model to understand process impacts of using a direct contact condenser with PZAS at low pressure and low temperature conditions in stripper. Study the impact of direct contact condenser at different packing heights on steam heater duty, condenser duty, gas cooling, and solvent preheating.
f. Use an economics scaling model to scale costs of different equipment impacted from their base case values to the newer designs and compare purchased equipment cost, operating cost, and total cost of capture for all design scenarios. Identify economically optimum packing height in direct contact condenser for all scenarios.

Chapter 2: Heat Loss in Amine Scrubbing Pilot Plants

2.1 INTRODUCTION

Pre-campaign pilot plant activities primarily deals with understanding the role of heat loss on energy performance of strippers for amine scrubbing at the pilot scale. This study combines process modeling in Aspen Plus®, pilot scale measurements of heat loss, and surface temperature measurements to understand heat loss mechanisms. The PZAS configuration is used as a case study, with some modeling applied to solvents like MEA and process configurations like the simple stripper to comparatively study the effect of heat loss between solvents and stripping systems.

An analysis of heat loss is necessary to interpret pilot plant heat duty. Heat loss could be 20-40% of the measured heat rate at pilot plants and its significance can depend on the solvent, stripper configuration, and location of heat loss. Many pilot demonstrations have evaluated the energy performance of strippers with different solvents and stripper configurations. For example, at the National Carbon Capture Center (NCCC), B&W demonstrated the RSAT™ process (Gayheart et al., 2012), Linde-BASF demonstrated post-combustion capture with the OASE® blue solvent (Krishnamurthy et al., 2017), and ION Engineering demonstrated the operation of the ION Advanced Solvent (Brown et al., 2017).

More testing was done by Hitachi Power Systems with the H3-1 solvent (Hitachi Power Systems, 2012), Chiyoda Corporation with the T-3 solvent (Chiyoda Corporation, 2014), and Cansolv, with the DC103 solvent (Cansolv, 2017). A common feature among these demonstrations was the concentration of CO_2 in the flue gas, 12%, pertaining to coal-fired power plant conditions. Moreover, only Carbon Clean Solutions (Patkar and Bumb, 2015) and Cansolv (Campbell, 2014) evaluated and reported the energy performance of

their respective solvents at NGCC conditions. Most of the above pilot demonstrations do not appear to correct the measured heat rate for heat loss except Hitachi and Chiyoda Corporation, but they do not delineate the method used to obtain the heat loss value.

Heat loss is important at the pilot scale for several reasons:

1. At NGCC conditions, for a given pilot plant, the effect of heat loss will be more pronounced compared to coal conditions due to the lower steam rate. Heat loss relative to steam heat rate was calculated to be 8-12% (Stec at al., 2016) and 6-16% (Knudsen et al., 2007) for 30 wt% MEA, and 10% for AMP-PZ (Artanto et al., 2012). Heat loss relative to heat rate is also expected to increase with decreasing plant capacity due to the larger exposed surface area of the plant relative to the gas rate processed.
2. There is lack of sufficient data for heat loss in amine scrubbing systems. Besides the work cited above, few authors have studied heat loss for amine scrubbing. Some authors have ignored heat loss in the stripper (Bui et al., 2016; Gao et al., 2017) due to large fluctuations in ambient temperature and non-insulated pipes. Others have assumed that heat loss is negligible in the stripper (Cousins et al., 2012). Some authors have investigated heat loss theoretically outside the context of CCS (Teymourtash et al., 2009; Merkin, 1994).
3. The effects of heat loss on heat rate with scale, ambient temperature, location of heat loss, flue gas CO_2 concentration are poorly understood. Heat loss can impact stripper performance by causing temperature pinches or CO_2 reabsorption in some cases. Incorrect heat loss estimation or the lack of heat loss estimation could result in incorrect field optimization of lean loading. For several solvents, optimization of heat duty or lean loading at pilot plants is done

by observing the sensitivity of heat duty to L/G (liquid-to-gas ratio) (Meuleman et al., 2010; Artanto et al., 2014; Mangalapally et al., 2011; Kwak et al., 2012).

4. Heat loss also impacts the interpretation of pilot plant data and data reconciliation. The ability process models to predict steam heater duty of a pilot plant is strongly related to the value of heat loss estimated at the pilot plant. Process models ignore heat loss and assume perfect mass and energy balance and therefore, heat duty estimated by process models must be compared to the "net" heat duty of a pilot plant (after correction for heat loss) versus a "gross" heat duty (before correction for heat loss). Previously, deviations between modeled and measured variables such as heat duty and stripper temperature profiles have been explained using heat loss but have not estimated heat loss at the pilot plant rigorously (Simon et al., 2011; Brúder et al., 2012; Li et al., 2016).
5. There is a lack of consensus on the methodology used to estimate heat loss.. Some authors have used a simple correction to heat loss (Seibert et al., 2011) that was built using water-based measurements, while others estimated heat loss using energy balance conducted with loaded amine with the help of process models (Lin, 2016). Lin showed that both these methods yielded very similar heat loss for the overall pilot plant (Lin, 2016). A study of controlling heat transfer mechanisms in heat loss could highlight the importance of the choice of fluid used to measure heat loss relative to ambient conditions. Most often, the average of the heat loss by water has been used to correct heat duty, and changes in ambient conditions or scale have been ignored in the estimation of heat loss for solvent-based test runs in the pilot plant.

Parts of this chapter have been published in the *International Journal of Greenhouse Gas Control* (Suresh Babu and Rochelle, 2022).

2.2 OBJECTIVES

The following are the objectives of the pilot scale heat loss tests.

1. Create a test plan to conduct heat loss measurements at the UT-SRP pilot plant and the NCCC pilot plant over a wide range of operating conditions and ambient temperature. Estimate a representative value of heat loss for each pilot plant and correct the measured heat rate for heat loss during solvent testing.
2. Conduct modeling studies to estimate the process effects of heat loss in different stripper configurations, solvents, and locations of heat loss.
3. Conduct surface temperature measurements at the UT-SRP and NCCC pilot plants at high temperature locations to compare driving forces for heat transfer in heat loss.
4. Conduct a qualitative analysis of heat loss at different pilot plants, ambient conditions, and steam flowrates.

2.3 PILOT PLANT OVERVIEW

This section introduces the Piperazine Advanced Stripper™ (PZAS) process at the National Carbon Capture Center and the UT-SRP pilot plant, and the simple stripper process at the National Carbon Capture Center (NCCC). The modeling studies that follow this section have been conducted using the PZAS process and the simple stripper process at NCCC as case studies, at representative operating conditions. The surface temperature measurements and heat loss measurements were conducted for the PZAS process only at both NCCC and UT-SRP pilot plants.

2.3.1 PZAS at PSTU, NCCC

The Pilot Solvent Test Unit (PSTU) is located in Birmingham, Alabama. The Piperazine Advanced Stripper™ (PZAS) is part of this integrated absorption-stripping system. This 0.5 MW pilot plant treats flue gas from a coal-fired power plant. Figure 2.1 shows the PZAS flowsheet with important heat loss locations. The process uses efficient heat-recovery using three cross exchangers. The cold and hot cross exchangers recover sensible heat from the hot lean stream and add sensible and latent heat to the rich solvent. The CO_2 exchanger is used to partially condense the water in the stripper overhead gas. The cold rich bypass and warm rich bypass are extracted at their optimal flow fractions, mixed, and sent to the top of the stripper to partially condense water vapor in the column. The total bypassed solvent is counter-currently contacted with vapor in a stripper containing 2 sections of random packing. The top section contains 2 m of RSR No. 0.5 packing, and the bottom section contains 2 m of RSR No. 0.7 packing. The internal diameter of the column is 0.25 m (10 in). High-pressure CO_2 is produced in the stripper which reduces the compression work.

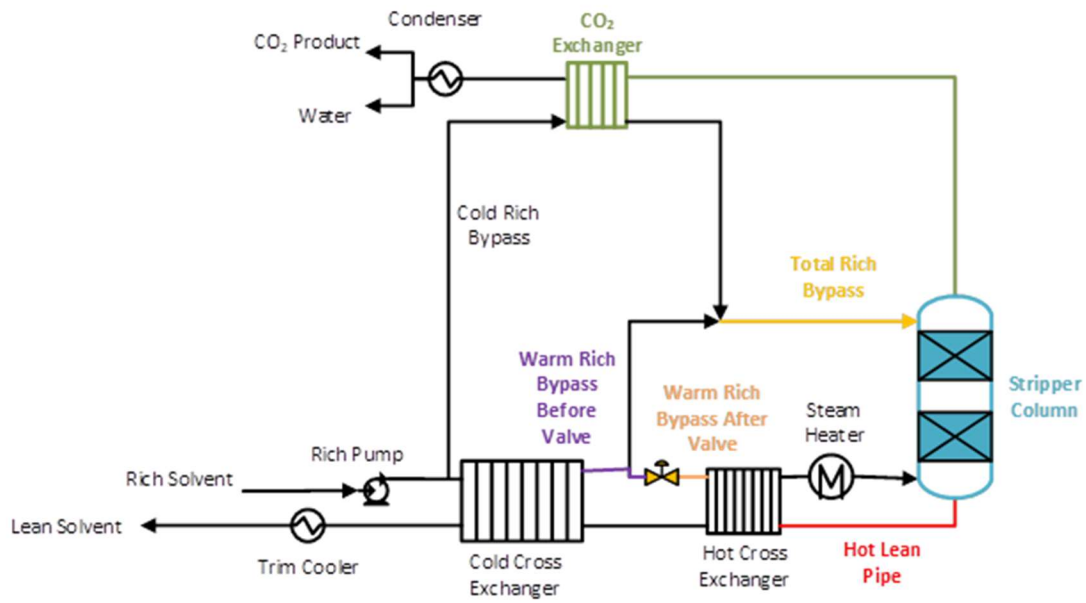

Figure 2.1: PZAS flowsheet with important heat loss locations

2.3.2 PZAS at UT-SRP Pilot Plant

The process configuration of PZAS at the UT-SRP pilot plant is very similar to that shown in Figure 2.1. The pilot plant captures CO_2 from simulated flue gas. The pilot plant is smaller in scale (0.2 MW) compared to NCCC. The stripper has an internal diameter of 0.83 ft (10 in) with 6.6 ft of RSR No. 0.3 coarse random packing in a single section. Figure 2.2 shows the PZAS process at the UT-SRP pilot plant with the heat loss measurement boundary.

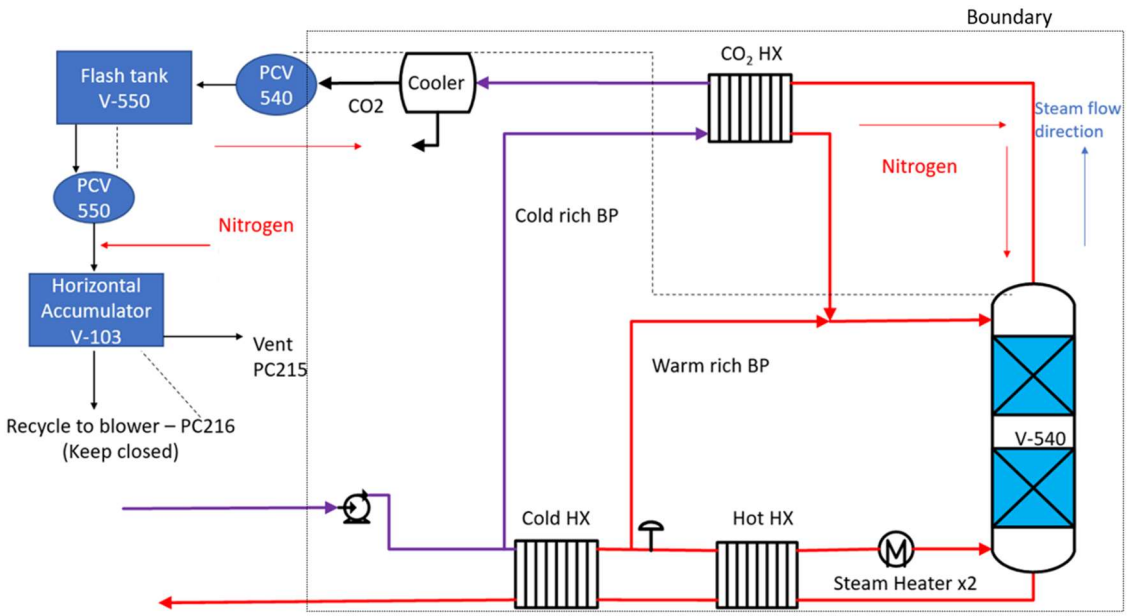

Figure 2.2: PZAS process at the UT-SRP pilot plant with the heat loss measurement boundary

2.3.3 Simple Stripper Process at PSTU, NCCC

The flowsheet of the simple stripper at NCCC is shown in Figure 2.3 along with important heat loss locations. The hot rich solvent from the cold cross exchanger is sent to a flash drum from which the vapor is directly mixed with the stripper overhead vapor. The hot liquid from the flash tank is sent to the top of the stripper. The simple stripper includes a thermosiphon reboiler and has a 0.42 m ID with 12 m of M252Y packing, making it much larger than the PZAS column. The lean solvent from the stripper is cooled in the cold cross exchanger and trim cooler and recycled back to the absorber.

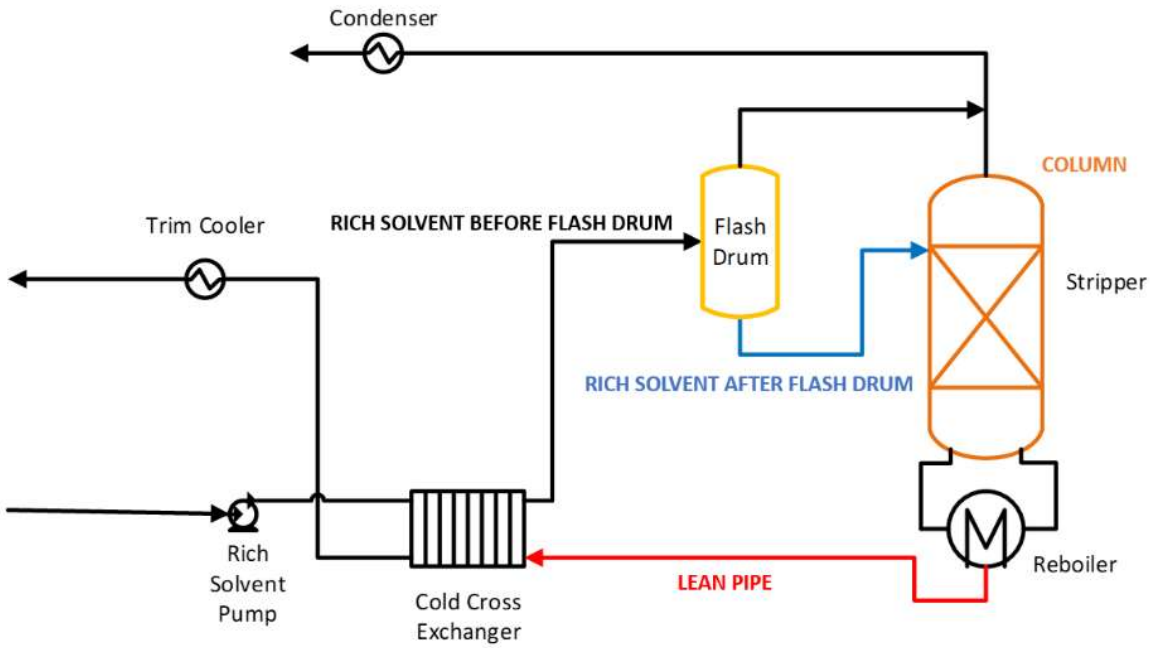

Figure 2.3: Flowsheet of the simple stripper process at NCCC

2.4 HEAT TRANSFER STUDIES FOR HEAT LOSS

Heat transfer studies for heat loss were done using surface temperature measurements at various locations at two pilot plants. The surface temperature data was used to quantify driving forces for heat loss on the solvent-side and on the ambient-side. A comparison of driving forces was done to identify controlling heat transfer mechanisms in heat loss, which indicates the importance of the choice of fluid used to measure heat loss in pilot plants.

2.4.1 Surface Temperature Measurements at Pilot Plant

Surface temperature measurements over 3 locations of heat loss were done using an infrared temperature gun. These locations included insulation, insertions (any sensors

that may heat up due to conduction), and bare metal. Appendix E.1 shows pictures of locations over which surface temperature measurements were made for UT-SRP.

Figure 2.4 shows a section of pipe with exposed metal, insertion, and insulation. The temperatures of exposed metal, insertions, and insulations were measured using an infrared temperature gun from Fischer Scientifc and an FLIR camera, and the temperature of the fluid in the pipe was measured using an online temperature sensor. With a known ambient temperature, using Equation 2.1, a temperature difference can be calculated for the fluid-side and for natural convection, and the ratio of these two represented the relative heat transfer resistance for heat loss. In the measurement of surface temperature, any local variations of temperature were ignored.

$$\frac{\Delta T \text{ natural convection}}{\Delta T \text{ fluid-side}} = \frac{\text{UA fluid-sid}}{\text{UA natural convection}} = \text{Relative Resistance} \tag{2.1}$$

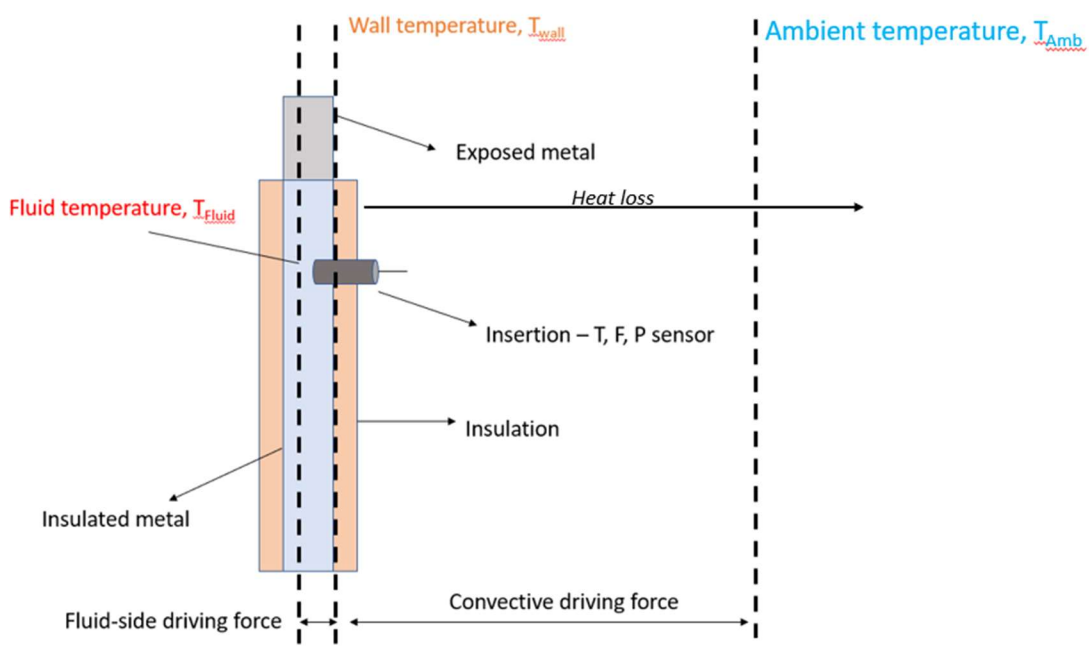

Figure 2.4: Schematic for surface temperature measurements at pilot plant

2.4.2 Heat Transfer Characteristics of Heat Loss at UT-SRP Pilot Plant (2021-22 campaign)

Figure 2.5 shows the measured temperature difference for natural convection in heat loss. The temperature difference represents the maximum value observed for each source and each run of heat loss test. The figure shows that heat loss by convection is most significant from exposed metal, with the highest temperature driving force, followed by heat loss from insertions, and insulation. Although some high values for temperature difference are also observed in insertions and insulations, these values may be skewed by the effect of solar radiation on localized heating of material at the pilot plant.

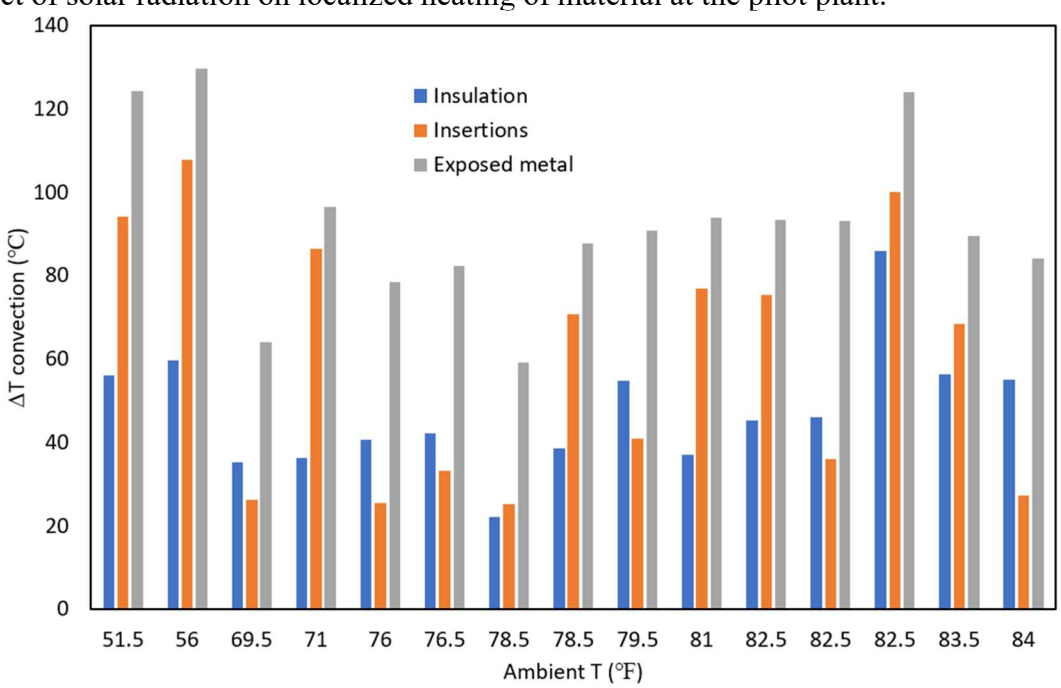

Figure 2.5: Maximum temperature driving force for heat loss through natural convection for 3 locations at variable ambient temperature

Figure 2.6 shows the ratio of the temperature driving force for natural convection to the temperature driving force on the fluid side. A ratio of at least 1 indicates that heat loss is 50% controlled by natural convection. For all four locations, the ratio is greater than

or equal to 1. For most runs, the ratio is greater than or equal to 3, indicating that the heat transfer mechanism for heat loss is at least 75% natural convection controlled. Two important conclusions can be derived from this analysis. First, heat loss is primarily a function of ambient conditions and exposed surface area, and fluid side-properties matter to a lesser extent. Second, water-based heat loss measurements can be used to reasonably represent the heat loss from amine scrubbing pilot plants. In this work, water will be used to measure and represent heat loss in a piperazine system.

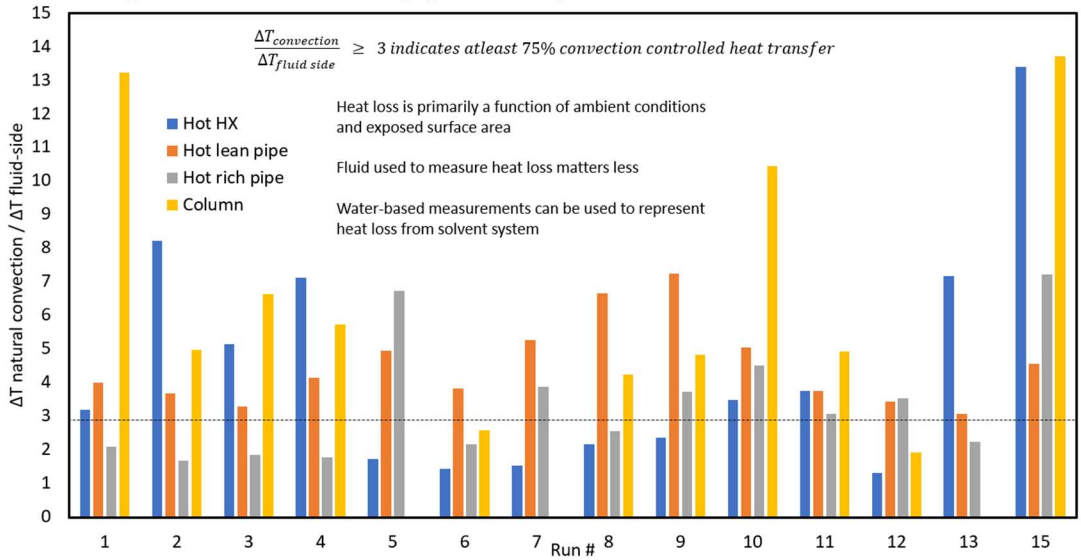

Figure 2.6: Heat transfer in heat loss is primarily controlled by natural convection for the UT-SRP pilot plant between 51 and 84 °F ambient temperature

2.4.3 Heat Transfer Characteristics of Heat Loss at NCCC (2023 campaign)

Surface temperature measurements were made using an FLIR Infrared Thermal Imaging Gun at several high temperature locations. The data from these measurements are shown in Figures 2.7 and 2.8. Appendix E.2 shows pictures of surface temperature measurements at NCCC.

Figures 2.7 and 2.8 show results from a representative group of measurements. Other measurement runs yielded very similar results and therefore are not shown here. Figure 2.7 compares the temperature driving force for convection from bare metal, insulation, and insertions at different locations. Heat loss from bare metal dominates in all locations, with the maximum temperature driving force. The driving force for heat loss from insulation and insertion was similar in almost all cases and was negligible compared to that from bare metal.

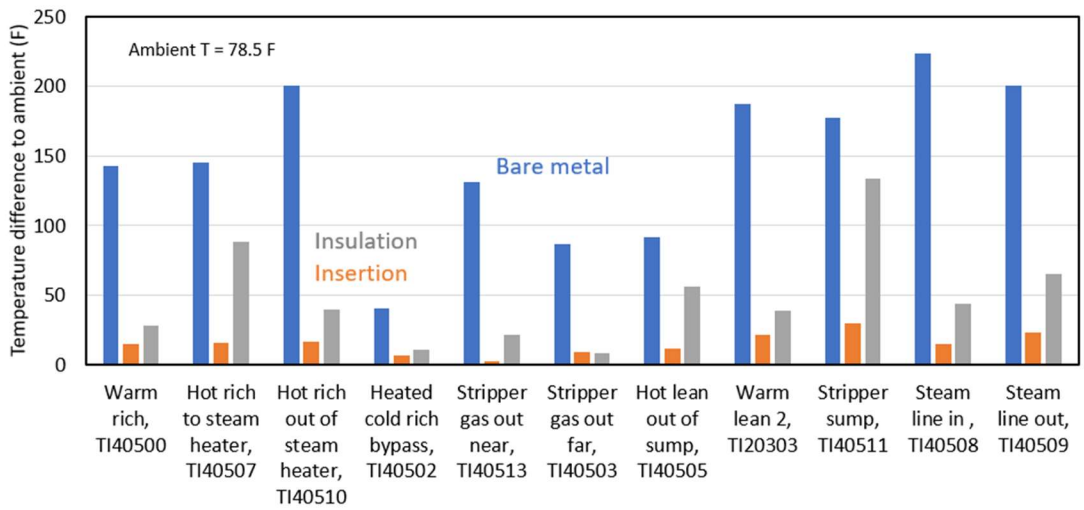

Figure 2.7: Temperature driving force to ambient for heat loss for Run 4

The surface temperature measurements were made close to process temperature measurements that recorded using temperature sensors. The proximity of the two measurements allows the analysis of heat loss to be made in the form of a ratio of temperature driving forces at different locations. An identical surface area for heat loss both on the fluid-side and ambient-side, and an equal heat-flux on both sides are important assumptions in this analysis.

Figure 2.8 shows the driving force ratio for the same locations shown in Figure 2.7. 7 out of 11 locations analyzed showed a ratio greater than 1, and almost all these locations had a ratio of almost at least 2 or above. This indicates that in these locations, heat loss is at least 60% controlled by natural convection. In some other locations, the ratio was closer or lower than 1. This was observed for these locations in all the surface temperature runs.

One explanation for the low ratio of ambient to fluid-side temperature driving force could be the lower measured surface temperature as shown by Figure 2.7 for these locations. For the measurements made on the stripper gas outlet, the N_2 used to pressurize the stripper could cool the metal surface locally leading to a lower measured temperature than usual.

The low surface temperature measurements for the hot lean pipe and the heated cold rich bypass pipe could be a result of local temperature variations during measurement. When the surface temperature was measured, the IR camera measured the temperature of a single point on the metal surface. A different point on the metal could have resulted in a different temperature recorded by the instrument. Other reasons for lower metal surface temperature measurement could be local cooling by wind or shade.

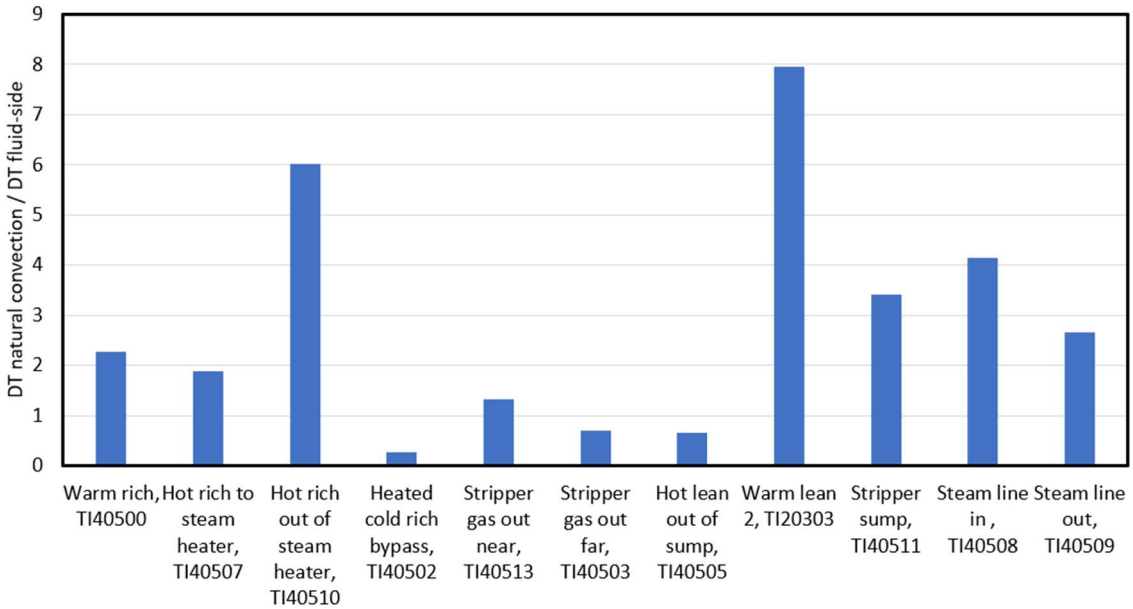

Figure 2.8: Ratio of ambient-side to fluid-side temperature driving force for heat loss for Run 4 across several locations

2.5 HEAT LOSS MODELING

This section uses the rate-based process model to analyze the significance of heat loss at different locations at the pilot plant with different solvents and process configurations. This section also forms the basis for the correction of measured heat rate at pilot plants for heat loss. This is important to interpret measured heat rate at pilot plants appropriately by accounting for the effect of heat loss.

2.5.1 Modeling Methodology

Heat loss in PZAS and the simple stripper was simulated by heater blocks with a negative heat duty and zero pressure drop at different locations. The modeling relied on Aspen Plus® predictions of process temperature in various parts of the system. Heat loss in the stripper was assigned using the built-in "heat loss" feature uniformly across the entire

column. All the heat loss was assumed to be in the liquid phase in contact with the walls of the column.

The locations of interest for the heat loss in PZAS are the hot lean pipe, warm rich pipe after the valve, warm rich pipe before the valve, stripper column, total rich bypass, and the CO_2 product line. In the simple stripper, the locations of interest are hot lean pipe, rich pipe before flash drum, flash drum, rich pipe after flash drum, and the stripper column. Heat loss in the flash drum is assigned using a pressure-heat duty (P-Q) flash, with negative duty and the pressure equaling the stripper pressure.

The above locations were chosen due to their high temperatures and the ability of heat loss at these locations to interact with column performance. Heat loss is more significant at higher process temperature due to larger temperature driving force for convective heat transfer. The specifications for heat loss modeling for different cases are shown in Table 2.1. The specifications were obtained from representative pilot plant data under coal and NGCC conditions with PZ and MEA.

Table 2.1: Process specifications of cases investigated for heat loss modeling

Specification	NGCC PZAS	NGCC Simple Stripper with 5 m PZ	Coal with PZAS	NGCC Simple Stripper with 7 m MEA (commercial scale)	NGCC Simple Stripper with 5 m PZ (compared to 7 m MEA)
Rich loading (mol CO_2/mol alkalinity)	0.41	0.41	0.40	0.43	0.41
Lean loading (mol CO_2/mol alkalinity)	0.23	0.23	0.24	0.1, 0.15, 0.17, 0.2, 0.23	0.24
Stripper temperature (°C)	151	150	152	120	150
Rich solvent rate (kg/s)	1.26	1.26	2.14	1341	1.26

Lean-side cold HX NTU	14	11	14	16	16
Lean-side hot HX NTU	4	-	3.6	-	-
Lean-side CO_2 HX NTU	0.8	-	0.8	-	-

The thermodynamics and rate behavior of PZAS were calculated using the Independence™ model (Frailie, 2014) developed in Aspen Plus® containing the CO_2 solubility, kinetics, specific heat capacity, and amine volatility regressed in the e-NRTL framework. The mass transfer model was developed by Wang (2015) and contains the interfacial area (a_e), liquid-phase mass-transfer coefficient (k_L), and gas-phase mass-transfer coefficient (k_G) for random packing. The loading and PZ concentration used by the model were calculated from density and viscosity correlations developed by Freeman (2011). A correction factor of 0.16 was used in the effective area model to bridge the deviation between modeled and measured diffusivity of the PZ at high temperature (Lin, 2016). Reactions are assumed to be at equilibrium in the stripper. The model uses measured conditions of the rich solvent including flow rate, temperature, pressure, loading, and PZ concentration. The bypass flow rates, stripper sump temperature, and pressure were specified to be the measured values at NCCC. The main model outputs are the heat rate, lean loading, and the stripper overhead CO_2 flow rate.

The 7 m MEA simple stripper was simulated using the "gold standard" MEA model (Chinen et al., 2016). The packing type, heat exchanger performance, and packing height were the same for both PZ and MEA and are outlined in Table 2.1.

2.5.2 Effect of Heat Loss in Different Locations in PZAS

Figure 2.9 shows the increase in heat duty per unit increase in heat loss (represented by the slopes) for different locations in PZAS. Heat duty is most sensitive to heat loss in the hot lean pipe and the warm rich pipe after the valve, shown by a 1:1 relation between additional heat duty and incremental heat loss. The heat duty is directly impacted by the heat loss at these locations by a decrease in the performance of the hot heat exchanger. In the warm rich pipe before the valve, stripper column, total rich bypass line, and CO_2 heat exchanger, the additional heat duty required to make-up for incremental heat loss is lower, making heat loss less important. The importance of heat loss is correlated with the process temperature of the location. A similar trend was also observed by Van Wagener (2011) in the modeling of the stripper at the SRP pilot plant.

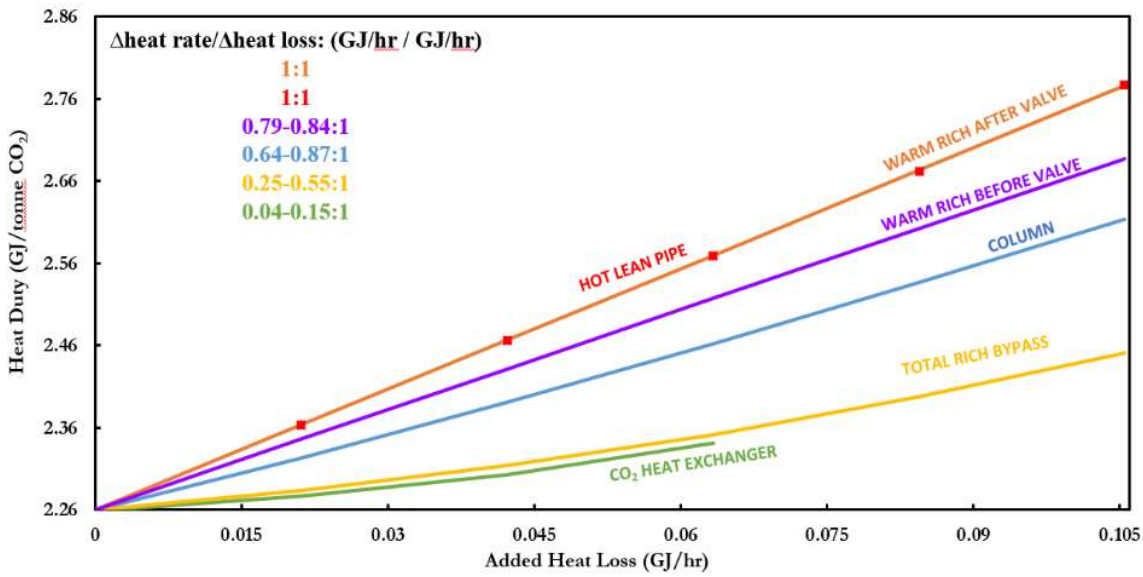

Figure 2.9: Sensitivity of heat duty to heat loss in different locations in PZAS

Figure 2.9 indicates that heat loss affects heat duty at locations other than the source itself. Correcting measured heat duty for heat loss on a 1:1 basis therefore assumes that heat loss only occurs at the source. This type of correction has been used previously by several authors (Lin, 2016; Stec et al., 2015; Van Wagener, 2011) and can lead to incorrect estimation of measured heat duty as it does not account for the process impacts of heat loss.

For PZAS at NCCC, the warm rich pipe before the valve dominates other locations in available surface area. Heat loss here can degrade stripper performance by lowering the total rich bypass temperature and reducing the flashing across the valve. For unit change in heat loss at this location, heat duty increases by only about 80% (79-84%) of the absolute heat loss value. Heat duty is therefore corrected for 80% of the heat loss value according to Equation 2.13.

2.5.3 Effect of Heat Loss on Stripper Performance in PZAS

Heat duty could be sensitive to heat loss in some parts of the regeneration system without affecting the stripper efficiency. In other parts, heat loss leads to a reduction in stripper efficiency by causing CO_2 to reabsorb. The sensitivity of the CO_2 flux in the PZAS column for a typical heat loss of 0.07 GJ/hr at different locations is shown in Figure 2.10. CO_2 flux remains unchanged for zero or 0.07 GJ/hr of heat loss in the lean hot pipe and warm rich pipe, indicating that stripper efficiency is unaffected. Heat loss in the stripper column and the total rich bypass changes the CO_2 flux compared to the case with no heat loss. The column approaches a top-side pinch with more stripping done at the bottom to maintain a constant CO_2 flow rate. Further sensitivity analysis revealed that reabsorption is likely to occur only for heat loss greater than 0.14 GJ/hr in the column. This is unlikely

in PZAS at NCCC as the measured heat loss for the entire system was found to be only 0.07 GJ/hr on average (discussed in upcoming sections).

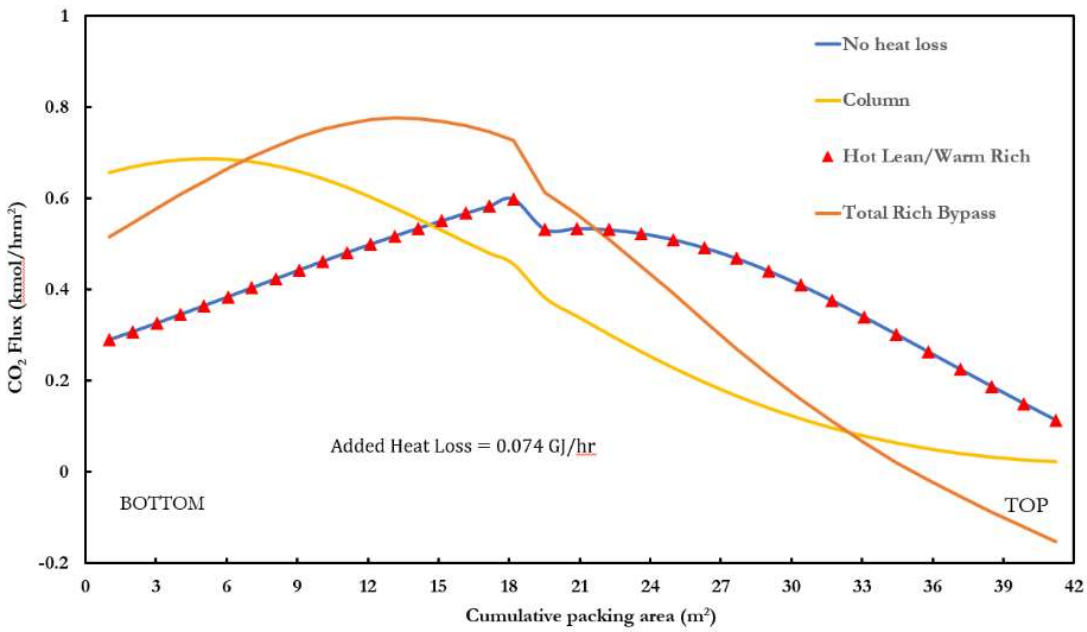

Figure 2.10: Sensitivity of CO_2 flux in the PZAS stripper to heat loss in different locations; negative flux indicates reabsorption of CO_2

2.5.4 Effect of Heat Loss in Different Locations of Simple Stripper with 5 m PZ

Figure 2.11 shows the sensitivity of heat duty to heat loss in the simple stripper with 5 m PZ. Unlike PZAS, the column is the most important location for heat loss in the simple stripper. This could be because of multiple reasons. The solvent entering the column is hotter in the simple stripper compared to PZAS making heat loss more significant in the column. Secondly, the overdesigned nature of the simple stripper gives a large top-side pinch in the column. This makes heat duty very sensitive to heat loss in the column, which causes CO_2 to reabsorb at the top. Top-side temperature pinches in the stripper were observed by authors with 2.5 m packing and proprietary solvents

(Mangalapally et al., 2012) and 4 m packing with MAPA activated with DMMEA (Brúder et al., 2012). In these columns, any additional heat added by the reboiler to mitigate reabsorption must travel from the reboiler to the top of the column, making it more susceptible to heat loss. For these types of strippers, it may be justified to correct heat duty for heat loss on a 1:1 basis.

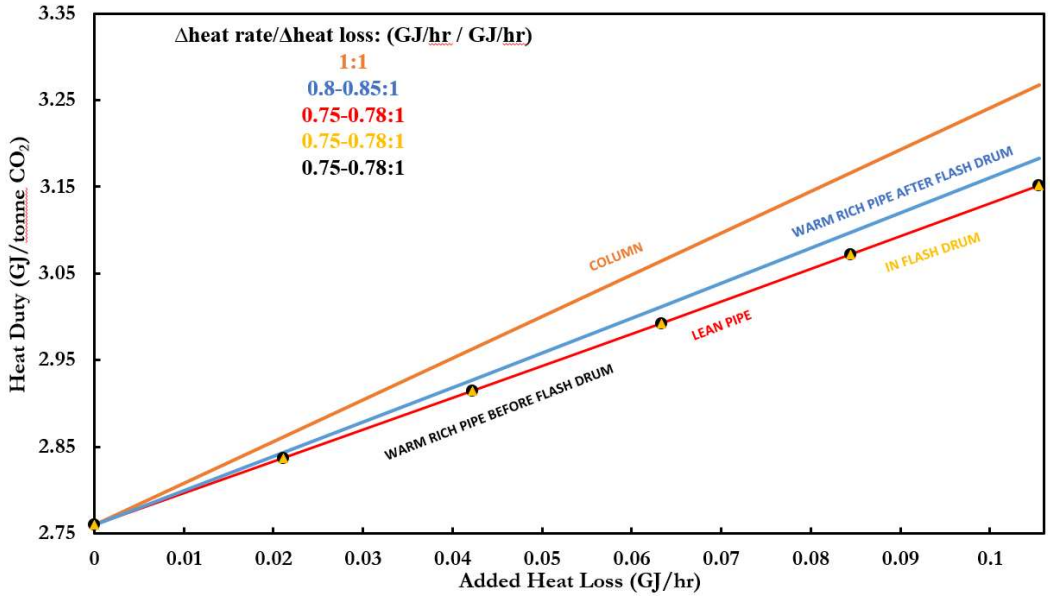

Figure 2.11: Sensitivity of heat duty to heat loss in different locations of the simple stripper with 5 m PZ

2.5.5 Effect of Heat Loss on Simple Stripper Performance

Figure 2.12 also shows that the effect of heat loss is more pronounced at the location of pinch compared to other locations for the simple stripper. Sensitivity analysis revealed that reabsorption occurs in the PZ-simple stripper even with a low heat loss of 0.03 GJ/hr in the column. This threshold is low compared to PZAS, where reabsorption occurs only for heat loss greater than 0.14 GJ/hr. This is due to the large packing height (40 ft) in the

PZ-simple stripper compared to PZAS (13 ft). Designing pilot strippers with excessive packing therefore needs to be avoided to mitigate the effects of heat loss.

Overdesigned columns with pinches have been observed in pilot plant tests of the simple stripper. Oh et al. (2020), Bui et al. (2016), and Cousins et al. (2012) have shown a bottom side pinch in the stripper with MEA with packing height ranging from 4-10 m. In these columns, heat loss might be less significant compared to PZ-simple stripper due to the bottom side pinch offered by lower lean loading and L/G.

PZ operates at higher lean loading (~0.23 mol/mol) due to possible precipitation issues at low lean loading (Freeman et al., 2010). In MEA strippers with low lean loading and L/G, the additional heat supplied by the reboiler to mitigate reabsorption does not travel all the way to the top of the column. Low lean loading solvents may therefore be affected less by heat loss and heat loss may require lesser attention in these strippers. This hypothesis is explored in Section 1.5.6.

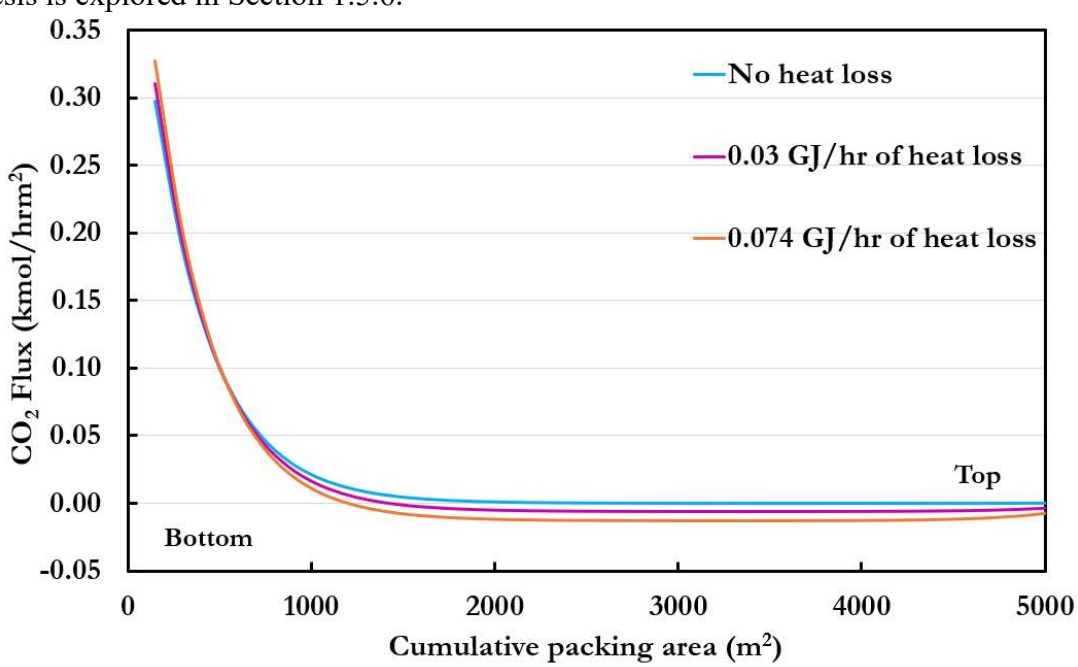

Figure 2.12: Reabsorption in simple stripper with 5 m PZ occurs at low heat loss value; heat loss was added to the column

2.5.6 Effect of Lean Loading on Heat Loss: 5 m PZ vs 7 m MEA

Figure 2.13 compares the increase in heat duty for given heat loss in the column for the simple stripper with 5 m PZ and 7 m MEA at variable lean loading. Figure 2.13 shows that the importance of heat loss increases with greater absolute value of heat loss and lean loading.

At typical lean loading between 0.1-0.2 mol/mol for 7 m MEA, the increase in heat duty due to heat loss in the column ranged between 1-13%. The heat loss range used for MEA was 0.14-0.47 GJ/tonne, higher than the gross heat loss values reported in literature for MEA, representing conservative evaluations of the effect of heat loss (Stec at al., 2015; Knudsen et al., 2007). For 5 m PZ, this increase was 120-150% at its typical heat loss value and lean loading of 0.23 mol/mol. The heat loss used for the simple stripper (0.7-1.8 GJ/tonne) was scaled-up from the heat loss of PZAS (0.38 GJ/tonne) based on the surface area of the stripper which is 2-5 times larger.

At low lean loadings, the MEA stripper increasingly approached a bottom-side pinch that made heat duty less sensitive to heat loss due to the reasons discussed in Section 5.2. The PZ stripper on the other hand had a large top-side pinch in the column at lean loading of 0.23 mol/mol. This analysis can also explain the much higher heat duty (4.2 – 5.5 GJ/tonne) observed in the test of 5 m PZ with the simple stripper at NCCC, compared to 3.5 GJ/tonne for 7 m MEA (Moser et al., 2011), despite PZ being the superior solvent.

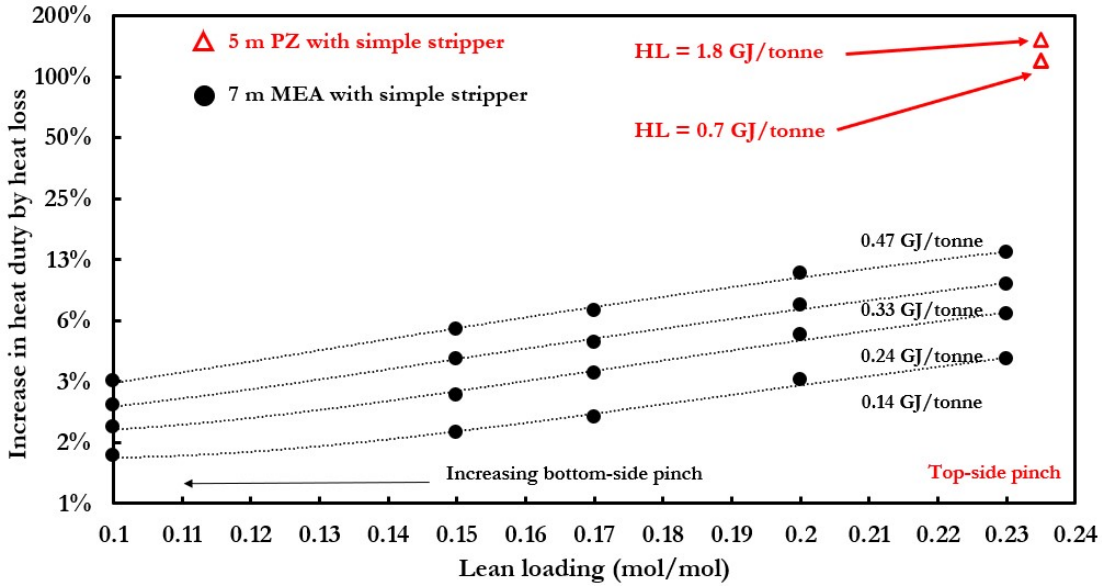

Figure 2.13: Effect of heat loss is less pronounced in 7 m MEA compared to 5 m PZ with the simple stripper

2.5.7 Implications of Heat Loss in Coal vs NGCC CO_2 Capture Using PZAS

Heat loss affects the pilot plant heat duty at NGCC conditions (4.3% CO_2) more than at coal conditions (12% CO_2). The same heat loss (0.07 GJ/hr) at the hot lean pipe increased heat duty for the NGCC case by 12.3% and by 9.6% for the coal case. The NGCC case is affected more due to its lower heat rate and CO_2 production compared to the coal case. Heat loss in pilot scale NGCC strippers therefore requires more attention.

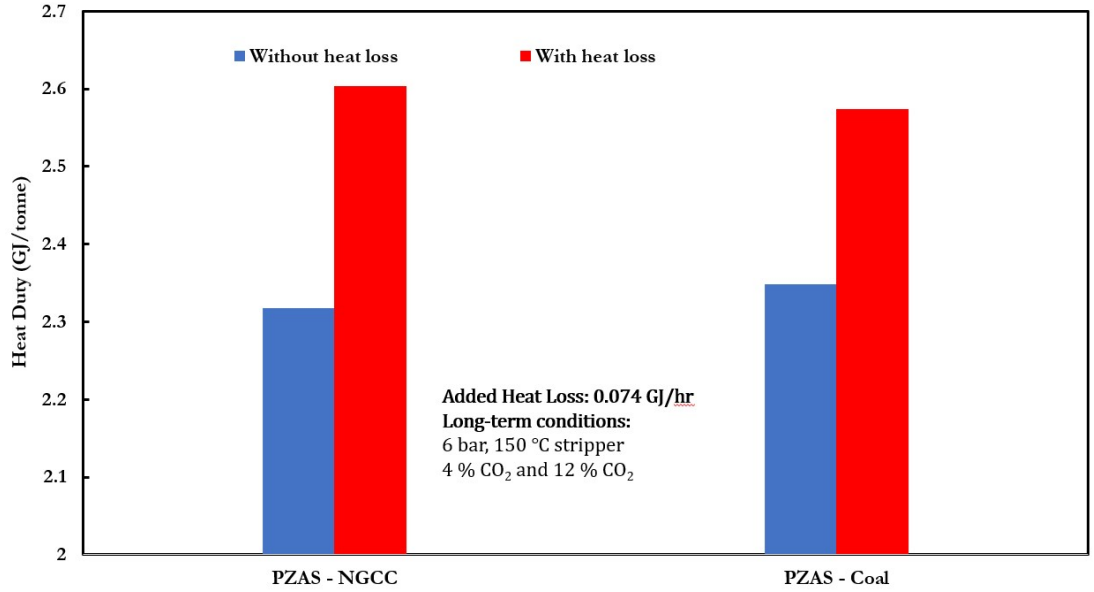

Figure 2.14: Effect of heat loss on heat duty with PZAS applied for NGCC and coal flue gas conditions

2.6 STEAM FLOW MEASUREMENT

This section gives the details of steam flow measurement at pilot plants. The accuracy of the measured steam flowrate was important in the measurement of heat loss at the pilot plants.

2.6.1 Steam Flowrate Correction for Temperature and Pressure in the Coal 2018 and NGCC 2019 Campaigns

Intermediate pressure steam flowrate at NCCC was measured using a vortex flowmeter in the 2018 campaign at coal conditions and 2019 campaign at NGCC conditions. The flowmeter converted the velocity of steam to a mass flowrate using a constant area term and a calibration density. While the factory setting of the density of the device was 0.23 lb/ft^3, the steam density which changes with temperature and pressure was not accounted for. The steam flow measurement was corrected by incorporating the

density of the steam at the pressure and temperature of the steam as shown by Equation 2.2.

$$F_{corrected} = \frac{F_{measured}\,\rho_{steam}}{0.23} \tag{2.2}$$

Steam condensate from the steam trap was directed to a tote where the cumulative weight gain was measured in one-hour intervals. A total of 22 condensate tests were done in the coal and NGCC campaigns, and this condensate measurement was found to deviate from the vortex flow measurement by 12% on average. Figure 2.15 shows the schematic for condensate tests done in the 2018 coal and 2019 NGCC campaigns.

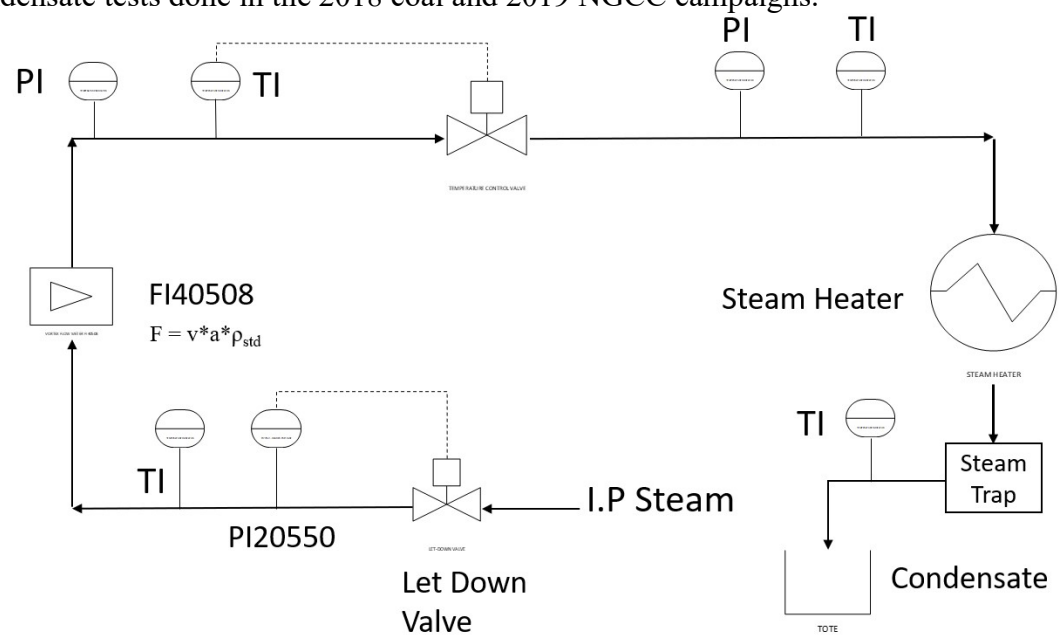

Figure 2.15: Steam flow arrangement with condensate measurement at NCCC

Equation 2.2 could be generalized as shown in Equation 2.3.

$$F_{corrected} = \frac{F_{measured}\,\rho_{steam}}{\rho_{standard}} \tag{2.3}$$

Two approaches to calculating the standard pressure of the device were considered. The first approach corrects the steam flow using the factory setting of the standard density,

as shown in Figure 2.15. The second approach was to use the condensate measurements as the correct flowrate ($F_{corrected}$) and back-calculate a standard density for the device based on the density of the steam at its temperature and pressure. This calculated standard density was however found to depend linearly on the measure steam flowrate as shown in Figure 2.16. At low steam flow rate, the calculated value of the standard density converged with the factory setting of 0.23 lb/ft^3. Due to a significant deviation in standard density of the flowmeter from the factory setting value, the measurement was corrected simply using the factory setting value per Equation 2.2.

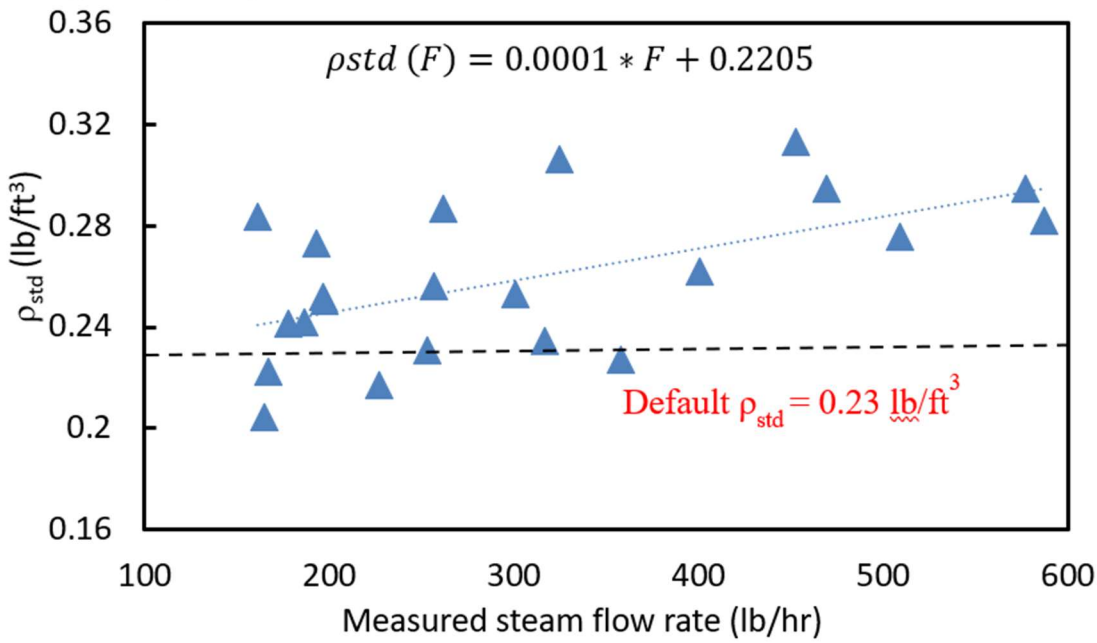

Figure 2.16: Back-calculated value of standard density of the flowmeter deviated significantly from the factory-setting value at high steam flow

2.6.2 Steam Flowmeter Calibration in the NGCC 2023 Campaign at NCCC

The former vortex flowmeter used to measure steam flowrate at NCCC was replaced by a V-Cone flowmeter in the 2023 campaign that corrected the flowrate of the

steam for its temperature and pressure. To accurately estimate the steam flowrate in this campaign, 10 condensate tote measurements were conducted wherein the condensate was allowed to accumulate in a tote and the change in mass of tote was measured over 1 to 2-hour intervals. The measured steam flowrate varied between 157 and 670 lb/hr during these tests. Additionally, this campaign also measured the condensate flowrate using a V-Cone flowmeter. Figure 2.17 compares the condensate and steam flowmeter measurement with the tote measurement. Steam flowrate appeared to be consistently lower than the condensate measurement by about 15% and the condensate flowrate appeared to be higher than the tote measurement by about 10%.

The deviation in steam flowrate may be a result of steam conditions deviating from their saturation conditions. This could result in the production of some liquid water in the steam line. The condensate measurement was confounded by the fluctuations in sensor data over the time intervals considered. The large fluctuations in condensate measurement were a result of sudden releases in condensate from the steam trap that was upstream of the condensate measurement. Ultimately, the steam flowrate measurement was used for heat loss measurements and solvent runs with a constant adjustment factor of 1.15 applied to match the condensate measurements.

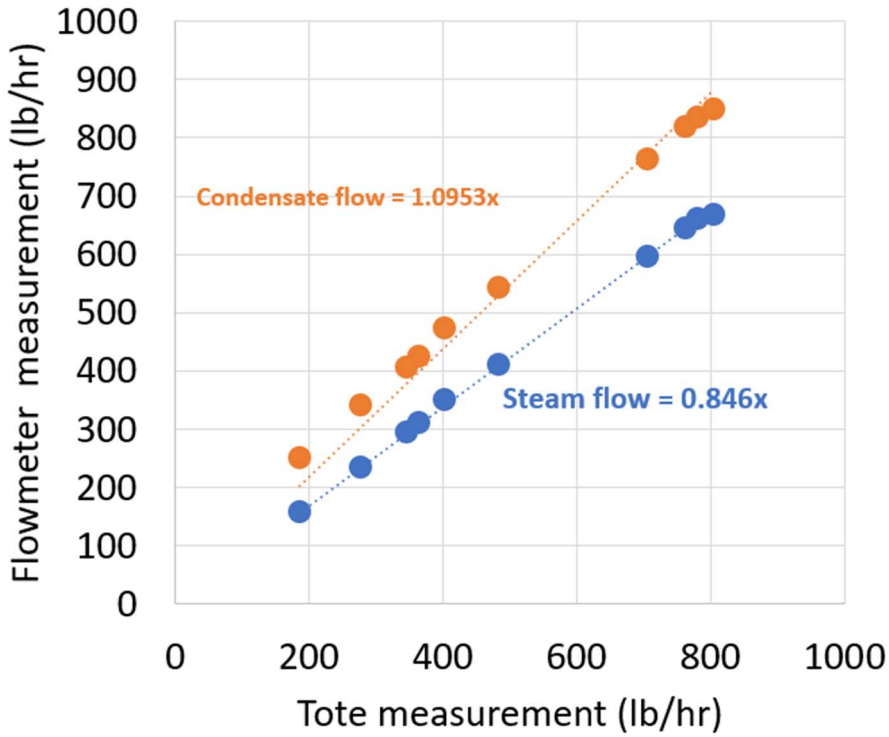

Figure 2.17: Steam flowrate and condensate flowrate measurements compared to the tote measurements

2.7 HEAT LOSS MEASUREMENT

This section details the procedure used to measure heat loss at pilot plants using water recirculation tests and studies the variation of measured heat loss with pilot plant operating conditions and ambient conditions.

2.7.1 NCCC Coal 2018 and NGCC 2019 Campaigns

Heat loss at NCCC was measured by conducting energy balances across PZAS using 27 steady-state water recirculation tests. The boundary for energy balance included the 3 cross exchangers, steam heater, stripper column, and condenser. Water was chosen as the test solvent as its physical properties are known with precision. Previous work also

showed that the product of overall heat transfer coefficient and heat transfer area (U*A) for heat loss calculated using water and PZ are similar (Lin, 2016). Water testing has also been used at other pilot facilities for heat loss measurements (Owrang and Svendsen, 2010). Since heat loss only depended on the external surface area of equipment, and is controlled by natural convection, the measured value based on water can be used to represent the value based on loaded piperazine. The average heat loss was calculated from the final 11 runs where the cold rich bypass flow was 0.06 kg/s, the warm rich bypass flow was 0.13 kg/s, and the stripper sump temperature was between 150 and 160 °C.

Equations 2.4 to 2.13 were used in the calculation of heat loss. Enthalpies were calculated using measured steady-state temperatures from the pilot plant. The reference temperature was fixed at 21 °C. The heat of vaporization of steam was calculated using the inlet pressure of steam.

$$Q_{rich} = L_{rich}\, C_{p,water}(T_{rich} - T_{ref}) \tag{2.4}$$

$$Q_{steam} = \left(F_{corrected}\, \Delta H_{vap}\right) + F_{corrected}\, C_{p,water}\, (T_{steam\ in} - T_{cond}) \tag{2.5}$$

$$Q_{in} = Q_{steam} + Q_{rich} \tag{2.6}$$

$$Q_{CW} = L_{CW}\, C_{p,water}\, (T_{CW\ out} - T_{CW\ in}) \tag{2.7}$$

$$Q_{lean} = L_{lean}\, C_{p,water}\, (T_{lean} - T_{ref}) \tag{2.8}$$

$$Q_{condensate} = L_{condensate}\, C_{p,water}\, (T_{condensate} - T_{ref}) \tag{2.9}$$

$$L_{condensate} = L_{rich} - L_{lean} \tag{2.10}$$

$$Q_{loss} = Q_{in} - (Q_{CW} + Q_{lean} + Q_{condensate}) \tag{2.11}$$

$$\text{Net heat duty} = Q_{net} = Q_{steam} - \frac{\Delta Q}{\Delta Q_{loss}} * \Delta Q_{loss} \tag{2.12}$$

$$Q_{net} = Q_{steam} - 0.8\, \frac{\sum Q_{loss}}{N} \tag{2.13}$$

The average measured heat loss was 0.078 GJ/hr (0.38 ± 0.1 GJ/tonne CO_2) and represented about 30% of the heat supplied by steam, Q_{steam}. The higher relative heat loss for PZAS compared to measurements for MEA (Stec et al., 2015; Knudsen et al., 2007)

and AMP-PZ (Stec et al., 2016) may be due to the higher operating temperature of PZAS, different ambient conditions, and/or differing equipment configurations and insulation.

2.7.2 UT-SRP NGCC Campaign 2021-22

Heat loss at the UT-SRP pilot plant was estimated by conducting an energy balance around the boundary highlighted in Figure 2.18. Heat loss was also estimated in the heat exchangers and piping using a similar energy balance method. Mass balance closure was ensured by adjusting the average lean water flow, assuming that the average rich water flow and average condensate water flow were accurate over the measurement interval. Equations 2.14, 2.15, and 2.16 were used to calculate heat loss for the entire system, heat exchangers, and piping.

$$\text{Heat loss, overall} = Q_{\text{water in,}} + Q_{\text{steam}} + Q_{\text{CW,in}} - Q_{\text{waater out,}} - Q_{\text{CW,out}} \quad (2.14)$$

$$\text{Heat loss, heat exchanger} = \sum_{i=1}^{n} m_{i,in}\, C_{p,i}\left(T_{in,i} - T_{amb}\right) - \sum_{i=1}^{n} m_{i,out}\, C_{p,i}\left(T_{out,i} - T_{amb}\right) \quad (2.15)$$

$$\text{Heat loss, pipe section} = m_{\text{water flow}} * C_{p,\text{water}} * (T_{in} - T_{out}) \quad (2.16)$$

Overall, 16 water tests were conducted to measure heat loss at varying steam flowrates. The steam flowrate ranged from 14-100 lb/hr compared to the high steam flowrates tested at NCCC. This led to colder stripper temperatures than usual due to subcooled water in the sump. Heat loss was measured at low stripper temperature in this campaign. The water flowrate leaving the absorber was controlled approximately at 5 gpm. No correction was applied to the steam flowrate measurement in this pilot plant campaign,

and the raw steam flowrate measurement was averaged for the time intervals considered. The stripper was started up using N_2 pressurization and the stripper pressure ranged from 14-45 psig. The cold and warm rich bypass flowrates were varied between 0 and 5% and 0 and 45%, respectively.

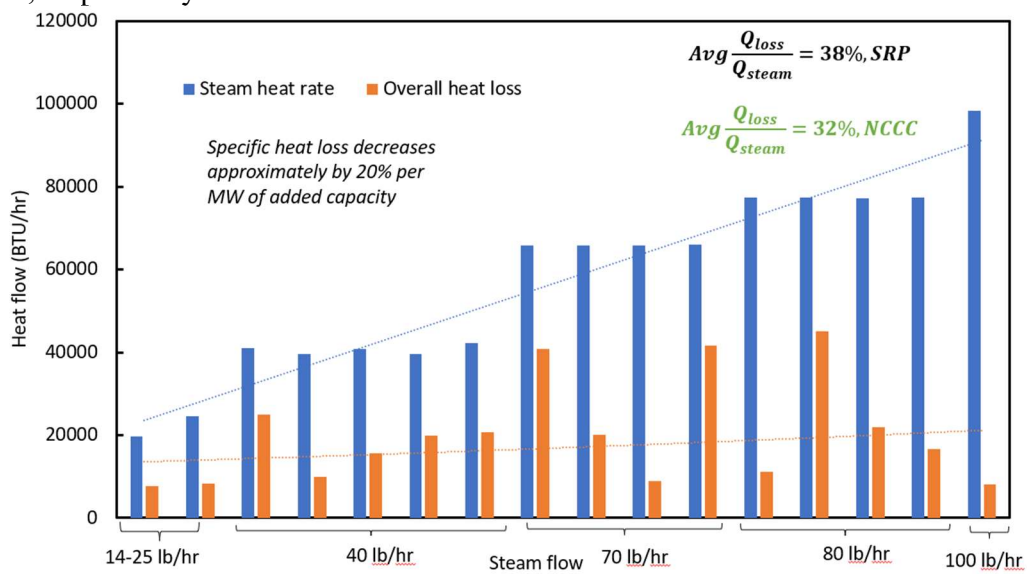

Figure 2.18: Measured heat loss showed no dependence on steam rate

Measured heat loss was found to be 20100 ± 12400 BTU/hr at the pilot plant. Figure 2.18 groups the measured heat rate and heat loss by steam flow rate. This figure indicates that heat loss has no significant relation to the steam heat rate and is constant irrespective of the steam flow rate. The relative heat loss (heat loss/heat rate) when compared between NCCC and SRP, increases by about 6% for the SRP pilot plant due to its smaller scale. This represents an approximate 20% decrease in relative heat loss per MW of added capacity at the pilot scale.

Heat loss in the hot rich pipe, hot heat exchanger, hot lean pipe, and cold exchanger are represented as a fraction the sum of the total heat loss in the equipment in Figure 2.19. Heat loss in the hot rich pipe and hot exchanger together constitute between 50 and 80%

of the total heat loss from equipment. This indicates that heat loss for this pilot plant can be corrected on a 1:1 basis, based on the correction method proposed by Suresh Babu and Rochelle for the NCCC pilot plant (2022).

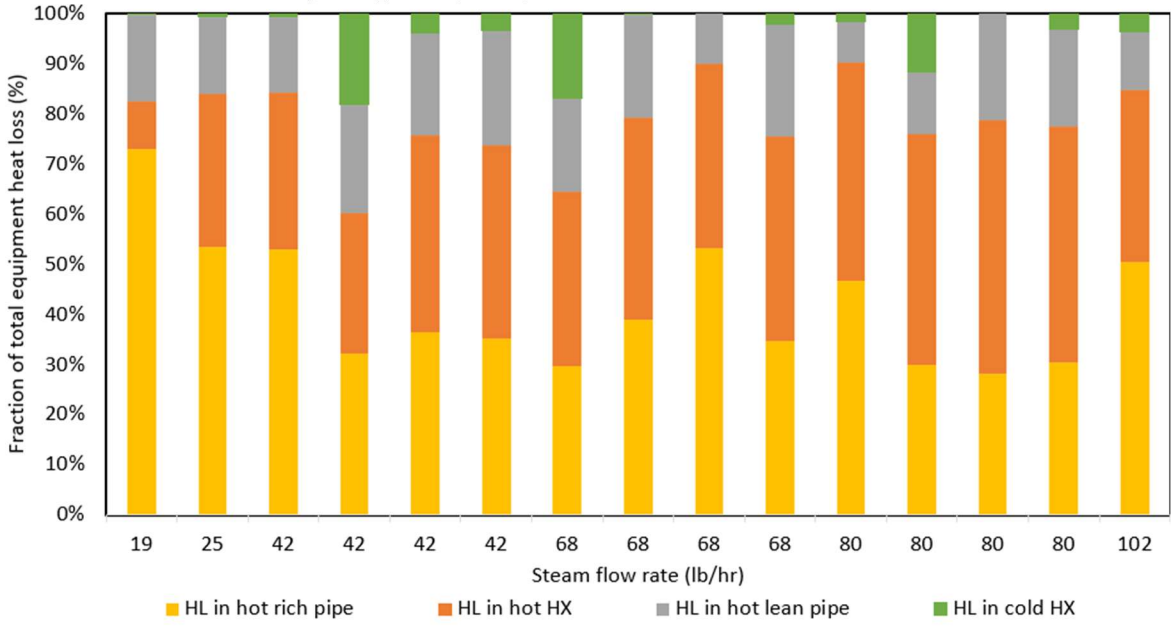

Figure 2.19: Heat loss in equipment in PZAS as fraction of total heat loss

2.7.3 NCCC NGCC Campaign 2023

In the NGCC campaign at NCCC in 2023, heat loss was measured using 5 steady state water recirculation runs. The ambient temperature ranged between 66 and 79 °F. The water flowrate leaving the absorber was between 10000 and 12000 lb/hr. Steam flowrate ranged between 231 and 412 lb/hr. The energy balance boundary used for heat loss calculations was the same as shown in Figure 2.2. The stripper sump temperature ranged between 291 and 314 °F. The cold and warm rich bypasses were changed through the heat loss measurements between 0 and 11% and 29 and 40%, respectively. Measurement of stripper overhead water vapor flowrate was challenging in these tests given that the steam

flowrates were lower than typical flowrates during regular operation under NGCC conditions at NCCC. Moreover, starting the stripper up with N_2 required a higher steam flowrate to produce vapor through the stripper with a measurable flowrate.

Stripper overhead water vapor flowrate was measured by observing the change in the level of the S-602 tank where all the water vapor condensed ultimately. It was observed that in 3 out of the 5 runs, the level in the tank did not change, indicating no condensation or accumulation of water. A zero overhead condensate flow was used for these runs. In the remaining 2 runs that used higher steam flowrate, there was a measurable change in the water level in tank S-602. The level indicator LI20211 was used to measure the water level in this tank, and the total height measured by L120211 was 99.4 in. Figure 2.20 shows the calculated level in the tank for runs 4 and 5 with time.

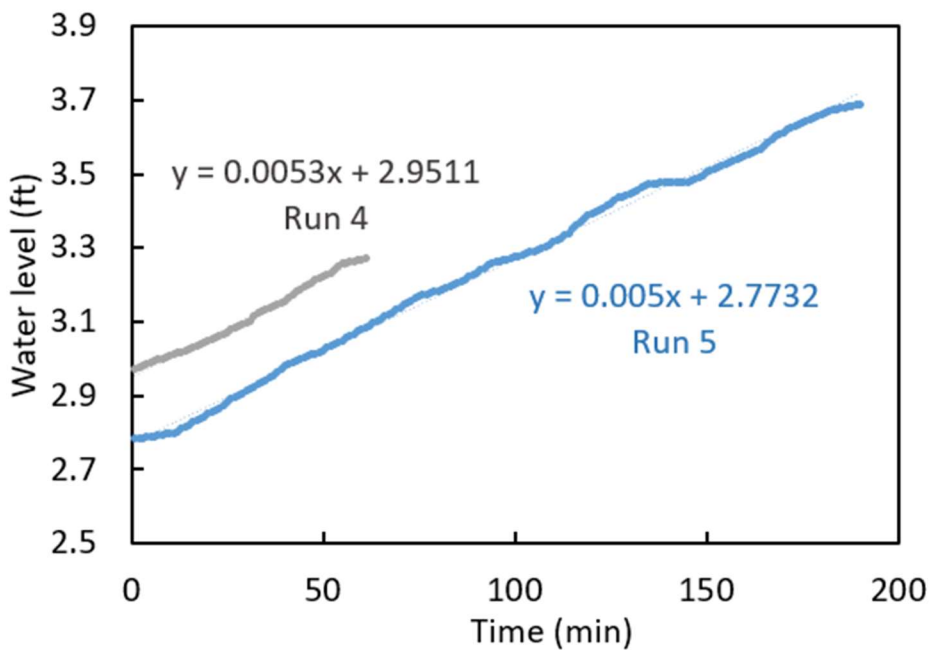

Figure 2.20: Change in water level in tank S-602 for heat loss runs 4 and 5

A linear fit through the data revealed the slope which can be interpreted as the change in tank level every minute. Using this value for each run, density of water, and the cross-sectional area of the tank, a mass flowrate of water was estimated in lb/hr. Using this value, the mass balance in the heat loss boundary closed with an average difference of about 0.5%. Figure 2.21 compares the total mass flow in with the total mass flow out of the boundary. The mass flow out was the sum of the lean water flow rate and the condensed water flowrate measured in S-602 by level change.

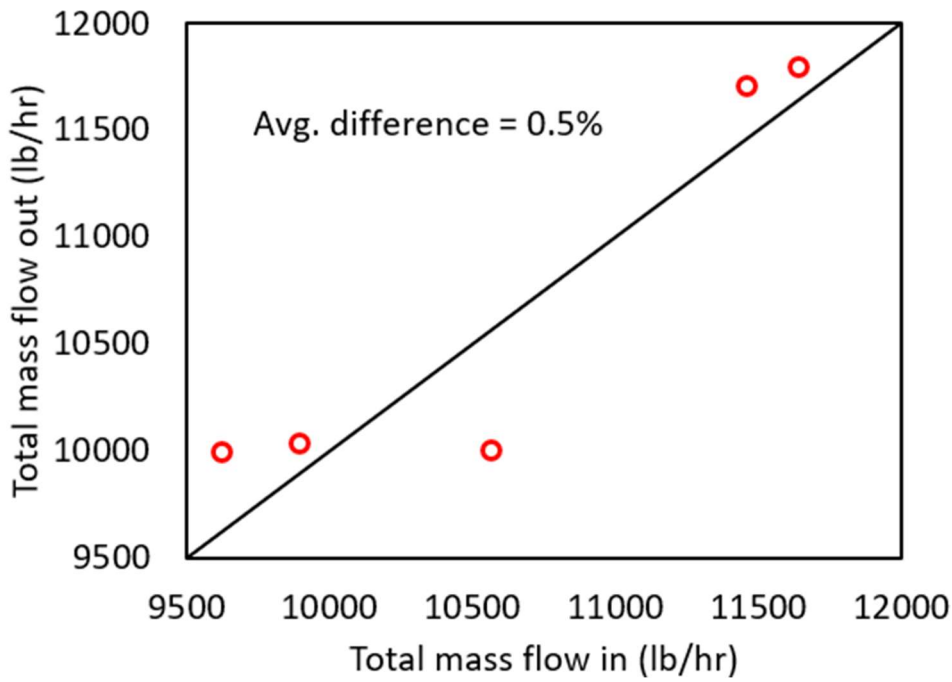

Figure 2.21: Mass balance closed within 0.5% for heat loss runs

The amount of steam used influences the stripper temperature measurements. At low steam rate, the sump temperature is more sensitive than the column temperatures due to sub-saturation of water in the sump of the column. The rest of the stripper is cold in this case. Heat loss may therefore only occur from the lower part of the stripper and the solvent

heat exchangers. This heat loss may however be negligible due to a cold sump temperature and low steam rate.

At higher steam rates, the water vapor rises through the column, increasing the upper column temperature measurements as well, but the sump temperature will remain relatively constant at the boiling point of water, at the stripper pressure. In this case, the exposed surface area for heat loss increases. At high enough steam rates, the entire stripper will attain equilibrium at the boiling point of water at its pressure. Heat loss in this case will increase due to an overall temperature increase of the stripping system. This effect of steam flowrate on sump and stripper overhead gas temperature for NCCC is shown in Figure 2.22. A similar plot is also shown for the UT-SRP pilot plant in Figure 2.23.

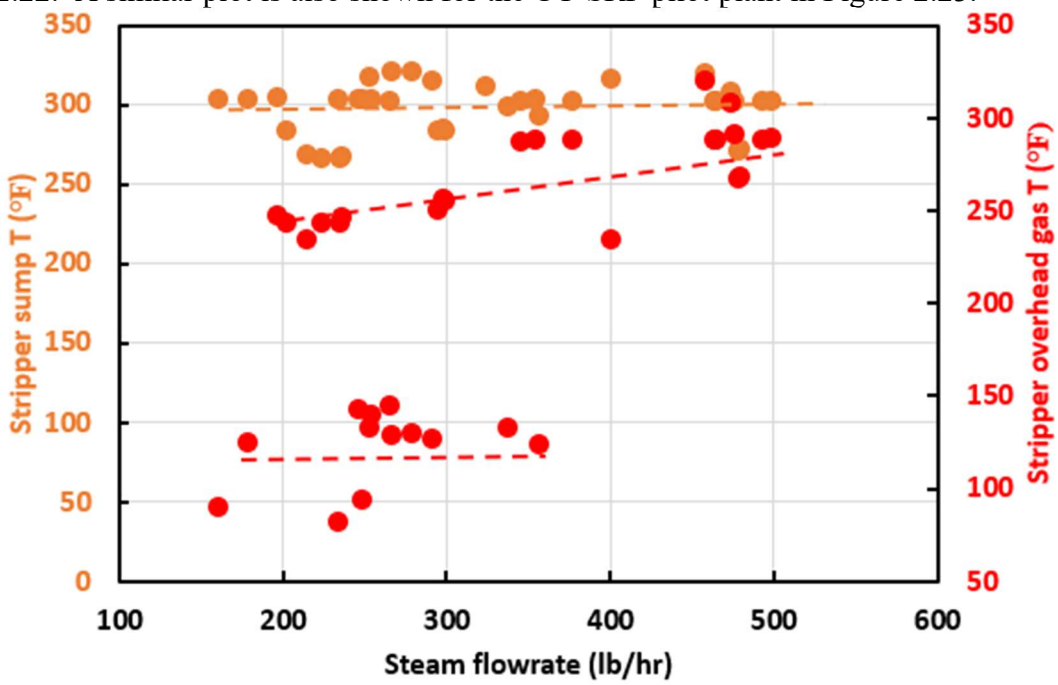

Figure 2.22: Stripper sump and overhead gas temperature as a function of steam flow rate for water testing at NCCC across all campaigns between 2018 and 2023

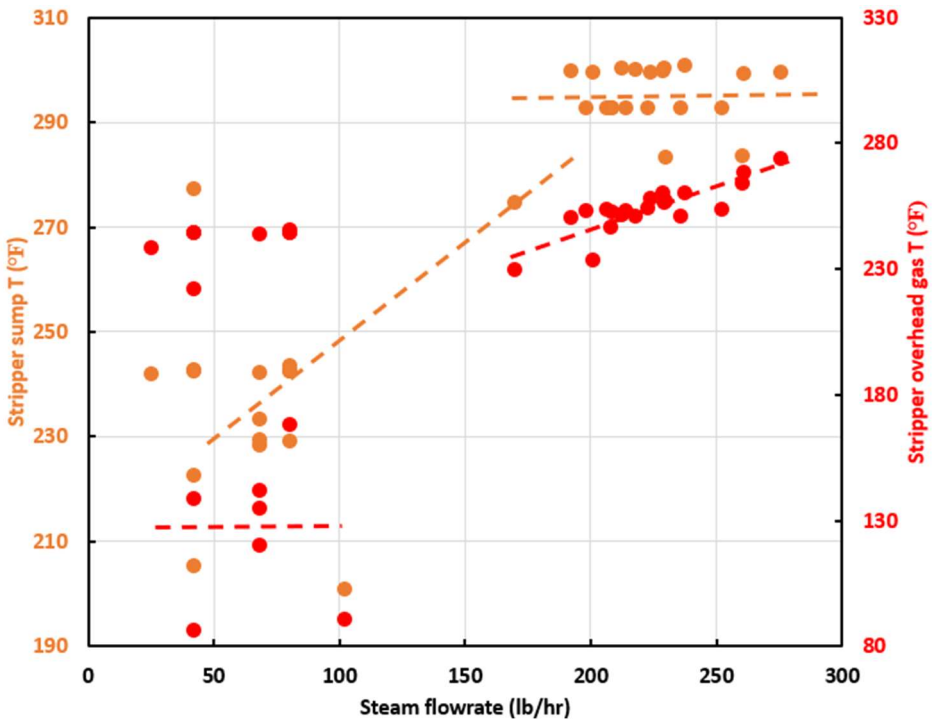

Figure 2.23: Stripper sump and overhead gas temperature as a function of steam flow rate for water testing at UT-SRP pilot plant across all campaigns between 2015 and 2013 (except for the MTR and Osaka Gas campaigns)

The effect shown above is different from what will typically be observed during solvent testing at the pilot plant. With loaded PZ, there will be a temperature gradient in the column with finite packing. While the measured value of heat loss may be identical for water and solvent, this phenomenon interferes with modeling of heat loss. Heat loss modeled using water data represents higher temperatures in the upper sections of the column which is typically not observed with solvent. The average measured heat loss for this campaign was 146,000 ± 44000 BTU/hr.

2.7.4 Consolidated Heat Loss Data from all Pilot Campaigns

Figure 2.24 combines the measured heat loss data from 5 different pilot plant campaigns and two different pilot plants as a function of the temperature driving force

between the stripper sump and the ambient conditions. Except for the SRP 2015 data taken from Lin (2016), all heat loss data were measured using water recirculation tests. Lin measured heat loss directly from solvent test runs using physical properties of the solvent from Aspen Plus®.

Figure 2.24 shows that the SRP pilot plant has a smaller heat loss than the NCCC pilot plant due to its smaller scale, exposed surface area, and steam flowrate. There is a systematic dependence between measured heat loss and the temperature driving force to ambient from the sump of the stripper, the hottest point in the stripper. Figure 2.24 also shows the ranges of sump temperature, stripper overhead temperature, and wind speed for the different water tests. Sump temperature provides an idea about the magnitude of steam flowrate. Stripper overhead temperature indicates the rise of steam through the stripper column, making the upper sections also exposed to heat loss in addition to the sump. Wind speed shows the influence of forced convection on heat loss at different pilot plants. Most of the data in Figure 2.24 can be explained by a combination of these three variables.

Figure 2.24 also shows the effect of flue gas type on heat loss. At the same pilot plant (UT-SRP), heat loss appears to be much higher for coal flue gas (yellow) than for NGCC flue gas (orange). This is a combination of the use of a higher steam rate in the coal campaign, reflected by a higher range of sump temperature and stripper overhead temperature. More of the stripper external surface area was exposed to heat loss in the coal campaign at SRP. Moreover, the wind speed during this campaign was much higher than that observed in the NGCC campaign, which is correlated with the much higher heat loss. The ambient temperature range was very similar for these two campaigns (50-87 °F), making heat loss only a function of wind speed, sump temperature, and stripper overhead temperature.

The high heat loss at the NCCC pilot plant can be explained by the higher steam rate (high sump temperature), high stripper overhead gas temperature, and seasonal changes. The red outlier (triangle) in the NGCC 2023 campaign is explained by the high stripper overhead vapor temperature and high wind speed compared to other data in this campaign. The NCCC coal campaign heat loss measurements were made in the winter. The two green triangle outliers were a consequence of near-freezing ambient temperature in these runs. The green and red NCCC points have a higher heat loss compared to the blue points primarily due to the consistently higher stripper overhead vapor temperature. The NCCC campaign in 2019 also operated at higher ambient temperature (max 96 °F) compared to the campaigns in 2018 (max 60 °F) and 2023 (max 78 °F) at NCCC and the SRP coal campaign in 2015 (max 83 °F).

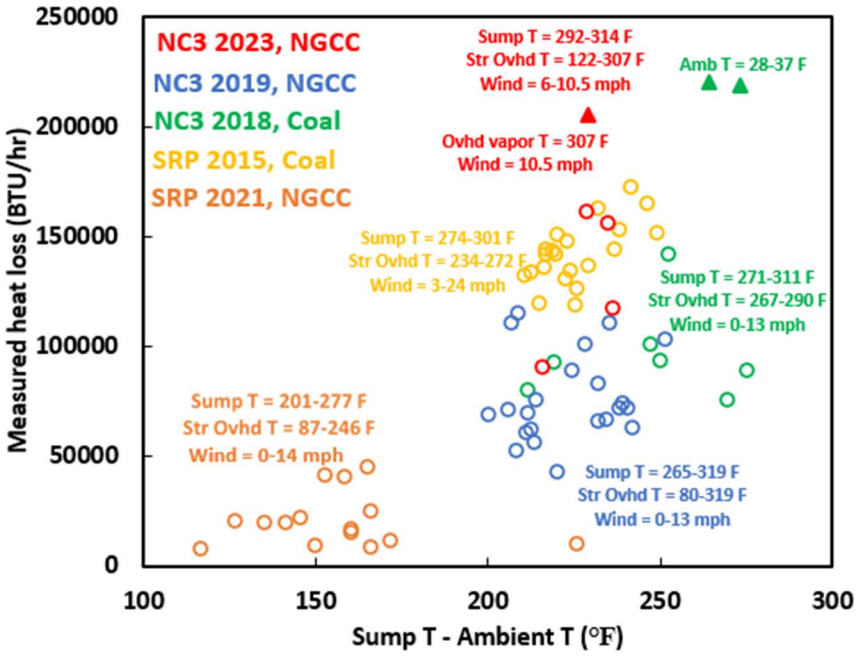

Figure 2.24: Measured heat loss as a function of temperature driving force from the stripper sump to ambient from 5 different pilot plant campaigns; SRP 2015 data taken from Lin (2016)

The effect of steam rate has been removed by normalizing the heat loss by steam flowrate. This removes the dependence of heat loss on the stripper sump temperature. Under these conditions, heat loss normalized by steam flowrate appears to be inversely proportional to ambient temperature. This is shown in Figure 2.25. Heat loss becomes less important at high ambient temperature primarily due to a lower driving force for heat loss. Pilot plants may therefore benefit from summer operation to mitigate the detrimental effect of heat loss on the energy performance.

At the same pilot plant (NCCC), processing NGCC (blue) flue gas increases the relative importance of heat loss compared to coal conditions (green). Heat loss appears to be more important in general for NGCC conditions. The average fraction of heat lost relative to steam heat rate across all the campaigns is about 35.4%, but this varies depending on ambient conditions and pilot plant operation.

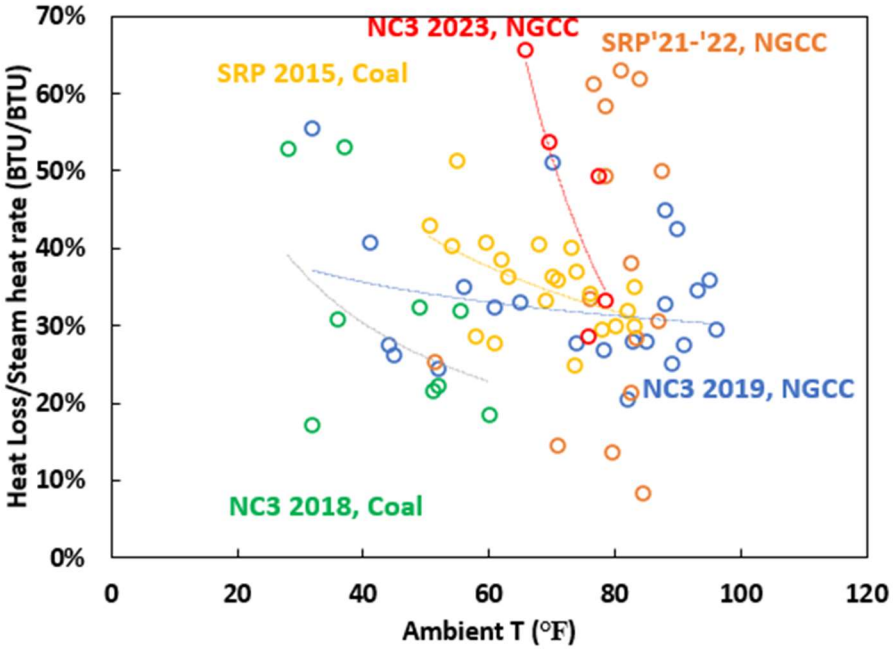

Figure 2.25: Heat loss normalized by steam heat rate removes its dependence on sump temperature; heat loss per unit steam flow depends inversely on ambient temperature

Heat loss could also be enhanced by forced convection through the interaction of local wind with the surface of the exposed metal at pilot plants. Figure 2.26 plots the measured heat loss as a function of wind-speed and the temperature driving force from the sump to the ambient. Wind speed data for Austin and Alabama were obtained from https://www.wunderground.com/ for the analysis of all heat loss data.

Most of the heat loss data appears to be concentrated in the low wind speed region. At the same temperature driving force from the sump to ambient, a higher wind speed points to a higher heat loss, but it is unclear if this effect is purely due to wind speed or is also due to the factors described previously such as pilot plant scale and flue gas type. The current dependence of heat loss on wind speed appears to be statistically insignificant and must be verified using data from future pilot plant tests.

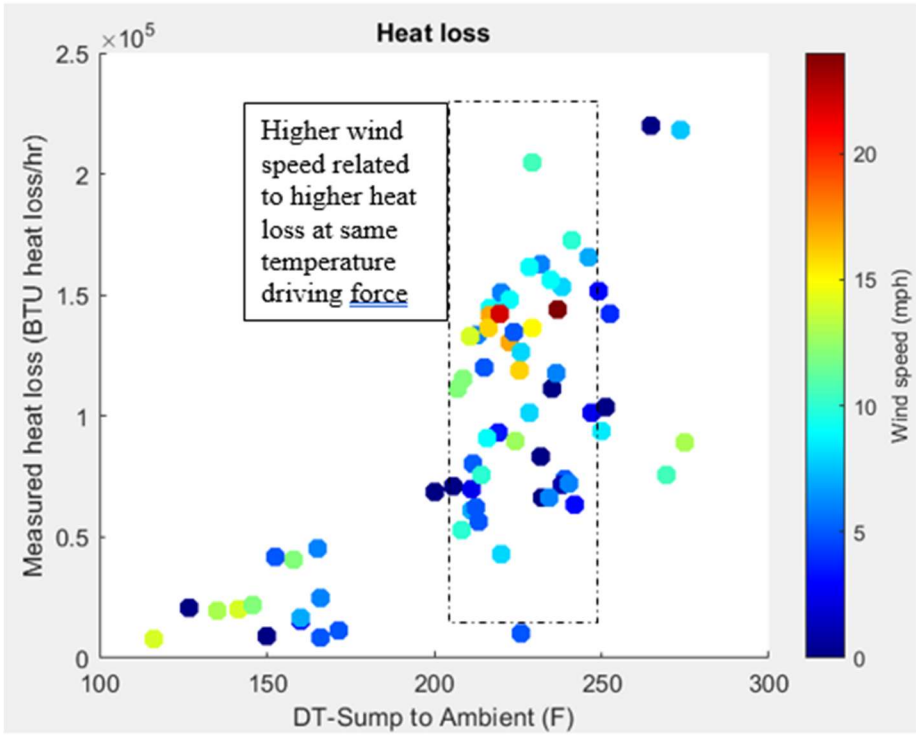

Figure 2.26: Heat loss shows a weak dependence on local wind speed

Overall, heat loss appears to have a complicated dependence on pilot plant scale, type of flue gas, process temperatures, and ambient conditions. Heat loss data is confounded by variation in process variables and ambient conditions in the measurement window, which leads to large standard deviations in measured data. The current understanding of heat loss could benefit from more data from water testing and solvent testing, especially in the lower sump temperature region for NCCC and higher sump temperature range for SRP at NGCC conditions.

2.8 CONCLUSIONS

The following conclusions were made from heat loss modeling for PZAS:

- Heat duty is most sensitive to heat loss in the hot lean pipe and the warm rich pipe after the valve at NCCC. The warm rich pipe before the valve, stripper column, total rich bypass line, and CO_2 heat exchanger require less additional heat duty to make up for incremental heat loss, indicating that heat loss is less important in these areas.
- Heat loss impacts heat duty at locations beyond the source, suggesting that adjusting measured heat duty for heat loss on a 1:1 basis assumes heat loss only occurs at the source or the hottest regions of the process. In PZAS at NCCC, the warm rich pipe before the valve has the largest surface area, and heat loss in this location can degrade stripper performance. Correcting for heat loss at this location is done at 80% of the heat loss value for the 2018 and 2019 campaigns.
- In the simple stripper, the column is the most important location for heat loss. Its large top-side pinch makes heat duty highly sensitive to heat loss, which may justify correcting heat duty for heat loss on a 1:1 basis for these types of strippers.
- Heat loss causes pinches and CO_2 reabsorption, reducing stripper performance. The simple stripper is more vulnerable to this effect at a lower heat loss value of 0.03 GJ/hr compared to PZAS at 0.14 GJ/hr. In PZAS at NCCC, reabsorption due to heat loss is unlikely since the average measured heat loss for the entire system was only 0.07 GJ/hr. To minimize the harmful effects of heat loss, strippers such as the one at the NCCC pilot plant should not be overdesigned.
- The lower measured heat duty value for 7 m MEA with the simple stripper at NCCC compared to 5 m PZ may be due to the less harmful effects of heat loss on 7 m MEA,

caused by a large bottom-side pinch in MEA strippers achieved by using lower liquid rate and lower lean loading than 5 m PZ.

- Heat loss in pilot scale strippers at NGCC conditions are more important than in strippers operating at coal conditions primarily because the NGCC case has lower absolute heat rate compared to the coal case for the same absolute heat loss.

<u>The following conclusions were made from surface temperature measurements for PZAS:</u>

- Natural convection is the most significant heat loss mechanism from exposed metal in both the UT-SRP and NCCC pilot plants, accounting for at least 75% and 60% of heat loss in most measurements, respectively. Heat loss is primarily dependent on ambient and process conditions, as well as exposed surface area, with fluid side-properties having a lesser effect. Water-based heat loss measurements can be used to accurately estimate heat loss from amine scrubbing pilot plants.

<u>The following conclusions were made from heat loss measurements for PZAS:</u>

- The NCCC pilot plant had an average measured heat loss of 0.078 GJ/hr (0.38 ± 0.1 GJ/tonne CO2) for the NGCC 2019 and Coal 2018 campaigns, representing about 30% of the average steam heat rate. At the UT-SRP pilot plant in the 2021-22 campaign, measured heat loss was found to be 0.021 ± 0.013 BTU/hr, with no significant relation to steam heat rate. The average measured heat loss for the NCCC NGCC campaign was 0.154 ± 0.046 BTU/hr.
- The relative heat loss (heat loss/heat rate) at SRP was 6% higher than at NCCC and SRP, resulting in an approximate 20% decrease in relative heat loss per MW of added capacity at the pilot scale.

- The SRP pilot plant has a smaller heat loss value compared to the NCCC pilot plant due to the higher scale, larger surface area, and steam flowrate employed in the NCCC pilot plant.
- Higher heat loss is observed for coal flue gas compared to NGCC flue gas at the UT-SRP pilot plant, due to a combination of factors including a higher steam rate, higher sump and stripper overhead temperature ranges, and higher wind speed during the coal campaign.
- NGCC flue gas test at NCCC confirms that heat loss is relatively more important for NGCC conditions compared to coal conditions, as supported by modeling results. The average fraction of heat loss relative to steam heat rate across all campaigns is approximately 35.4%, although it varies based on pilot plant operation and ambient conditions.

RECOMMENDATIONS FOR FUTURE WORK

- The current understanding of heat loss could benefit from more data from water and solvent testing, especially at low sump temperature for NCCC and high sump temperature for UT-SRP.
- Heat loss measurements must be made as close to steady state conditions as possible, or smaller time intervals of pilot plant data must be used to avoid large scatter in measured data. The source of variation in heat loss data must be identified by observing the sensitivity of heat loss to flow measurements and temperature measurements.
- An empirical heat loss model using temperature driving forces and wind speed could be developed to correct heat rate as a function of varying operating and ambient

conditions. This could aid in better model reconciliation of heat duty during pilot plant campaigns.

- The impact of heat tracing as a mitigation method for heat loss must be investigated in detail.

ACKNOWLEDGEMENTS

The author acknowledges Dr. Gary Rochelle and Dr. Frank Seibert for guiding the pilot plant heat loss tests at NCCC and SRP, respectively. The author also thanks Laura Uhrig and Jason Arriazola at the NCCC pilot plant, and Dr. Frank Seibert and Jarrett Spinhirne at the UT-SRP pilot plant for their help with measurements. The author expresses gratitude to the operators at the NCCC pilot plant and Texas Carbon Engineers for their help during the campaign, especially during night shifts.

Chapter 3: Pilot Plant Data Reconciliation and Stripper Model Validation

3.1 INTRODUCTION

In aqueous amine-based absorption/stripping, steam is the major component of total energy use (Rochelle, 2009). Reductions in energy consumption could come from appropriate solvent selection and designing advanced stripper configurations. Aqueous concentrated piperazine (PZ) has been shown to outperform the conventional alternative monoethanolamine (MEA) due to its greater absorption rate, CO_2 capacity, and low energy requirement (Rochelle et al., 2011; Lin et al., 2016; Li et al., 2016; Plaza and Rochelle, 2011). Different advanced configurations have previously been modeled and/or tested at the pilot scale including lean vapor compression, inter-heated stripper, and two-stage flash with cold rich bypass, and all have shown energy reductions compared to the simple stripper (Knudsen et al., 2011; Madan et al., 2013). The Advanced Stripper with PZ improved energy performance more than other options, according to a simulation study (Lin, 2016). When tested in a pilot plant at UT-SRP, it gave a heat duty of 2.1-2.5 GJ/tonne (Lin et al., 2016). Other technology providers such as Linde-BASF (Jovnovic et al., 2012), ION Engineering (Brown et al., 2017), Hitachi Power Systems (https://www.nationalcarboncapturecenter.com/wp-content/uploads/2021/01/Hitachi-Power-Systems-America-Testing-of-Hitachi-H3-1-Solvent-2012.pdf) etc. have tested their solvents and process configurations at the National Carbon Capture Center, but most this testing appears to be at coal-fired conditions. Moreover, many of the tests do not report the net heat duty of the pilot plant after a correction for heat loss at NGCC conditions. This work measures and reports the net heat duty of the PZAS process between 4 and 12% CO_2 in flue gas at the NCCC and UT-SRP pilot plants over 4 pilot plant campaigns and a wide

range of operating conditions. Pilot plant data will also be used to validate a rate-based process model and assess its performance.

3.1.1. Modeling and Data Reconciliation Approaches for Strippers

Pilot plant experimentation can validate the process model in its representation of mass transfer, reaction kinetics, and solvent equilibrium. Prior to this work, other Texas Carbon Engineers had developed methods to reconcile pilot plant data with the predictions from the process model.

Several modeling approaches have been considered for strippers in CO_2 capture. Van Wagener (2011) used equilibrium reactions with mass transfer to model different stripper configurations with MEA and PZ under coal conditions. Oyenekan (2007) used both equilibrium and rate-based methods to model the stripper using Aspen Plus®. Madan (2013) used a rate-based approach with equilibrium reactions to model the stripper, and Lin (2016) used a rate-based stripper with equilibrium reactions at high temperature.

Van Wagener (2011) lumped the deviations between measured data and modeled results using an adjustable heat loss in the stripper. The heat loss values predicted by the process model were 35-179% different from that measured at the pilot plant for 9 m MEA using the simple stripper. A similar approach was also used for data reconciliation of lean loading by Van Wagener (2011) using 8 m PZ. In this case, heat loss in the model varied between 0 and 127% of the measured heat loss value for the simple stripper.

In the reconciliation of stripper data with 5 m K^+/2.5 m PZ and 6.4 m K^+/1.6 m PZ, Oyenekan (2007) adjusted the wetted area of the column in the top half to 10% of the dry packing area and 70% of the dry packing area in the lower half.

Madan (2013) conducted rigorous data reconciliation using the Data Fit functionality in Aspen Plus® to minimize an "error" objective function for each steady state run at the pilot plant. Rich CO_2 content was adjusted by 4.6% to minimize the error between modeled and measured pilot plant data.

Lin (2016) used a similar approach in Aspen Plus® Data Fit™ but adjusted the rich loading and packing interfacial area of the stripper which resulted in a correction factor of about 0.152 (~0.16) applied to the interfacial area. This correction was attributed to the overprediction of PZ diffusivity and mass transfer coefficient by the model compared to the measurement.

Other researchers have modeled the stripper with equilibrium only (Bhattacharyya et al., 2011), equilibrium reactions with rate-based mass transfer (Tobiesen et al., 2006), kinetic reactions with rate-based mass transfer (Sipöcz et al., 2011), kinetic reactions with Murphree efficiencies (Karimi et al., 2012), and rate-based mass transfer with enhancement factors for reactions (Borhani et al., 2019). Modeling methods and tools employed by researchers outside the Texas Carbon Management Program have also been listed in Chapter 1 in Table 1.1.

This work will use rate-based mass transfer with equilibrium reactions in the stripper to model pilot plant data and validate the process model. Data reconciliation is done using two approaches: the first simply inputs time-averaged input data into the model and estimates predicted values of outputs (input-output) method, and the second uses the Aspen Plus® Data Fit™ to rigorously minimize the deviation between measured and modeled variable values.

Parts of this chapter have been published in the *International Journal of Greenhouse Gas Control* (Suresh Babu and Rochelle, 2022; Rochelle et al., 2022).

3.2 PILOT PLANT AND CAMPAIGN OVERVIEW

The PZAS process was tested in the PSTU (Pilot Solvent Test Unit) at NCCC in Wilsonville, Alabama in 2018, 2019, and 2023 and the UT-SRP (Separations Research Program) pilot plant in Austin, Texas in 2021-22. The NCCC 2018 campaign tested system performance at coal-fired flue gas conditions with approximately 12% CO_2 and the NCCC 2019, NCCC 2023, and UT-SRP 2021-22 campaigns tested system performance at NGCC conditions (about 4% CO_2). Flue gas at NCCC was obtained from a gas-fired boiler with air dilution for the 2023 campaign and was diluted from coal flue gas using injection of air for 2018 and 2019. Flue gas at UT-SRP was a gas mixture of air and CO_2.

3.2.1. NCCC 2018 Coal and NGCC 2019

The NCCC 2018 Coal campaign treated a slip-stream of flue gas (roughly 0.5 MW) from the total flue gas that is generated from Plant Gaston Unit 5 coal-fired boiler. This supercritical pulverized coal boiler has a capacity of 880 MW. In the NCCC 2019 NGCC campaign, the same flue gas was diluted with air to bring down the CO_2 concentration to about 4.3% CO_2. The flue gas at the main boiler was pretreated for the control of NO_x, SO_x, and particulate matter using selective catalytic reduction, sodium bicarbonate injection, hot-side electrostatic precipitation, wet flue gas desulfurization, and a fabric filter with $Ca(OH)_2$ injection. The 0.5 MW slip-stream of flue gas was taken after the flue gas desulfurization unit and sent to the PZAS unit. A simplified flowsheet of the absorber and advanced stripper configuration is shown in Figure 3.1.

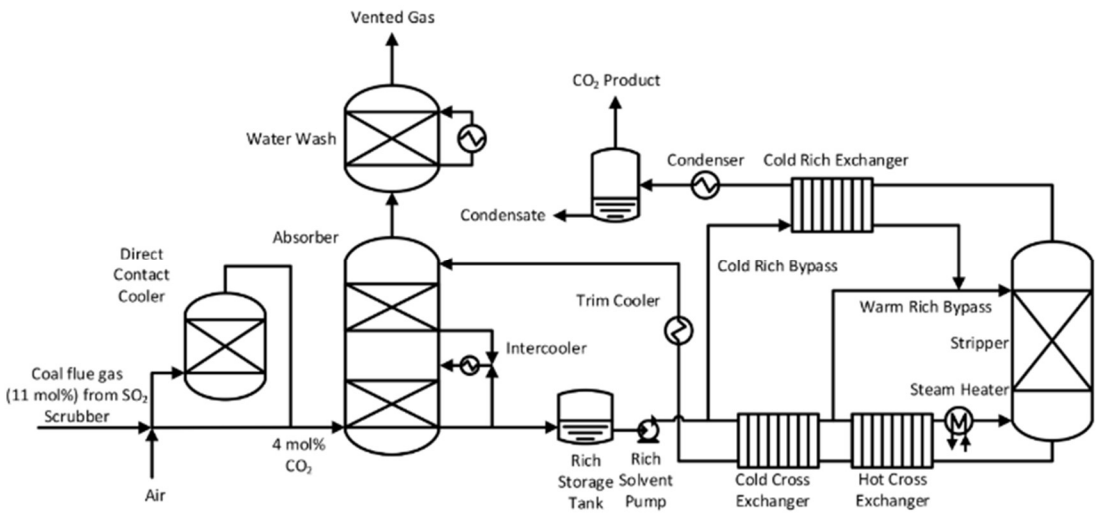

Figure 3.1: Simplified process flow diagram of PZAS at NCCC

The stripper section uses efficient heat-recovery using a network of three cross exchangers. The cold and hot cross exchangers recover sensible heat from the hot lean stream and add sensible and latent heat to the rich solvent. The CO_2 exchanger is used to partially condense the water vapor in the stripper overhead gas. The cold and warm rich bypasses are extracted at their optimal flow fractions, mixed, and sent to the top of the stripper column to partially condense the water vapor rising through the column by direct contact. The total bypassed solvent is counter-currently contacted with vapor in a stripper containing 2 sections of random packing. The top section contains 2 m of RSR No. 0.5 packing, and the bottom section contains 2 m of RSR No. 0.7 packing. The internal diameter of the column is 0.25 m. High-pressure CO_2 is produced in the stripper which is expected to reduce compressor work.

In the NGCC 2019 campaign, 50% more flue gas was processed. Two types of tests were conducted in the pilot campaigns: parametric tests, to measure system

performance in response to changes in operating conditions, and long-term tests, to measure stability of the system and its response to solvent composition and degradation.

3.2.2 UT-SRP 2021-22 NGCC Campaign

Figure 3.2 shows a simplified process flow diagram of the PZAS process at the UT-SRP pilot plant. The stripper configuration is the same as that in NCCC. The flue gas treated by the absorber is a synthetic mixture of CO_2 and air. The captured CO_2 is cooled by the cold rich exchanger (CO_2 exchanger) and the condenser and is recycled back to the inlet air to the absorber. The condensate water is recycled back to the absorber with the cold lean solvent.

This pilot plant treats about 0.2 MW of flue gas. The stripper was designed for coal-fired flue gas but was used at NGCC conditions in this campaign, which possibly resulted in much lower vapor rates and flooding in this campaign compared to those at NCCC. The stripper diameter was 0.83 ft and consisted of a single section of RSR No. 0.3 random packing. Two shell-and-tube steam heaters in series are used after the hot cross exchanger.

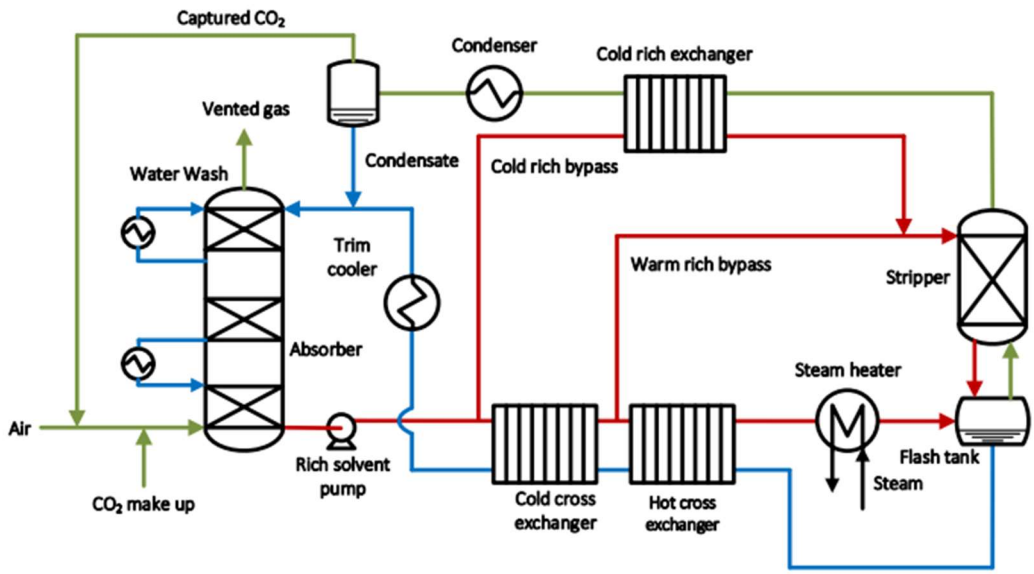

Figure 3.2: Simplified process flow diagram of PZAS at UT-SRP pilot plant

3.2.3 NCCC 2023 NGCC Campaign

The simplified process flow diagram of PZAS at NCCC in 2023 was very similar to the one shown in Figure 3.1. Flue gas with approximately 4% CO_2 by volume from a real natural gas boiler was processed by the absorber. Parametric and long-term tests in this campaign primarily dealt with high CO_2 removal at low lean loading of about 0.2 mol/mol. Both in-and-out and pump-around intercooling were employed in the absorber. Minimization of energy requirement of stripping in this campaign was done by evolutionary optimization of cold and warm rich bypass flowrates at the pilot plant during real-time operation. The total bypassed solvent is counter-currently contacted with vapor in a stripper containing 2 sections of random packing. The top section contains 2 m of RSR No. 0.5 packing, and the bottom section contains 2 m of RSR No. 0.7 packing. The internal diameter of the column is 0.25 m. Operation with high fractional total bypass was also tested in this campaign to confirm reliable steam heater performance, enhancement of

energy performance, and test the process with flashing total rich bypass (at the entry point in the stripper).

3.3 ANALYTICAL METHODS AND PILOT PLANT MEASUREMENTS

3.3.1 NCCC 2018 Coal and 2019 NGCC Campaigns

Gao (2021) reports the gas and liquid measurements pertaining to the absorber that were used to study material balances in the process. The inlet and outlet gas composition of CO_2 in the absorber were determined using nondispersive infrared (NDIR) analyzers. The stripper side did not have a direct measurement of gas composition. Instead, in the stripper side, a total CO_2 flowrate in the vapor was measured. Figure 3.3 shows the stripper side measurements at the pilot plant.

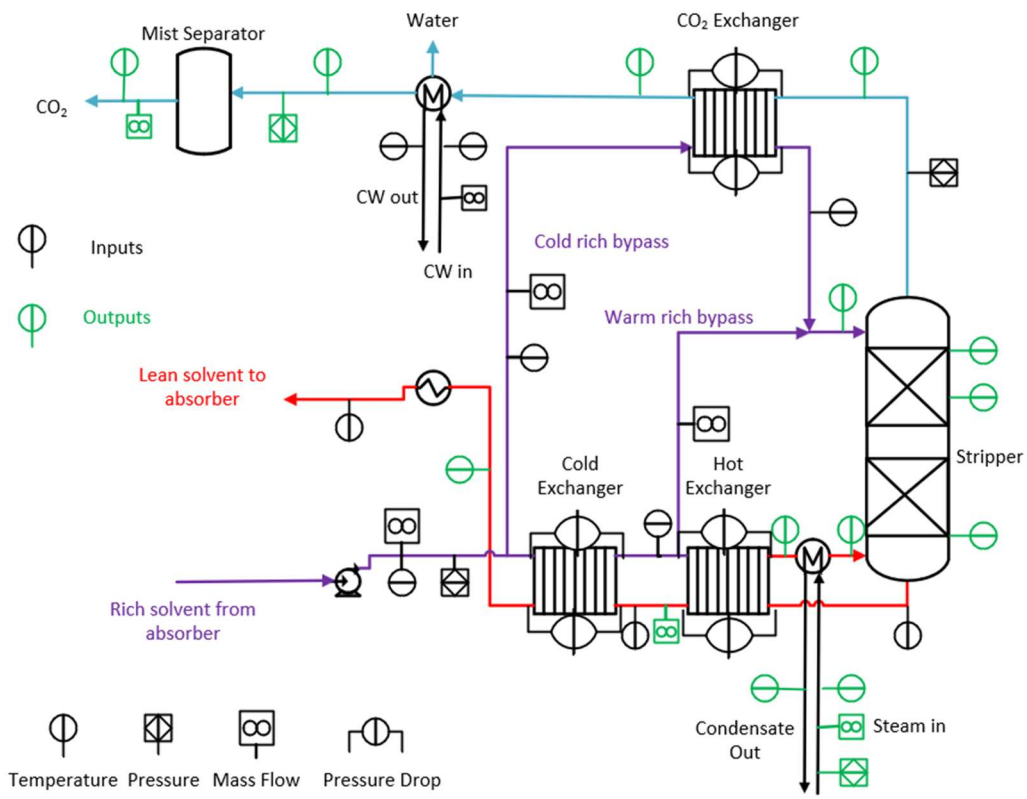

Figure 3.3: Stripper-side pilot measurements showing key model inputs and outputs for PZAS at NCCC

On the liquid-side, the campaign relied on online titrated measurements of PZ and CO_2 in lean and rich solvent. The samples for online titration were collected approximately every 70 minutes. In addition to this, the density and viscosity of the solvent were also measured continuously by online micromotion flowmeters and viscometers. Density accurately represents the CO_2 content of the solvent and viscosity accurately represents the PZ content of the solvent and when coupled together, yielded the CO_2 loading from Equations 3.1 to 3.3. These equations were regressed using experimental data for 2 to 9 m PZ at different loadings by Freeman (2011). Gao (2021) showed that these equations accurately represent solvent composition of 5 m PZ at lean and rich conditions.

$$\rho_{PZ} = \rho_w \cdot (0.0407 \cdot C_{CO_2} + 0.008 \cdot C_{PZ} + 0.991) \quad (3.1)$$

$$\mu = \mu_w \cdot exp[\,(26.16/T - 0.0265) \cdot (7.69 \cdot C_{PZ} - 7.80 \cdot C_{CO_2} + 3.37 \cdot C_{PZ} \cdot C_{CO_2}) \quad (3.2)$$

$$\mu_W = 2.41 \times 10^{-5} \times 10\,247.8/(T-140) \quad (3.3)$$

Other sample analyses included gas chromatography (GC) and total inorganic carbon (TIC) for PZ and CO_2, and cation chromatography (IC) for PZ at UT-Austin (Wu and Rochelle, 2022). Figure 3.4 shows the liquid and gas-side online measurements made at the pilot plant for lean and rich samples.

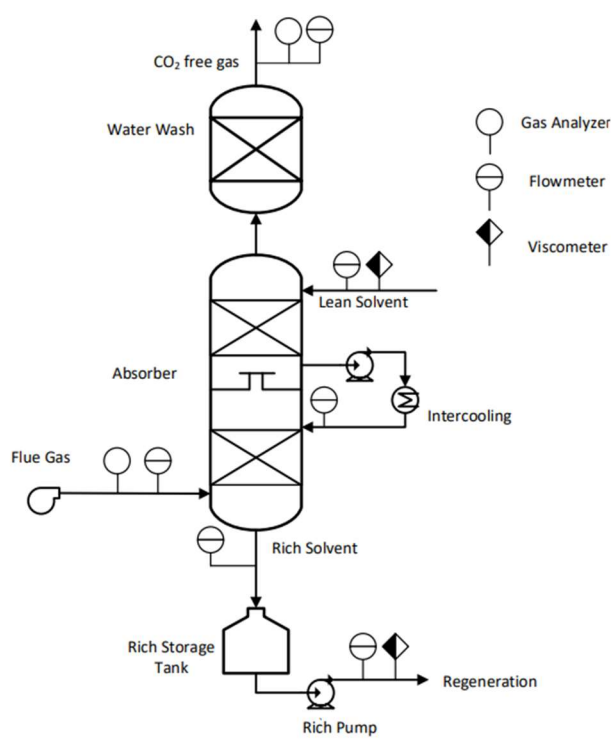

Figure 3.4: On-line measurements for rich and lean samples around the absorber (Gao, 2021)

3.3.2 UT-SRP 2021-22 NGCC Campaign

In the UT-SRP campaign, samples were analyzed for PZ by manual titration at UT Austin with 0.5 N HCl, automatic inflection point-based titration with 1 N H_2SO_4, and cation chromatography. CO_2 content in the solvent was determined from solvent density measurements. Solvent density was measured using a Mettler Toledo DE40 densitometer (Mettler-Toledo, Inc., Columbus, OH) and was related to the CO_2 content in the solvent using Equation 3.4 by Freeman (2011).

$$\rho_{\text{densitometer}} = \rho_W \cdot (0.0407 \cdot C_{CO_2} + 0.008 \cdot C_{PZ} + 0.991) \tag{3.4}$$

$$\rho_W = 2.41 \times 10^{-5} \times 10\,247.8/(T-140) \tag{3.5}$$

The PZ content in the solvent was required for Equation 3.4, which was obtained from the sample analyses for PZ. Unlike the NCCC 2018 and 2019 campaign, reliable viscosity and density measurements for lean and rich samples were not available in this campaign, and therefore CO_2 content had to be measured using PZ content by other analysis methods and the density measurement made in the lab. Ultimately, CO_2 loading was calculated using multiple combinations of CO_2 and PZ measurements. 6 different measurements of loading were obtained in this campaign. Loading calculated purely by the manual titration of PZ and CO_2 were used as the baseline in this campaign as these data were the most reproduceable, with the lowest standard deviation. The same loading measurement was used as an input in process modeling.

In addition to analytical and correlation-based loading measurements, online pilot plant measurements of solvent flowrate, pressure, temperature, and pressure drop were also used for data reconciliation and process modeling. Figure 3.5 shows the simplified process

flow diagram of the stripper side measurements that were important for data reconciliation and process modeling.

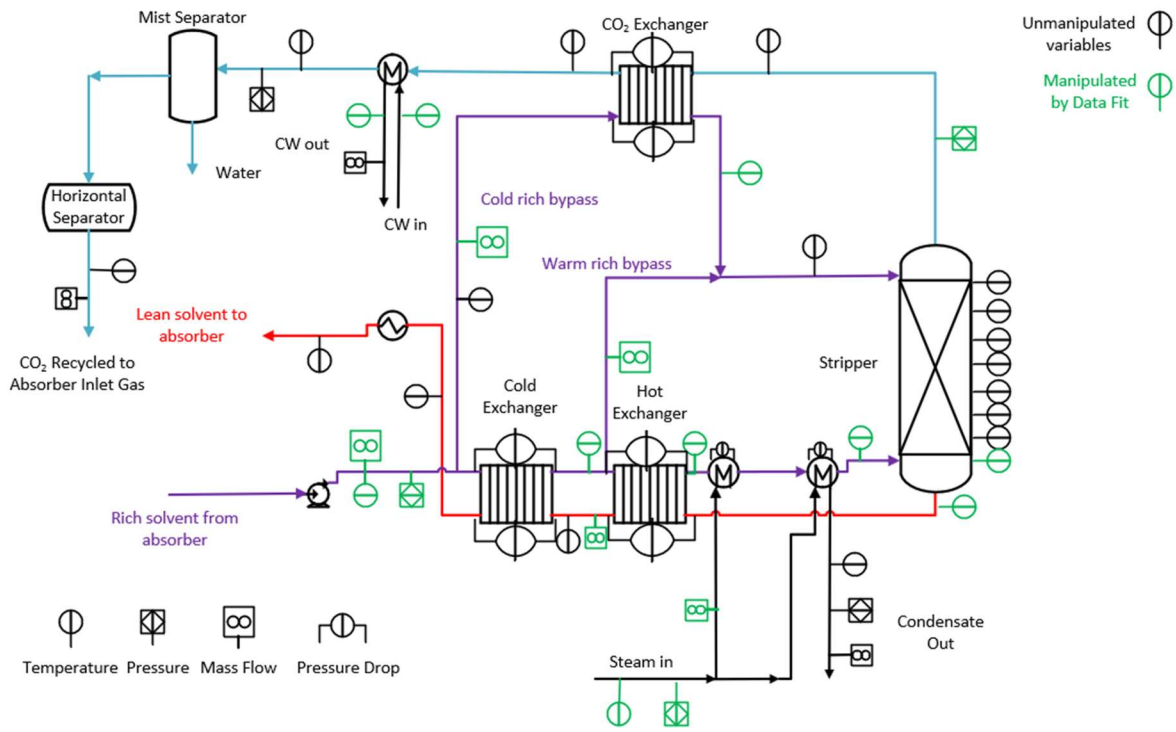

Figure 3.5: Flowsheet of PZAS at UT-SRP showing measurements and variables manipulated and not manipulated by Aspen Plus® Data Fit™

3.3.3 NCCC 2023 NGCC Campaign

In this campaign, PZ was measured using Gas Chromatography (GC), Ion Chromatography (IC), online titration at the pilot plant, and total alkalinity analysis. CO_2 content in the solvent was measured using Total Inorganic Carbon (TIC) analysis at UT Austin, TIC analysis at NCCC, density measurement, and online titration at the pilot plant. Solvent density was measured using a Mettler Toledo DE40 densitometer (Mettler-Toledo, Inc., Columbus, OH) and is related to the CO_2 content in the solvent using Equation 3.4 by

Freeman (2021). Reliable viscosity measurements at the pilot plant were not available in this campaign.

Online pilot plant measurements are shown in Figure 3.6. An additional temperature sensor (TI40513) was added in this campaign at the top of the stripper to measure the temperature of the gas leaving. This aided in better reconciliation of column temperatures between the model and measurement in this campaign.

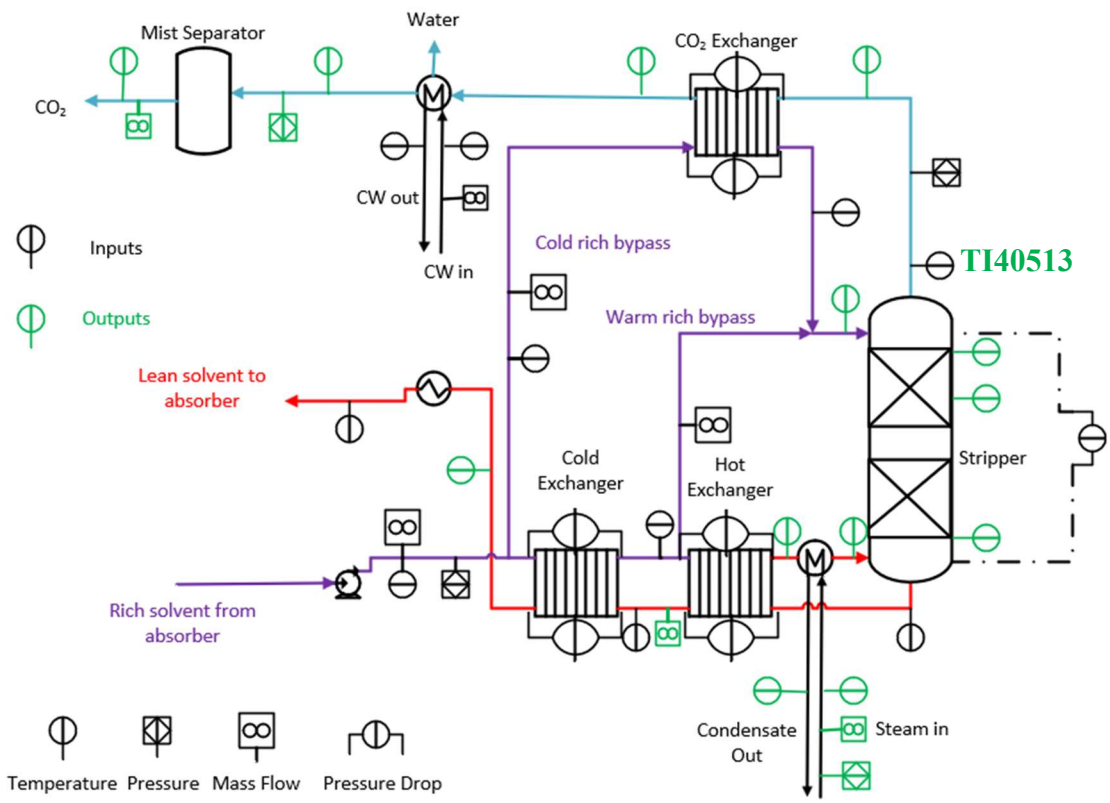

Figure 3.6: Flowsheet of PZAS at NCCC in the 2023 campaign showing key model inputs and outputs

3.4 MODELING METHOD

3.4.1 Coal 2018 and NGCC 2019 Campaigns at NCCC

The thermodynamics and rate behavior of PZAS were calculated using the Independence™ model (Frailie, 2014) developed in Aspen Plus® containing the CO_2 solubility, kinetics, specific heat capacity, and amine volatility regressed in the e-NRTL framework. The mass transfer model was developed by Wang (2015) and contains the interfacial area (a_e), liquid-phase mass-transfer coefficient (k_L), and gas-phase mass-transfer coefficient (k_G) for random packing. The Song (2017) model was also used to estimate energy performance of PZAS. This model was built from a broad database of mass-transfer properties of both structured and random packing and is applicable to both the absorber and stripper packing. The loading and PZ concentration used by the model were calculated from density and viscosity correlations developed by Freeman (2011).

A correction factor of 0.16 was used in the effective area model to bridge the deviation between modeled and measured diffusivity of the PZ at high temperature (Lin, 2016). Reactions are assumed to be at equilibrium in the stripper. The model uses measured conditions of the rich solvent including flow rate, temperature, pressure, loading, and PZ concentration. The bypass flow rates, stripper sump temperature and pressure, and heat exchanger terminal temperatures were specified to be the measured values at NCCC. The main model outputs are the heat rate, lean loading, and the stripper overhead CO_2 flow rate. Time-averaged steady state data over 60 minutes of the process were selected for modeling.

3.4.2 UT-SRP NGCC 2021-22 Campaign

The thermodynamics and rate behavior of the process were represented by the Independence model by Frailie (2014). Mass transfer in random packing in the stripper column was represented by the Song model (Song, 2017). A constant correction factor of 0.16 on the wetted area of packing was applied in the column to bridge the discrepancy between the measured and modeled diffusivity of PZ under stripper conditions.

Aspen Plus® Data Fit™ was used for model reconciliation. This rigorous method allowed the measured variables in the pilot plant to be adjusted within a given range to best fit the variables predicted by the model. An optimization problem is defined as the minimization of the weighted sum of squared error between the measured ($X_{i,meas)}$ and estimated variable ($X_{i,est)}$ value, by varying the estimated value within 3 standard deviations ($\sigma_{i,x}$) of the measured value. The weights (w_i) used for optimization are automatically selected by the model in proportion to the standard deviation of each adjusted variable. Equations 3.6 to 3.8 show the objective function minimized by Aspen Plus® to do rigorous data reconciliation.

$$\min \sum_{i=1}^{16} w_i \left(X_{i,est} - X_{i,meas}\right)^2 \tag{3.6}$$

$$X_{i,meas} - 3 * \sigma_{i,X} \leq X_{i,\ est} \leq X_{i,meas} + 3 * \sigma_{i,X} \tag{3.7}$$

$$w_i\ \alpha\ \sigma_{i,X} \tag{3.8}$$

The variables chosen for this analysis had a significant effect on the results and ultimately the following 16 variables were chosen as it was the only combination that resulted in reasonable changes in the variable values:

- Rich solvent flow, temperature, PZ content, and CO_2 content

- Cold rich and warm rich bypass flow rates
- Warm rich, hot rich, hot lean, stripper sump, heated cold rich bypass, and condenser temperatures.
- Temperature of rich solvent exiting steam heater
- Lean loading from manual titration, lean solvent flow rate
- Net heat rate and stripper pressure.

The following variables were calculated outside of Data Fit™: CO_2 flow rate, rich loading, and net heat duty. This analysis allowed the standard deviation of measured heat loss to be included as a part of the input heat rate. Measured heat loss has a high standard deviation, which could affect the results of data-fit significantly. Standard deviations of the measured variables were either directly measured from sensor data or repeating analytical measurements, or by indirectly calculating the standard deviation for a given dependent variable such as heat duty (heat rate/CO_2 flow) using the standard deviations of its independent variables.

In the modeled flowsheet, pressure was balanced at the point of entry of the total rich bypass and hot rich solvent into the stripper using valves with a specified pressure drop to match the downstream stripper pressure. Heat rate was manipulated in a separate heater block that represented the steam heater to set a desired value of vapor temperature leaving the stripper sump. The pressure of the sump was set to obtain a modeled lean loading. Heat loss in the hot lean pipe was incorporated into the model by using a heater block with no pressure drop and a measured temperature change from the pilot plant.

3.4.3 NCCC 2023 NGCC Campaign

This campaign used a modeling approach like the one in NCCC 2018 and 2019 campaign. Time-averaged steady state values of process variables were directly provided as inputs to the model. Figure 3.6 summarizes the inputs and outputs to the model. The thermodynamics and rate behavior of the process were represented by the Independence Model built by Frailie (2014). Mass transfer in random packing in the stripper column was represented by the Song model (Song, 2017). A constant correction factor of 0.16 on the wetted area of packing was applied in the column to bridge the discrepancy between the measured and modeled diffusivity of PZ under stripper conditions.

Heat loss in the hot lean pipe and warm lean pipe were also simulated in the model. Heater blocks with no pressure drop and a measured temperature change was provided as input to the model to simulate heat loss. Pressure was balanced at the point of entry of the total rich bypass into the stripper overhead and at the point of the rich solvent entry into the sump of the stripper using valves with a specified pressure drop.

3.5 PILOT PLANT EXPERIMENTAL RESULTS

3.5.1 Reconciliation of Solvent Composition

3.5.1.1 NCCC 2018 Coal and 2019 NGCC Campaigns

Gao (2021) provides a detailed account of absorber-side comparisons of PZ and CO_2 content measured using different analytical methods for both the campaigns. While the lean viscometer did not work correctly for the 2018 campaign, it worked fine for the 2019 campaign. The PZ content in the rich and lean solvent were assumed to be equal in this campaign, with the rich composition estimated by a rich viscometer and flowmeter.

Lean and rich viscosity agreed very well in the 2019 campaign and Gao confirmed that the lean viscosity calculated by the assumption of equal PZ content was sufficient.

In the 2018 campaign, PZ calculated by density and viscosity measurements deviated from that calculated by cation IC and titration by 1% and 3% respectively. PZ by gas chromatography was consistent with density viscosity measurements within 5% for most of the campaign, except for some analytical issues in the beginning. PZ measurements by density and viscosity were deemed to be the base method for reconciliation of data due to good data availability, precision, and a low standard deviation of about 2% (Gao, 2021). In the 2019 campaign, PZ by IC and titration were within 6% and 3% of that measured by online density and viscosity. PZ by GC agreed with density-viscosity based measurements within 3%.

CO_2 measurements differed more significantly than PZ measurements in both campaigns. In the 2018 campaign, online titration-based CO_2 deviated from density-viscosity based measurements by 17%, which translated to a 14% difference in loading. In the 2019 campaign, titration-based CO_2 deviated from density viscosity-based measurements by 18%, which translated to a 15% difference in loading by the two methods. Overall, loading reconciliation by different methods lead to similar conclusions in both campaigns.

Figure 3.7 is a parity plot comparing the model-predicted lean loading with lean loading calculated from density and viscosity correlation for 2018 coal and 2019 NGCC campaign together. The process model used the stripper sump temperature and pressure to predict a lean loading based on thermodynamics. The model-predicted lean loading was within 10% of the measured lean loading, and the scatter in the data was a result of random variations in stripper sump temperature.

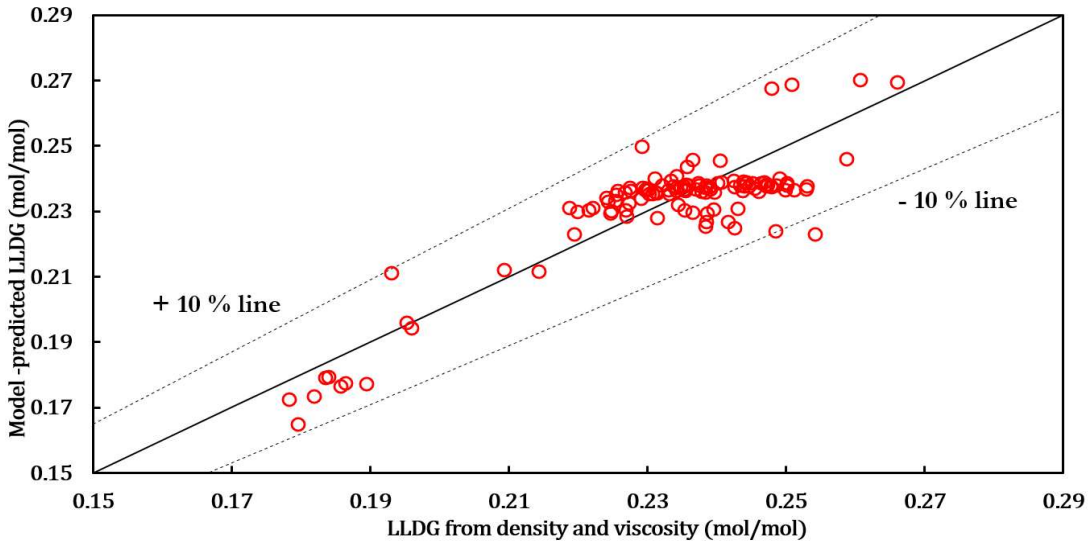

Figure 3.7: Density-viscosity based lean loading agreed within 10% of the model-predicted lean loading

In the long-term measurements, a deviation from the party line was observed, which was the effect of carbon treating on lean loading estimated from density and viscosity. Prior to carbon treating of solvent, the model appears to predict a constant lean loading at fixed temperature and pressure, while the density-viscosity lean loading appears to vary significantly due to accumulation of degradation products in the solvent, which influenced viscosity of the solvent. After the removal of products by the carbon bed, the density and viscosity measurements accurately represented model predicted value.

The process model does not account for solvent degradation. This effect is shown in Figure 3.8. The red data indicates that measured lean loading increased for a relatively constant model predicted lean loading. Degradation products likely impacted the density and viscosity of the solvent at approximately constant piperazine content to produce this effect.

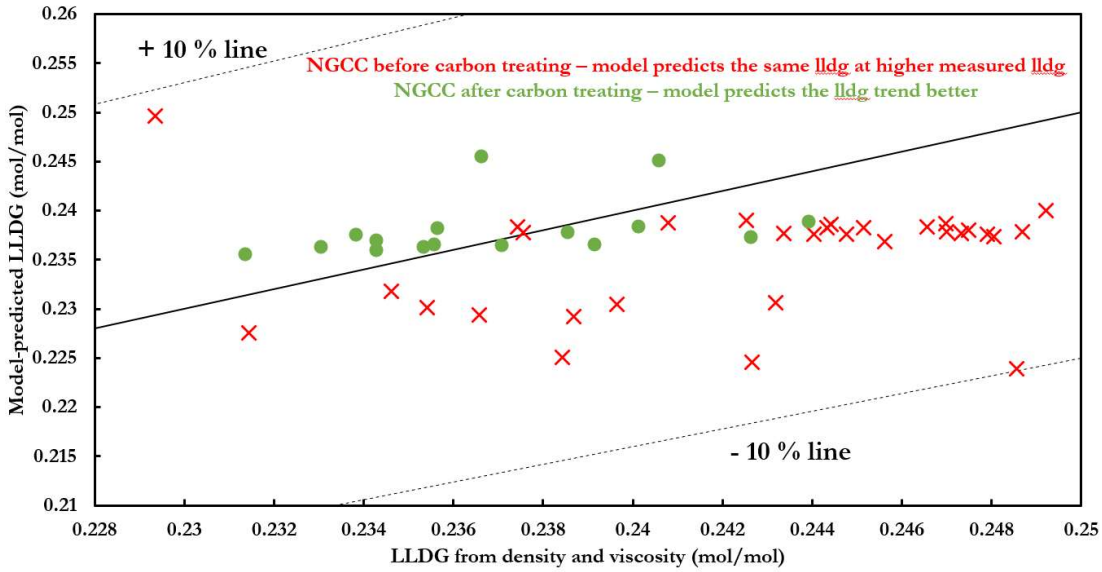

Figure 3.8: Density-viscosity based lean loading agrees better with modeled lean loading with the use of a carbon bed

3.5.1.2 UT-SRP 2021-22 NGCC Campaign

PZ was measured using anion IC, manual titration, and auto-titration in this campaign. Figure 3.9 shows the relative error between different measurement pairs with calendar time in the campaign. PZ from auto titration and manual titration agreed with each other to a good extent with an average difference of about 2.6%. Measurements made using anion IC significantly over-predicted the other PZ measurements. IC measurements deviated from manual titration measurements by +10% on average and from auto-titrated measurements by +13.3% on average. This deviation was a result of calibration issues with anion chromatography. Ultimately, the manual titrated value of PZ was used as the base method for this campaign due to its low standard deviation.

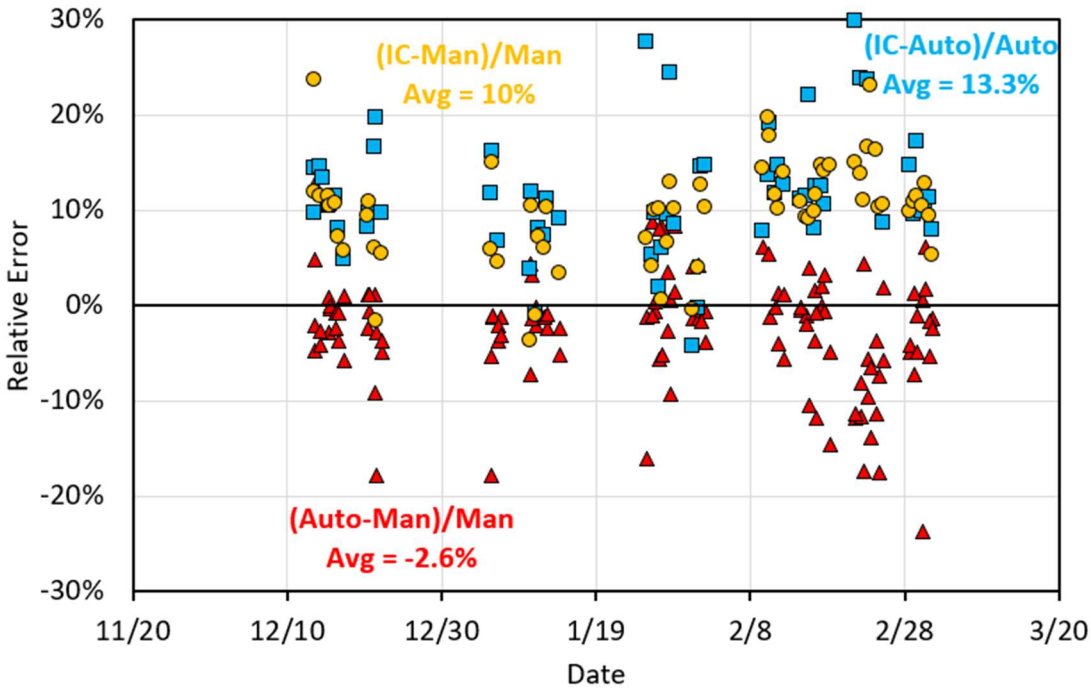

Figure 3.9: Relative error in PZ concentration from ion chromatography, auto-titrated PZ, and manually titrated PZ

CO_2 was measured using density-based measurements, manual titration, and TIC (total inorganic carbon) analysis. The absence of viscosity measurements or reliable online viscosity measurements in this campaign made the estimation of CO_2 fully reliant on density only. Density of the solvent was measured and coupled with the PZ concentration from manual and auto-titration to obtain a CO_2 concentration.

Figure 3.10 compares the relative error between CO_2 measurements from density and manual titration-based-PZ with that by TIC and manual titration. The TIC and manual titration-based CO_2 appear to be lower than density-based value by 5.2% and 8.6% on average, respectively.

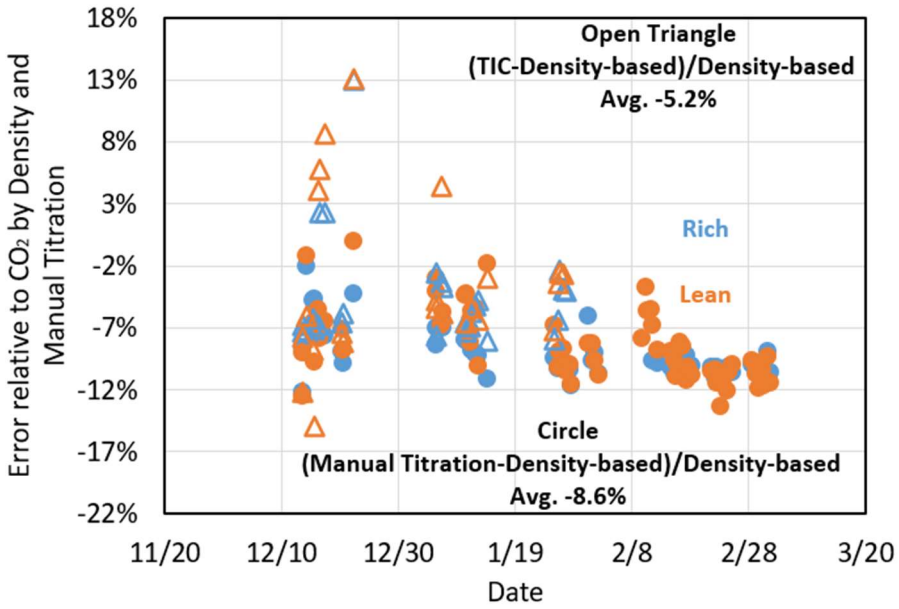

Figure 3.10: Relative error of CO_2 by density and manual titration PZ compared to TIC and manual titration of CO_2, orange points are lean samples, blue points are rich samples

Figure 3.11 compares the relative error between CO_2 measurements made by coupling density and auto titration-based PZ with that by TIC and manual titration. The TIC and manual titration-based CO_2 appear to be lower than density-based value by 4.6% and 9.3% on average, respectively.

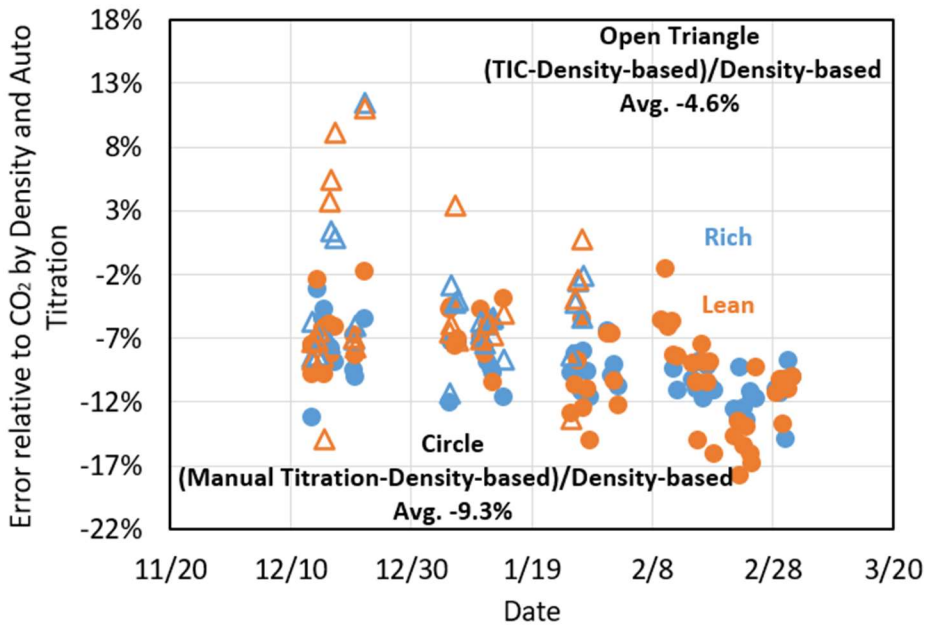

Figure 3.11: Relative error of CO_2 by density and auto titration PZ compared to TIC and manual titration of CO_2, orange points are lean samples, blue points are rich samples

The consistent over-prediction of density-based CO_2 in both cases could be due to the lack of viscosity measurements, an important indicator of solvent composition that was missing in the analysis of samples in this campaign. The correlations used to estimate CO_2 concentration from density and a PZ concentration use parameters that were originally regressed from density and viscosity data.

Figure 3.12 shows the CO_2 loading calculated using 6 different methods compared to CO_2 loading from manual titration of PZ and CO_2 only. Most loading measurements were within 10% of the loading measured using manual titration. Loading that involved only density calculations for CO_2 significantly deviated from the parity line due to the overestimation of density-based CO_2.

Loading measured using PZ from ion-chromatography deviated consistently on the lower side compared to loading from manual titration due to a consistently higher PZ content. PZ measured by IC was consistently higher by 10% compared to PZ from manual titration, while the PZ measured by auto-titration was more consistent with that from manual titration. Ultimately, the loading calculated by manual titration of CO_2 and PZ was used as the base method for process modeling inputs.

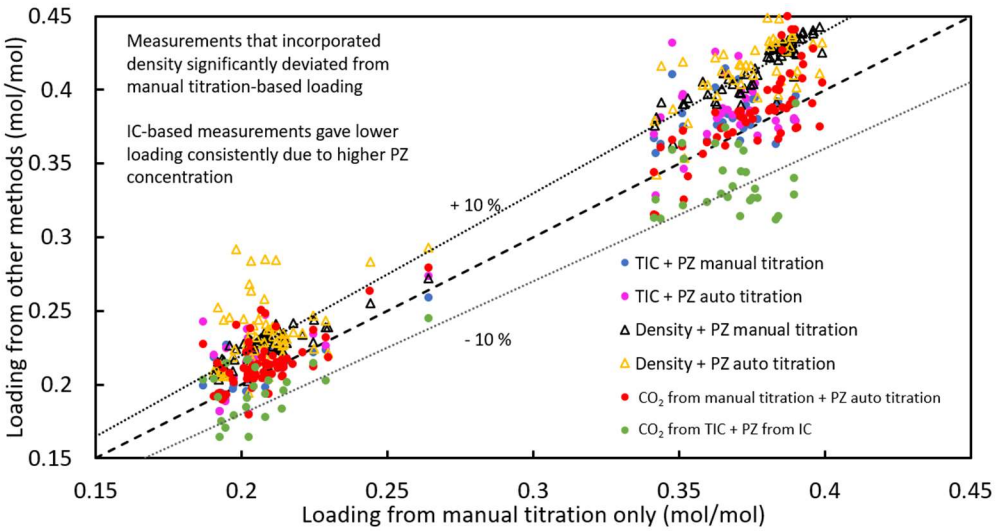

Figure 3.12: Loading measurements done 6 different ways in the SRP campaign

3.5.1.3 NCCC 2023 NGCC Campaign

In this campaign, PZ was measured using Gas Chromatography (GC), Ion Chromatography (IC), online titration at the pilot plant, and total alkalinity analysis. CO_2 content in the solvent was measured using Total Inorganic Carbon (TIC) analysis at UT Austin, TIC analysis at NCCC, density measurement combined with alkalinity-based PZ, and online titration at the pilot plant. Solvent density was measured using Mettler Toledo DE40 densitometer (Mettler-Toledo, Inc., Columbus, OH) and is related to the CO_2 content

in the solvent using correlations given by Freeman (2011). Reliable viscosity measurements at the pilot plant were not available in this campaign.

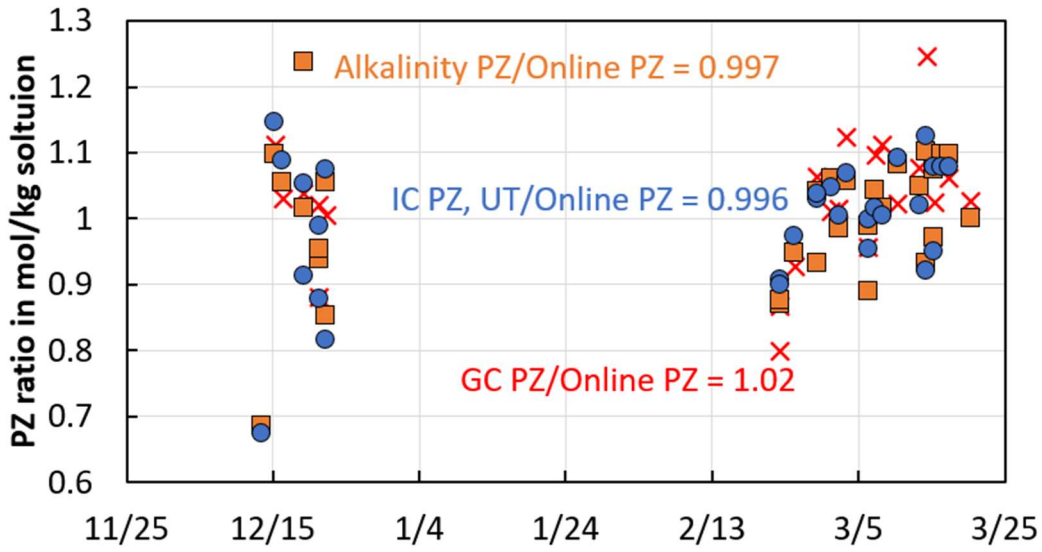

Figure 3.13: Comparison of PZ concentration using 3 different methods with online titration; IC PZ data after recalibration of instrument in April 2023

PZ measurements showed good agreement with online titration with very little deviation, as shown in Figure 3.13. The online titration and the manual titration at UT Austin had similar methods, which confirmed that the deviation in IC-based PZ observed in the SRP 2022 campaign was due to calibration issues. Figure 3.13 also confirms alkalinity-based method as a reliable to procedure to estimate PZ concentration. As seen from the SRP campaign, this method also agreed with PZ from manual titration.

However, PZ from online titration was the base method for PZ in the 2023 campaign due to its ready daily availability compared to other methods. This method also provided the data for modeling.

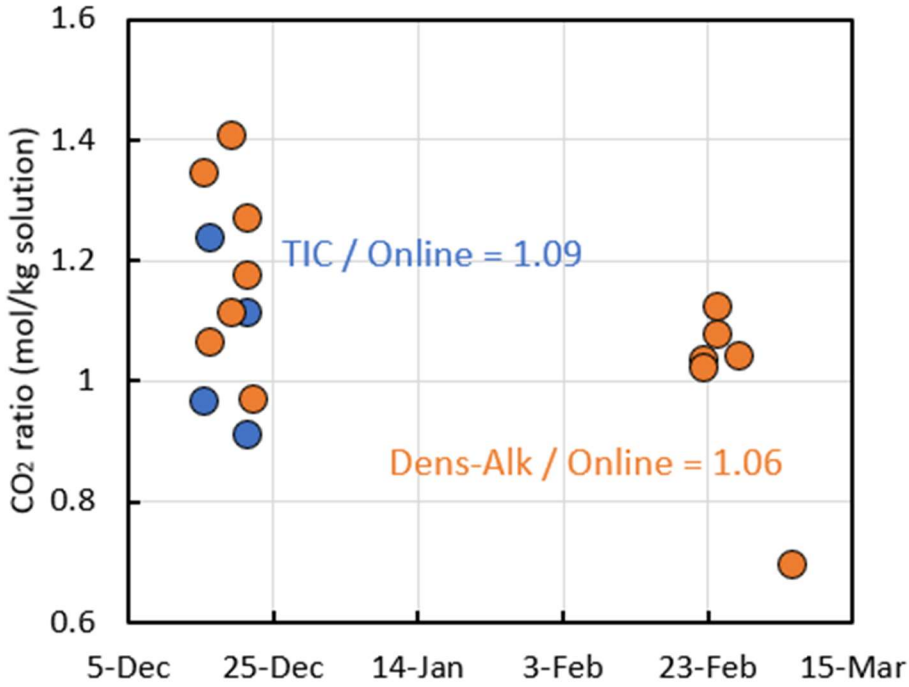

Figure 3.14: Comparison of CO_2 concentration using 2 different methods with online titration; CO_2 concentration from online titration was adjusted by +15% per Gao (2021) to match density-viscosity based CO_2 concentration

When compared with online titration, CO_2 measurements deviated more significantly than PZ measurements. TIC measurements overpredicted the online titration measurements by 9% on average and density-based measurements overpredicted the online titration measurements by 6%. The deviation in density-based CO_2 from online titration was very similar to that observed in the 2022 SRP campaign (against manual titration-based CO_2). The deviation in CO_2 loading is caused by CO_2 measurement only and not PZ, as seen from the great agreement of methods for PZ from Figure 3.13. There appears to be a bias between the measurements made for CO_2 by combining density and alkalinity, and CO_2 by online titration at NCCC/manual titration at UT Austin. This could be corrected by adjusting the density-alkalinity values by -6 to -9% for future applications.

3.5.2 Energy Performance of Stripper at Pilot Plants

3.5.2.1 NCCC 2018 Coal and 2019 NGCC Campaigns

Net heat duty was evaluated in the 2018 coal and 2019 NGCC campaigns by correcting the heat rate of the steam for 80% of the measured average heat loss. The heat loss measurement details are provided in Chapter 2. Steam heat rate was calculated using the measured flowrate of the steam and the heat of vaporization at the steam pressure, assuming saturated conditions. 60-minute intervals of data were obtained at steady state to evaluate energy performance. Net heat duty increased with capture efficiency due to the increased solvent circulation and sensible heat at higher removal. This is shown in Figure 3.15.

In the coal campaign, higher removal was achieved with a lower penalty in heat duty due to unchanging rich loading at greater removal (Gao, 2019). More scatter is seen in the NGCC data due to the larger number of parametric tests. This could also be the effect of correcting heat loss using a single averaged value rather than adjusting heat loss for variations in ambient and process conditions during the campaign.

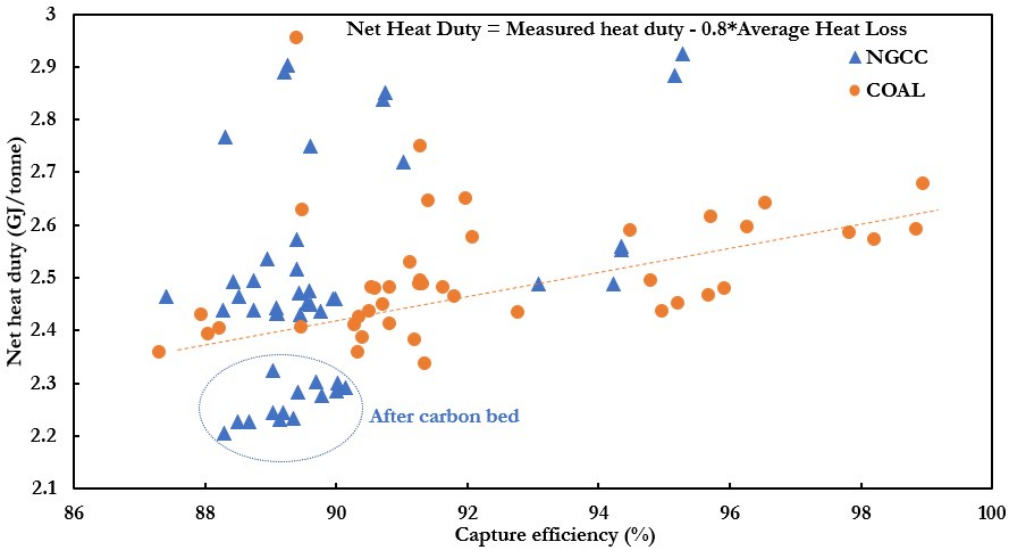

Figure 3.15: Net heat duty increased with CO_2 removal in the coal and NGCC campaigns at NCCC

At long-term conditions of 90% CO_2 removal, the average net heat duty for the NGCC and coal campaign was identical at about 2.45 GJ/tonne. At similar CO_2 removal, carbon treating in the NGCC campaign gave a lower heat duty of about 2.3 GJ/tonne which is due to increased heat exchanger performance from lower solvent viscosity.

In the test of PZAS at the UT-SRP campaign under natural gas conditions (Osaka Gas campaign), at similar CO_2 removal, the heat duty was found to be comparable at 2.67 GJ/tonne (Chen et al., 2018). In the MTR-UT Austin campaign at the UT-SRP pilot plant, the heat duty for PZAS at NGCC conditions at 90% removal was comparable at 2.21 GJ/tonne. In this campaign, the plant was also operated under coal conditions. Compared to the heat duty at NGCC conditions, the average heat duty at 90% removal for coal conditions was similar at 2.43 GJ/tonne CO_2 (Chen et al., 2019). In both these campaigns, measured heat rate was corrected for heat loss calculated from water tests.

The long-term heat duty of PZAS before carbon treating was 21-32% lower than the heat duty of the APBS solvent of Carbon Clean Solutions, with the simple stripper, at NGCC conditions, in the removal range of 85.5-92.5%. Unlike PZAS, APBS had 10-22% lower heat duty at coal conditions compared to NGCC conditions (Bumb et al., 2014), while for PZAS, the heat duty was identical at both coal and NGCC conditions. This could be the effect of not accounting for heat loss in the NGCC case where it may be more important.

Improved energy performance of PZAS was observed at higher rich loading. Increased rich loading lowered the amount of solvent circulated between the absorber and the stripper, reducing the sensible heat requirement and heat duty. This is shown in Figure 3.16. At long-term conditions of 90% removal and a rich loading of 0.40 mol/mol, the average net heat duty for the coal and the NGCC campaign is 2.45 GJ/tonne. The apparent increase of rich loading to 0.41 after carbon treating gave a lower heat duty at 2.3 GJ/tonne. This apparent increase in rich loading was due to the removal of dense and viscous solvent degradation products that skewed density and viscosity measurements used for estimating the loading.

The NGCC heat duty data in the range of 2.7-3.0 GJ/tonne at rich loading of 0.41 that deviate from the general trend belong to runs with low solvent rate where there could be poor gas-liquid distribution due to low flooding in the stripper. This results in poor mass transfer and high heat duty despite a high rich loading. Another reason could be the lower lean loading (0.18 mol/mol) of these runs compared to the typical lean loading of 0.2-0.23 mol/mol. This could have resulted in over stripping and increased the heat duty.

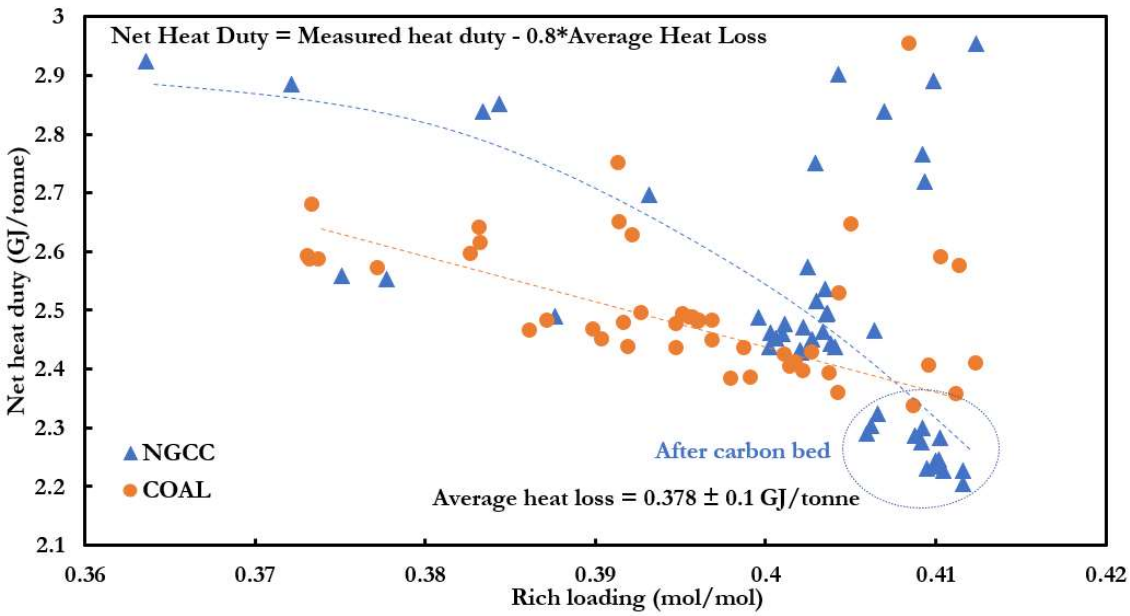

Figure 3.16: Net heat duty decreased with increasing rich loading

Carbon treating was added to the rich amine towards the end of the NGCC campaign. Carbon treating refers to the filtration of solvent using activated carbon to remove solvent degradation products. To do this, a slip stream was drawn from the rich amine exiting the absorber and sent to the carbon bed, and then recycled back to mix with the main rich solvent leaving the absorber.

The measured viscosity of the rich and lean solvent decreased due to carbon treating. This was accompanied by a decrease in alkalinity of the solvent, by the removal of alkaline degradation products. Carbon treating also improved heat exchanger performance by reducing solvent viscosity. Figure 3.17 shows the dependence of heat exchanger NTU on solvent viscosity before and after carbon treating. The NTU of the heat exchangers are defined based on the positive temperature difference of the lean solvent. The NTU calculations are shown in Equations 3.9 and 3.10.

$$NTU_{cold} = \frac{(T_{HL}-T_{WL})}{\frac{(T_{HL}-T_{HR})-(T_{WL}-T_{WR})}{LN\frac{(T_{HL}-T_{HR})}{(T_{WL}-T_{WR})}}} \quad (3.9)$$

$$NTU_{hot} = \frac{(T_{WL}-T_{CL})}{\frac{(T_{WL}-T_{WR})-(T_{CL}-T_{CR})}{LN\frac{(T_{WL}-T_{WR})}{(T_{CL}-T_{CR})}}} \quad (3.10)$$

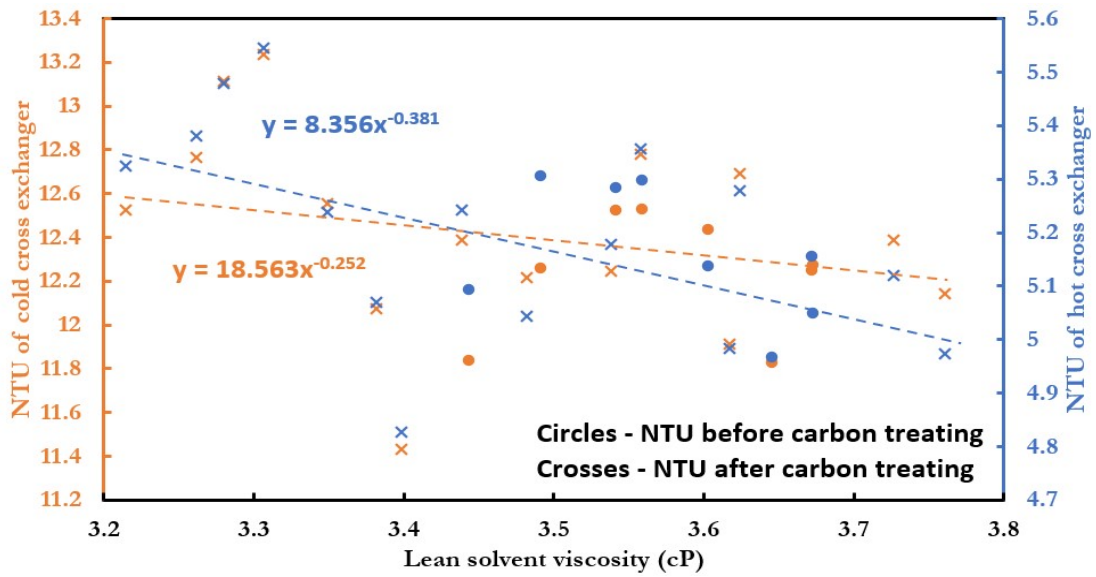

Figure 3.17: Carbon treating improved heat exchanger performance

The dependence between NTU and viscosity is similar to that described by Lin (2016). The NTU of the cold and hot exchanger increased by 1.8% and 1.5% respectively after carbon treating, but the apparent change in measured heat duty (8%) was much larger.

3.5.2.2 UT-SRP 2021-22 NGCC Campaign

Compared to the NCCC campaigns, the objective of the SRP campaign was to operate at relatively lower lean loading and measure the net heat duty at the pilot plant at these conditions. Most of the lean loading data from the NCCC campaign was between

0.21 and 0.25 mol/mol. In the SRP campaign, lean loading was controlled mostly between 0.19 and 0.21 using the stripper temperature at constant stripper pressure.

Figure 3.18 shows the combined dependence of the measured heat duty from the pilot plant on lean loading (by manual titration) and cold rich bypass flow rate. The measured heat duty has been corrected for heat loss. The figure shows that there exists an optimum lean loading between 0.2 and 0.21 mol/mol where the heat duty is between 2 and 2.4 GJ/tonne CO_2.

A similar energy consumption was measured at the National Carbon Capture Center and was reported by Rochelle et al. (2022). At a higher lean loading, the higher solvent requirement due to the lower cyclic capacity increases the sensible heat requirement of the system. At a lower lean loading, the heat duty begins to increase again due to over stripping of the solvent. This is shown at approximately constant cold rich bypass flow rate (yellow points). Figure 3.18 showed that PZAS provides favorable energy performance even at low lean loading.

Heat duty is also a function of cold rich bypass. As the flow rate of the cold rich bypass decreases, less heat is recovered by the CO_2 exchanger (lower water condensation). This, in combination with the high lean loading, gives heat duty as high as 3.8 GJ/tonne CO_2.

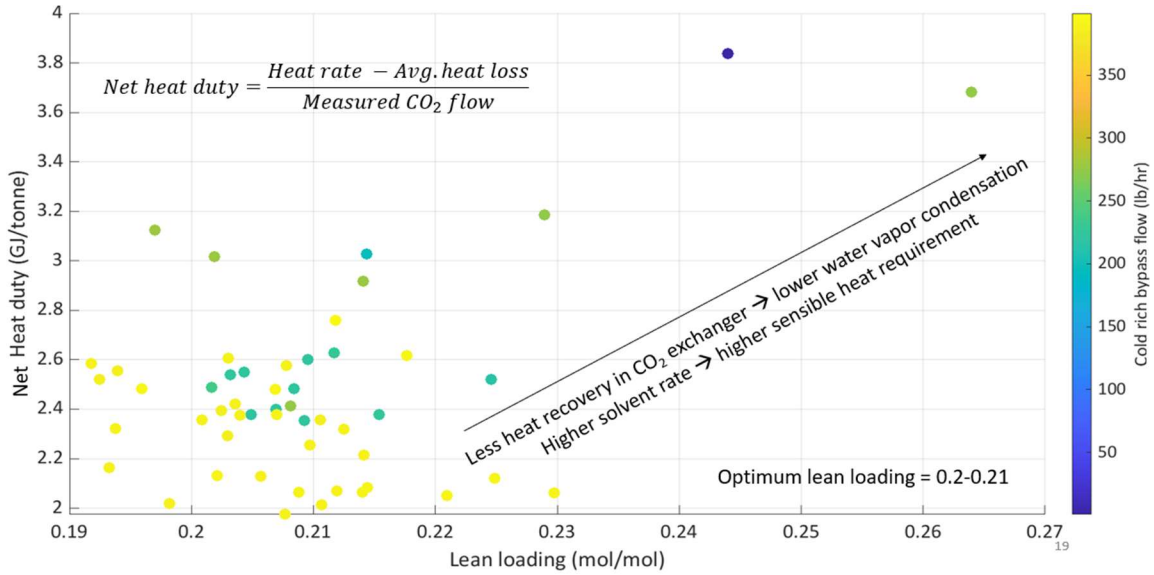

Figure 3.18: Measured heat duty depends on measured lean loading and cold rich bypass flowrate

Figure 3.19 plots the lean loading as a function of stripper sump temperature. The figure indicates that the stripper was operated at almost constant pressure of 70 psig. This figure shows that the higher lean loading points were a result of the intentional manipulation of the stripper sump temperature at constant pressure, and therefore cannot be classified as outliers. Further, there exists a smooth function of lean loading versus stripper sump temperature that is shown by the equation in Figure 3.19.

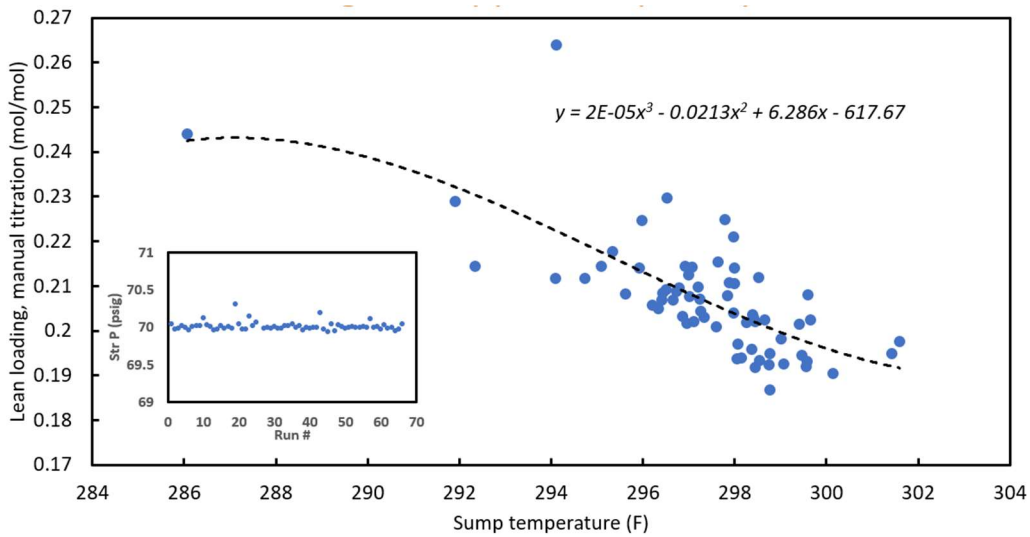

Figure 3.19: Measured lean loading is correlated with stripper sump temperature at constant pressure

3.5.2.3 NCCC 2023 NGCC Campaign

In this campaign, the objective was to measure energy performance and ensure stable operation at high CO_2 removal, low lean loading, and high total rich bypass. Heat duty of the stripper was calculated using an adjusted steam flowrate based on condensate measurements (Chapter 2). Heat duty from steam not only came from the latent heat of steam but also sensible heat due to a significant change in temperature from the steam side to condensate side in the steam heater. The absorber was operated with both I/O intercooling and PA intercooling. The operational periods for these strategies are shown in Figures 3.20 and 3.21.

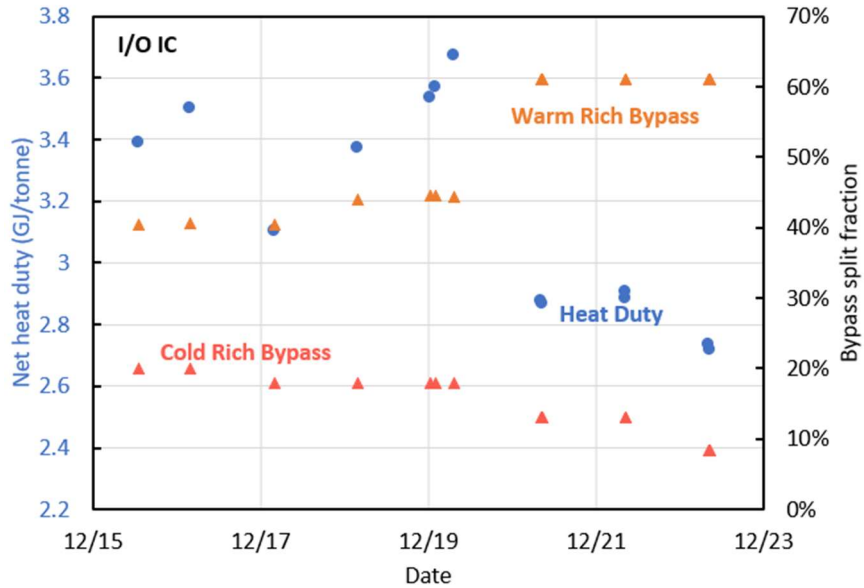

Figure 3.20: Measured heat duty during evolutionary optimization of bypass flowrates for I/O IC

Minimization of heat duty of the stripper was done in real-time through evolutionary optimization. Step changes in cold and warm rich bypass flowrates were made to observe its effect on heat duty. The direction of change that reduced the heat duty was pursued until heat duty reached a minimum.

In the in-and-out intercooling period, heat duty initially was about 3.1 GJ/tonne, at 20% cold rich bypass and 40% warm rich bypass as shown in Figure 3.20. Bypass flowrates were adjusted until the heat duty reached about 2.73 GJ/tonne at a cold rich bypass of 8.3% and warm rich bypass of about 61%. All reported heat duties were adjusted for an average measured heat loss.

After a plant shutdown, the stripper started up on February 22 with pump-around intercooling in the absorber. However, one of the pump-around loops did not extract solvent from the sump of the absorber, but instead from the middle of one of the packing sections, leading to ineffective performance compared to regular pump-around

intercooling. The cold rich bypass at the beginning was 10% of the total rich solvent, and the warm rich bypass was about 40%. Heat duty was about 3.6 GJ/tonne. A step change in cold rich bypass split fraction from 10% to 20% was made which reduced the heat duty to 2.6-2.8 GJ/tonne. High heat duty during start-up conditions could be attributed to lower PZ concentration, lower removal, and unstable operating conditions.

Around March 5, the cooling in the absorber was switched to pump-around intercooling with all the solvent extracted from the sump of the absorber for both the intercooling loops. This enhanced the rich loading in the solvent. Accompanied with this increased was a reduction in cold rich bypass that was required to minimize heat duty. Ultimately, 8% cold rich bypass and 64% warm rich bypass minimized the heat duty to 2.4 GJ/tonne.

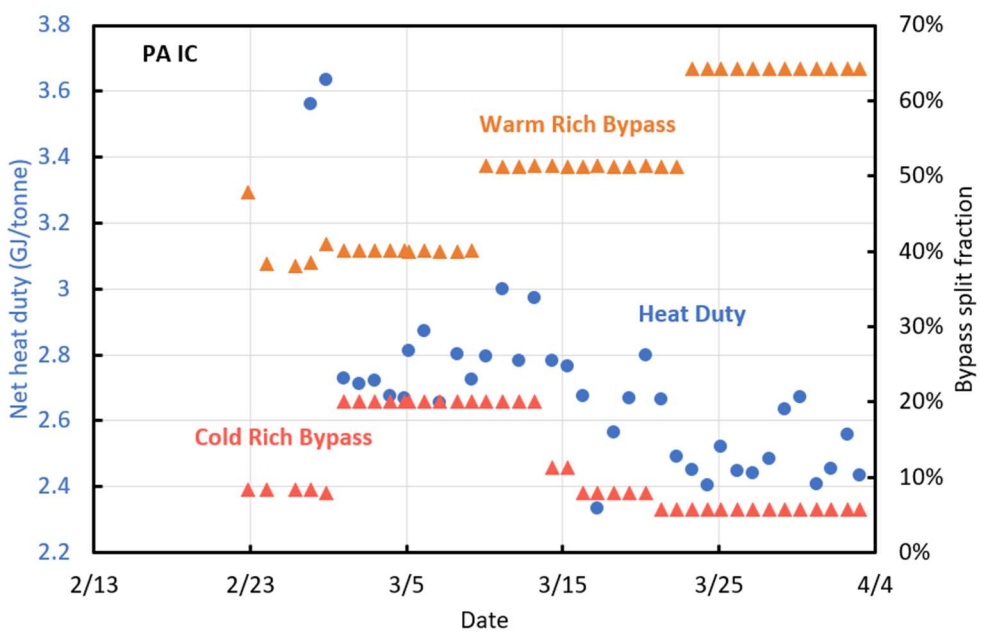

Figure 3.21: Measured heat duty during the evolutionary optimization of bypass flowrates for PA IC

In this campaign, the stripper operated without issues at high bypass split fraction of about 73% with a favorable energy performance in the removal range of 66-98%, with most of the removal around 97%. The sump temperature was maintained at about 302 °F at a stripper pressure of 66 psig.

Heat duty was also a function of the solvent loading. From Figure 3.22, high heat duty during startup was also a result of lower rich loading and higher lean loading, leading to a low cyclic capacity of the solvent. A combination of bypass control and maximization of delta loading lowered the heat duty of the process. In Figure 3.22, at about 0.2 lean loading and 0.4 rich loading, the heat duty was 2.4-2.7 GJ/tonne. The data at 2.4 GJ/tonne were more impacted by the high total rich bypass that led to a step decrease in heat duty at the same cyclic capacity. The total rich bypass for these data varied from 70-73.2% and the cold rich bypass was optimized at 5 to 9%.

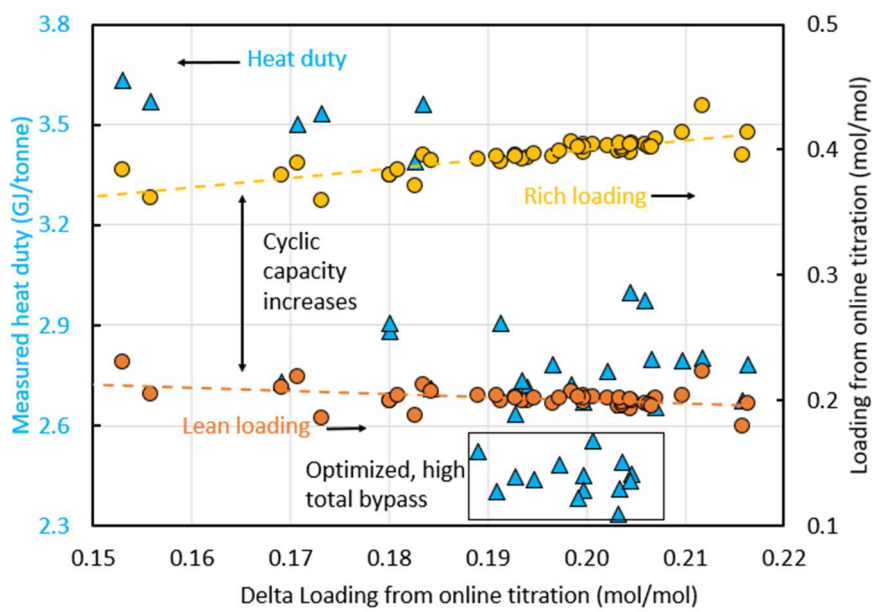

Figure 3.22: Measured heat duty as a function of solvent loading from online titration

An increase in total rich bypass was related to a decrease in heat duty, as was reported by modeling studies by Suresh Babu and Rochelle (2022) with the hot rich bypass. This decrease in heat duty is linked to an increase in warm rich bypass temperature, which leads to a higher total rich bypass temperature and vapor fraction. These effects are shown in Figures 3.23 and 3.24.

Figure 3.23 shows that a high bypass split fraction makes the total rich bypass hotter than the stripper overhead gas temperature (orange data points). Low heat duty is associated with a negative temperature difference in the overhead of the stripper (between -5 and -10 °F). This indicates that enhancement of energy performance can occur if the temperature of the total rich bypass is raised above its bubble point at the stripper pressure, giving rise to significant vapor in this line. The high heat duty data points at around 60% total rich bypass Figure 3.23 are affected by startup conditions with lower delta loading.

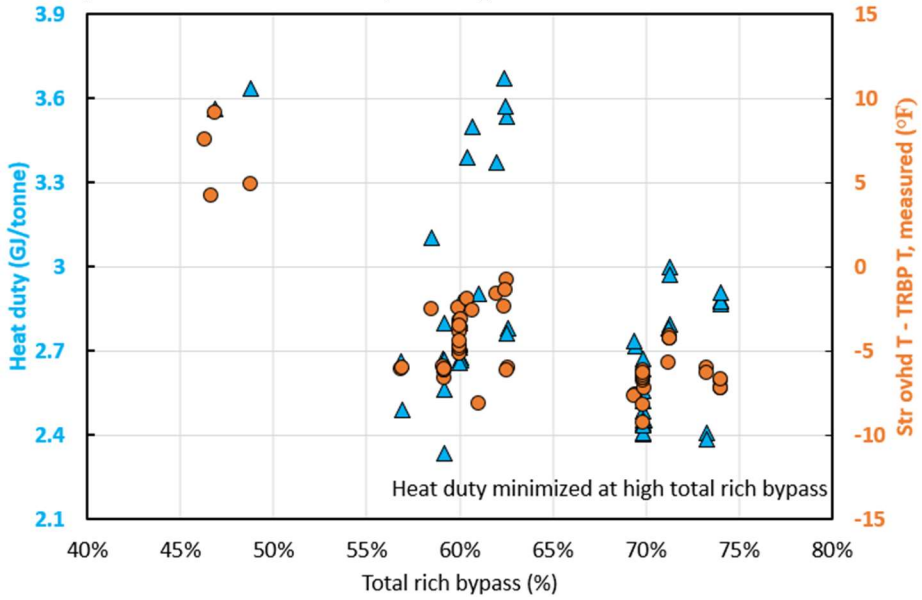

Figure 3.23: Effect of total rich bypass split fraction on measured heat duty and stripper overhead temperature difference

Figure 3.24 shows that a high total rich bypass gives a higher vapor fraction in the total rich bypass. The vapor fraction was predicted by the model at the point where the total rich bypass enters the stripper. While this was strictly a model result, the total rich bypass temperature was specified to be almost equal to that of the measured value. Given that the rich solvent properties were specified using measured rich loading, temperature, pressure, and temperature around the cold heat exchanger, the vapor fraction in the total rich bypass line can be used as a good estimate for the vapor fraction in this pipe at NCCC.

Suboptimal bypass brings the total rich bypass to its bubble point (0 vapor fraction). This corresponded to using a large cold rich bypass. For these data, the cold rich bypass leaving the CO_2 exchanger was colder than the other points (in blue) due to poor preheating. This suppressed the flashing in the total rich bypass.

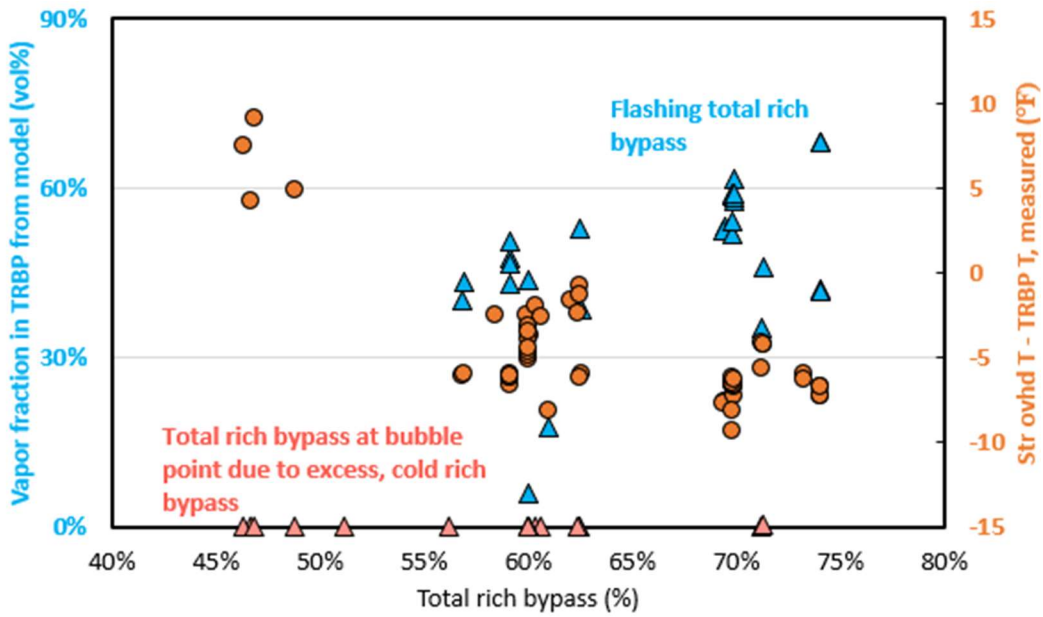

Figure 3.24: Effect of total rich bypass split fraction on estimated vapor fraction in the total rich bypass; pink triangles represent total rich bypass at bubble point with suboptimal cold rich bypass

Combining the conclusions from Figures 3.23 and 3.24 shows that energy performance at low lean loading and high removal under NGCC conditions will benefit from total rich bypass not at its bubble point, but with significant vapor content. The large volume fraction of vapor in this line however could result in slug, churn, or annular flow which could cause operational disturbances, although none have been identified thus far in this campaign. A high total rich bypass reduced the heat duty by promoting flashing in the total rich bypass line, but this was only valid for an optimum cold rich bypass.

To minimize the heat duty, the cold rich bypass must be chosen to both cool the CO_2 vapor stream adequately and sufficiently preheat the cold rich bypass leaving the CO_2 exchanger. The latter implies that the cold rich bypass be adjusted to recover as much heat as possible from the gas-side water vapor. This implies the importance of a hot-side pinch in the CO_2 exchanger. Figure 3.25 compares the cold CO_2 temperature that leaves the CO_2

exchanger (TI40518), the heated cold rich bypass temperature (TI40502), and the hot gas inlet temperature (TI40503) around the CO_2 exchanger as a function of the cold rich bypass split fraction.

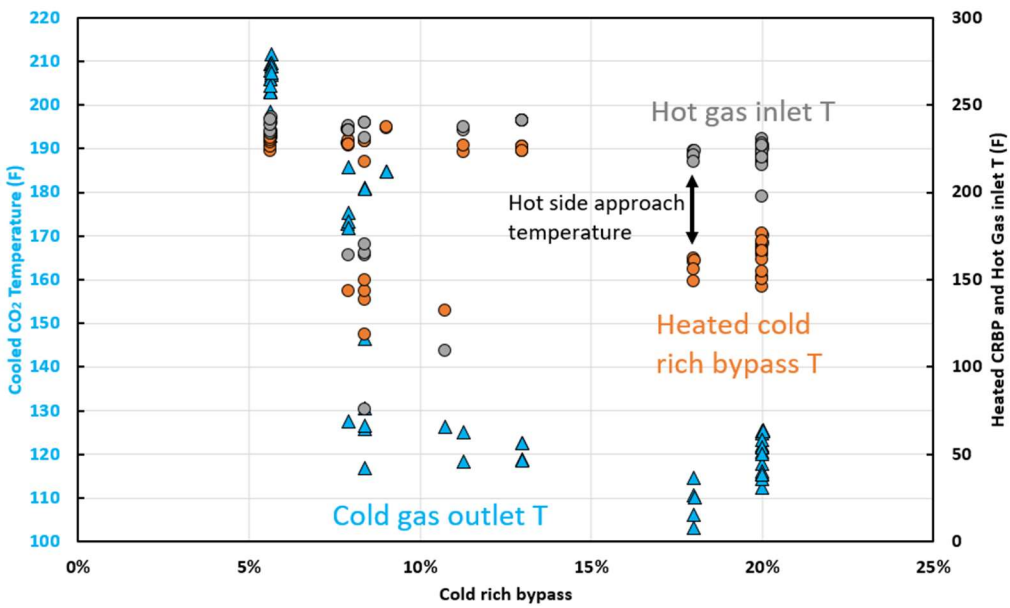

Figure 3.25: Temperatures around the CO_2 exchanger as a function of cold rich bypass split at NCCC

Figure 3.25 shows that the temperature of the gas stream leaving the CO_2 exchanger is sensitive to the cold rich bypass. While using a high amount of cold rich bypass cools the CO_2 stream effectively by condensing most of the water vapor from the gas, it does not effectively preheat the cold rich bypass, which suppresses flashing in the total rich bypass and increases heat duty. For example, at a cold rich bypass split of about 18%, the cooled CO_2 temperature is at its apparent minimum between 100 and 110 °F, but the hot-side approach temperature in the CO_2 exchanger is large. The heated cold rich bypass temperature is 150 °F. This shows that the optimum cold rich bypass value is not one that

cools the gas steam to the lowest possible temperature. For data points between 5 and 8% cold rich bypass, the CO_2 is cooled to 180-210 °F while there is a hot-side pinch in the CO_2 exchanger shown by the closeness of points in grey and orange. From Figure 3.25, it is the cold rich bypass fraction that yielded the lowest heat duty in this campaign.

The warm rich bypass must be optimized to elevate the total rich bypass temperature above the gas temperature leaving the stripper, as shown in Figure 3.24. The bypass flowrates can be controlled automatically by adjusting the cold rich bypass to control the cooled CO_2 temperature between 180-210 °F and by adjusting the warm rich bypass to make the stripper overhead temperature difference to be about -5 to -10 °F (total rich bypass temperature minus the overhead gas temperature).

3.6 MODEL VALIDATION

3.6.1 NCCC 2018 Coal and 2019 NGCC Campaign

112 steady state runs from the coal and NGCC campaign were used to validate the Independence™ model. Figure 3.26 shows the ratio of predicted heat duty to the measured net heat duty as a function of rich loading calculated from density and viscosity. The model underpredicts measured heat duty with a mean error of 9%. Model performance is affected by inherent defects in the model as well as the measured heat loss. Higher values of heat loss will reduce the model error while low values of heat loss will increase the model error. Moreover, heat duty was corrected in the campaign for a constant value of heat loss but not adjusted for the effects of ambient conditions or process conditions. Inherent defects in the model may include incorrect representation of column hydraulics at different solvent rates and incorrect estimation of heat of absorption or heat of reaction of ionic species in the liquid phase.

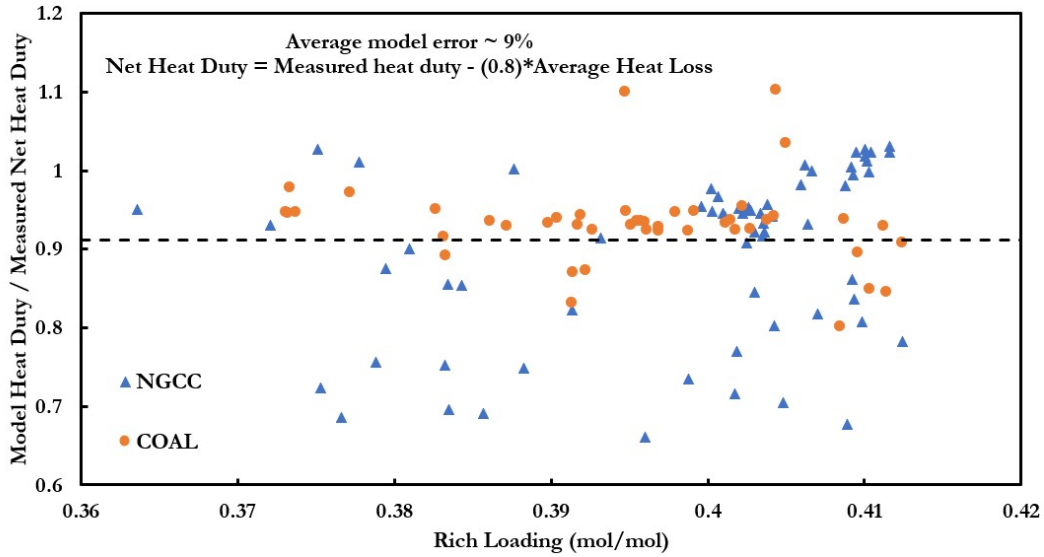

Figure 3.26: Model underpredicts net heat measured heat duty at NCCC with a 9% average error

In these campaigns, both net heat rate and CO_2 flowrate were predicted reasonably well by the rate-based model. The model predicted heat duty using two different mass transfer models. The Song model differs from the Wang model in its ability to predict liquid-phase mass transfer coefficient as a function of liquid viscosity. The model also accounts for the effect of column height on mass transfer. Select steady state runs were modeled using the Song model to cover the entire range of steam heat rate in both the coal and NGCC campaigns.

Figure 3.27 reveals that compared to the Wang model the Song model only slightly changed the predicted heat rate. A similar effect is observed in the comparison of error in heat duty predictions from Figure 3.28. Compared to the Wang model, the Song model only slightly reduced the deviation between the modeled and measured net heat duty at NCCC, possibly by accounting for liquid viscosity and packing height effects.

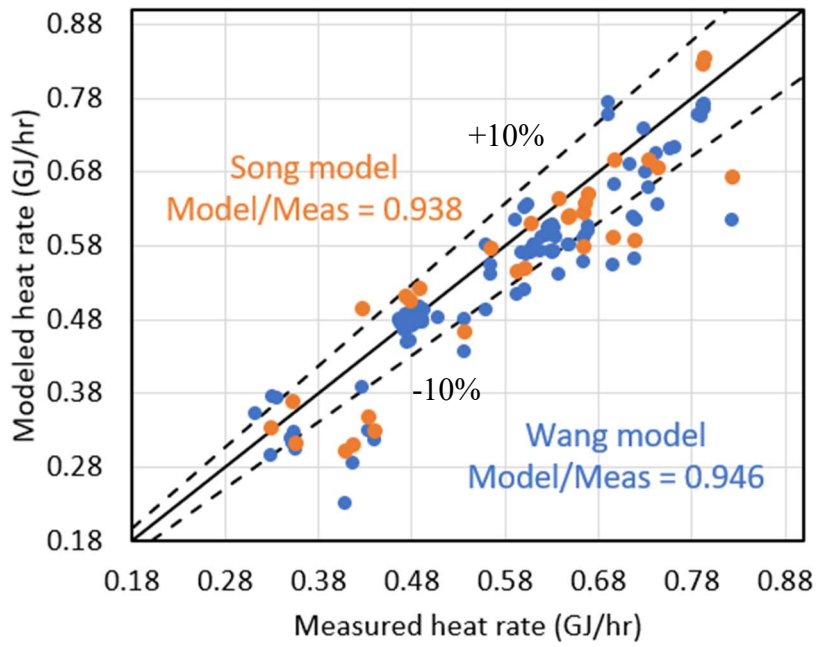

Figure 3.27: Error comparison in steam heat rate between two mass transfer models for NGCC and coal campaigns

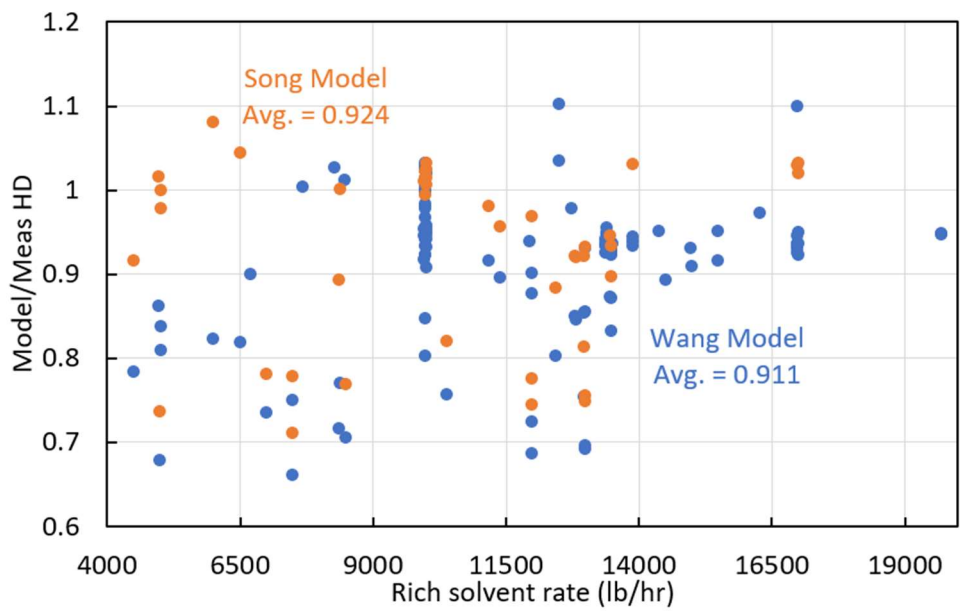

Figure 3.28: Comparing error in heat duty for NGCC and coal campaigns with two mass transfer models

The long-term steady state data from each campaign was used to validate the stripper temperature profile. There were only three temperature measurements in the stripper column at NCCC in the 2018 and 2019 campaigns. Figure 3.29 shows the validation of the temperature profile in the NGCC campaign. Steady state run #72 was used to validate the temperature profile. The rich solvent flow rate was about 10,000 lb/hr, the cold rich bypass was 6%, the warm rich bypass was 21%, the stripper sump temperature was 302 °F at 77 psig, rich loading was about 0.41, and lean loading was about 0.23.

The temperature measurements appeared to agree more with the liquid temperature profile than the vapor temperature profile. The average error with the liquid temperature profile was about 2% compared to about 6% with the vapor temperature profile. The model predicts a bottom-side temperature pinch in the column as indicated from the measurements, which validates the high-temperature thermodynamics of the model. The deviation in temperatures at the colder end of the column could be indicative of the incorrect representation of mass transfer or reaction kinetics in the column. The CO_2 flowrate predicted by the model is close to that measured, making the general temperature profile in the column predictable by the model, due to approximately similar vapor-to-liquid ratio in both cases.

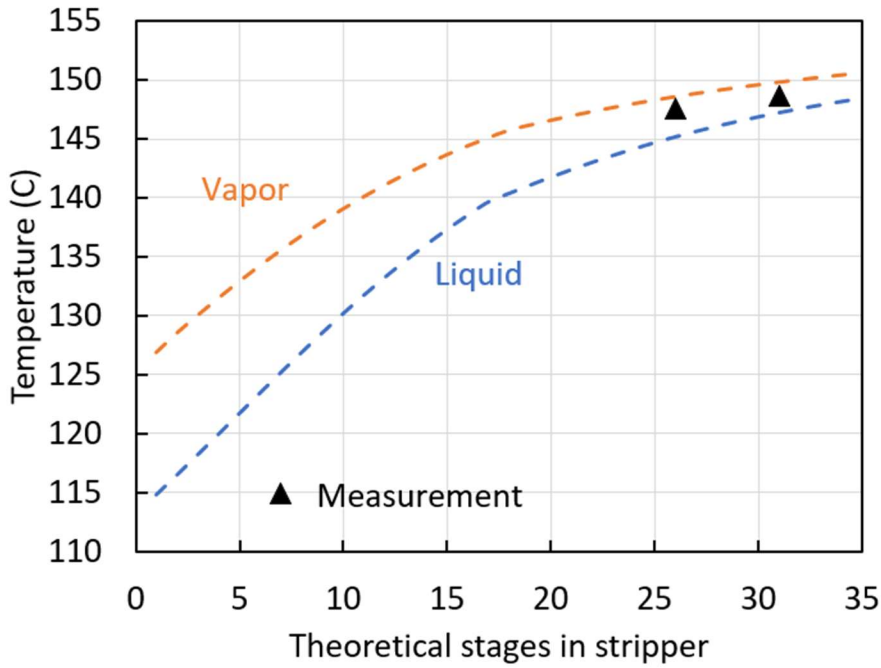

Figure 3.29: Validating stripper temperature profile in the NGCC campaign using the rate-based model, run 72, wetted area correction factor = 0.16, stage 1 is the top, stage 35 is the bottom; stages represent computational segments

For the coal campaign, run #52 at steady state was used to validate the stripper temperature profiles. The rich solvent flowrate was about 17000 lb/hr, the sump temperature was 302 °F, the cold rich bypass fraction was 6.2%, the warm rich bypass fraction was 28%, the stripper pressure was 77 psig, the rich loading was 0.395, and the lean loading was 0.24. Similar to the NGCC case, the measured temperatures agreed more with the liquid temperature profile of the column. The average error with the liquid temperature was 1% and the vapor temperature was 3%. There was no pinch observed in the column either from measurements or the model and there was general agreement between the temperature profiles. This is shown in Figure 3.30.

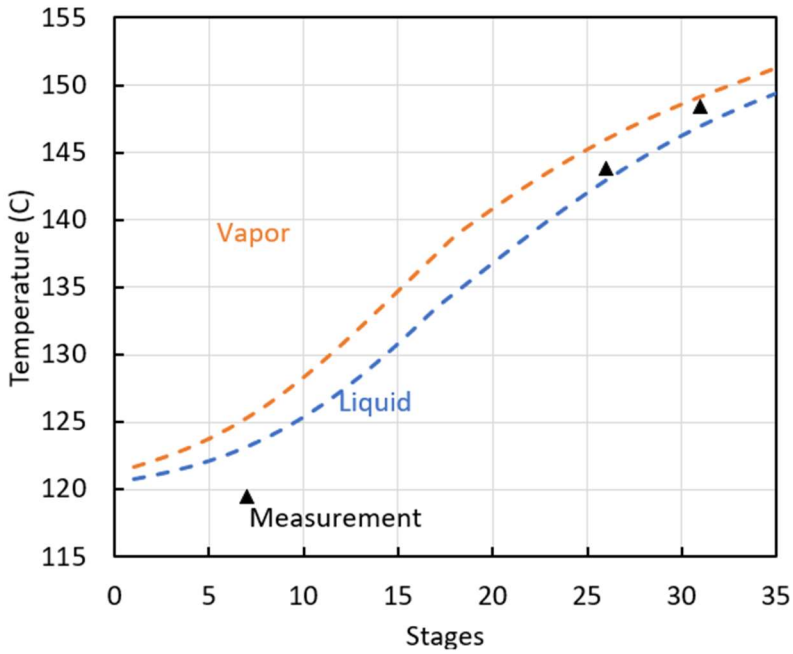

Figure 3.30: Validating stripper temperature profile in the coal campaign using the rate-based model, run 52, wetted area correction factor = 0.16, stage 1 is the top, stage 35 is the bottom; stages represent computational segments

3.6.2 NGCC NCCC 2023 Campaign

Model prediction of heat duty is shown in Figure 3.31. The rich loading obtained from either density-alkalinity analysis in the lab or online titration at NCCC was used to specify rich solvent properties in the rate-based model. In the absence of online titration data, the density-alkalinity values were used. The figure shows that the rate-based model can predict the heat duty well for three different intercooling strategies that were used in this campaign. The average ratio of the predicted heat duty to the measured heat duty was about 1. The modeled heat duty also tracks the measured heat duty with time, indicating that the rate-based model predicts energy performance as a function of changing cold and warm rich bypass split fractions.

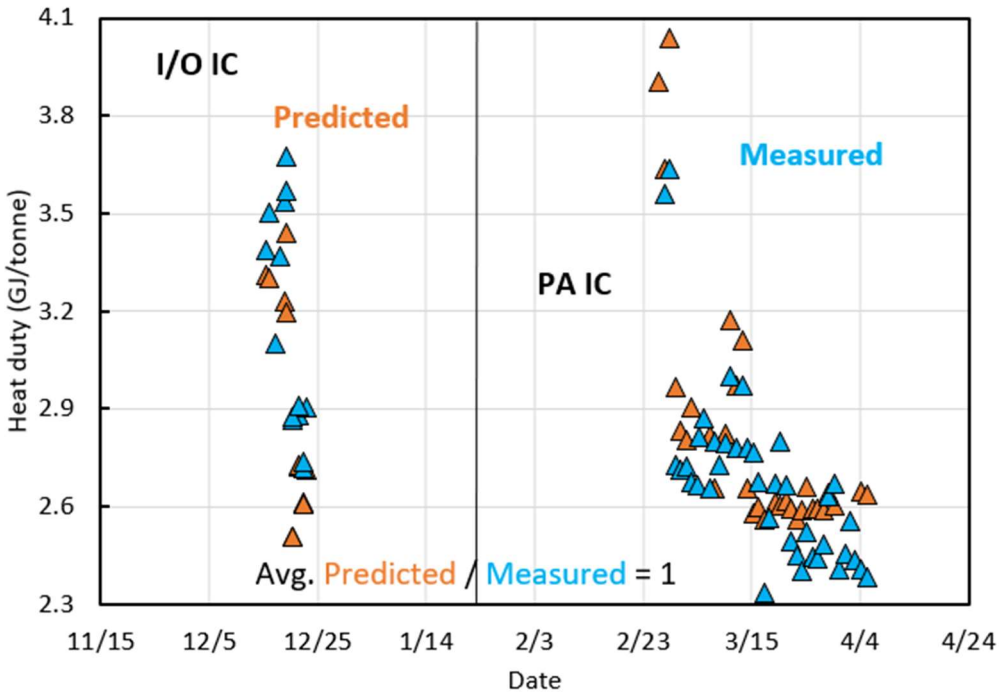

Figure 3.31: Model predicted heat duty and measured net heat duty versus time for NCCC 2023 campaign; blue points represent measured values; orange points represent model-predicted values

Figure 3.32 breaks down the error in heat duty to its individual components – error in CO_2 flowrate and error in heat rate. Both CO_2 flowrate and heat rate were overpredicted by the model by 8.6% and 9.5% respectively which makes the ratio of predicted to measured heat duty (normalized by CO_2 flow rate) approximately 1. The deviations, however, accounted for startup conditions as well where the piperazine concentration was not constant and the system was not at steady state. At startup conditions (right after 12/5 and before 3/5), the error in heat rate and CO_2 flowrate were larger compared to later in the campaign. Towards 4/4, the measured heat duty is constantly lower than the predicted heat duty which was due to a good agreement between measured and modeled CO_2 flowrate but a higher predicted heat rate compared to a measured heat rate. This could be related to

differences between the equilibrium constant predicted by the equilibrium model and the kinetics model at high temperature, or the mass transfer model.

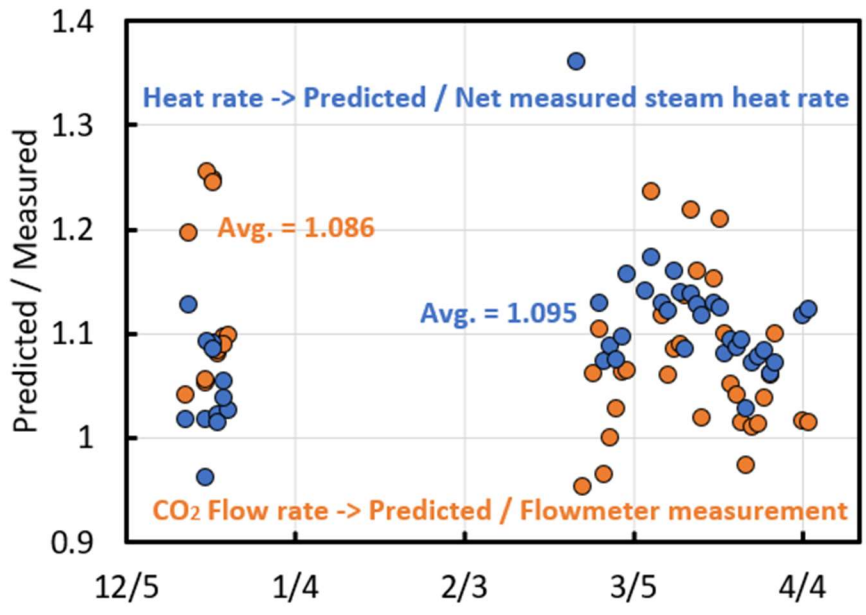

Figure 3.32: Ratio of model-predicted to measured heat rate (blue) and CO_2 flowrate (orange)

Figure 3.33 compares the solvent CO_2 loading measured using online titration at NCCC, density combined with alkalinity measurements at UT Austin, and temperature-pressure-based lean loading predictions made by the rate-based model. The stripper sump temperature and pressure were specified to the rate-based model using time-averaged measurements made at the pilot plant at steady state. The thermodynamics model uses this pressure and temperature to calculate a lean loading, which has been compared to measured values from UT Austin and NCCC.

Historically, at NCCC, loading was also measured by coupling online density and viscosity measurements using correlations provided by Freeman (2011). In the absence of

reliable viscosity measurements in this campaign, the online titration-based CO_2 wt % was calibrated to match that of density-viscosity, as proposed by Gao (2021). The online titration-based CO_2 measurement acted as a proxy for the density-viscosity measurements of CO_2 after applying a constant 1.15 correction factor. Online titration-based PZ measurement was not adjusted.

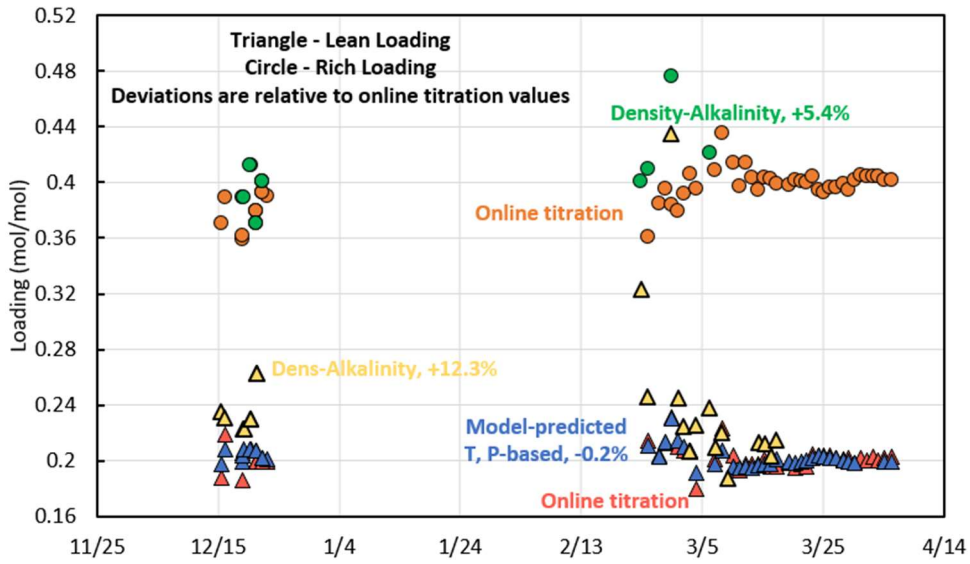

Figure 3.33: Loading comparison from different methods used in the NGCC NCCC 2023 campaign

Figure 3.33 shows that there is great agreement between the lean loading predicted by the model and the online titration at NCCC, with a deviation of only 0.2% on average. There exists a larger deviation between the density-alkalinity-based lean loading and the model-predicted lean loading, with the density-alkalinity values greater by 12.3%, but this includes the two outlier data points in the yellow triangles. Similarly, density-alkalinity-based rich loading was higher than that from online titration by 5.4%. Density-alkalinity-based lean loading was also higher than the model-predicted lean loading by 11.6%. Given

that the PZ measurements all agreed well in this campaign, the overprediction of loading from density-based method was related to the overprediction of CO_2 only, as shown by Figures 3.13 and 3.14.

The stripper temperature profile predicted by the rate-based model is shown in Figure 3.34. Also plotted are temperature measurements taken from 6 different locations around the stripper. These include temperature measurements in the sump, column, overhead vapor, and total rich bypass. There is a general agreement between temperatures measured and predicted by the model. The sump temperature measurements agree more with the vapor temperature predictions than with the liquid temperature predictions. The rest of the measurements in the column agree more with the liquid temperature predictions.

A new temperature sensor (TI40513) was added at the pilot plant to measure the stripper overhead gas temperature at the top of the stripper. Interestingly, this temperature agrees more with the liquid temperature predicted by the model as well and is close to the prediction of the temperature of the total rich bypass solvent. This indicates that the gas-phase mass (and heat) transfer coefficient is underpredicted by the model, leading to excessive heat leaving with the vapor, thereby predicting a higher vapor temperature. This indicates that the vapor and liquid at the top of the stripper are close to each other in reality, indicating a pinch. The model, on the other hand, predicts a larger temperature difference between the liquid and the vapor. This may also be related to kinetics/reaction equilibrium.

This is another reason for the higher heat duty predicted by the model compared to measured value in the long-term case. The vapor leaving the column could still contain uncondensed water vapor (thus the higher temperature), but the measurements indicate a lower gas temperature and a temperature pinch. The Song mass transfer model appears to be adequate at predicting liquid-side temperatures in the column.

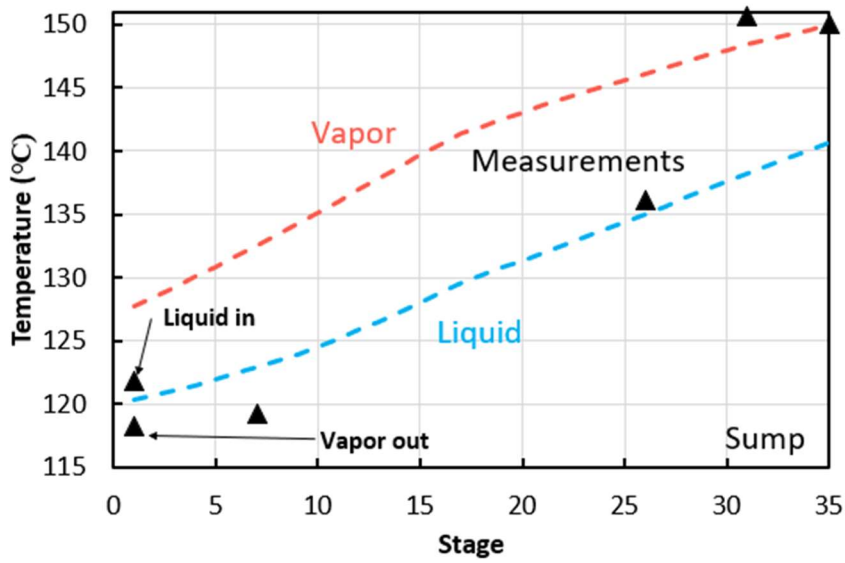

Figure 3.34: Validation of stripper temperature profile for a long-term pump-around intercooling case (Run 58); stages represent computational segments

3.7 OVERALL MODEL ERROR ANALYSIS

This section analyzes the model error in heat duty across all pilot plant campaigns conducted for PZAS. The model error has been evaluated for a wide range of rich solvent rates, ambient conditions, and liquid loads in the stripper from the SRP and NCCC pilot plants. Heat rate at each pilot plant was corrected for the average heat loss. The Song (2017) mass transfer model and Independence™ (Frailie, 2014) thermodynamic model were used in Aspen Plus®. Data from the NCCC 2018, 2019, 2022-23 campaigns and SRP 2021-22 campaign were combined with older data obtained from the SRP 2018 campaign (MTR (4-20% CO_2) and Osaka Gas (4% CO_2)) and SRP 2015 campaign at coal conditions (Lin, 2016).

Figure 3.35 plots the ratio of modeled heat duty to the measured net heat duty as a function of specific liquid rate in the stripper. The specific liquid rate was calculated using

the mass flowrate of the total rich bypass, its density, and the cross-sectional area of the stripper for each pilot plant run using the rate-based model at the point of entry at the top of the stripper column (theoretical stage 1).

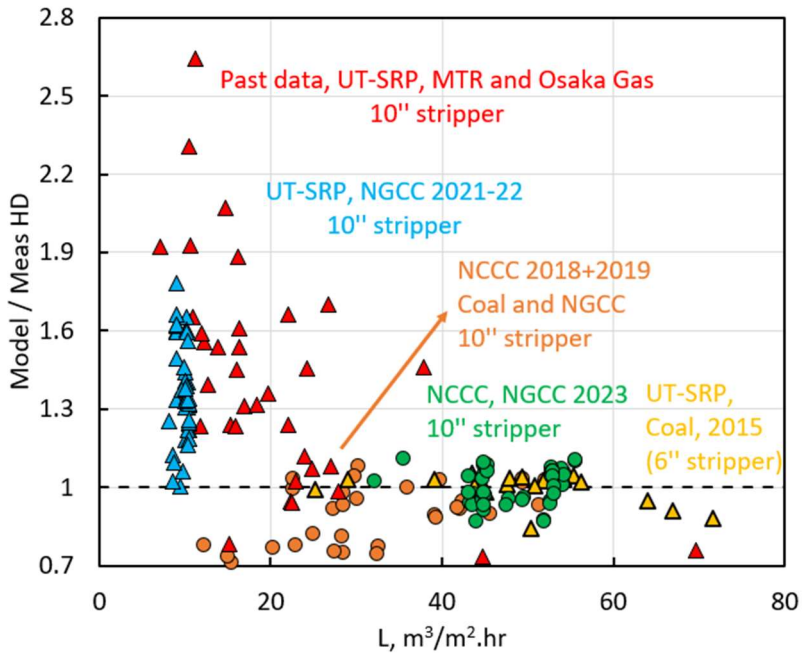

Figure 3.35: Model error across all pilot plant campaigns with PZAS as a function of liquid load in the stripper; measured heat duty corrected for heat loss

The result suggests that the model performs poorly at low liquid flux, typically observed at UT-SRP operating conditions. Model predictions are consistently better at higher liquid flux. One possible explanation for the improved performance of the model at high liquid flux is the better ability of the mass transfer model to predict the film-wetting of packing in the stripper. At lower solvent rates, there may be droplet wetting on the packing that is not accounted for by the Song mass transfer model. The model assumes film-wetting regardless of the liquid rate (Abreu, 2022). In the presence of droplets, the velocity or Reynold's number of the droplets become more significant than that of the bulk-

liquid that is being used by the mass transfer model. The vapor or liquid flow at low liquid load may also be closer to laminar than turbulent, as assumed by the model. The model for k_l was regressed over a healthy range of liquid load ranging from 6 to 73 m^3/m^2 h, but the k_G model was only regressed at two distinct values of vapor velocity (24 and 37 m^3/m^2h). Moreover, the k_G model uses a 0.5 exponent on gas diffusivity as opposed to the 0.67 exponent from seen in literature (Bravo et al., 1985; Rocha et al., 1996; Billet and Schultes, 1993). The error in the mass transfer model could be more of an issue with the k_G model than the k_L model. This is also reflected in the validation of temperature profile for the NCCC 2023 campaign as explained previously in section 3.6.3.

Interestingly, at the UT-SRP pilot plant, data taken from Lin (2016) had much smaller model error compared to the UT-SRP 2018 and 2021-22 campaigns. The liquid flux in the 2015 campaign (Lin, 2016) was higher (yellow data) because of the smaller stripper diameter (0.54 ft), compared to 0.83 ft in the later SRP campaigns (red and blue data). This shows a clear dependence of model performance on liquid and vapor rates in the stripper.

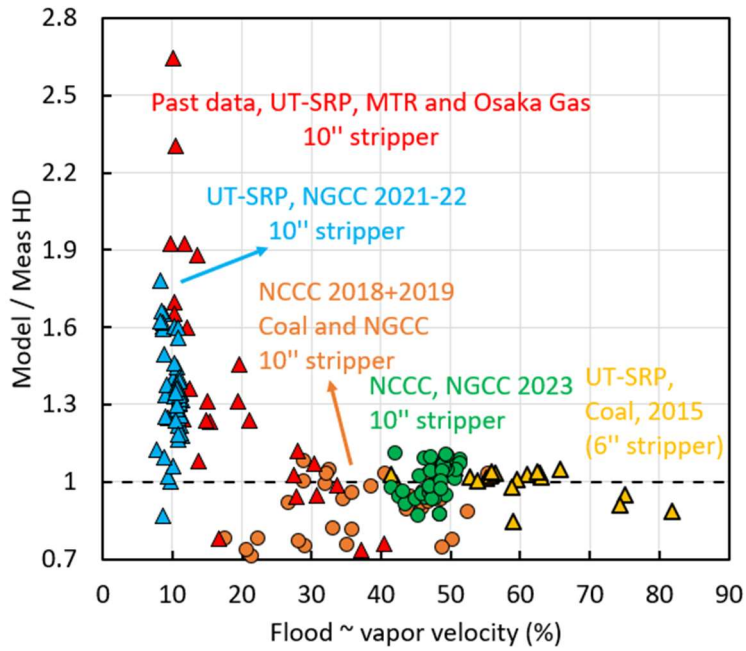

Figure 3.36: Model error across all pilot plant campaigns with PZAS as a function of flooding in the stripper; flooding estimated from the model; measured heat duty corrected for heat loss

The low liquid flux in the stripper column also resulted in low flooding in the column as predicted by the rate-based model for UT-SRP. Figure 3.36 shows that below about 20% flood, the mass-transfer model appears to break down and underpredict the wetted area of packing, resulting in consistently higher heat duty compared to the measured value. Flooding (or vapor velocity) in the stripper appears to be well correlated with the liquid load in the stripper column, as shown by Figure 3.37, which explains the similar trend in error from Figures 3.35 and 3.36.

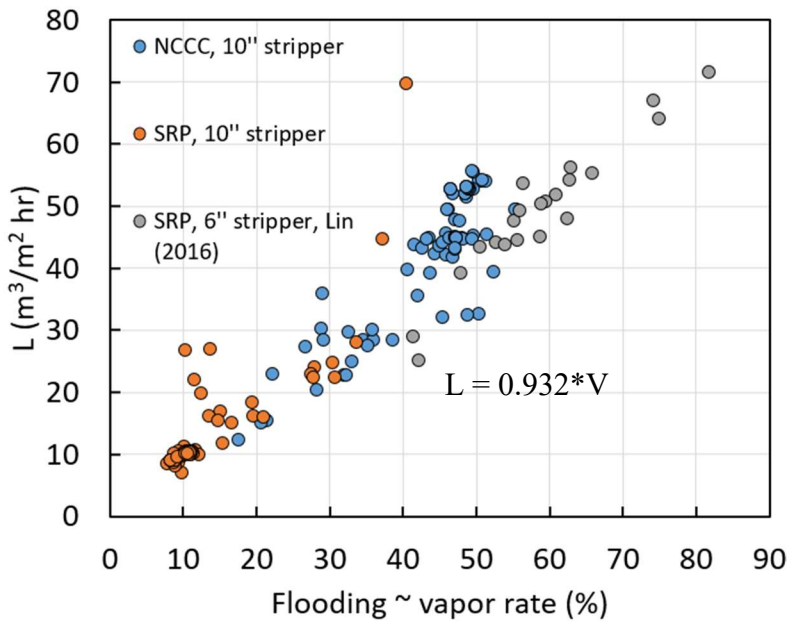

Figure 3.37: Liquid load and flooding in the stripper are well correlated; smaller stripper column resulted in higher liquid loading, flooding and better model performance

Error in heat duty at UT-SRP was also compounded by a disagreement between modeled and measured values of CO_2 flowrate, which relates to issues with the ability of the thermodynamic model to predict lean loading at a measured temperature and pressure. The disagreement in heat rate and CO_2 flowrate are less significant at NCCC than at SRP, making the overall model error much smaller for this pilot plant. This is seen by a variance in model error for the SRP data at approximately constant liquid and vapor load in the stripper. The above analyses show that at high liquid loads (NCCC or smaller diameter stripper), the model error is a weaker function of mass transfer and could be more related to thermodynamics and the handling of heat loss. At lower liquid loads, the mass transfer also compounds the error in addition to thermodynamics and heat loss.

The Independence model works adequately at predicting heat duty at two different pilot plants at high liquid loads but performs poorly at liquid loads below 20 m^3/m^2 h. The

model can be used for design of stripper columns with high solvent rate/bypass rate and/or smaller diameters.

3.8 MODEL RECONCILIATION

An adjustable heat loss measurement was used to reconcile the difference between the modeled and measured heat duty. This was done by minimizing the difference between the measured and modeled heat duty for every steady state run in the NCCC and SRP campaigns. This reconciliation lumps any error in mass and heat balance into the heat loss value.

Figure 3.45 shows that the adjusted heat loss is an inverse function of ambient temperature for the NCCC data. This suggests that the driving force for heat loss is lower as ambient temperature increases. Heat loss must be corrected as a function of ambient temperature rather than using an average value for the pilot plant campaigns at NCCC.

For the SRP pilot plant, the low heat loss value suggests that heat loss could be ignored at low steam rates. The heat loss measurements made from water agree well with the adjusted values shown in Figure 3.45, validating the measured data. This also serves as an alternate method of estimating heat loss during solvent runs in the pilot plant campaign, instead of relying on water-based data.

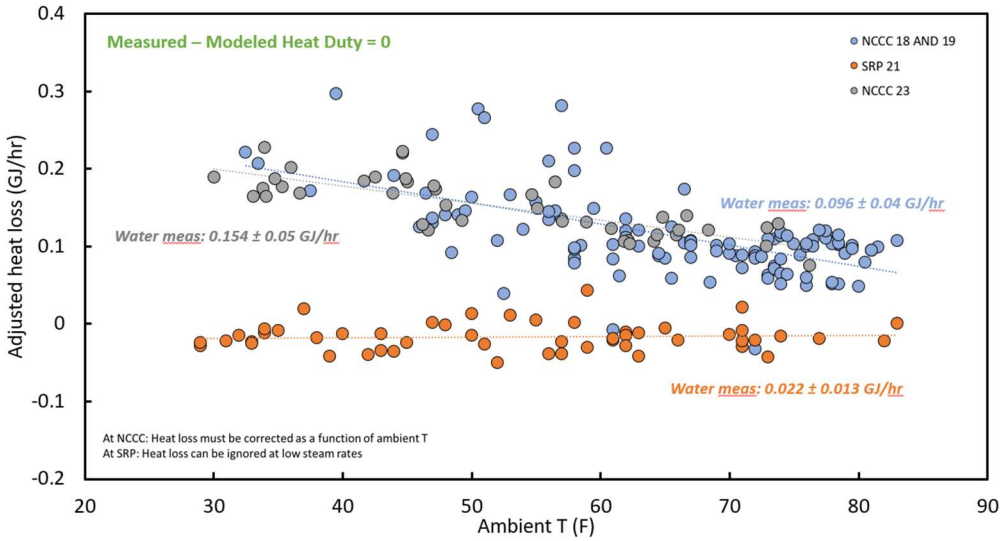

Figure 3.38: Adjusted heat loss for perfect model reconciliation of heat duty for SRP and NCCC data

While heat loss is not expected to be a strong function of ambient temperature, the trend shown in Figure 3.45 could be attributed to error in mass and heat balance. For example, in the NCCC 2023 campaign, the stripper overhead water flowrate measured using a flow measurement (FI20248) was often greater than the water flowrate predicted by the model.

At low ambient temperature, large amount of heat loss could occur in the stripper which results in internal water condensation, leaving less water detected by the downstream flowmeter. This effect could be lesser at a higher ambient temperature. At the UT-SRP campaign, differences in CO_2 flowrate between the model and the measurement were also lumped into heat loss, which lead to the reconciled heat loss being negative (heat gain) at times. This also led to a lack of ambient temperature dependence of measured heat loss.

3.9 CONCLUSIONS

Solvent Composition Analysis:

- In general, the methods for liquid PZ were consistent with each other at both the SRP and NCCC pilot plants. However, there were notable variations in the estimated CO_2 in the solutions and subsequently in the estimated loading, depending on the specific method used.

Measured Energy Performance

- After a correction for heat loss, the long term heat duty at NCCC in both coal and NGCC conditions at 90% removal was 2.4 GJ/tonne. In the NGCC campaign, heat duty was reduced to 2.2 GJ/tonne at long term conditions using carbon treating of solvent.
- Carbon treatment improved heat exchanger performance by removing bulky degradation compounds from the solvent that contributed to increased solvent viscosity.
- In the SRP 2021 campaign, heat duty was measured at low lean loading between 0.19 and 0.21 mol/mol. Measured net heat duty was between 2 and 2.4 GJ/tonne at long term conditions and was positively correlated with lean loading and inversely correlated with cold rich bypass flow rate.
- In the NCCC 2023 campaign at NGCC conditions, heat duty was measured to at high removal of 97%, low lean loading of 0.2 mol/mol, and high total rich bypass split fraction with pump around intercooling in the absorber to be about 2.4 GJ/tonne.
- Real-time evolutionary optimization of bypasses was identified as a tool to minimize heat duty over a wide range of CO_2 removal in NCCC 2023..

- Increase in total rich bypass with an optimized cold rich bypass was linked to low heat duty. The optimal total rich bypass was about 73% with an optimal cold rich bypass between 5 and 9%.
- Cold rich bypass flowrate dictated the performance of the CO_2 exchanger and its optimum corresponded to a cooled CO_2 gas temperature between 180 and 210 °F. Optimal cold rich bypass was also linked to a hot-side pinch in the CO_2 exchanger. Warm rich bypass dictated the temperature difference in the overhead of the stripper with the optimal value corresponding to the total rich bypass temperature being 5-10 °F hotter than the exit gas.
- The cooled CO_2 gas temperature and stripper overhead temperature difference can be used as self-optimizing control variables for real time optimization of cold rich bypass and warm rich bypass flow rate.
- Under optimal bypass conditions, the total rich bypass was found to be flashing at the entry point into the stripper with a volume vapor fraction between 30 and 60%.

<u>Model Performance:</u>

- Model validation of heat duty in NCCC at coal and gas conditions showed an average underprediction of net heat duty by 9%.
- Model validation of heat duty in the SRP campaign showed an average overprediction of net heat duty by 33% primarily due to an overprediction of lean loading by 13%, resulting in an underprediction of CO_2 flow by 20%. The deviation in CO_2 flow was much larger than that of heat rate.
- Heat duty in the NCCC 2023 gas campaign was predicted with almost no error on average by the model.

- At NCCC, the measured and modeled temperature profiles in the column agreed with each other better than at SRP, primarily due to a difference in CO_2 flowrate. Temperatures near the sump agreed more with the model-predicted vapor temperatures and the rest agreed more with the liquid temperatures.
- The overall ability of the model to predict net heat duty was related to the gas and liquid velocities in the stripper. Significant overprediction of heat duty occurred at low liquid and gas velocities, typical of the SRP campaign with a 10 inch stripper column. At the SRP plant, the use of a 6 inch stripper significantly improved the ability of the model to predict heat duty. The effect of low vapor rates was not captured in the gas phase mass-transfer model and mass-transfer in stagnant liquid films or low Re number flow was not accounted for in the mass transfer model.
- At NCCC, most of the data was in the moderate to high liquid and vapor velocity range, leading to better predictions of heat duty. The mass transfer model assumes film wetting which is more likely the case at high liquid and vapor rates. With the error from the mass transfer and thermodynamic models being minimal at high liquid/vapor rates, the error in heat duty could be explained by the accounting of heat loss in the measurement of net heat duty.
- At low liquid and vapor rates, modeling of heat duty is confounded by not only heat loss but also inherent defects in the model with thermodynamics and mass transfer.

RECOMMENDATIONS FOR FUTURE WORK

- Pilot plant work will benefit from a systematic analysis of the effect of the mass transfer, heat transfer, and thermodynamic models on heat rate and CO_2 loading. More

thermodynamic data can be included in the model from high temperature measurements, or the model can be adjusted to represent the stripper performance.

- To adjust the heat of absorption, heats of formation for species relevant to low lean loading and high temperature conditions need to be modified. Liquid and gas phase mass transfer coefficient models must be expanded to apply to low liquid and vapor rates where the flow is likely stagnant or laminar. Reevaluation and analysis of UT-SRP data must be done after adjusting the models.
- The accuracy of CO_2 flow measurements at NCCC and UT-SRP must be verified. The CO_2 flowmeters may need to be calibrated, especially the one at UT-SRP.
- Specific heat capacity models of loaded amine must be corrected to ensure more accurate estimation of heat exchanger terminal temperatures.
- The heat transfer models used in the stripper column require more study. Either adjusting the heat transfer models to accurately predict temperatures in the column at the pilot plant, or creating a new heat transfer model relevant to high temperature stripping would aid interpretation of pilot plant results.
- Reaction kinetics model must be fixed to represent high temperature conditions. Stripper modeling suffers from an incorrect estimate of equilibrium at high temperature, possibly due to an incorrect estimate of reverse reaction rate constants. One fix for this would be adjusting the reverse reaction rate constant as a function of temperature to match the equilibrium constant as a function of temperature in the stripper.
- The stripper could be modeled only using kinetic reactions just as the absorber if the kinetic and equilibrium models match at high temperature. This method could be validated against pilot data.

- A systematic analysis of the solvent analytical methods must be conducted to determine the most accurate method to measure CO_2 loading. Past pilot plant campaigns suffer from the use of different analytical methods in each campaign due to instrument issues.
- Offline solvent viscosity measurements can be made, and coupled with the density measurements that are already available to measure a loading based on density and viscosity. The density-viscosity method has proven to be a very reliable pilot plant method to estimate loadings.
- Automatic bypass control for PZAS must be tested at the pilot scale by adjusting the cold rich bypass to control the CO_2 temperature leaving the CO_2 exchanger and the warm rich bypass to control the temperature difference in the overhead of the stripper.
- The stripper model validation could benefit from additional temperature measurements in the stripper column at NCCC.

ACKNOWLEDGMENTS

The author would like to thank all members of the Texas Carbon Management Program that were involved in the planning for the campaigns. Special thanks to Laura Uhrig, Jason Arriazola, and operators at NCCC for making timely changes to operating conditions. Thanks go to Dr. Frank Seibert, Jarett Spinhirne, and JR Campos at the UT-SRP pilot plant for their help with plant operation. Plant operation would also not have been possible without the help of Yee Lee Chen and Miguel Abreu who assisted with night shifts. Thanks also go to Yuying Wu, Ching-Ting Liu, Ariel Plantz, Chih-I Chen, Miguel Abreu, Sara Cardenas, Arya Balasubramanian, and Kahiso Erickson for solvent analysis in the NCCC and SRP campaigns.

Chapter 4: Commercial Stripper Design for a FEED on a 460 MW NGCC

Piperazine with the Advanced Stripper™ (PZAS™) is a second-generation amine regeneration system for CO_2 capture that has been extensively tested at the pilot scale at coal (Chen et al., 2019) and NGCC conditions (Rochelle et al., 2022, Suresh Babu and Rochelle, 2022). This chapter investigates the scale-up of PZAS for a Front-End Engineering Design (FEED), which will be used to develop a comprehensive cost estimate for the commercial design. This work is part of the FEED conducted by The University of Texas at Austin for a 460 MW NGCC power plant in Denver City, Texas.

The host site includes two gas turbine generators and one steam turbine generator. Supplementary firing of duct burners will be used to increase electricity output and CO_2 captured. Details on the host site and high-level aspects of the project have been discussed by Closmann et al. (2021). At design conditions the plant will capture 1.7 million tonnes CO_2/year.

This chapter specifically discusses the design of the regeneration system only. This includes a base case design and an advanced design with the potential to reduce the energy, packing, and heat exchanger requirement compared to the base case. Packing height, column contactor, column diameter, and heat exchanger size selection, and the effect of seasonal changes on energy performance for the base case design are some of the cases investigated. Finally, the benefits of the advanced design are compared with existing stripper configurations and its operational limits are described.

Details on the absorber-side design are excluded from this paper but are described in detail by Gao and Rochelle (2022). Given the low natural gas price in west Texas, the primary objective of this FEED is to reduce capital investment. This can be achieved by

using smaller heat exchangers and coarse packing in the stripper, resulting in a higher energy requirement compared to that of the pilot plant at NCCC. Additionally, minimization of heat duty for PZAS has been the focus of this work, as minimization of equivalent work was not necessary due to the presence on site of packaged natural gas boilers that enable high pressure steam delivery with low losses.

Parts of this chapter have been published in the *International Journal of Greenhouse Gas Control (Suresh Babu and Rochelle, 2022).* Practically all other FEED results for these technologies are proprietary and provide few if any public details.

4.1 DESIGN METHODOLOGY

4.1.1 Simulation Method

Aspen Plus® was used for modeling the stripper column and the heat exchangers. Equilibrium reactions at high temperature with rate-based mass transfer was used to simulate the transport phenomena in the column. In-house thermodynamic and mass transfer models were used for the PZ-CO_2-H_2O system. The Independence thermodynamic model and the Song mass transfer models were used (Frailie, 2014, Song, 2017). A correction factor of 0.16 was used on mass transfer interfacial area to bridge discrepancies between measured and modeled diffusivity of PZ (Lin, 2016).

4.1.2 Process Description and Design Rationale

Figure 4.1 shows a simplified process flow diagram for PZAS with the design specifications for the base case. This design shows 1 of 2 parallel process trains. The rich solvent from the absorber is pumped to high pressure to overcome the pressure drop through the cross exchangers. The cold cross exchanger exchanges the sensible heat of the warm lean solvent with the cold rich solvent. The hot cross exchanger exchanges both

sensible and latent heat, resulting in flashing hot rich solvent. The cold rich bypass is drawn before the cold cross exchanger to recover latent heat of vaporization from the stripper overhead gas. This results in partial condensation of water and reduces lost work in the process. The warm rich bypass is drawn typically at the bubble point after the cold cross exchanger and is mixed with the heated cold rich bypass and sent as reflux to the top of the stripper. Both bypasses are optimized for every design case in the process model to operate at the lowest stripper heat duty. The total reflux sent to the top of the stripper has three important functions: 1) it acts as a direct contact cooler to partially condense some water vapor in the stripper; 2) it balances the lean and rich flows in the cross exchangers; and 3) it balances the L/G in the stripper and avoids temperature pinches in the column.

Flue gas specifications for the NGCC unit and gas-fired boiler have been given by Gao and Rochelle (2022). Decisions related to process design on the stripper side have been taken by considering a single process train and were modified to represent a two-train operation. Heat exchanger performance and bypass optimization in the process are not affected by scale-down. The stripper column diameter was adjusted to produce 80% flood at the scaled-down condition.

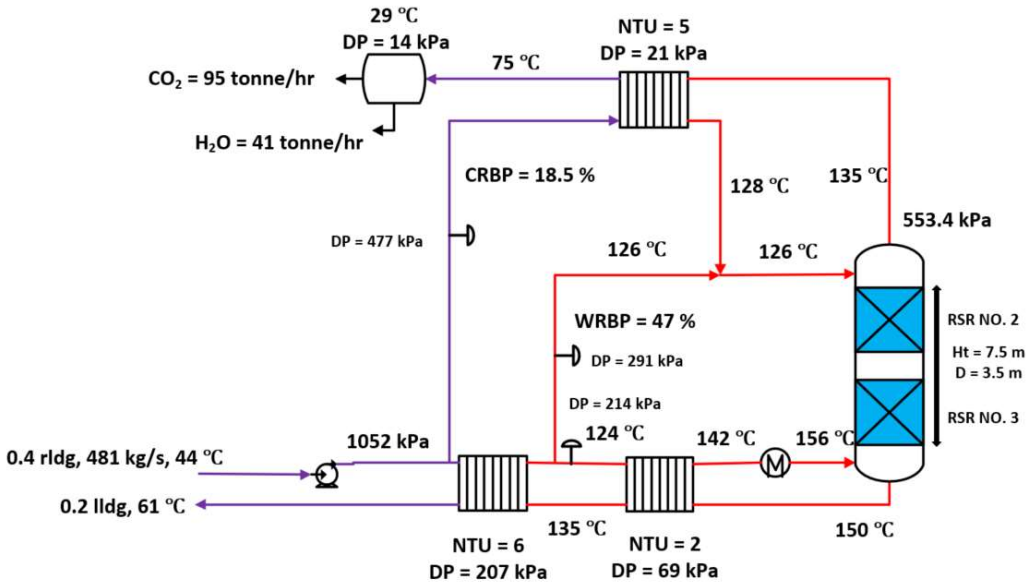

Figure 4.1: Base case design specification of PZAS (1 of 2 parallel trains)

4.1.3 Bypass Optimization Procedure

Optimization of the cold and warm rich bypass was important to ensure a near-optimum operation of the advanced stripper. Specifically, in this work, bypass flowrates or their respective split-fractions (fractional flow with respect to the total rich flowrate) were optimized to minimize the steam heater duty. For this, data of heat duty as a function of cold rich and warm rich bypass split fractions were collected for each design case investigated in this chapter and other subsequent chapters. The heat duty was then regressed as a quadratic function of bypass split fractions using Microsoft Excel®. This quadratic function was then optimized to minimize the heat duty using MATLAB Optimization Toolbox®. The optimization code is provided in Appendix A.

4.1.4 Design of Heat Exchangers

Heat exchangers were modeled using NTU that directly relates to heat exchanger performance for a given flow, excluding any dependence of their performance on solvent flow rate. NTU of a heat exchanger is defined as the ratio between the UA (product of overall heat transfer coefficient and heat exchanger area) and the flow heat capacity, mC_p of the lean solvent. Similar dependencies of U and mC_p on solvent flow rate, as observed in pilot plant data from NCCC, removes the dependence of NTU on flow rate (Abreu, 2021). Equation 4.1 is used for calculating heat exchanger NTU.

$$\mathbf{NTU} = \frac{\textbf{Overall heat transfer coefficient} * \textbf{Heat exchange area}}{\textbf{Lean solvent mass flow rate} * \textbf{Specific heat capacity of lean solvent}} = \frac{\mathbf{U} * \mathbf{A}}{\mathbf{m} * \mathbf{C_p}} \qquad (\mathbf{4.1})$$

This method of representing heat exchangers allows for easy scale-up and rating of at different solvent rates. Heat exchanger sizes were scaled from pilot plant data at NCCC. This procedure is explained in detail by Closmann et al. (2021). Given that the physical properties of solvent and heat transfer mechanism in the heat exchangers at NCCC and the FEED are similar, designing the FEED exchangers for the same NTU as NCCC would mean that the ratio of heat exchange area to flow is kept constant. This also means that the flow velocity per channel length and pressure drop are similar. Given a heat exchanger of known channel length, one could determine the number of passes required in the exchanger using the ratio of NTU between NCCC and the FEED.

If the NTU of the FEED was half that at NCCC, it would mean that while the heat exchanger for the FEED will be larger in its area than NCCC simply due to the scale (flowrate) of the plant, the heat exchanger would be less effective at transferring heat

between the rich and lean solvent. This will result in colder hot-side temperatures around the heat exchanger for the FEED.

In modeling, the heat exchangers were split into “flashing” and “non-flashing” zones to monitor temperature crossovers. This was especially important in the design of PZAS with hot rich bypass, which will be discussed in upcoming sections.

4.1.5 Column Design

The stripper column was designed with two sections of random packing. The diameter of the column is influenced by the fractional flood that depends on the vapor rate and the solvent bypass rates. For every design case, the diameter of the column was adjusted to give approximately 80% flood. Random packing was used for the commercial design to reduce the column diameter, which resulted in a compact and cost-effective column with a diameter that will allow offsite fabrication. Random packing is also used to reduce the capital investment in the column associated with the packing. The stripper sump was designed with the same diameter as the column. The height of the sump was evaluated on a case-by-case basis to provide a residence time of 1 minute for the hot lean solvent leaving the sump. The rich solvent pump pressure was back-calculated from the stripper sump pressure by accounting for pressure drop in the heat exchangers, control valves, stripper liquid head, and pressure drop in the warm rich bypass line.

4.1.6 Water Balance in PZAS

Water vapor in the stripper overhead line was partially condensed in the CO_2 exchanger and then mostly removed in the condenser. The condensate was returned to the absorber water wash to manage emissions. A check on water balance between the absorber

and the stripper side was critical to the design as simulations were done independently for the two systems. The net water production rate was evaluated in the absorber depending on ambient temperature and has been explained by Gao (2021). The net water produced in the absorber is mixed with the rich solvent and returned to the solvent inventory. To close the water balance, the total water in the rich solvent from the absorber was compared to the sum of the condensate flow rate and the water in the lean solvent. The mass balance closed within 0.3%.

4.2 SUMMARY OF BASE CASE DESIGN

The stripper column consists of two sections of coarse random packing, each with a packing height of 3.7 m, and a diameter of 3.35 m at 80% flood. The rich loading was 0.4 mol/mol and the stripper sump was designed for 150 °C to give a lean loading of 0.2 mol/mol at 5.5 bar. The rich solvent was pumped to 10.5 bar to overcome pressure drop through heat exchangers and the control valve. On an NTU basis, the cross exchangers were half the size of those at the NCCC pilot plant, resulting in higher approach temperature. The cold cross exchanger was designed for 6 transfer units and the hot cross exchanger was designed for 2 transfer units. The CO_2 exchanger was designed for 5 transfer units. The cold and warm rich bypasses were optimized at 19% and 47% of the total rich flow, respectively.

The heat duty for the base case is about 2.85 GJ/tonne, which represented an acceptable energy cost at the low natural gas prices in west Texas. The design benefits from the low capital cost associated with fewer transfer units in the heat exchangers and coarse packing in the stripper. The flowsheet with the base case design specifications is shown in Figure 4.1.

4.3 SELECTION OF PACKING TYPE

Three sets of coarse random packing were considered for the top and bottom sections of the stripper column. Compared to those in the NCCC stripper, these packings had lower metal surface area. Table 4.1 shows a comparison of metal surface area of the pilot and the commercial design, and the packing height, diameter, and flooding evaluated for each section. To select the most economical packing type, the total area of packing and heat duty was considered for each pair. With capital cost reduction being the main objective, packing with minimum total required area was chosen at the expense of slightly increased energy requirement.

According to Song (2017), the $k_L a_e$ of packing depends on the packing metal surface area to the 0.73 power. Assuming that mass transfer in the stripper is mostly liquid-side controlled, the packing height required for each packing type in each packing section can be scaled up from the NCCC stripper using Equation 4.2.

$$\frac{h_{FEED}}{h_{NCCC}} = \left\{\frac{a_{FEED}}{a_{NCCC}}\right\}^{0.73} \tag{4.2}$$

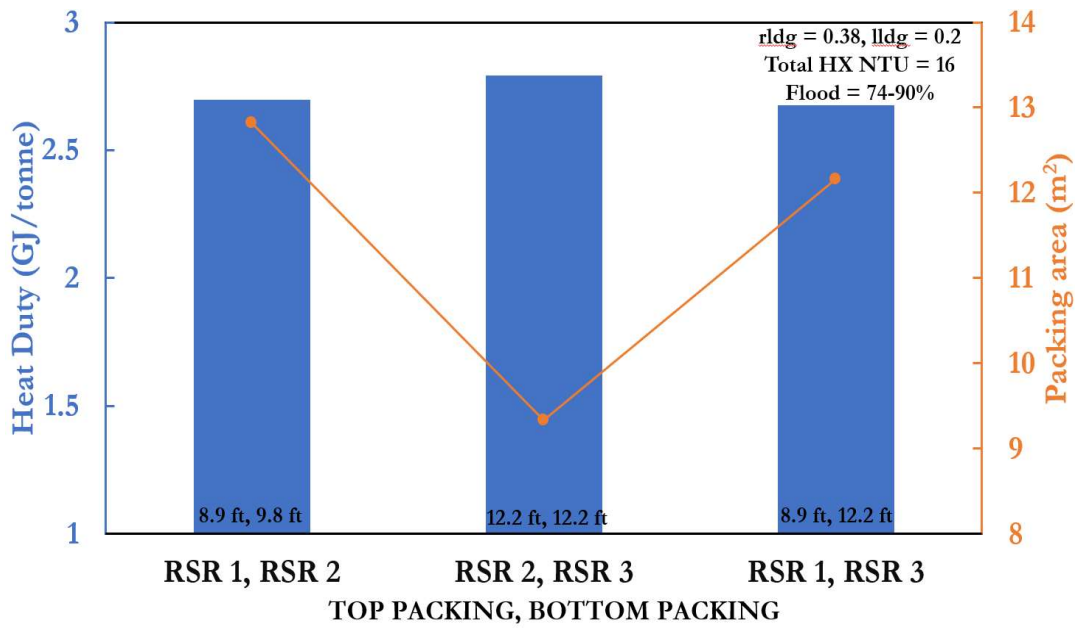

Figure 4.2: Packing area and heat duty comparison for 3 different sets of packing

From Figure 4.2, while the energy requirement for cases 1 and 3 is about 8% lower than case 2, the total packing area required for case 2 is about 30% lower, reducing the expected capital cost. Therefore, RSR 2 was chosen for the top section and RSR 3 for the bottom section. This combination of packing types also provided equal flooding in both sections of the column compared to the other types. The height of packing added to each section in the stripper was the average of the packing heights estimated from scaling-up. This ensured that both the packing sections were geometrically similar.

Table 4.1: Packing height per section and column diameter for 3 different sets of packing

Design Case	Packing Type	a_p (m^2/m^3)	Packing Height per Section (m)	d (m)	Flooding per section (%)
NCCC Pilot	RSR 0.5	236.2	2	0.25	~ 30-60% during operation
	RSR 0.7	176	2		
FEED case 1	RSR 1	155.5	2.7	4.7	83
	RSR 2	100.6	3		76
FEED base case	RSR 2	100.6	3.7	4.3	85
	RSR 3	74.9	3.7		83
FEED case 2	RSR 1	155.5	2.7	4.6	90
	RSR 3	74.9	3.7		74

4.4 SELECTION OF PACKING HEIGHT

Figure 4.3 shows the trade-off between packing height and energy requirement. As expected, the steam heater duty drops as the packing height is increased, eventually reaching a minimum that corresponds to low energy costs with a fixed total heat exchanger NTU. This comes at the expense of excess packing height in the stripper. To the far left of the figure, the energy costs are high due to the low packing height, resulting in high natural gas energy cost. At the design packing height of 7.5 m, the steam heater duty is 2.85 GJ/tonne at 0.4 mol/mol rich loading. This is shown by the blue curve. The red curve shows

a similar trade-off between heat duty and packing height at twice the heat transfer units in the cross exchangers, and lower rich loading (and cyclic capacity). This curve is representative of the pilot plant heat exchanger performance at NCCC, albeit at lower cyclic capacity, resulting in higher energy requirement than typically observed at the pilot plant.

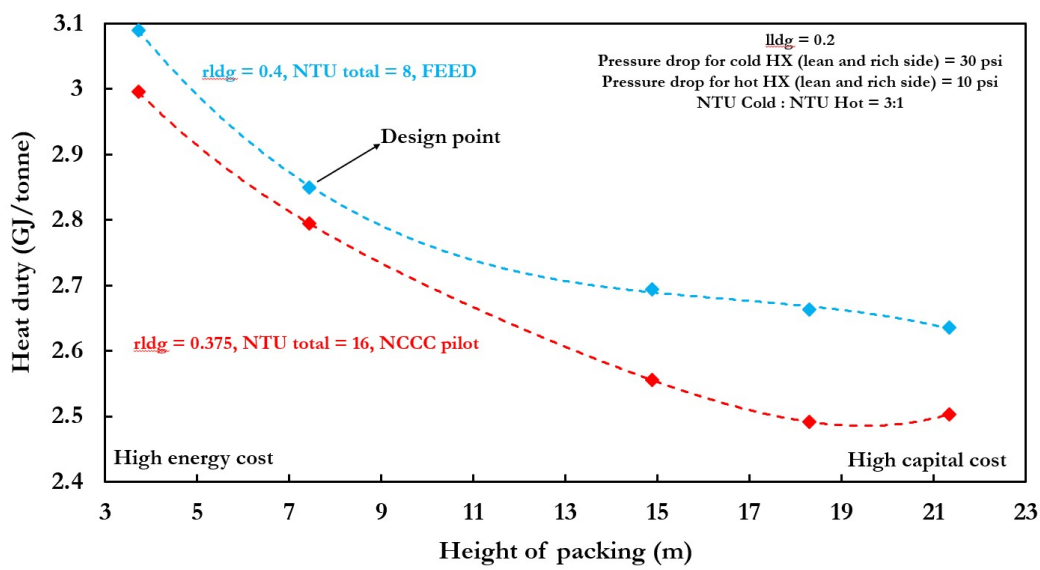

Figure 4.3: Trade-off of heat duty and packing height

The stripper column begins to approach a top-side temperature pinch with about 70 ft of packing with a rich loading of 0.4 mol/mol, lean loading of 0.2 mol/mol, and a total heat exchanger NTU of 8. However, a closer temperature pinch in the column may be observed at packing height > 70 ft, thus resulting in a slightly lower minimum heat duty of separation. This would ultimately translate to a slightly lower heat duty at the design point as well for an assumed value of Q/Q_{min}.

4.5 ESTIMATION OF MINIMUM HEAT RATE

Both the heat exchanger performance and packing performance dictate the energy requirement of the PZAS. For the minimum heat duty, both excessive packing and heat exchanger transfer units are used. 21.3 m of RSR 2 and RSR 3 packing was used in the stripper. The stripper diameter was adjusted for 80% flood. A total of 16 transfer units were used in the cross exchangers. This NTU was assumed to be excessive as it resulted in a hot-side temperature pinch between the cross exchangers. The CO_2 exchanger was designed for 5 transfer units. At a rich loading of 0.4 mol/mol and a lean loading of 0.2 mol/mol, the minimum heat duty was estimated to be 2.34 GJ/tonne CO_2.

Compared to the minimum heat duty, the base case heat duty was only 21% higher (Q/Q_{min} = 1.21). This represents an acceptable energy performance given the low price of natural gas in west Texas, while minimizing capital investment by using smaller heat exchangers and less packing in the stripper. Compared to the design at minimum heat duty, the base case design used 65% lower packing height and the heat exchangers were 50% smaller on an NTU basis.

4.6 IMPACT OF SUMP TEMPERATURE ON COLUMN DIAMETER

An analysis was performed to demonstrate the effect of stripper sump temperature on column diameter and heat duty. Small column diameter was preferred as it allowed for off-site fabrication and transportation to the plant. As the sump temperature increased from 140 to 160 °C, the pressure increased from 4 to 7.5 bar (+87.4%). While the high temperature reduced the density of the gas, the effect of increased pressure dominated, resulting in a net increase in the density of the vapor. This resulted in lower vapor velocity in the stripper and flooding lower than 80%. At 80% flood, increasing the sump temperature by 10 °C reduced the column diameter by 0.3 m. The energy performance

decreased from about 3 GJ/tonne CO_2 at 140 °C to 2.81 GJ/tonne CO_2 at 160 °C due to the increased selectivity of CO_2 over H_2O. These results are shown in Figure 4.4.

While this analysis showed high temperature operation could reduce stripper diameter, compression requirement, and heat duty, it has three major disadvantages: 1) the solvent degrades thermally and oxidatively at higher temperature (Freeman, 2011); 2) corrosion may be severe at higher temperature (Liu, 2022); and 3) compressors would be under-designed if PZAS were operated at low temperature to minimize oxidation and corrosion. Therefore, a stripper sump temperature of 150 °C was chosen for the FEED. At this temperature, two parallel process trains were used to further reduce the liquid load and flooding in the column, which resulted in a stripper diameter of 3.35 m.

For both energy performance and electricity consumption, the use of a low temperature (and pressure) stripper at constant lean loading is not beneficial with PZ due to the higher heat duty (higher water/CO_2 ratio) and higher compression requirement. PZ may benefit from low temperature operation when the solvent is heavily degraded or with corroded piping/equipment. Another reason to use PZ at low temperature especially at the pilot scale would be to mitigate heat loss from the stripper column, or when low pressure steam is available, or a low temperature solvent is used in the stripper column.

Other reasons to operate at low temperature include low pressure rating of the stripper.

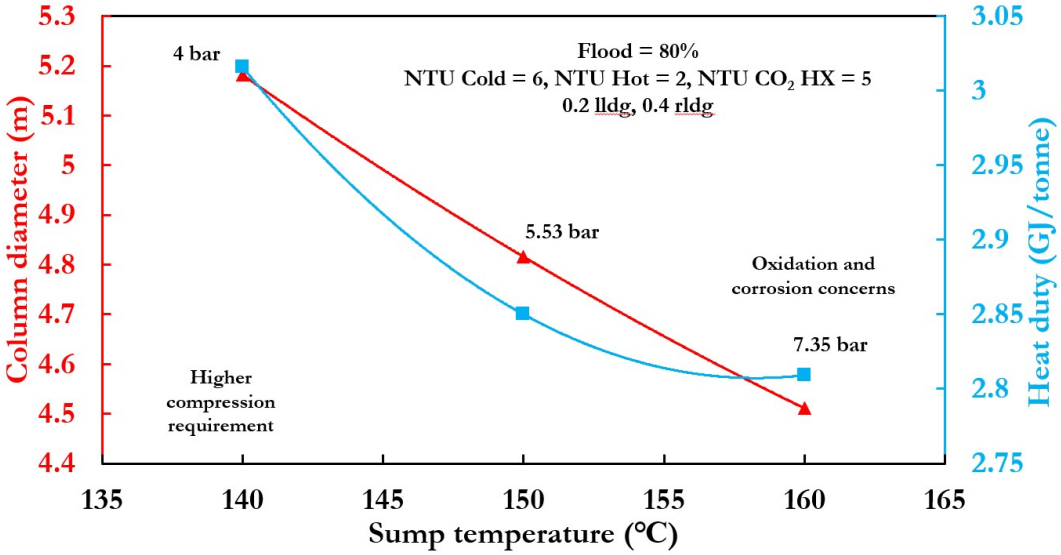

Figure 4.4: Higher stripper temperature (and pressure) would reduce column diameter

4.7 SELECTION OF HEAT EXCHANGER NTU

Another important process variable that required consideration was the cross-exchanger size. The NTU concept, as defined by Equation 4.1, was chosen to represent the area of heat exchangers for a fixed solvent rate. Figure 4.5 shows the effect of total NTU of cross exchangers on steam heater duty at fixed lean and rich loading, stripper packing height, and CO_2 heat exchanger size. The total NTU was the sum of the NTU of the cold and hot cross exchangers. The ratio of the cold cross exchanger to the hot cross exchanger was maintained at 3:1.

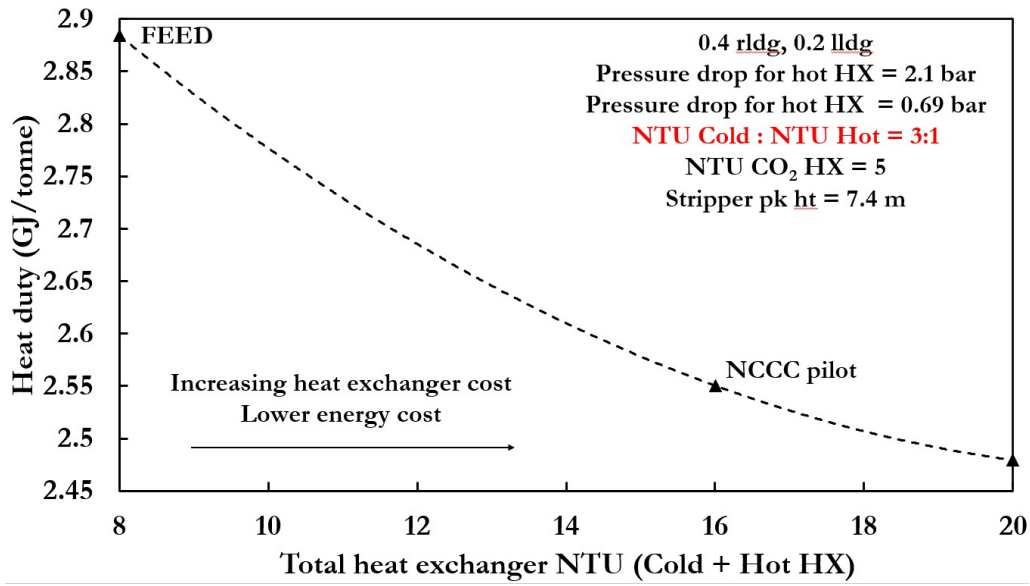

Figure 4.5: Effect of heat exchanger NTU on steam heater duty

As the total NTU is varied from the design value of 8 to 20, the steam heater duty decreases from 2.85 GJ/tonne CO_2 to 2.48 GJ/tonne CO_2. At a total NTU of 16, which corresponds roughly to the heat exchanger sizes at NCCC, the calculated heat duty is 2.55 GJ/tonne CO_2, comparable to the measured heat duty at the pilot plant.

Low heat duty at high values of total NTU can be attributed to greater sensible and latent heat exchange through the cold and hot cross exchangers. This analysis revealed that reducing the heat exchanger area by 50% compared to the pilot plant only increased heat duty by 12%. Given the cheap energy prices in west Texas, 2.85 GJ/tonne CO_2 represents an acceptable energy cost with low heat exchanger cost.

4.8 ALTERNATIVE PROCESS CONFIGURATIONS

4.8.1 Distribution of Heat Exchanger NTU

With a fixed total NTU of 8 in the cross exchangers, the distribution of NTU between the cold and hot cross exchangers provided was another degree of freedom. This allows variation in the relative sizes of the two exchangers. The ratio of cold exchanger NTU to hot exchanger NTU is 3:1 for the base case, indicating that the cold exchanger is three times as large as the hot exchanger. This ratio (NTU cold : NTU hot) has been varied from 2:6 to 7:1, and its effect on steam heater duty is shown in Figure 4.6. This analysis has been done at a slightly lower rich loading of 0.375 compared to the base case design, which explains the higher heat duty in Figure 4.6.

As the ratio of the heat exchanger sizes was increased from 2:6 to 7:1, the steam heater duty decreased by 11.5%. Below a cold exchanger NTU of 4, the hot exchanger is bigger than the cold exchanger. Above a cold exchanger NTU of 4, the cold exchanger is bigger than the hot exchanger. Figure 4.6 importantly shows that increasing the size of the hot exchanger at the expense of the size of cold exchanger (left of the vertical blue line) can only reduce the energy requirement from 3.35 GJ/tonne to 3.2 GJ/tonne (6%). Increasing the cold exchanger size at the expense of the hot exchanger size (right of the vertical blue line) yields a greater reduction in energy requirement, from 3.2 GJ/tonne to 2.95 GJ/tonne (8%). This highlights the importance of the size of the cold exchanger in PZAS which dictates the temperature of the warm rich bypass and ultimately, the total rich bypass temperature.

At higher cold exchanger NTU, the warm rich bypass temperature increases, thereby increasing the total rich bypass temperature. A higher total rich bypass temperature reduces the lost work in the column from temperature driving forces (lower LMTD) by

reducing the approach temperature at the top of the column and introducing more flashing in the total rich bypass line. Higher temperature at the feed point in the stripper could locally increase the selectivity of CO_2 over H_2O at constant pressure, thereby reducing energy requirement. The solvent is also leaner going into the top of the stripper at higher temperature. This results in pre-stripping of some CO_2 that directly leaves with the stripper vapor. The reduced rich loading in the liquid reduces the heat rate for the stripper. The total CO_2 separated ultimately remains the same, which results in lower heat duty.

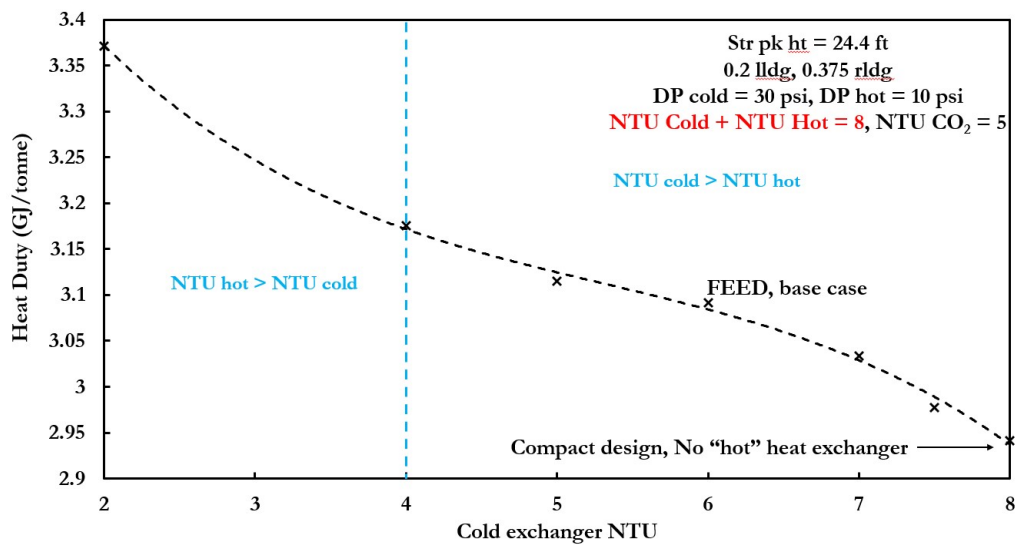

Figure 4.6: Effect of relative size of cold and hot cross exchanger on steam heater duty

4.8.2 Use of a Hot Rich Bypass Flow

The previous analysis resulted in a variant of the PZAS called the PZAS with hot rich bypass. This configuration corresponds to a case where heat transfer occurs in the cold cross exchanger only, with an NTU of 8 (extreme right of Figure 4.7), bearing all the pressure drop. The CO_2 exchanger and the steam heater were assumed to have no pressure drop. The performance of this configuration was evaluated using a single capture train,

resulting in a higher diameter than the PZAS design, to regulate the flooding in the column to about 80%.

The hot cross exchanger is not required in this design. Practically, this configuration allows the two exchangers to be combined into one large exchanger. The second bypass stream is drawn after the heat exchangers instead of in between them, resulting in a hotter, flashing solvent. To simulate this configuration, a single cross exchanger was assigned 8 transfer units and was divided into "flashing" and "non-flashing" sections to avoid temperature crossovers. A simplified flowsheet of this configuration is shown in Figure 4.7 with representative temperatures for the base case design.

This configuration further reduced the energy requirement of the base case design to 2.78 GJ/tonne. A flat optimum in heat duty was observed for this design, as a function of cold rich and hot rich bypass split fractions. The hot rich bypass was at a higher temperature (140 °C) than the warm rich bypass (126 °C) used in the base-case PZAS design, which resulted in more flashing of both CO_2 and H_2O in this line and the total rich bypass line. This also resulted in a higher total rich bypass temperature and a higher rich solvent temperature exiting the steam heater, dictating a higher steam quality.

More importantly, this configuration required a higher cold rich bypass split fraction (20%) than that in the PZAS design (18.5%), to condense the larger amount of water vapor generated from the flashing total bypass. This water vapor must be condensed in addition to the water vapor generated in the stripper column. The benefits and drawbacks of this design are evaluated in the upcoming sections.

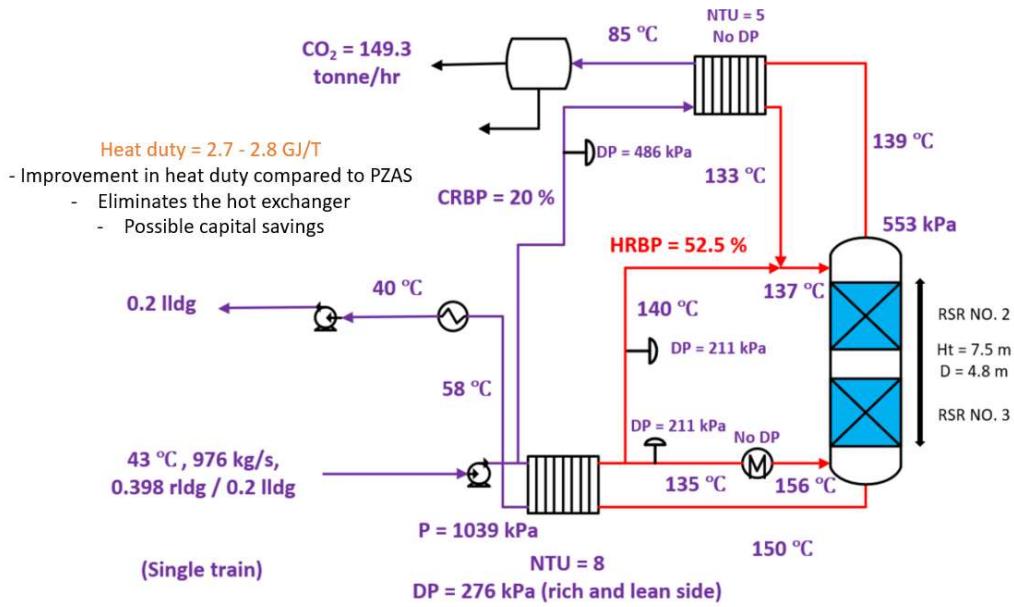

Figure 4.7: Use of hot rich bypass with base case design of stripper for FEED

4.8.3 Benefits of Using a Hot Rich Bypass

A hotter total rich bypass solvent was shown to reduce the LMTD in the stripper column. The LMTD of the stripper was calculated using temperatures of liquid and vapor at the top and bottom stages of the column as shown in Equation 4.3. Subscript "top" refers to the topmost stage in the column and subscript "bot" refers to the bottom stage of the column. Subscript "L" refers to liquid and subscript "V" refers to the gas.

$$\textbf{LMTD of stripper} = \frac{(T_{L,top} - T_{V,top}) - (T_{L,bot} - T_{V,bot})}{\ln(\text{DT top}/\text{DT bottom})} \tag{4.3}$$

This effect is shown in Figure 4.8, which compares the stripper LMTD for PZAS and PZAS with hot rich bypass for heat exchanger NTU of 8, 12, and 16. PZAS with hot rich bypass always has a hotter total rich bypass temperature and lower stripper LMTD than PZAS. The hotter total rich bypass temperature lowered the approach temperature of the stripper at the top. This resulted in lower lost work and lower equivalent work by

approaching a more reversible stripper operation. The stripper LMTD of the PZAS with hot rich bypass with a total NTU of 8 is also shown to be comparable to that of the simple stripper with a CO_2 heat exchanger. The simple stripper with CO_2 exchanger lacks a convective steam heater and uses a reboiler in the stripper. Due to this, there is no solvent bypassed to the bottom of the stripper and all the hot rich solvent is sent to the top of the stripper. The enthalpy of the hot rich solvent is enhanced in this case, giving rise to a similar equivalent work compared to the PZAS with hot rich bypass at equal total heat exchanger NTU.

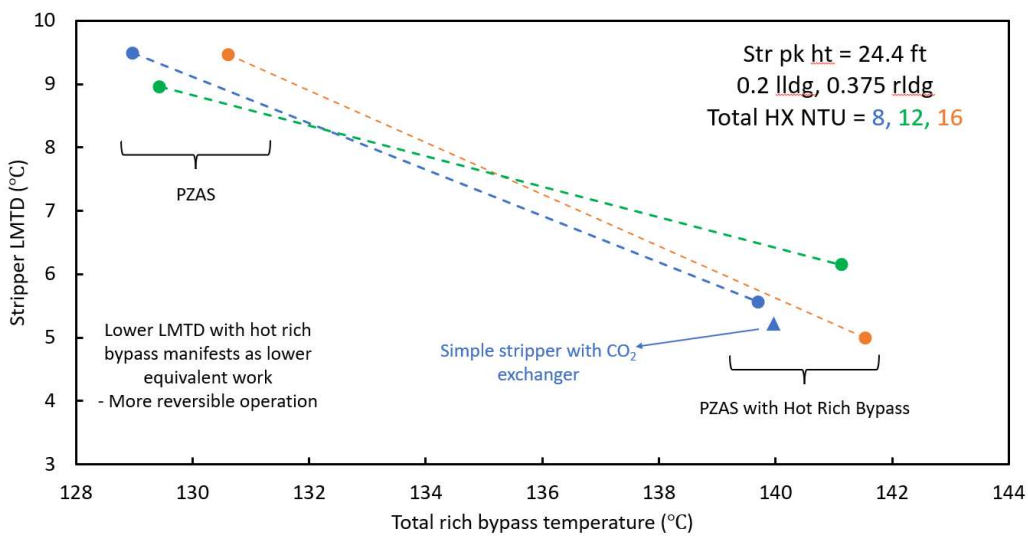

Figure 4.8: Reduction in stripper LMTD associated with higher total rich bypass temperature

4.8.4 Benefits of Flashing Total Rich Bypass

When heat duty is minimized using the hot rich bypass, at the optimum cold rich bypass, the top-side stripper approach temperature is about 0 to -2 °C. The hot rich bypass is not at its bubble point like the warm rich bypass in the PZAS, but is flashing, resulting in a higher molar vapor fraction in the total rich solvent entering the stripper. This shows

that further energy reduction in PZAS is possible when the total rich bypass solvent approaches equilibrium with the vapor leaving the stripper, which is possible when the hot rich bypass is used. This is shown in Figure 4.9. The x-axis on Figure 4.9 refers to the fractional hot rich bypass relative to the total rich solvent. The secondary y-axis in Figure 4.9 shows the molar vapor fraction in the total rich bypass line as a function of the hot rich bypass. PZAS with hot rich bypass provides significantly higher molar vapor fraction in the solvent entering the stripper (1 mol%) compared to PZAS (0.3 mol%). This shows that flashing more solvent as it enters the stripper can result in a reduction in energy requirement in PZAS.

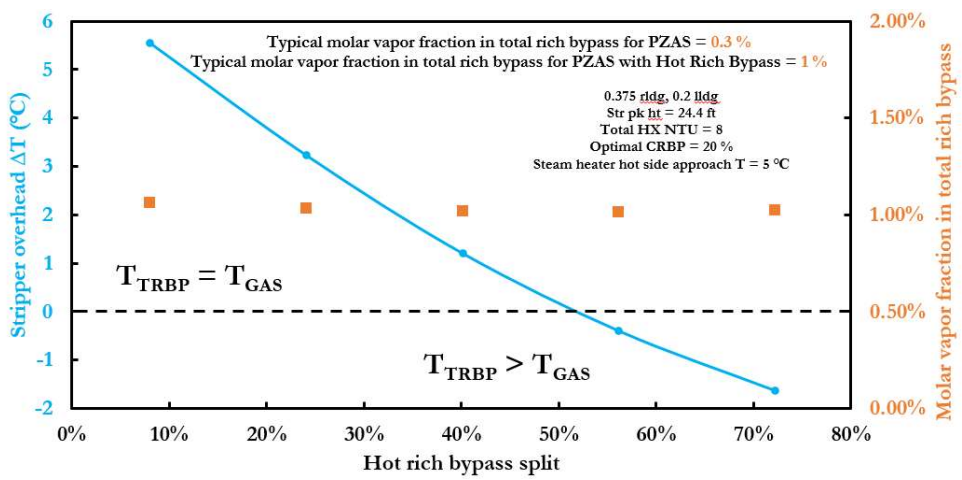

Figure 4.9: Hot rich bypass produces more vapor in total rich bypass line than warm rich bypass

4.9 EQUIVALENT WORK OF STRIPPING AND COMPARISONS WITH OTHER PROCESS CONFIGURATIONS

The energy requirement of PZAS with hot rich bypass has been evaluated at total NTU values of 8, 12, and 16, and has been compared with their PZAS counterparts at a rich loading of 0.375 and lean loading of 0.2. Equivalent work was used to quantify the

energy requirement as it considers steam quality. PZAS with hot rich bypass requires a higher quality steam due to the higher temperature of the rich solvent exiting the steam heater.

The equivalent work of stripping was calculated as the sum of the rich pump work, compression work, and heat duty work, as shown in Equation 4.4. The pump work is estimated directly from the simulations using a pump efficiency of 65%. The compression work was calculated as a function of stripper pressure, P_{str}, as shown in Equation 4.5. The heat duty work converts the process heat duty, Q_p, into electricity by accounting for the turbine efficiency (assumed to be 90%) and the Carnot cycle efficiency. This is shown in Equation 4.6. In this equation, T_{stm}, is the condensing temperature of the steam, which is assumed to be 5 °C greater than the temperature of the rich solvent exiting the steam heater. The calculated work in all three cases is normalized by the total moles of CO_2 produced by the stripper.

$$\mathbf{W_{eq} = W_{pump} + W_{compression} + W_{heat}} \tag{4.4}$$

$$\mathbf{W_{compression} = -3.476 * \log\left(\frac{P_{str}}{100000}\right) + 14.845} \tag{4.5}$$

$$\mathbf{W_{heat} = 0.9 * \frac{T_{stm} - 313}{T_{stm}} * Q_p = 0.9 * \frac{(T_{rich\ out,\ steam\ heater} + 5) - 313}{(T_{rich\ out,\ steam\ heater} + 5)} * Q_p} \tag{4.6}$$

Compared to PZAS, the PZAS with hot rich bypass reduced the equivalent work by 1.5–3.5% over the entire range of total NTU investigated. Increasing total NTU provided diminishing returns in equivalent work compared to PZAS. For example, at an

NTU of 16, PZAS with hot rich bypass had an equivalent work similar to that of PZAS. This was due to a hot-side pinch between the non-flashing and flashing regions of the cross exchanger, that led to an approximately constant hot rich solvent temperature at higher NTU, giving rise an unchanging equivalent work between the PZAS and PZAS with hot rich bypass. This change was 3.5% for a total NTU of 8. These results are shown in Figure 4.10.

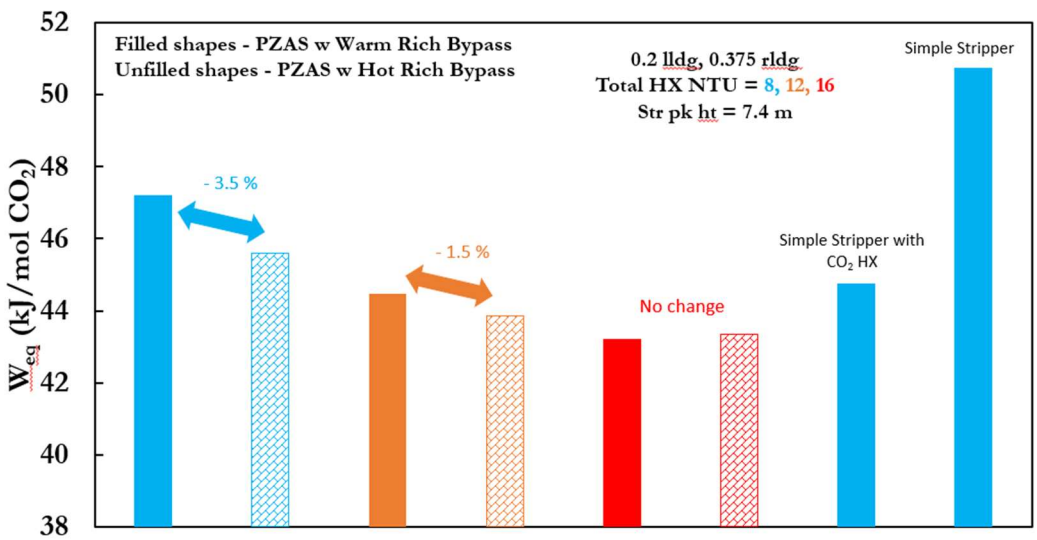

Figure 4.10: Equivalent work comparison between different stripper configurations

PZAS with hot rich bypass outperforms the simple stripper in equivalent work for the same total NTU in the cross exchanger. The simple stripper does not employ any heat integration and the lost work comes from condensing the water vapor in the gaseous product in the condenser. This also indicates the importance of the CO_2 exchanger in minimizing the lost work in the simple stripper process.

To investigate the effect of the CO_2 exchanger, the PZAS with hot rich bypass is also compared to the simple stripper with CO_2 exchanger alone. The simple stripper with

CO_2 exchanger slightly outperforms the PZAS with hot rich bypass at an NTU of 8. The simple stripper with CO_2 exchanger lacks a convective steam heater and uses a reboiler in the stripper. Due to this, there is no solvent bypassed to the bottom of the stripper and all the hot rich solvent is sent to the top of the stripper. The enthalpy of the hot rich solvent is enhanced in this case, which reduces the equivalent work compared to PZAS with hot rich bypass. Moreover, a lower quality steam can be used for the simple stripper with CO_2 exchanger than for PZAS with hot rich bypass due to the lack of convective steam heater.

It is interesting however that while at lower NTU, the use of the hot rich bypass will reduce the heat duty and equivalent work of the process compared to the warm rich bypass, as the NTU increases, this is not the case. At high heat exchanger size (NTU=16), due to a pinch in the middle of the cold and hot cross exchangers, the hot rich solvent in PZAS is almost at the same temperature as the hot rich bypass in PZAS with hot rich bypass, necessitating the requirement of the same steam quality in the steam heater. This makes the equivalent work and heat duty similar for the warm rich and hot rich bypass configurations.

The overall benefit of the hot rich bypass over the warm rich bypass for any heat exchanger size can be understood as the balance between the reduction of heat duty through a reduction of stripper LMTD and the quality of steam that is required. At lower heat exchanger sizes, the former appears to outweigh the latter, and at high heat exchanger size, the benefit from the former is diminished through the need of high-quality steam.

4.10 EFFECT OF AMBIENT TEMPERATURE ON ENERGY REQUIREMENT

Rich loading has an important effect on heat duty, which is shown by the quadratic relation in Figure 4.11. Rich loading was obtained from absorber simulations which

accounted for the effect of ambient temperature, flue gas temperature, and intercooling employed in the column. Heat duty was estimated by stripper simulations at different rich loadings. A 13% increase in rich loading from 0.354 to 0.4, decreased heat duty from 3.3 GJ/tonne CO_2 to 2.85 GJ/tonne CO_2, at fixed heat exchanger performance and stripper packing height. At approximately constant lean loading, this can be interpreted as the effect of increasing cyclic capacity and decreasing solvent circulation.

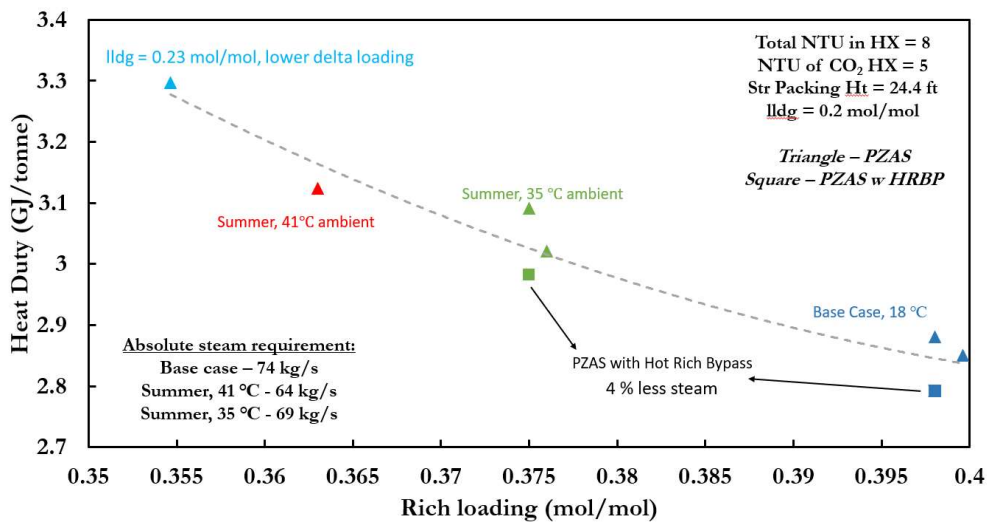

Figure 4.11: Effect of rich loading on energy performance at different ambient temperatures

Figure 4.11 shows that the energy performance dropped by 6–10% in the summer compared to the base case. In the summer, high ambient temperature coupled with the high flue gas temperature led to a hotter absorber bottom, resulting in low rich loading. However, in absolute steam requirement, the summer months require 8–15% less the base case requirement due to the lower capture efficiency.

This shows that the PZAS can be operated in the summer with a small penalty on energy performance, at lower absolute steam requirement. Figure 4.11 also shows that

PZAS with hot rich bypass uses 4% less steam than PZAS at the same rich loading. This has been shown for a 35 °C summer case, indicating that an alternative method to achieve further reduction in heat duty during summer months would be to switch to the hot rich bypass. The benefits of this configuration are discussed in the next section.

4.11 OPERATIONAL BOUNDS OF PZAS WITH HOT RICH BYPASS

A limitation of the PZAS with hot rich bypass is that it outperforms the PZAS only at low to moderate packing height in the stripper. Figure 4.12 presents a comparison of heat duty as a function of stripper packing height for PZAS and PZAS with hot rich bypass. The analysis was done at fixed heat exchanger NTU, lean loading, and rich loading. In both cases, the heat duty decreases with increasing packing height, eventually approaching a minimum at fixed heat exchanger performance. However, the curve flattens much sooner for PZAS with hot rich bypass, at about 15 m of packing compared to 21 m for PZAS. Below 15 m of packing, PZAS with hot rich bypass outperforms PZAS and after 15 m, PZAS outperforms PZAS with hot rich bypass.

The hot rich bypass primarily reduces the energy requirement by reducing stripper LMTD and this advantage diminishes beyond 15 m of packing due to little change in the LMTD of the column from a pinch. Importantly, Figure 4.12 demonstrates that PZAS with hot rich bypass requires significantly less packing to strip CO_2 to give the same lean loading (0.2 mol/mol) in the solvent as PZAS. For example, at a heat duty of 2.9 GJ/tonne, the hot rich bypass requires about 13 m of packing compared to 15 m of packing with the warm rich bypass. This indicates that hot rich bypass can enable both energy savings from its lower heat duty and capital savings from its lower packing requirement.

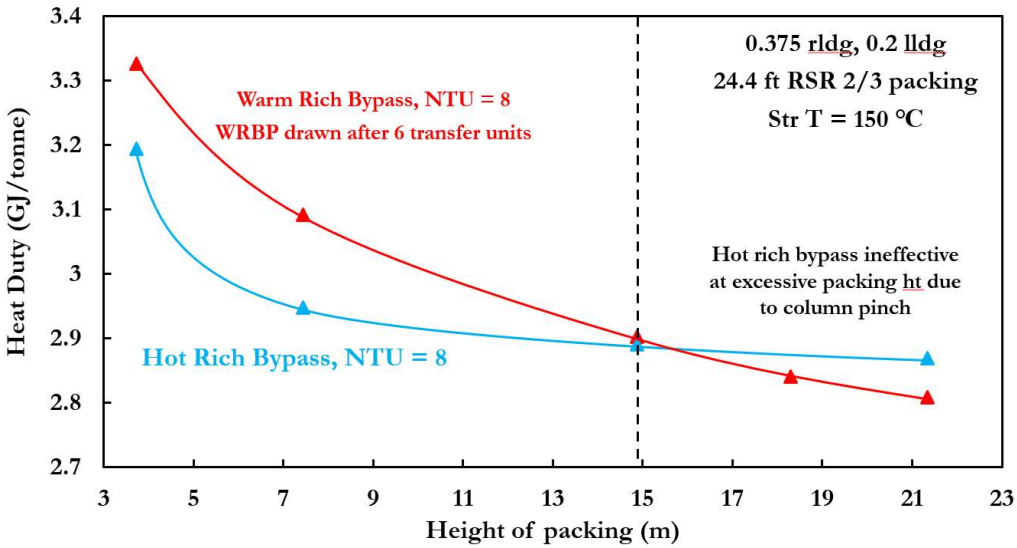

Figure 4.12: PZAS with hot rich bypass outperforms PZAS only at packing height less than 15 m

Figure 4.13 compares the stripper LMTD between the warm rich bypass and hot rich bypass as a function of packing height. LMTD of the column was calculated using the temperature driving force between the gas and liquid at the top and bottom stages of the column. Figure 4.13 shows that the hot rich bypass operates with a lower column LMTD compared to warm rich bypass over the entire range of packing height considered, which is due to the higher temperature of the total rich bypass. However, the change in heat duty observed over the same range of packing height is a function of the change in LMTD observed in the column.

For PZAS and PZAS with hot rich bypass, this change is significant from 3.7 m to 15 m of packing. The LMTD of PZAS drops by 45% and the LMTD of PZAS with hot rich bypass drops by 53%, and this is reflected in the steeper change in heat duty for PZAS with hot rich bypass compared to PZAS in this range of packing height (Figure 4.13). However, beyond 15 m of packing, the LMTD in the column for PZAS with hot rich bypass

diminishes faster than for PZAS, shown by the earlier flattening of the blue curve in Figure 4.12 and Figure 4.13. Between 15 m and 21.3 m of packing, the LMTD in the column for PZAS with hot rich bypass only decreases by 19% compared to 29% for PZAS. Therefore, in this range of packing height, the heat duty does not change for PZAS with hot rich bypass but continues to decrease for PZAS.

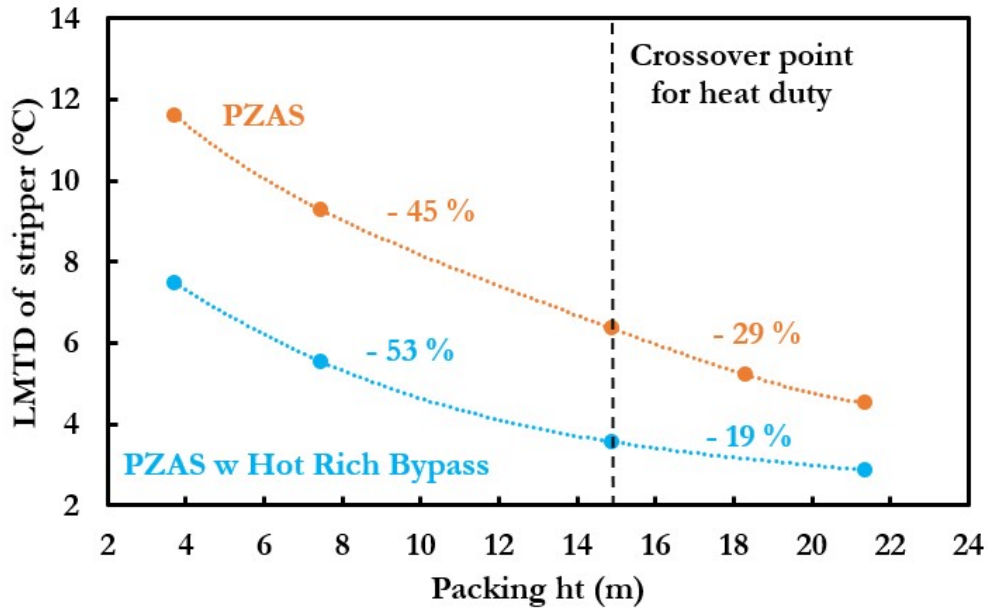

Figure 4.13: Stripper LMTD comparison of PZAS and PZAS with hot rich bypass as a function of packing height

4.12 OPERATIONAL CHALLENGES WITH PZAS WITH HOT RICH BYPASS

In the field, heat duty optimization will be done by fixing the cold rich bypass value and manipulating the hot rich bypass to give a minimum heat duty. Figure 4.14 shows that this results in a flat optimum for the hot rich bypass split fraction at about 72%. Due to this, there is a small amount of solvent bypassed to the steam heater, resulting in unfavorably high temperatures in the rich solvent exiting the steam heater.

At the apparent optimum value of hot rich bypass split fraction, this temperature is about 165 °C. This temperature will increase oxidative and thermal degradation, and corrosion in the pipes at lean conditions. A higher steam pressure would also be required in this case (with a condensing temperature of 170 °C).

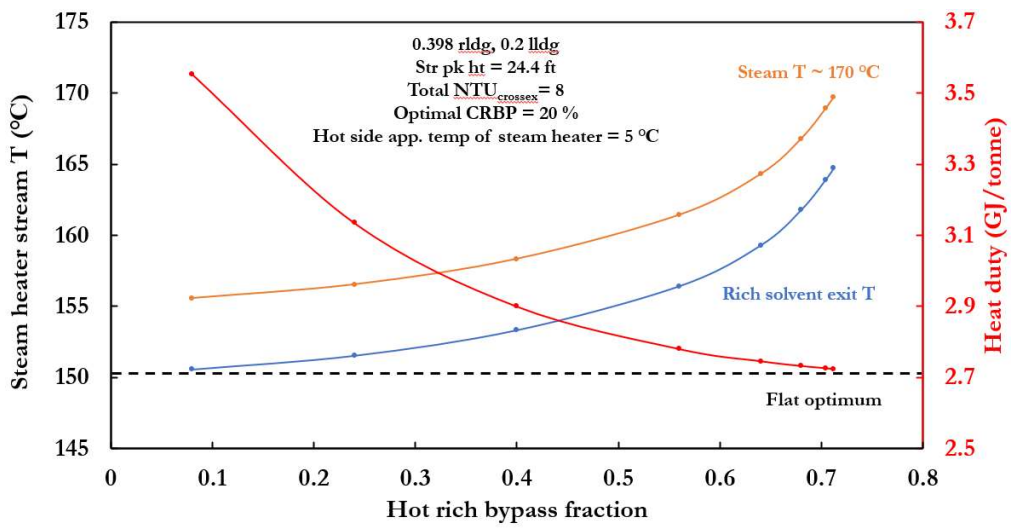

Figure 4.14: Optimizing heat duty for hot rich bypass results in high quality steam requirement

To avoid this, the optimum for the hot rich bypass split fraction must be found by minimizing the equivalent work in the process. This is shown in Figure 4.15. This analysis accounts for the steam temperature used in the process. Although the equivalent work shows a similar trend to that of heat duty with increasing hot rich bypass, there exists a clear optimum for the hot rich bypass split fraction at about 60%. Beyond this value, the required steam temperature increases drastically, giving rise to lower Carnot efficiency of the power plant.

At 60% hot rich bypass, the temperature of the hot rich solvent exiting the steam heater is 157 °C, which is now within the degradation limit for PZ. The required steam

temperature is lower at 162 °C, compared to the steam temperature in the previous case where heat duty was optimized, representing a 5 °C hot side approach temperature in the steam heater. Irrespective of whether heat duty or equivalent work is used to minimize heat duty, the optimum hot rich bypass (and cold rich bypass) value appears to be much higher than the optimum warm rich bypass value (and cold rich bypass) used in PZAS, possibly due to the higher amount of water that needs to be condensed due to the flashing total rich bypass.

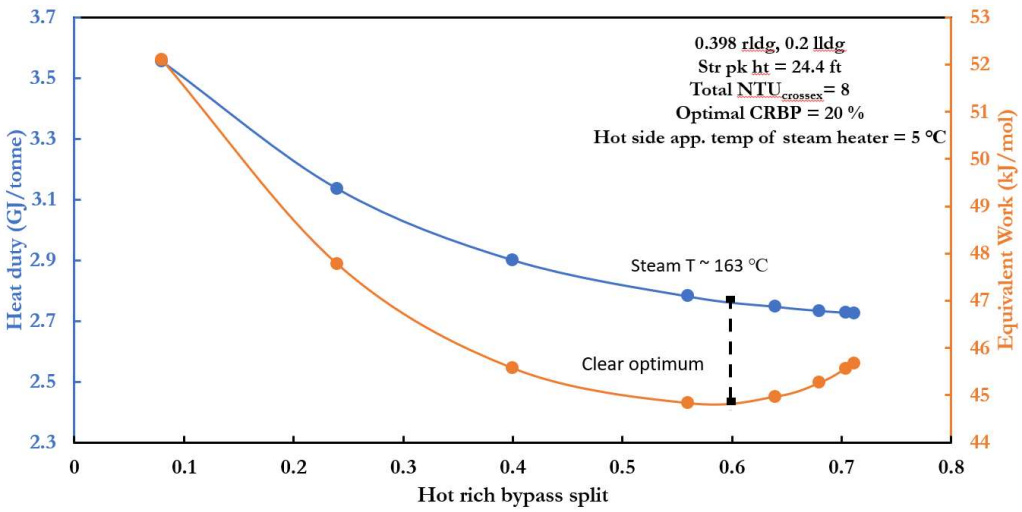

Figure 4.15: Optimizing equivalent work for hot rich bypass results in lower quality steam requirement

For PZAS, when heat duty is optimized using the warm rich bypass at the optimum cold rich bypass split fraction, a flat optimum is observed at about 60% warm rich bypass. At this condition, the temperature of the solvent exiting the steam heater is about 159 °C, which is already within the degradation limit for PZ. The steam temperature required at this condition is 164 °C, which is much lower than the steam temperature required for the hot rich bypass counterpart (170 °C). This result is shown in Figure 4.16.

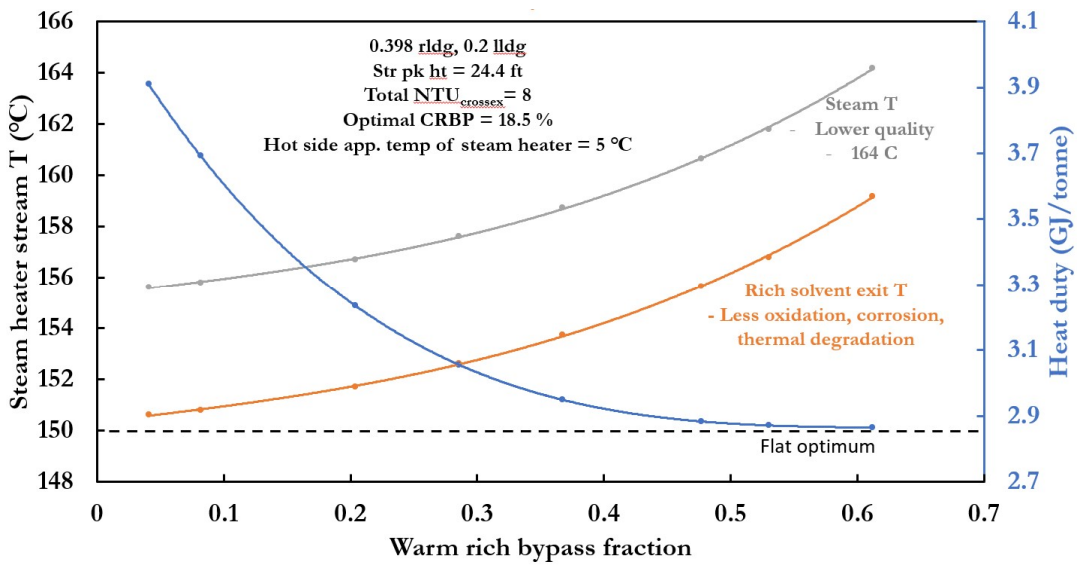

Figure 4.16: Steam inlet temperature and rich solvent temperature exiting steam heater when heat duty is optimized using warm rich bypass for PZAS

When equivalent work is optimized using the warm rich bypass, at the optimum cold rich bypass split fraction, the temperature of the solvent exiting the steam heater (155 °C) and the corresponding steam temperature (160 °C) are lower compared to their counterparts with the PZAS with hot rich bypass. This is shown in Figure 4.17.

Overall, this demonstrated that optimizing heat duty instead of equivalent work for PZAS did not pose a practical challenge as it did for the PZAS with hot rich bypass.

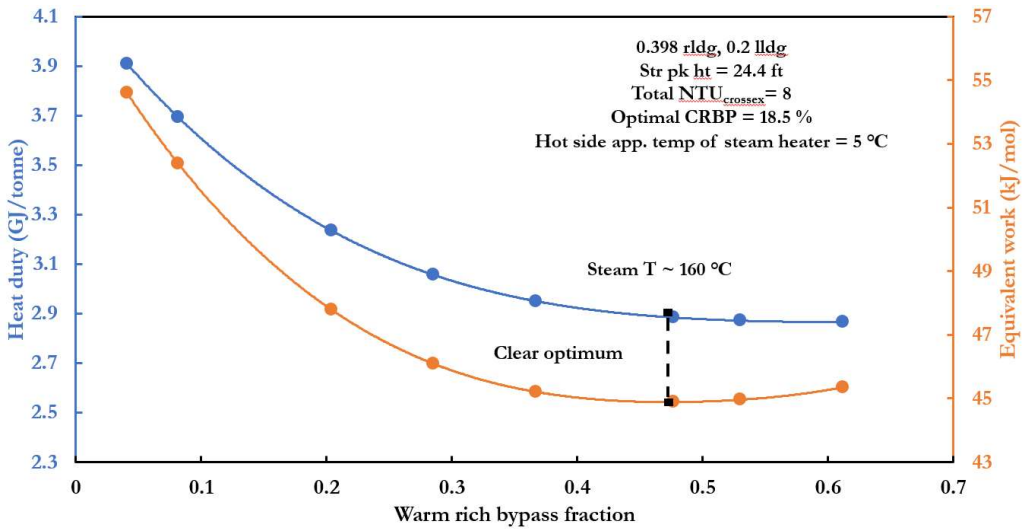

Figure 4.17: Optimizing equivalent work for warm rich bypass with representative steam temperature

4.13 CONCLUSIONS

- Based on a rigorously validated model for PZ at NGCC conditions, a commercial design for the PZAS™ process is proposed for a 460 MW NGCC with the following specifications (1 out of 2 stripper trains):
  - Stripper Packing: 3.75 m RSR 2 in top, 3.75 m RSR 3 in bottom, 7.5 m total
  - Column diameter: 3.5 m
  - Lean and rich loading: 0.2 and 0.4 mol CO_2/ equivalent N
  - Heat exchanger NTU: 6 for cold cross exchanger, 2 for hot cross exchanger, and 5 for CO_2 exchanger
  - Energy performance: 2.85 GJ/tonne CO_2, 74 kg/s steam required
  - Ratio of design energy requirement to minimum energy requirement (Q/Q_{min}): 1.21
- By using random packing in the column and lower heat transfer units compared to the pilot plant at NCCC, the capital cost in this design should be reduced. This also results

in a slightly higher energy requirement but is offset by the low natural gas price in west Texas. The baseline energy performance is likely to increase to about 3.1 GJ/tonne during the summer months and represents a small penalty in energy performance at about 8–15% lower absolute steam requirement due to lower capture rates. Increasing the cold exchanger size relative to the hot exchanger size at fixed total heat exchanger NTU was key to reducing the energy performance of the system.

- The energy requirement in terms of equivalent work can further be reduced by 1.5–3.5% (and heat duty to 2.78 GJ/tonne) by drawing the second bypass stream after the hot cross exchanger (PZAS with hot rich bypass). This reduces the lost work in the stripper by lowering the stripper LMTD. However, this benefit ceases to exist at packing height > 15 m due to a column pinch. PZAS with hot rich bypass can also operate at lower packing height compared to PZAS to achieve the same separation. A higher quality steam would be required for PZAS with hot rich bypass due to the higher temperature of rich solvent leaving the steam heater. This advanced configuration offers the potential to reduce energy costs by lowering the heat duty and capital costs by reducing the packing and heat exchanger requirement.

RECOMMENDATIONS FOR FUTURE WORK

- Future work could investigate process configurations that intentionally increase the vapor content in the solvent such as using heat exchanger networks at an elevation.
- A more robust method to optimize bypass flowrates could be investigated. This could involve the creation or use of an equation-oriented modeling and optimization platform to model PZAS instead of Aspen Plus®.

- Unification of absorber and stripper flowsheets could be attempted to automatically close the mass balance between the two sides.
- This work has assumed liquid-side mass transfer control in the stripper. Future work could involve studying mass transfer mechanisms in the stripper in detail to better estimate mass transfer correction factors and a design a stripper that more realistically represents mass transfer at high temperature.
- Further packing height reduction in strippers could be possible through wetted area creation by surface phenomena such as boiling. Future work could involve experimental and modeling studies of boiling in stripper columns, and appropriately correcting the wetted area in the stripper for its effects.
- Future work could involve a study of a change in mass transfer mechanisms in the stripper column with scale-up, with the use of different packing types and packing height.
- The hot rich bypass concept could be tested at NCCC. Piping has already been modified at NCCC to bypass hot rich solvent to the top of the stripper.

Chapter 5: Off-Design Performance of Commercial Stripper Design

The Texas Carbon Management Program developed a Front-End Engineering Design (FEED) of the Piperazine Advanced Stripper (PZAS) process at an existing 460 MW NGCC in west Texas. The details of the design of the absorber, stripper, and other equipment are provided by Gao (2022), Suresh Babu (2022), Closmann et al. (2021). Additional details on the FEED are reported by Rochelle et al. (2022, 2022).

With a finalized design for the plant in Aspen Plus®, off-design (rating) models for the absorber, stripper, air coolers, water wash, and compressors are developed by incorporating real equipment performance data obtained from vendors. The rating models are used to identify equipment that limited the performance of the facility. This chapter provides details of the rating models for the stripper-side and compressor train and explores their operational limits. For details on the other equipment such as absorber, air coolers, and water wash models, refer to the report by Rochelle et al. (2022). Miguel Abreu constructed the models for the absorber-side and Benjamin Drewry constructed the models for the air coolers for intercooling and water wash.

Once the rating model for the stripper-side is built, the data from the rating model is used to construct algebraic surrogate models of variables on the stripper-side and for compressor performance using the ALAMO Model Building Tool (Cozad et al., 2014). These algebraic equations are pivotal in increasing the ease of convergence of the process simulation compared to Aspen Plus® and resulted in much faster simulation times. These models, however, are very specific to the PZAS process, particularly for its FEED. These models can be applied only over the range specified for the individual variables, but can be used for locations with different gas and power price.

The surrogate models are simultaneously solved using MATLAB with 7 major independent variables that determined system performance. These are lean solvent rate, number of air cooler bays (for intercooling and water wash), cold rich bypass flowrate, warm rich bypass flowrate, number of water wash pumps, number of intercooler pumps, and lean loading at constant stripping temperature of 150 °C. The MATLAB model also involves several operational constraints that are explained in detail in this section.

The converged steady-state values of the variables from the MATLAB model will be used to estimate variable profit of the process as a function of energy price, power price, and the value for CO_2. The variable profit will be maximized to obtain optimal operating conditions. This is explained in Chapter 6.

The optimization code and surrogate models can be found in Appendices B and F.

Parts of this chapter have been submitted for publication in the *Industrial and Engineering Chemistry Research* journal.

5.1 MODELING METHODS

The rating models developed in this work were created in the Aspen Plus® software. The Independence™ model was used to estimate solvent thermodynamics, reaction kinetics, and the physical properties of the 5 m PZ solvent (Frailie, 2014). The performance of the structured packing in the absorber and random packing in the stripper was estimated using the model developed by Song at the University of Texas Separations Research Program (UT-SRP) (Song, 2017).

The stripper column was simulated with rate-based modeling in Aspen Plus® using the RadFrac. A 0.16 correction factor was applied to the wetted mass transfer area (Lin, 2016) in the stripper column to bridge discrepancies between measured and modeled

diffusivity of PZ in the column. The heat exchangers were modeled using pairs of heater blocks for ease of convergence. The NTU of the heat exchangers using the lean solvent temperature difference was specified to define their areas. The NTU of the cold and hot cross exchangers were defined using the lean-side temperature difference and the Log-Mean Temperature Difference (LMTD) of the cross exchangers as shown by Equation 5.1. This method of defining heat exchanger performance yields the same set of temperatures on both sides of the cross exchanger irrespective of scale or flowrate.

$$\mathrm{NTU} = \frac{\Delta \mathrm{T}_{\mathrm{lean}}}{\mathrm{LMTD}} \tag{5.1}$$

5.2 SUMMARY OF BASE CASE STRIPPER DESIGN

Chapter 4 proposed a base case design for PZAS by considering several tradeoffs associated with packing type selection, packing height selection, heat exchanger size selection etc. The base case design was slightly modified at the end after consulting with equipment vendors. This modification was specifically associated with the NTU of the cross exchangers and the CO_2 exchanger, the ability to accommodate the pressure drop in these exchangers, and practical maintenance issues associated with these exchangers. The final design used 2 stripper trains, and each train had three cold cross exchangers in parallel, two hot cross exchangers, a stripper column, a CO_2 exchanger, and a condenser.

Each stripper column had a total height of 7.5 m and consisted of two sections of random packing: 3.75 m of RSR 2 packing at the top and 3.75 m of RSR 3 packing at the bottom. The cold cross exchanger was designed with a NTU of 5.3, the hot cross exchanger with a NTU of 1.7, and the CO_2 exchanger with a NTU of 3.88. The base case design with its design specifications is shown in Figure 5.1. The stripper operated with a bottoms

temperature of 150 °C at 5.6 bar which resulted in a lean loading of 0.2 mol/mol. With a rich loading of 0.4 mol/mol, the energy required for stripping was 3 GJ/tonne CO_2. This heat duty was slightly higher than the heat duty described for the base case design in Chapter 4 primarily due to slightly smaller heat exchanger NTU.

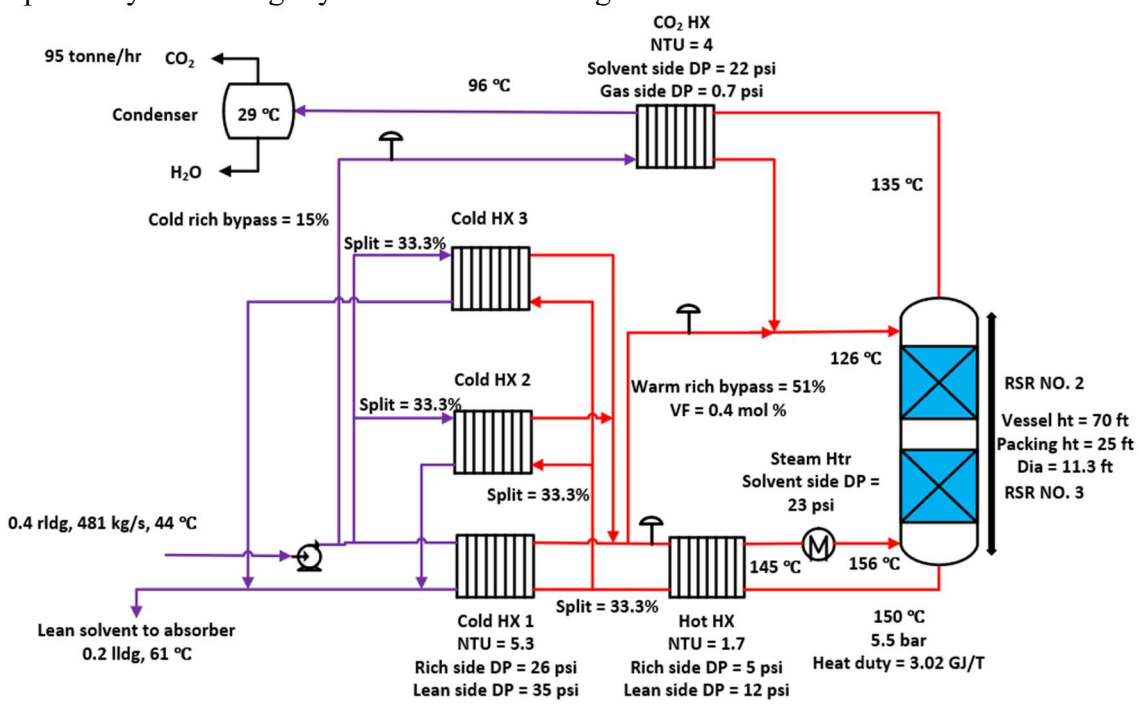

Figure 5.1: Final base case design of PZAS for FEED

5.3 DEVELOPMENT OF OFF-DESIGN (RATING) MODELS

The rating model was built in Aspen Plus® to represent semi-dynamic process performance. This involved including in the design model the performance of pumps and fans, pressure drop in heat exchangers and elevation head. Some of the equipment in the process was modeled by either coding an algebraic model into the Aspen Plus® software using calculator blocks or by using other Aspen Plus® tools such as the EDR software (Aspen Technology, Inc., 2013). This section describes the construction of the rating

models for the stripper system. The absorber side models were constructed by Miguel Abreu and the air cooler models were constructed by Benjamin Drewry. All the models are available in the report by Rochelle et al. (2022).

The stripper model automatically updated heat exchanger pressure drops as a function of rich solvent flowrate, bypass flowrates, and lean solvent flowrate. The rich and lean pumps were simulated by incorporating pump performance curves obtained from vendors. The model also automatically calculated and accounted for the elevation head in the solvent lines that extend from the level of the sump to the feed point in the stripper.

The heat exchanger NTU was kept constant in these simulations at their respective final design values. The cold cross exchanger was simulated with a NTU of 5.3, the hot cross exchanger with a NTU of 1.7, and the CO_2 exchanger with a NTU of 3.88. Three cold heat exchangers work in parallel in this design along with two hot exchangers, one CO_2 exchanger, and 2 steam heaters in series. The pressure drop through the stripper packing was assumed to be negligible and constant at 2 psi.

The elevation head from the lean pump to the solvent entry point in the absorber was calculated to determine the operating point of the lean pump, which had a variable speed drive (VSD). This considered the height of the feed point from the bottom of the absorber sump and liquid level calculation in the sump of the stripper. The calculation methods for the above are given in detail in the upcoming sections.

Heat exchanger pressure drop was estimated using Equation 5.2. Table 5.1 shows the pressure drop and flowrates for the base case which were used to size the heat exchangers. The mass flow through the rich side of the heat exchangers was only a function of the bypass values. The mass flow on the lean side of the heat exchangers only depended on the total rich solvent rate, which changed with rich loading.

$$\Delta P_{new} = \Delta P_{base} * \left[\frac{L_{new}}{L_{base}}\right]^2 \quad (5.2)$$

Table 5.1: Scaling of pressure drop in heat exchangers

Solvent line	L_{base} (kg/s)	Base-case pressure drop (psi)
Cold HX rich side	408	26
Cold HX lean side	440	33.8
Hot HX rich side	160	14
Hot HX lean side	440	14
CO_2 HX solvent side	73	26
Steam heater solvent side	160	20

The lean pump was a variable speed pump, but the performance curves were only provided for a fixed speed of 705 rpm. Performance at other speeds (N, in rpm) was extrapolated using the pump affinity laws in Equations 5.3 to 5.5.

$$\text{Vol. Flow}_{LeanPump} \; \alpha \; N_{LeanPump} \quad (5.3)$$

$$\text{Head}_{LeanPump} \; \alpha \; N^2_{LeanPump} \quad (5.4)$$

$$\text{Power}_{LeanPump} \; \alpha \; N^3_{LeanPump} \quad (5.5)$$

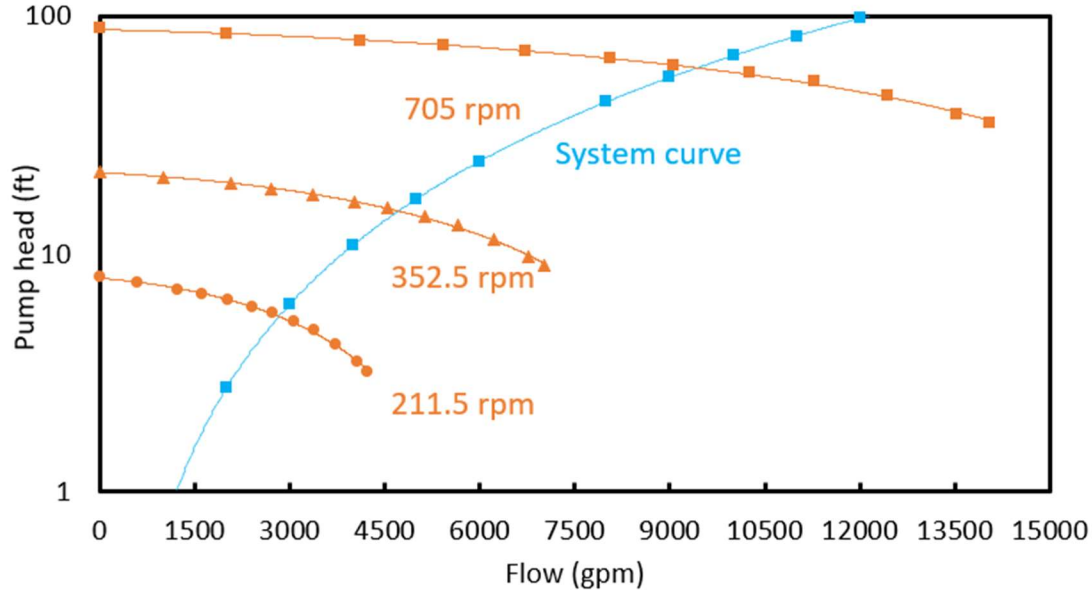

Figure 5.2: Extrapolated pump head from design curve for the lean pump

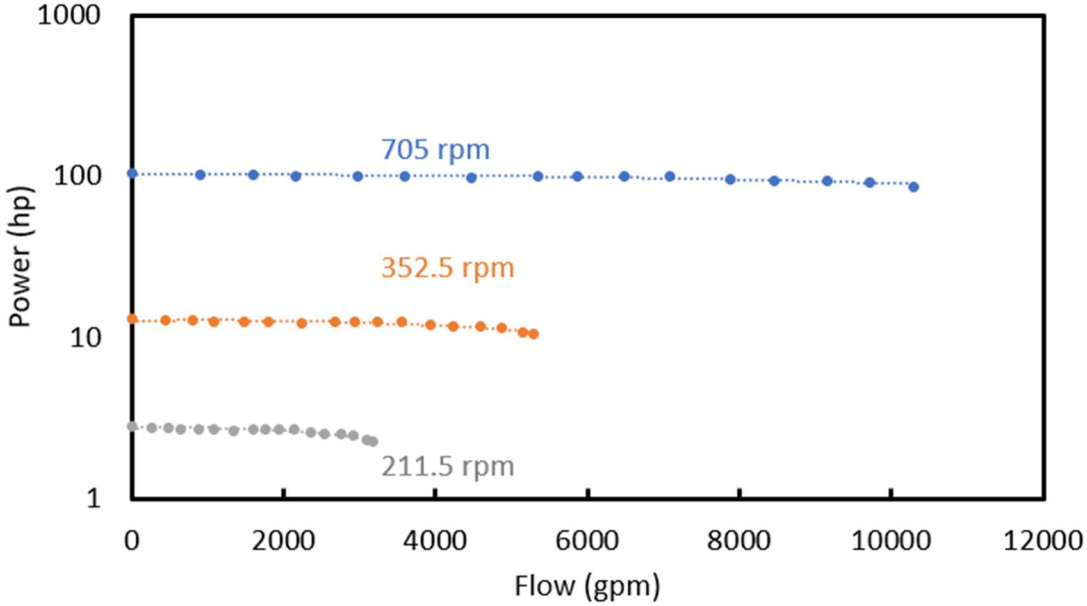

Figure 5.3: Extrapolated lean pump power from design curve

The lean pump speed was a function of the lean solvent volumetric flow and thus a function of temperature and composition. It also depended on the pressure drop in the lean

solvent line downstream of the lean pump. This pressure drop mainly considered the elevation head and frictional loss (which was assumed to be 10 psi), due to the pump being a cold lean pump. Future chapters will describe the use of a hot lean pump in certain design scenarios where the rating model is modified to include the pressure drop in the lean side of heat exchangers with the elevation head and frictional loss in the lean line, to calculate a hot lean pump pressure.

The elevation head in the lean solvent line was calculated using Equation 5.6. It depended on the difference between the stripper sump level and the lean solvent entry point in the absorber (approximately 85 ft). The stripper sump level was estimated by assuming 2-minute residence time in the sump and using the hot lean solvent flowrate. The sump diameter was the same as the stripper diameter.

$$\Delta P_{elevation,lean} = 10 + \frac{(85 - h_{stripper\ sump}) * \rho_{cold\ lean}}{144} \tag{5.6}$$

The lean pump speed was calculated using Equation 5.7 and used the base-case speed of 705 rpm and base-case head of 36 ft (15.6 psi).

$$RPM_{new} = 705 * \left(\frac{\Delta P_{elevation,lean}}{15.603}\right)^{0.5} \tag{5.7}$$

The total rich bypass line extends from the sump level of the stripper to the solvent entry point in the stripper column, giving rise to an elevation head. This must be accounted for to accurately balance the pressures in the cold rich bypass, warm rich bypass, and the remaining solvent line. This elevation head was calculated using Equation 5.8 by using the density of the flashing total rich bypass solvent and the total elevation of the stripper column (about 69 ft).

$$\Delta P_{elevation,TRBP} = 0.0301 * \frac{\rho_{liquid} + \rho_{mixed}}{2} \quad (5.8)$$

Three control valves were used to balance the pressure in the solvent lines. This was necessary due to the different pressure drop through each line and the use of a fixed rich pump outlet pressure. The cold rich and the warm rich bypass lines were mixed and sent to the top of the stripper column, where the pressure was slightly lower than the sump pressure due to the pressure drop through the packing and column internals. The remaining solvent line goes to the stripper sump.

Equations 5.9 to 5.12 represent the pressure drop in these three lines and were used to determine the valve opening (or pressure drop) required to balance the lines. They were also used as an indicator for infeasible cases, which correspond to operation requiring negative values of pressure drop through the valve.

$$\Delta P_{valve,CRBP} = P_{rich\ pump} - \Delta P_{rich\ side,CO2\ HX} - \Delta P_{elevation,TRBP} - P_{stripper\ overhead} \quad (5.9)$$

$$\Delta P_{valve,WRBP} = P_{warm\ rich\ solvent} - \Delta P_{elevation,TRBP} - P_{stripper\ overhead} \quad (5.10)$$

$$\Delta P_{valve\ 3} = P_{warm\ rich\ solvent} - \Delta P_{rich\ side,steam\ heater} - \Delta P_{rich\ side,hot\ HX} - P_{sump} \quad (5.11)$$

$$P_{stripper\ overhead} = P_{sump} - 2 \quad (5.12)$$

5.3.1 Operational Limit of Rich Pump

Being a fixed speed pump, the rich pump can only operate over a narrow range of rich solvent rate. In addition to this, the output pressure decreases with increasing solvent rate, making it impossible to satisfy the stripper pressure requirement of approximately 5.5 bar for 0.2

lean loading and a 150 °C stripper sump for certain bypass flow rates. This issue could be avoided by a variable speed rich pump or by operating at lower lean loading (pressure) at constant stripper sump temperature. Upcoming sections describe the use of stripper pressure or lean loading also as a decision variable.

Figure 5.4 shows the rich pump limit using the pressure drop through the valve in the solvent line going to the stripper sump. This is calculated using Equation 5.11. When this pressure drop is exactly 0, the output pressure of the rich pump and the stripper pressure are balanced, leaving no room for pressure drop through this valve (no flow control, fully open valve). When this pressure drop is negative, the operating condition is infeasible due to insufficient pressure at the pump. When this pressure drop is positive, the operating condition is feasible, and flow can be manipulated in the valve by inducing a pressure drop through the valve to balance the pressure requirement. Figure 5.4 can therefore be used to classify feasible operating conditions from infeasible operating conditions for PZAS at a lean loading of 0.2 and stripper sump temperature of 150 °C.

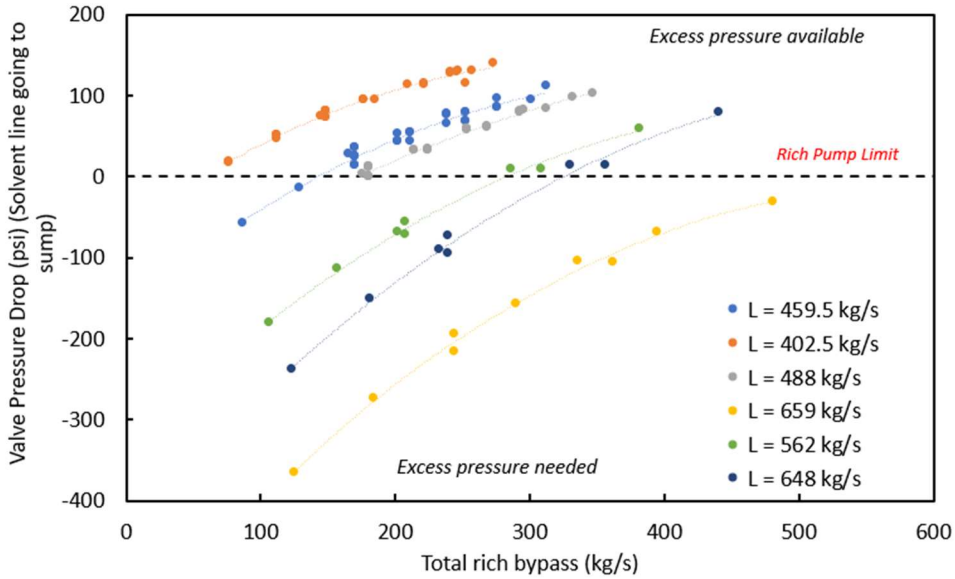

Figure 5.4: Limits of rich pump for a 150 °C and 5.5 bar stripper; feasible cases are above the zero line; infeasible cases are below the zero line.

Figure 5.4 shows that the rich pump limitation can also overcome during operation by using a lower rich solvent rate (or higher rich loading) at fixed lean loading, or by using a higher total rich bypass flow. As the rich solvent rate increases, the room for the feasible operation becomes increasingly limited.

5.4 OFF-DESIGN PERFORMANCE OF CO_2 COMPRESSOR

The CO_2 compressor was not modeled rigorously. Only a model for the power requirement of the compressor was included, which was regressed from data provided in vendor quotes. These included data for ambient temperature of 65 and 105 °F, which were used to regress compressor performance at 40 °F. Compressor performance curves are shown in Figure 5.5 for the design pressure of the stripper.

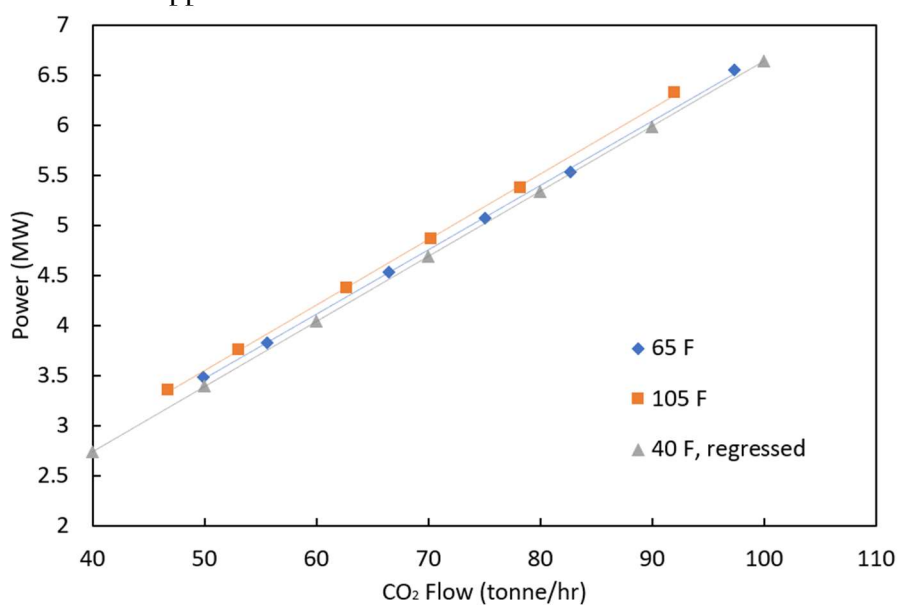

Figure 5.5: Compressor power as a function of CO_2 flow and ambient temperature

When operating at an off-design lean loading, the pressure and density of the CO_2 delivered to the compressor will differ from the base case. The pressure affects the power requirement, and the density affects the maximum inlet flowrate. The effect of pressure was estimated using an equation for the CO_2 compression work developed by Lin (2016). The effect of density was estimated using Aspen Plus® to determine the change in density for each case using Equations 5.13 to 5.18. Q_{CO2} in equation 5.16 refers to the mass flow rate of CO_2.

$$\mathrm{Power_{Compressor}} = \frac{(0.1295+0.0047\times \mathrm{T_{Amb.}}+0.065\times \mathrm{Q_{mass,CO_2}})\mathrm{W_{Comp}}}{\mathrm{W_{Comp,Base}}} \tag{5.13}$$

$$\mathrm{W_{Comp,Base}} = 8.87\,\frac{\mathrm{kJ}}{\mathrm{mol}} \tag{5.14}$$

$$\mathrm{W_{Comp}} = 15.3 - 4.6\ln(\mathrm{P_{in,comp}}) + 0.81(\ln(\mathrm{P_{in,comp}}))^2 - 0.24(\ln(\mathrm{P_{in,comp}}))^3 + 0.03(\ln(\mathrm{P_{in,comp}}))^4 \tag{5.15}$$

$$\mathrm{Q_{CO_2,Max}} = \frac{(-0.22\times \mathrm{T_{Amb.}}+101.2)\rho_{\mathrm{CO_2,P_{in}}}}{\rho_{\mathrm{CO_2,Base}}} \tag{5.16}$$

$$\rho_{\mathrm{CO_2,Base}} = 4.71\,\frac{\mathrm{kg}}{\mathrm{m^3}} \tag{5.17}$$

$$\rho_{\mathrm{CO_2,P_{in}}} = -552\mathrm{LDG_{Lean}^2} + 238\mathrm{LDG_{Lean}} - 20.8 \tag{5.18}$$

5.5 DEVELOPMENT OF SURROGATE MODELS FOR PZAS

This section details the surrogate model variables and ranges of applicability for the stripper section of the PZAS process. The surrogate models are presented in Appendix B. For details on the surrogate models for the absorber, water wash, and air coolers for intercooling and the water wash, refer to the report by Rochelle et al. (2022).

Surrogate models on the stripper side were constructed for the heat duty, CO_2 production rate, lean solvent temperature, stripper flooding in the top section of packing, stripper flooding in the bottom section of the packing, and average of cold lean and cold rich solvent temperatures

(to monitor solvent precipitation). These were the main variables on the stripper side that needed to be computed in MATLAB as a part of the process surrogate model. All the remaining variables were dependent variables and could be computed after the convergence of the MATLAB script.

The heat duty surrogate model used rich loading, rich solvent rate, cold rich bypass split fraction, warm rich bypass split fraction, rich solvent temperature, and lean loading as the independent variables. The rich loading varied from 0.35 to 0.44, the rich solvent rate from 250 to 550 kg/s, the cold rich bypass split fraction from 0.1 to 0.3, the warm rich bypass split fraction from 0.1 to 0.66, the rich solvent temperature from 44 to 52 °C, and the lean loading from 0.18 to 0.22 mol/mol. A total of 207 data points for heat duty were obtained using rating model simulations. The mathematical form of the model is shown in Appendix F with its R-squared value.

The CO_2 flowrate surrogate model used rich loading, rich solvent rate, cold rich bypass split, warm rich bypass split fraction, rich solvent temperature, and lean loading as the independent variables. The rich loading varied from 0.35 to 0.44, the rich solvent rate from 250 to 550 kg/s, the cold rich bypass split fraction from 0.1 to 0.3, the warm rich bypass split fraction from 0.1 to 0.66, the rich solvent temperature from 44 to 52 °C, and the lean loading from 0.18 to 0.22 mol/mol. A total of 205 data points for heat duty were obtained using rating model simulations. The mathematical form of the model is shown Appendix F with its R-squared value.

The lean solvent surrogate model used rich loading, rich solvent rate, cold rich bypass flowrate, warm rich bypass flowrate, rich solvent temperature, and lean loading as the independent variables. The rich loading varied from 0.35 to 0.44, the rich solvent rate from 250 to 550 kg/s, the cold rich bypass flowrate from 25 to 146 kg/s, the warm rich bypass flowrate from 20 to 275 kg/s, the rich solvent temperature from 44 to 52 °C, and the lean loading from

0.18 to 0.22 mol/mol. A total of 202 data points for heat duty were obtained using rating model simulations. The mathematical form of the model is shown in Appendix F with its R-squared value.

The stripper flooding surrogate models used rich loading, rich solvent rate, cold rich bypass flowrate, warm rich bypass flowrate, and CO_2 flowrate as the independent variables. The rich loading varied from 0.35 to 0.44, the rich solvent rate from 250 to 550 kg/s, the cold rich bypass flowrate from 25 to 146 kg/s, the warm rich bypass flowrate from 17.5 to 275 kg/s, and the CO_2 flowrate from 9 to 39 kg/s. A total of 189 data points for heat duty were obtained using rating model simulations. The mathematical form of the model is shown in Appendix F with its R-squared value.

In addition to the above models, a surrogate model of the average of the cold lean solvent and cold rich solvent temperatures was constructed to monitor the possibility of solvent precipitation as a function of lean loading. The model used rich loading, rich solvent rate, cold rich bypass flowrate, warm rich bypass flowrate, rich solvent temperature, and lean loading as the independent variables. The rich loading varied from 0.35 to 0.44, the rich solvent rate from 250 to 550 kg/s, the cold rich bypass flowrate from 25 to 146 kg/s, the warm rich bypass flowrate from 17.5 to 275 kg/s, the rich solvent temperature from 44 to 52 °C, and the lean loading from 0.18 to 0.22 mol/mol. A total of 146 data points for heat duty were obtained using rating model simulations.

5.6 PROCESS SURROGATE MODEL

All the surrogate models were combined in a MATLAB script to create an overall "process" surrogate model that can simulate the off-design performance of the absorber, stripper, air coolers, and water wash at much smaller convergence times compared to Aspen Plus®. This

method allows combination of the complex unit operations into a simpler code. Figure 5.6 shows the flow of data in the process surrogate model.

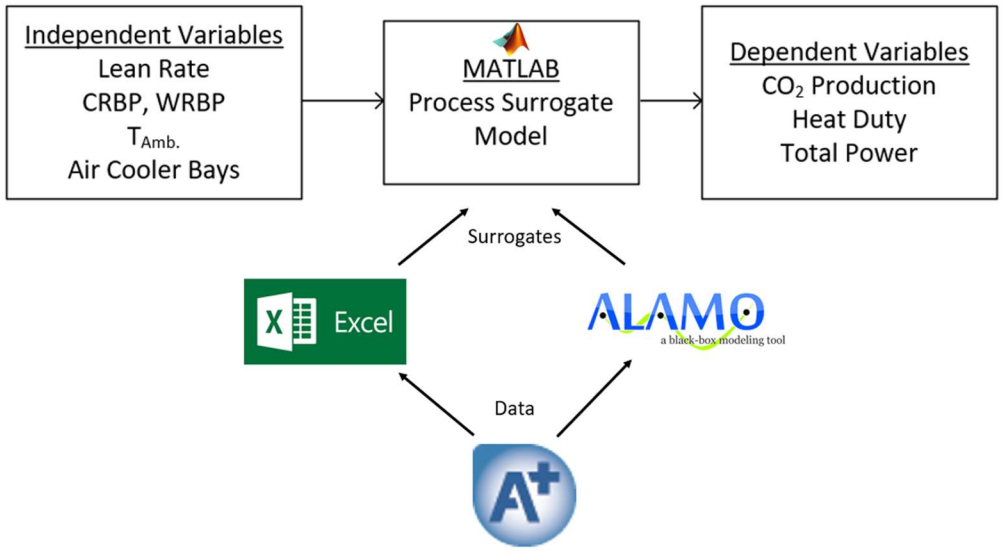

Figure 5.6: Interaction between different models and their data in the working of the process surrogate model

5.6.1 Convergence of Process Surrogate Model

The PZAS process script was used to determine the performance of the process at different values of the independent variables. These are: cold rich bypass fraction (CRBP), warm rich bypass fraction (WRBP), lean solvent flowrate, number of intercooler air cooler bays in operation, number of intercooler pumps, number of water wash pumps, and lean loading. The split fraction of the cold rich bypass was with respect to the total rich solvent, but the split of the warm rich bypass was calculated relative to the warm rich solvent flow rate leaving the cold cross exchanger.

This script includes the surrogate models for the absorber, stripper, air coolers, water wash, and compressor, and uses the algorithm shown in Figure 5.7. The script produces a matrix with the converged values of produced CO_2, heat rate, total power, and a "feasibility" variable (which is discussed in the upcoming sections), for all combinations of the 7 independent variables within user-defined ranges.

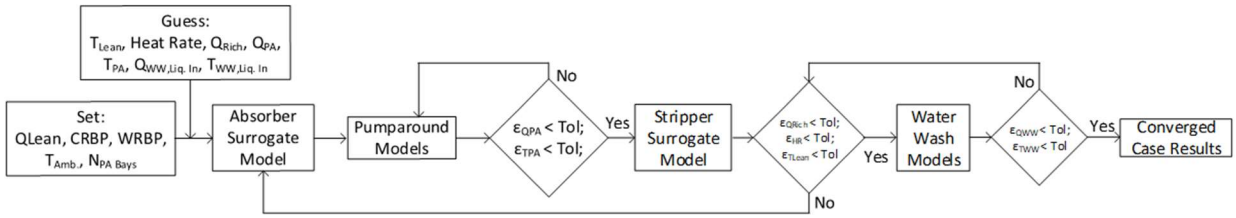

Figure 5.7: Convergence scheme to attain steady state using PZAS process surrogate model

To start the convergence process, guesses for key variables were required to initialize the models. These variables were: lean temperature, rich solvent flowrate, heat rate, flowrate, temperature of the outlet pump-around intercooling stream, and flowrate and temperature of the water wash liquid inlet stream.

The values pertaining to the design case were assigned as initial guesses, with the exceptions of the rich solvent flowrate and the water wash inlet flowrate. The initial guess for the rich solvent flowrate was set to the value of the lean solvent flowrate plus unity, since this was found to produce a faster convergence for the cases studied. Figure 5.8 shows a typical run for convergence of the process surrogate model for a fixed lean loading at 0.2 mol/mol at a fixed lean solvent rate. This particular run had an approximate convergence time of about 0.2 seconds to reach steady-state.

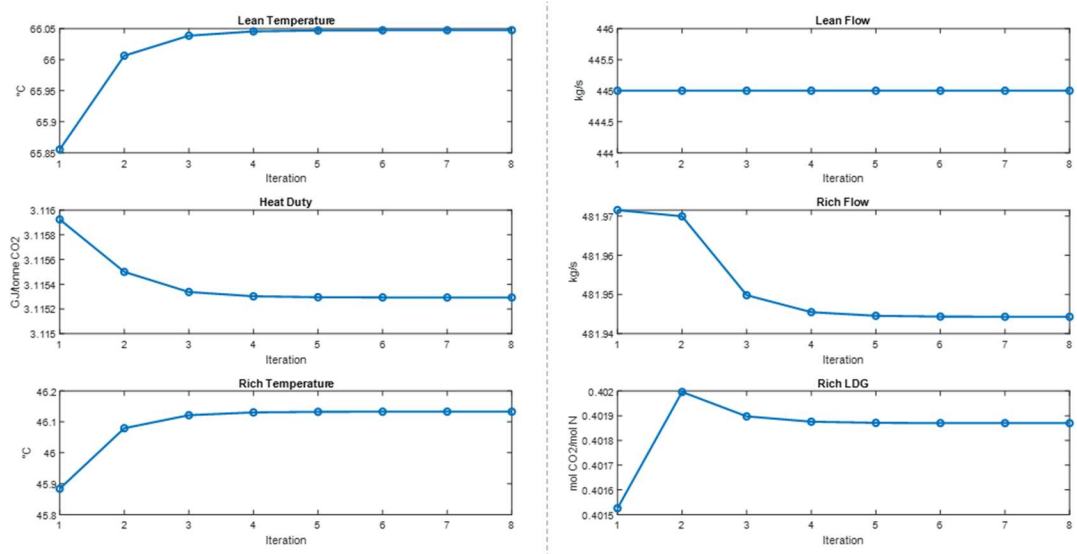

Figure 5.8: Process surrogate model reaches steady state in about 8 iterations

The initial guess for the water wash inlet flowrate was set to 1500 kg/s. This was because it was observed that using fewer than 20 air cooler bays in the water wash can allow for a flowrate higher than that of the design case (1300 kg/s). Setting the initial guess to the design case value was found to artificially set the upper limit of the flowrate to that value, which did not correspond to reality.

There are three main loops in the PZAS process script: the absorber loop, the stripper loop, and the water wash loop. The error in these key variables was tracked between subsequent iterations, and all loops were iterated upon until all errors were lower than 0.1%. The error in the flowrate and temperature of the outlet pump-around intercooling stream were tracked in the absorber loop; the error in the rich solvent flowrate, the heat rate, and the lean solvent temperature were tracked in the stripper loop; and the error in the flowrate and temperature of the water wash liquid inlet stream were tracked in the water wash loop.

The absorber loop contains the ALAMO surrogate models for the absorber and the air coolers used for the pump-around intercooler. The pump-around intercooler model included a

check to ensure the pumps can provide an outlet pressure above the head requirement. When the pressure was not sufficient, the MATLAB function *fzero* was used to determine a viable flowrate. The result depends on the number of intercooler air cooler bays in operation.

The stripper loop contains the ALAMO surrogate models for the stripper side of the process. A correction was made to the rich flowrate estimated by the absorber model to reflect the amount of water added to the rich solvent stream to achieve a PZ concentration of 5 molal. The corrected rich flowrate was used as an input variable to the stripper-side ALAMO surrogate models.

The water wash loop section contains the ALAMO surrogate models for the water wash, for the absorber gas outlet stream, and for the air coolers used in the water wash. The water wash intercooler model included a check to ensure the pump outlet pressure was above the head requirement for all cases. If the pressure was not sufficient, *fzero* was used to determine a new flowrate.

The water balance in the absorber was calculated as the difference between the water flowrate entering the absorber unit and the water flowrate in the water wash gas outlet. Because the latter depends on the number of air cooler bays in operation, the water balance closure was calculated for 5 to 20 bays. This result was then used to determine the number of air cooler bays that would more closely balance the water in the system for every case.

All calculations pertaining to the power requirements of the different equipment were done outside the three loops. These can be calculated using the final converged values of the PZAS process variables, avoiding multiple intermediary calculations that substantially slow down the execution time of the script. The calculation of the absorber mass transfer units, absorber flooding, and stripper flooding were also done outside of the three loops, for the same reasons.

The lean solvent pump power requirement was determined by calculating the required pump speed to overcome the total head requirement for the lean solvent line. This was done by finding the solution to Equation 5.19 using the MATLAB function *fzero*, and then using the pump affinity laws shown in Equations 5.20 and 5.21 to calculate the required pump speed and power requirements.

$$\Delta P_{N_2,ft} = \left(-1.92E-7Q_{1gpm}^2 - 7.23E-4Q_{1gpm} + 5.01\ E1\right) * \left(\frac{Q_{2gpm}}{Q_{1gpm}}\right) \tag{5.19}$$

$$N_2 = \frac{Q_{2gpm}}{Q_{1gpm}} * N_1 \tag{5.20}$$

$$Power_{N_2} = \left(\left(-2.1E-7Q_{1gpm}^2 + 8.3E-4Q_{1gpm} + 1.02E2\right) * \left(\frac{N_2}{N_1}\right)^3\right) 1341 \tag{5.21}$$

Equations 5.22 to 5.24 were used to calculate the power requirements of the rich solvent pump, the intercooler pumps, and the water wash pumps. All these curves were obtained by regression of the corresponding vendor-provided power performance curve. The calculations done for the lean pump were not required for these units as they were all fixed speed pumps.

$$Power_{Rich\ Pump} = \frac{967.5-3.9E-3T_{Rich}^2+4.4E-4Q_{mass,Rich}^2}{1341} \tag{5.22}$$

$$Power_{IC\ Pumps} = \frac{\left(N_{PA}\left(337.2-0.13\frac{Q_{mass,PA}}{N_{PA}}-2E4\left(\frac{Q_{mass,PA}}{N_{PA}}\right)^2+1.25E-6\left(\frac{Q_{mass,PA}}{N_{PA}}\right)^3-1.02E-9\left(\frac{Q_{mass,PA}}{N_{PA}}\right)^4\right)\right)}{1341} \tag{5.23}$$

$$Power_{WW\ Pumps} = \frac{N_{WW}*289.4+Q_{mass,WW}*0.26}{1341} \tag{5.24}$$

Equations 5.25 to 5.27 were used to calculate the power requirement of the intercooler and water wash air cooler bay fans. Equation 5.27 was used to calculate the number of fans in service for both the intercooler and water wash air cooler units.

$$\mathrm{Power}_{\mathrm{IC\ Fans}} = 29.4\,\frac{\mathrm{N}_{\mathrm{IC\ Fans}}}{1341} \tag{5.25}$$

$$\mathrm{Power}_{\mathrm{WW\ Fans}} = 36.6\,\frac{\mathrm{N}_{\mathrm{WW\ Fans}}}{1341} \tag{5.26}$$

$$\mathrm{N}_{\mathrm{Fans}} = \mathrm{N}_{\mathrm{Bays}} * 3 \tag{5.27}$$

The power requirements of the HRSG flue gas and gas-fired boiler flue gas fans were calculated with the respective surrogate model equations shown in Appendix B. The power requirement of the HRSG flue gas fan was doubled since the surrogate model pertained to a single fan only. The standalone natural gas boiler efficiency was 94% as noted from the boiler performance data.

The total power requirement of the PZAS process was calculated as the sum of the power requirements of all pieces of equipment multiplied by the number of process trains online.

5.6.2 Operational Constraints in Process Surrogate Model

The PZAS process script has several Boolean feasibility flags that represent process constraints. The flags were initialized as true and were automatically switched to false if any of the constraint conditions were not met during the convergence process. This automatically stopped the execution of the case and flagged it as infeasible. Feasibility flags were used for the cold and rich bypasses, the lean solvent pump, the rich solvent pump, the CO_2 compressor, the gas-fired boiler, the gas-fired boiler fan, the stripper flooding, the absorber flooding, and solvent precipitation. Table 5.2 summarizes these feasibility flags.

Table 5.2: Feasibility flags incorporated in optimization model

Feasibility flag	Constraint addressed
Cold and Warm Rich Bypass Flowrate	CO_2 exchanger cold-side pinch
Lean Pump Operation	Pump cavitation
Rich Pump Operation	Max. head
CO_2 Compressor Operation	Max. Capacity
Gas-Fired Boiler	Max. Capacity
Gas-Fired Boiler Fan	Max. Capacity
Absorber Flooding	Max. Capacity (100%)
Stripper Flooding	Max. Capacity (100%)
Solvent Precipitation	Minimum Temperature

The feasibility flag for cold and warm rich bypasses represents a process constraint and a limitation of the stripper surrogate model. This flag was set to false in cases where the cold rich bypass fraction was equal to 0.3 and the warm rich bypass fraction was larger than 0.3. A cold side pinch in the CO_2 heat exchanger was observed in Aspen Plus® beyond this limit, which represents a performance limitation.

The feasibility flag for the lean solvent pump represents cavitation of the pump. The feasibility flag was set to false for cases where the lean solvent bubble point pressure was higher than pressure at the pump inlet minus the required NPSH. Equations 5.28 to 5.31 were used for this purpose. Equation 5.2 was used to calculate the lean side pressure drop at the cold and hot heat exchangers.

$$P_{Bubble,Lean} = 4E-5 * T_{Lean}^3 - 4.8E-3 * T_{Lean}^2 + 0.26 * T_{Lean} - 4.54 \quad (5.28)$$

$$P_{Lean\ Pump\ In} = P_{Stripper\ Sump} - \Delta P_{Lean,Hot\ HX} - \Delta P_{Lean,Cold\ HX} \quad (5.29)$$

$$P_{Stripper\ Sump} = \frac{m_{Lean} * \tau_{Sump}}{A_{Stripper} * 2310 * 0.3048} \rho_{Lean} \quad (5.30)$$

$$NPSH_{Req.\ Lean} = \frac{9.41E-8 * Q_{Lean}^2 - 8.6E-4 * Q_{Lean} + 1.11E1}{\frac{2310}{\rho_{Lean}}} \quad (5.31)$$

The feasibility flag for the rich pump represents two different limits. The first was whether the volumetric flowrate was smaller than the minimum stable continuous flow as defined in the vendor-provided specification sheet. The second was a check on the rich-side pressure balance to determine the valve pressure drop required to achieve 80 psia at the stripper. This flag was set to false if the calculated valve pressure drop was negative.

The CO_2 compressor, gas-fired boiler, and gas-fired boiler fan feasibility flags each represent the upper operating limit of the respective equipment as defined in the vendor quotes. The CO_2 compressor flag was set to false when the amount of CO_2 produced was higher than that determined by Equation 5.16. The gas-fired boiler feasibility flag was set to false when the heat rate was higher than 311.6 MMBtu/hr. The gas-fired boiler fan feasibility flag was set to false when the fan speed was higher than 1756 RPM.

The flags for stripper flooding and absorber flooding represent the typical operating limit of 100% flooding. The respective flag was set to false when either of the packing sections in the stripper or the absorber had a flooding above 100%.

The solvent precipitation flag represents the solubility window for 5 m PZ. The flag was set to false when the average of the cold lean and cold rich temperature was below the transition temperature for the formation of PZ•6H_2O. The transition temperature for 5 m PZ was calculated as a function of lean loading using Equation 5.32.

$$T_{Trans} = -499 * LDG_{Lean}^2 + 6.8 * LDG_{Lean} + 41 \quad (5.32)$$

To avoid low lean solvent temperatures and risk solids precipitation at a given rich solvent temperature, the cold rich bypass and warm rich bypass flow rates can be increased, as they increase the lean temperature. This can be particularly useful on cold winter days when the rich solvent temperature is low. Figure 5.9 shows the effect of cold rich bypass and rich solvent temperature on lean solvent temperature.

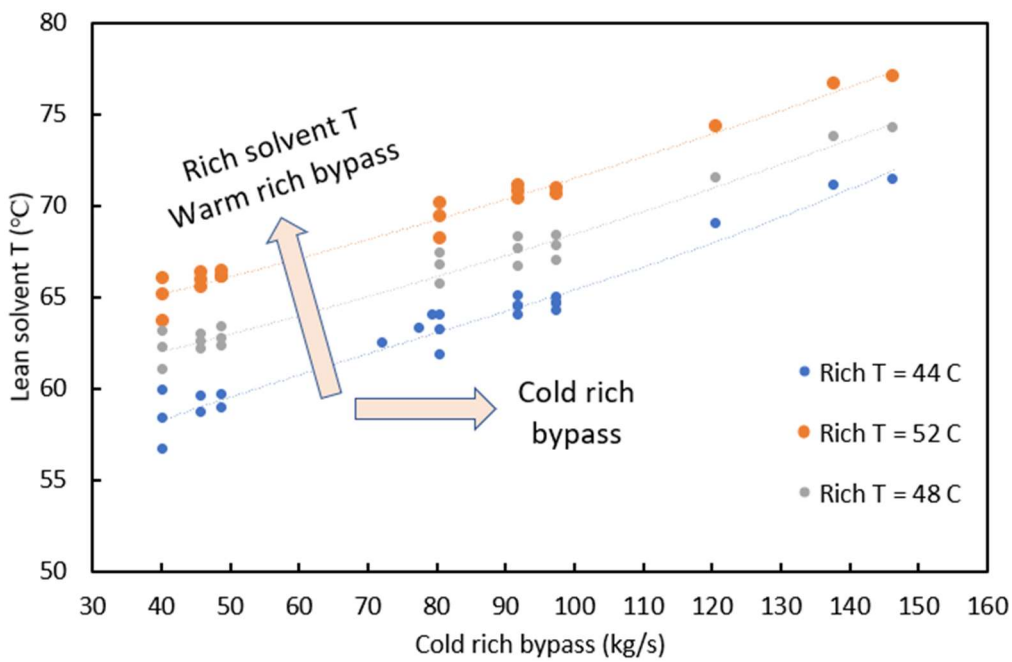

Figure 5.9: Effect if rich solvent temperature and cold rich bypass flow on lean solvent temperature

5.6.3 Modified Bypass Extraction Strategy for FEED of PZAS

A modified bypass extraction strategy for the FEED of PZAS was simulated using the rating model for the stripper side. This was done to eliminate the vapor content in solvent lines upstream of control valves.

The base case consists of two cold cross exchangers in parallel, each with an NTU of 5.3, a hot exchanger with an NTU of 1.7, and CO_2 exchanger with an NTU of 4. The three major solvent lines have individual control valves to control the flow through these lines, as shown in Figures 5.10 and 5.11. Once the cold rich bypass is extracted, the remaining solvent is split in half and sent through the cold cross exchangers. Downstream of the cold cross exchangers, the warm rich bypass is drawn and sent to the top of the stripper. The remaining solvent goes through the hot exchanger and steam heater to the bottom of the stripper.

On the lean side, similarly, the warm lean solvent is split into two and sent into the two cold exchangers. The lean side of the cross exchangers are identical in their flow paths, requiring equal flow through this side. The warm rich solvent entering the control valve contains 0.4 mol % vapor. All the specifications for this design case are shown in Figure 5.10.

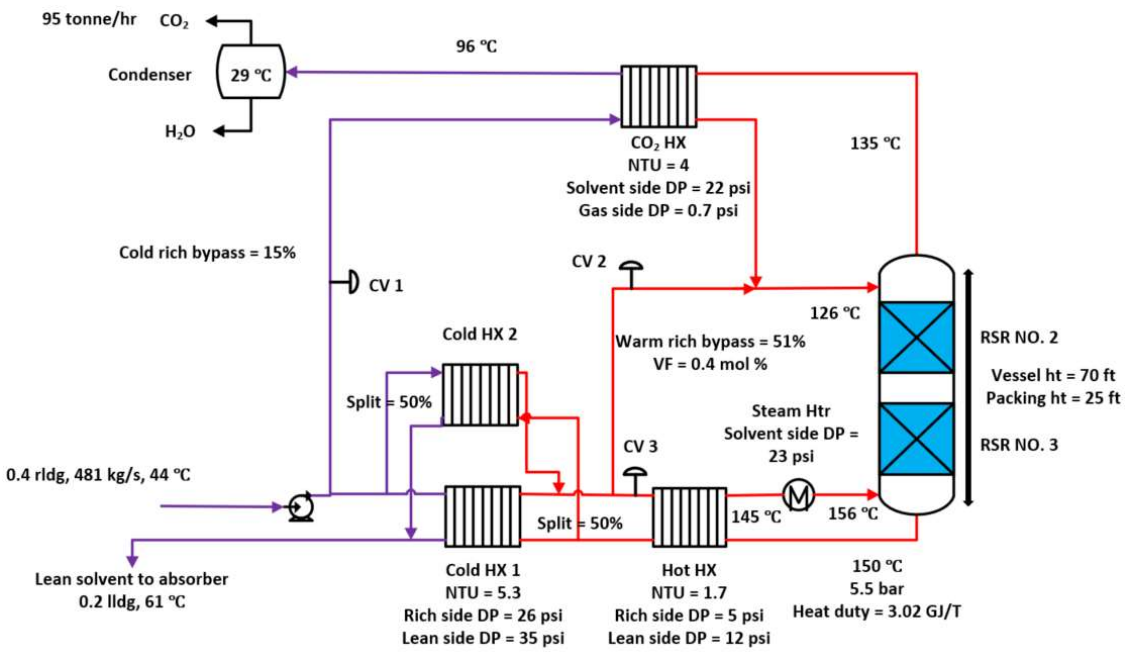

Figure 5.10: Design specifications at base case conditions

The vapor fraction in the warm rich solvent as it enters the control valve (CV2) interferes with valve design and performance. To avoid this, a modified bypass extraction is considered where the bypasses are extracted at high pressure after the rich solvent pump, upstream of heat exchangers. This modified scenario will be evaluated for its performance using the rating model.

In the modified configuration, shown in Figure 5.11, the flow through the heat exchangers will change compared to the base case design due to the extraction of bypasses upstream of the cold cross exchanger. The cold rich bypass still passes through the CO_2 heat exchanger. The warm rich bypass passes through the 2nd cold cross exchanger and the remaining rich solvent passes through the 1st cold cross exchanger, the hot cross exchanger, and the steam heater. The cold and warm rich bypasses are reoptimized to reflect these changes. The method for scaling pressure drop is shown in Equation 5.2 and Table 5.1 compares the base case flows with the flows in the modified design. The lean solvent split is maintained at 50% to provide equal flow

through the lean side of the cross exchangers. The lean side of the exchangers are identical in their path and therefore require the same flow.

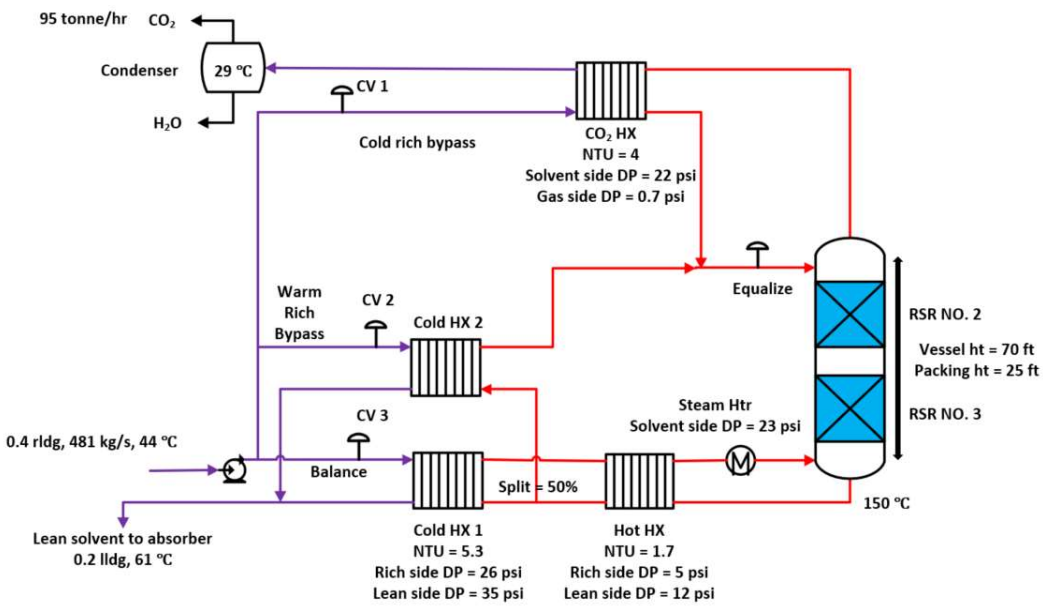

Figure 5.11: Modified bypass extraction for PZAS to avoid flashing in solvent lines entering control valves

The lean side solvent flow rate (for the same path length) remains unchanged for the hot exchanger compared to the base case. Therefore, the lean side pressure drop of the hot exchanger remains the same as that of the base case. The split of the warm-lean solvent is an additional degree of freedom presented by the modified configuration. For this case, this split is maintained to be 50% just as in the base case design, and therefore the lean side pressure drop of the two cold cross exchangers also remains equal to that of the base case design.

5.6.3.1 Simulation of Modified Configuration

In the simulation of the modified PZAS configuration, the total rich-side pressure drop in the three main solvent lines was calculated. In the cold rich bypass, this includes the sum of

the pressure drop across CV 1 and pressure drop in the solvent side of the CO_2 exchanger. In the warm rich bypass line, this includes the sum of the pressure drop across CV 2 and pressure drop in the rich side of the 2nd cold cross exchanger. In the "balance" solvent line, this includes the sum of the pressure drop in the rich side of the 1st cold cross exchanger, pressure drop in the rich side of the hot cross exchanger, solvent side pressure drop in the steam heater, and pressure drop across CV 3.

The line with the greatest pressure drop determined the pump output pressure and the control valve in this line is kept fully open ($\Delta P = 0$). The pressure drop in the remaining control valves needs to be changed to balance pressure and flow control. This was done in the absence of rich pump performance curves at the time of this design.

The heat exchanger pressure drops are a function of flow and are fixed for every combination of cold rich and warm rich bypass. The pressure drop in the control valves CV 1 and CV 2 is adjusted to satisfy an isobaric condition before and after the mixing point of the bypasses. Additionally, the "equalize" valve exists right before the total rich bypass enters the stripper to simulate the flashing at the entry point in the stripper. The pressure drop in this valve must equal the elevation head in the total rich bypass line calculated based on solvent density. This valve also ensures that the total rich bypass enters the stripper at the same pressure as the top-most stage in the stripper, which is 2 psi lower than the sump pressure to account for pressure drop through the packing (2 in water/ft at flooding).

5.6.3.2 Scenario 1: Fluid Density in Total Rich Bypass Line Determines Elevation Head

In this scenario, to evaluate the elevation head in the total rich bypass line, the mixed fluid density is used. The average mixed density of the total rich bypass line before and after the control valve is used along with the total stripper vessel height (69 ft) to give an elevation head.

The final design for this scenario is shown in Figure 5.12. The calculated elevation head matches the pressure drop across the control valve in the total rich bypass line at 9.5 psi. The optimum cold rich bypass and warm rich bypass are 18.5% and 43% respectively, with the remaining 38.5% passing through the hot cross exchanger and steam heater. This is like the base case design where 34% of the solvent passes through the hot cross exchanger and steam heater.

Most importantly, Figure 5.12 shows that this design eliminates flashing in the solvent lines entering the three control valves upstream of the cross exchanger at slightly reduced energy requirement (2.95 GJ/tonne) compared to the base case value of 3 GJ/tonne.. This design requires flow control in the cold rich bypass and warm rich bypass line with the valve in the "balance" line kept open. The required rich pump pressure is 137 psia and the pump work is 0.57 MW.

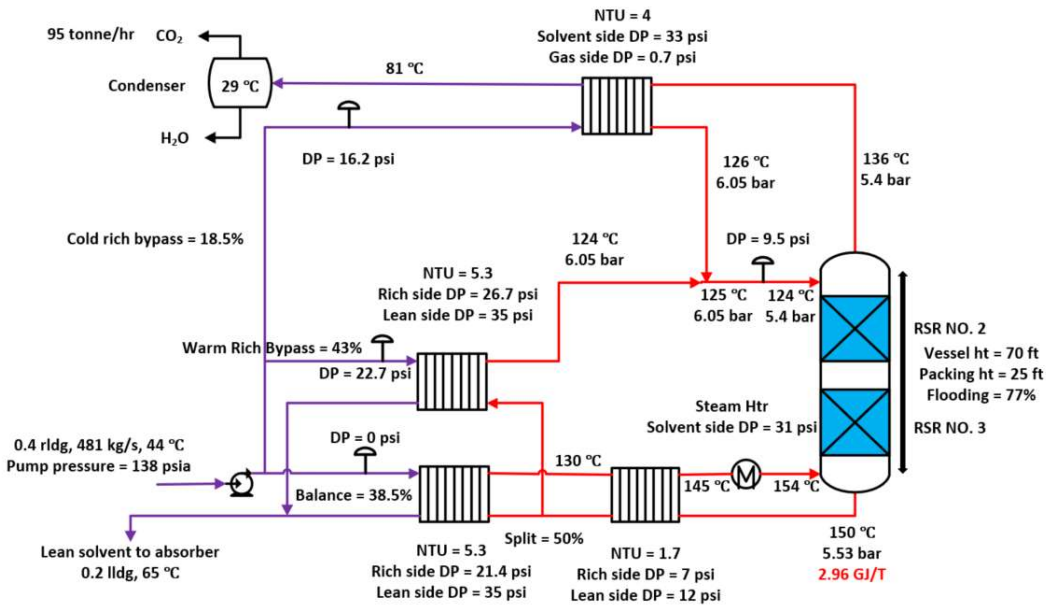

Figure 5.12: Design specifications of scenario 1 with the modified bypass extraction; this alternative to the base case design eliminates two phase flow in the warm rich lines until just before the stripper.

5.6.3.3 Scenario 2: Liquid Density in Total Rich Bypass Line Determines Elevation Head

In this scenario, to evaluate the elevation head in the total rich bypass line, the average of the liquid density before and fluid density after the control valve on the total rich bypass line is used along with the stripper vessel height. This combination of densities is likely to more closely approximate the liquid-only density of the line compared to an average density calculated using liquid densities only. This is because the solvent is likely to be flashing as it enters the stripper during regular operation. The final design for this scenario is shown in Figure 5.13.

The calculated elevation head in this case is higher than in scenario 1 and matches the pressure drop across the control valve in the total rich bypass line at 20.3 psi. The optimum cold rich bypass and warm rich bypass are 20.3% and 42.3% respectively, with the remaining 37.4% passing through the hot cross exchanger and steam heater. Flashing is eliminated in solvent lines entering the control valves and the energy requirement is 2.96 GJ/tonne. In this design, flow control is required in the "balance" line and the warm rich bypass line, while the control valve in the cold rich bypass line can be kept open. The required rich pump pressure is 139 psia and the pump work is 0.58 MW.

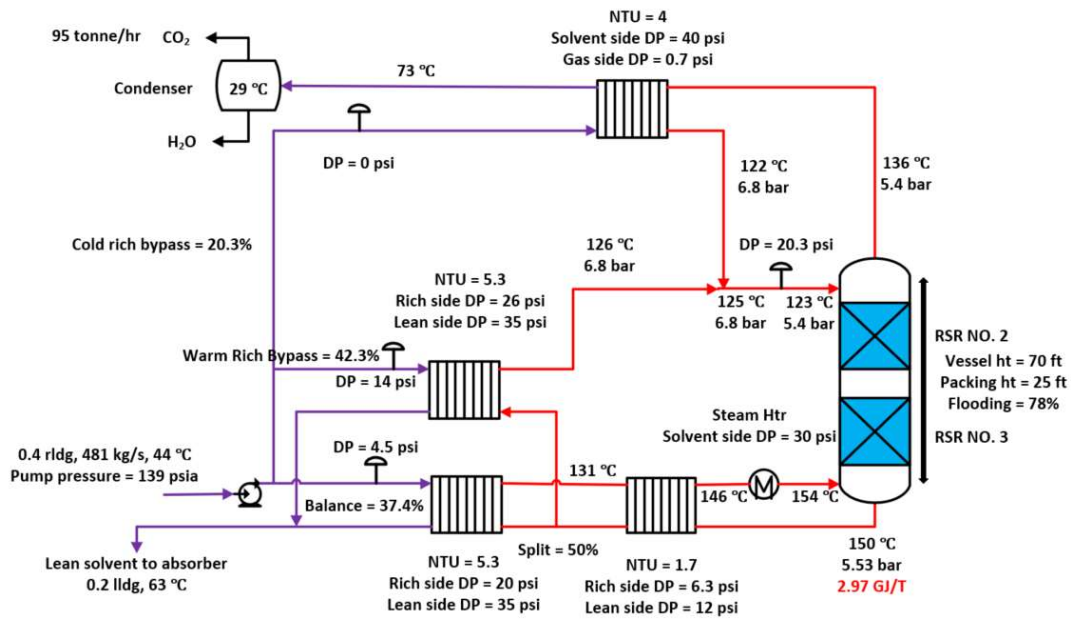

Figure 5.13: Design specifications of scenario 2 with the modified bypass extraction; this alternative to the base case design eliminates two phase flow in the warm rich lines until just before the stripper.

5.6.3.4 Control Valve Operation

The operation of the control valve in each major solvent line is shown as a function of total rich bypass in Figure 5.14. At fixed heat exchanger performance, the line with the greatest pressure drop is assumed to dictate the pump output pressure in the absence of pump performance curves. The valve in this line is kept open (no flow control, pressure drop = 0 psi), and flow control must be implemented in the remaining two solvent lines (non-zero control valve pressure drop).

In Figure 5.14, control valve operation is classified into two modes: mode "1" represents an operating valve (flow control) and mode "0" represents an open valve. Figure 5.14 shows that for total rich bypass up to about 60%, flow control is required in the cold rich bypass and warm rich bypass lines. At total rich bypass greater than 60%, flow control is required in the

"balance" solvent line. For design scenario 1, flow control in the cold rich bypass and warm rich bypass lines with the valve in the "balance" line kept open. For design scenario 2, flow control is required in the "balance" line and the warm rich bypass line while the control valve in the cold rich bypass line can be kept open.

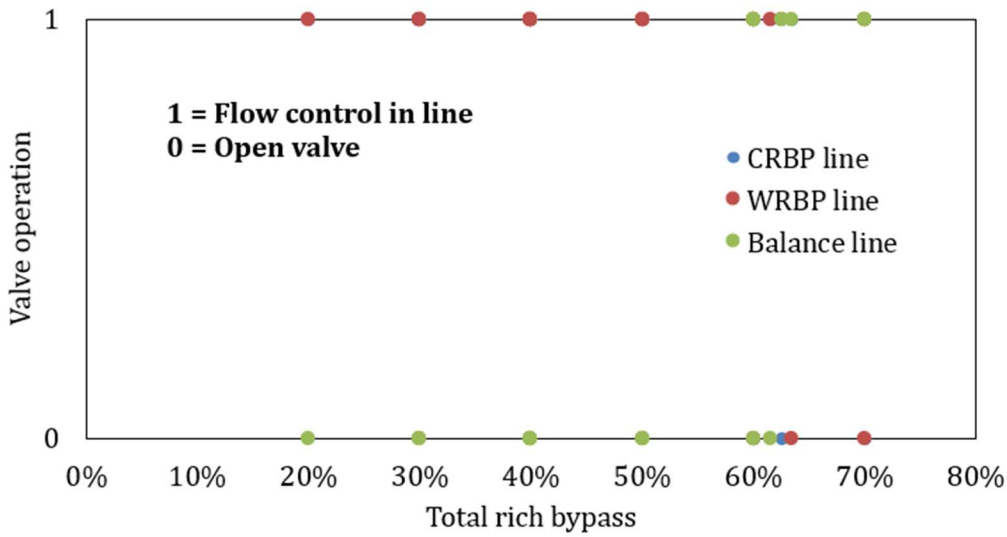

Figure 5.14: Valve operation as a function of total rich bypass

5.6.3.5 Vapor Content in Solvent Lines

Table 5.3 reports the vapor mole fraction in the heated warm rich bypass line, heated cold rich bypass line, and total rich bypass line after the control valve. The heated warm rich bypass and cold rich bypass lines are horizontal while the total rich bypass line is vertical until it enters the stripper at the top. While the vapor content ranges only from 0.45% to 1% for horizontal lines and from 0.66% to 1.16% for vertical lines on a mole basis, the volume vapor fraction is much higher at 46–70% for horizontal lines and 56–74% for vertical lines, possibly resulting in slug or annular flow in both vertical and horizontal lines. While the modified configurations

eliminated flashing as the solvent entered the valves CV1, CV2, and CV3 (Figure 5.11), there is always two-phase flow downstream of all the valves.

Table 5.3: Vapor content in solvent lines after control valves for two design scenarios with modified bypass extraction

Stream	Design Scenario	Mole vapor fraction (%)	Volume vapor fraction (%)
Heated Warm Rich Bypass	1	0.9	65.9
Heated Cold Rich Bypass	1	1.04	69.1
Total Rich Bypass	1	0.94–1.16	66.9–73.7
Heated Warm Rich Bypass	2	0.77	59.5
Heated Cold Rich Bypass	2	0.45	45.9
Total Rich Bypass	2	0.66–1.1	55.7–71.9

5.7 CONCLUSIONS

- A rating model of the PZAS process for the FEED was created to evaluate off-design performance of the stripper by incorporating the effect of pressure drop/elevation head in solvent lines and heat exchangers as a function of mass flow, and pump performance as a function of solvent flowrate.
- The rich pump, being a fixed speed pump, delivered solvent at a lower pressure at higher solvent flowrate. During design, one way to overcome this would be to operate at lower lean loading at constant stripper sump temperature, thereby operating the stripper with a lower pressure requirement. During operation, the rich pump limitation can be overcome by using a lower rich solvent rate (or higher rich loading) at fixed lean loading, or by using a higher total rich bypass flow. As the rich solvent rate increases, the room for the feasible operation becomes increasingly limited.

- The rating model showed that to avoid low lean solvent temperatures and risk solids precipitation at a given rich solvent temperature, the cold rich bypass and warm rich bypass flow rates can be increased, as they increase the lean temperature, which could be particularly useful on cold winter days when the rich solvent temperature is low.
- The vapor fraction in the warm rich bypass in the base case design was about 0.4 mol% upstream of a flow control valve, which could lead to issues with valve operation and maintenance. A modified bypass extraction strategy where both the cold and warm rich bypasses were extracted at high pressure downstream of the rich pump and upstream of the cross exchangers was evaluated to mitigate this issue. The modified bypass extraction eliminated vapor upstream of control valves and reduced the heat duty to about 2.95 GJ/tonne CO_2 from 3 GJ/tonne in the base case. Vapor content downstream of control valves ranged from 46-74 vol% resulting in possible slug or annular flow in horizontal and vertical lines.
- Surrogate models on the stripper side were constructed using ALAMO Model Building Tool for the heat duty, CO_2 production rate, lean solvent temperature, stripper flooding in the top section of packing, stripper flooding in the bottom section of the packing, and average of cold lean and cold rich solvent temperatures (to monitor solvent precipitation) using the data obtained from the rating model.
- The operational ranges for different input variables in the surrogate model are given below:
    - Rich loading: 0.35-0.44 mol/mol
    - Lean loading: 0.18-0.22 mol/mol
    - Rich solvent rate: 250 to 550 kg/s
    - Cold rich bypass split: 0.1-0.3
    - Warm rich bypass split: 0.1-0.66
    - Rich solvent temperature: 44-52 °C

- CO_2 flowrate: 9-39 kg/s

- Stripper-side surrogate models were combined with absorber, air-cooler, and water wash surrogate models into a process surrogate model script in MATLAB™ which was solved using a back-substitution method for steady state values of output variables in the process. The independent variables were cold rich bypass fraction (CRBP), warm rich bypass fraction (WRBP), lean solvent flowrate, number of intercooler air cooler bays in operation, number of intercooler pumps, number of water wash pumps, and lean loading. The surrogate model improved ease of convergence and reduced time of convergence compared to Aspen Plus®.
- The process surrogate model contained several process constraints to avoid infeasible operational conditions in the steady state operation, which were coded in as feasibility flags. Feasibility flags were used for the cold rich bypass limits, cavitation of the lean solvent pump, the rich solvent pump pressure, the CO_2 compressor limit, the gas-fired boiler limit, the gas-fired boiler fan limit, the stripper flooding limit, the absorber flooding limit, and solvent precipitation.

RECOMMENDATIONS FOR FUTURE WORK

- Future iterations of the rating and surrogate models could include larger variable ranges or incorporate different heat exchanger sizes, stripper packing height, stripper diameter etc. as additional variables. This will aid in design optimization in addition to rating optimization, and make the models applicable to other flue gas sources and plant locations.
- Process optimization and convergence of PZAS could be better implemented in equation-oriented platforms unlike Aspen Plus®, that simultaneously solve all differential equations involved in the process flowsheet. This will not only further improve convergence time and ease, but also remove the need for the creation of surrogate models that tend to be data and time intensive.

- The effect of water cooling for intercooling and water wash instead of air cooling should be investigated as a cheaper alternative, and should be modeled, rated, and optimized.

ACKNOWLEDGEMENTS

The author would like to acknowledge the contributions of Miguel Abreu, Benjamin Drewry, and Yee Lee Chen for the creation of rating models for the absorber side, air coolers for water wash and intercooling, and for the collection of absorber and stripper data in Aspen Plus® to create surrogate models, respectively. The author would like to acknowledge the contribution of Miguel Abreu in the creation of the MATLAB process surrogate model.

Chapter 6: Optimization of Off-Design Performance of PZAS

Chapter 5 dealt with the construction of rating and surrogate models for the stripper and compressor system. Chapter 6 builds on Chapter 5 by overlaying an optimization model on the process surrogate model to optimize 7 independent variables to maximize variable profit. Details on the optimization model and its code are provided in Appendix B and Chapter 5.

The variable profit considers the cash flow for gas and power consumption, and revenue from CO_2. These depend on gas price, power price, and value for CO_2. All dependent variables like rich loading, CO_2 removal, and heat duty were calculated from the optimized independent variables. This analysis was done with variable flue gas specifications for 3 different ambient temperatures – 40, 65, and 105 °F. The results of this chapter will guide plant operation to maximize the variable profit.

Parts of this chapter have been submitted for publication in *Industrial and Engineering Chemistry Research* journal.

The author would like to acknowledge the contributions of Miguel Abreu in the construction of absorber-side rating and surrogate models, and the steady-state process surrogate model in MATLAB, Benjamin Drewry in the construction of rating and surrogate models for the air coolers for intercooling and water wash, and Yee Lee Chen in obtaining data from Aspen Plus® for absorber and stripper-side rating models to construct the surrogate models.

6.1 FLUE GAS CASES INVESTIGATED

The process surrogate model that was built in MATLAB (Chapter 5) was used to estimate off-design process performance of PZAS for different flue gas specifications (shown in Table 6.1).

Table 6.1: Flue gas conditions considered for process optimization

Case (Amb. T, HRSG Flue Gas %, Duct Burn.)	A 40 °F, 95%, No DB	B 65 °F, 72%, No DB	C 65 °F, 95%, No DB	D 65 °F, 100%, DB	E 105 °F, 95%, No DB
Temperature, °F	222.1	220.1	220.1	220	217.4
Flowrate, lb/hr	3,432,795	2,283,803	3,010,027	3,172,189	2,841,211
CO_2, mol %	3.84	3.84	3.84	3.99	3.82
H_2O, mol %	7.93	8.53	8.53	8.81	10.08
N_2, mol %	75.54	75.05	75.05	74.24	73.80
O_2, mol %	12.69	12.58	12.58	12.95	12.30

For cases shown in Table 6.1, the HRSG flue gas flowrate, temperature, and composition were different. While for cases at 65 °F and 105 °F ambient temperature, these values were directly obtained from the mass balance data provided by GSEC (Golden Spread Electric Cooperative), the values for the 40 °F case were obtained through interpolation. More details on absorber side rating and surrogate models are by Rochelle et al. (2022).

6.2 OPTIMIZATION OF VARIABLE PROFIT

For cases defined in Table 6.1, a sensitivity of process performance over specified ranges of the 7 independent variables was conducted and the steady state results recorded. This was done by the process surrogate model whose construction and working are explained in Chapter 5.

In this sensitivity analysis, cold rich bypass split fraction was varied between 0.1 and 0.3 with a step size of 0.02 (9 intervals). Warm rich bypass split fraction was varied between 0.05 and 0.6 with a step size of 0.029 (19 intervals). The lean solvent rate varied between 250 and 550 kg/s with a step size of 1.2 kg/s (249 intervals). Air cooler bays for intercooling varied between 6 and 20 with a step size of 1 (14 intervals). Pumps for intercooling varied between 1 and 2 with a step size of 1 (2 intervals). Pumps for water wash varied between 1 and 2 with a step size of 1 (2 intervals). Lean loading varied between 0.18 and 0.22 mol/mol with a step size of 0.004 mol/mol (9 intervals).

Lean loading has an uncertain constraint associated with the precipitation of piperazine hexahydrate when the system must shut down. During normal operation the process can be constrained by monitoring the loading and temperature of the cold lean solvent. However, there is a concern that precipitation may occur if the system shuts down and leaves lean solvent that cools to a much lower temperature. Therefore, arbitrarily low lean loading values of 0.2 and 0.18 have been considered for this work.

Once steady state was attained, for each combination of these independent variables, an independent variable profit was calculated according to Equation 6.1. This calculation was repeated over a range of gas and power prices expected in west Texas. Two gas prices, \$3 and \$5/MMBtu were considered for this analysis. The price of electricity was calculated using a nominal heat rate of 7000 Btu heat/kWh electricity to which a surcharge of \$5/MWh was added. The variable profit was calculated by considering 2 process trains for the FEED. Ultimately these resulted in 2 subcases for each case shown in Table 6.2, related to gas and power price.

$$\text{Profit} = \text{N}_{\text{Trains}}\left(\$_{\text{CO}_2}\text{Rate}_{\text{CO}_2} - \$_{\text{Elect.}}\text{Power} - \$_{\text{NG}}\text{Rate}_{\text{NG}}\right) \tag{6.1}$$

Table 6.2: Flue gas cases with gas and power price considered

HRSG flue gas (%)	Ambient T (°F)	Gas price ($/MMBtu)	Power price ($/MWh)
95% with no duct burning	40	3	26
		5	40
100% + duct burning	65	3	26
		5	40
72% with no duct burning	65	3	26
		5	40
95% with no duct burning	65	3	26
		5	40
95% with no duct burning	105	3	26
		5	40

6.3 EFFECT OF PROCESS CONSTRAINTS ON MAXIMUM ACHIEVABLE PROFIT

The optimization of variable profit used 9 constraints in total. This section analyzes the change in optimized profit (%) as a function of increasing the process constraints in the system. In the figure below, going from left to right, more constraints are being added to the optimization. The case on the far right in Figure 6.1 represents the lowest attainable profit with all 9 process constraints. The optimum profit achieved for other cases is compared to the lowest attainable profit to calculate a change in maximum profit (%).

In Figure 6, going from right to left, one constraint at a time is removed on the optimization problem to observe its impact on equipment capacity and profit. For example, first, the precipitation constraint is removed on the optimization. Next, the compressor capacity constraint is removed along with the precipitation constraint, and so on. As more constraints are removed, the optimization problem is more relaxed, resulting in a higher

attainable profit at the cost of added capacity to equipment. The data for change in profit and added capacity relative to the most constrained problem for 0.18 lean loading is shown in Appendix H and summarized in Figure 6.1 This analysis was done for a gas price of $3/MMBtu as a function of lean loading for three different ambient temperatures, with 95% HRSG flue gas.

The precipitation constraint was not violated under any condition, so removing it did not change the minimum profit at any ambient temperature or lean loading.

At 40 °F ambient temperature:

Removing the compressor capacity constraint sizably increased the attainable maximum profit by about 20.9% for 0.18 lean loading. At low lean loading, a higher CO_2 flowrate is processed owing to the high rich loading, and the compressor capacity constrains the system. The compressor capacity is exceeded by 20–30% with varying lean loading. The absorber and stripper flooding did not limit the variable profit. Removing the boiler fan constraint required that the boiler fan capacity and compressor capacity be increased by 8 and 24% respectively to increase profit by 21.1%. Removing the boiler capacity constraint required that the boiler, boiler fan, and compressor be increased by 33, 34, and 30%, respectively, to increase the profit by 21.45%. The pumps and bypass constraints did not affect profit.

At 0.2 lean loading, only the compressor limited the process. A 2% increase in compressor capacity can increase the variable profit by 1.7%.

At 0.22 lean loading, only the stripper flooding limited the profit. A 3% increase in stripper capacity can change the variable profit by 0.52%. This was due to the highest solvent rate at high lean loading.

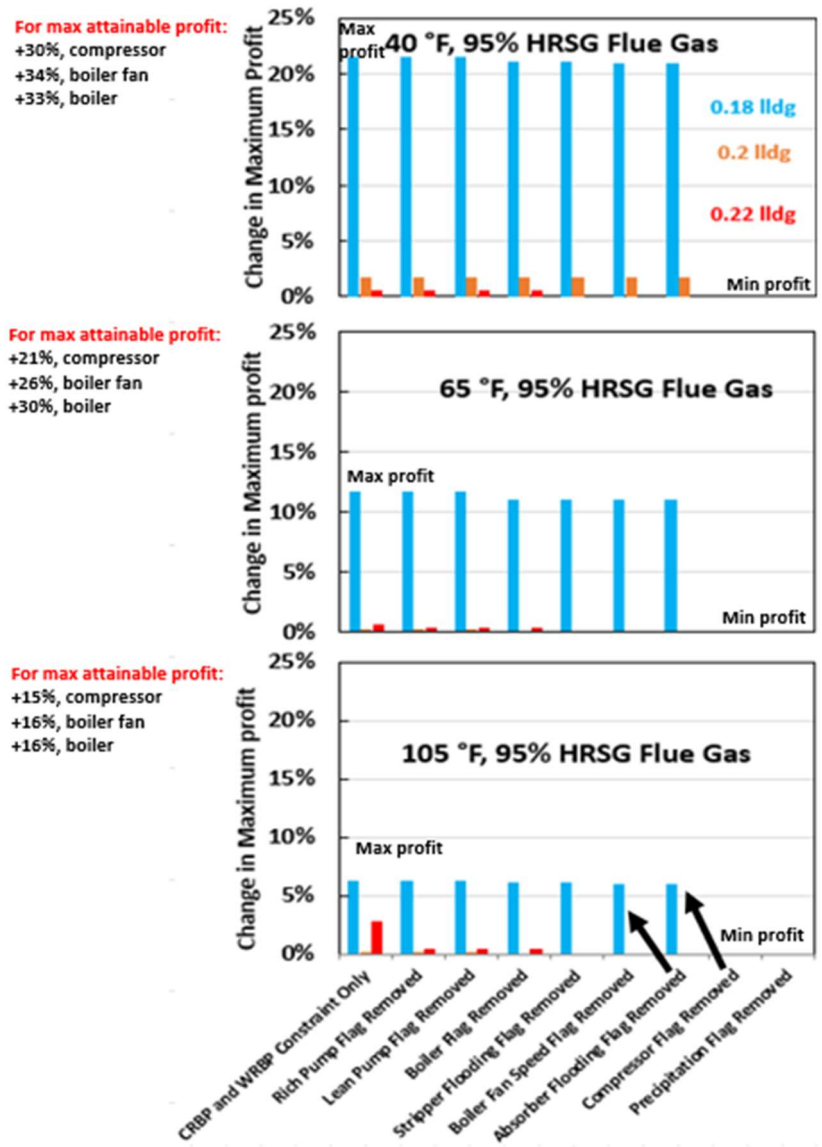

Figure 6.1: Effect of removing different process constraints on profitability at 40 °F with 95% HRSG flue gas; vertical bars to the left of the constraint removed represent the respective change in maximum variable profit; figure is read right to left, going from the most constrained to the least constrained case

At 65 °F ambient temperature:

At 0.2 lean loading, like the low temperature case, the compressor, boiler fan, and boiler were the only limiting equipment. Profitability was impacted by a smaller degree due to the lower CO_2 flowrate already processed by the system. Increasing compressor capacity by 15% can result in a 11% increase in profit. A 2% increase in boiler fan capacity had to be accompanied by a 16% increase in compressor capacity to increase profit (+11.03%). A 30% increase in boiler capacity had to be accompanied by a 26 and 21% increase in boiler fan and compressor capacity, respectively, to increase profit (+11.62%).

At 0.2 lean loading, removing the boiler capacity constraint required a 4% increase in boiler fan capacity to yield marginal increase in profit (+0.06%).

At 0.22 lean loading, increasing stripper and rich pump capacity minimally impacted profit (+0.32-0.56%).

At 105 °F ambient temperature:

At 0.18 lean loading, an 11% increase in compressor capacity only resulted in 5.9% increase in profit. Boiler fan capacity can be increased by 16% and boiler capacity can be increased by 2-16% to increase profit (+6.05-6.24%) if the compressor capacity was also increased by 12-15%. Other equipment did not limit the profit.

At 0.2 lean loading, increasing the capacity of the boiler required a 3% increase in boiler fan capacity to obtain marginal improvement (+0.1%) in profit.

At 0.22 lean loading, increasing the rich pump capacity impacted profit (+2.78%) more than increasing the stripper capacity (+0.33%).

6.4 DEPENDENCE OF OPTIMAL HEAT DUTY ON GAS PRICE

Figure 6.2 shows the dependence of optimum heat duty for a wide range of gas prices on lean loading and ambient temperature, for 95% HRSG flue gas. The figure indicates that a lower lean loading will provide a lower heat duty irrespective of gas price and ambient temperature. This demonstrates that PZAS can operate flexibly with an energy requirement of 2.2–3 GJ/tonne at variable ambient temperature and lean loading. A similar decrease in regeneration energy requirement with decreasing lean loading was observed in the pilot test of the PZAS at the UT-SRP pilot plant by Suresh Babu and Rochelle (2022).

Figure 6.2 demonstrates an independent effect of gas price on heat duty. At 0.22 lean loading and gas price between $3 and 4/MMBtu, heat duty is the highest compared to other lean loading. As the gas price increases to $5/MMBtu, the heat duty drops to about 2.3 GJ/tonne and from there on monotonically decreases with increasing gas price. This can be explained by calculating a "breakeven" gas price that produces a value for the emitted C from natural gas exactly equal to $80/tonne (45Q value for captured C).

Assuming natural gas is methane, the LHV (low heating value) of 21496 Btu/lb was used for this calculation. Assuming the complete combustion of methane, the breakeven gas price was $4.6/MMBtu. Below this value, the variable profit was maximized at high lean loading by increasing the boiler heat rate. In this region, carbon in natural gas was cheaper than carbon in captured CO_2. Therefore, natural gas combustion drove profitability of the capture system.

When the gas price exceeds $4.6/MMBtu, C in captured CO_2 becomes more valuable than C in natural gas, requiring a reduction in boiler heat rate and consequently, specific heat duty.

At lower lean loading (0.2, 0.18 mol/mol), this dynamic was not observed. Heat duty was almost constant at around 2.2 GJ/tonne for the whole range of gas prices studied. Due to the low solvent rate at low lean loading, the process operates at low heat duty irrespective of gas price, thereby requiring less combustion of natural gas.

As the ambient temperature increased to 65 °F, the trend in heat duty at a lean loading of 0.22 lean loading obeyed the dynamic described before, which was optimized to 2.7 GJ/tonne below the breakeven gas price and 2.3 GJ/tonne above the breakeven gas price. This is because of the lower CO_2 production at higher ambient temperature, making the process unprofitable at a gas price higher than $3/MMBtu unless the heat duty of the stripper and natural gas boiler is sharply decreased. At this ambient temperature and a lean loading of 0.2 and 0.18 mol/mol, the optimum heat duty remained unaffected as the gas priced changed due to the sufficiently high CO_2 production.

In Figure 6.2, as the ambient temperature increased to 105 °F, the rich loading and CO_2 flowrate decreased further for all three lean loadings. In this case, at low gas price, a high heat duty was required for both 0.2 and 0.22 lean loading, and only the 0.18 lean loading case was profitable at any gas price without increasing the boiler heat rate. The lean loading that required an increase in the boiler heat rate showed a much steeper transition to a lower heat duty as the gas price and ambient temperature increased. This can be understood as the effect of decreasing rich loading at higher ambient temperature.

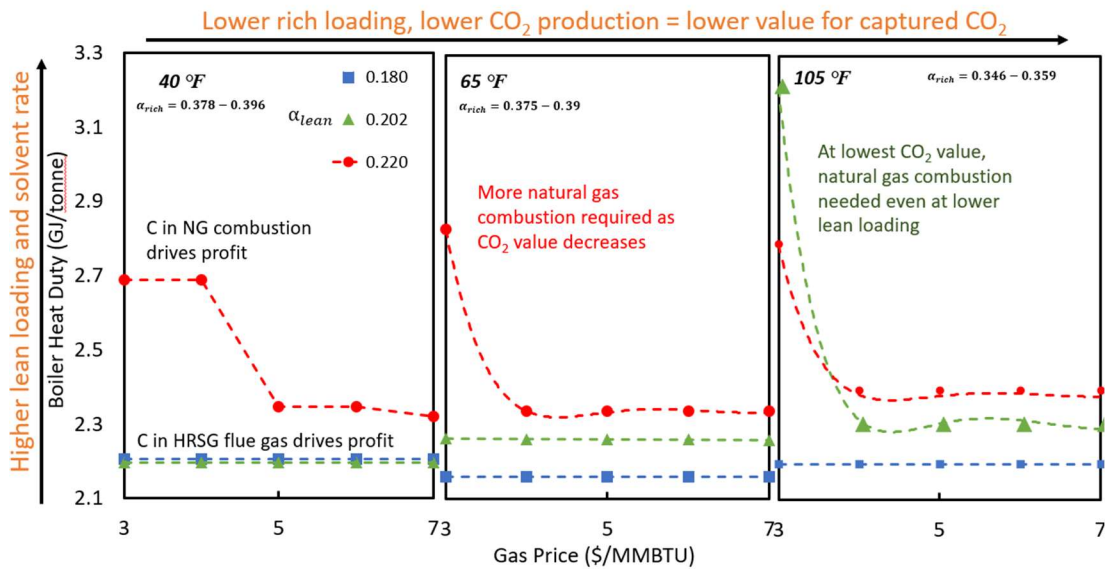

Figure 6.2: Variation of optimum specific heat duty with gas price as a function of lean loading and ambient temperature, where α_{lean} denotes the lean solvent CO_2 loading.

6.5 SUMMARY TABLE OF OPTIMIZATION RESULTS WITH VARIABLE LEAN LOADING (STRIPPER PRESSURE)

Table 6.3 summarizes the optimized process variables to attain maximum variable profitability for any given case. These results will be discussed in more detail in upcoming sections.

Table 6.3: Summary table of results from optimization of variable profit for 5 different flue gas cases; gas price = $3/MMBtu; all numbers except profit and electric power are for one process train; CO_2 value: $80/tonne

Case (Amb. T, HRSG Flue Gas %, Duct Burn.)	A 40 °F, 95, No DB	B 65 °F, 72, No DB	C 65 °F, 95, No DB	D 65 °F, 100, DB	E 105 °F, 95, No DB	Design Case (Unoptimized)
Hourly Profit, $/hr	14,116	10,594	12,938	13,724	11,637	12,968
CO_2 Production, tonne/hr	102	76	93	99	84	94.8
CO_2 Removal, %	93.6	98	96	94	93	90
Lean Loading, mol/mol	0.207	0.180	0.193	0.207	0.184	0.2
Rich Loading, mol/mol	0.381	0.365	0.368	0.377	0.352	0.4
Lean solvent rate, kg/s	549	386	503	546	475	450
Air cooler bays for intercooling	18	18	20	17	20	20
Intercooler solvent T, out (°C)	23	30.5	31	31.8	45.6	29.4
Rich solvent T (°C)	43	44	46	47	53	44
Air cooler bays for water wash	6	5	8	10	18	18
Total electric power, MW	31	21	28	30	28	34

Heat Duty, MMBtu/hr	233	169	209	221	186	272
Specific heat duty (GJ/t)	2.26	2.208	2.22	2.21	2.19	3.0
Cold lean solvent temperature, °C	71	71	73	74	78	61
Boiler capacity (%)	71.8	52.1	64	68.1	57.3	98.2
Compressor capacity (%)	100	89	99	100	100	96
Boiler fan speed capacity (%)	91.7	63.3	81	85.7	76	99.7

6.6 DISCUSSION OF OPTIMIZATION RESULTS

6.6.1 Air Cooler Operation for Rich Loading Maximization

For 40 °F ambient temperature, 18 air cooler bays and both pumps were used for absorber intercooling. At ambient temperature of 65 °F and 105 °F, the number of intercooler bays increased to 20 with both pumps in use. This was expected since the number of bays used is directly proportional to the absorber performance, and higher ambient temperatures required more cooling to maximize the rich loading at the bottom of the absorber. The temperature of the rich solvent leaving the intercooler was 23, 31, and 45.6 °C at 40, 65, and 105 °F ambient temperature respectively, with 95% HRSG flue gas. The increase in rich solvent temperature reflects the increase in the temperature of the ambient air used in the air cooler bays.

In general, the number of intercooler bays was close to maximum for each case due to the hot flue gas at 112 °C or higher. Due to the lack of a direct contact cooler, the pump-around section was used to cool the flue gas and consequently the absorber column.

Temperature management in the absorber was compounded by the lack of a trim cooler in the design, which gave a high lean solvent temperature ranging from 71 to 78 °C. However, the presence of a trim cooler would likely not produce a drastically different profit optimum, unless cooling water were to be used, which would likely increase the profit for all cases. Cooling water would produce more uniform optimum conditions between cases since the system would be less exposed to differences in ambient temperature.

6.6.2 Stripper Flooding

The highest observed stripper flooding was 97% in the bottom section of the column for the 40 °F case with 95% HRSG flue gas. The 65 °F and 105 °F cases had lower flooding at 88% and 84% respectively in the bottom section of packing. This is due to a monotonic decrease in lean solvent rate and CO_2 flowrate with increase in ambient temperature. Both the liquid and vapor rate in the stripper determined the flooding in the column. This flooding was usually the greatest at the bottom of the lower packing section where the liquid and vapor rate is usually the highest. At this point, the liquid has picked up the most water through condensation and the vapor has the highest velocity due to the lowest pressure drop experienced. Figure 6.3 shows the relationship between lean solvent rate, CO_2 flowrate, and stripper flooding.

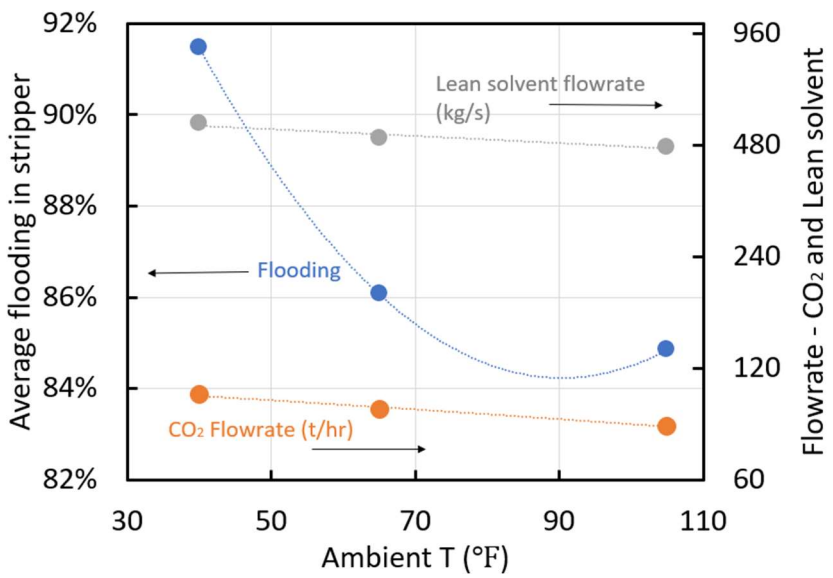

Figure 6.3: Relation between stripper flooding, ambient temperature, solvent rate, and CO_2 flowrate; gas price = $3-5/MMBtu

6.6.3 Approach to Maximum Boiler Heat Rate

The boiler heat rate did not exceed the maximum boiler capacity in any of the cases. The approach to maximum boiler heat rate (%) ranged from 56.5–70.9%. The approach to maximum boiler capacity was correlated well with the percentage of HRSG flue gas processed by the system at constant temperature. With increasing ambient temperature at 95% HRSG flue gas, the approach to maximum boiler capacity decreased monotonically, which is related to the consistent decrease in boiler heat rate (and flue gas produced) with increasing ambient temperature.

Although rich loading decreased with increasing temperature, the gross heat rate of the boiler is only related to the amount of CO_2 processed by the system, which decreased monotonically with ambient temperature. Higher ambient temperature cases also had a lower mass flowrate of flue gas due to a lower gas density. This is shown in Figure 6.4.

6.6.4 Approach to Maximum Boiler Fan Speed

The approach to maximum boiler fan speed showed a dependence on ambient temperature similar to that of maximum boiler heat rate. This is also shown in Figure 6.4.

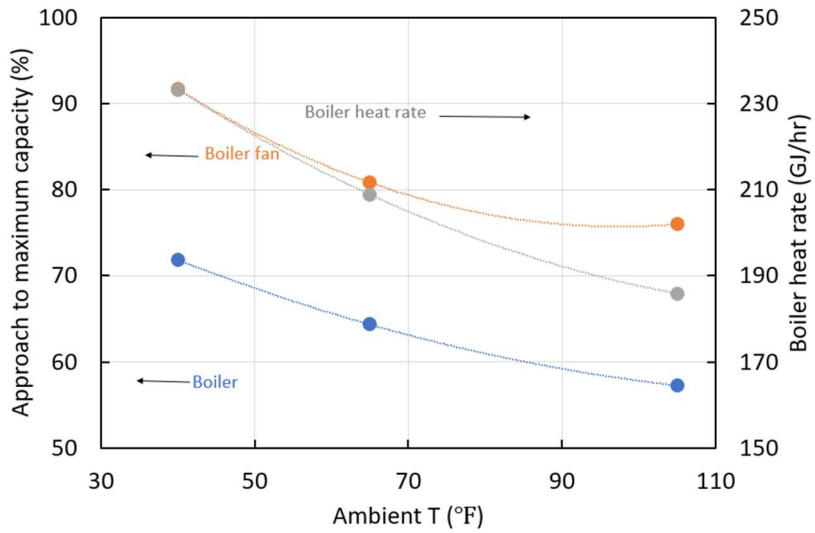

Figure 6.4: Relation between approach to maximum capacity of boiler equipment, ambient temperature, and boiler heat rate

6.6.5 Approach to Maximum Compressor Capacity

For 95% HRSG flue gas, the approach to maximum compressor capacity ranged from 99-100% between 40 and 105 °F. The compressor was at its maximum capacity for both the low (40 °F) and high temperature (105 °F) cases. This is expected because CO_2 flowrate is an important driver of variable profit of the plant, which was maximized at any given condition.

At a fixed ambient temperature of 65 °F, with increasing percentage of HRSG flue gas, the approach to maximum compressor capacity (%) increased owing to the larger amount of CO_2 in the flue gas.

6.6.6 Maximum Variable Profit and Optimum Variables

Variable profit was highest for the 40 °F ambient temperature case, and monotonically decreased as the ambient temperature increased, reaching a minimum at 105 °F. This trend is shown in Figure 6.5 and resulted primarily through the optimization of

lean solvent rate which showed a similar trend. Variable profit also systematically decreased as the gas price increased to $5/MMBtu, primarily due to the higher cash flow for natural gas. Optimal process variables however did not change with gas price between $3 and 5/MMBtu due to the optimization of lean loading.

Lean solvent rate (and CO_2 flowrate) also decreased with increasing ambient temperature to accommodate the reduced maximum CO_2 flowrate through the compressor. Because the HRSG flue gas flowrate decreased as the ambient temperature increased, so did the optimum lean solvent rate. A higher ambient temperature also required lower pressure stripping, which increased the compressor power requirement. A lower lean solvent rate decreased the electricity consumption from pump work, which was required to maintain optimum profitability given the higher compressor power requirement.

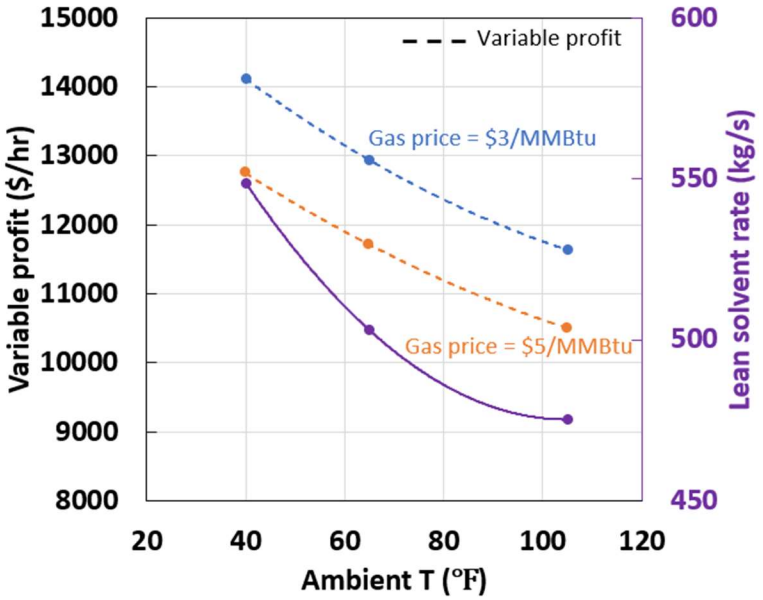

Figure 6.5: Optimum variable profit for the different scenarios is driven by lean solvent rate, 150 °C stripper, CO_2 value: $80/tonne

The use of a high lean solvent rate at low ambient temperature resulted in the highest amount of CO_2 being captured. The highest amount of CO_2 captured at 40 °F was also related to the highest maximum working capacity of the compressor. As the ambient temperature increased, the lower lean solvent rate and decreased delta loading resulted in less CO_2 being captured and thus a lower profit. Lean solvent rate was found to be an important driver of profitability and optimal plant operation.

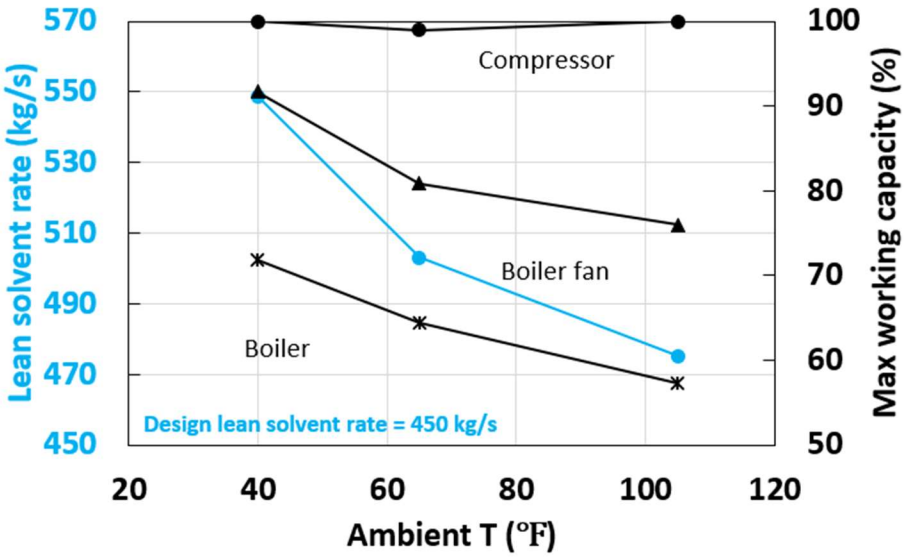

Figure 6.6: Lean solvent rate drives optimum operation but is limited by compressor operation, 150 °C stripper, CO_2 value: \$80/tonne, gas price = \$3–5/MMBtu

Figure 6.6 shows the optimum lean solvent rate for the different scenarios considered. The optimum lean solvent rate for the 40 ºF case was at the upper limit of the range in which the surrogate model was applicable. However, this was not limited by the lean solvent rate but by the CO_2 compressor which was operating at or close to its maximum capacity. While the amount of solvent processed was a significant driver for the profitability of the plant, this was only true while the CO_2 compressor could handle the

amount of CO_2 produced. This suggested that a good lean pump design would be one that can match the CO_2 compressor limit. This is especially true considering that both the capital cost and operating cost of the CO_2 compressor are much higher than those of the lean pump. The lean solvent rate exceeded that of the design case (450 kg/s) for all 3 ambient temperatures, which meant that the actual maximum capacity of the lean pump was not fully utilized. The boiler fan and boiler were not limiting the optimal operation of the process, as shown by Figure 6.6.

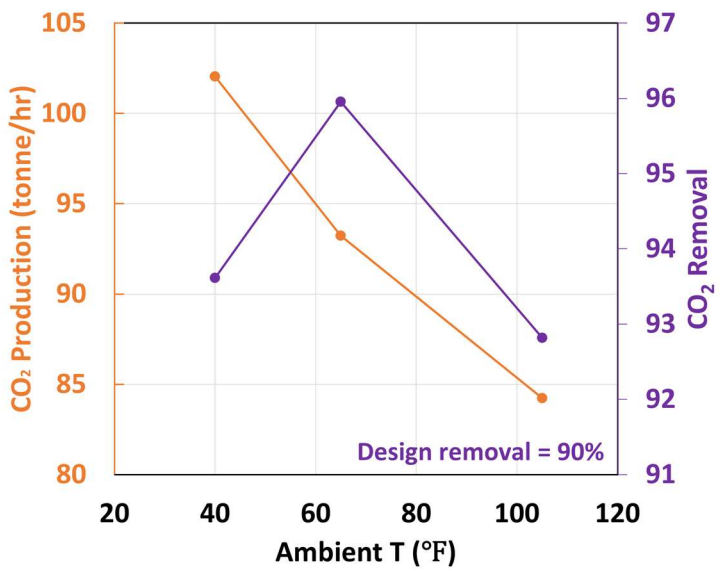

Figure 6.7: Optimum CO_2 flowrate for a single process train and removal indicate that high removal is important for optimization of operation, 150 °C stripper, CO_2 value: \$80/tonne, gas price = \$3–5/MMBtu

The variation in CO_2 production with ambient temperature is shown in Figure 6.7. Figure 6.7 also shows CO_2 removal as a function of ambient temperature. Notably, the CO_2 removal was always higher than the design removal of 90% and achieved a peak of 96%

for the 65 ºF case. This also shows the importance of high CO_2 removal for optimal plant operation and maximization of variable profit.

The 65 °F case had 14% lower flue gas flowrate but only about 9% lower lean solvent rate compared to the 40 °F case. This combined with the use of pump-around intercooling and lower pressure stripping (to 0.193 lean loading at 65 °F versus 0.207 lean loading at 40 °F), the delta loading approximately remained constant between 40 and 65 °F. This resulted in the highest removal for the 65 °F case. However, CO_2 flowrate monotonically decreased from 40 to 105 °F, being only limited by the lean solvent rate and maximum working capacity of the compressor, both of which showed the same behavior with temperature.

Figure 6.8 shows the CO_2 loading in the rich and lean solvent as a function of ambient temperature along with the number of air cooler bays for intercooling used as a function of ambient temperature. Rich loading decreases monotonically with an increase in ambient temperature. At 65 and 105 °F ambient temperature, all the air cooler bays (20) had to be used to maximize the rich loading, while at lower ambient temperature (40 °F), effective cooling at the bottom of the absorber was possible with 18 air cooler bays.

Figure 6.8 also shows that at low ambient temperature the optimum lean loading is higher compared to higher temperatures. Because of the more effective intercooling at 40 °F, increasing the lean solvent rate to 550 kg/s was sufficient to produce enough CO_2 to match the capacity of the CO_2 compressor, avoiding the need to utilize lower pressure stripping to achieve lower lean loadings.

A lower lean loading was necessary at higher ambient temperatures to maximize variable profit by maintaining the cyclic capacity of the solvent. This was done to make-

up for the reduced intercooler effectiveness and lean solvent flowrate at high ambient temperature as shown in Figure 6.8.

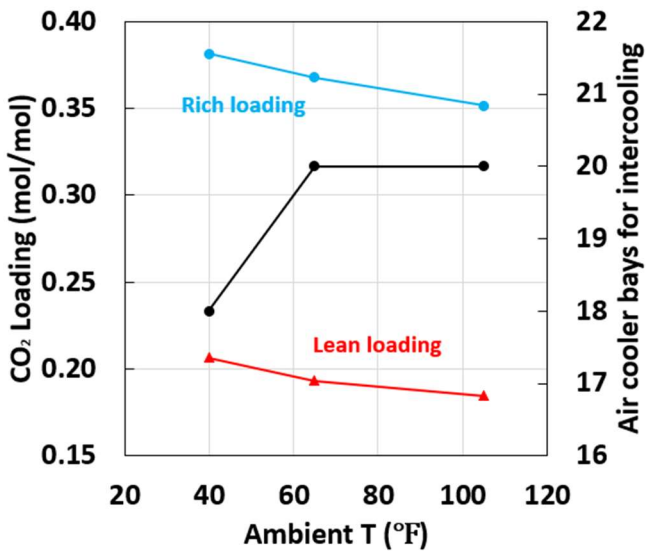

Figure 6.8: Optimum rich and lean loading for different scenarios; rich loading is maximized at high ambient temperature by using more air cooler bays for intercooling; optimum profit requires low lean loading at high ambient temperature, 150 °C stripper, CO_2 value: \$80/tonne, gas price = \$3–5/MMBtu

Figure 6.9 shows the optimum heat duty as a function of ambient temperature. Overall, the heat duty appears to be between 2.2 and 2.3 GJ/tonne regardless of delta loading, lean solvent rate, or ambient temperature primarily through the optimization of the cold and warm rich bypasses. This enabled efficient recovery of heat from the water vapor leaving the stripper, an important source of irreversibility in the stripper. For all three ambient temperatures, the optimum bypass split fractions are flat at 27.8 % for the cold rich bypass and 60% for the warm rich bypass (relative to the warm rich solvent flowrate).

Almost always, over 70% of the rich solvent being bypassed to the top of the stripper column, leaving a maximum of 30% of total rich solvent leaving the steam heater. Due to the lack of rigorous steam heater modeling in this work, the temperature of the solvent exiting the steam heater could be prohibitive, giving rise to higher rates of thermal degradation and corrosion, especially at the low lean loading that the system self-optimized to in this study.

Suresh Babu and Rochelle (2022) conducted a study of the steam heater for the base case FEED for PZAS at a lean loading of 0.2 mol/mol that indicated that the steam temperature required and rich solvent temperature exiting the steam heater are 164 °C and 159 °C respectively, at 60% warm rich bypass.

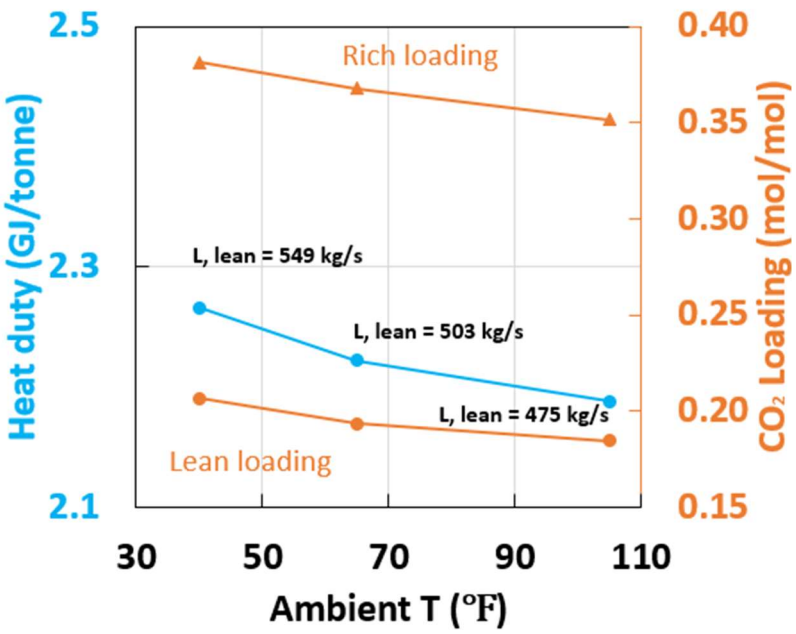

Figure 6.9: Stripper operated at low heat duty even at high ambient temperature by manipulating lean loading and solvent rate, 150 °C stripper, CO_2 value: \$80/tonne, gas price = \$3–5/MMBtu; numbers inside the bars represent rich loading

As seen in Figure 6.9, heat duty monotonically decreases with ambient temperature by using a lower lean solvent rate and lower lean loading. Lower lean loading operation has also been related to favorable energy performance of the advanced stripper from pilot plant tests conducted by Suresh Babu and Rochelle (2022). The manipulation of stripper pressure to change lean loading with increasing ambient temperature allowed the cyclic capacity of the solvent to be maintained between 0.167-0.175 mol/mol regardless of the decrease in rich loading with ambient temperature. This demonstrated that the PZAS process could operate flexibly at different ambient temperatures with a heat duty of 2.2–2.3 GJ/tonne while maximizing variable profit.

Consequently, the boiler heat rate was between 186 and 233 MMBtu/hr. As the ambient temperature increased, the boiler heat rate decreased due to the lower amount of CO_2 captured by the system because of lower lean solvent rate, and lower maximum permissible flowrate of the compressor. The boiler never exceeded 72% of its maximum capacity, as seen in Figure 6.6.

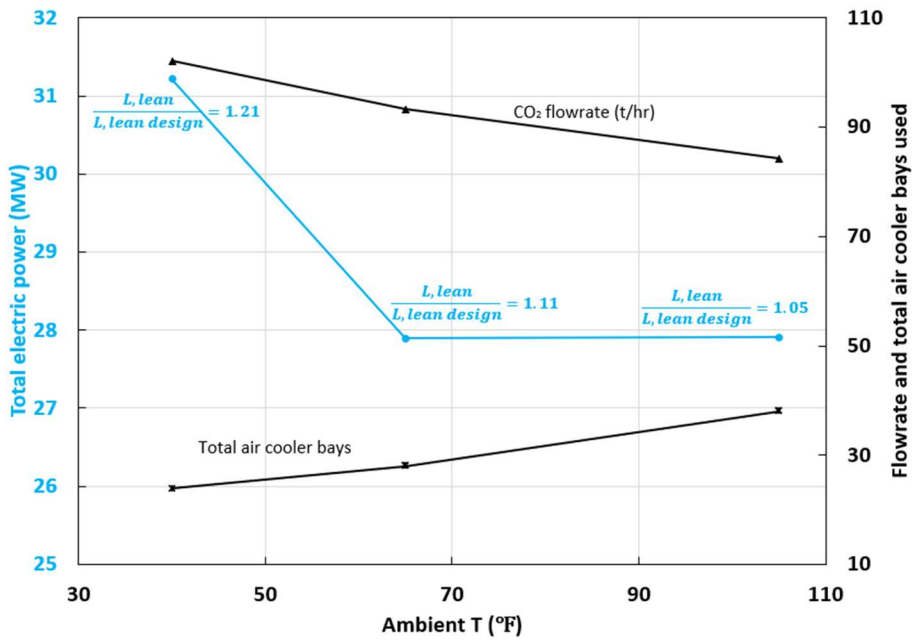

Figure 6.10: Total electric power requirement was highest at low ambient temperature due to maximization of lean solvent rate and CO_2 flowrate, 150 °C stripper, CO_2 value: \$80/tonne, gas price = \$3–5/MMBtu, total air cooler bays for intercooling = 20, total air cooler bays for water wash = 18, design lean solvent rate = 450 kg/s

Figure 6.10 shows the variation of total electrical power requirement with ambient temperature. Total power appears to be correlated with optimum lean solvent rate and CO_2 flowrate. The total power consumption was at a maximum at 40 °F because it corresponded to the highest CO_2 flowrate and lean solvent rate of all the cases. The CO_2 flowrate dictates the compressor power requirement, and the lean solvent rate dictates the power requirement of the pumps. The compressor power requirement is also related to the working pressure (lean loading) of the stripper.

As the ambient temperature increased, the total power consumption decreased. At 65 °F, this decrease was due to a lower lean solvent flowrate and a lower CO_2 flowrate, despite an increase in total air cooler bays used, indicating that the electrical power

requirement for pumps and compressors likely were more important than that of the air coolers.

Although the CO_2 flowrate and lean solvent rate were even lower at 105 °F compared to 65 °F, the power consumption was approximately the same compared to that at 65 °F due to an increase in air cooler bays and compression requirement from the use of a low-pressure stripper. At 105 °F, the power requirement of the air coolers and compressor (for low pressure stripping) likely were more important than that of the pump.

6.7 SOLVENT PRECIPITATION

It was important to consider the possibility of solvent precipitation in the process optimization of PZAS™ especially given that the ambient temperature varied from 40–105 °F and lean loading varied from 0.18 to 0.22 mol/mol.

From the Solid-Liquid-Equilibrium diagram shown in Figure 6.11 (adapted from Chen et al. (2014)), precipitation in 5 m PZ occurs at low temperature and low lean loading. The coldest point in the system was the metal temperature in the cold end of the cold cross exchanger which was approximated in the model using an average of cold lean and cold rich temperature.

Figure 6.11 plots this average temperature against optimum lean loading for all the cases considered in this work. A high lean solvent temperature due to the absence of the trim cooler downstream of the cold exchanger avoided precipitation in the system even at lean loading as low as 0.18 mol/mol.

Nevertheless, there is still the lingering possibility that operation at lower lean loading will expose the system to precipitation in the event of an unplanned shutdown during low ambient temperature. At the selected limit of 0.18 lean loading, the solution will precipitate if it cools to 26 ºC.

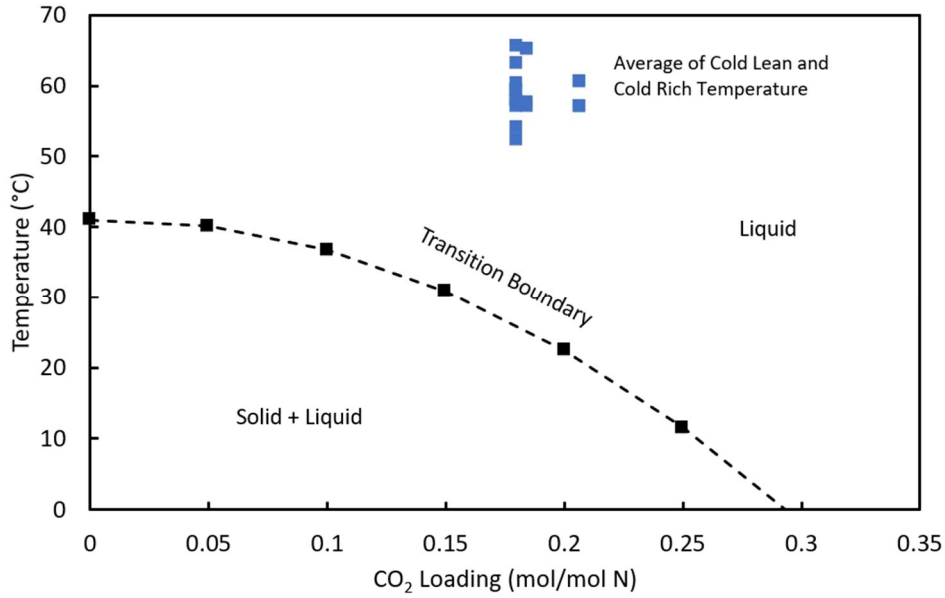

Figure 6.11: Profitable operation of PZAS at different ambient temperatures is possible while avoiding solvent precipitation

6.8 AMINE VOLATILITY

The cold lean solvent temperature at the optimized operating conditions was between 71 and 78 °C. While this avoided solvent precipitation, it also made for hot lean solvent inlet to the absorber. This high temperature will result in a larger concentration of vapor PZ in the flue gas entering the water wash. A modified water wash design may be necessary to avoid excessive emissions of PZ in the cleaned flue gas.

6.9 CONCLUSIONS

Optimization of variable profit for retrofit on a 460 MW NGCC operation indicated that:

- Low lean loading of about 0.18 mol CO_2/equiv. N generally resulted in lower reboiler heat duty. Optimum heat duty was found to be 2.2-2.3 GJ/tonne compared to the original fixed design of 3 GJ/tonne
- The process was profitable at a higher lean loading of 0.2 mol/equiv. N at lower ambient temperature (heat duty: 2.2-2.3 GJ/tonne). High ambient temperature required lower lean loading to maximize variable profit by maintaining the cyclic capacity of the solvent.
- The lean solvent rate was decreased with increasing ambient temperature to maximize the variable profit.
- Only at 0.18 lean loading and 40 °F was the profit significantly constrained by the compressor, boiler, and boiler fan capacity, with an effect of about 21%. As ambient temperature increased, a larger compressor, boiler, and boiler fan would only increase the profit by 6-11%.
- Size of the rich pump constrained variable profit to a smaller extent, especially at low cyclic capacity (0.22 lean loading, 105 °F ambient temperature). Making the rich pump larger could increase the profit only by 2% at most, in the absence of the compressor constraint.
- Optimal CO_2 removal was always higher than the design case removal of 90% indicating that the plant was overdesigned. From 40 °F to 65 °F, the removal increased to its maximum of 96% from 94% due to a much larger decrease in the mass flowrate of flue gas (14%) than lean solvent rate (9%). Intercooling and low pressure stripping

also helped maintain the cyclic capacity of the solvent to be constant at 0.175 mol/mol between 40 °F and 65 °F.

- Lean solvent rate was higher than the design value of 450 kg/s in all cases, making it a key driver of plant profitability. Optimum lean solvent rate was 5-21% higher than the design value of 450 kg/s.
- Solvent precipitation was avoided even at low lean loading (0.18 mol/mol) in the absence of a trim cooler for the lean solvent between the absorber and the cold cross exchanger.
- The breakeven gas price is $4.6/MMBtu, and below this value, the variable profit was maximized at high lean loading (0.22 lean loading) by increasing the boiler heat rate. Above a gas price of $4.6/MMBtu, CO_2 becomes more valuable than natural gas, requiring a reduction in boiler heat rate and consequently, specific heat duty, especially at 0.22 lean loading. As the ambient temperature increases, a similar trend in heat duty is observed at 0.22 lean loading, but the transition to lower heat duty occurs earlier at $4/MMBtu. This is because of the lower CO_2 production at higher ambient temperature, making the process unprofitable at gas price higher than $3/MMBtu unless the heat duty of the stripper and natural gas boiler is steeply decreased. At lower lean loading (0.2, 0.18 mol/mol), this behavior is not observed at low gas price due to the high value for CO_2.

RECOMMENDATIONS FOR FUTURE WORK

- Process optimization was found to be independent of gas price at $3-5/MMBtu. The optimization can be extended to locations where gas price is higher to observe the dependence of process variables on gas price.

- The variable profit optimization model can be combined with a capital cost model for different equipment of PZAS to obtain an optimized cost of capture ($/tonne) as a function of ambient temperature, power plant operation, and operating conditions throughout the year.
- The lean loading range in this work can be expanded to lower values (< 0.18 mol/mol). While this optimization indicated that lower lean loading is preferable for better energy performance, an optimum lean loading is yet to be estimated for application on Mustang Station.
- The effect of power plant operation on variable profit optimization can be studied in greater detail by using the instantaneous power production profile of the plant through the year. This work assumes an average capacity factor for the power plant.
- The effect of renewables penetration into the grid in West Texas can also be studied for its impact on optimal operation of PZAS through the year.
- Absorber and stripper operation at high liquid flux or high removal must be investigated in detail and tested at the pilot plant to verify the optimization results of this work.
- Long-term operation of the stripper at low lean loading (~0.18 mol/mol), high fractional bypass (~70%), and high liquid flux in the absence of a lean amine trim cooler must be studied at the pilot scale to ensure reliable process operation without precipitation of PZ, steam heater operation, and favorable heat duty.
- Study of amine volatility (or emissions) in the absorber is required at the pilot scale at high lean solvent temperature representative of the optimal FEED conditions. A multi-stage water wash and/or acid wash may be used to deal with PZ emissions with high lean solvent temperature.

ACKNOWLEDGEMENTS

The author would like to acknowledge the contributions of Miguel Abreu in the construction of absorber-side rating and surrogate models, and the steady-state process surrogate model in MATLAB, Benjamin Drewry in the construction of rating and surrogate models for the air coolers for intercooling and water wash, and Yee Lee Chen in obtaining data from Aspen Plus® for absorber and stripper-side rating models to construct the surrogate models. The author would also like to acknowledge the contribution of Miguel Abreu in the construction of the PZAS process surrogate model in MATLAB. This chapter was written by the author. Parts of this chapter have been submitted for peer reviewed publication, which had contributions from Miguel and Benjamin for the absorber section and air cooler section, respectively. The rest of the paper was written by the author.

Chapter 7: Alternative Stripper Designs for FEED of PZAS

Chapters 4-6 discussed the design, operation, and optimization of the PZAS process for a 460 MW NGCC. The base case stripper design resulted in a high heat duty (3 GJ/tonne) compared to pilot measurements made at NCCC and the UT-SRP (Rochelle et al., 2022, Suresh Babu and Rochelle, 2022). This was primarily a product of small heat exchanger transfer units (NTU), coarse packing in the stripper, and a low gas price at the time of the design. Detailed cost estimates for the equipment are reported by Rochelle et al. (2022).

The cost estimates revealed that the total direct field cost of the solvent cross exchangers for both parallel process trains were surprisingly low ($1.54 MM) compared to the total direct field cost of the FEED. The cost of the gas-liquid CO_2 exchangers was roughly 2.3 times that of the solvent cross exchangers. A breakdown of a portion of the total direct field cost that can be reduced by using design modifications is shown in Figure 7.1.

Air cooling, compressors, and the standalone gas boilers occupied a major chunk of this direct field cost shown in Figure 7.1. Design modifications that can reduce the heat duty of stripping will potentially reduce the cost of the above equipment. A reduction in heat duty directly translates to a reduction in steam heater and boiler size, reducing their capital costs. A lower heat duty will also yield a lower cold lean solvent temperature, allowing smaller air coolers in the water wash. The water wash acts as the heat sink for the lean solvent.

This chapter presents process strategies that can reduce the energy requirement of stripping compared to the base case design.

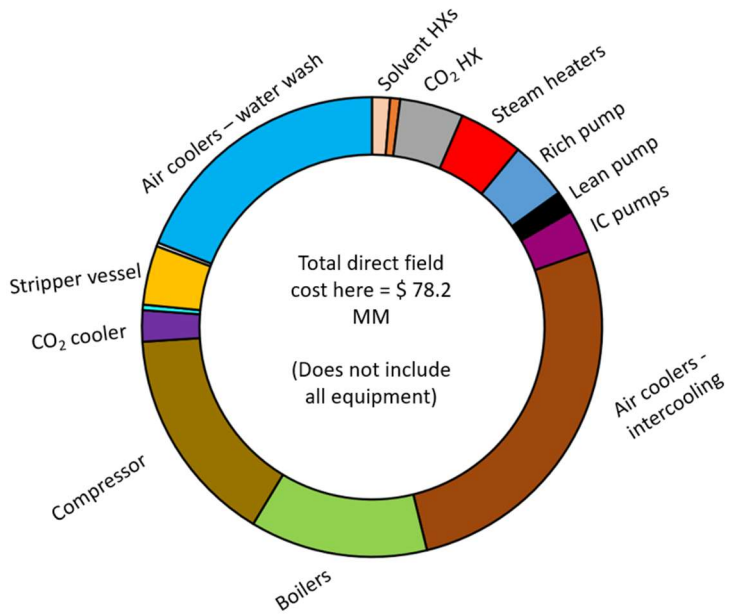

Figure 7.1: Fraction of the total direct field cost of the FEED likely to be affected by the direct contact condenser

7.1 ADVANCED SCENARIOS CONSIDERED

The energy requirement of the stripper might be reduced at the expense of a small added capital for doubling the heat transfer units in the cross exchangers. Per process train, this would double the number of cross exchangers. The new design scenario would consist of 6 cold cross exchangers, 2 sets of 3 (in parallel) in series, and 4 hot cross exchangers, 2 sets of 2 (in parallel) in series.

A second strategy to reduce the energy requirement would be to replace the CO_2 exchangers with a packed section atop the stripper column that would serve as a direct contact condenser. This yields a new process configuration that is referred to as PZAS with a Direct Contact Condenser.

A third strategy would result from the combination of strategies 1 and 2. These strategies could possibly reduce the annualized investment of the FEED through the effects of having a lower energy requirement.

The direct contact condenser is compared with stripper designs operating at different pressure levels. For this, a low temperature/pressure stripper for the PZAS process is designed and compared with the high-pressure stripper. Further, the low-pressure stripper is also coupled with a direct contact condenser and its performance compared to its high-pressure counterpart.

7.2 LITERATURE REVIEW ON ADVANCED STRIPPER CONFIGURATIONS

Several authors investigated advanced stripper configurations to reduce the energy requirement of CO_2 stripping compared to the simple stripper process (Bottoms, 1930).

Liu et al. (2020) investigated the use of cold bypass split, lean and rich vapor compression, and a warm bypass split for CO_2 capture using ammonia-based solvents. The stripper is operated at high pressure with a single cross exchanger and a reboiler.

Karimi et al. (2011) have shown capital cost and energy reductions with advanced configurations compared to the simple stripper using MEA at low pressure. They investigated the split-stream configuration with rich bypasses entering the stripper at two different locations, a multi-pressure stripper configuration that works in the pressure range of 2–4 atm, vapor recompression with the simple stripper, and a compressor integration with the simple stripper where the hot, compressed CO_2 is used as an additional heat source to strip the CO_2 from the rich amine.

Oh et al. (2020) have shown improvements in energy requirement compared to the simple stripper with lean vapor compression, cold solvent split, and stripper overhead compressor, but at low pressure around 1 bar.

The flash-stripping process with a cold rich split only has been used by Jiang et al. (2017) for ammonia-based post-combustion CO_2 capture at high stripper pressure.

A multi-feed stripper configuration using a cold rich, warm rich, and hot rich split with a flashing heat exchanger was used Jung et al. (2013) at 2 bar stripper pressure.

Thompson et al. (2017) have demonstrated the use of a secondary air-stripper column with the conventional simple stripper to lower the CO_2 content in the lean solvent before it enters the absorber. They also utilize a cold rich split in the secondary air stripper. They used 30 wt % MEA that required low pressure stripping.

Zhao at al. (2017) demonstrated advancements to the stripper process using a cold rich split, a cold rich and a warm rich split using a gas-liquid heat exchanger to recover water vapor from the stripper overhead gas, and an inter-heated stripper. The stripper operates at a low pressure of about 2 bar with MEA and PZ+MDEA as solvent.

Dubois et al. (2018) conducted a modeling study showed that a cold rich split, lean vapor compression, rich vapor compression reduced the stripping energy requirement compared to the simple stripper with MEA and PZ+MDEA in the pressure range of 2–6 bar.

Li et al. (2016) showed that a cold rich bypass sent directly into the stripper, a cold rich bypass heated using a gas-liquid exchanger, and an inter-heated stripper all reduced the stripper energy requirement of MEA at 2 bar.

Jung et al. (2015) used lean vapor compression, cold rich bypass, rich vapor compression, and a combination of these strategies with MEA to bring down the stripping energy requirement.

Rochelle et al. (2011) evaluated regeneration of aqueous solutions through multi-stage flashing and stripping.

This chapter discusses the use of a direct contact condenser with a combination of cold rich bypass, warm rich bypass, and a second generation solvent (5 m PZ) that operates at high pressure (5 bar) and high temperature in the stripper. This is an improvement on the Piperazine with the Advanced Stripper (PZAS), where the cold rich bypass is directly sent to a packed direct contact condenser on top of the stripper column, which replaces the CO_2 exchanger. This configuration is shown in Figure 7.2.

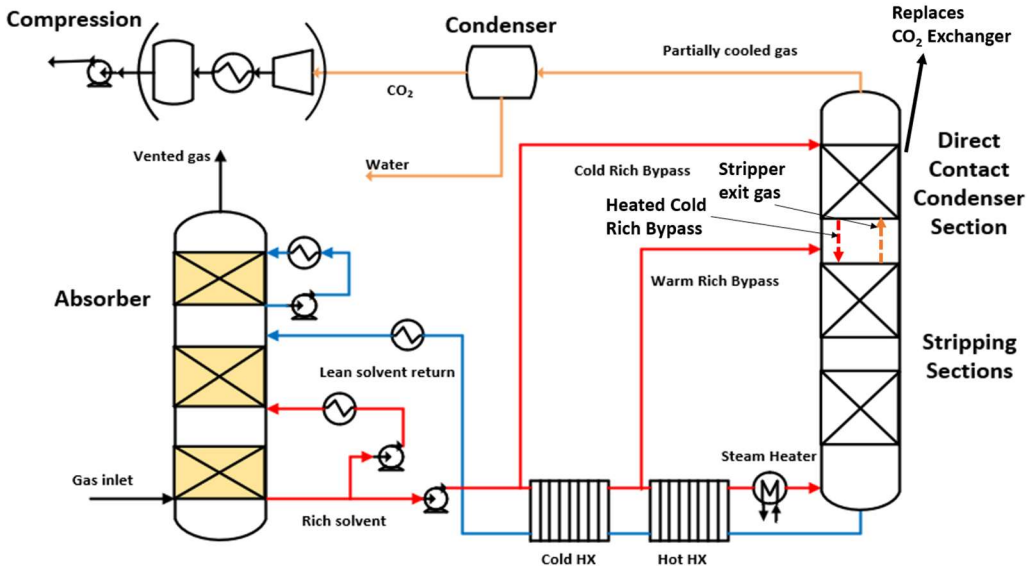

Figure 7.2: Simplified absorber and advanced stripper with PZ and the direct contact condenser (DCC) for the FEED

The cold rich bypass condenses the water vapor leaving the stripper while enabling some additional stripping in the high temperature regions, which leads to additional cooling of gas and a lowering of rich loading prior to solvent entry into the stripper column. In the direct contact condenser, the cold rich bypass is preheated using the vapor leaving the stripper and is mixed with the warm rich bypass from between the cold and hot cross exchangers. The total rich bypass is sent to the top of the stripper column, which operates at high pressure and temperature.

7.3 SUMMARY OF BASE CASE DESIGN

The stripper design consists of two parallel process trains, each with 3 cold cross exchangers, 2 hot cross exchangers, 1 stripper column, 1 gas-liquid CO_2 exchanger, and a condenser. Each stripper has a total packed height of 7.5 m with two sections of random packing (RSR 2 at the top and RSR 3 at the bottom). The cold cross exchanger was designed with a NTU of 5.3, the hot cross exchanger with a NTU of 1.7, and the CO_2 exchanger with a NTU of 3.9. The stripper operated with a bottoms temperature of 150 °C at 5.6 bar which resulted in a lean loading of 0.2 mol/mol. With a rich loading of 0.4 mol/mol, the energy required for stripping equals 3 GJ/tonne CO_2.

With 15.2% cold rich bypass through the CO_2 exchanger, the vapor stream leaving the stripper is partially cooled to about 96 °C. At these conditions, the lean solvent leaving the cold exchanger is at 61 °C and this residual heat is ultimately transferred to the water wash section and removed by the water wash air coolers. Figure 7.3 shows the flowsheet of the stripper at base case design conditions.

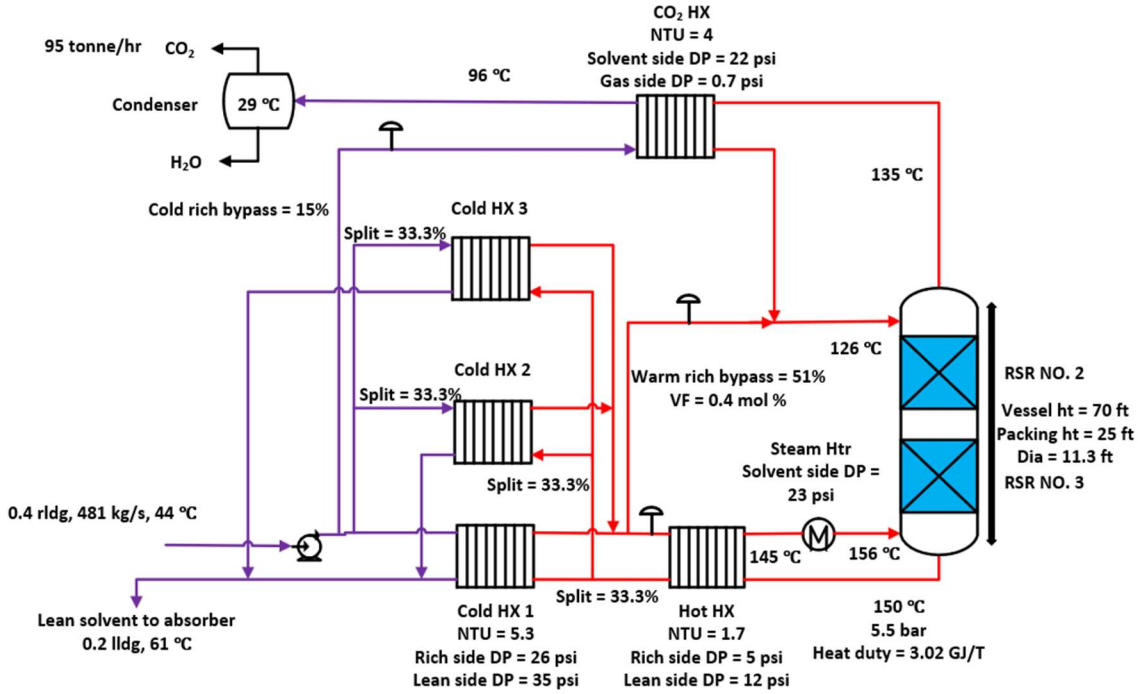

Figure 7.3: Flowsheet of the base case design of PZAS (Rochelle et al. (2022))

7.4 STRIPPER MODELING METHOD AND TOOLS

The models used in this work were created in Aspen Plus®. Two types of process models were used to evaluate the design scenarios. The "design model" was used to evaluate the base case performance of PZAS with the CO_2 exchanger as a function of heat exchanger area and stripper pressure/temperature. The scenarios consisting of the direct contact condenser were modeled using a "rating model". The rating model differs from the design model in its ability to automatically account for the pressure drop in heat exchangers, columns, and elevation head vertical solvent lines as a function of flow. Moreover, the rating model also consists of real equipment performance data obtained from vendor quotes for pumps, fans, blowers etc. More details on the design, rating, and optimization models are provided in Chapters 4 to 6.

The Independence™ model was used to estimate solvent thermodynamics, reaction kinetics, and the physical properties of 5 molal PZ (Frailie, 2014). The performance of the random packing in the stripper column and direct contact condenser section was estimated using the mass transfer model developed by Song (2017). A correction factor of 0.16 on wetted area in the stripper column was applied (Lin, 2016). This factor was an empirical correction from data reconciliation at UT-SRP pilot plant using the Wang mass transfer model (Lin, 2016), and may not be accurate for the Song (2017) mass transfer model. This correction serves to correct the modeled diffusivity of PZ at high temperature to match the measured values estimated by the Stokes-Einstein equation (Equation 7.1) (Snijder et al., 1993; Versteeg et al., 1988). This equation estimates the diffusivity of PZ in aqueous PZ solvent from the diffusivity of PZ in water using the ratio of viscosity of the water to amine.

$$\frac{D_{PZ-}}{D_{PZ-Water}} = \left(\frac{\mu_{Water}}{\mu_{PZ}}\right)^{0.6} \tag{7.1}$$

Equilibrium reactions with finite mass transfer rates were assumed in the stripper column (bottom 2 sections of packing) owing to the high operating temperature of these regions.

The equilibrium reactions in the stripper are shown in Equations 7.2 to 7.5. Unlike absorber modeling, in high temperature stripper modeling, the equilibrium constants of reactions 7.2 to 7.5 are directly calculated using the temperature dependencies of free energy, heat of formation, and specific heat capacity.

$$PZ + CO_2 + PZ \rightleftharpoons PZH^+ + PZCOO^- \tag{7.2}$$

$$PZCOO^- + CO_2 + PZCOO^- \rightleftharpoons PZH^+ + PZ(COO)_2^{2-} \tag{7.3}$$

$$PZCOO^- + CO_2 + H_2O \rightleftharpoons H^+PZCOO^- + HCO_3^- \quad (7.4)$$

$$PZ + H^+PZCOO^- \rightleftharpoons PZH^+ + PZCOO^- \quad (7.5)$$

7.5 MODELING THE DIRECT CONTACT CONDENSER

The direct contact condenser (topmost section of packing) was modeled as an absorber. In rate-based absorber modeling, the solvent equilibrium is defined by the ratio of forward and reverse reaction rates of CO_2 absorption reactions as shown by Equations 7.6 to 7.9 below.

$$2PZ + CO_2 \leftrightarrow PZCOO^- + PZH^+ \quad (7.6)$$

$$2PZCOO^- + CO_2 \leftrightarrow PZ(COO)_2^{2-} + H^+PZCOO^- \quad (7.7)$$

$$PZCOO^- + H_2O + CO_2 \leftrightarrow H^+PZCOO^- + HCO_3^- \quad (7.8)$$

$$PZ + H^+PZCOO \leftrightarrow PZH^+ + PZCOO^- \quad (7.9)$$

The direct contact condenser works in the range of 40-130 °C, which required modeling the liquid film with finite reaction rates. The liquid film was discretized into 20 segments to accurately calculate the reaction and mass transfer flux across the film. Unlike the stripping sections, a correction factor for wetted area was not applied in the direct contact condenser section.

It is not clear if this correction is applicable for mass transfer at low temperature, as observed in this column. In the absence of a more appropriate correction factor, the wetted area is not corrected, and its correction factor is left at its default value of 1.

7.6 DISCUSSION OF THE MODELING METHODS

This section investigates the modeling of mass transfer and reaction kinetics in the stripper and direct contact condenser, and the effect of modeling methods on the results in this chapter. The temperature profile, speciation, heat rate, and CO_2 flow rate will be compared with different modeling methodologies for the base case design with a direct contact condenser. The packing height in the direct contact condenser is fixed at 15 ft and the packing type used is RSR 2. The remaining design specifications for the stripper are same as the base case as shown in Figure 7.3.

7.6.1 Reaction Kinetics

The reaction kinetics in the stripper assumes that the high operating temperature results in reaction equilibrium. This assumption needs to be confirmed by comparing two different kinetics models in the stripper. Moreover, the equilibrium constant of the reactions may have an unusual temperature dependence at high temperature. The kinetic models were regressed using data from relatively low temperature (40-100 °C), more pertinent to absorber conditions (Frailie, 2014). It is also likely that the forward reaction rate constants have an unusual temperature dependence at stripper conditions, which may result in incorrect estimation of reverse reaction rate constants and the equilibrium constant.

The kinetic model that uses the finite reaction rates will be referred to as "R-KIN" and the kinetic model that uses equilibrium reactions will be referred to as "R-EQB".

7.6.2 Mass Transfer

The model for packing performance used by the stripper and direct contact condenser is developed by Song (2017) and is fixed in this analysis. For the base case, the

stripper contains an area correction factor of 0.16 and the direct contact condenser does not use an area correction factor. The default value is set at 1. The effect of using a unified correction factor for both the direct contact condenser and the stripper will be tested. Instead of applying a correction factor on area, an equivalent correction is applied on liquid-side mass transfer coefficient (k_L). To obtain an equivalent correction, the factor on k_L is adjusted to obtain the same heat duty as the base case (2.9 GJ/tonne) with 15 ft of packing and the original correction factors (0.16 for wetted area in stripper and 1 for wetted area in direct contact condenser). This equivalent correction was found to be 0.1 on k_L.

The correction factor on area was an empirical result used to correct the modeled liquid-phase diffusivity of PZ (Lin, 2016). However, an area correction will affect not only k_La but also k_Ga, resulting in a double-correction. Moreover, there is no evidence that suggests that the product of gas phase mass-transfer coefficient and wetted area must be corrected to account for discrepancies in liquid phase diffusivity of PZ.

7.6.3 Diffusivity of PZ

Another approach is considered to study the transport phenomena in the stripper and the direct contact condenser by directly correcting the diffusivity model of PZ. Figure 7.4 shows that the measured diffusivity of PZ from the Stokes-Einstein model is about 4.2 times on average lower than the model-predicted value for diffusivity of PZ-PZ.

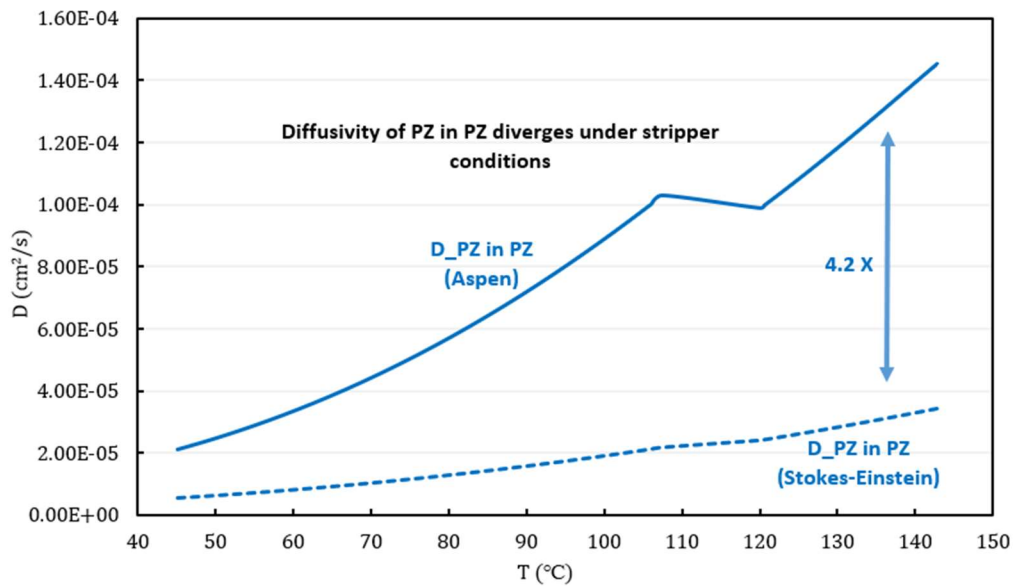

Figure 7.4: Diffusivity of PZ at high temperature is overpredicted by the model; 15 ft of packing in direct contact condenser and 24 ft of packing in the stripper

The diffusivity model for PZ in Aspen Plus® Fortran subroutine '*dlou'* is calculated using the model proposed by Frailie (2014) using a temperature and viscosity dependence. This is also shown in Equation 7.10. This model is modified in the subroutine by applying a factor (1/4.2) directly to force the predicted diffusivities to match the values predicted by the theory proposed by Stokes-Einstein (Equation 7.1).

$$D_{PZ-P} = 2.26 * 10^{-10} \left(\frac{T}{313.15}\right)^{-2.58} \left(\frac{\mu}{0.0155}\right)^{-1.45} \tag{7.10}$$

Once this model has been corrected, there is no requirement for other correction factors to be applied on wetted area. The correction factors are set to their default values of 1 with this diffusivity correction. The corrected model is shown in Equation 7.11.

$$D_{PZ-PZ} = 5.38 * 10^{-1} \left(\frac{T}{313.15}\right)^{-2.58} \left(\frac{\mu}{0.0155}\right)^{-1.45} \quad (7.11)$$

Figure 7.5 compares the uncorrected diffusivity model predictions and the corrected diffusivity model predictions with the values estimated by Stokes-Einstein.

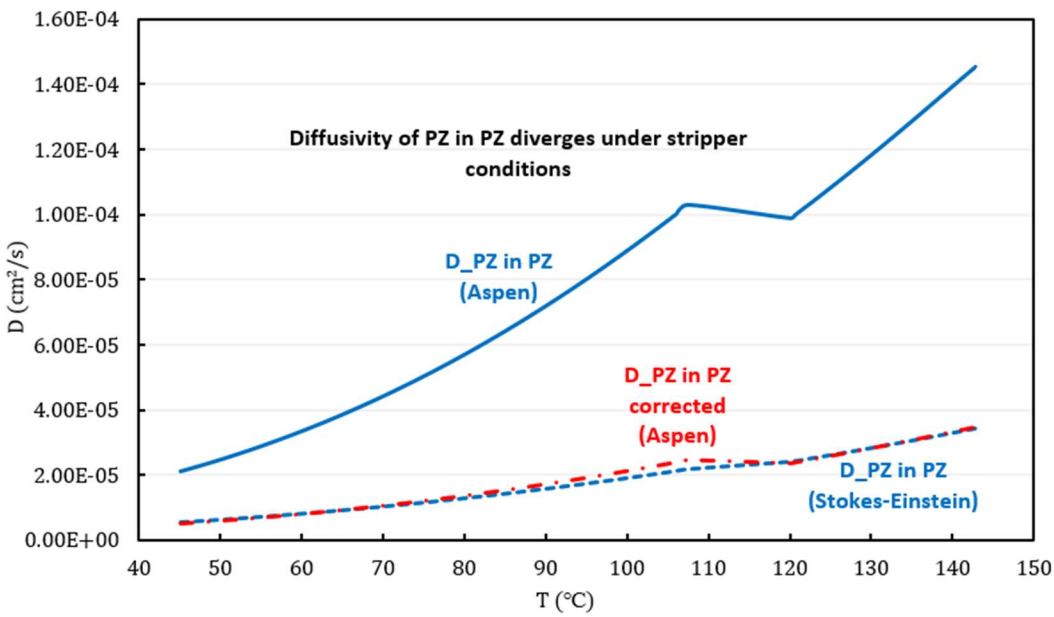

Figure 7.5: Effect of correcting diffusivity model for PZ

The effects of changing the diffusivity model, mass transfer model, and kinetics model are studied together for their synergistic effects on heat duty and temperature profile in the columns.

7.6.4 Cases Studied

Ultimately, 6 cases were studied with different combinations of mass transfer, reaction kinetics, and diffusivity method in the model. These are presented in Table 7.1 along with the heat rate and CO_2 flow rate for these cases. All these cases pertain to PZAS

with a direct contact condenser (DCC) for the base case design with 15 ft of packing in the direct contact condenser, and a 150 °C stripper. The rich loading was 0.4 and the lean loading was 0.2.

Table 7.1: Cases studied to analyze the impact of mass transfer, kinetics, and diffusivity method on stripper modeling

Case	Reaction kinetics method		Mass transfer correction factor		Diffusivity model		Heat rate	CO_2 Flow
	Stripper	DCC	Stripper	DCC	Stripper	DCC	GJ/hr	tonne/hr
Base	R-EQB	R-KIN	a, 0.16	None (1)	Uncorrected		275.9	94.9
2	R-EQB	R-KIN	k_L, 0.1		Uncorrected		274.9	94.9
3	R-KIN		k_L, 0.1		Uncorrected		284.5	94.9
4	R-EQB	R-KIN	k_L, 0.1		Corrected		279	94.9
5	R-EQB	R-KIN	none		Corrected		271	94.9
6	R-KIN		none		Corrected		271	94.9

7.6.5 Impact of Modeling Method Choice on Heat Duty

Comparing the cases in Table 7.1 provides insight into mass-transfer and kinetic mechanisms in the stripper and direct contact condenser. Comparing the base case and case 2 reveals that a 10% correction in k_L in both columns yields almost the same heat duty as that of a 16% correction in area in the stripper only.

Case 3 reveals that when all reactions are kinetic in both columns with the same mass transfer correction, the heat rate increases by 3.5% compared to case 2.

Comparing case 4 and case 2 reveals that for the same mass transfer correction in both columns, correcting the diffusivity model of PZ increases the heat rate by 1.5%. This

can be attributed to the lower diffusivity of PZ in case 4 estimated by the corrected model as shown in Figure 7.5.

Comparing case 5 with the base case shows that with the same reaction kinetics in both columns, correcting the diffusivity model (with no other area or k_L correction) reduces the heat duty by only 2%. At worst, the modeling method of the base case estimates a conservative heat duty compared to case 5.

Comparing cases 5 and 6 reveals that with a corrected diffusivity model, making both DCC and stripper reactions kinetic does not change the heat duty at all.

In all the cases shown in Table 7.1, the CO_2 flowrate is unchanging. The overall change in heat duty with all these modeling methods is only 5% at most, which is likely from differences in the amount of water condensed inside the column.

This analysis reveals that the mass-transfer method, diffusivity model and reaction kinetics model do not appreciably affect the heat duty or the CO_2 flow rate. The cost of the boilers, compressors, air coolers for water wash, and steam heaters that are estimated in this chapter can be reasonably accurate.

The modeling methods may however have a more pronounced effect on temperature profiles in the columns, which affects the downstream condenser duty and its cost. This is discussed in the next section.

7.6.6 Impact of Modeling Method Choice on Temperature Profile

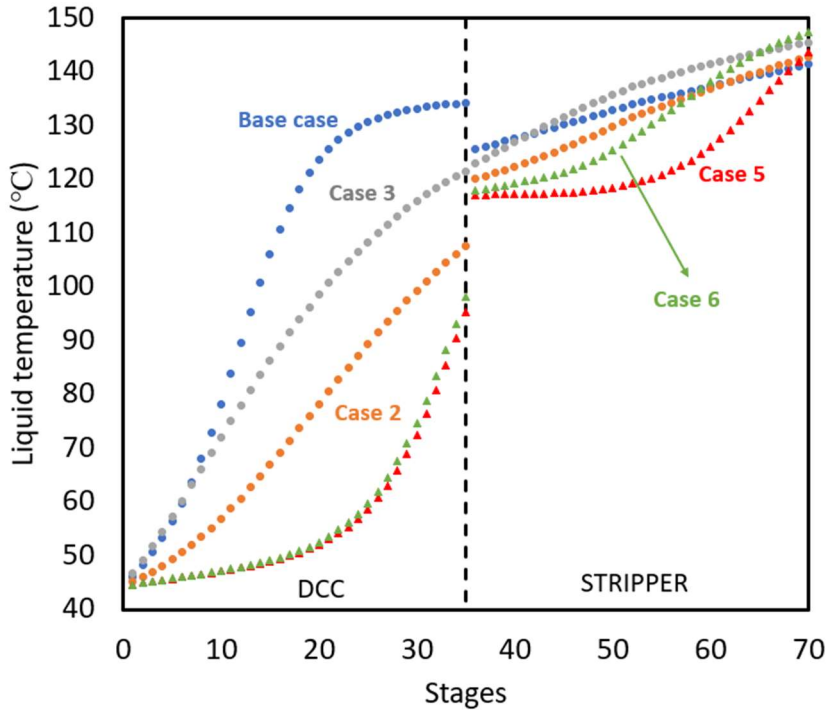

Figure 7.6: Effect of different modeling methods on liquid temperature profile; stages represent computational segments in the stripper

Figure 7.6 shows the impact of modeling methods on liquid temperature profile. In all cases, the terminal liquid temperature at the top of the DCC and bottom of the stripper are the same which indicates that stripping is equilibrium limited. The liquid temperature at the top of the stripper column changes with different modeling methods at most by about 8 °C. This indicates that with a finite amount of packing like in the bottom two sections of the stripper, the mass-transfer and reaction kinetics may matter but with large amounts of packing, the stripper becomes equilibrium limited.

Comparing the temperature profile of the base case with case 5 or case 6 shows that both correcting the diffusivity model and changing the reaction kinetics model will affect the liquid temperature in the stripper and consequently the rich loading. The ultimate effect

of these changes is once again reflected in the heat duty of the process which is discussed in section 7.5.4.

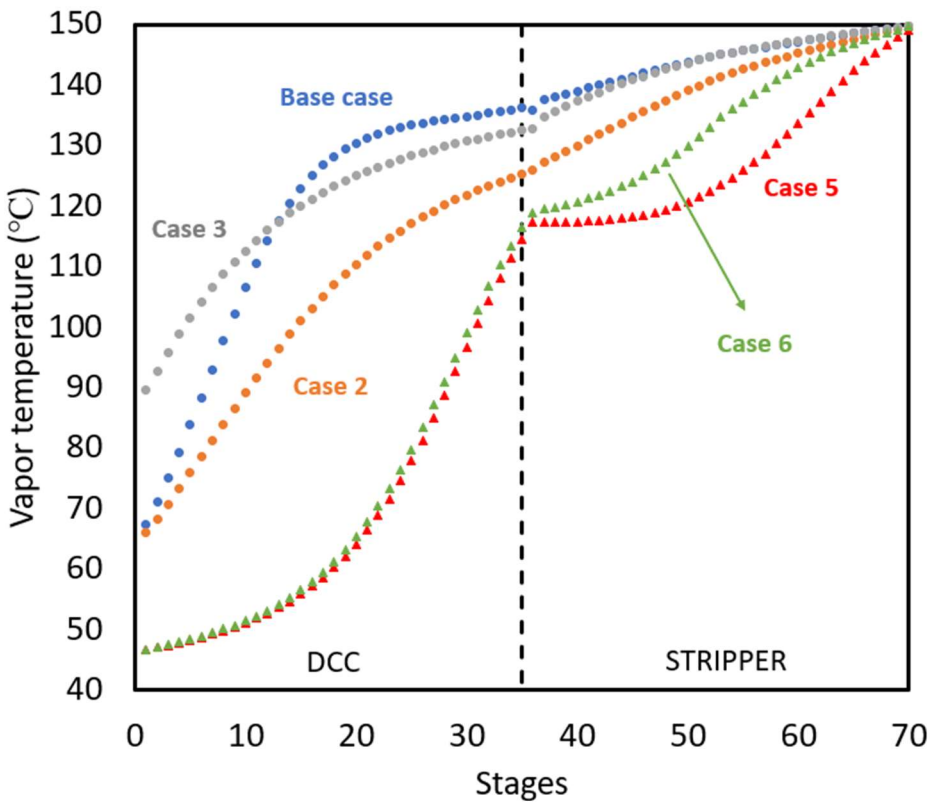

Figure 7.7: Effect of different modeling methods on vapor temperature profile; stages represent computational segments in the stripper

Figure 7.7 shows that the different modeling methods affects the vapor temperature more than the liquid temperature. While the vapor temperature at the bottom of the stripper was constant for all cases, the temperature of the vapor leaving the direct contact condenser depended on the modeling method.

The base case and case 2 have identical temperatures at the top and the bottom and therefore, the same heat duty and vapor rate for both cases. Using kinetic reactions in both

columns yielded a higher vapor temperature at the top of the direct contact condenser (case 3 versus case 2).

Cases 5 and 6, when compared to the base case show that when the liquid diffusivity model is corrected, and the mass transfer correction factors removed, the net result is a decrease in vapor temperature throughout both columns compared to the base case. This would translate to a much lower cooling duty in the condenser downstream.

This comparison shows that the modeling method used for the base case is at worst a conservative approach to estimating the condenser duty and its cost. The terminal vapor temperature was also correlated with the heat rate for each modeling method, indicating that it is related to the water vapor content leaving the stripper.

7.6.7 Differences in Kinetics Method

Case 3 in Figures 7.6 and 7.7 showed that rate-based kinetics for both columns yielded a continuous liquid and vapor temperature profile. While this method is the preferred choice for modeling, it can accurately represent the kinetics at high temperature only if the rate-based kinetics model converges to equilibrium at high temperature.

Figure 7.8 compares the equilibrium constant for Equation 7.12 calculated using speciation with that calculated using the ratio of forward and reverse reaction rates.

$$2PZCOO^- + CO_2 \rightleftharpoons H^+PZCOO^- + PZ(COO)_2^{2-} \tag{7.12}$$

The results were not a function of loading but only liquid temperature. Pre-exponential factors and activation energies for forward and reverse reactions shown in Equation 7.12 was obtained from Frailie (2014). The speciation and activity coefficients at a given loading as a function of temperature were obtained by conducting flash calculations in Aspen Plus®.

Figure 7.8 showed that equilibrium constants from forward and reaction rates agreed very well with that from thermodynamics between 40 and 90 °C, which is the region of regression and data acquisition for the kinetics model. Beyond 90 °C, the thermodynamics and kinetics do not agree as perfectly. This shows that the kinetics model does not converge to thermodynamics at high temperature and cannot be used for modeling the stripper column without adjustments. As temperature increases beyond 90 °C, the equilibrium constant from thermodynamics is lower than that from kinetics, reaching a maximum deviation of -30% at 150 °C.

The direct contact condenser could be better modeled by separating the columns at the crossover point at 90 °C between the two curves in Figure 7.8. Below 90 °C, the direct contact condenser can be modeled with the regular kinetics model. Beyond 90 °C, the direct contact condenser and stripper must be modeled with a modified kinetics model where the reverse reaction rate is adjusted to reconcile differences in equilibrium constant calculated by kinetics and equilibrium model.

A piece-wise adjustment for a range of temperatures can be used, or a continuous adjustment by segmenting the high temperature parts of the column into smaller sections can be used. Another option would be to include a user subroutine for the adjusted high temperature kinetic model in Aspen Plus®.

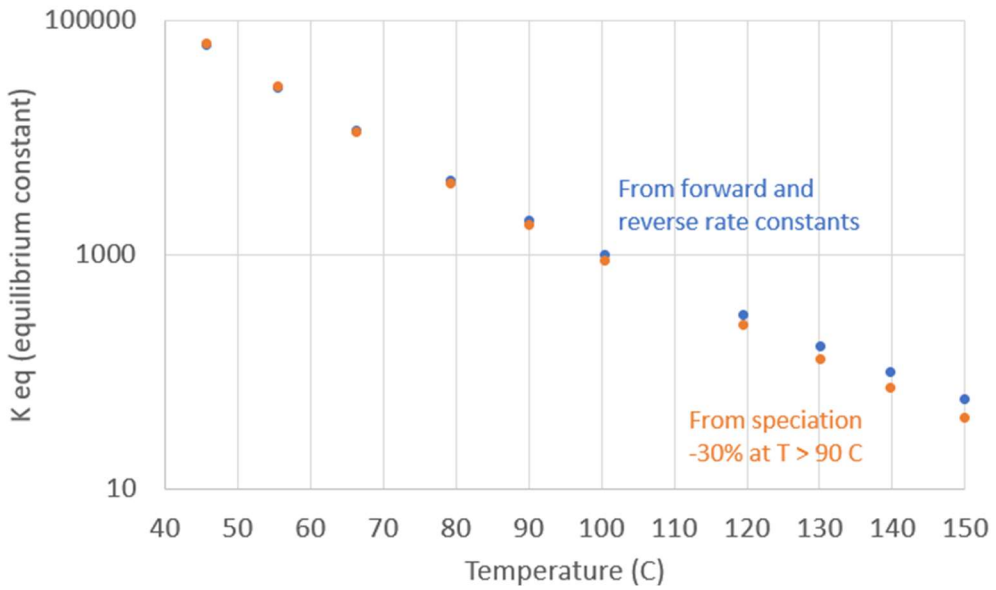

Figure 7.8: Differences between equilibrium constant from speciation and rate-based kinetics between 40 and 150 °C; 0.2 to 0.4 loading

7.7 PZAS WITH DOUBLE THE NUMBER OF SOLVENT CROSS EXCHANGERS

Figure 7.9 describes the base case design with double the number of cross exchangers. This is represented by doubling the number of transfer units and pressure drop of the cold and hot cross exchangers. This configuration would consist of two sets of three parallel cross exchangers, in series, and two hot cross exchangers. The number of steam heaters and CO_2 exchangers remain the same as the base case design. The stripper is identical to the base case design in packing type, height, and diameter.

Rochelle et al. (2022) suggested that doubling the number of transfer units in the solvent cross exchangers would lower the CAPEX and OPEX of the process by reducing the heat duty, and thereby reducing the size of equipment such as steam heaters and standalone natural gas boilers. The direct field cost of the cross exchangers will double in this case.

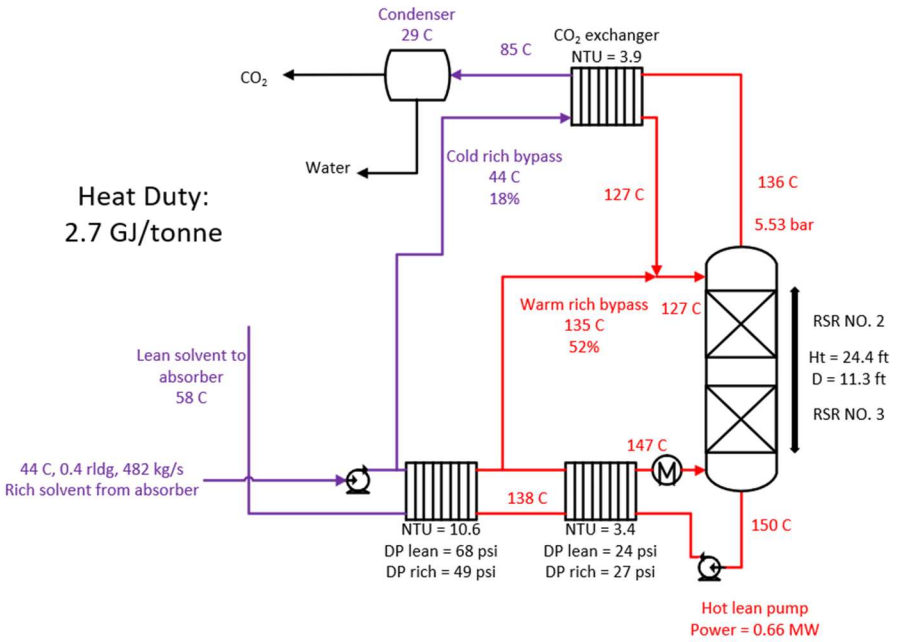

Figure 7.9: Design specifications of PZAS with double the solvent cross exchanger area

The reoptimized bypass flowrates are shown in Figure 7.9. The heat duty of this configuration is about 2.7 GJ/tonne CO_2, 12% lower than the base case. Due to the better heat recovery in the cross exchangers compared to the base case, the lean solvent recycled back to the absorber is colder (58 °C) compared to the base case design (61 °C). This will reduce the cooling duty of the air coolers for the water wash, which acts as the heat sink for the cold lean solvent. The higher cold rich bypass used by this design also cools the stripper overhead gas to a lower temperature (85 °C) compared to the base case design, in the CO_2 exchanger (96 °C). This will reduce the cooling duty in the downstream condenser and partially eliminate some of the capital associated with the condenser and the KO drums.

In addition to the added capital for the solvent cross exchangers, this design will also require a hot lean pump instead of a cold lean pump used in the base case design. This

is a direct consequence of the larger pressure drop in the lean side of the hot and cold exchangers and consequently the larger elevation head that the lean pump counteracts.

The lean pump was modeled in a design mode using a 65% thermodynamic efficiency and its electric power consumption was about 0.7 MW. The pressure change across the lean pump was specified equal to the sum of the total lean side pressure drop and the elevation head to the absorber inlet. Elevation head calculations are described in Chapter 5.

7.8 PZAS WITH A DIRECT CONTACT CONDENSER

This section investigates the performance of PZAS with the CO_2 exchanger replaced by a direct contact condenser section atop the stripper column. This configuration will be referred to as PZAS with the Direct Contact Condenser.

The direct contact condenser will be used to condense the water vapor leaving the main stripper column using the cold rich bypass using direct contact on random packing (RSR 2) unlike the CO_2 exchanger, where there exists a barrier for heat and mass transfer between the gas and liquid phases. This method of contact will promote both heat and mass transfer which could offer several advantages. The direct contact condenser is expected to:

1. Directly eliminate the capital associated with the CO_2 exchanger.
2. Cool the vapor leaving the main stripper to a lower temperature compared to the CO_2 exchanger by condensing water vapor. This could partially or fully eliminate the downstream condenser and knock-out drums, reducing the overall CAPEX of the process.

3. Enable some further stripping in addition to the main stripper. This will reduce the energy requirement of the process further compared to the base case, which will reduce OPEX.
4. Reduce the CAPEX of the process by requiring smaller steam heaters, gas boilers, condenser and knock-out drums, and fewer air coolers for the water wash section.
5. Allow vertical integration of the direct contact condenser on top of the stripper column unlike horizontally in the case of the CO_2 exchanger, which will be especially useful when used in locations with space constraints.
6. Be more economical effective with a high pressure and high temperature stripper by reducing the stripper diameter. This will be useful especially with solvents that are resistant to thermal degradation, such as 5 molal Piperazine.

Figure 7.10 shows the design specifications of PZAS with the Direct Contact Condenser. The NTU of the solvent cross exchangers are held at the same values as the base case. In this scenario, the cold and hot cross exchangers have the same pressure drop as the base case, and therefore the rich and lean pumps have approximately the same electric power requirement as the base case.

The cold and warm rich bypass flow rates have been specified to be the same as that of the base case to individually highlight the effect of replacing the CO_2 exchanger with a direct contact condenser. The packing height in the direct contact condenser was varied to observe its effects on heat duty, downstream condenser duty, gas temperature, and rich loading.

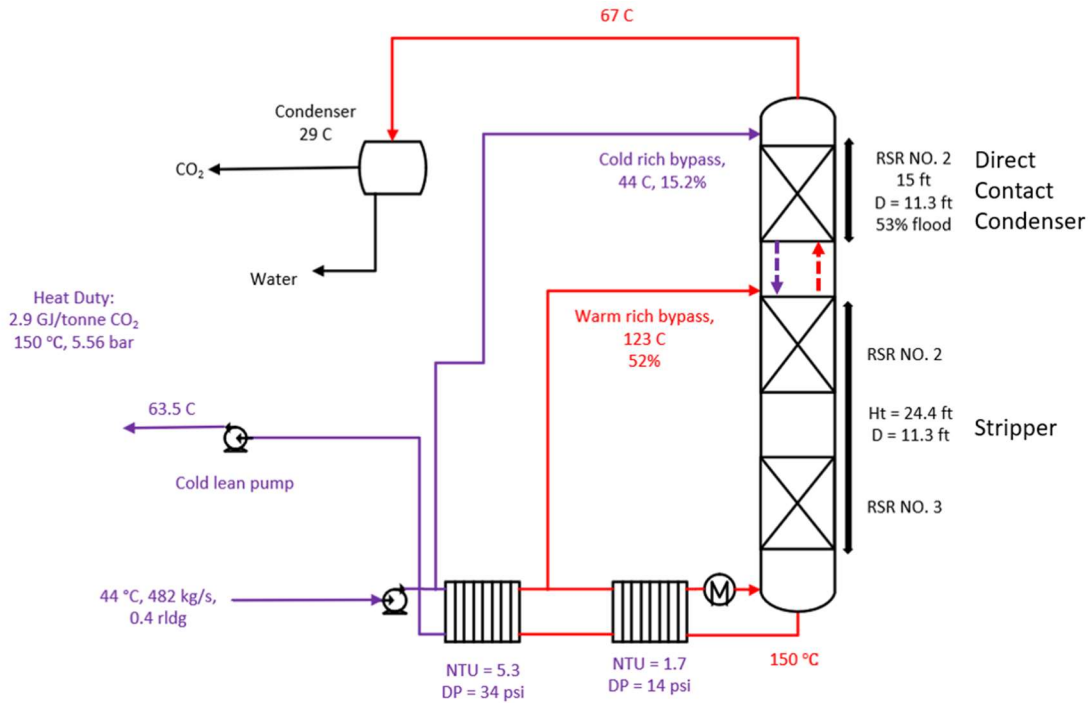

Figure 7.10: Design specifications of PZAS with the direct contact condenser with base case heat exchanger sizes

7.8.1 Impact of Direct Contact Condenser on Steam Heater Duty

The packing height in the direct contact condenser was increased from 2 ft to 30 ft to observe its effect on heat duty. The packing type used was RSR 2. Below 5 ft of packing, the direct contact condenser underperformed compared to the CO_2 exchanger, resulting in a higher heat duty.

Only 5 ft of packing in the direct contact condenser was adequate to match the heat duty of the base case design. Below 5 ft of packing, the cold rich bypass leaving the direct contact condenser is at a lower temperature compared the CO_2 exchanger. This results in a higher rich loading in this stream compared to the base case design. The temperature of the vapor leaving the stripper is also higher than the base case, caused by little water condensation.

As the packing height increased further, the heat duty decreased, ultimately approaching 2.9 GJ/tonne where the direct contact condenser pinched at the bottom. This was due to enhanced water condensation in the column.

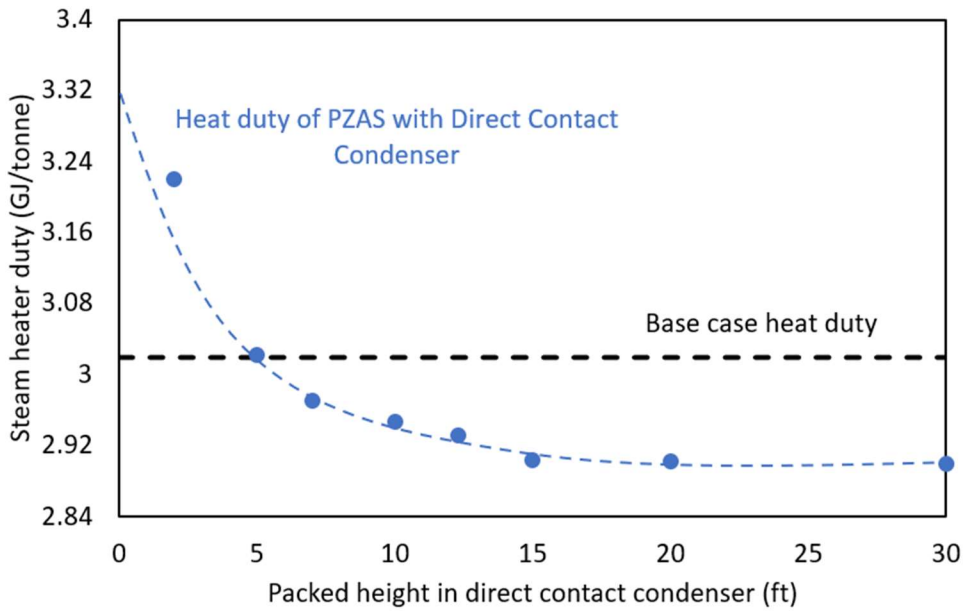

Figure 7.11: Sensitivity of heat duty to packing height in direct contact condenser; base case heat exchanger size

7.8.2 Temperature and Flux Profile in Direct Contact Condenser

The temperature and flux profiles in the direct contact condenser with a packed height of 12.3 ft are shown in Figure 7.12. The stripper has three symmetric sections on top of each other. The diameter of the direct contact condenser was equal to that of the main stripper column.

Figure 7.12 shows that the direct contact condenser works partially as an absorber at the top and as a stripper at the bottom. This is shown by the positive CO_2 flux at the top, representing reabsorption and negative CO_2 flux at the bottom, representing stripping.

Water is always being condensed in the direct contact condenser, shown by the positive flux on the primary y-axis.

Figure 7.12 also shows a bottom-side temperature pinch in the direct contact condenser indicating that the cold rich bypass is preheated to the maximum possible temperature and stripped to the lowest possible loading as it leaves the direct contact condenser. The lower liquid temperature at the top requires the treatment of the direct contact condenser as a classic absorber with finite reaction rates in the liquid film.

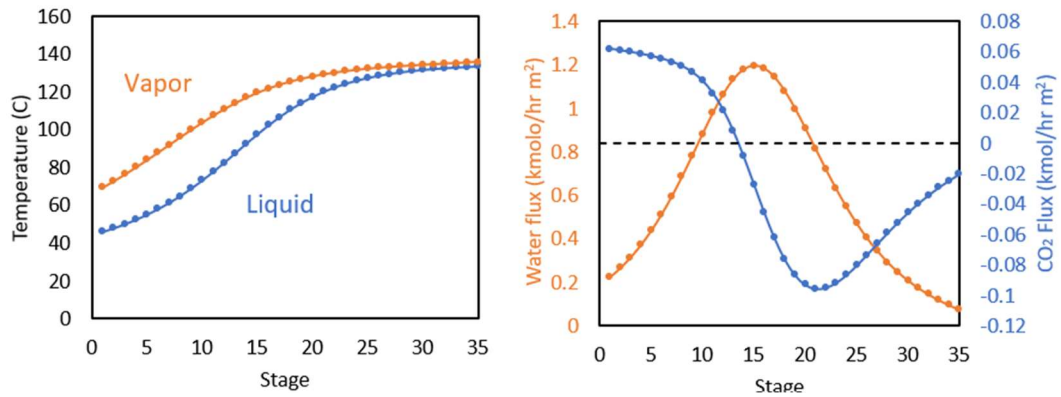

Figure 7.12: Temperature and flux profiles in the direct contact condenser; stage 1 is the top of the column; stage 35 is the bottom of the column; base case heat exchanger size; packed height = 12.3 ft; stages represent computational segments

Overall, despite the partial reabsorption at the top, the direct contact condenser effectively cools the vapor, preheats the cold rich bypass, and strips the CO_2 from the solvent prior to entry into the main stripper column. This is represented by the rich loading profile through the column in Figure 7.13, and the rich loading in the cold rich bypass leaving the column in Figure 7.14.

7.8.3 Effect of Direct Contact Condenser on Rich Loading

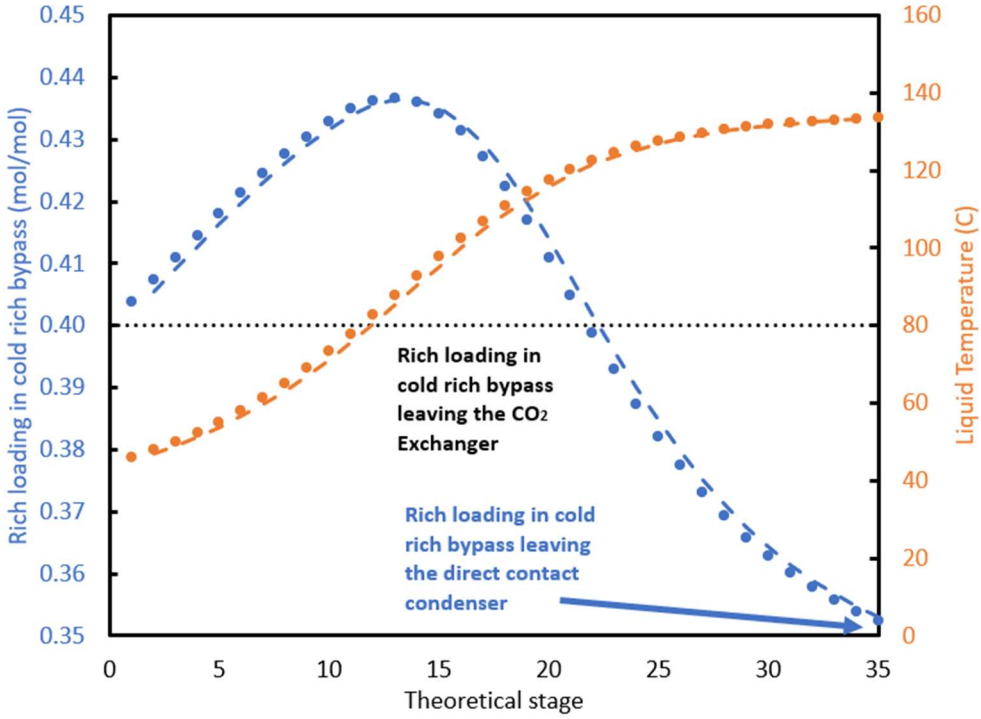

Figure 7.13: Rich loading profile in direct contact condenser for a symmetric stripper; 12.3 ft of packing in direct contact condenser; base case heat exchanger size; theoretical stage represents computational segments

The rich loading profile reveals that as the cold rich bypass gets preheated, partial stripping of solvent occurs prior to entry into the stripper column. This is shown in Figure 7.13. Towards the bottom 3rd of the column, between a temperature of 120 and 130 °C, the rich loading is lower compared to that in the cold rich bypass leaving the CO_2 exchanger in the base case. The exchanger is unable to exchange mass because of a physical barrier. Ultimately the cold rich bypass leaves the direct contact condenser at a rich loading of 0.35, 12.5% lower than the base case.

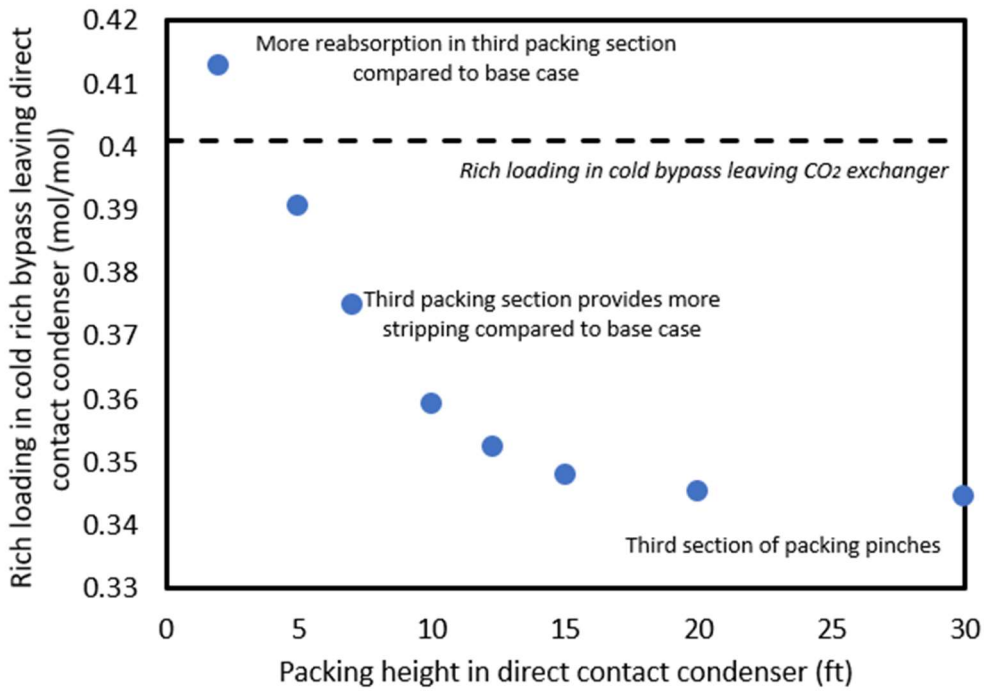

Figure 7.14: Rich loading in cold rich bypass leaving direct contact condenser as a function of packing height in the direct contact condenser; base case heat exchanger size

Figure 7.14 plots the rich loading in the solvent leaving the direct contact condenser as a function of packing height. Compared to the rich loading in the cold rich bypass leaving the CO_2 exchanger, at very low packing height, the direct contact condenser performs poorly, giving rise to a higher rich loading.

As packing height is increased, the rich loading is lower compared to the base case ultimately becoming constant at about 0.34 at very high packing height. This occurs due to a temperature and flux pinch at large packing height. Overall, the direct contact condenser can be expected to reduce the rich loading in the cold rich bypass by up to 15% compared to the base case.

7.8.4 Impact of Direct Contact Condenser on Gas Cooling and Condenser Duty

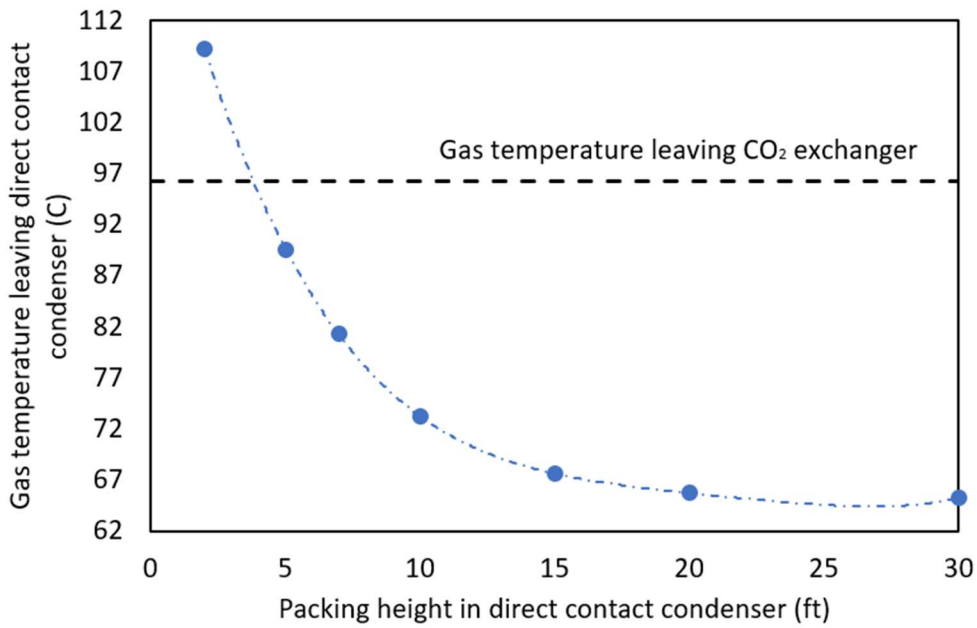

Figure 7.15: Gas cooling as a function of packed height in direct contact condenser; base case heat exchanger size

Figure 7.15 shows that above a packing height of about 5 ft, the gas temperature leaving the direct contact condenser can be decreased below the gas temperature leaving the CO_2 exchanger for the same cold rich bypass. Direct contact results in more condensation of water in the column, ultimately resulting in better cooling of gas leaving the column. This results in a lower condenser duty as shown in Figure 7.16, which indicates that using the direct contact condenser could result in partial or complete elimination of the condenser and knock out drums.

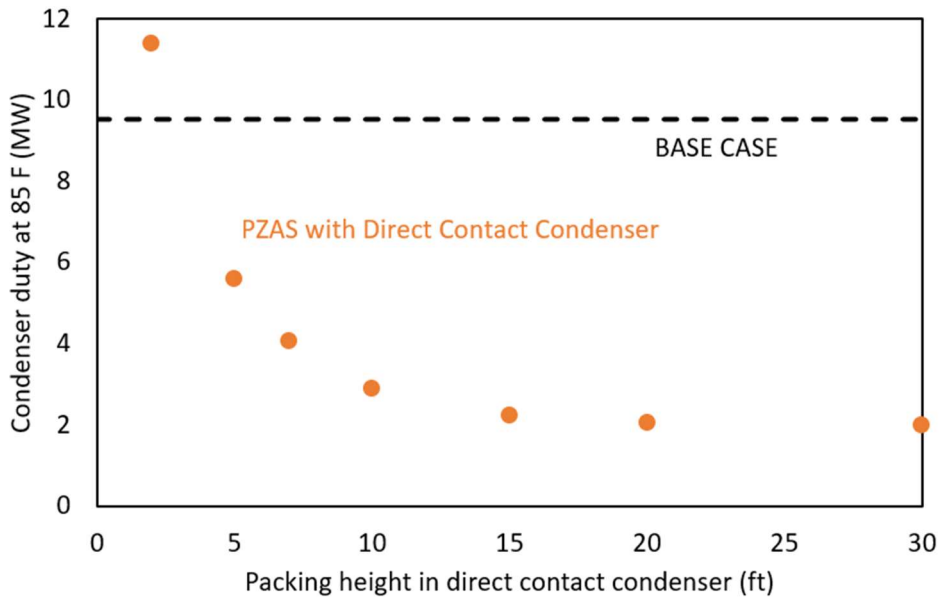

Figure 7.16: Downstream condenser duty as a function of packed height in direct contact condenser; base case heat exchanger size

Figure 7.16 shows that the additional cooling of the gas in the direct contact condenser reduces the downstream condenser duty with increasing packing height. This will give lower cost for condenser and KO drums when the base case costs are scaled using condenser duty for a new design.

At a packing height of 30 ft, the condenser duty is only 2 MW compared to the base case duty of 10 MW, indicating that the condenser may be completely eliminated from the design, but this point may not be economically optimal considering that the cost of stripper packing and internals will be the greatest at this high packing height.

7.9 PZAS WITH A DIRECT CONTACT CONDENSER AND DOUBLE THE NUMBER OF SOLVENT CROSS EXCHANGERS

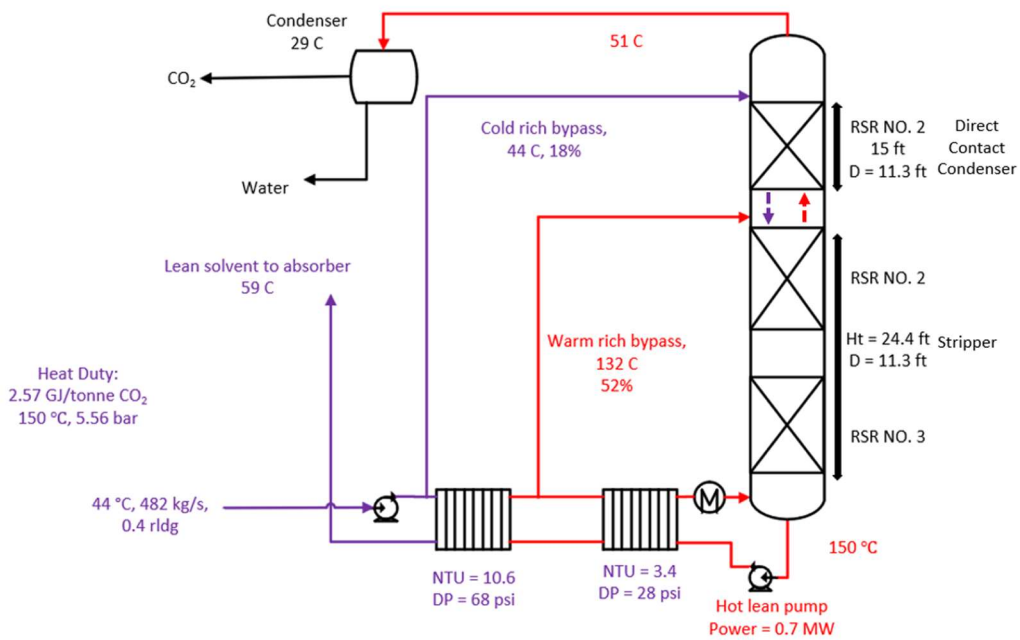

Figure 7.17: Design specifications of PZAS with a direct contact condenser and double the solvent cross exchanger area

This section evaluates the process impacts of a design that combines the key elements of sections 7.7 and 7.8. This design will consist of direct contact condenser and double the number of heat transfer units in the cold and hot cross exchangers. The rich pump design and performance is not expected to change under this scenario as it is a fixed speed pump that outputs a given pressure for a given flow.

The lean pump will need to be placed downstream of the stripper sump and before the hot exchanger, as explained in section 7.7. Figure 7.17 shows the process flow diagram for this design at the economically optimum packing height of 15 ft in the direct contact condenser.

7.9.1 Impact of Direct Contact Condenser on Steam Heater Duty

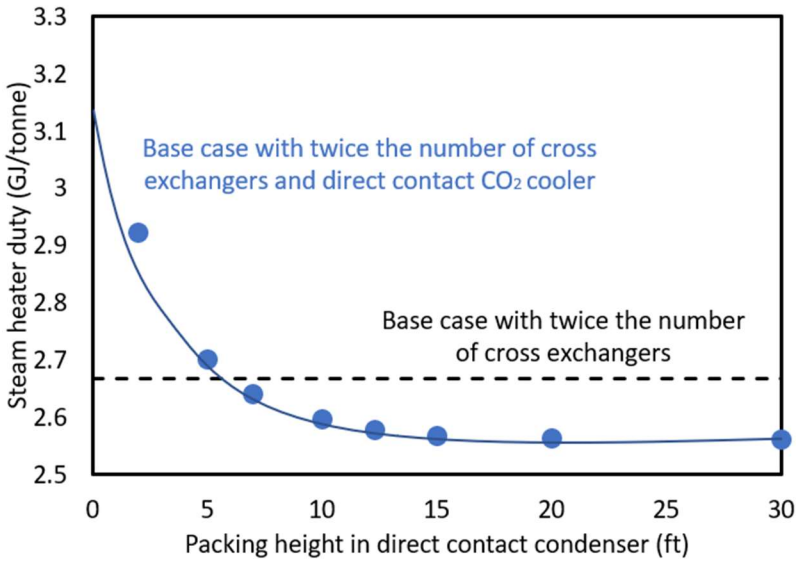

Figure 7.18: Sensitivity of heat duty to packing height in direct contact condenser; double the solvent cross exchanger area

Figure 7.18 shows the sensitivity of heat duty to packing height in the direct contact condenser. Compared to the base case design (3 GJ/tonne), the heat duty is lower, directly correlating with the increased heat exchange area.

Only 5 ft of packing in the direct contact condenser section is sufficient to match the heat duty (2.7 GJ/tonne) and performance of the CO_2 exchanger in the base case with double the number of cross exchangers. Below 5 ft of packing, the base case design with double the number of cross exchangers outperforms the configuration with a direct contact condenser due to ineffective cooling and condensation. At high packing height, the column pinches resulting in a constant heat duty.

7.9.2 Temperature and Flux Profile in Direct Contact Condenser

Temperature and flux profile in the direct contact condenser for a packing height of 12.3 ft is shown in Figure 7.19. This represents a column with 3 identical packing sections.

As observed in section 7.8.2, the cold rich bypass enters at about 44 °C at the top of the column (stage 1) and is preheated as it flows down the column by the condensing vapor. Ultimately the vapor is partially cooled as leaves the section to about 55 °C and the liquid is preheated to 130 °C before it enters the main stripper column (2nd and 3rd sections of packing). Consequently, owing to the lower liquid temperature at the top of the column, CO_2 reabsorption is noticed, and the process reverses to stripping as the temperature increases down the column. Meanwhile, water vapor is always being condensed in the column, shown by the positive flux for water through the entire column.

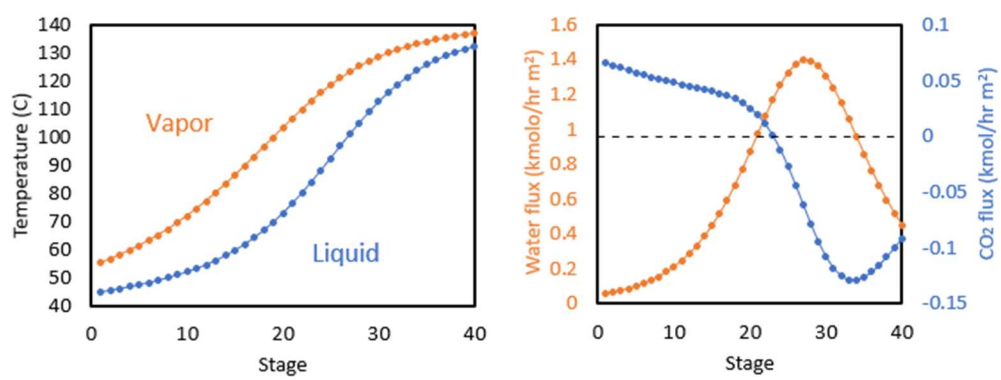

Figure 7.19: Temperature and flux profiles in the direct contact condenser; stage 1 is the top of the column; stage 40 is the bottom of the column; double the solvent cross exchanger area; packed height = 12.3 ft; stages represent computational segments

7.9.3 Impact of Direct Contact Condenser on Rich Loading

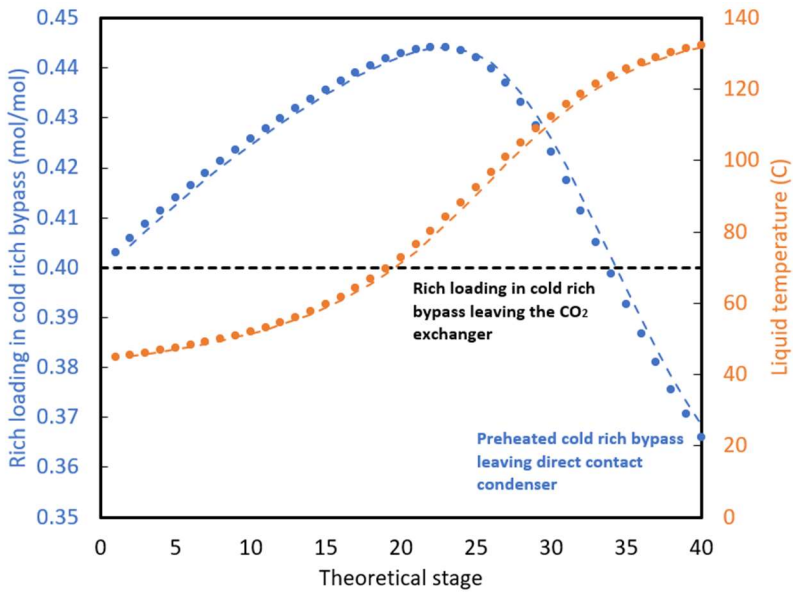

Figure 7.20: Rich loading profile in direct contact condenser for a symmetric stripper; 12.3 ft of packing in direct contact condenser; double the solvent cross exchanger area; theoretical stage represents computational segment

The low liquid temperature in the top section of packing and reabsorption of CO_2 results in a higher rich loading compared to the base case design at a similar location. As the liquid gets preheated by the condensing vapor, some CO_2 is stripped off the solvent, which is shown by the decreasing rich loading towards the bottom of the column. Ultimately, the preheated cold rich bypass this section of packing at a rich loading of 0.37 mol/mol, which is 8% lower than the rich loading of the cold rich bypass that would leave the CO_2 exchanger in the base case design. This demonstrates that despite some reabsorption of CO_2, using the direct contact condenser will partially strip the solvent before it enters the main stripper, which enables the reduction in heat duty.

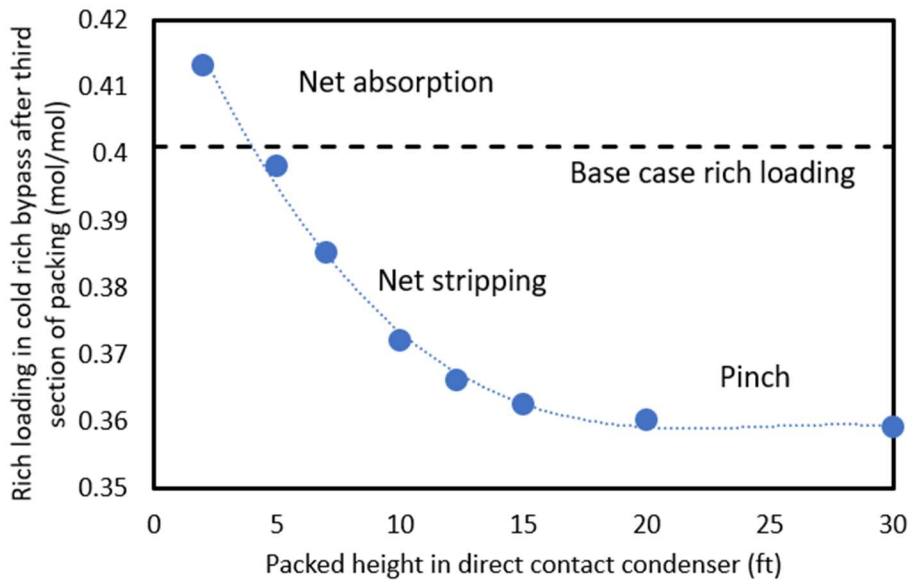

Figure 7.21: Rich loading in cold rich bypass leaving direct contact condenser as a function of packing height in the direct contact condenser; double the solvent cross exchanger area

This phenomenon is observed less as the packing height in the direct contact condenser increases. Beyond 15 ft of packing, the reduction in rich loading is not significant due to a column pinch leading to approximately constant bottom-side liquid temperature in the direct contact condenser.

7.9.4 Impact of Direct Contact Condenser on Gas Cooling and Residual Condenser Duty

Figure 7.22 shows that the gas temperature leaving the direct contact condenser can be lower than with the case with base case heat exchanger sizes for the same packing height primarily due to the higher amount of cold rich bypass. This independently highlights the effect of cold rich flow through the section.

At a packing height of 20 ft or above, the gas temperature leaving the condenser is about 42 °C bringing it almost in equilibrium with the cold rich bypass entering the column.

In this case, the condenser duty downstream will be close to zero due to almost complete condensation of water in the stripper column. This will further reduce the cost of the condenser and KO drum compared to the other designs and may almost eliminate the need for this equipment. This effect is highlighted in Figure 7.23.

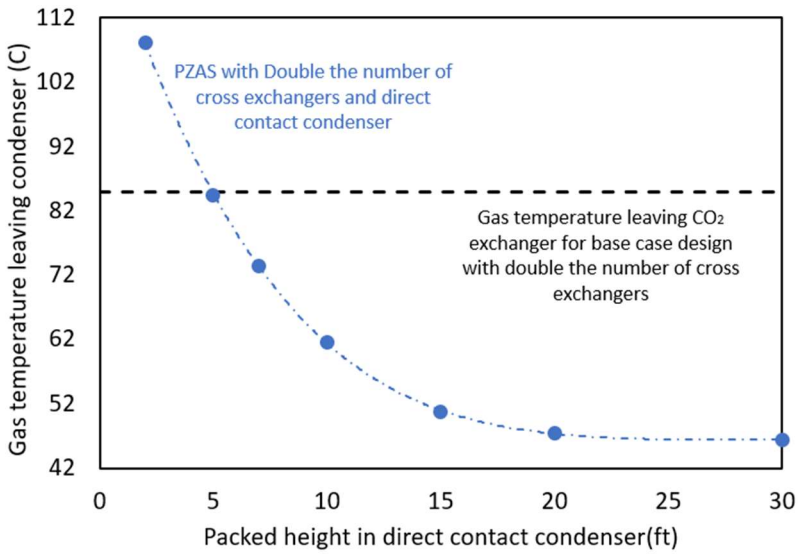

Figure 7.22: Gas cooling as a function of packed height in direct contact condenser; double the solvent cross exchanger area

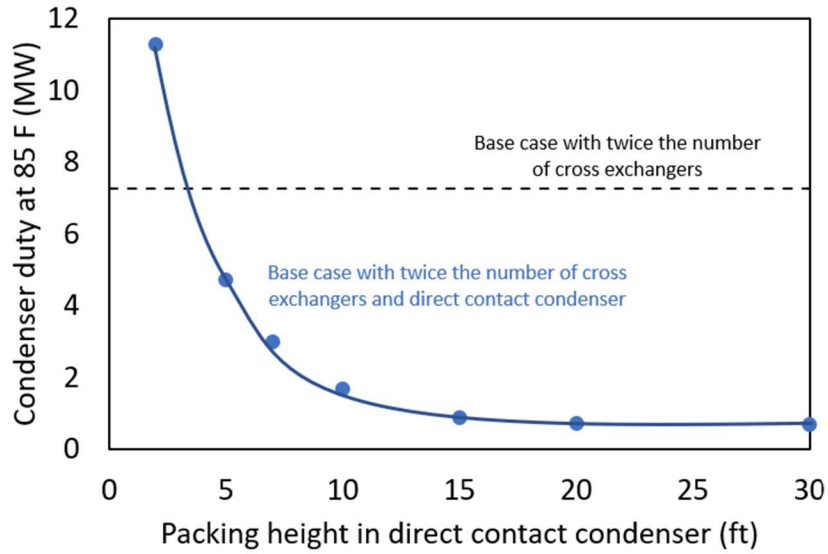

Figure 7.23: Downstream condenser duty as a function of packed height in direct contact condenser; double the solvent cross exchanger area

Figure 7.23 shows that as the packing height in the direct contact condenser increases, the condenser duty drops just as, but slightly lower than with the direct contact condenser and base case heat exchanger sizes, due to the higher cold rich bypass. At very high packing height, the condenser duty can be reduced to almost zero compared to that of the base case design with double the cross exchangers (8 MW).

7.10 EFFECT OF BYPASS FLOWRATE ON PERFORMANCE OF DIRECT CONTACT CONDENSER

The scenarios developed in the previous sections were evaluated at the optimum bypass flow rates for their respective base cases with the CO_2 exchanger. This section shows the dependence of heat duty on the bypass flowrate keeping the stripper packing height fixed at the optimum value of 15 ft.

In Figures 7.24 and 7.25, heat duty decreases when more total rich bypass is used. At one extreme, when very low cold rich bypass or very low total rich bypass is used, the

heat duty is higher than that of the optimized case. At this condition, due to the very little cold rich bypass, there is little change in vapor temperature in the direct contact condenser due to poor water condensation. This also results in a large temperature pinch from the middle to the bottom of the column.

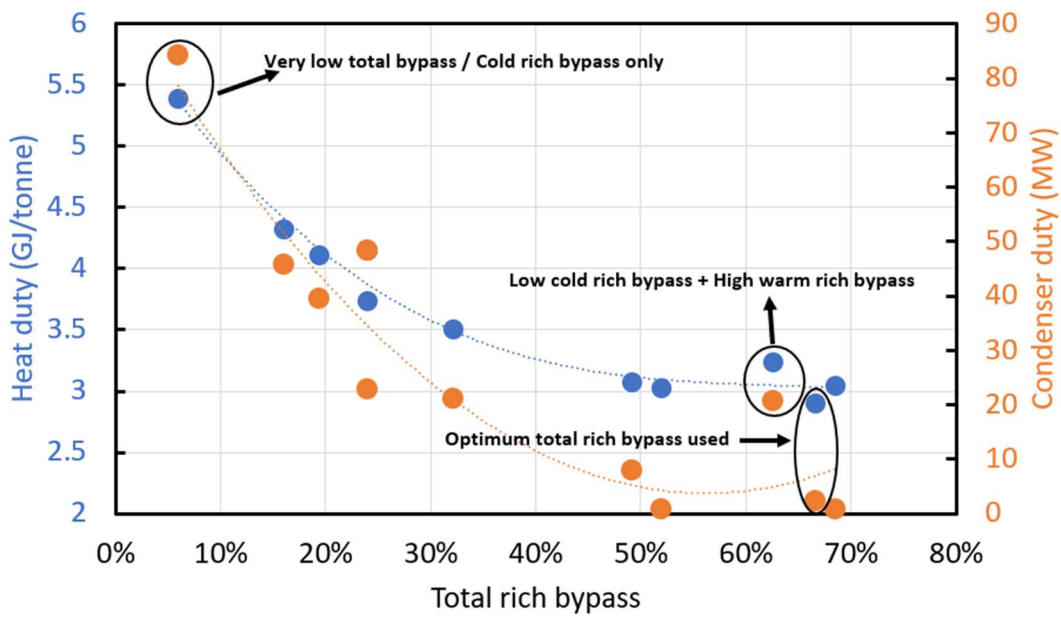

Figure 7.24: Sensitivity of heat duty and condenser duty to total rich bypass; base case heat exchanger size

In another case where a combination of low cold rich bypass and high warm rich bypass is used, the heat duty is much lower but still not at its optimum value, however, the residual condenser duty is still about 20 MW.

At the optimum value of bypasses, both heat duty and condenser duty are minimized as shown in Figures 7.24 and 7.25. This demonstrates that the performance of the direct contact condenser will likely be suboptimal with either the cold rich or warm rich

bypass only, rather than both bypasses at their optimal values irrespective of solvent heat exchanger size.

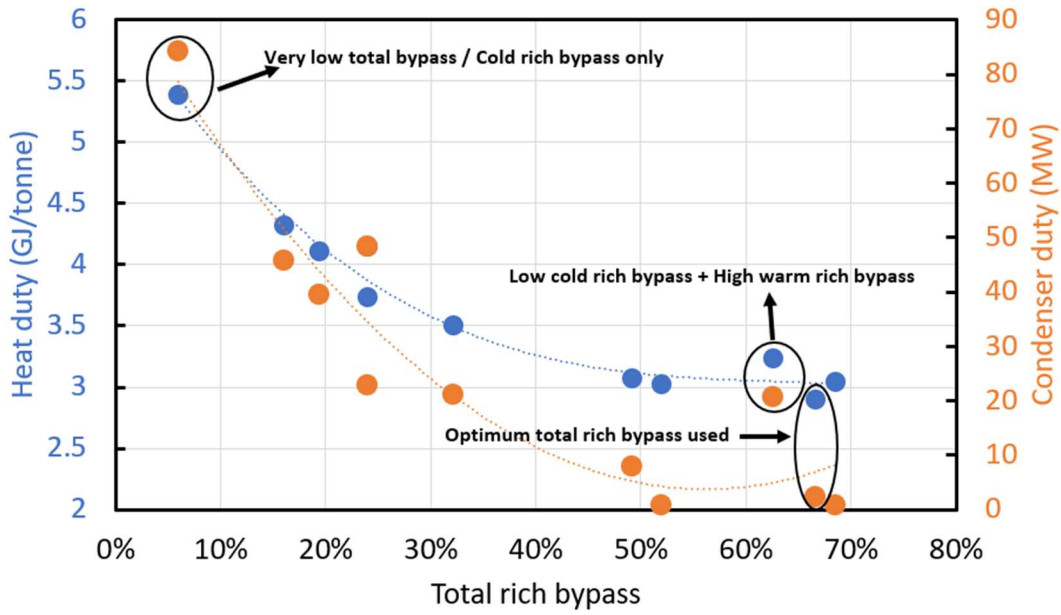

Figure 7.25: Sensitivity of heat duty and condenser duty to total rich bypass; double the solvent cross exchanger area

7.11 LOW PRESSURE STRIPPING WITH PZAS

7.11.1 Impact on Process Equipment

Use of low pressure and low temperature in the stripper impacts the energy performance as well as the capital cost of the equipment. As shown in Figure 7.26, the base case design has been evaluated with a lower temperature and pressure stripper at a fixed lean loading of 0.2 mol/mol. The bypasses have been optimized to minimize the heat duty. The stripper bottoms temperature is 120 °C and the corresponding stripper pressure for a lean loading of 0.2 mol/mol is 2.04 bar.

The vapor density in the stripper is lower compared to a stripper operated at 5.6 bar and 150 °C. This increases the velocity of vapor in the stripper, thereby flooding the column with the diameter fixed at 11.3 ft. To avoid this, the diameter of the stripper column is increased to 15 ft, bringing the flooding down to about 80%. This increased diameter directly impacts the direct field cost of the stripper column.

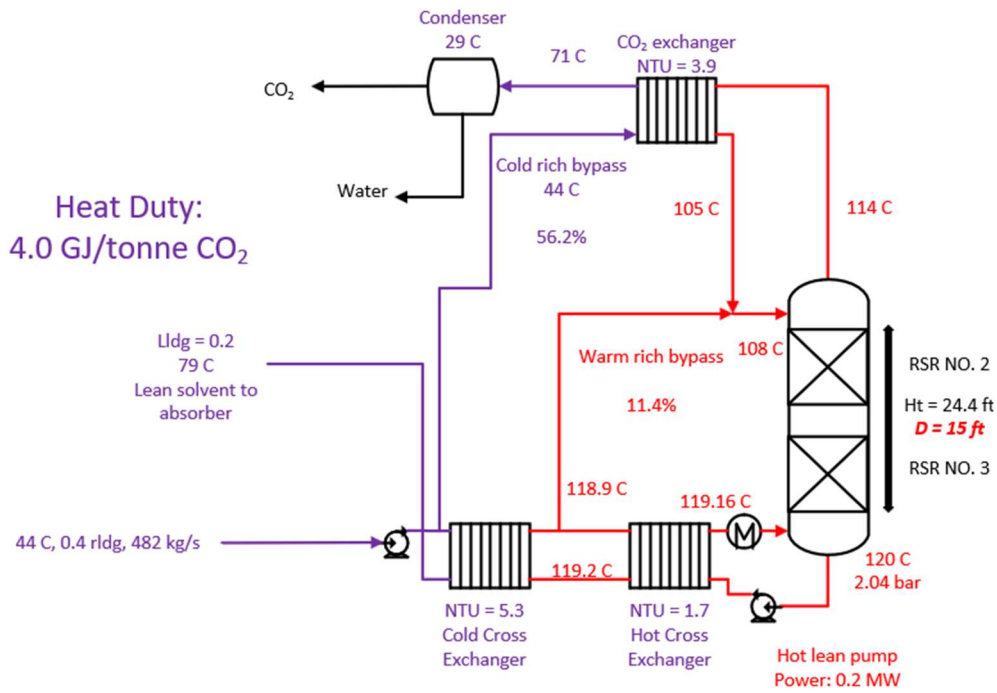

Figure 7.26: Design specifications of PZAS with a low temperature and low pressure stripper

The lower pressure of the stripper also impacts compressor cost. Compared to the base case design, the compressor cost would increase due to a greater pressure swing across the compressor. This would require more compressor stages for the same CO_2 flow through the compressor.

The use of a low-pressure stripper requires a hot lean pump downstream of the stripper sump and upstream of the hot cross exchanger. The stripper pressure is not high enough to compensate for the pressure drop through the lean side of the cross exchangers and the elevation head to the absorber. The electric power of this pump was calculated using a pump efficiency of 65% and was estimated to be about 0.2 MW.

7.11.2 Impact on Stripper Performance

At low temperature and pressure in the stripper, the ratio of partial pressure between CO_2 and H_2O in the stripper is lower compared to a high pressure stripper. Equation 7.13 shows this dependence between equilibrium partial pressures of CO_2 and water vapor, and heat of absorption and vaporization in the stripper. The heat of vaporization is typically lower than the heat of absorption of CO_2. At lower temperature, Equation 7.13 shows that the ratio of partial pressure of CO_2 to water decreases.

$$\frac{P^*_{CO_2}(T)}{P^*_{H_2O}(T)} = \frac{P^*_{CO_2}(T_{ref})}{P^*_{H_2O}(T_{ref})} \exp\left[\left(\frac{\Delta H_{abs} - \Delta H_{vap}}{R}\right)\left(\frac{1}{T_{ref}} - \frac{1}{T}\right)\right] \tag{7.13}$$

From Figure 7.27, as the temperature of the stripper is increased from 120 to 150 °C, as expected, the partial pressure ratio of CO_2 to H_2O increases from 0.4 to 0.95, decreasing the heat duty. The heat duty of this design is 4 GJ/tonne compared to 3 GJ/tonne with the base case for the same heat exchanger sizes and packing height in the stripper.

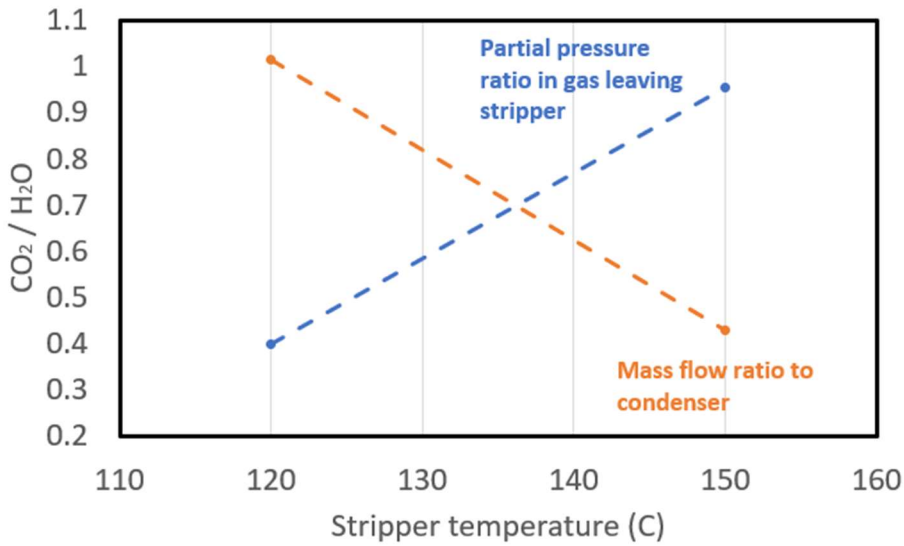

Figure 7.27: Comparison of ratios of mass flow and partial pressure between CO_2 and water at two different pressure and temperature levels in stripper

The second effect is requiring a large amount of cold rich bypass through the CO_2 exchanger to condense the large amount of water vapor. Ultimately, the optimum cold rich bypass was 56.2% and the optimum warm rich bypass was 11.4% of the total rich solvent from the absorber. Interestingly, the total rich bypass does not change significantly compared to the base case even with lower stripper temperature and pressure.

The large cold rich bypass cools the stripper gas to a lower temperature (71 °C) compared to the base case design (96 °C), in the CO_2 exchanger. However, the residual condenser duty downstream of the CO_2 exchanger is still expected to be larger than the base case design due to the much larger mass flowrate of water vapor being condensed. The ratio of mass flow of CO_2 to H_2O going to the condenser decreases from 1 to 0.4 as the temperature of stripping is increased from 120 to 150 °C. This translates to a change in ratio of mole flow from 0.95 to 0.4.

However, this has detrimental effects on the solvent cross exchangers. All the solvent cross exchangers have a sharp hot-side pinch and the lean solvent recycled back to the absorber is hotter (79 °C) compared to the base case design (61 °C). This is a direct consequence of using a much larger cold rich bypass, resulting in a smaller flow through the cold cross exchanger compared to the base case. This is expected to increase the cooling duty of the air coolers employed for the water wash, thereby increasing their capital cost.

7.12 PZAS WITH LOW PRESSURE/LOW TEMPERATURE STRIPPER AND DIRECT CONTACT CONDENSER

Figure 7.28 shows the process flow diagram of PZAS with the direct contact condenser and a low-pressure stripper at 120 °C and 2 bar. The flowrates of the cold rich and warm rich bypass have been fixed at their corresponding optimum for the base case design with a low-pressure stripper as described in section 7.11.

The packing height in the direct contact condenser is 10 ft, which was estimated to be the economic optimum. The diameter of the stripper column and direct contact condenser was increased to 15 ft compared to the base case to account for the higher vapor rate in the column. This represented a 33% increase in column diameter compared to the base case. A similar increase in column diameter with decreasing stripper sump temperature has been shown by Suresh Babu and Rochelle (2022), albeit at slightly different operating conditions.

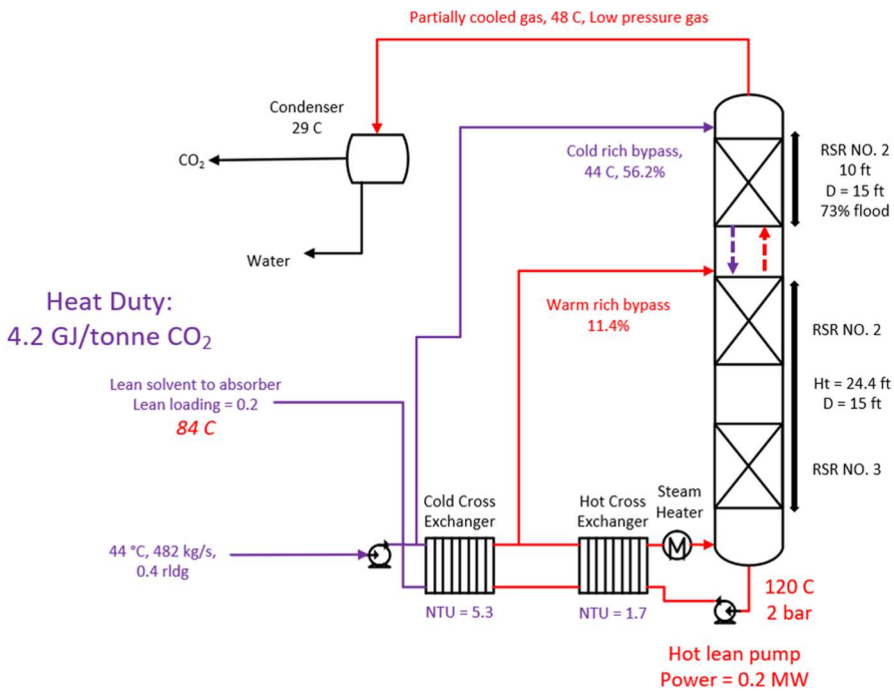

Figure 7.28: PZAS with a low pressure stripper and direct contact condenser; base case heat exchanger sizes

The heat duty with 10 ft of packing in the direct contact condenser is 4.2 GJ/tonne CO_2, which is 40% higher than the base case design (3 GJ/tonne), and 5% higher than the base case design with a low-pressure stripper (4 GJ/tonne). The higher heat duty compared to the base case design is directly explained by the higher water-to-CO_2 ratio.

The higher heat duty compared to the base case design with a low pressure stripper indicates that, while using the direct contact condenser with the low pressure stripper cools the gas to a lower temperature (48 °C) compared to the base case design with a low pressure stripper (71 °C), for the same cold rich bypass flowrate, the CO_2 exchanger may be more effective than the direct contact condenser at reducing the heat duty. This is investigated in the upcoming sections.

7.12.1 Impact of Direct Contact Condenser on Steam Heater Duty

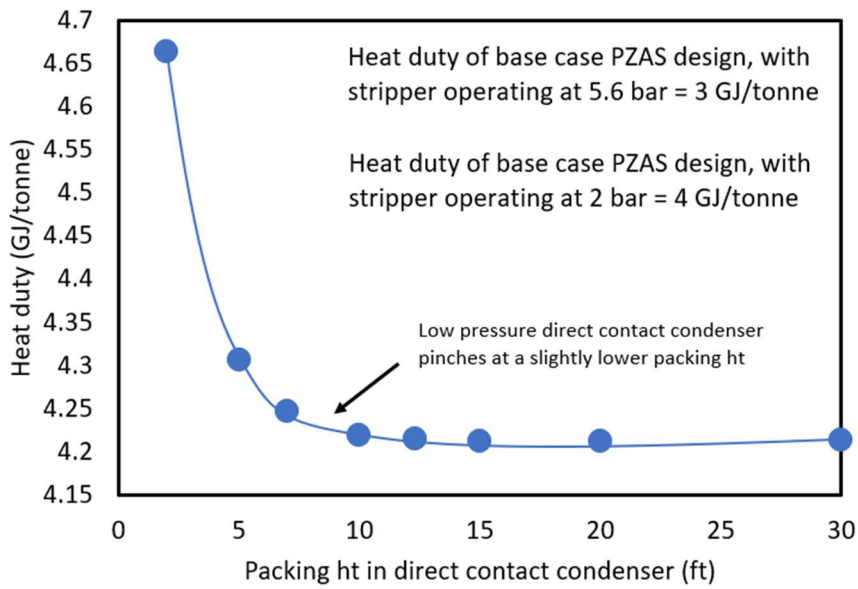

Figure 7.29: Heat duty as a function of packing height in direct contact condenser; low pressure stripper and base case heat exchanger sizes

Figure 7.29 shows the sensitivity of heat duty with added packing height in the direct contact condenser. As the packing height increases, the heat duty decreases but quickly becomes constant at a relatively lower packing height compared to the other design cases with the direct contact condenser. This is due to the high cold rich bypass. Using 56.2% cold rich bypass induces a top-side pinch in the direct contact condenser at a lower packing height. At no packing height in the direct contact condenser is this design equivalent to the base case design in its heat duty.

7.12.2 Temperature and Flux Profile in Direct Contact Condenser

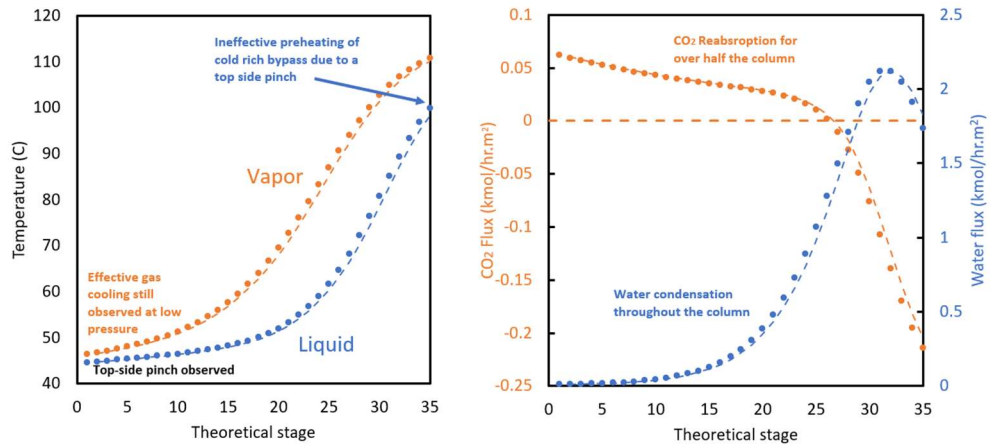

Figure 7.30: Temperature and flux profile in direct contact condenser for a symmetrical stripper; stage 1 is the top of the column; stage 35 is the bottom of the column; low pressure stripper with base case heat exchanger sizes; theoretical stages represent computational segments

The top-side pinch described in section 7.12.1 is shown in Figure 7.30. The high cold rich bypass pinches the section at the top for a packing height of 12.3 ft.

A major disadvantage of this top-side pinch is the larger temperature difference at the bottom of the column, leading to ineffective preheating of the cold rich bypass. However, the vapor temperature still decreases effectively as it rises through the column through water vapor condensation. This indicates that the direct contact condenser will always effectively cool the vapor stream irrespective of stripper pressure, but its effect on heat duty and rich loading is dependent on the location of pinch in the direct contact condenser section.

A bottom-side pinch, or a lower cold rich bypass is generally preferred because this achieves effective preheating of solvent in addition to effective cooling of gas. A high cold rich bypass as used in the low-pressure stripper will not reduce the rich loading in the

solvent significantly due to poor preheating of solvent. This also makes the low-pressure stripper with the direct contact condenser unfavorable relative to its high-pressure counterpart.

7.12.3 Impact of Direct Contact Condenser on Rich Loading

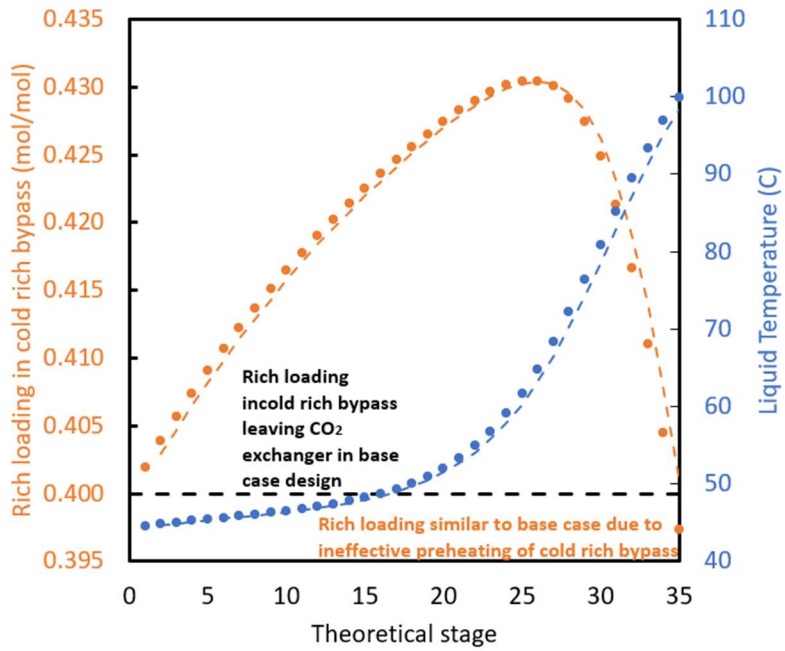

Figure 7.31: Rich loading profile in the direct contact condenser for a symmetrical stripper; low pressure stripper with base case heat exchanger sizes; theoretical stages represent computational segments

As a result of the poor preheating of the cold rich bypass leaving the direct contact condenser, the rich loading is like that of the cold rich bypass leaving the CO_2 exchanger in the base case. This effect is shown in Figure 7.31.

As the liquid flows down the packed section, the low temperature increases the rich loading through CO_2 reabsorption more compared to the high-pressure cases, shown in Figures 7.13 and 7.20. The low pressure in the stripper makes it difficult to preheat and pre-strip the solvent at the inherently low temperature. Due to this effect, as seen in Figure

7.32, the ultimate rich loading in the cold rich bypass leaving the direct contact condenser is not significantly different from that leaving the CO_2 exchanger in the base case.

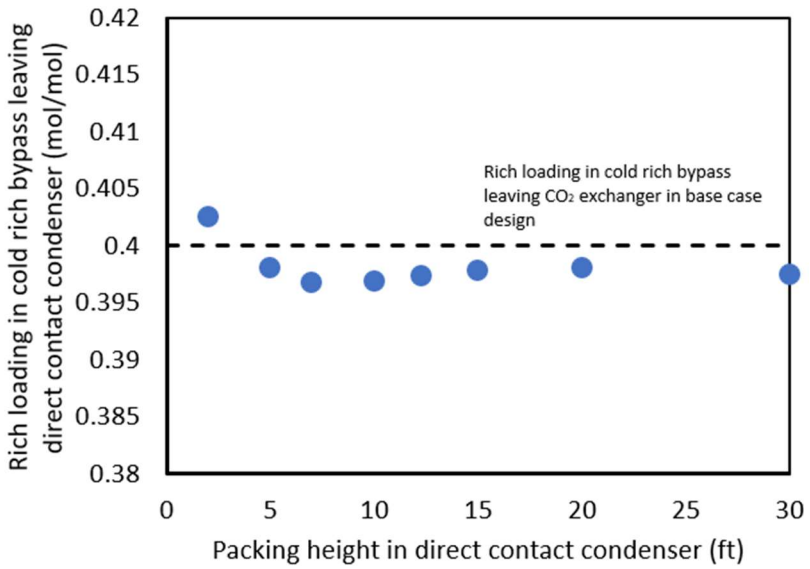

Figure 7.32: Rich loading in the cold rich bypass leaving the direct contact condenser as a function of packing height in the direct contact condenser; low pressure stripper with base case heat exchanger sizes

This is observed over a wide range of packing height in the direct contact condenser. Between 2 and 30 ft of packing in the direct contact condenser, the rich loading in the cold rich bypass leaving the section is not significantly lower compared to the that in the cold rich bypass leaving the CO_2 exchanger in the base case. This also contributes to the higher heat duty of this design compared to the base case design with a low-pressure stripper and a CO_2 exchanger.

7.12.4 Impact of Direct Contact Condenser on Gas Cooling and Residual Condenser Duty

Figure 7.33 shows that despite the poor preheating of the cold rich bypass by the direct contact condenser, it achieves effective cooling of the gas and consequently reduces the condenser duty by a large amount compared to the base case design. This is due to the large cold rich bypass employed by this design.

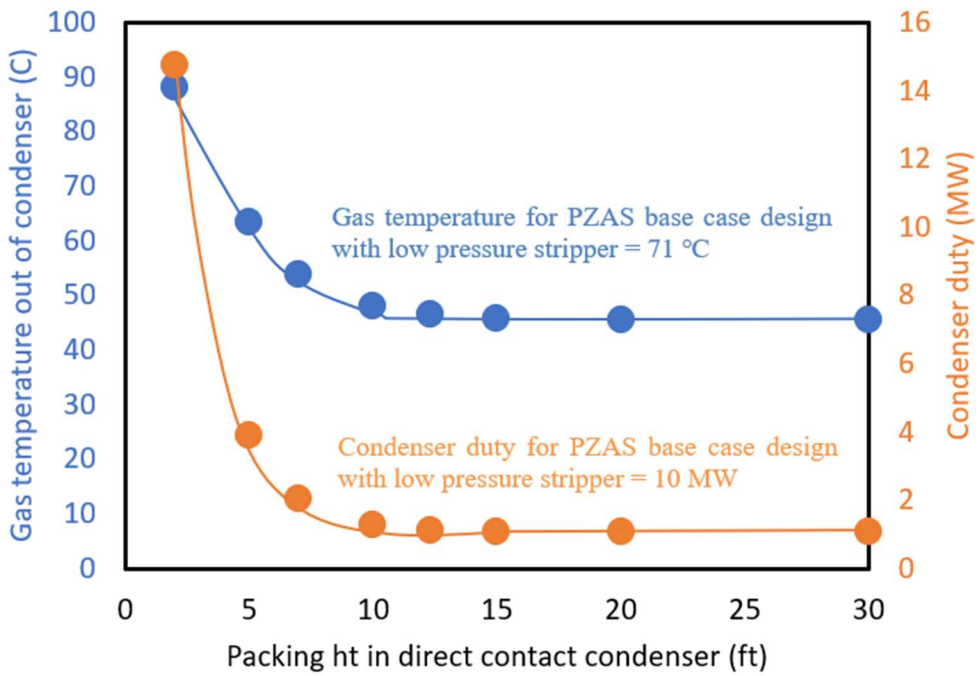

Figure 7.33: Gas temperature and condenser duty as a function of packing height in direct contact condenser; low pressure stripper with base case heat exchanger sizes

7.13 SUBOPTIMIZATION OF FEED POINT FOR WARM RICH BYPASS

In the previous sections, the optimization of packing height for the direct contact condenser was done with a fixed feed point for the warm rich bypass. The preheated cold

rich bypass leaving the direct contact condenser was mixed with the warm rich bypass and sent to the top of the stripper just as in the base case.

This method of feeding the total rich bypass to the column could result in a suboptimal heat duty due to irreversibility in the process that arises from enthalpy of mixing at the feed point. One way to minimize the enthalpy of mixing would be to match the rich loading or temperature at the feed point. The other will be to minimize the enthalpy of mixing and simultaneously optimize the feed point by conducting a sensitivity analysis of heat duty versus feed point for the warm rich bypass.

The feed point that minimizes the heat duty will be picked for the warm rich bypass.

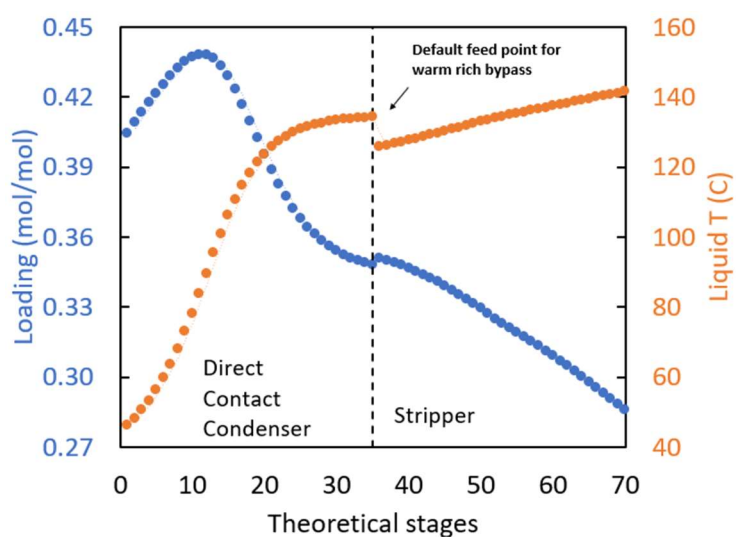

Figure 7.34: Liquid temperature and loading profile in the direct contact condenser and stripper for PZAS with the base case design and direct contact condenser; packed height = 15 ft (optimum); theoretical stages represent computational segments

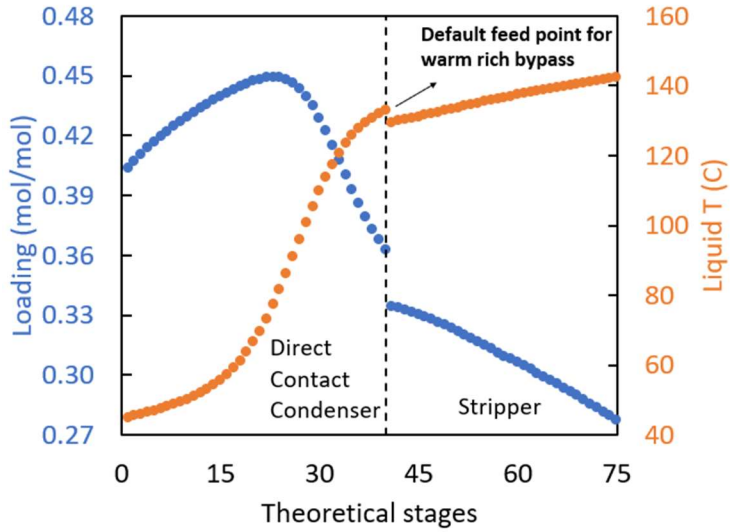

Figure 7.35: Liquid temperature and loading profile in the direct contact condenser and stripper for PZAS with the base case design and double the number of solvent cross exchangers and direct contact condenser; packed height = 15 ft (optimum); theoretical stages represent computational segments

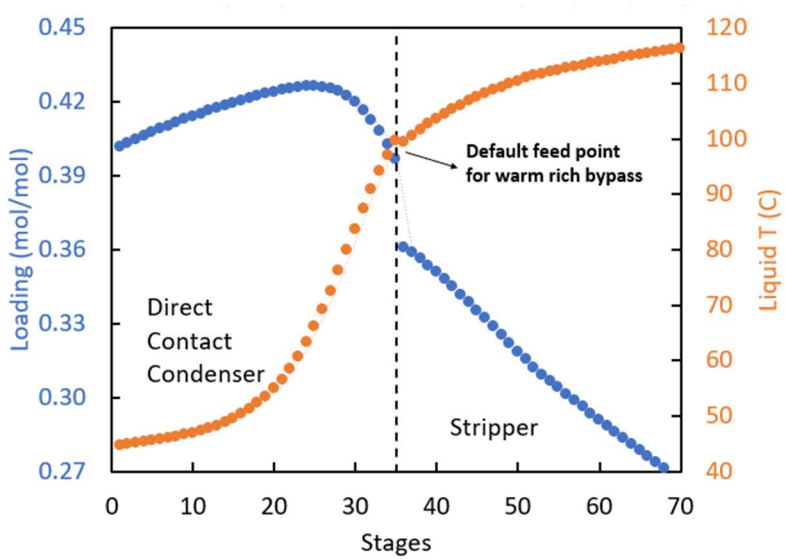

Figure 7.36: Liquid temperature and loading profile in the direct contact condenser and stripper for PZAS with the low pressure stripper and direct contact condenser; packed height = 10 ft (optimum); theoretical stages represent computational segments

Figures 7.34 to 7.36 show the loading and liquid temperature in the direct contact condenser and the stripper for three design cases.

The rich loading and temperature of the warm rich bypass for the base case design with the direct contact condenser are 0.4 mol/mol and 123.3 °C. Figure 7.34 shows that compared to these specifications, the temperature of the liquid in the column at the default feed point was higher at 125.6 °C with a rich loading of 0.35 mol/mol. The heat duty for this case is 2.9 GJ/tonne CO_2. The warm rich bypass feed point was at $Z/Z_{total} = 0.51$, where Z/Z_{total} is the fractional packing height from the bottom to the top of the column.

The rich loading and temperature of the warm rich bypass for the base case design with double the number of cross exchangers and the direct contact condenser are 0.4 mol/mol and 129.1 °C. Figure 7.35 shows that compared to these specifications, the temperature of the liquid in the column at the default feed point was similar at 129.4 °C with a rich loading of 0.33 mol/mol. The heat duty for this case is 2.57 GJ/tonne CO_2. The warm rich bypass feed point was at $Z/Z_{total} = 0.54$.

The rich loading and temperature of the warm rich bypass for the base case design with the low-pressure stripper are 0.4 mol/mol and 107.5 °C. Figure 7.36 shows that compared to these specifications, the temperature of the liquid in the column at the default feed point was lower at 99.4 °C with a rich loading of 0.36 mol/mol. The heat duty for this case is 4.2 GJ/tonne CO_2. The warm rich bypass feed point was at $Z/Z_{total} = 0.51$.

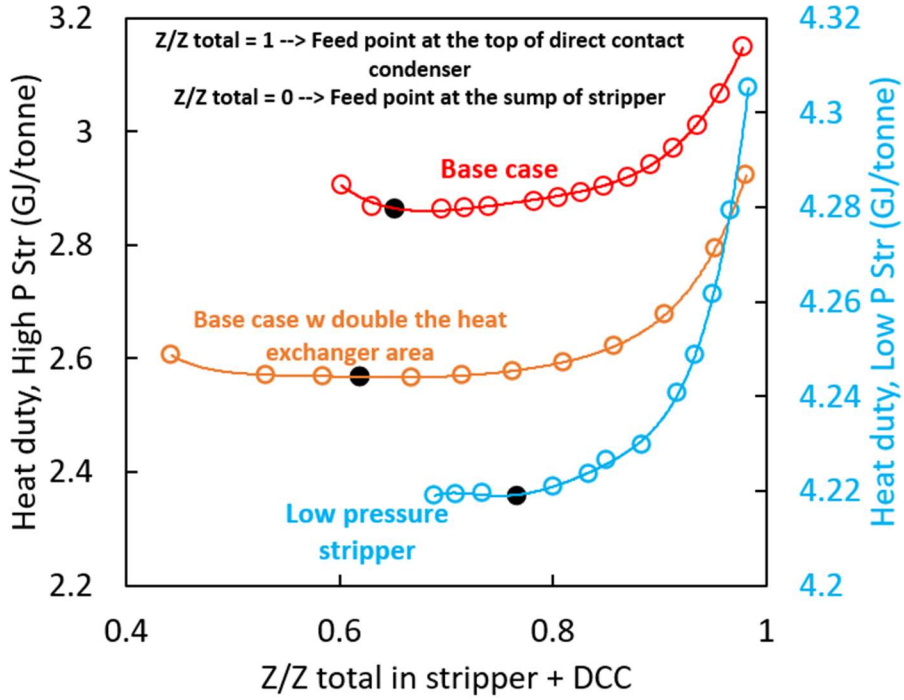

Figure 7.37: Suboptimization of feed point of warm rich bypass for PZAS with the direct contact condenser in 3 design scenarios; black points represent optimal feed point for warm rich bypass

Figure 7.37 shows the feed point optimization for the warm rich bypass for three designs with the direct contact condenser. In all three cases, the optimum feed point (black circle) provides the minimum heat duty of stripping compared to a feed point at Z/Z_{total} = 1. At this feed point, all the solvent is fed to the top of the column.

For the base case design and direct contact condenser, the feed point for the warm rich bypass moved up the column (Z/Z_{total} = 0.652) after optimization and the heat duty reduced by 1% to 2.864 GJ/tonne.

For the base case design with double the number of cross exchangers and direct contact condenser, the feed point for the warm rich bypass moved up the column (Z/Z_{total} = 0.62) and the heat duty approximately stayed constant.

For the base case design with a low pressure stripper and direct contact condenser, the feed point of the warm rich bypass also moved up the column ($Z/Z_{total} = 0.77$) and the heat duty approximately stayed constant.

7.14 CONCLUSIONS

<u>For PZAS with a direct contact condenser and base case heat exchanger sizes:</u>

- Only 5 ft of packing in the direct contact condenser was adequate to match the heat duty of the base case design. As the packing height was increased, heat duty ultimately approached 2.9 GJ/tonne. This was due to better preheating of the cold rich bypass and more water condensation in the direct contact condenser.
- The direct contact condenser works partially as an absorber at the low temperature zone and as a stripper at the high temperature zone, but water vapor is always condensed.
- With 12.3 ft of packing, the direct contact condenser has a bottom temperature pinch, indicating efficient preheating of the cold rich bypass to the maximum possible temperature and lowest possible loading as it leaves the section. This loading is lower than the rich loading in the solvent leaving the CO_2 exchanger.
- Above a packing height of 5 ft, the gas temperature leaving the direct contact condenser can be decreased below the gas temperature leaving the CO_2 exchanger at the same flow of cold rich bypass through these units. This reduces the downstream condenser duty. At a packing height of 30 ft, the condenser duty is only 2 MW compared to the base case duty of 10 MW.

<u>For PZAS with a direct contact condenser and double the number of solvent cross exchangers as the base case:</u>

- A lean pump is required downstream of the stripper sump and before the hot exchanger to counteract the large lean side pressure drop in the cross exchangers.
- Only 5 ft of packing in the direct contact condenser section is sufficient to match the heat duty (2.7 GJ/tonne) and performance of the CO_2 exchanger in the base case design with double the number of cross exchangers.
- The preheated cold rich bypass leaves the direct contact condenser with a loading that is 8% lower than that of the cold rich bypass leaving CO_2 exchanger in the base case design.
- At a packing height of 20 ft or above, the gas temperature leaving the condenser is 42 °C bringing it almost to equilibrium with the cold rich bypass entering the column. This almost brings the downstream condenser duty to 0 MW compared to 8 MW in the base case design with double the cross exchangers.

<u>For PZAS with a low pressure (2 bar) and low temperature (120 °C) stripper:</u>

- The low pressure and low temperature stripper required a larger diameter of 15 ft compared to the base case value of 11.3 ft, owing to the lower vapor density/velocity in the column.
- A hot lean pump is required downstream of the stripper sump and upstream of the hot cross exchanger to compliment the low stripper pressure.
- The heat duty of this design is 4 GJ/tonne compared to 3 GJ/tonne with the base case design, for the same heat exchanger sizes and packing height in the stripper. This is due to the much larger water to CO_2 ratio in the column with a low temperature stripper.
- A large amount of cold rich bypass (56.2%) through the CO_2 exchanger is required to effectively condense the large amount of water vapor.

- The large cold rich bypass effectively cooled the stripper overhead gas to 71 °C, but the residual downstream condenser duty was still high due to a large mass flow rate of water with low temperature stripping. The mole flow rate ratio of CO_2 to water processed by the condenser decreases from 0.95 to 0.4 as the stripper temperature decreases from 150 to 120 °C.
- All the solvent cross exchangers have a tight hot-side pinch and the lean solvent recycled back to the absorber is hotter (79 °C) compared to the base case design (61 °C). This is a direct consequence of drawing a much larger cold rich bypass, resulting in less heat recovery in the cold cross exchanger compared to the base case design.

<u>For PZAS with a low pressure (2 bar) and low temperature (120 °C) stripper and a direct contact condenser with base case heat exchanger:</u>

- The heat duty with 10 ft of packing in the direct contact condenser is 4.2 GJ/tonne CO_2, which is 40% higher than the base case design (3 GJ/tonne), and 5% higher than the base case design with a low-pressure stripper (4 GJ/tonne).
- The low pressure/temperature stripper with a direct contact condenser is ineffective at reducing the heat duty compared to the CO_2 exchanger mainly due to the large cold rich bypass (56.2%) that causes a cold side pinch in the column, leading to ineffective preheating of solvent, reduction in rich loading, and stripping.
- The direct contact condenser still effectively decreases the vapor temperature leaving the column (to 45 °C) through water condensation, and can be used to reduce the duty (to 1 MW) and capital of the downstream condenser.

RECOMMENDATIONS FOR FUTURE WORK

- The modeling of the direct contact condenser could be done with an updated high kinetics model for the stripper. The same could be done with an updated mass transfer model.
- Pilot testing of the direct contact condenser will allow for validation of the mass transfer model. This validation can be used to tune the mass transfer coefficients or wetted area for the application of the direct contact condenser. Pilot testing of the direct contact condenser can also be used to study VLE and kinetics over a wide range of stripper temperature.
- PZAS must be tested at low temperature and pressure over a long period of time to measure its energy performance compared to the typical high pressure and high temperature application.
- An equation-oriented model that can be used to simultaneously optimize design and operation to minimize total cost of capture can be used to select packing height in the stripper and direct contact condenser for a wide range of operating conditions and heat exchanger sizes. This work only accounts for two such heat exchanger sizes and its optimum has not been determined.
- The direct contact condenser will eliminate some horizontal footprint of the plant by integrating the process vertically. The cost avoided by implementing the direct contact condenser must be evaluated in detail.
- The performance of the direct contact condenser must be compared to a scenario where the condensed water from the vapor (in the downstream condenser) is returned to the stripper column.

Chapter 8: Process Economics with Alternative Stripper Designs

Chapter 8 discusses the economic methods, variations in total capital investment and operating costs for designs with and without the direct contact condenser. Chapter 8 builds on Chapter 7 that dealt with the optimal design of a direct contact condenser instead for PZ with the advanced stripper. In this chapter, direct field cost of different equipment that are impacted by the direct contact condenser are estimated using a cost-scaling methodology. An economically optimum packing height in the direct contact condenser with three different designs is estimated by calculating tradeoffs between capital and operating cost as a function of packing height. The total cost of capture ($/tonne) is compared for different scenarios with and without the direct contact condenser.

8.1 COST SCALING METHODOLOGY

To translate the benefits of using additional cross exchangers, direct contact condenser, or high-pressure stripper over a low-pressure stripper, the Direct Field Cost (DFC) of certain equipment were scaled from their respective base case values using appropriate scaling variables. The scaling variables chosen for each equipment are shown in Table 8.1.

The economics of the base case is given in detail by Rochelle et al. (2022), and Closmann et al. (2021). All costs scaled were for both the process trains together.

Table 8.1: Base case direct field cost (DFC) and scaling variable chosen for some equipment

Equipment	Base case FEED DFC ($MM)	Scaling variable/constant chosen
Cold cross exchanger	0.99	1 or 2, constant multiplier
Hot cross exchanger	0.55	1 or 2, constant multiplier
CO_2 exchanger	3.49	0, equipment eliminated
Steam heaters	3.54	Steam heater heat rate

Rich solvent pump	3.22	Power
Lean solvent pump	1.22	Power
Packaged boilers	9.76	Boiler heat rate
CO_2 compressor	12	CO_2 flow rate (at constant stripper pressure), compressor power (at variable stripper pressure)
CO_2 condenser and KO drum	1.72	Condenser duty
Stripper packing	0.3 (60% of total quoted internal cost)	Area of packing
Stripper vessel	3.26	External surface area, power law factor = 1 (instead of 0.6)
Stripper distributors and support plates	0.2 (40% of total quoted internal cost)	1.5, constant multiplier
Air cooler for water wash	14.87	Steam heater heat rate

For scaling the direct field cost, the six-tenth's rule was used as shown in Equation 8.1.

$$\frac{\text{New DFC of equipment}}{\text{Base case FEED DFC of equipment}} = \left[\frac{\text{Updated scaling variable}}{\text{Scaling variable for base case FEED}}\right]^{0.6} \tag{8.1}$$

For scaling the cost of the stripper shell, the 0.6 exponent was replaced with 1 to represent a direct proportionality between cost and external shell surface area (steel cost).

For the stripper distributors and support plates, a 1.5 multiplier was used. The base case stripper design consisted of 2 support plates and 2 distributors for 2 sections of packing. For a 3rd section of packing, 1 support plate and distributor each were assumed in addition to the 2 support plates and distributors that existed in the stripper column, resulting in the 1.5 multiplier for direct field cost.

For scaling the compressor cost for cases with the low-pressure stripper, compressor power was used as the scaling variable instead of CO_2 flow rate as shown in

Table 8.1. This is because as the stripper pressure changed, the compressor pressure increased for the same CO_2 flow.

While the cost scaling factor exponent could range from 0.3 to above 1 in some cases, 0.6 presents a reasonable estimate of direct field cost especially when the new design scenarios do not exceed 10 times the base case capacity of the plant (Peters et. al, 2003). This was true in all the design cases considered.

8.2 PROCESS ECONOMICS

The cost of the equipment considered for cost-scaling are expected to be impacted the most by the design changes described in Chapter 7. The equipment considered are the cold cross exchangers, hot cross exchangers, CO_2 exchangers, steam heaters, rich and lean solvent pumps, natural gas boilers, CO_2 compressor, CO_2 condenser and knock-out drums, stripper vessel (packing and other internals), and air coolers for water wash.

The economic impacts of the design changes were compared to the total capital investment for the FEED which was about $760.5 MM (Rochelle et. al, 2022). The economics were also compared by calculating an annualized capital investment for the base case and upgraded designs using Equation 8.2.

A capacity factor of 52% was used for the plant to estimate the total CO_2 flow through the year. This capacity factor was obtained from year-round actual flue gas availability data of the NGCC facility. The flue gas availability for the plant is shown in Figure 8.1. A capital cost scaling factor (α = 1.98) was used to account for indirect costs such for construction, commissioning, contractor's fee etc., and an annualizing factor (β = 0.2) was used to convert the total investment on a yearly basis. The annualizing factor

includes depreciation, return on investment, local and federal taxes, maintenance, and other expenses related to investment.

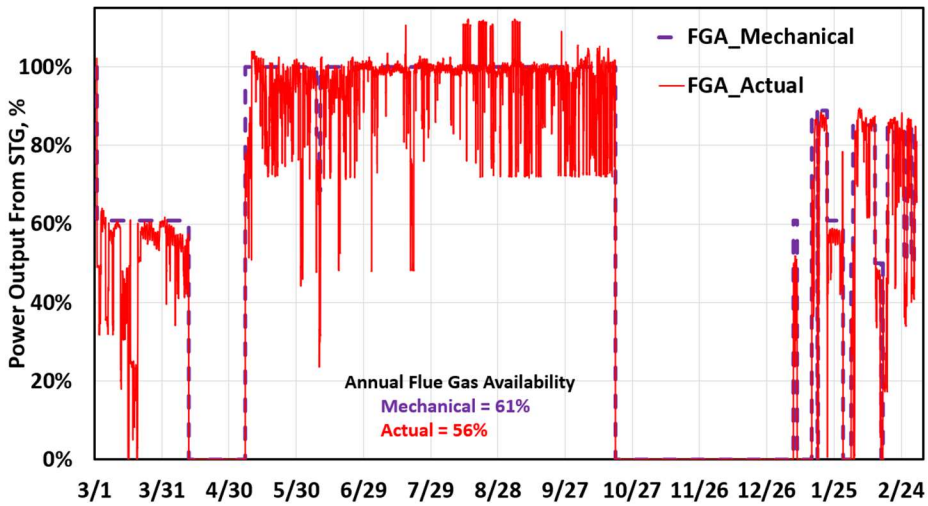

Figure 8.1: Mechanical and actual availability of flue gas from steam turbine generator (STG) for capture plant at Mustang Station for 2018-19

$$\text{Annualized capital}\left(\frac{\$}{\text{tonne } CO_2}\right) = \text{Total Direct Field Cost} * \alpha * \frac{\beta}{CO_2 \text{ flow}} \quad (8.2)$$

The annual operating cost of the base case and upgraded designs were estimated using a gas price of $3/MMBtu and electric power price of $25/MWh, according to Equation 8.3. The primary component of the cost for heating was the heat rate of the standalone gas-fired boilers.

For electric power, the power of the rich pump, lean pump, and compressor were considered. Electric power of other equipment such as air coolers and absorber intercooler pumps were ignored as they were not expected to be impacted by the design changes. This data was obtained from the FEED report (Rochelle et al., 2022).

Pump power was estimated by the design and rating models, and the compressor power was estimated using the surrogate model explained by Suresh Babu et al. (2023).

$$\text{Operating cost} = \frac{\text{Heat rate of gas boiler} * \$_{\text{GAS}} + \text{To} \quad \text{electric power} * \$_{\text{POWER}}}{\text{CO}_2 \text{ flow}} \tag{8.3}$$

Ultimately, the annualized capital and the annual operating cost were added to estimate a total cost of capture (\$/tonne CO_2) for the base case design and compare it with the advanced design scenarios.

8.3 REDUCTION IN DIRECT FIELD COST

The direct field cost (DFC) of the condenser and KO drums, packaged natural gas boilers, steam heaters, water wash air coolers, and stripper column are shown as a function of packing height in the direct contact condenser for each design scenario.

The savings in DFC for each of these equipment relative to their base case DFC are deduced at their respective optimum packing heights in the direct contact condenser. Ultimately, the annualized investment and the annual operating cost are calculated as a function of packing height in the direct contact condenser for each design.

Figure 8.2 shows the sensitivity of the direct field costs of condenser and KO drums as a function of packing height in the direct contact condenser. The triangle data represent the DFC of the equipment at the optimum packing height in the direct contact condenser for any given scenario. DFC decreases with added packing height in all scenarios due to the condensation of water and cooling of gas. The optimum DFC of condenser and KO drums was lower compared to that of the base case design for all three design scenarios with the direct contact condenser. This showed that the direct contact condenser was

effective at cooling the gas leaving the stripper to a lower temperature compared to the base case design in all design scenarios.

In the low pressure case, despite the high water vapor content in the stripper, the direct contact condenser is able to efficiently cool the gas using the high cold rich bypass. For the low pressure configuration, despite the effective gas cooling in the CO_2 exchanger, the large amount of water to be condensed made the cost of condenser and KO drums the highest.

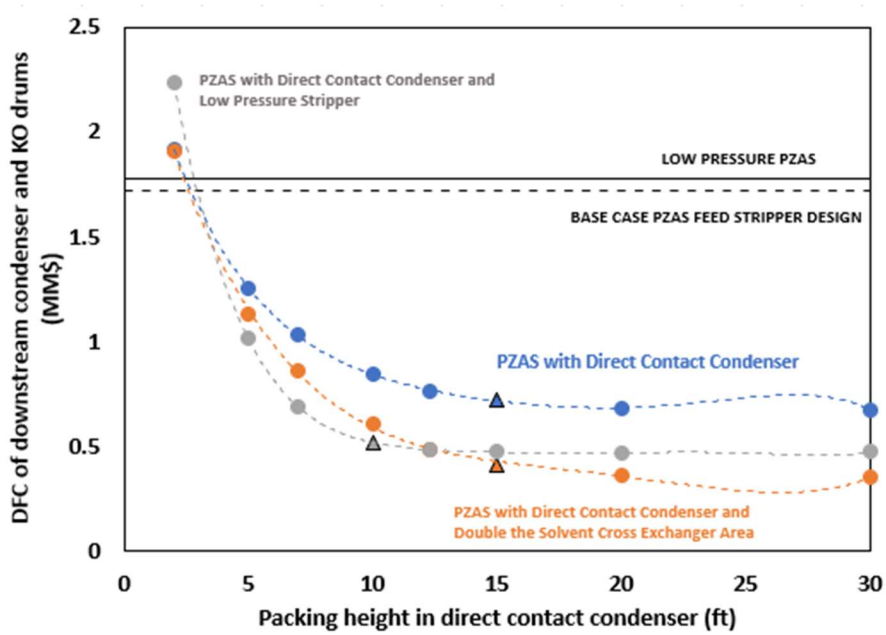

Figure 8.2: Effect of packing height in direct contact condenser on DFC of condenser and KO drums

The DFC of natural gas boilers at the optimum packing height was lower compared to the base case value only for high pressure stripper cases. The low-pressure stripper with a direct contact condenser had a higher heat duty compared to the base case design. The trend in DFC observed is a direct consequence of the relation between boiler heat duty and

packing height in the direct contact condenser. Interestingly, the direct contact condenser is not effective at reducing the heat duty with the low pressure stripper due to ineffective preheating of the cold rich bypass. This is caused by a top-side pinch in the column that is explained in Chapter 7 in detail.

A similar trend in steam heater cost is also observed, which is also a function of the heat duty of the process. This is shown in Figures 8.3 and 8.4.

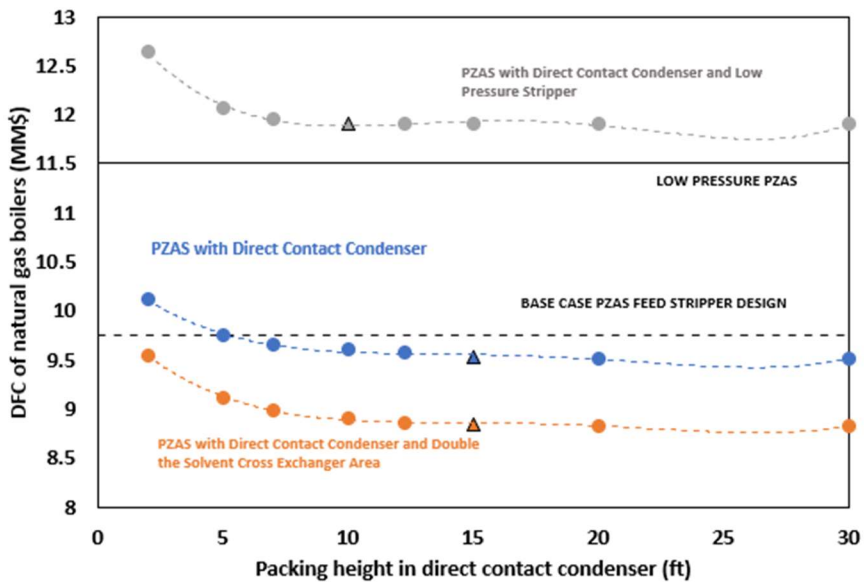

Figure 8.3: Effect of packing height in direct contact condenser on DFC natural gas boilers

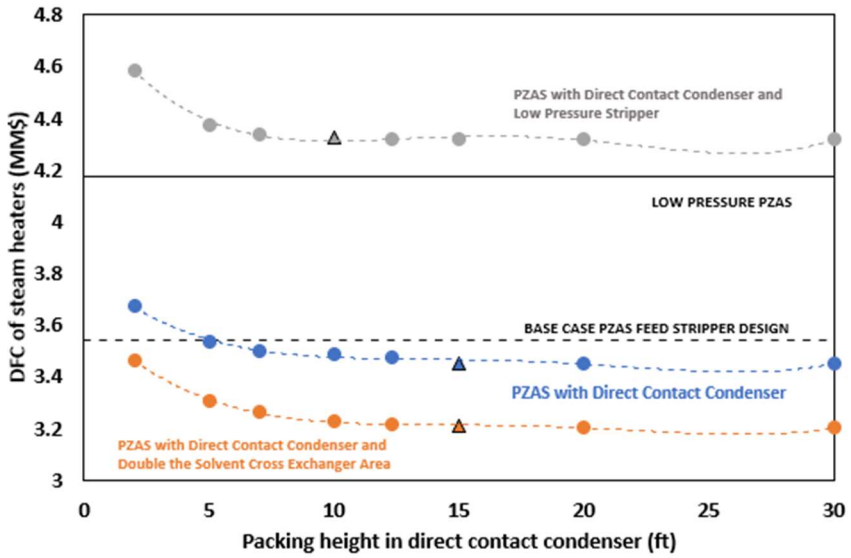

Figure 8.4: Effect of packing height in direct contact condenser on steam heaters

Figure 8.5 shows the variation in the DFC of air coolers for water wash with increasing packing height in the direct contact condenser. The high heat duty for the low-pressure stripper increased the cold lean solvent temperature compared to the base case design. This heat was ultimately removed by the air coolers for the water wash, thereby increasing their cost.

The high-pressure stripper cases had a lower cold lean solvent temperature due to the lower heat duty compared to the base case. Therefore, the air-cooling duty for the water wash was also consequently lower. This effect is directly reflected in the cost of the water wash air coolers.

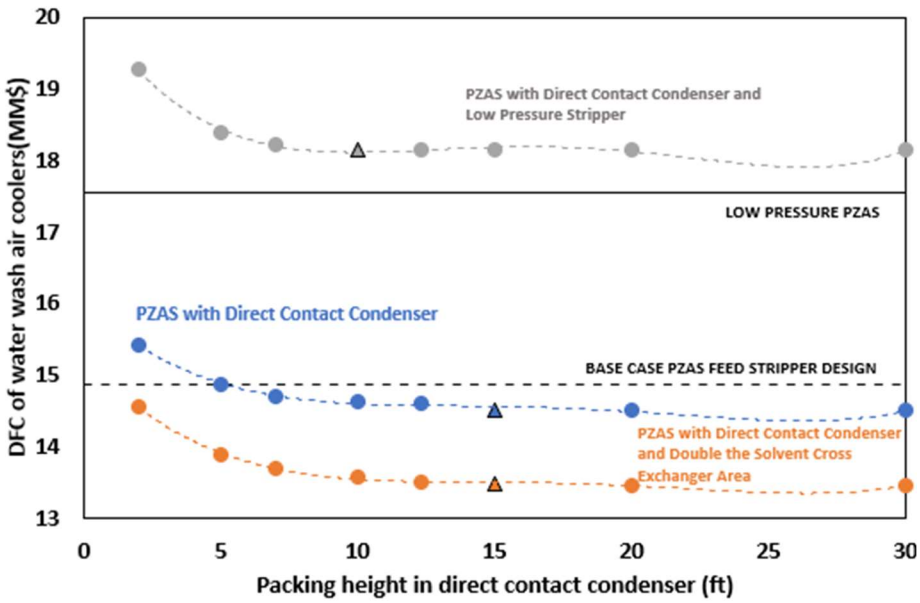

Figure 8.5: Effect of packing height in direct contact condenser on water wash air coolers

8.4 ADDED COST OF STRIPPER COLUMN

While the above costs decreased with increasing packing height in the direct contact condenser, the cost of the stripper vessel increased due to the added packing height, added packing section, and changes to column diameter. Figure 8.6 shows the effect of added packing height in the direct contact condenser on the DFC of the stripper column.

All design scenarios had a higher stripper DFC compared to the base case design simply due to the added cost of a 3rd packing section for the direct contact condenser. The low-pressure stripper had the highest DFC of the stripper compared to the base case due to added cost of packing and column internals, but also because of the higher stripper diameter.

Both the high-pressure stripper cases had the same DFC of stripper due to the same column diameter and cost of added packing, but the DFC of the high-pressure cases were

consistently lower compared to that of the low-pressure cases due to the lower column diameter only. The cost of added packing, and internals were similar in all cases.

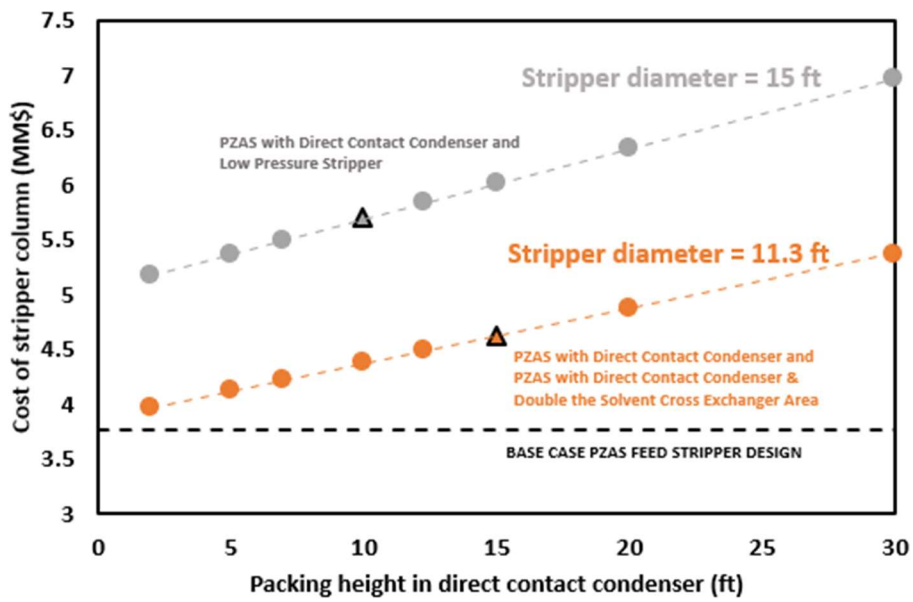

Figure 8.6: Comparison of direct field cost for stripper column between a high pressure and low pressure stripper

8.5 MISCELLANEOUS COSTS

Some other changes to DFC of equipment were required, which were not correlated with packing height in the direct contact condenser. All the scenarios that used the direct contact condenser eliminated the DFC associated with the CO_2 heat exchanger ($3.49 MM).

The cases with double the heat exchanger area required a larger, hot lean pump instead of the cold lean pump at an added cost of about $0.03 MM. The low-pressure stripper cases required a larger CO_2 compressor at an added cost of about $2.85 MM.

8.6 BREAKDOWN OF DIRECT FIELD COSTS BY DESIGN

Table 8.2 breaks down the direct field costs of the equipment considered in the economic analysis for the different design scenarios investigated.

Table 8.2: Direct field cost (DFC) of equipment for 6 design scenarios

Design	Base case	Base case with 2x cross exchangers	Base case with low P stripper	Base case with DCC	Base case with DCC and 2x cross exchangers	Base case with DCC and low P stripper
Pk ht. (ft)	12.3	12.3	12.3	15	15	10
Str. Pressure (bar)	5.5	5.5	2	5.5	5.5	2
Str Dia (ft)	11.3	11.3	15	11.3	11.3	15
Boilers (MM$)	9.8	9.1	11.5	9.5	8.9	11.9
Steam heaters (MM$)	3.5	3.3	4.2	3.5	3.2	4.3
WW air coolers (MM$)	14.9	13.8	17.6	14.5	13.5	18.2
Exchangers (MM$)	1.6	3.1	1.6	1.6	3.1	1.6
CO_2 exchanger (MM$)	3.5	3.5	3.5	0	0	0
Stripper (MM$)	3.8	3.8	5.1	4.6	4.6	5.7
Compressor (MM$)	12	12	14.9	12	12	14.9

Condenser and KO drums (MM$)	1.7	1.5	1.8	0.7	0.41	0.52
Rich and lean pumps (MM$)	4.5	6	3.9	4.5	6	4.5
Total incremental DFC (MM$)	55.2	56	63.8	50.8	51.6	61.5
Annual operating cost ($/tonne)	13.7	12.6	17.3	13.3	12.3	18
Annualized investment ($/tonne)	176.9	174.7	180.9	174	174.3	178.9
Cost of capture ($/tonne)	190.6	187.4	198.2	187.2	186.7	196.8

8.7 ANNUALIZED TOTAL CAPITAL INVESTMENT AND ANNUAL OPERATING COST

Figures 8.7, 8.8, and 8.9 show the sensitivity of annualized capital investment and annual operating cost as a function of packing height added to the direct contact condenser for three design scenarios.

Annualized capital investment, as calculated by Equation 8.2, decreases until an optimum packing height that minimizes the PEC and consequently the total cost of capture (Annualized capital investment + Annual Operating Cost) and increases beyond that packing height.

Below the optimum packing height, the economic benefits of using the direct contact condenser outweigh the economic disadvantage that comes with added stripper cost (for all cases), cost for larger compressor (low-pressure case only), and hot lean pump (case

with double the heat exchanger area). Above the optimum packing height, the opposite is observed, and the direct contact condenser no longer is economically beneficial.

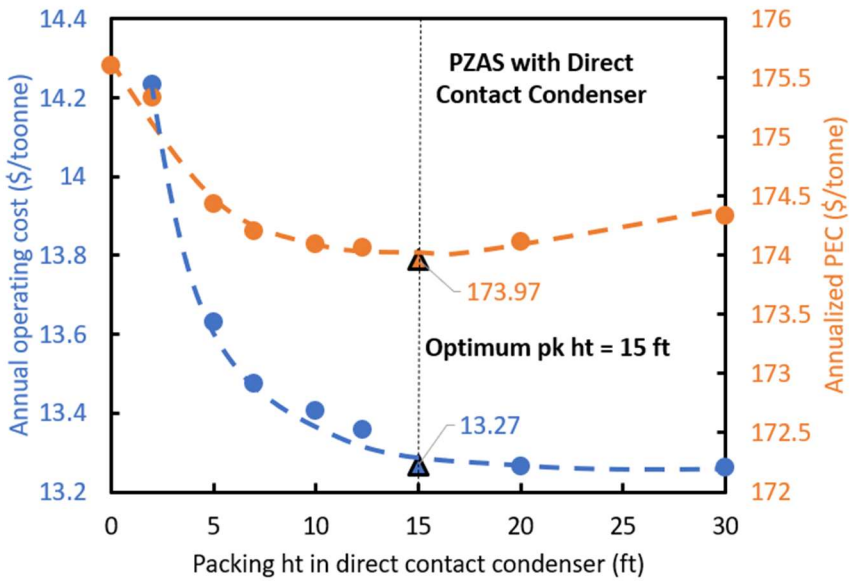

Figure 8.7: Optimum packing height for PZAS with the direct contact condenser

In all three cases the annual operating cost, being a function of natural gas consumption, decreases monotonically with added packing in the direct contact condenser and ultimately becomes constant at high packing height when the column pinches. This is directly linked to the relation between heat duty and packing height in the direct contact condenser for any scenario.

PZAS with the direct contact condenser and double the cross exchanger area gave the lowest operating cost at about $12.32/tonne at its optimum packing height of 15 ft. PZAS with the direct contact condenser increased the operating cost to about $13.27/tonne at a similar optimum packing height of about 15 ft. PZAS with the direct contact condenser and low pressure stripper gave the highest operating cost at about $18/tonne at a lower

optimum packing height of about 10 ft. The packing pinched sooner with a low pressure stripper due to the higher cold rich bypass flow compared to the other two cases.

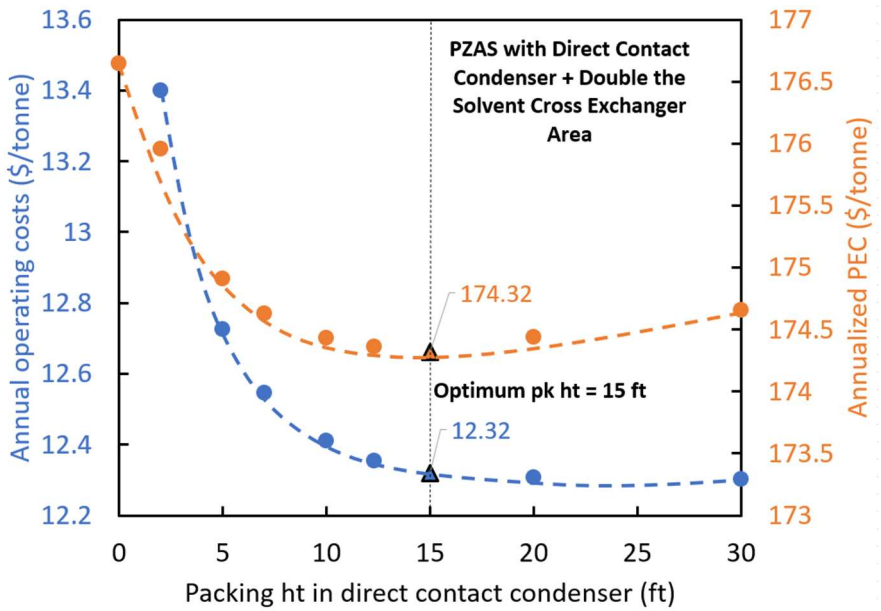

Figure 8.8: Optimum packing height for PZAS with the direct contact condenser and double the number solvent cross exchangers

This optimum packing height was estimated to be 15 ft for both high pressure stripper cases (PZAS with Direct Contact Condenser and PZAS with Direct Contact Condenser and Double the Cross Exchanger Area), and about 10 ft for the PZAS with Direct Contact Condenser and Low-Pressure Stripper. The low-pressure stripper case had a lower optimum packing height possibly due to a column pinch at a lower packing height because of the use of a large cold rich bypass.

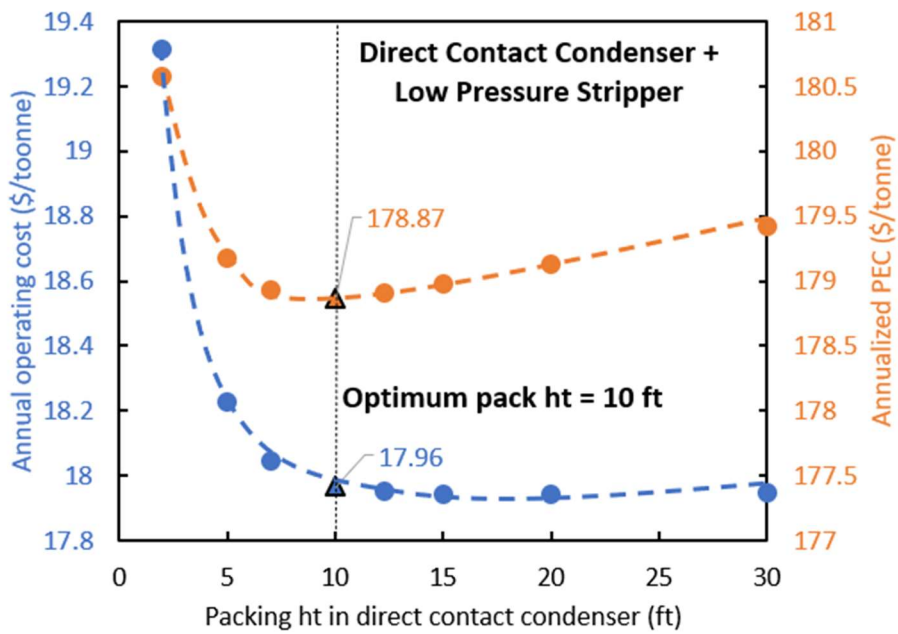

Figure 8.9: Optimum packing height of PZAS with the direct contact condenser and a low pressure stripper

8.8 TOTAL COST OF CAPTURE

Figure 8.10 summarizes the total cost of capture ($/tonne) in 6 design scenarios with PZAS.

Scenario 1 is the variant of the base case design with double the solvent cross exchanger area. Scenario 2 is the variant of the base case design with a direct contact condenser replacing the CO_2 exchanger. Scenario 3 is the variant of the base case design with a low-pressure stripper. Two additional scenarios exist which are combinations of scenario 1 and 2 (PZAS with double the solvent cross exchanger area and direct contact condenser replacing the CO_2 exchanger), and scenario 1 and 3 (PZAS with low pressure stripper and direct contact condenser replacing the CO_2 exchanger).

Compared to the base case design, both scenarios that used a low-pressure stripper were more expensive. This shows that using a low-pressure stripper or a low temperature solvent would not be economically favorable with the direct contact condenser. Using a direct contact condenser with a low-pressure stripper reduces the total cost of capture by about \$1.4/tonne CO_2 compared to scenario 3 (PZAS with a low-pressure stripper).

Using the direct contact condenser with a high-pressure stripper always reduced the cost of capture compared to the base case design. Interestingly, simply doubling the number of solvent cross exchangers reduced the cost of capture by about \$3.2/tonne CO_2. Using the direct contact condenser with PZAS or doubling the cross-exchanger area approximately had the same economic benefit.

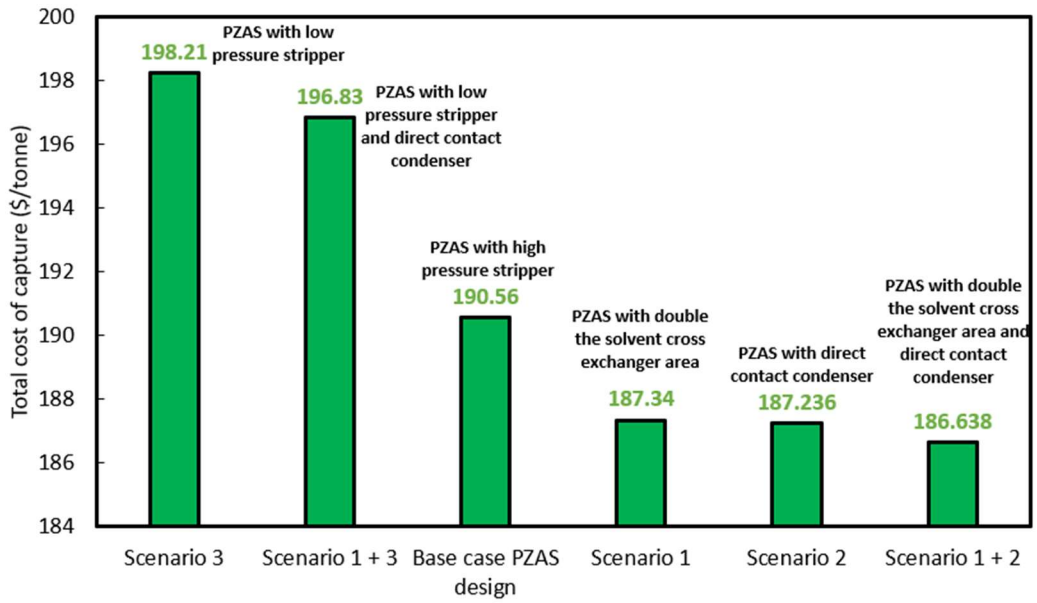

Figure 8.10: Comparison of total cost of capture; cases with direct contact condenser have been optimized for packing height in the direct contact condenser; stripper packing height constant = 24.4 ft (for all cases)

One potential advantage of replacing the CO_2 exchanger with a direct contact condenser instead of simply doubling the solvent cross exchanger area would be the reduction of footprint at the plant. Using a direct contact condenser allows vertical integration of the condenser into the stripper column, while the former design scenario would still incorporate the horizontal footprint from having the CO_2 exchangers and additional solvent cross exchangers.

The scenario with the direct contact condenser and double the solvent cross exchanger area yielded the most economical benefit (scenario 1+2). The cost of capture for this scenario was about $4/tonne lower compared to the PZAS base case design with a high-pressure stripper ($190.56/tonne) and about $11.6/tonne lower compared to PZAS base case design with a low-pressure stripper ($198.21/tonne).

8.9 CONCLUSIONS

- The optimum direct field cost of condenser and KO drums was lower compared to that of the base case for all three design scenarios with the DCC. The DCC was effective at cooling the gas leaving the stripper to a lower temperature compared to the base case in all design scenarios.
- The direct field cost of natural gas boilers at the optimum packing height was lower compared to the base case only for high pressure stripper. The low-pressure stripper with a DCC had a higher heat duty and boiler cost compared to the base case design. A similar trend in steam heater cost is also observed, which is also a function of the heat duty of the process.
- The high heat duty for the low-pressure stripper increased the cold lean solvent temperature compared to the base case. This heat was ultimately removed by the air coolers for the

water wash, thereby increasing their cost. The high-pressure stripper cases had a lower cold lean solvent temperature due to the lower heat duty compared to the base case. Therefore, the air-cooling duty for the water wash was also lower. This effect is directly reflected in the cost of the water wash air coolers.

- All design scenarios had a higher stripper DFC compared to the base case due to the added cost of a 3rd packing section for the DCC. The low-pressure stripper had the highest increase in DFC of the stripper compared to the base case due to added cost of packing, column internals, and larger stripper diameter.
- PZAS with the direct contact condenser and double the cross exchangers gave the lowest operating cost at about $12.32/tonne at its optimum packing height of 15 ft. PZAS with the direct contact condenser increased the operating cost to about $13.27/tonne at a similar optimum packing height of about 15 ft. PZAS with the direct contact condenser and low pressure stripper gave the highest operating cost at about $18/tonne at a lower optimum packing height of about 10 ft.
- The total cost of capture for the base case design was $190.56/tonne CO_2. Scenarios that used a low-pressure stripper were more expensive. The base case design with low pressure stripper costed about $198.21/tonne CO_2. Using a direct contact condenser with low pressure stripping reduced the cost by about $1.4/tonne CO_2 only. Using a low-pressure stripper with PZ would not be economically favorable with the advanced stripper and direct contact condenser.
- Simply doubling the number of solvent cross exchangers reduced the cost of capture by about $3.2/tonne CO_2 (to $187.36/tonne CO_2) compared to the base case cost. Using the direct contact condenser with PZAS or doubling the cross-exchanger area approximately had the same economic benefit.

- PZAS with the direct contact condenser and double the cross exchangers yielded the most economical benefit. The total cost of capture was about $4/tonne lower compared to the PZAS base case ($190.56/tonne) and about $11.6/tonne lower compared to PZAS base case with a low-pressure stripper ($198.21/tonne).

RECOMMENDATIONS FOR FUTURE WORK

- The effect of different equipment-specific cost-scaling factors can be investigated for its role on the total cost of capture.
- Optimal design as a function of varying lean loading and gas/power price is required for the direct contact condenser.
- The performance of an advanced reboiled stripper must be studied as an alternative to the PZAS especially at high lean loading or low temperature stripping.
- The role of the direct contact condenser with steam extraction and water cooling can be investigated.

Chapter 9: Summary of Conclusions and Recommendations for Future Work

9.1 PILOT PLANT TESTING

The following are the conclusions from pilot plant testing:

- Modeling studies showed that the impact of heat loss on heat duty depends on the location of heat loss, stripper type, solvent and CO_2 content in flue gas.
    - Heat loss is more impactful under NGCC conditions than coal conditions due to the relatively lower heat rate for equal exposed surface area.
    - Overdesign of strippers like the simple stripper at NCCC makes the column more vulnerable to heat loss even at values as low as 0.03 GJ/hr, resulting in temperature pinches and reabsorption of CO_2.
    - Low lean loading with 7 m MEA causes a bottom-side pinch in the stripper making it less susceptible to heat loss compared to 5 m PZ, that causes a top-side pinch.
    - For PZAS, the most important location for heat loss was the warm rich pipe after the valve. Heat duty at NCCC is corrected for 80% of the measured average heat loss corresponding to heat loss at this location.
    - The column is the most important location for heat loss in the simple stripper, requiring that heat duty be corrected for 100% of the heat loss.
- Heat loss measurements from water recirculation tests represented heat loss with solvent reasonably well.

- Surface temperature measurements at NCCC and UT-SRP showed that heat loss is 50-75% convection controlled, making it less dependent on fluid properties.
- While absolute heat loss decreased with lower steam flowrate, heat loss relative to heat rate increased by about 6% at UT-SRP compared to NCCC. A 20% decrease in relative heat loss per MW of added pilot capacity can be expected.
- Measured heat loss increases with increasing steam flowrate and wind speed.

- Measured heat duty corrected for heat loss was similar for coal and NGCC conditions for a fixed CO_2 removal.
  - At 90% removal, net heat duty of PZAS was 2.4 GJ/tonne at coal and NGCC conditions at NCCC.
  - Low lean loading and optimal cold rich bypass was shown to reduce energy consumption of PZAS at UT-SRP with NGCC flue gas.
  - NGCC testing at high removal of 97%, 0.2 lean loading using a high total bypass (73%) at NCCC was linked to a decrease in heat duty through increased flashing in solvent as it entered the stripper.
  - Evolutionary optimization was a useful tool to minimize heat duty over a wide range of CO_2 removal at NCCC. The cold rich bypass must be adjusted to control the cooled CO_2 gas at temperature of 180-210 °F, and the warm rich bypass must be adjusted to set the total rich bypass temperature to be 5-10 °F hotter than the stripper exit gas.

The following are the recommendations for future pilot plant testing:

- Source of variation in measured heat loss data must be identified by observing the sensitivity of heat loss measurements to flow and temperature measurements.
- Heat loss should be measured at low sump temperature for NCCC and high sump temperature for UT-SRP closer to steady state conditions.
- An empirical heat loss model that uses steam flowrate, temperature driving forces, and wind speed and/or direction could be developed to correct heat rate as a function of varying process and ambient conditions.
- A systematic analysis of analytical methods for solvent should be conducted to determine the most accurate method for CO_2 loading. Offline viscosity measurements can be coupled with existing density measurements to determine CO_2 loading.
- Automatic bypass control can be tested at the pilot plant by adjusting the cold rich bypass to control CO_2 temperature leaving the exchanger and warm rich bypass to control the stripper overhead temperature difference.
- Absorber and stripper performance at high liquid flux, low lean loading (0.18 mol/mol) could be tested to ensure reliable process operation without solvent precipitation and steam heater issues.
- Amine volatility studies for absorber and stripper are required at higher lean solvent temperature representative of commercial design conditions.

9.2 STRIPPER MODELING

The following are the conclusions for stripper modeling:

- Model predictions of heat duty were significantly impacted by mass transfer, mass balance issues, and heat loss.
    - At higher flooding at NCCC, the mass transfer model performed significantly better leading to much better predictions of heat duty. Model error in heat duty at NCCC is likely linked to error in heat loss estimation. Average model error was 3%.
    - At low flooding, especially with a larger stripper diameter, the mass transfer performance was underpredicted by the model for SRP, leading to higher heat duty than measurements. Error in heat duty was also due to differences between measured and modeled CO_2 flowrate. These data increased the average model error to 11%
    - Reconciliation of measured and modeled heat duty using heat loss as an adjustable parameter showed that heat loss must be corrected as an inverse function of ambient temperature for NCCC. This analysis showed that heat loss could be ignored at SRP, but this is a result of overcorrection caused by mass balance issues at this plant.

The following are the recommendations for future stripper modeling:

- The accuracy of the CO_2 flowmeter at NCCC and UT-SRP must be verified and calibrated if necessary. Re-evaluation of UT-SRP 2021 results must be done.
- Mass transfer models, especially gas-phase, must be expanded to apply to low vapor rates where flow through the packing is likely stagnant or laminar.

- Reaction kinetics model must be fixed to represent high temperature conditions by adjusting reverse reaction rate constant. Other functionalities used to represent high temperature kinetics could be considered for the stripper.
- Heat transfer models used by the stripper require more study. Adjusting the models to accurately predict temperatures in the column or creating a new heat transfer model for stripping would aid interpretation of pilot plant data.
- Heat of formation of species relevant to stripper conditions could be adjusted to better represent the thermodynamics at high temperature. This could reconcile some differences in lean loading between the pilot plant and model.

9.3 STRIPPER DESIGN AND OPTIMIZATION

The following are the conclusions for stripper design and optimization:

- Modeling studies showed that a hot rich bypass when combined with PZAS improved energy performance at NGCC conditions.
    - The hot rich bypass reduces heat duty and equivalent work of the advanced stripper by 1.5-3.5% by reducing the LMTD of the stripper and increasing vapor content in the total rich bypass.
    - The hot rich bypass works better than the warm rich bypass at low to moderate packing height (< 15 m). At high packing height, a column temperature pinch provides diminishing returns with the hot rich bypass. The warm rich bypass outperforms the hot rich bypass with excess packing height.
- Replacing the CO_2 exchanger with a direct contact condenser (DCC) was beneficial for gas cooling, energy requirement, and total cost of capture of the FEED.

- The DCC when used with a high pressure (5.5 bar) and high temperature stripper (150 °C) resulted in a lower heat duty (2.9 GJ/tonne) and downstream condenser duty (as low as 2 MW) compared to the base case (heat duty = 3 GJ/tonne, condenser duty = 10 MW). With double the number of cross exchangers, the heat duty was lower (2.7 GJ/tonne) and the condenser duty was almost eliminated.
- The DCC with a low temperature (120 °C) and low pressure (2 bar) stripper did not improve the heat duty (4 GJ/tonne) but reduced the condenser duty (1 MW) compared to the base case. Use of PZ at low temperature and pressure results in large water vapor content which increases the heat duty. The DCC could work best with a solvent with high heat of absorption and resistance to thermal degradation.
- PZAS with DCC and double the number of cross exchangers gave the lowest cost of capture at $186.7/tonne compared to the base case value of $190.56/tonne. Simply using the DCC with the base case decreased the cost of capture to $187.2/tonne. Doubling the number of cross exchangers had a similar cost of capture at $187.34/tonne. Designs that used a low pressure stripper increased the cost of capture compared to the base case. The DCC with low pressure stripper had a cost of $196.83/tonne and the low pressure PZAS had a cost of $198.2/tonne.

- Lean solvent rate and lean loading can be used as effective handles to maximize the variable profit of the plant as a function of ambient temperature.
  - Optimum lean solvent rate decreased with increase in ambient temperature to accommodate the lower flue gas mass flowrate and compressor capacity. Its

value was always higher than the design value by 5-21%, meaning that the lean pump was overdesigned.

- 0.2 lean loading was sufficient at low ambient temperature while 0.18 lean loading was required at high ambient temperature to maximize cyclic capacity of the solvent. Low pressure stripping at 150 °C at high ambient temperature was required to maximize variable profit.
- Optimum heat duty was between 2.2 and 2.3 GJ/tonne irrespective of reduced rich loading at high ambient temperature due to the lower lean solvent rate and lean loading.
- At 0.18 lean loading and 40 °F ambient temperature, the compressor, boiler, and boiler fan capacities could be increased to increase the variable profit by upto 21%. This increase was less significant (6-11%) at higher ambient temperature (lower rich loading) or higher lean loading.

The following are the recommendations for future stripper design:

- The direct contact condenser can be reevaluated with a corrected high temperature kinetics model. The same could be done with an updated mass transfer model.
- The direct contact condenser could be tested at the pilot scale, which can be used to tune mass transfer coefficients or wetted area over a wide range of operating temperature.
- Cost avoided by the direct contact condenser by eliminating horizontal footprint could be studied in detail.
- Other scenarios of direct contact condensation could be modeled and compared to the performance of the direct contact condenser. For example, a process scheme where the

condensed water from the condenser is directly sent into the stripper column could be studied.

- The direct contact condenser could be studied at higher lean loading and lower stripper temperature.
- The performance of an advanced reboiled stripper with the direct contact condenser at low temperature and pressure could be studied as a design alternative.
- The hot rich bypass must be tested at NCCC with the existing modified piping.
- Process configurations that increase vapor content in rich solvent line, such as using heat exchangers at an elevation could be modeled.
- Stripper optimization could incorporate heat exchanger size, stripper packing height and type, stripper diameter etc. as design variables.
- The effect of water cooling for intercooling and water wash instead of air cooling should be modeled, rated, and optimized. The surrogate and rating models can be expanded for water cooling.
- Lower lean loading values can be considered to optimize lean loading for PZ. Solvent concentration is another variable that could be included in the optimization.
- The effect of the power plant operation and penetration of renewables on the capture system can be studied in greater detail.
- Performance of PZAS at low temperature and pressure must be tested at long term conditions.
- Unification of absorber and stripper flowsheets along with a more robust bypass optimization method could be investigated.
- Equation-oriented modeling of PZAS could further reduce convergence time and remove the need for creation of data-intensive surrogate models.

- Phenomena such as nucleate boiling on the surface of packing in strippers have the potential to further reduce heat duty. Future work could experiment and model these phenomena.

Appendices

Appendix A

Appendix A provides the MATLAB code used for optimization of bypasses for all design cases evaluated using Aspen Plus®.

MATLAB Code for Bypass Optimization using Surrogate Model

```
clc

clear

% FUNCTION DEFINITION

%f = @(x,y) 5.375939 - 14.5893*x - 3.96382*y + 21.11915*x.^2 + 15.59102*x*y;

%f = @(x,y) 5.331786 - 13.9513*x - 3.82755*y + 18.8787*x.^2 + 13.92045*x*y;

% OPTIMIZE FUNCTION

x = zeros(1,2);

% 2x packing RSR 2 3

%f = @(x) 5.74998-15.1657*x(1)-9.82456*x(2)+21.92128*x(1).^2+7.499774*x(2).^2 +22.43328*x(1)*x(2);

%f = @(x) 5.892816-9.64111*x(1)-10.2514*x(2)+7.771058*x(2).^2+22.876438*x(1)*x(2);

%0.5X PACKING CASE

%f = @(x) 5.375054 - 11.5281*x(1) - 3.67751*x(2) + 19.0409*x(1).^2 + 2.078922*x(2).^2 + 5.556759*x(1)*x(2);

%f = @(x) 5.960497-13.1505*x(1)-3.63429*x(2)+19.96403*x(1).^2+1.99617*x(2).^2+5.967985*x(1)*x(2);

%initial packing selection

%f = @(x) 5.805343 - 17.0975*x(1) - 6.72839*x(2) + 30.49224*x(1).^2 + 4.250841*x(2).^2 + 15.32088*x(1)*x(2);

%f = @(x) 5.27215 - 14.7203*x(1) - 5.03628*x(2) + 28.6222*x(1).^2 + 2.862003*x(2).^2 + 10.68447*x(1)*x(2);

%f = @(x) 5.435696 - 16.4467*x(1) - 4.6328*x(2) + 32.39525*x(1).^2 + 2.356966*x(2).^2 + 9.986946*x(1)*x(2);

%LOW NTU case

%f = @(x) 5.788285-16.5664*x(1)-5.24181*x(2)+29.30272*x(1).^2+2.5301*x(2).^2+12.14015*x(1)*x(2);
```

```
%High NTU case

%f = @(x) 5.628314-17.1493*x(1)-5.7575*x(2)+32.53623*x(1).^2+3.314378*x(2).^2+12.591*x(1)*x(2);

%60 ft RSR 2 3

%f = @(x) 5.592344-13.4542*x(1)-9.3822*x(2)+18.07681*x(1).^2+6.886032*x(2).^2+20.04015*x(1)*x(2);

%f = @(x) 6.05823-13.7725*x(1)-9.67838*x(2)+16.85469*x(1).^2+7.167833*x(2).^2+20.29344*x(1)*x(2);

%70 ft RSR 23

%f = @(x) 5.859883-15.3399*x(1)-11.3478*x(2)+22.32312*x(1).^2+9.494585*x(2).^2+24.33025*x(1)*x(2);

%f = @(x) 6.313967-15.6405*x(1)-11.5309*x(2)+21.23036*x(1).^2+9.611255*x(2).^2+24.38811*x(1)*x(2);

%0.5x NTU case

%f = @(x) 6.218806-17.384*x(1)-6.26681*x(2)+29.41762*x(1).^2+3.656006*x(2).^2+14.20645*x(1)*x(2);

%steam heater pressure drop

%f = @(x) 5.639841-15.8713*x(1)-5.43425*x(2)+28.44283*x(1).^2+3.036539*x(2).^2+11.33882*x(1)*x(2);

%CROSS EXCHANGER NTU REDISTRIBUTION

%f = @(x) 5.676182-13.9152*x(1)-6.56373*x(2)+24.69033*x(1).^2+5.950473*x(2).^2+14.54378*x(1)*x(2); % NTU C 2 NTU H 6

%f = @(x)  6.258939-16.9712*x(1)-5.82715*x(2)+26.73927*x(1).^2+3.12708*x(2).^2+12.57773*x(1)*x(2); % NTU C 7 NTU H 1

%f = @(x) 6.19343-17.8096*x(1)-6.40524*x(2)+30.89076*x(1).^2+4.097681*x(2).^2+14.36976*x(1)*x(2); % NTU C 5 NTU H 3

%f = @(x) 6.235189-17.7436*x(1)-7.50451*x(2)+30.01084*x(1).^2+5.563988*x(2).^2+17.49792*x(1)*x(2); % NTU 4 4

%f = @(x) 6.09026-16.677*x(1)-5.48123*x(2)+27.85586*x(1).^2+2.705174*x(2).^2+12.72247*x(1)*x(2); %base case 0.5x NTU, NTUCO2 = 5

%f = @(x) 6.229591-16.9555*x(1)-5.0943*x(2)+26.20941*x(1).^2+2.298199*x(2).^2+11.15423*x(1)*x(2);

%ntu H =7.5

%f = @(x) 6.177306-17.3728*x(1)-4.19181*x(2)+27.21185*x(1).^2+1.550187*x(2).^2+9.481534*x(1)*x(2);

% no hot exchanger

%EFFECT OF CROSS EXCHANGER DP

%f = @(x) 6.262574-16.9869*x(1)-5.83117*x(2)+26.78646*x(1).^2+3.130203*x(2).^2+12.59878*x(1)*x(2); %Cold DP = 0
```

```
%f = @(x) 6.261907-16.9949*x(1)-5.82855*x(2)+26.80396*x(1).^2+3.127887*x(2).^2+12.58883*x(1)*x(2); %Cold DP = 15

%f = @(x) 6.260562-17.0323*x(1)-5.8704*x(2)+26.95684*x(1).^2+3.167512*x(2).^2+12.66876*x(1)*x(2); %Hot DP = 0

%f = @(x) 6.258857-16.9965*x(1)-5.84468*x(2)+26.83938*x(1).^2+3.144059*x(2).^2+12.61421*x(1)*x(2); % Hot DP = 5

%EFFECT OF STEAM HEATER DP

%f = @(x) 6.26125-16.8797*x(1)-5.75504*x(2)+26.35215*x(1).^2+3.054733*x(2).^2+12.44233*x(1)*x(2); %STMHTR = 10

%f = @(x) 6.263478-16.7913*x(1)-5.71314*x(2)+25.93797*x(1).^2+3.008793*x(2).^2+12.39514*x(1)*x(2); %STMHTR = 20 DP

%EFFECT OF LEAN LOADING

%f = @(x) 5.099508-17.5361*x(1)-3.54723*x(2)+54.87366*x(1).^2+2.037554*x(2).^2+12.89302*x(1)*x(2); %LLDG = 0.23

%CONDENSATE COOLING

%f = @(x) 5.837119-7.30029*x(1)-8.24651*x(2)+30.90274*x(1).^2+7.073981*x(2).^2+6.089088*x(1)*x(2); %CASE 2

%f = @(x) 5.703189-10.4425*x(1)-6.57284*x(2)+15.13773*x(1).^2+4.304503*x(2).^2+13.25365*x(1)*x(2); %CASE 3

%0.5x PK NTU 8,0

%f = @(x) 5.952716-14.1199*x(1)-3.38771*x(2)+20.32205*x(1).^2+1.178323*x(2).^2+7.176675*x(1)*x(2);

%f = @(x) 6.186633-16.1961*x(1)-3.51831*x(2)+26.48725*x(1).^2+1.265992*x(2).^2+7.524438*x(1)*x(2);

%2xPK NTU 8,0

%f = @(x) 6.55405-19.6011*x(1)-7.37177*x(2)+28.20104*x(1).^2+3.907919*x(2).^2+18.39175*x(1)*x(2);

%f = @(x) 6.728305-22.593*x(1)-7.44741*x(2)+38.54874*x(1).^2+3.816773*x(2).^2+19.35835*x(1)*x(2);

%NTU = 16, NTU HOT = 0

%f = @(x) 5.358452-13.9246*x(1)-3.80328*x(2)+24.76136*x(1).^2+1.428118*x(2).^2+8.114901*x(1)*x(2);

%NTU 8 0 WITH NO STEAM HEATER

%f = @(x) 6.146254-18.7123*x(1)-3.858628*x(2)+33.94018*x(1).^2+1.357835*x(2).^2+8.591627*x(1)*x(2);

%LATEST FEED DESIGN CASE, 6-2 NTU, 0.398 RLDG, GAS FROM 1 GT + 0.5 GFB

%f = @(x) 5.956382-14.869*x(1)-5.8317*x(2)+21.73723*x(1).^2+3.139909*x(2).^2+11.7179*x(1)*x(2);

%HOT RICH BYPASS 8 0, WEQ SURROGATE OPTIMIZATION, 0.398 RLDG, GAS FROM 1 GT + 0.5 GFB

%f = @(x) 75.48538-172.415*x(1)-45.7477*x(2)+280.8186*x(1).^2+20.08299*x(2).^2+96.85671*x(1)*x(2);
```

```
%40 TURNDOWN MODE,6-2 NTU, 0.398 RLDG, GAS FROM 1 GT + 0.5 GFB

%f = @(x) 5.835286-13.817*x(1)-6.942*x(2)+20.57826*x(1).^2+4.44372*x(2).^2+12.65584*x(1)*x(2);


%NTU 12 0 CASE

%f = @(x) 5.740957-17.0736*x(1)-3.91686*x(2)+31.40873*x(1).^2+1.392628*x(2).^2+9.044591*x(1)*x(2);

%NTU 8 0 HRBP case with 70 ft RSR 2 3 packing

%f = @(x) 5.697887-9.41915*x(1)-6.24816*x(2)+3.2505*x(2).^2+12.57809*x(1)*x(2);

%NTU 6 2 HRBP WITH WRBP BASE CASE 95 F

%f = @(x) 5.974698-15.5231*x(1)-5.56014*x(2)+24.88846*x(1).^2+3.027063*x(2).^2+11.6455*x(1)*x(2);

%NTU 6 2 HRBP WITH WRBP BASE CASE 105 F

%f = @(x) 6.143497-17.4582*x(1)-5.58843*x(2)+31.28653*x(1).^2+3.1887*x(2).^2+12.042428*x(1)*x(2);

%HIGHER NTU CASES WITH 0.398 RLDG BASE CASE

%NTU = 20

%f = @(x) 5.616499-16.077*x(1)-6.1107*x(2)+26.43477*x(1).^2+3.309911*x(2).^2+12.78087*x(1)*x(2);

%NTU=16

%f = @(x) 5.688137-15.8235*x(1)-6.16621*x(2)+25.07515*x(1).^2+3.373354*x(2).^2+12.87632*x(1)*x(2);

%FIXING NTU = 12, NTU = 16 data to accomodate NTU CO2 = 5

%NTU TOTAL = 12

%f = @(x) 5.784816-16.4787*x(1)-5.23234*x(2)+29.28293*x(1).^2+2.810452*x(2).^2+10.90132*x(1)*x(2);

%NTU TOTAL = 16

%f = @(x) 5.786122-17.4407*x(1)-5.96447*x(2)+31.83739*x(1).^2+3.546613*x(2).^2+12.67261*x(1)*x(2);

%PACKING HEIGHT ANALYSIS ON FINAL BASE CASE, rldg = 0.3996

%48.8 ft

%f = @(x) 6.128735-15.2367*x(1)-9.82011*x(2)+22.00223*x(1).^2+7.250904*x(2).^2+19.0273*x(1)*x(2);

%70 ft
```

```
%f = @(x) 6.288086-17.3613*x(1)-10.8133*x(2)+28.95638*x(1).^2 + 8.129422*x(2).^2 + 22.07811*x(1)*x(2);

%60ft

%f = @(x) 6.16214-15.1691*x(1)-10.3797*x(2)+19.41048*x(1).^2 + 7.362336*x(2).^2 + 22.485*x(1)*x(2);



%12.2 ft

%f = @(x) 5.773073-11.4777*x(1)-3.65595*x(2)+14.9361*x(1).^2+1.884261*x(2).^2+5.224098*x(1)*x(2);

%Effect of sump T on column diameter

% 160 C

%f = @(x) 5.516978-17.4396*x(1)-4.78198*x(2)+34.35142*x(1).^2+2.641129*x(2).^2+11.45499*x(1)*x(2);

%140 C

%f = @(x) 6.371727-10.8022*x(1)-6.70668*x(2)+9.125277*x(1).^2+3.608583*x(2).^2+9.669362*x(1)*x(2);

%base case with flue gas duct firing

%f = @(x) 5.96657-15.0055*x(1)-5.90897*x(2)+21.51502*x(1).^2+3.133785*x(2).^2+12.12028*x(1)*x(2);

%105 F rating for base case, rldg 0.366

%f = @(x)6.032203-15.674*x(1)-5.51117*x(2)+25.4481*x(1).^2+3.009564*x(2).^2+11.6048*x(1)*x(2);

%Alfa Laval design, vary stm ht dp

%f = @(x)

%6.166495-14.536*x(1)-7.00337*x(2)+18.64096*x(1).^2+4.116852*x(2).^2+15.30873*x(1)*x(2);

%DP = 30 psi

%f = @(x)

%6.069231-15.0918*x(1)-6.08209*x(2)+21.59051*x(1).^2+3.27341*x(2).^2+12.58762*x(1)*x(2);

%DP = 0 psi

%f = @(x) 6.042068-13.607*x(1)-6.55576*x(2)+16.90134*x(1).^2+3.654698*x(2).^2+13.96637*x(1)*x(2);

%DP = 20psi

%Qmin estimation
```

```
%f = @(x) 6.072179-16.5349*x(1)-12.8278*x(2)+23.54339*x(1).^2+10.98683*x(2).^2+27.06704*x(1)*x(2);

%Bypass optimization for NGCC NCCC Run 44 Superheating Concept

%f = @(x) 3.848071-11.2071*x(1)-5.707*x(2)+30.43144*x(1).^2+5.1507*x(2).^2+13.94299*x(1)*x(2);


%Bypass optimization for 284 F sump T design case for superheat test

%f = @(x) 2.516952-10.472*x(1)-0.32853*x(2)+111.0852*x(1).^2+0.775299*x(2).^2+2.276303*x(1)*x(2);

%Bypass optimization for 320 F sump T design case for superheat test

%f = @(x) 8.066808-9.90915*x(1)-13.2541*x(2)+5.08332*x(2).^2+19.5964*x(1)*x(2);

%Bypass optimization for superheat analysis, Q vs packing ht plot

%13.2 ft

%f = @(x) 3.548302-5.77014*x(1)-4.40666*x(2)+3.660223*x(2).^2+8.144037*x(1)*x(2);

%6.56 ft

%f = @(x) 4.061795-14.5385*x(1)-5.3196*x(2)+40.88126*x(1).^2+4.629157*x(2).^2+15.43417*x(1)*x(2);

%3.28 ft

%f = @(x) 3.889731-11.1604*x(1)-3.05283*x(2)+26.49899*x(1).^2+2.052604*x(2).^2+8.192508*x(1)*x(2);

%1.64 ft

%f = @(x) 4.417674-16.88728*x(1)-1.95642*x(2)+41.3364*x(1).^2+0.714833*x(2).^2+6.337727*x(1)*x(2);

%26.4 ft

%f = @(x) 4.267802-15.1143*x(1)-9.58633*x(2)+47.777548*x(1).^2+11.11212*x(2).^2+26.42417*x(1)*x(2);

%52.8 ft

%f = @(x) 4.290336-15.4293*x(1)-9.79981*x(2)+49.77704*x(1).^2+11.42241*x(2).^2+27.2049*x(1)*x(2);

%105 F PZAS High Upstream Pressure

%f = @(x) 6.330061-14.1107*x(1)-9.96722*x(2)+19.02511*x(1).^2 + 8.007749*x(2).^2+19.68526*x(1)*x(2);

%After carbon bed bps optimization

%f = @(x) 3.789895-9.77507*x(1)-7.24409*x(2)+22.23316*x(1).^2+8.248271*x(2).^2+15.43519*x(1)*x(2);
```

```
%Before carbon bed bps optimization

%f = @(x) 3.79956-9.80317*x(1)-7.25262*x(2)+22.26566*x(1).^2+8.255919*x(2).^2+15.50156*x(1)*x(2);

%FEED, boiling, 12.2 ft packing

%f = @(x) 5.875403-12.0726*x(1)-4.33203*x(2)+15.9669*x(1).^2+2.638617*x(2).^2+6.533399*x(1)*x(2);


%FEED,boiling, 6.1 ft packing

%f = @(x) 6.0023-11.4803*x(1)-2.49484*x(2)+13.55733*x(1).^2+1.022072*x(2).^2+4.039887*x(1)*x(2);

%FEED boiling, 3.05 ft packing

%f = @(x) 6.911633-16.0616*x(1)-1.55444*x(2)+20.17011*x(1).^2+0.400714*x(2).^2+2.227756*x(1)*x(2);

%FEED boiling, 50 ft packing

%f = @(x) 6.137544-12.8656*x(1)-11.1191*x(2)+11.8962*x(1).^2+9.359555*x(2).^2+19.83205*x(1)*x(2);

%FEED boiling, 70 ft packing

%f = @(x) 6.199223-11.2053*x(1)-12.5505*x(2)+4.141402*x(1).^2+11.51804*x(2).^2+18.25276*x(1)*x(2);

%Effect of changing packing to NCCC - FEED boiling

%f = @(x) 6.44777-18.6012*x(1)-8.88412*x(2)+27.07166*x(1).^2+5.4287748*x(2).^2+20.85336*x(1)*x(2);

%split HX lean split 50%, assumed column head and WRBP head

%f = @(x) 7.530093375-17.2574868*x(1)-12.81962306*x(2)+23.48863618*x(1).^2+10.60019292*x(2).^2+18.15169382*x(1)*x(2);

%split HX, 2CHXs, real stripper and real head

%f = @(x) 8.176015297-21.94693458*x(1)-14.66225944*x(2)+32.45348094*x(1).^2+12.07132038*x(2).^2+23.04276123*x(1)*x(2);

%split HX, 2CHXs, real stripper and real head liquid only

%f = @(x) 7.925920972-19.28294353*x(1)-14.00513683*x(2)+25.725831*x(1).^2+11.5403895*x(2).^2+20.926001*x(1)*x(2);

%split HX, 3CHXs (2,1), real stripper and real head, 66% lsplit

%f = @(x) 7.862478438-20.40382565*x(1)-10.38765005*x(2)+31.0519335*x(1).^2+5.11410775*x(2).^2+18.245175*x(1)*x(2);

%split HX, 3CHXs (1,2), real stripper and real head, 33% lsplit

%f = @(x) 8.12187791-21.9682036*x(1)-17.734411*x(2)+28.9748295*x(1).^2+18.213668*x(2).^2+31.6249885*x(1)*x(2);
```

```
%split HX, 2CHXs, real stripper and liquid hd only, 50% lsplit

%f = @(x) 7.84974717-18.90240717*x(1)-13.87180092*x(2)+25.533441*x(1).^2+11.52050688*x(2).^2+20.52307*x(1)*x(2);

%packing type effect in FEED boiling, RSR 1 2

%f = @(x) 6.273485243-16.69703195*x(1)-7.863403717*x(2)+22.638131*x(1).^2+4.6667765*x(2).^2+17.7171885*x(1)*x(2);

%packing type effect in FEED boiling, RSR 1 3

%f = @(x) 6.316983177-17.1824231*x(1)-8.062636229*x(2)+23.67246121*x(1).^2+4.806704054*x(2).^2+18.37551079*x(1)*x(2);


%packing type effect in FEED boiling, RSR 0.1 0.3

%f = @(x) 6.322726361-15.68247002*x(1)-10.1920262*x(2)+20.177328*x(1).^2+7.784446875*x(2).^2+18.9282515*x(1)*x(2);

%packing type effect in FEED boiling, RSR 0.1 0.5

%f = @(x) 6.364899234-16.39809762*x(1)-10.17350204*x(2)+21.9030256*x(1).^2+7.446583986*x(2).^2+19.94022811*x(1)*x(2);

%packing type effect in FEED boiling, RSR 0.3 0.5

%f = @(x) 6.183057576-14.43963034*x(1)-9.341337286*x(2)+16.81236696*x(1).^2+6.727721656*x(2).^2+17.56496471*x(1)*x(2);

%srp 2021 campaign

%precampaign 0.4 rldg 0.2 lldg

%f = @(x) 6.653330994-21.12487227*x(1)-16.7432525*x(2)+29.67980787*x(1).^2+15.82630469*x(2).^2+42.18822307*x(1)*x(2);

%precampaign 0.37 rldg 0.2 lldg

%f = @(x) 6.292715442-13.79481625*x(1)-16.32823155*x(2)+3.884043374*x(1).^2+17.69600286*x(2).^2+30.11785295*x(1)*x(2);

%precampaign 0.409 rldg 0.2 lldg

%f = @(x) 6.321732961-13.55926561*x(1)-16.6862572*x(2)+4.100234341*x(1).^2+17.11923051*x(2).^2+28.01529235*x(1)*x(2);

%precampaign 0.411 rldg 0.2 lldg

%f = @(x) 6.385287662-14.40167314*x(1)-17.11075286*x(2)+6.120248755*x(1).^2+17.51952553*x(2).^2+31.21639673*x(1)*x(2);

%HRBP NTU 8,0, rldg 0.375, Weq optimization

%f = @(x) 75.15857153-173.1999425*x(1)-43.83808078*x(2)+302.1828413*x(1).^2+21.53728368*x(2).^2+87.16776185*x(1)*x(2);

%HRBP NTU 12,0, rldg 0.375, Weq optimization
```

```
%f = @(x) 66.38870992-69.16764516*x(1)-43.70483962*x(2)+22.78306707*x(2).^2+74.6902826*x(1)*x(2);

%HRBP NTU 16,0, rldg 0.375, Weq optimization

%f = @(x) 64.19090351-62.49552281*x(1)-42.38973269*x(2)+21.58754754*x(2).^2+75.4395101*x(1)*x(2);

%WRBP NTU 6,2, rldg 0.375, Weq optimization

%f = @(x) 79.70166791-180.2351004*x(1)-59.29896203*x(2)+300.915673*x(1).^2+29.27058524*x(2).^2+137.5648648*x(1)*x(2);

%WRBP NTU 9,3, rldg 0.375, Weq optimization

%f = @(x) 73.41606024-141.1595736*x(1)-70.66457213*x(2)+212.0589363*x(1).^2+53.58714188*x(2).^2+125.9332725*x(1)*x(2);


%WRBP NTU 12,4, rldg 0.375, Weq optimization

%f = @(x) 65.82559561-71.938567*x(1)-56.53447543*x(2)+33.52547732*x(2).^2+106.7262079*x(1)*x(2);

%65 F, rich solvent T = 44 C, surrogate models for heat duty

% 0.4 rldg, 0.2 lldg

%f = @(x) 5.53088716-11.5413999*x(1)-5.12919625*x(2)+16.6663045*x(1).^2+2.9210475*x(2).^2+10.0708585*x(1)*x(2);

% 0.39 rldg, 0.2 lldg

%f = @(x) 5.57257318-12.6638324*x(1)-4.58276725*x(2)+20.870428*x(1).^2+2.3678145*x(2).^2+9.809531*x(1)*x(2);

% 0.44 rldg, 0.2 lldg

%f = @(x) 5.803732071-10.02009523*x(1)-7.91173665*x(2)+6.7611985*x(1).^2+5.048178375*x(2).^2+13.4650885*x(1)*x(2);

%65 F, rich solvent T = 52 C, surrogate models for heat duty

% 0.4 rldg, 0.2 lldg

%f = @(x) 5.396124605-8.759717258*x(1)-5.53421355*x(2)+8.83581575*x(1).^2+3.5272815*x(2).^2+8.859048*x(1)*x(2);

% 0.39 rldg, 0.2 lldg

%f = @(x) 5.477904095-9.548602642*x(1)-5.3583286*x(2)+11.51523925*x(1).^2+3.4149825*x(2).^2+8.868934*x(1)*x(2);

%0.44 rldg, 0.2 lldg

%f = @(x) 5.667195531-9.0863424*x(1)-7.5961722*x(2)+5.226676*x(1).^2+5.200399875*x(2).^2+11.238756*x(1)*x(2);

%65 F, rich solvent T = 48 C, surrogate models for heat duty
```

```
% 0.4 rldg, 0.2 lldg

%f = @(x) 5.287497492-8.499324643*x(1)-4.947124653*x(2)+9.375715294*x(1).^2+2.943159941*x(2).^2+7.876142*x(1)*x(2);

% 0.39 rldg, 0.2 lldg

%f = @(x) 5.370923217-9.211154543*x(1)-4.811333993*x(2)+11.87361908*x(1).^2+2.915156709*x(2).^2+7.804817381*x(1)*x(2);

% 0.44 rldg, 0.2 lldg

%f = @(x) 5.394834773-7.512985388*x(1)-6.522377575*x(2)+2.871565625*x(1).^2+4.1714445*x(2).^2+8.835809*x(1)*x(2);

%proof of concept of surrogate model (heat duty as a func of rich T, rich

%solv rate, crbp, and wrbp)


%heat duty = f(Trich, Lrich, crbp flow rate, wrbp flow rate)

%f = @(x)4.620957996-0.0279539*x(1)-0.016841355*x(2)+7.32968E-05*x(1).^2+2.579E-05*x(2).^2+6.76E-05*x(1)*x(2)+7.00019E-

        06*(400).^2-4.61449E-05*(43).^2;

%heat duty = f(Trich, Lrich, crbp fraction, wrbp fraction)

%f = @(x) 5.05500154-(0.003292925*(52))+(4.68746E-06*(480).^2)-9.96632881*x(1)-7.304849168*x(2)+8.349393592*x(1).^2 +

        4.826839136*x(2).^2 + 11.96677839*x(1)*x(2);

%ALAMO heat duty model

%a = 43;

%b = 400;

%f = @(x) 0.348e-1*a + 0.248e-1*b - 11.827*x(1) - 12.571*x(2) - 0.1786e-4*(b).^2 + 10.2490*x(1).^2 + 14.903*x(2).^2 - 8.247*x(2).^3 -

        0.102e-3*a*b + 0.214e-1*a*x(2) + 20.737*x(1)*x(2) - 55.0709*(x(1)*x(2)).^2 + 0.656e-4*(b*x(1)*x(2)).^2 - 0.653

%NCCC precampaign modeling

%0.18 lldg, 99% removal

%f = @(x) 6.595366591-12.42249883*x(1)-10.14708599*x(2)+9.258304354*x(1).^2 + 6.268604914*x(2).^2 + 17.72674964*x(1)*x(2);

%0.2 lldg, 99% removal

%f = @(x) 5.425885663-9.919489524*x(1)-9.486502439*x(2)+6.931817643*x(1).^2+8.074961453*x(2).^2+15.0133031*x(1)*x(2);
```

```
%case 1

%f = @(x) 5.406569056-9.573453217*x(1)-9.491904843*x(2)+5.523270312*x(1).^2+8.035200936*x(2).^2+14.53371296*x(1)*x(2);

%rating model, double the HX NTU

%f = @(x) 5.518999067-11.40642937*x(1)-7.243639683*x(2)+11.66731633*x(1).^2+4.128660583*x(2).^2+12.507758*x(1)*x(2);

%scenario 2, DCCC, 15ft of packing

%f = @(x) 5.678477592 -14.76335844*x(1)-6.845086503*x(2) + 24.17841051*x(1).^2 + 4.555710004*x(2).^2 + 11.84758787*x(1)*x(2);

%scenario 1, DCCC, 15ft of packing

%f = @(x) 6.070405253-14.51087795*x(1)-7.396702959*x(2)+21.19006107*x(1).^2 + 5.070094075*x(2).^2 +13.60179774*x(1)*x(2);


%LOW T/P Stripping FEED

f = @(x) 9.140670287-13.33485123*x(1)-10.33808854*x(2)+8.545843459*x(1).^2 + 4.999155089*x(2).^2 +13.78524242*x(1)*x(2);

x0 = [0.3,0.3];

LB = [0.3, 0.1];

UB = [0.6, 0.5];

A = [0,0];

b = 0;

Aeq = [0,0];

beq = 0;

options = optimoptions('fmincon','Algorithm','active-set');

options.Display = 'iter'

[x, fval] = fmincon(f,x0,A,b,Aeq,beq,LB,UB)   %gradient based optimization

%[x, fval] = fminsearch(f,x0) %gradient free optimization

fval

%SURFACE PLOT OF FUNCTION

%a = 44;
```

```
%b = 488;

%f = @(x,y) 0.348e-1*a + 0.248e-1*b - 11.827*x - 12.571*y - 0.1786e-4*(b.^2) + 10.2490*x.^2 + 14.903*(y.^2) - 8.247*(y.^3) - 0.102e-3*a*b
            + 0.214e-1*a*y + 20.737*x*y - 55.0709*(x*y).^2 + 0.656e-4*(b*x*y).^2 - 0.653

%f = @(x,y) 4.620957996-0.0279539*x-0.016841355*y+7.32968E-05*x.^2+2.579E-05*y.^2+6.76E-05*x*y+7.00019E-06*(490).^2-4.61449E-
            05*(48).^2;

%fsurf(f,[0.1 0.3 0.1 0.7],'ShowContours','on')

%zlim([2.8,4])

%ylim([0.1, 0.7]);

%title('Rich solvent rate = 488 kg/s and Rich Temperature = 52 C')

%ylabel('WRBP (kg/s)')

%xlabel('CRBP (kg/s)')

%zlabel('Heat Duty (GJ/tonne CO2)')
```

Appendix B

Appendix B provides the MATLAB surrogate model code used for the process optimization of PZAS for the FEED.

PZAS Process Surrogate Model for FEED Optimization

F.1 PZAS Process Script

```
%%
clc
clear

%array for iteration storage
MaxIt = 100; %Nr of max iterations per case
```

```
% Table creator for optimum calc

% Nr of points for each independent variable - odd numbers produce whole
% numbers in the independent variable

% NrPoints include the upper and lower bound

CRBPNrPoints = 10;

WRBPNrPoints = 20;

LeanFNrPoints = 250;

NrICBaysNrPoints = 15;

NrPAPumpsNrPoints = 2;

NrWWPumpsNrPoints = 2;

LeanLDGNrPoints = 10;

% Lower bounds

CRBPLow = 0.1;

WRBPLow = 0.05;

LeanFLow = 250; %kg/s

NrICBaysLow = 6; % New Low is 6 - bc 5 doesnt work

NrPAPumpsLow = 1;
```

```
NrWWPumpsLow = 1;

LeanLDGLow = 0.18 ;

% Upper bounds

CRBPHigh = 0.3;

WRBPHigh = 0.6;

LeanFHigh = 550; %kg/s

NrICBaysHigh = 20;

NrPAPumpsHigh = 2;

NrWWPumpsHigh = 2;

LeanLDGHigh = 0.22;


%Step change

CRBPStep = (CRBPHigh - CRBPLow) / (CRBPNrPoints - 1 ) ;

WRBPStep = (WRBPHigh - WRBPLow) / (WRBPNrPoints - 1 ) ;

LeanFStep = (LeanFHigh - LeanFLow) / (LeanFNrPoints - 1 ) ;

NrBaysStep = (NrICBaysHigh - NrICBaysLow) / (NrICBaysNrPoints - 1 ) ;
```

```
NrPAPumpsStep = 1;

NrWWPumpsStep = 1;

LeanLDGStep = (LeanLDGHigh - LeanLDGLow) / (LeanLDGNrPoints - 1 ) ;

TotalPoints = CRBPNrPoints * WRBPNrPoints * LeanFNrPoints * NrICBaysNrPoints * NrPAPumpsNrPoints *
NrWWPumpsNrPoints * LeanLDGNrPoints

ResMatrix = zeros(TotalPoints, 9);

EntryNr = 1;

for i = WRBPLow:WRBPStep:WRBPHigh
    for j = CRBPLow:CRBPStep:CRBPHigh
        for m = LeanFLow:LeanFStep:LeanFHigh
            for n = NrICBaysLow:NrBaysStep:NrICBaysHigh
                for o = NrPAPumpsLow:NrPAPumpsStep:NrPAPumpsHigh
                    for p = NrWWPumpsLow:NrWWPumpsStep:NrWWPumpsHigh
                        for r = LeanLDGLow:LeanLDGStep:LeanLDGHigh

                            ResMatrix(EntryNr, 1) = i;
                            ResMatrix(EntryNr, 2) = j;
                            ResMatrix(EntryNr, 3) = m;
                            ResMatrix(EntryNr, 4) = n;
                            ResMatrix(EntryNr, 5) = o;
                            ResMatrix(EntryNr, 6) = p;
                            ResMatrix(EntryNr, 7 )= r;
```

```
                    EntryNr = EntryNr + 1;
                end
            end
        end
    end
  end
 end
end

%looping to get output data

tic
    for i = 1:1:TotalPoints

[LeanTcalc,RichFcalc,RichFPZAS,HRcalc,PATcalc,PAFlowcalc,RichLDG,RichT,HDcalc,TP,Feasible,Feasible1,Feasible2,Feasible3,
Feasible4,Feasible5,Feasible6,Feasible7,Feasible8,...
        CO2Flow,CO2Rem,LPP,RPP,ICPP,WWPP,HRSGFP,BLRFP,ICFP,WWFP,CP,Flood1,Flood2] =
convergence(ResMatrix(i,2),ResMatrix(i,1),ResMatrix(i,3),ResMatrix(i,4),ResMatrix(i,5),ResMatrix(i,6), ResMatrix(i,7));  %calling
the convergence function


        ResMatrix(i,8) = CO2Flow;

        ResMatrix(i,9) = HRcalc;

        ResMatrix(i,10) = TP;

        ResMatrix(i,11) = Feasible; %Rich Pump Flag

        ResMatrix(i,12) = Feasible1; %CRBP and WRBP Flag
```

```
            ResMatrix(i,13) = Feasible2; %Lean Pump Bubble point Flag

            ResMatrix(i,14) = Feasible3; %Gas-fired boiler capacity

            ResMatrix(i,15) = Feasible4; %Stripper Flooding Flag

            ResMatrix(i,16) = Feasible5; %Gas-fired boiler fan speed Flag

            ResMatrix(i,17) = Feasible6; %Absorber flooding flag

            ResMatrix(i,18) = Feasible7; %Compressor maximum capacity flag

            ResMatrix(i,19) = Feasible8; % Precipitation flag



        end
    toc

    %%
    save('Results_40F_95CF_DB_Full_VaryLLDG.mat','ResMatrix','-v7.3')



    function
[LeanTcalc,RichFcalc,RichFPZAS,HRcalc,PATcalc,PAFlowcalc,RichLDG,RichT,HDcalc,TP,Feasible,Feasible1,Feasible2,Feasible3,
Feasible4,Feasible5,Feasible6,Feasible7,Feasible8,CO2Flow,CO2Rem,LPP,RPP,ICPP,WWPP,HRSGFP,BLRFP,ICFP,WWFP,CP,Fl
ood1,Flood2] = convergence(CRBP,WRBP,LeanF,ICBays, NrPAPumps, NrWWPumps,LeanLDG);


    %% Independent Variables - Optimized Version
```

```
%           CRBP = 0.3;
%           WRBP = 0.3;
%           LeanF = 400;
%           ICBays = 20;
%           NrPAPumps = 2;
%           NrWWPumps = 2;
%           LeanLDG = 0.2;

        NrTrains = 2; %Number of process trains online
        TAmb = 4.444; %Ambient Temperature, °C ( 40 F - 4.444 C; 65 F - 18.3333 C; 105 F - 40.5556 C)
        TAmbF = ( TAmb * 9/5 ) + 32;

%           NrPAPumps = 2 ; % Number of pumparound pumps in service
%           NrWWPumps = 2 ; % Number of water wash pumps in service


        ICFans = ICBays * 3; %number of air cooler fans - Intercooler Performance Model assumes 3 Fans/Bay

        % Next two are determined by the WW loop to be the Number
        % of Bays that can more closely close the water balance

        %WWBays = 20; %Number of Pumparound air cooler bays active - Range: 5 to 20
        %WWFans = WWBays * 3; %number of water wash air cooler bays online - Water wash Performance Model assumes ???
Fans/Bay

        WWBayMin = 5 ;

        WWBayMax = 18 ;
```

```
%           Feasibility Check Var

        Feasible = true;
        Feasible1 = true;
        Feasible2 = true;
        Feasible3 = true;
        Feasible4 = true;
        Feasible5 = true;
        Feasible6 = true;
        Feasible7 = true;
        Feasible8 = true;


        %initial guesses

        LeanTcalc = 62; %Celsius, lean solvent temperature
        RichFcalc = LeanF+1; %kg/s, rich solvent flowrate
        HDcalc = 2.9; %GJ/tonne, heat duty
        PAFlowcalc = 1400; %kg/s, pumparound rate. Range: 800 - 1400 kg/s.
        PATcalc = 30; %Celsius, pumparound temperature. Range: 29.44 - 40.56 °C

        WWFlowcalcAux = 2000; %kg/s, pumparound rate. Range: 250 - 1300 kg/s.
        WWTcalcAux = 30; %Celsius, pumparound temperature. Range: 7 - 60 °C

        CO2Flow = 90; %tonne/hr
        HRcalc = (HDcalc*CO2Flow)/1.055; %heat rate


        % These are used to force the outer while loop to start
        LeanT = LeanTcalc + 10; %Celsius, lean solvent temperature
        RichF = RichFcalc + 10; %kg/s, rich solvent flowrate
        HR = HRcalc + 100; %heat rate, MMBTU/hr
```

```
Tol = 0.001 ; % Tolerance for while loops

ErrorRF = 1;
ErrorHR = 1;
ErrorLT = 1;


%while ( (RichF ~= RichFcalc) && (HR ~= HRcalc) && ( LeanT ~= LeanTcalc ) )
while ( ( abs(ErrorRF) >= Tol ) || ( abs(ErrorHR) >= Tol) || ( abs(ErrorLT) >= Tol ) )
%% absorber-intercooler loop

if ( (Feasible == false) || (Feasible1 == false) || (Feasible2 == false) || (Feasible3 == false) || (Feasible4 == false) || (Feasible5
== false) || (Feasible6 == false) || (Feasible7 == false) || (Feasible8 == false) )
    break;
end

% These are used to force the inner while loop to start
LeanT = LeanTcalc;
RichF = RichFcalc;
HR = HRcalc;

PAT = PATcalc + 1;
PAFlow = PAFlowcalc + 1;


ErrorPAF = 1;
ErrorPAT = 1;

%while ( (PAFlow ~= PAFlowcalc) | (PAT ~= PATcalc) )
```

```
while ( ( abs(ErrorPAF) >= Tol ) || ( abs(ErrorPAT) >= Tol) )

    % Refresh input variables
    PAFlow = PAFlowcalc;
    PAT = PATcalc;

    % Abs Model Vars
    % X 1 - LeanLDG
    % X 2 - HR
    % X 3 - PAFlow
    % X 4 - PAT
    % X 5 - LeanF
    % X 6 - LeanT


    % Absorber model

    RichFcalc =  - 127.696934086034 * LeanLDG - 0.00294906795659493 * HR + 0.0481844127148734 * PAFlow -
0.054796950793517 * PAT + 1.11647266586793 * LeanF + 0.0257756931513651 * LeanT + 495.147215592588 * LeanLDG^2 -
0.0000202722978695733 * PAFlow^2 - 0.0102160108621226 * PAT^2 + 0.0000138888793558139 * LeanF^2 - 0.0275216827152873
* LeanLDG*PAFlow - 0.216306712915534 * LeanLDG*LeanF + 0.0000114618859747042 * HR*PAFlow + 0.0000465397918255126
* PAFlow*LeanT + 0.000281832572993301 * PAT*LeanF - 0.00151365842797987 * LeanF*LeanT - 9.77792426634494E-08 *
HR*PAFlow*PAT;

    % Rich Stream LDG * 1.08

    RichLDG = ( 2.0934426511671 * LeanLDG - 0.000233006915028512 * HR + 0.000156401448758508 * PAFlow +
0.00318556419794584 * PAT + 0.00066567044512814 * LeanF - 4.00321832520057 * LeanLDG^2 - 2.04439506862554E-08 *
PAFlow^2 - 0.0000230714133451729 * PAT^2 - 7.97251162492881E-07 * LeanF^2 - 1.07744107744081E-10 * LeanF^3 +
0.000761728395062192 * LeanLDG*HR - 0.00020633750173639 * LeanLDG*PAFlow - 0.00919030107327374 * LeanLDG*PAT -
0.00229319747913229 * LeanLDG*LeanF + 1.78804170739637E-08 * HR*PAFlow + 7.8716049382737E-07 * HR*LeanF -
1.50577642322047E-06 * PAFlow*PAT - 2.53755611618102E-07 * PAFlow*LeanF - 1.96366542447555E-06 * PAT*LeanF -
```

7.46596398770412E-08 * LeanF*LeanT + 0.0000127215505648893 * (LeanLDG*LeanF)^2 - 2.87654320987757E-06 * LeanLDG*HR*LeanF + 6.48297491039487E-07 * LeanLDG*PAFlow*LeanF + 2.13019199061804E-09 * PAFlow*PAT*LeanF + 1.04184789508876E-10 * (LeanLDG*PAFlow*PAT)^2 + 1.04827510504808E-09 * (LeanLDG*PAT*LeanF)^2 + 0.0500591813614916)*1.08;

% Rich Stream PZ molality / 1.08

RichPZMolal = (4.60190788415253 * LeanLDG - 0.000441653466367968 * PAFlow + 0.0144326801166424 * PAT + 0.00197724438413336 * LeanF + 0.0144517765750211 * LeanT - 11.1657744562296 * LeanLDG^2 + 5.16233766233764E-07 * PAFlow^2 + 0.000209190932645793 * PAT^2 - 0.0000024443602693603 * LeanF^2 - 0.00303419952210228 * LeanLDG*PAFlow + 0.00166127041019521 * LeanLDG*LeanF - 5.08540921021141E-07 * HR*PAFlow + 2.62322775833737E-07 * HR*LeanF - 1.63381495395511E-06 * PAFlow*LeanF - 4.94567987469198E-06 * PAFlow*LeanT - 0.0000395302499366375 * PAT*LeanF + 9.17264038231694E-06 * LeanLDG*PAFlow*LeanF + 8.03110269871374E-10 * HR*PAFlow*LeanF + 5.72166547363202E-09 * PAFlow*LeanF*LeanT + 3.20756953490218E-07 * (LeanLDG*PAT*LeanT)^2 + 4.47283643830163)/1.08;

% Rich Temperature, °C

RichT = - 6.43700551663871 * LeanLDG + 0.0116695079176926 * HR - 0.0152432938561254 * PAFlow + 0.0606623593912515 * PAT - 0.00429083140630201 * LeanF + 0.00881212121212107 * LeanT + 68.1817489480989 * LeanLDG^2 - 0.00453672714585764 * PAT^2 + 0.0000208549663299662 * LeanF^2 - 3.53074504042524E-09 * PAFlow^3 - 0.028497634323922 * LeanLDG*PAFlow - 0.0621770753504335 * LeanLDG*LeanF - 0.0000996573137538904 * HR*PAT - 0.0000093829629629632 * HR*LeanF + 0.000636426253522741 * PAFlow*PAT + 0.0000232701070376378 * PAFlow*LeanF - 0.000283642266929694 * PAT*LeanF + 0.0000678022650597674 * (LeanLDG*PAFlow)^2 - 7.61753222619386E-10 * (PAFlow*PAT)^2 - 0.0000818945639187528 * LeanLDG*PAFlow*LeanF + 0.00184272659524971 * LeanLDG*PAT*LeanF - 1.29881525811587E-07 * PAFlow*PAT*LeanF + 51.6428560710706;

% Pumparound model

%Outlet Temperature - Converted to C

RichTF = (RichT * 9/5) + 32 ;

```
%Outlet Pressure for given Nr of Pumps
if NrPAPumps == 1
   PAPumpPOut = -7E-08*PAFlow.^3 + 9E-05*PAFlow.^2 - 0.0857*PAFlow + 82.883;
elseif NrPAPumps == 2
   PAPumpPOut = -8E-09*PAFlow.^3 + 2E-05*PAFlow.^2 - 0.0423*PAFlow + 82.699;
end

%Head Requirement - psia

PAPumpHeadReq =  - 1.856180567406373604910 6 * ICBays + 5.733580434139768478019 1 * log(PAFlow) - 5.398755531502583693281 8 * log(ICBays) - 0.889038510948132867806 62E-008 * exp(ICBays) + 0.771416688032617704296 00E-005 * PAFlow^2 + 0.897379810746132960952 44E-001 * ICBays^2 - 0.119863222212089381022 77E-007 * (PAFlow*ICBays)^2 + 0.108752274598139368234 91E-002 * (PAFlow/ICBays)^2 + 1106.4030109344764696289 * (ICBays/PAFlow)^2 - 0.133071327407808574446 77E-006 * (PAFlow/ICBays)^3 - 3523.5875487350531329866 * (ICBays/PAFlow)^3 + 18.046292238036127031364 ;

% Pumparound Pressure Drop - psia - Elevation
% head requirement is embedded here

PADeltaP = - 0.115546815787441761735 90 * RichTF + 0.338959714060505512556 18E-001 * PAFlow/ICBays - 0.511352786530429037625 82 * log(TAmbF) + 0.495319257436056229089 44E-003 * RichTF^2 + 0.162982617006901314357 65E-002 * (PAFlow/ICBays)^2 - 0.896256401484574341471 99E-006 * (PAFlow/ICBays)^3 - 0.161735894500716855516 72E-007 * (RichTF*(PAFlow/ICBays))^2 - 0.555515654418770976540 98E-008 * ((PAFlow/ICBays)*TAmbF)^2 + 9.271247461163287795216 1;

RichDens = 247.00780980117176000022 * RichLDG - 0.424861323769340049061 33 * RichT - 22.767822608800763362069 * (RichLDG).^2 - 0.981070184454102961479 90E-001 * RichLDG*RichT + 1033.0152450461619082489 ; %Rich density - kg/m3

% Absorber Sumb Elevation - psi - 28 ft

PAElev = 28 / (2.31 / (RichDens / 1000) );
```

```
%New Flowrate calculation if not enough head is generated
if PAPumpPOut < ( PAPumpHeadReq + PADeltaP - PAElev )

  if NrPAPumps == 1

    fun = @(PAFlow) (- 1.8561805674063736049106 * ICBays + 5.7335804341397684780191 * log(PAFlow) -
5.3987555315025836932818 * log(ICBays) - 0.88903851094813286780662E-008 * exp(ICBays) + 0.77141668803261770429600E-
005 * PAFlow^2 + 0.89737981074613296095244E-001 * ICBays^2 - 0.11986322221208938102277E-007 * (PAFlow*ICBays)^2 +
0.10875227459813936823491E-002 * (PAFlow/ICBays)^2 + 1106.4030109344764696289 * (ICBays/PAFlow)^2 -
0.13307132740780857444677E-006 * (PAFlow/ICBays)^3 - 3523.5875487350531329866 * (ICBays/PAFlow)^3 +
18.04629223803612703136 4 ...
        - 0.11554681578744176173590 * RichTF + 0.33895971406050551255618E-001 *
PAFlow/ICBays - 0.51135278653042903762582 * log(TAmbF) + 0.49531925743605622908944E-003 * RichTF^2 +
0.16298261700690131435765E-002 * (PAFlow/ICBays)^2 - 0.89625640148457434147199E-006 * (PAFlow/ICBays)^3 -
0.16173589450071685551672E-007 * (RichTF*(PAFlow/ICBays))^2 - 0.55551565441877097654098E-008 *
((PAFlow/ICBays)*TAmbF)^2 + 9.27124746116328779521 61 ...
        - PAElev ...
        - ( -7E-08*PAFlow.^3 + 9E-05*PAFlow.^2 - 0.0857*PAFlow + 82.883 ) );
    x = fzero(fun, PAFlow);

  elseif NrPAPumps == 2

    fun = @(PAFlow) (- 1.8561805674063736049106 * ICBays + 5.7335804341397684780191 * log(PAFlow) -
5.3987555315025836932818 * log(ICBays) - 0.88903851094813286780662E-008 * exp(ICBays) + 0.77141668803261770429600E-
005 * PAFlow^2 + 0.89737981074613296095244E-001 * ICBays^2 - 0.11986322221208938102277E-007 * (PAFlow*ICBays)^2 +
0.10875227459813936823491E-002 * (PAFlow/ICBays)^2 + 1106.4030109344764696289 * (ICBays/PAFlow)^2 -
0.13307132740780857444677E-006 * (PAFlow/ICBays)^3 - 3523.5875487350531329866 * (ICBays/PAFlow)^3 +
18.04629223803612703136 4 ...
        - 0.11554681578744176173590 * RichTF + 0.33895971406050551255618E-001 *
PAFlow/ICBays - 0.51135278653042903762582 * log(TAmbF) + 0.49531925743605622908944E-003 * RichTF^2 +
0.16298261700690131435765E-002 * (PAFlow/ICBays)^2 - 0.89625640148457434147199E-006 * (PAFlow/ICBays)^3 -
```

```
0.16173589450071685551672E-007 * (RichTF*(PAFlow/ICBays))^2 - 0.55551565441877097654098E-008 * ((PAFlow/ICBays)*TAmbF)^2 + 9.2712474611632877952161 ...
                    - PAElev ...
                    - ( -8E-09*PAFlow.^3 + 2E-05*PAFlow.^2 - 0.0423*PAFlow + 82.699));
            x = fzero(fun, PAFlow);

        end

        PAFlowcalc = x;

    end

    %Outlet Pressure for given Nr of Pumps
    if NrPAPumps == 1
        PAPumpPOut = -7E-08*PAFlow.^3 + 9E-05*PAFlow.^2 - 0.0857*PAFlow + 82.883;
    elseif NrPAPumps == 2
        PAPumpPOut = -8E-09*PAFlow.^3 + 2E-05*PAFlow.^2 - 0.0423*PAFlow + 82.699;
    end

    % Pumparound outlet temperature - °F

    PATcalcF = 0.13259278050795317294153 * RichTF - 2.42308296687131008440 02 * (PAFlow/ICBays) + 22.329977167065560905712 * log(RichTF) + 38.03139203535084078566 8 * log((PAFlow/ICBays)) + 14.39238431213591518087 5 * log(TAmbF) + 0.25112646171735045208528E-001 * (PAFlow/ICBays)^2 + 0.25039478162563874250046E-002 * TAmbF^2 - 0.13126478576938523665577E-003 * (PAFlow/ICBays)^3 + 0.25246161166776254612828E-006 * (PAFlow/ICBays)^4 + 0.60107017435266467313089E-007 * (RichTF*(PAFlow/ICBays))^2 - 0.67101263664322938653571E-007 * ((PAFlow/ICBays)*TAmbF)^2 - 182.21397697475541122003;

    % Pumparound outlet temperature - °C

    PATcalc = (PATcalcF - 32) * 5/9;
```

```
        ErrorPAF = (PAFlow - PAFlowcalc) / PAFlowcalc *100;
        ErrorPAT = (HR - HRcalc) / HRcalc *100;

    end




    %% PZAS model

      % Correct rich rate for water balance (water is added at rich
      % storage tank until 5 molal PZ is achieved)
        RichH2OwtFrac = 1 / ( 1 + RichPZMolal*86.136/1000 + RichLDG*RichPZMolal*2*44.01/1000);



        AddH2O = RichFcalc*RichH2OwtFrac * ( RichPZMolal/5 - 1);

      % Total H2O in Rich Stream after water balance fix
        totalh2o = RichH2OwtFrac*RichFcalc + AddH2O;

      % Rich PZ molality after water balance fix
%           RichPZMolal * RichH2OwtFrac*RichFcalc/(RichH2OwtFrac*RichFcalc+AddH2O);

      % Corrected Rich Flow after fix
        RichFPZAS = RichFcalc + RichFcalc*RichH2OwtFrac * ( RichPZMolal/5 - 1);

      %Bypass flowrates

        if CRBP == 0.3 && WRBP > 0.3    %setting range of operation for bypasses
          Feasible1 = false;
        end
```

```
LCRBP = CRBP*RichFPZAS; %CRBP flow rate, kg/s
LWRBP = RichFPZAS*(1-CRBP)*WRBP; %WRBP flow rate, kg/s


% Rich Pump Outlet Pressure - psia

RPOP = 329.7579981 + 67.36264733*RichLDG - 0.251043117*RichFPZAS ;

% Rich-side Cold HX Del P - psia

CHXDP = - 26 * ( LCRBP / 408.309).^2;

% Rich-side Hot HX Del P - psia

RHXDP = -14 * ( LWRBP / 160.58).^2;

% Rich-side Steam Heater DelP - psia

SHDP = -20 *  ( LWRBP / 160.58).^2;

% Control Valve DP to ensure 80 psia at the stripper - Has to
% positive

PStripper = 80; %Stripper pressure, psia, at 0.2 lldg, 150 C stripper ONLY

CVDP = RPOP + CHXDP + RHXDP + SHDP - PStripper;

% Rich Pump Check

RPMCSF = 3293; %Rich pump minimum stable continuous flow - GPM
```

RichDens = 247.00780980117176000022 * RichLDG - 0.42486132376934004906133 * RichT - 22.76782260880076336206 9 * (RichLDG).^2 - 0.98107018445410296147990E-001 * RichLDG*RichT + 1033.0152450461619082489 ; %Rich density - kg/m3

RichFGPM = RichF / RichDens * 60 * 264.172 ; % Rich volumetric flowrate - GPM

if ((RichFGPM <= RPMCSF) || (CVDP <= 0))

Feasible = false;

end

% ALAMO Equations - Stripper Model

LeanTcalc = 209.38220744636 * RichLDG - 0.0346684126445572 * RichFPZAS + 0.599095728584041 * RichT + 0.0449758734141336 * LCRBP + 0.0393726915516799 * LWRBP + 15.2955585774627 * LeanLDG - 363.069202778924 * RichLDG^2 + 0.00323886370542153 * (RichLDG*LWRBP)^2 + 1467.91292464058 * (RichLDG*LeanLDG)^2 + 1.15285874867922E-08 * (RichFPZAS*RichT)^2 - 0.0176608078277384 * (LWRBP*LeanLDG)^2 - 0.0000208691878440675 * (RichLDG*LWRBP)^3 + 0.000212753108487983 * (LWRBP*LeanLDG)^3 - 3.82921662822444E-07 * (RichLDG*RichT*LCRBP)^2 + 136.227903626607 * (LCRBP/RichFPZAS)^2;

HDcalc = - 39.5612206094863 * RichLDG + 0.00108832468036288 * RichFPZAS - 49.6791030223479 * CRBP - 6.15798102526132 * WRBP - 0.0153084036872078 * RichT - 190.534297534916 * LeanLDG + 44.4984309675978 * RichLDG^2 + 130.563904746233 * CRBP^2 - 43.6738614262279 * WRBP^2 + 390.192377462923 * LeanLDG^2 - 345.722071230588 * CRBP^3 + 49.3402383650732 * WRBP^3 + 6.18272224774559E-06 * (RichLDG*RichFPZAS)^2 + 487.192216837083 * (RichLDG*CRBP)^2 - 13.6169836577685 * (RichLDG*WRBP)^2 + 0.0014708294067233 * (RichLDG*RichT)^2 - 79.640813330341 * (RichLDG*LeanLDG)^2 - 0.0000139605447790558 * (RichFPZAS*CRBP)^2 + 543.662596139205 * (CRBP*WRBP)^2 + 2085.60281181739 * (CRBP*LeanLDG)^2 + 1203.51261288316 * (WRBP*LeanLDG)^2 - 0.00192884389972827 * (RichT*LeanLDG)^2 - 935.549851413922 * (RichLDG*CRBP)^3 + 13.4608143894934 * (RichLDG*WRBP)^3 - 2785.65626154557 * (CRBP*WRBP)^3 + 0.000177053935551814 * (CRBP*RichT)^3 + 6740.15113900706 * (CRBP*LeanLDG)^3 - 6098.0121453558 * (WRBP*LeanLDG)^3 - 0.000218049053387136 * (RichLDG*RichFPZAS*LeanLDG)^2 - 1951.9631715455 * (RichLDG*CRBP*WRBP)^2 - 9273.32234956026 * (RichLDG*CRBP*LeanLDG)^2 + 74.4040326454073 * (RichLDG*WRBP*LeanLDG)^2 - 0.128000689862346 * (CRBP*RichT*LeanLDG)^2 + 24036.5209441246 * (RichLDG*CRBP*WRBP)^3 + 39.7276639740566 ;

```
CO2Flow = - 32.8093344360339 * RichLDG + 0.16452689974639 * RichFPZAS + 1.22273377989589 * CRBP +
1.10569175487715 * WRBP - 232.880216121543 * LeanLDG + 681.997717226559 * RichLDG^2 - 0.000205920527000715 *
RichFPZAS^2 + 167.949581168539 * LeanLDG^2 - 877.232742746562 * RichLDG^3 + 1.22288022632859E-07 * RichFPZAS^3 +
0.00299374117557422 * (RichLDG*RichFPZAS)^2 + 581.858738951054 * (RichLDG*LeanLDG)^2 - 0.00503305052328248 *
(RichFPZAS*LeanLDG)^2 - 0.0000040481121653161 * (RichLDG*RichFPZAS)^3 + 0.0000105243221837983 *
(RichFPZAS*LeanLDG)^3;

%HEAT DUTY IN GJ/tonne
HRcalc = (HDcalc*CO2Flow/1.055); %MMBTU/hr

% Feasibility flag for Gas-fired boiler capacity
if ( HR > 311.6 * 0.94)
Feasible3 = false;
end

% Lean Pump Density and Volumetric flowrate

LeanDens = - 0.44475896421051980267336 * LeanTcalc - 0.24114481350928400205515E-006 * (LeanTcalc).^2 +
1081.6296369739688998379; %Lean Density - kg/m3

LeanFGPM = LeanF / LeanDens * 60 * 264.172;  % Lean volumetric flowrate - GPM


% Lean Pump net positive suction head required - ft - regressed from
% spec sheet

LNPSHR = 9.40656E-08*(LeanFGPM)^2 - 8.62945E-04*LeanFGPM + 1.10736E+01;

LNPSHRpsi = LNPSHR / (2.31 / (LeanDens / 1000) ) ;

% Stripper sump level - ft
```

```
% Lean Vol Flow * Residence Time / ( pi * stripper radius^2)

   SSL = ( LeanF / LeanDens * 60  * 2 / ( 3.1415 * (3.81/2).^2 ) ) /0.3048;



% Lean solvent bubble point entering lean pump, vapor
% fraction : 1e-5

   PLeanBubble = 4e-5*(LeanTcalc).^3 - 0.0048*(LeanTcalc).^2 + 0.2625*LeanTcalc - 4.5443;  % psia



% Cold exchanger lean side DP

   CHXLDP = -33.8*( LeanF / 440.3 ).^2;

% Hot exchanger lean side DP

   HHXLDP = -14*( LeanF / 440.3 ).^2;

%Balance pressure in lean solvent going into lean pump

   LeanBalP = PStripper + SSL / (2.31 / (LeanDens / 1000) ) + HHXLDP + CHXLDP ;

   % Lean solvent bubble point vs Lean Pump inlet P - NPSH
   % check

      if PLeanBubble > ( LeanBalP - LNPSHRpsi)

         Feasible2 = false;

      end
```

```
%                % Required NPSH vs available NPSH check
%
%                  if LNPSHRpsi > LeanBalP
%
%                    Feasible3 = false;
%
%                  end

count = 1;



ErrorRF = (RichF - RichFcalc) / RichFcalc *100;
ErrorHR = (HR - HRcalc) / HRcalc *100;
ErrorLT = (LeanT - LeanTcalc) / LeanTcalc *100;



        end



        %Electrical Work



        % Lean Pump Power Calculation

        % Lean Pump head requirements from absorber inlet height - ft

          LPHRAbs = 85 ;

        % Lean Pump frictional losses - psi

          LPFDP = 10;
```

```
%Lean Pump total DelP  - ft
% psi to ft formula from eng toolbox
   LPTDP = (LPHRAbs - SSL) + LPFDP * 2.31 / (LeanDens / 1000);

% Lean Pump Outlet Head Performance Curve at Design Speed (705 RPM)
% Regressed from Spec Sheet

   %LPHDesign = -1.91812E-07*(LeanFGPM)^2 - 7.23430E-04*LeanFGPM + 5.09233E+01 ;

% Lean Pump Outlet Head Performance Curve at Specified Speed
% Using Pump Laws

% LPH = LPHDesign * ( Desired RPM / Design RPM ) ^2

% Now we have a Del P and a Flow rate so we have to calculate what is
% the speed that produces a pump curve that intersects the system curve
% at the Op. point
% This is the same as getting the RPM such that LPTDP = LPH

   %LPMinRPM = 705 ; %This provides the initial guess for the solver

   LeanFGPMAux = 8000 ; %This provides the initial guess for the solver

   fun = @(LeanFGPMAux) ( LPTDP - (-1.91812E-07*(LeanFGPMAux)^2 - 7.23430E-04*LeanFGPMAux + 5.09233E+01) * ( LeanFGPM / LeanFGPMAux ) ) ;
   x = fzero(fun, LeanFGPMAux);

   LeanFGPMAux = x;  %finding the new speed of the pump that can output a pressure that satisfies the new head downstream of lean pump or (pump head - delP = 0)

% Calculating new pump speed
```

```
LPMinRPM = ( LeanFGPM  / LeanFGPMAux ) * 705;

% Now we calculate the power required

% Lean Pump Power Requirements at Design Speed (705 RPM)
% Regressed from spec sheet

LPPDesign = -2.07099E-07*(LeanFGPMAux)^2 + 8.25077E-04*LeanFGPMAux + 1.02094E+02 ;

% Lean Pump Power - MW

LPP = ( LPPDesign * ( LPMinRPM / 705 ) ^3 ) / 1341;

% RPP - Rich Pump Power, MW

% Rich Flow used is after addition of water
RPP = (967.5682566 - 0.003870061 * RichT.^2 + 0.00043598 * RichFPZAS.^2) / 1341 ;

% ICPP - intercooler pump power, MW

ICPP = NrPAPumps * ( (337.23421 - 0.1337.*PAFlow/NrPAPumps) - 0.0002.*((PAFlow/NrPAPumps).^2) + 1.249e-6.*((PAFlow/NrPAPumps).^3) - 1.0246e-9.*((PAFlow/NrPAPumps).^4) )./1341;

% HRSGFP - HRSG Fans power, for one HRSG fan, MW (2 HRSG Fans per Train)

HRSGFP = (0.467885362168682 * HR - 0.515645841463743 * PAFlow - 5.01162869498661 * PAT - 0.251447407492601 * LeanF - 0.0929320702096328 * LeanT + 0.000234948828341722 * PAFlow^2 + 0.103721993004652 * PAT^2 + 0.000129351851851876 * LeanF^2 - 0.108890164771078 * LeanLDG*PAFlow + 0.00548446436229834 * PAFlow*PAT + 0.000161862495927009 * PAFlow*LeanF - 0.000506732649071357 * PAFlow*LeanT + 0.00217727272727249 * LeanF*LeanT - 3.58505683355519E-08 * (PAFlow*PAT)^2 + 5.36799946007562E-06 * HR*PAT*LeanF + 0.0000364088289497072 * HR*PAT*LeanT + 2455.5898665727)/1000;
```

```
%Boiler fan power, MW (1 Boiler Fan per Train)

BLRFP = (1281.96032766061 * LeanLDG - 3.21171879539977 * HR + 0.184871693237126 * PAFlow - 0.462235589249222 * PAT - 0.00189869121320709 * LeanF + 1.295573884001 * LeanT - 1670.39965552172 * LeanLDG^2 + 0.0238743671100638 * HR^2 + 0.0000213508461235734 * PAFlow^2 + 0.0188763183167645 * PAT^2 - 0.0000379194209919668 * HR^3 - 1.06482974910381 * LeanLDG*HR - 1.36704562425306 * LeanLDG*PAFlow - 5.62197580645018 * LeanLDG*LeanT - 0.00028051171053515 * HR*PAFlow + 0.00115981878337941 * HR*PAT + 0.0000236591723688511 * HR*LeanF + 0.000250215997750067 * PAFlow*PAT + 0.0000681841805148263 * PAFlow*LeanF - 0.00217439743831444 * PAFlow*LeanT - 1.38170698404623E-07 * (HR*PAT)^2 + 0.00231772700119457 * LeanLDG*HR*PAFlow + 0.0126568100358397 * LeanLDG*PAFlow*LeanT - 1.95356793743892E-07 * HR*PAFlow*LeanF - 1.98580291100007E-06 * HR*PAFlow*LeanT)/1000;

%Boiler fan speed, RPM

BLRFRPM = 1.68044526495903 * HR - 0.209730430181217 * PAFlow - 0.29305829896423 * PAT - 0.0232641630391987 * LeanF - 0.141257402272628 * LeanT + 0.00421739087760222 * HR^2 + 0.0000752794625229565 * PAFlow^2 + 0.0286362985697147 * PAT^2 + 0.0000278221572518892 * LeanF^2 - 0.279589867433765 * LeanLDG*HR + 0.0662088645584766 * LeanLDG*PAFlow + 0.0000802567267608117 * HR*PAFlow + 0.00141608444014494 * HR*PAT - 0.000101919245117856 * HR*LeanF + 0.00140100081944559 * PAFlow*PAT + 0.0000394936312968411 * PAFlow*LeanF - 0.00149127410332858 * PAT*LeanF + 0.00115624152020181 * LeanF*LeanT - 1.14515552777163E-07 * (HR*PAT)^2 + 5.52947565398057E-08 * (PAT*LeanF)^2 - 1.69390314786943E-06 * HR*PAFlow*PAT + 1080.5331535315;

%Boiler fan speed feasibility flag
if (BLRFRPM > 1756)
   Feasible5 = false;
end

%Intercooler fans power

ICFP = 29.4 / 1341 * ICFans;

%          %Compressor power - MW - 65F
```

```
%
%                CP = 0.0644*CO2Flow + 0.2473;  %MW, power for 65 F
%
%              % Compressor Feasibility flag for 65F and 40F
%              if (CO2Flow > 97.32)
%                Feasible7 = false;
%              end
%

            % Compressor inlet pressure as a function of lean loading
            % (regressed from aspen) - bar

              CPInlet = 58.354*LeanLDG^2 - 6.5089 * LeanLDG + 4.4976;

            % Work at 0.2 LeanLDG / 5.5 bar from YJ correlation - kJ/mol

              WorkBaseCase = 8.876499867 ;

            % Compressor Power - MW - Regressed for all temperatures
            % and corrected for inlet P (using YJ Correlation)

            % CompWork =  15.3 - 4.6 * log(CPInlet) + 0.81 * log(CPInlet)^2 - 0.24 * log(CPInlet)^3 + 0.03 * log(CPInlet)^4;

            CP = (0.129590895 + 0.004676228*TAmb +0.064890173*CO2Flow) * ((15.3 - 4.6 * log(CPInlet) + 0.81 * log(CPInlet)^2
- 0.24 * log(CPInlet)^3 + 0.03 * log(CPInlet)^4)/WorkBaseCase) ;

%              %Compressor power - MW - 105F
%
%                CP = 0.0654*CO2Flow + 0.2854;  %MW, power for 105 F ONLY

            % Compressor Feasibility Flag - Regressed for all
            % temperatures and corrected for inlet density (from Aspen)
```

```
CompInDensBase = 0.29422; % lb/ft3 total gas density after stripper

MaxCO2Flow = (-0.2233*TAmb+101.15) * (-34.498*LeanLDG^2+14.868*LeanLDG-1.2995)/0.29422; % tonne/hr

% Compressor Feasibility flag for 105F
if (CO2Flow > MaxCO2Flow)
   Feasible7 = false;
end

%          %Compressor power - MW - 40F
%
%             CP = 0.0649*CO2Flow + 0.1504;  %MW, power for 65 F
%
%          % Compressor Feasibility flag for 65F and 40F
%          if (CO2Flow > 100.64)
%             Feasible7 = false;
%          end


% Water Wash Loop


% Absorber Gas Outlet Equations

   % Absorber - Gas Outlet Temperature - C

   AbsGOutT =  191.94641785965 * LeanLDG - 0.0192200276864391 * PAFlow + 0.140556884980275 * PAT +
0.141107514805723 * LeanF + 0.0516336945691948 * LeanT - 424.246903105767 * LeanLDG^2 + 9.43868148518392E-06 *
PAFlow^2 + 0.00180659293327299 * PAT^2 - 0.000115224631703959 * LeanF^2 - 0.000868552831562998 * LeanT^2 -
0.0416440885165723 * LeanLDG*PAFlow - 0.449273908895619 * LeanLDG*LeanF + 0.46192130210152 * LeanLDG*LeanT -
1.82352447730514E-06 * HR*PAFlow + 0.0000057935444556301 * HR*LeanF + 0.000198172633753265 * PAFlow*PAT -
```

0.0000382246306608415 * PAFlow*LeanF + 0.0000663964748293619 * PAFlow*LeanT - 0.000300008886540879 * PAT*LeanF + 0.000440452697018819 * PAT*LeanT + 0.000373683614730104 * LeanF*LeanT + 0.00126765455151938 * (LeanLDG*LeanF)^2 - 6.48666675223393E-10 * (PAFlow*PAT)^2 + 1.01437165565719E-08 * (PAT*LeanF)^2 + 0.000211212664277214 * LeanLDG*PAFlow*LeanF - 2.67607377614853E-07 * PAFlow*PAT*LeanF + 1.21918377321618E-07 * PAFlow*LeanF*LeanT - 3.83922223859236E-06 * PAT*LeanF*LeanT - 1.05049971033873E-08 * (LeanLDG*PAFlow*LeanT)^2 + 11.8759367810314;

% Absorber - Gas Outlet Flowrate - kg/s

AbsGOutF = 18.8952057344126 * LeanLDG + 0.128222074236995 * HR - 0.048346765531838 * PAFlow + 0.0333753756106103 * PAT - 0.11789176774976 * LeanF - 0.022350680188968 * LeanT - 228.962215351567 * LeanLDG^2 + 0.0000202775400104944 * PAFlow^2 + 0.010630126605324 * PAT^2 - 0.0000136734006734021 * LeanF^2 + 0.0280432347670281 * LeanLDG*PAFlow + 0.22074382716048 * LeanLDG*LeanF - 0.0000114359783190629 * HR*PAFlow - 0.0000212878787879199 * HR*LeanT - 0.000045986681329416 * PAFlow*LeanT - 0.000279757247744596 * PAT*LeanF + 0.00151827777777774 * LeanF*LeanT + 9.84819637368474E-08 * HR*PAFlow*PAT + 444.232557759862;

% Absorber - Gas Outlet Water Mol Frac

AbsGOutH2Omolfrac = 0.764028040207562 * LeanLDG + 0.0000254304567812879 * HR - 0.0000858635823450254 * PAFlow - 0.00296103010001061 * PAT + 0.000326598768533908 * LeanF + 0.00010949228519425 * LeanT - 1.61090248087824 * LeanLDG^2 + 6.51137199868883E-08 * PAFlow^2 + 0.000014764481525692 * PAT^2 - 1.22256992421349E-07 * LeanF^2 - 1.87768238149056 * LeanLDG^3 - 4.56509539843314E-10 * LeanF^3 - 0.000133405502242782 * LeanLDG*PAFlow + 0.0208779206059022 * LeanLDG*PAT - 0.00168784261879854 * LeanLDG*LeanF - 1.03453893776508E-08 * HR*PAFlow + 5.1919191919211E-08 * HR*LeanF - 2.57883675464314E-07 * PAFlow*LeanF + 9.58006002569599E-06 * PAT*LeanF + 3.74136363636384E-06 * LeanF*LeanT - 4.09377087394381E-07 * (LeanLDG*PAFlow)^2 + 8.32785569300346E-06 * (LeanLDG*LeanF)^2 - 2.43920775651785E-06 * LeanLDG*HR*LeanT + 1.32697132616483E-06 * LeanLDG*PAFlow*LeanF - 0.0000638161709672846 * LeanLDG*PAT*LeanF + 1.27219850693903E-09 * (LeanLDG*PAT*LeanF)^2;

% Absorber - Gas Outlet CO2 Mol Frac

AbsGOutCO2molfrac = + 0.995078840133856 * LeanLDG + 0.0000678601317835715 * HR - 4.32904768971773E-06 * PAFlow - 0.000418132334602045 * PAT - 0.000284864876412189 * LeanF - 0.0000424166666667429 * LeanT - 6.34905840285832 * LeanLDG^2 + 2.20000327954903E-09 * PAFlow^2 + 2.96356021854142E-06 * PAT^2 + 7.63153030429367E-

08 * LeanF^2 + 12.2858439082775 * LeanLDG^3 + 1.61560044893238E-10 * LeanF^3 - 0.000195123456789074 * LeanLDG*HR - 0.0000159834229390874 * LeanLDG*PAFlow + 0.00112210757610297 * LeanLDG*PAT + 0.00101808584560823 * LeanLDG*LeanF - 1.56239817530577E-09 * HR*PAFlow - 1.56989898989438E-07 * HR*LeanF + 3.95533656154912E-08 * PAFlow*PAT + 3.77294358606906E-07 * PAT*LeanF + 8.12626262627885E-08 * LeanF*LeanT - 3.71030689300026E-06 * (LeanLDG*LeanF)^2 + 6.25925925923725E-07 * LeanLDG*HR*LeanF - 1.87368495718553E-10 * (LeanLDG*PAT*LeanF)^2;

% Absorber - Gas Outlet PZ Mol Frac

AbsGOutPZmolfrac = - 0.00444706244720876 * LeanLDG + 2.89057239058017E-08 * HR + 1.62671383251766E-07 * PAFlow + 2.0531958755115E-07 * PAT + 1.78465905368324E-06 * LeanF - 9.99817060494936E-07 * LeanT + 0.0391781071284128 * LeanLDG^2 + 1.66202255797819E-08 * PAT^2 - 1.03488537579099E-09 * LeanF^2 + 2.06439393939307E-08 * LeanT^2 - 0.0723412821203043 * LeanLDG^3 - 1.02007923169832E-06 * LeanLDG*PAFlow - 5.67179516498254E-06 * LeanLDG*PAT - 9.00241966154559E-06 * LeanLDG*LeanF - 0.0000116655092592648 * LeanLDG*LeanT - 6.9696969697084E-10 * HR*LeanT - 3.99579830563436E-10 * PAFlow*LeanF - 2.14442815249102E-10 * PAFlow*LeanT + 8.82648986928887E-10 * PAT*LeanF + 8.26220175165871E-09 * PAT*LeanT + 6.26606060605993E-09 * LeanF*LeanT + 7.77418042788147E-10 * (LeanLDG*PAFlow)^2 + 2.03227309465134E-08 * (LeanLDG*LeanF)^2 - 4.55696320566985E-10 * LeanLDG*PAFlow*PAT + 1.82925627240016E-09 * LeanLDG*PAFlow*LeanF;

% Absorber - Gas Outlet O2 Mol Frac

AbsGOutO2molfrac = - 0.0000210557239057183 * HR + 0.0000164939512671575 * PAFlow + 0.0000266589987213829 * PAT + 2.13422935407686E-06 * LeanF + 0.0000161136363636547 * LeanT - 9.07899791751642E-09 * PAFlow^2 - 3.52816478427082E-06 * PAT^2 + 2.50168350168359E-08 * LeanF^2 + 0.0952249820773028 * LeanLDG^3 + 0.0000126803165239915 * LeanLDG*PAFlow + 0.0000352043682785317 * LeanLDG*LeanF - 2.06498316498379E-08 * HR*LeanF - 2.51515151515656E-08 * HR*LeanT - 8.79898518626836E-08 * PAFlow*PAT + 2.54008522048717E-08 * PAFlow*LeanF - 1.07407800409873E-08 * PAT*LeanF - 6.08434343434376E-07 * LeanF*LeanT + 5.26849681431565E-08 * (LeanLDG*PAFlow)^2 - 1.57064640776448E-07 * LeanLDG*PAFlow*LeanF + 3.09090909091003E-10 * HR*LeanF*LeanT + 1.91545942803074E-10 * PAFlow*PAT*LeanF + 0.122580180176811;

% Absorber - Gas Outlet N2 Mol Frac

AbsGOutN2molfrac = 1 - AbsGOutH2Omolfrac - AbsGOutCO2molfrac - AbsGOutPZmolfrac - AbsGOutO2molfrac;

% Absorber - Gas Outlet Flowrates - kg/h

AbsGOutH2OF = 3600 * AbsGOutF * (18.015 * AbsGOutH2Omolfrac) / (18.015 * AbsGOutH2Omolfrac + 44.01 * AbsGOutCO2molfrac + 86.136 * AbsGOutPZmolfrac + 31.998 * AbsGOutO2molfrac + 28.0134 * AbsGOutN2molfrac);

AbsGOutCO2F = 3600 * AbsGOutF * (44.01 * AbsGOutCO2molfrac) / (18.015 * AbsGOutH2Omolfrac + 44.01 * AbsGOutCO2molfrac + 86.136 * AbsGOutPZmolfrac + 31.998 * AbsGOutO2molfrac + 28.0134 * AbsGOutN2molfrac);

AbsGOutPZF = 3600 * AbsGOutF * (86.136 * AbsGOutPZmolfrac) / (18.015 * AbsGOutH2Omolfrac + 44.01 * AbsGOutCO2molfrac + 86.136 * AbsGOutPZmolfrac + 31.998 * AbsGOutO2molfrac + 28.0134 * AbsGOutN2molfrac);

AbsGOutN2F = 3600 * AbsGOutF * (28.0134 * AbsGOutN2molfrac) / (18.015 * AbsGOutH2Omolfrac + 44.01 * AbsGOutCO2molfrac + 86.136 * AbsGOutPZmolfrac + 31.998 * AbsGOutO2molfrac + 28.0134 * AbsGOutN2molfrac);

AbsGOutO2F = 3600 * AbsGOutF * (31.998 * AbsGOutO2molfrac) / (18.015 * AbsGOutH2Omolfrac + 44.01 * AbsGOutCO2molfrac + 86.136 * AbsGOutPZmolfrac + 31.998 * AbsGOutO2molfrac + 28.0134 * AbsGOutN2molfrac);

% Water Balance

% Boiler Flue Gas Stream - Flowrate - kg/h

BFGFlow = (983.65 * HRcalc + 4546.1) * 0.453592;

% Water in Boiler Flue Gas Stream - Flowrate - kg/h

BFGH2O = BFGFlow * (18.015 * 0.1786) / (18.015 * 0.1786 + 44.01 * 0.0834 + 31.998 * 0.0247 + 28.0134 * 0.7133);

% Water in HRSG Flue Gas - kg/h - Select Case According to model

% 40°F 95% No Duct Burning

```
    HRSGH2O = 77482.5;

  % 65°F 100% w/ Duct Burning

    %HRSGH2O = 80717.3;

  % 65°F 95% No Duct Burning

    %HRSGH2O = 73252.4;

  % 65°F 72% No Duct Burning

    %HRSGH2O = 55578.9;

  % 105°F 95% No Duct Burning

    % HRSGH2O = 82257.5;

% Water at the WW Outlet - kg/h

  WWH2OTarget = BFGH2O + HRSGH2O ;

% Matrix to store results

  WWRes = zeros(WWBayMax - WWBayMin + 1,3);

for WWBays = WWBayMin : ( WWBayMax )

  WWFlowcalc = WWFlowcalcAux; %kg/s, pumparound rate. Range: 250 - 1300 kg/s.
  WWTcalc = WWTcalcAux; %Celsius, pumparound temperature. Range: 7 - 60 °C
```

```
ErrorWWF = 1;
ErrorWWT = 1;

%while ( (PAFlow ~= PAFlowcalc) | (PAT ~= PATcalc) )
while ( ( abs(ErrorWWF) >= Tol ) || ( abs(ErrorWWT) >= Tol) )

% Water Wash - Liquid Inlet Flowrate - kg/s

   %WWLinF

% Water Wash - Liquid Inlet Temperature - C

  %WWLinF

% Refresh input variables
  WWLinF = WWFlowcalc;
  WWLinT = WWTcalc;



% Water Wash - Liquid Outlet Flowrate - kg/s

    WWLOutFlow = 0.6756595399605727081393 5 * WWLinF + 3.9936647965887743794156 * WWLinT + 5.1819491490754270301977 * AbsGOutT - 0.1607595108871247846504 8 * AbsGOutF - 0.1461860394435116343621 3E-003 * AbsGOutH2OF ...
        - 0.1368876453022583304132 4E-003 * WWLinF^2 - 0.2726210191459630532984 1E-001 * WWLinT^2 - 0.1032520148692993161576 6 * AbsGOutT^2 + 0.2031885698942904026637 8E-003 * AbsGOutF^2 + 0.5504430683049139768641 3E-007 * WWLinF^3 ...
        - 0.4603217899276820588422 5E-005 * WWLinT^3 + 0.5970246455470963912667 8E-003 * AbsGOutT^3 + 0.2195490456793956421388 5E-002 * WWLinF*WWLinT + 0.6767649011719391663466 4E-002 * WWLinF*AbsGOutT - 0.1591113080271574120767 9E-003 * WWLinF*AbsGOutF ...
```

+ 0.23284053765919169313431E-006 * WWLinF*AbsGOutH2OF + 0.10794957763848339166473E-007 * WWLinF*AbsGOutCO2F - 0.39454198456892831947673E-001 * WWLinT*AbsGOutT - 0.18460343722826071718307E-002 * WWLinT*AbsGOutF - 0.18325117778472335649094E-005 * WWLinT*AbsGOutH2OF ...

+ 0.51636416437517119407824E-003 * AbsGOutT*AbsGOutF - 0.27431194750106307564549E-006 * AbsGOutF*AbsGOutH2OF - 0.67894371328860351342159E-008 * (WWLinF*WWLinT)^2 - 0.20020444947368072089086E-007 * (WWLinF*AbsGOutT)^2 + 0.29568223946639886295744E-005 * (WWLinT*AbsGOutT)^2 ...

+ 0.34097904955822584526829E-007 * (WWLinT*AbsGOutF)^2 - 0.76100001526902231199995E-005 * WWLinF*WWLinT*AbsGOutT - 0.26404507208373318004216E-005 * WWLinF*WWLinT*AbsGOutF + 0.35019621395778556999278E-005 * WWLinF*AbsGOutT*AbsGOutF ...

+ 0.48199241289003804281457E-005 * WWLinT*AbsGOutT*AbsGOutF + 0.11961237016758635182995E-008 * WWLinT*AbsGOutF*AbsGOutH2OF - 4.27763684518971132320 08 * WWLinF/WWLinT + 20.702360109524512665757 * WWLinF/AbsGOutT - 34.30541153917639718429 2 * WWLinF/AbsGOutF ...

- 0.94142798490628742946740 * WWLinF/AbsGOutCO2F + 3188.5612305959193690796 * WWLinT/WWLinF - 502.64364031061580817550 * WWLinT/AbsGOutT - 16357.311079544420863385 * WWLinT/AbsGOutH2OF - 1175.1346880367693756853 * AbsGOutT/WWLinF + 37.71291553262107498767 4 * AbsGOutT/WWLinT ...

- 7.72372723065920663287 90 * AbsGOutF/WWLinF - 0.18182342874903956175814 * AbsGOutF/WWLinT + 0.70828886374227198463593E-001 * AbsGOutH2OF/WWLinF - 0.33639738708849797194089E-003 * AbsGOutH2OF/WWLinT + 0.20229576487739476392536E-001 * (WWLinF/WWLinT)^2 ...

- 0.95321767626147579921536E-001 * (WWLinF/AbsGOutT)^2 + 2.8103969243837467750780 * (WWLinF/AbsGOutF)^2 - 9786.4598622414705459960 * (WWLinT/WWLinF)^2 + 216.77925257980322726326 * (WWLinT/AbsGOutT)^2 + 937.42694328308732565347 * (AbsGOutT/WWLinF)^2 ...

- 1.2381621181442918899762 * (AbsGOutT/WWLinT)^2 + 0.39285893914609919871079E-008 * (AbsGOutH2OF/WWLinT)^2 - 0.42705942566107106604482E-004 * (WWLinF/WWLinT)^3 + 14575.049643033182292129 * (WWLinT/WWLinF)^3 - 45.75065281859887278415 0 * (WWLinT/AbsGOutT)^3;

% Water Wash - Liquid Outlet Temperature - C

WWLOutT = - 0.25867835624733886978888 * WWLinF - 0.44756198469824531871453 * WWLinT + 4.10795627958760256603 91 * AbsGOutT - 1.22401394327788559657 22 * AbsGOutF - 0.20731901517892799128619E-003 * AbsGOutH2OF ...

+ 0.12065440088339570714419E-003 * WWLinF^2 - 0.88844211687093346818678E-002 * WWLinT^2 + 0.15148795195701997631788E-001 * AbsGOutT^2 + 0.35552632750278818918321E-002 * AbsGOutF^2 ...

- 0.160315787449596061499 52E-007 * WWLinF^3 + 0.397155708152316451096 07E-004 * WWLinT^3 - 0.316479758890267570819 47E-005 * AbsGOutF^3 + 0.183865623350857221481 04E-002 * WWLinF*WWLinT ...

+ 0.114885500920810005275 05E-002 * WWLinF*AbsGOutT + 0.186081722138640114332 79E-003 * WWLinF*AbsGOutF + 0.205368364389833559907 05E-006 * WWLinF*AbsGOutH2OF + 0.420048284313736825651 42E-002 * WWLinT*AbsGOutT ...

- 0.764038294122142201507 40E-003 * WWLinT*AbsGOutF - 0.147745317767203585610 61E-005 * WWLinT*AbsGOutH2OF + 0.324201546748051567040 09E-002 * AbsGOutT*AbsGOutF + 0.219078348150186237093 23E-006 * AbsGOutF*AbsGOutH2OF ...

- 0.382785937019579276137 97E-008 * (WWLinF*WWLinT)^2 - 0.914443639546060237224 94E-008 * (WWLinF*AbsGOutT)^2 + 0.322880669055549461178 15E-006 * (WWLinT*AbsGOutT)^2 + 0.168048731007219018746 60E-007 * (WWLinT*AbsGOutF)^2 ...

- 0.282240185322902320962 07E-007 * (AbsGOutT*AbsGOutF)^2 - 0.394086341699609475408 34E-005 * WWLinF*WWLinT*AbsGOutT - 0.134227750292221301475 26E-005 * WWLinF*WWLinT*AbsGOutF - 0.416824356528791467352 45E-005 * WWLinF*AbsGOutT*AbsGOutF ...

+ 0.184513915956911909177 78E-005 * WWLinT*AbsGOutT*AbsGOutF + 0.148434528872062813493 00E-008 * WWLinT*AbsGOutF*AbsGOutH2OF - 0.262868167360916338282 10 * WWLinF/WWLinT + 0.980724674874588253636 89 * WWLinF/AbsGOutT - 29.831708534808974775387 * WWLinF/AbsGOutF ...

+ 9843.3589284918307384942 * WWLinF/AbsGOutH2OF + 201.51054112631700832026 * WWLinT/WWLinF + 75.256745574607890603147 * AbsGOutT/WWLinF + 2.963224696756595388791 3 * AbsGOutT/WWLinT + 16.207121836579560181235 * AbsGOutF/WWLinF ...

- 0.373117826152912501758 15 * AbsGOutH2OF/WWLinF - 0.290598139768875311664 35E-004 * AbsGOutH2OF/WWLinT - 42.531480208656645913834 * AbsGOutPZF/AbsGOutH2OF + 0.676508084664684803712 09E-003 * (WWLinF/WWLinT)^2 ...

- 0.601982304497329853698 60E-001 * (WWLinF/AbsGOutT)^2 + 2.113619730428611731554 2 * (WWLinF/AbsGOutF)^2 - 120257.25196515479183290 * (WWLinF/AbsGOutH2OF)^2 - 132.33958353999480550556 * (WWLinT/WWLinF)^2 ...

- 0.976980032965299310943 05E-001 * (AbsGOutT/WWLinT)^2 + 0.252930880787468031611 20E-003 * (AbsGOutH2OF/WWLinF)^2 - 0.748957108286607542992 25E-007 * (AbsGOutH2OF/WWLinF)^3;

% Water Wash - Gas Outlet Water - kg/h

WWGOutH2O = 1188.9198723501435779326 * WWLinF - 19216.119908903103350895 * WWLinT - 18331.361527666249457980 * AbsGOutT + 451.97444853281490395602 * AbsGOutF + 1.8295105850455941620680 * AbsGOutH2OF + 0.49578910293857803015527 * WWLinF^2 ...

+ 105.98129171821275917864 * WWLinT^2 + 368.60573547238698211004 * AbsGOutT^2 - 0.58114100784905986518680 * AbsGOutF^2 - 0.20092083698522748488879E-003 * WWLinF^3 - 0.33476776415901500494332E-001 * WWLinT^3 ...

- 2.2506879787349864940893 * AbsGOutT^3 - 7.9970728824652272948015 * WWLinF*WWLinT - 24.684491041193695082256 * WWLinF*AbsGOutT + 0.57297198931944115507520 * WWLinF*AbsGOutF - 0.87401931131169102034972E-003 * WWLinF*AbsGOutH2OF ...

+ 176.31634866498006886104 * WWLinT*AbsGOutT + 0.52468557509900237700862 * WWLinT*AbsGOutF + 0.81516963600253430303338E-003 * WWLinT*AbsGOutH2OF - 1.2928390294135565508071 * AbsGOutT*AbsGOutF + 0.62949060938057325650941E-003 * AbsGOutF*AbsGOutH2OF ...

+ 0.24715834332021998493139E-004 * (WWLinF*WWLinT)^2 + 0.74145062501006204049372E-004 * (WWLinF*AbsGOutT)^2 - 0.10347117300181712246099E-001 * (WWLinT*AbsGOutT)^2 - 0.11437307535392826770507E-003 * (WWLinT*AbsGOutF)^2 ...

+ 0.26033892656804846071905E-001 * WWLinF*WWLinT*AbsGOutT + 0.95967220937339271086275E-002 * WWLinF*WWLinT*AbsGOutF - 0.12501047884719984279456E-001 * WWLinF*AbsGOutT*AbsGOutF + 0.79578480786615238273818E-001 * WWLinT*AbsGOutT*AbsGOutF ...

+ 15576.090030825764188194 * WWLinF/WWLinT - 75669.385226789658190683 * WWLinF/AbsGOutT + 127220.72376775630982593 * WWLinF/AbsGOutF - 11604397.007413940504193 * WWLinT/WWLinF + 2056418.5374479894526303 * WWLinT/AbsGOutT ...

+ 4290368.2129641529172659 * AbsGOutT/WWLinF - 136691.53479166806209832 * AbsGOutT/WWLinT + 27586.425619011766684707 * AbsGOutF/WWLinF + 694.85725082377757644281 * AbsGOutF/WWLinT - 259.21056888891325797886 * AbsGOutH2OF/WWLinF ...

+ 0.69209215959911807303229 * AbsGOutH2OF/WWLinT - 73.657310380518538295291 * (WWLinF/WWLinT)^2 + 352.15082102723681600764 * (WWLinF/AbsGOutT)^2 - 10451.743176654665148817 * (WWLinF/AbsGOutF)^2 + 35589420.217154972255230 * (WWLinT/WWLinF)^2 ...

- 810201.75561299384571612 * (WWLinT/AbsGOutT)^2 - 3417403.9432997256517410 * (AbsGOutT/WWLinF)^2 + 4514.9254708111866420950 * (AbsGOutT/WWLinT)^2 - 0.10209401015669982741509E-004 * (AbsGOutH2OF/WWLinT)^2 + 0.15536425396746431082384 * (WWLinF/WWLinT)^3 ...

- 52999214.156288452446461 * (WWLinT/WWLinF)^3 + 172085.36848503412329592 * (WWLinT/AbsGOutT)^3;

% Water Wash - Gas Outlet PZ - kg/h

WWGoutPZ = 0.8626181108287670623591 1E-002 * WWLinF + 0.3015259976366178595874 6 * WWLinT + 16416739408.736368179321 * AbsGOutT - 2305088556.4248495101929 * AbsGOutF + 0.2608014344196067248031 0E-004 * AbsGOutH2OF + 0.8969990425341487242857 9E-004 * AbsGOutCO2F ...

- 0.1533693200940166830644 6E-003 * AbsGOutPZF - 0.8029218273568125786699 8E-006 * AbsGOutN2F - 0.3371809489941218419730 8E-005 * WWLinF^2 - 0.1857090527249373760818 0E-002 * WWLinT^2 - 301811922.27702516317368 * AbsGOutT^2 ...

+ 5885332.4845005385577679 * AbsGOutF^2 - 0.2313295166071468433685 3E-009 * AbsGOutCO2F^2 + 0.1172225673647257774082 5E-006 * AbsGOutPZF^2 + 0.3522325707134361490196 3E-009 * WWLinF^3 + 0.1773086884900383950565 1E-004 * WWLinT^3 ...

+ 1829163.1653038859367371 * AbsGOutT^3 - 4904.4437370861087401863 * AbsGOutF^3 - 0.1033963601078316058318 1E-009 * AbsGOutPZF^3 - 0.9460241263146134803752 7E-004 * WWLinF*WWLinT - 0.2361144165563049555282 7E-004 * WWLinF*AbsGOutT ...

- 2031077.5481123365461826 * WWLinF*AbsGOutF + 564.18820777741689198592 * WWLinF*AbsGOutH2OF + 564.18820766934936727921 * WWLinF*AbsGOutCO2F + 564.18820775371170839207 * WWLinF*AbsGOutPZF + 564.18820780808562176389 * WWLinF*AbsGOutN2F + 564.18820780804890091531 * WWLinF*AbsGOutO2F ...

- 0.3328406316542660905999 4E-002 * WWLinT*AbsGOutT + 0.4507873217481701589052 7E-004 * WWLinT*AbsGOutF + 0.1833796134971430192428 7E-005 * WWLinT*AbsGOutCO2F - 0.3760299267016319361631 2E-003 * AbsGOutT*AbsGOutF + 0.8318961092552468125649 1E-006 * AbsGOutT*AbsGOutCO2F ...

+ 0.2581580127744866318093 2E-007 * AbsGOutF*AbsGOutH2OF + 0.2128294834192347597242 4E-006 * AbsGOutF*AbsGOutCO2F - 0.1532641261733907633732 0E-006 * AbsGOutF*AbsGOutPZF + 0.6003945805896345691613 8E-009 * (WWLinF*WWLinT)^2 + 0.3704384515310796089929 6E-009 * (WWLinF*AbsGOutT)^2 ...

+ 0.1828170519691769923444 5E-006 * (WWLinT*AbsGOutT)^2 - 0.6432672850992853470060 1E-009 * (WWLinT*AbsGOutF)^2 - 0.2757157793860868001384 5E-006 * WWLinF*WWLinT*AbsGOutT + 0.1099133381795728590237 7E-006 * WWLinF*WWLinT*AbsGOutF ...

- 0.3460301842420873268948 4E-009 * WWLinF*WWLinT*AbsGOutCO2F + 0.1715057173300456531155 0E-006 * WWLinF*AbsGOutT*AbsGOutF + 0.2677046785065278636294 5E-008 * WWLinF*AbsGOutT*AbsGOutCO2F + 0.4855224432450189414037 1E-008 * WWLinT*AbsGOutT*AbsGOutH2OF ...

- 0.2606949149982049804699 9E-007 * WWLinT*AbsGOutT*AbsGOutCO2F - 0.1920197991761270997431 9E-008 * WWLinT*AbsGOutF*AbsGOutCO2F - 0.5007820753002247910056 2E-008 * AbsGOutT*AbsGOutF*AbsGOutCO2F + 0.1277503283493447012882 4E-007 * AbsGOutT*AbsGOutF*AbsGOutPZF ...

- 0.1162442597356114085474 5E-002 * WWLinF/WWLinT - 0.9961367988790271743582 1 * WWLinF/AbsGOutCO2F - 4.4290625460298738147458 * WWLinT/WWLinF - 4.0788686396249689281035 * WWLinT/AbsGOutT + 35.21096778616730205158 1 * WWLinT/AbsGOutCO2F ...

+ 23.76797028491381169601 5 * AbsGOutT/WWLinF - 0.4110021821584277507133 4E-001 * AbsGOutT/WWLinT - 63.89674753073968105354 7 * AbsGOutT/AbsGOutCO2F + 17977.39664583010016940 5 * AbsGOutT/AbsGOutN2F + 0.2092195134911689971546 3E-001 * AbsGOutF/WWLinT ...

+ 5.944190915644515627036 5 * AbsGOutF/AbsGOutCO2F + 0.9923400191736680541615 4E-003 * AbsGOutH2OF/WWLinF + 0.1775044355774887949728 2E-001 * AbsGOutH2OF/AbsGOutCO2F - 0.5231675676426170151778 2E-002 * AbsGOutCO2F/WWLinF - 0.1426755990978519333251 0E-003 * AbsGOutCO2F/WWLinT ...

- 66.45683924903397610251 0 * AbsGOutCO2F/AbsGOutN2F - 21.74059936485433652819 7 * (WWLinT/WWLinF)^2 - 34.28491586529038670505 5 * (AbsGOutT/WWLinF)^2 + 38.57528969107301008989 5 * (WWLinT/AbsGOutF)^3;

```
%% Air Cooler Model - Water Wash

% WW Liquid Outlet Temperature - Converted to C

WWLOutTF = ( WWLOutT * 9/5 ) + 32 ;


%Outlet Pressure for given Nr of Pumps
if NrWWPumps == 1
   WWPumpPOut = -1E-5 * WWLinF^2 -0.008*WWLinF +82.091;
elseif NrWWPumps == 2
   WWPumpPOut = -1E-5*WWLinF^2 -0.0015 * WWLinF + 83.572;
end

%Head Requirement (includes elevation
%head requirement) - psia
```

WWPumpHeadReq = 0.5698758897779058335553 2E-001 * WWLinF - 8.9672977995880387425132 * WWBays - 0.1408436144475112731871 4E-004 * WWLinF^2 + 0.3207310271785659416821 1 * WWBays^2 + 0.7188195565352902818498 4E-003 * (WWLinF/WWBays)^2 + 11724.707366977560013765 * (WWBays/WWLinF)^2 + 63.69316149396208714961 2;

%Water Wash Pressure Drop - psia

WWDeltaP = 0.3031195717408632570033 5E-001 * (WWLinF/WWBays) + 0.2308961575793424050862 0E-001 * WWLOutTF + 0.9890431131976771400582 4E-003 * (WWLinF/WWBays)^2 - 0.1918010067508249039992 8E-003 * WWLOutTF^2 + 0.2529764186778504170303 5E-008 * WWLOutTF^4 - 0.2325793943900340495353 3E-008 * ((WWLinF/WWBays)*WWLOutTF)^2 + 0.7526268689164367087229 8E-002 * (TAmbF/(WWLinF/WWBays))^2 - 0.4042286600482670744227 7 * (TAmbF/WWLOutTF)^2 + 0.1452173223958162090463 4E-001 * ((WWLinF/WWBays)/TAmbF)^2 + 0.3481202112098243373061 7 * ((WWLinF/WWBays)/WWLOutTF)^2;

% Water Wash Elevation (97 ft) - psia (Water
% Density Assumed)
% Apparently there's tank before the WW pumps?
% Find out if head requirements include tank
% level

WWElev = 91 / (2.31 / (1000 / 1000));

%New Flowrate calculation if not enough head is generated

if (WWPumpPOut < (WWPumpHeadReq + WWDeltaP)) %- WWElev))

if NrWWPumps == 1
fun = @(WWLinF) (0.5698758897779058335553 2E-001 * WWLinF - 8.9672977995880387425132 * WWBays - 0.1408436144475112731871 4E-004 * WWLinF^2 + 0.3207310271785659416821 1 * WWBays^2 + 0.7188195565352902818498 4E-003 * (WWLinF/WWBays)^2 + 11724.707366977560013765 * (WWBays/WWLinF)^2 + 63.69316149396208714961 2 ...
+ 0.3031195717408632570033 5E-001 * (WWLinF/WWBays) + 0.2308961575793424050862 0E-001 * WWLOutTF + 0.9890431131976771400582 4E-003 * (WWLinF/WWBays)^2 - 0.1918010067508249039992 8E-003 * WWLOutTF^2

+ 0.25297641867785041703035E-008 * WWLOutTF^4 - 0.23257939439003404953533E-008 * ((WWLinF/WWBays)*WWLOutTF)^2 + 0.75262686891643670872298E-002 * (TAmbF/(WWLinF/WWBays))^2 - 0.40422866004826707442277 * (TAmbF/WWLOutTF)^2 + 0.14521732239581620904634E-001 * ((WWLinF/WWBays)/TAmbF)^2 + 0.34812021120982433730617 * ((WWLinF/WWBays)/WWLOutTF)^2 ...

- (-1E-5 * WWLinF^2 -0.008*WWLinF +82.091));

x = fzero(fun, WWLinF);

elseif NrWWPumps == 2

fun = @(WWLinF) (0.56987588977790583355532E-001 * WWLinF - 8.9672977995880387425132 * WWBays - 0.14084361444751127318714E-004 * WWLinF^2 + 0.32073102717856594168211 * WWBays^2 + 0.71881955653529028184984E-003 * (WWLinF/WWBays)^2 + 11724.707366977560013765 * (WWBays/WWLinF)^2 + 63.69316149396208714961 2 ...

+ 0.30311957174086325700335E-001 * (WWLinF/WWBays) + 0.23089615757934240508620E-001 * WWLOutTF + 0.98904311319767714005824E-003 * (WWLinF/WWBays)^2 - 0.19180100675082490399928E-003 * WWLOutTF^2 + 0.25297641867785041703035E-008 * WWLOutTF^4 - 0.23257939439003404953533E-008 * ((WWLinF/WWBays)*WWLOutTF)^2 + 0.75262686891643670872298E-002 * (TAmbF/(WWLinF/WWBays))^2 - 0.40422866004826707442277 * (TAmbF/WWLOutTF)^2 + 0.14521732239581620904634E-001 * ((WWLinF/WWBays)/TAmbF)^2 + 0.34812021120982433730617 * ((WWLinF/WWBays)/WWLOutTF)^2 ...

- (-1E-5*WWLinF^2 -0.0015 * WWLinF + 83.572));

x = fzero(fun, WWLinF);

end

WWFlowcalc = x;

end

% WW Liquid inlet temperature - °F

WWTCalcF = 0.6037442618447635966916 2 * TAmbF + 0.34141115807038441287702 * (WWFlowcalc/WWBays) + 0.23725521826315518029993E-002 * WWLOutTF^2 - 0.12362683527553394878984E-004 * (WWFlowcalc/WWBays)^3 + 0.34590849142711767113834E-007 * (WWFlowcalc/WWBays)^4- 0.29780128573303977183356E-007 * WWLOutTF^4 - 0.54427764926301215643278E-007 * (TAmbF*(WWFlowcalc/WWBays))^2 + 0.43174059428732749634990E-007 * ((WWFlowcalc/WWBays)*WWLOutTF)^2 + 0.56384775784102592055547 * (TAmbF/(WWFlowcalc/WWBays))^2 + 0.47247441792662775439382 * ((WWFlowcalc/WWBays)/TAmbF)^2 -

```
1.7601265182155445554457 * ((WWFlowcalc/WWBays)/WWLOutTF)^2 - 0.3926393956795063977516 2 *
(WWLOutTF/TAmbF)^2 - 0.2602248950873893296176 2 * (WWLOutTF/(WWFlowcalc/WWBays))^2;

            % WW Liquid inlet temperature - °C

            WWTcalc = (WWTCalcF - 32) * 5/9;

            ErrorWWF = (WWLinF - WWFlowcalc) / WWFlowcalc *100;
            ErrorWWT = (WWLinT - WWTcalc) / WWTcalc *100;

        end

        WWRes(WWBays-WWBayMin + 1,1) = WWBays;

        WWRes(WWBays-WWBayMin + 1 ,2) = abs ( WWGOutH2O - WWH2OTarget) ;

        WWRes(WWBays-WWBayMin + 1,3) = WWLinF;


    end

    % Picks Number of WW Bays that most closely closes the water balance

    [Min, Indx] = min(WWRes(:,2));

    WWBays = WWRes(Indx,1);

    WWLinF = WWRes(Indx, 3);

    WWFans = WWBays * 3; %number of water wash air cooler fans online

    % WWPP - water wash pump power, MW
```

```
WWPP = (( NrWWPumps * 289.393290544082+(WWLinF*0.261441079045139))/1341);

%Water wash fans power

WWFP = 36.6 / 1341 * WWFans;

% Total Power (Both Trains) - MW

TP = NrTrains * ( 2*HRSGFP + BLRFP + LPP + RPP + ICPP + ICFP + WWPP + WWFP + CP);

%Other Output Variables - Converged values

% Precipitation feasibility flag

%Avg of cold lean and cold rich T - coldest poit in the
%system - degC

ColdSolvT = - 43.8063809526129 * RichLDG - 0.0807568034515082 * RichFPZAS + 0.993277402829918 * RichT +
0.0492069357094608 * LCRBP + 0.0321325425492939 * LWRBP + 278.455340145426 * LeanLDG + 24.5719855130343 *
RichLDG^2 + 0.0000939696632544697 * RichFPZAS^2 + 0.00133300013235813 * LCRBP^2 + 0.0000772121217417357 *
LWRBP^2 - 507.787854777207 * LeanLDG^2 - 2.72340248415663E-09 * LWRBP^4 - 0.00095354264099311 *
(RichLDG*LCRBP)^2 + 0.00284613221060037 * (RichLDG*LWRBP)^2 + 3.11907041825435 * (RichLDG*LeanLDG)^2 +
6.56057609068488E-09 * (RichFPZAS*RichT)^2 - 5.17491350858627E-09 * (RichFPZAS*LCRBP)^2 + 0.0000633929540155873 *
(RichFPZAS*LeanLDG)^2 - 9.78403009676175E-08 * (RichT*LCRBP)^2 - 0.0612484215622779 * (RichT*LeanLDG)^2 -
0.02085327257272 * (LWRBP*LeanLDG)^2 - 0.0000251718838114076 * (RichLDG*LWRBP)^3 + 0.000380671178962947 *
(LWRBP*LeanLDG)^3 + 2.42492558438432E-06 * (LCRBP*LeanLDG)^4 + 0.151507699653368 * (RichLDG*RichT*LeanLDG)^2;

% SLE line for 5 m PZAS regressed from GHGT-12 "Pilot
```

```
% Plant Activities with Concentrated Piperazine"

SLELine = -499.14 * LeanLDG^2 + 6.7881*LeanLDG + 41.046 ; % Precipitation temp - degC

if (ColdSolvT < SLELine)
   Feasible8 = false;

end

%Absorber - Number of transfer units
%
NTUAbs = 9.14312517878722 * LeanLDG - 0.00226004445816395 * HR + 2.34273977862223E-06 * PAFlow - 0.00255141358384102 * PAT + 0.00147369453243037 * LeanF + 0.00341482323231971 * LeanT - 36.5205310519848 * LeanLDG^2 - 4.08711668889046E-07 * PAFlow^2 - 0.000797438445669041 * PAT^2 + 0.0000440378300177219 * LeanF^2 + 111.269931347429 * LeanLDG^3 + 0.0000102144488835438 * PAT^3 - 3.52553310886692E-08 * LeanF^3 + 0.0131682098765513 * LeanLDG*HR + 0.00284520484706134 * LeanLDG*PAFlow + 0.086724301906328 * LeanLDG*PAT - 0.0740624622261413 * LeanLDG*LeanF - 3.45079830563932E-07 * HR*PAFlow + 0.0000148860803849213 * HR*PAT - 4.66841750841656E-06 * HR*LeanF - 6.35902611549355E-06 * PAFlow*PAT + 6.15244599713333E-06 * PAFlow*LeanF + 0.000026742346467296 * PAT*LeanF - 0.0000121611111111039 * LeanF*LeanT + 0.000076767743988736 * (LeanLDG*LeanF)^2 - 1.79710544084351E-09 * (PAT*LeanF)^2 - 0.0000193678315412073 * LeanLDG*PAFlow*LeanF - 1.51454270721386E-08 * PAFlow*PAT*LeanF + 1.6965350939786E-09 * (LeanLDG*PAFlow*PAT)^2;
%
%          %Absorber - CO2 Removal
%
 CO2Rem = (1 - exp(-NTUAbs)) * 100;
%
%
CO2Flowkgs = CO2Flow*1000/3600;

% Stripper fractional flood - Top section
```

Flood1 = 5.36069508764744 * RichLDG + 0.0107984122363325 * RichFPZAS - 0.00149407379501041 * LCRBP - 0.110710124811398 * CO2Flowkgs - 10.2925139112505 * RichLDG^2 - 0.0000350378191776623 * RichFPZAS^2 + 7.56768479212756E-06 * LCRBP^2 + 6.21858290039045E-06 * LWRBP^2 - 0.00641994037333848 * CO2Flowkgs^2 + 2.09904764393935E-08 * RichFPZAS^3 + 0.00010697079455567 * CO2Flowkgs^3 + 0.000110345136121645 * (RichLDG*RichFPZAS)^2 - 0.0000347834435511722 * (RichLDG*LWRBP)^2 - 1.05702951682425E-08 * (RichFPZAS*CO2Flowkgs)^2 - 6.68605324355561E-08 * (LCRBP*CO2Flowkgs)^2 + 6.09886132273307E-10 * (RichLDG*RichFPZAS*LCRBP)^2 + 1.96880548927528E-07 * (RichLDG*LCRBP*CO2Flowkgs)^2 + 0.00192039234201981 * (LCRBP/CO2Flowkgs)^2 + 0.00106397060517638 * (CO2Flowkgs/RichLDG)^2 + 322.461152684524 * (CO2Flowkgs/RichFPZAS)^2 - 1.66735222265824;

% Stripper fractional flood - Bottom section

Flood2 = - 5.10605202217549 * RichLDG - 0.00256429067746952 * RichFPZAS - 0.00223410055982649 * LCRBP - 0.0000317439134494403 * LWRBP + 0.157224676477044 * CO2Flowkgs + 5.78508079693367 * RichLDG^2 + 5.92157824045019E-07 * RichFPZAS^2 + 0.000028926162027239 * LCRBP^2 + 1.14913582054721E-06 * LWRBP^2 - 0.00622988706179911 * CO2Flowkgs^2 - 3.46715068205913E-08 * LCRBP^3 - 2.88889893711406E-08 * LWRBP^3 + 0.0000970232584326045 * CO2Flowkgs^3 - 0.000009153097159151 * (RichLDG*RichFPZAS)^2 + 0.0000403545973091811 * (RichLDG*LCRBP)^2 + 0.0000282822195260201 * (RichLDG*LWRBP)^2 - 1.29621767681603E-10 * (RichFPZAS*LCRBP)^2 + 1.09271328499506E-10 * (LCRBP*LWRBP)^2 - 6.31615571822203E-08 * (LCRBP*CO2Flowkgs)^2 + 5.15104230711193E-07 * (RichLDG*LWRBP)^3 + 1.47567516125977E-09 * (RichLDG*RichFPZAS*LCRBP)^2 + 1.50518413227041E-10 * (RichLDG*RichFPZAS*LWRBP)^2 - 1.06782509147456E-07 * (RichLDG*LWRBP*CO2Flowkgs)^2 + 0.000519185700127981 * (RichFPZAS/CO2Flowkgs)^2 + 0.00025265581057433 * (CO2Flowkgs/RichLDG)^2 + 0.507445967623614;

% Stripper Flooding Feasibility flag

```
if ( (Flood1 > 1) || (Flood2 > 1) )
    Feasible4 = false;
end
```

% Absorber - Top Section Flooding

```
AbsTopFlood = - 0.0825147779819776 * LeanLDG + 0.000109652872814164 * HR - 0.000108051063433676 *
PAFlow - 0.00168282575346653 * PAT + 0.000312344097792582 * LeanF - 0.000186818181818151 * LeanT - 0.723635937241577
* LeanLDG^2 + 3.82615014760462E-08 * PAFlow^2 + 9.76202343289259E-06 * PAT^2 - 3.30500552255948E-07 * LeanF^2 +
0.000215199763199703 * LeanLDG*PAFlow + 0.0110786992996768 * LeanLDG*PAT + 0.000235030533883034 *
LeanLDG*LeanF - 1.12495927012039E-08 * HR*PAFlow + 4.59259259259196E-08 * HR*LeanF + 5.40434038066441E-06 *
PAT*LeanF + 2.12929292929287E-06 * LeanF*LeanT - 2.28053675974098E-07 * (LeanLDG*PAFlow)^2 + 2.38599888808561E-06
* (LeanLDG*LeanF)^2 - 0.0000346025857933418 * LeanLDG*PAT*LeanF + 7.39397009285713E-10 * (LeanLDG*PAT*LeanF)^2
+ 0.449781117899782;

%                % Absorber - Bottom Section Flooding

AbsBotFlood =- 0.0191026961694554 * LeanLDG + 0.000136160312805471 * HR + 0.000226648743711837 *
PAFlow - 0.0000105513064974603 * PAT + 0.000210395804723814 * LeanF + 0.0000378853046594635 * LeanT -
2.83041453495997E-08 * PAFlow^2 + 2.08912752310065E-06 * PAT^2 + 1.43634395863373E-08 * LeanF^2 +
0.000187862355906623 * LeanLDG*LeanF + 1.38400130335587E-08 * HR*PAFlow + 1.23905723905824E-08 * HR*LeanF +
1.96851067977663E-08 * PAFlow*PAT - 4.01147126556175E-08 * PAFlow*LeanF + 4.56989247311578E-08 * PAFlow*LeanT -
2.1302598350706E-07 * PAT*LeanF - 1.84848484848368E-07 * LeanF*LeanT - 8.72006359013312E-07 * (LeanLDG*LeanF)^2 -
2.18278704136758E-08 * LeanLDG*PAFlow*LeanF + 0.472307267896646;

if ( AbsTopFlood > 1 || AbsBotFlood > 1)
   Feasible6 = false;
end
end
```

F.2 Optimum Profit Rate Script

```
%% Optimum Profit Rate Script - 40F, 95% CF, No Duct Burning

gp = 3:1:10; % Natural Gas Price range

%% Value of CO2
```

```
    CarbCred = 80; % $/tonne CO2 Captured, 45Q
    %CarbCred = 45; % $/tonne CO2 Captured, storage
    %CarbCred = 30; % $/tonne CO2 Captured, EOR - low

    % Matrix of profit rate for each gas price
    ProfMatrix = zeros(size(ResMatrix,1),length(gp));

% Optimum profit rate calculation
for i = 1:length(gp)

    NGPrice = gp(i) ; %Natural gas price $/MMBTU

    EPrice = NGPrice * (7000) / 1000 + 5; % Equation to calculate electricity price from NG price, $/MWh

    for j = 1:size(ResMatrix,1)


      % Feasiblity Flags from PZASTM process Script

%           ResMatrix(i,11) = Feasible; %Rich Pump Flag
%
%           ResMatrix(i,12) = Feasible1; %CRBP and WRBP Flag
%
%           ResMatrix(i,13) = Feasible2; %Lean Pump Bubble point Flag
%
%           ResMatrix(i,14) = Feasible3; %Gas-fired boiler capacity
%
%           ResMatrix(i,15) = Feasible4; %Stripper Flooding Flag
%
%           ResMatrix(i,16) = Feasible5; %Gas-fired boiler fan speed Flag
%
%           ResMatrix(i,17) = Feasible6; %Absorber flooding flag
```

```
%
%           ResMatrix(i,18) = Feasible7; %Compressor maximum capacity flag
%
%           ResMatrix(i,19) = Feasible8; % Precipitation flag


        % Fully Constrained
        Feasibility = ResMatrix(j,11)  * ResMatrix(j,12) * ResMatrix(j,13)  * ResMatrix(j,14) *  ResMatrix(j,15) *  ResMatrix(j,16)  *
ResMatrix(j,17) * ResMatrix(j,18)  * ResMatrix(j,19)  ;

%        %Partially Constrained
      %  Feasibility = ResMatrix(j,11) * ResMatrix(j,12) * ResMatrix(j,13) * ResMatrix(j,19) ;

      % Profit for 2 process trains online

        ProfMatrix(j,i) = Feasibility *( 2*CarbCred*ResMatrix(j,8) - ( 2*NGPrice*ResMatrix(j,9)/0.94 + EPrice*ResMatrix(j,10) ) );
     %                    Profit  =  Feasible*Feasible1*Feasible2*(  CarbCred*CO2Flow  -  1  *  (gp(i)*HRcalc/Boiler  Eff.  +
OptMatrix(CountAux,8)*TP) );

     end

     % Optimum profit rate for each gas price
        % Column 1 - Maximum Profit Rate
        % Column 2 - Corresponding index in ResMatrix

     [ opt(i,1), opt(i,2) ] = max(ProfMatrix(:,i));


   end


   % Algorithm to calculate optimum profit rate cases and other dependent variables of interest
```

```
% Optimum profit rate cases
    for i = 1:length(gp)

        % WRBP
        OptMatrix(i,1) = ResMatrix(opt(i,2),1);

        % CRBP
        OptMatrix(i,2) = ResMatrix(opt(i,2),2);

        % Lean Flow
        OptMatrix(i,3) = ResMatrix(opt(i,2),3);

        % Nr IC Bays
        OptMatrix(i,4) = ResMatrix(opt(i,2),4);

        % Nr PA Pumps
        OptMatrix(i,5) = ResMatrix(opt(i,2),5);

        % Nr WW Pumps
        OptMatrix(i,6) = ResMatrix(opt(i,2),6);

        % Lean Loading
        OptMatrix(i,7) = ResMatrix(opt(i,2),7);

        OptMatrix(i,8) = gp(i);


          % Electricity price ( gas price * 7000 MMBTU/kWh / 1000 + 5 $/kWh)

        OptMatrix(i,9) = gp(i) * (7000) / 1000 + 5;
```

```
% Running PZASTM Process Script

[LeanTcalc,RichFcalc,RichFPZAS,HRcalc,PATcalc,PAFlowcalc,RichLDG,RichT,HDcalc,TP,Feasible,Feasible1,Feasible2,Feasible3,
Feasible4,Feasible5,Feasible6,Feasible7,Feasible8,...

CO2Flow,CO2Rem,LPP,RPP,ICPP,WWPP,HRSGFP,BLRFP,BLRFRPM,ICFP,WWFP,CP,Flood1,Flood2,AbsTopFlood,
AbsBotFlood,WWBays,PAFlow, PAT, MaxCO2Flow] =
convergence(OptMatrix(i,2),OptMatrix(i,1),OptMatrix(i,3),OptMatrix(i,4),OptMatrix(i,5),OptMatrix(i,6),OptMatrix(i,7)); %calling
the convergence function

OptMatrix(i,10) = opt(i,1); % Profit Rate

OptMatrix(i,11) = CO2Flow; % CO2 Flow

OptMatrix(i,12) = CO2Rem; % CO2 Removal

OptMatrix(i,13) = OptMatrix(i,3); %Lean Flow

OptMatrix(i,14) = HDcalc; % Heat Duty

OptMatrix(i,15) = RichLDG; % Rich Loading

OptMatrix(i,16) = OptMatrix(i,7); % Lean Loading

OptMatrix(i,17) = OptMatrix(i,4); % Air cooler bays

OptMatrix(i,18) = WWBays; % Nr WW Bays

OptMatrix(i,19) = OptMatrix(i,6); % Water Wash Pumps
```

```
    OptMatrix(i,20) = Flood1; % Stripper top flooding

    OptMatrix(i,21) = Flood2; % Stripper bot flooding

    OptMatrix(i,22) = OptMatrix(i,1); % WRBP

    OptMatrix(i,23) = OptMatrix(i,2); % CRBP

    OptMatrix(i,24) = OptMatrix(i,5); % PA Pumps

    OptMatrix(i,25) = TP; % Total Power - MW

    OptMatrix(i,26) = HRcalc/0.94; % Boiler Heat Rate - MMBTU

    OptMatrix(i,27) = BLRFRPM; % Boiler fan speed

    OptMatrix(i,28) = LeanTcalc; % Lean temperature

    OptMatrix(i,29) = RichT; % Rich temperature

    OptMatrix(i,30) = AbsTopFlood; %absorber top flood

    OptMatrix(i,31) = AbsBotFlood; %absorber bottom flood

    OptMatrix(i,32) = PAT; %Pumparound T

    OptMatrix(i,33) = PAFlow; %Pumparound flow

    OptMatrix(i,34) = MaxCO2Flow; % Maximum Compressor CO2 flow
end
```

```
function
[LeanTcalc,RichFcalc,RichFPZAS,HRcalc,PATcalc,PAFlowcalc,RichLDG,RichT,HDcalc,TP,Feasible,Feasible1,Feasible2,Feasible3,
Feasible4,Feasible5,Feasible6,Feasible7,Feasible8,CO2Flow,CO2Rem,LPP,RPP,ICPP,WWPP,HRSGFP,BLRFP,BLRFRPM,ICFP,W
WFP,CP,Flood1,Flood2,AbsTopFlood, AbsBotFlood,WWBays,PAFlow, PAT , MaxCO2Flow] =
convergence(CRBP,WRBP,LeanF,ICBays, NrPAPumps, NrWWPumps,LeanLDG);
    %% THE PZASTM PROCESS SCRIPT CORRESPONDING TO THE CASE BEING ANALYZED HAS TO BE PASTED HERE
    %% (EVERYTHING BETWEEN "function [..]" and "end" FROM THE CORRESPONDING SCRIPT)

End
```

Appendix C

Appendix C provides the standard operating procedures for the density and total alkalinity analysis performed on solvent samples during pilot plant campaigns.

C.1 Analysis of Solvent Density

Risk Assessment

Hazardous Chemicals: *(List chemicals used. Include chemical name, common name and abbreviation)*

Common Name	Chemical Name	Abbreviation
Acetone	Acetone	

Potential Hazard(s): *(Describe the potential hazards associated with the chemicals or procedure.)*

Acetone
Danger! Extremely flammable liquid and vapor. Vapor may cause flash fire. Causes eye irritation. Breathing vapors may cause drowsiness and dizziness. Causes respiratory tract irritation. Aspiration hazard if swallowed. Can enter lungs and cause damage. Prolonged or repeated contact may dry the skin and cause irritation.
Target Organs: Central nervous system, respiratory system, eyes, skin.

Control Measures

Personal Protective Equipment (PPE): *(List all applicable personal protective equipment needed for procedure)*

Nitrile Gloves
Lab Coat
Safety Glasses

Cleanup Procedures: *(Describe the process for cleaning the work area during and after the procedure.)*

- Flammable liquids should be put back in the flammable cabinet immediately following use.
- Densitometer will not reset itself to room temperature. Always set the instrument to 20 °C when finished.
- In between each run the instrument will prompt a cleaning sequence. The first rinse will be DDI water, the second rinse is acetone, and the purge is air.

Storage Procedures: *(Describe how and where the chemical will be safely stored)*

Acetone
Flammable Cabinet

Waste Disposal Procedures: (*Description of how waste will be disposed)*

Waste is collected in a vessel and will need to be disposed of in a liquid waste carboy when full.

Emergency Procedures: *(Describe what procedures should be followed in the event of an emergency)*

Spills or Releases: Clean up any spills using spill kit found in Safety Supplies cabinet.

Fire: Ensure that all flammable chemicals are put away, shut down instrument.

Emergency Shut Offs: Instrument is unable to be stopped mid-run. In case of emergency, turn off instrument using switch on back.

Exposures: Rinse affected area with water for 15 minutes.

Material Safety Data Sheets (MSDS): *(Describe how personnel will access MSDS in the lab. Include a copy of the MSDS with this SOP)*

Personnel will access MSDS by using technology to look them up either here or online.

Acetone

Training Requirements: OH102

Review of Procedure: SOP should be reviewed annually

Protocol:

- Choose a method (each method is the same, the only difference is the temperature of the measurement)
- Instrument will read "ready" when the system is stable
- Place inlet tube in beaker of analyte
- Press green measure button. Instrument will draw up ~5mL analyte and heat to desired temperature. The instrument will wait until it is stable before giving a reading. If it doesn't stabilize in 10 minutes, it will give the most accurate reading it can.
- Place inlet in DDI for rinse one, press enter
- Instrument will then finish first rinse and prompt rinse 2
- Rinse 2 is with acetone
- Instrument will finish rinse 2 and prompt air purge
- Purge with air
- Switching between methods/temperatures:
- When changing temperatures, the instrument must be allowed time to stabilize.
- Increasing temperature: +10C = wait 30 minutes; +35C = wait 45 minutes
- Decreasing temperature: -10C = wait 60 minutes; -35C = wait 90 minutes

C.2 Analysis of Total Alkalinity

Risk Assessment

Hazardous Chemicals: *(List chemicals used. Include chemical name, common name and abbreviation)*

Common Name	Chemical Name	Abbreviation
Sulfuric Acid	Sulfuric Acid	H_2SO_4

Potential Hazard(s): *(Describe the potential hazards associated with the chemicals or the procedure.)*

- Sulfuric Acid
  - Danger! Causes eye and skin burns. Causes digestive and respiratory tract burns. May be fatal if mist inhaled. Strong inorganic acid mists containing sulfuric acid may cause cancer. Concentrated sulfuric acid reacts violently with water and many other substances under certain conditions. May cause lung damage. Hygroscopic (absorbs moisture from the air). Corrosive to metal.
  - Target Organs: Lungs, teeth, eyes, skin.

Control Measures

Personal Protective Equipment (PPE): *(List all applicable personal protective equipment needed for procedure)*

- Nitrile Gloves
- Lab Coat
- Safety Glasses

Cleanup Procedures: *(Describe the process for cleaning the work area during and after the procedure.)*

- Take extreme caution when handling the dosing line or the acid.
- Probe must be rinsed with DDI water in between runs

Storage Procedures: *(Describe how and where the chemical will be safely stored)*

- Sulfuric Acid
  - Inorganic Acids bin in Acid cabinet

Waste Disposal Procedures: (*Description of how waste will be disposed)*

Waste will be disposed in specified titration waste carboy.

Emergency Procedures: *(Describe what procedures should be followed in the event of an emergency)*

Spills or Releases: Clean up any spills using spill kit found in Safety Supplies cabinet.

Fire: Ensure that all flammable chemicals are put away, shut down instrument.

Emergency Shut Offs: Stop run using software.

Exposures: Rinse affected area with water for 15 minutes.

Material Safety Data Sheets (MSDS): *(Describe how personnel will access MSDS in the lab. Include a copy of the MSDS with this SOP)*

Personnel will access MSDS by using technology to look them up either here or online.

- Sulfuric Acid

Protocol:

- Add 200 microliters of sample to an empty beaker and record the mass. Add 60mL DDI water. Place beaker with stir bar on stirring platform.
- Arrange dosing line and probe so that the dosing line remains above the liquid level and the probe is submerged
- Make sure dosing line is free of large bubbles, if necessary, manually dose 5mL of acid until the line is filled (see instructions below)
- Using PC Control software, choose load method, internal memory, show all. Choose a method.
    - Method "PZ total alkalinity" doses in 0.1mL increments and stops analyzing at either 2mL of acid or when 3 endpoints are found (whichever happens first)
    - Method "20200925" doses 0.5 mL/min and stops analyzing at either pH = 2 or when 3 endpoints are found (whichever happens first)
- Once a method has been loaded, click start.
- Record the sample ID, mass of sample, endpoint pH, acid vol (mL) to reach endpoint, concentration of acid

Changing the Acid/Base:

- Changing just the concentration, not changing out acid for base or base for acid:
    - There is a vessel inside the automatic titrator that must be emptied. From the home page, click manual, dosing, dosing fixed volume, and then dose at least 50mL to empty the vessel and dosing line. When the new acid is in the

removable bottle, dose in 5mL increments until the dosing vessel and line are filled with the new acid.

- Changing out an acid for a base, or a base for an acid

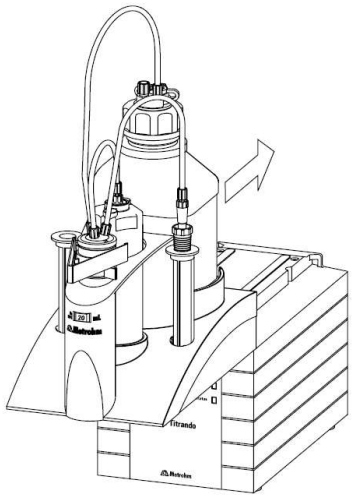

Fig. 10: Attaching the exchange unit to the Titrando

  -
  - When you need to change out the acid for a base (or vice versa) you must change out the entire exchange unit. Locate the exchange unit you intend to use.
  - In the software, click manual, dosing, fill. This will move the piston into the lowest position, and allow the exchange unit to be removed.
  - Remove the pH probe – this will be moved into the new exchange probe. (no need to unplug it)
  - Slide the exchange unit off the front.
  - Slide the new exchange unit on.
  - On the software, click on manual, dosing, prepare. This will prepare the column for use. Make sure the column inside the green plastic tube is full. If it is not full, press manual, dosing, fill. If the line from the exchange unit to the dosing tube is not full, press manual, dosing, dosing fixed vol, and dose 5mL at a time until the tube is full.
  - Make sure to check that the method that is loaded is the one that you need.
  - Proceed normally

Experimental Method*:
***Adapted from Freeman 2011**
In PZ titrations, there were usually two prominent equivalence points identified. The first equivalence point represented the conversion of anhydrous PZ species into monoprotonated PZ (protonated PZ or PZH+).

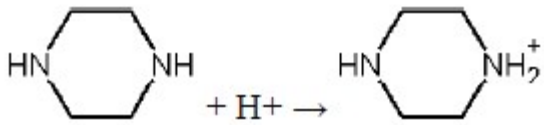

The second equivalence point represented the further conversion to diprotonated PZ.

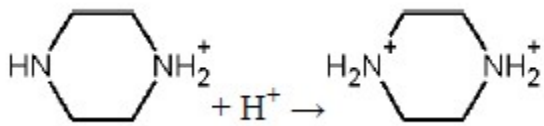

The equilibrium constant for an equilibrium reaction, Ka, can be defined for each of the two dominant reactions. The two protonation reactions written in reverse as deprotonations are shown in equations:

$$H^{+}PZ \rightarrow PZ + H^{+}$$

$$H^{+}PZH^{+} \rightarrow H^{+}PZ + H^{+}$$

Rearranging each Ka equation yields the Henderson-Hasselbalch equation relating the pH of a solution to the pKa of the species and the concentration of the species and its conjugate acid.

$$pH = pK_{a,1} + \log\left(\frac{[PZ]}{[H^{+}PZ]}\right)$$

$$pH = pK_{a,2} + \log\left(\frac{[H^{+}PZ]}{[H^{+}PZH^{+}]}\right)$$

The measured pKa of the first protonation, pKa,1, ranges from 9.71 to 9.73 at 25 °C (Enea et al., 1972; Hamborg and Versteeg, 2009; Hetzer et al., 1968; Khalili et al., 2009). The measured pKa value of the second protonation, pKa,2, ranges from 5.33 to 5.41 at 25 °C, with Enea and colleagues reporting a value as low as 4.63 at 25 °C (Enea et al., 1972; Hamborg and Versteeg, 2009; Hetzer et al., 1968; Khalili et al., 2009). Using the pH equations, the ratio of the two pairs of species can be calculated over the range of pH experienced during the titration, as shown in the table:

Solution pH	$\frac{[PZ]}{[H^{+}PZ]}$	$\frac{[H^{+}PZ]}{[H^{+}PZH^{+}]}$
11	15.1	251189
10	1.51	25119
9	0.151	2512
8	0.0151	251
7.5	0.00479	79.4

7	0.00151	25.1
6	0.000151	2.51
5	1.514E-05	0.251
4	1.514E-06	0.0251
3.9	1.202E-06	0.0200
3	1.514E-07	0.00251
2.4	3.802E-08	0.000631

When the first equivalence point at pH of 7.5 is reached, the concentration of PZ is only a fraction (0.000479) of the concentration of PZH+, indicating that nearly all the PZ has been protonated once. At the second equivalence point of 3.9 pH, the concentration of PZH+ is only a small fraction (0.02) the concentration of H+PZH+, indicating that most of the singly protonated PZ is now diprotonated. This second equivalence point, therefore, represented the amount of acid needed to fully protonate all of the amino groups on the PZ species.

The calculation of total alkalinity from the titration data is very direct and can be demonstrated assuming a case where 0.2 gram of a test sample required 8.4 mL of 0.2 N H2SO4 to reach a pH of 3.9. First, the amount of alkalinity in the sample can be calculated from the amount of acid added. Then, the concentration can be calculated in terms of moles of alkalinity per kilogram of solution using the original sample mass.

$$8.4\ \text{mL}\ H_2SO_4 * \frac{0.2\ \text{mol}\ H_2SO_4}{1000\ \text{mL}} * \frac{1\ \text{mol Alk}}{1\ \text{mol}\ H_2SO_4} = 0.00168\ \text{mol Alk}$$

$$\frac{0.00168\ \text{mol Alk}}{0.2\ \text{g soln}} * \frac{1000\text{g}}{1\text{kg}} = 8.4\ \frac{\text{mol PZ}}{\text{kg soln}}$$

In the instance of an undegraded PZ sample, for instance those used for physical property measurements, the PZ concentration can be calculated as well if the CO2 loading of the sample is known. Starting with the calculation demonstrated above for total alkalinity, the PZ concentration can be calculated in units of either mole PZ per kg of solution or molal. The first calculation is direct using the two amino functions in the PZ molecule.

$$\frac{0.00168\ \text{mole Alk}}{0.2\ \text{g soln}} * \frac{1\ \text{mole PZ}}{1\ \text{mole Alk}} * \frac{1000\ \text{g}}{1\ \text{kg}} = 4.2\ \frac{\text{mole PZ}}{\text{kg soln}}$$

To calculate the concentration in molal, the CO2 loading must be known or estimated. When the CO2 concentration is measured (see Section 3.1.3), the units first calculated are moles of CO2 per kg of solution. Therefore, the CO2 loading can be calculated directly using this value and the value calculated above for the PZ concentration.

$$\text{CO2 loading} = \frac{\frac{\text{mole CO2}}{\text{kg soln}}}{\frac{\text{mole PZ}}{\text{kg soln}} * \frac{\text{2 mole Alk}}{\text{mole PZ}}} = \frac{\text{mole CO2}}{\text{mole Alk}}$$

This calculation procedure avoids the need to assume either a PZ concentration or CO2 concentration when analyzing either set of data. Once the CO2 concentration is calculated as a loading (units of mole CO2 per mole alkalinity), this value can be used in the calculation of PZ concentration in molality. Continuing the example given above with an additional assumption of a CO2 loading of 0.3 mole CO2 per mole alkalinity, the concentration of CO2 in the sample is then calculated in terms of the amount of water in the sample.

$$\frac{\text{0.3 mole CO2}}{\text{mole Alk}} * \frac{\text{2 mole Alk}}{\text{mole PZ}} * \frac{\text{8 mole PZ}}{\text{kg H2O}} * \frac{\text{44.01 g CO2}}{\text{mole CO2}} = 211.2 \frac{\text{g CO2}}{\text{kg H2O}}$$

Next, the mass of CO2 in the sample is calculated by using the sample mass and the mass fraction of CO2 in the sample. The mass fraction is calculated by assuming a basis of 1 kg of water and a nominal PZ concentration.

$$\text{0.2 g sample} * \left[\frac{\left(\frac{\text{211.2 g CO2}}{\text{kg H2O}}\right)}{\frac{\text{211.2 g CO2}}{\text{kg H2O}} + \left(\frac{\text{8 mole PZ}}{\text{kg H2O}} * \frac{\text{86.14 g PZ}}{\text{mole PZ}}\right) + \frac{\text{1000 g H2O}}{\text{kg H2O}}}\right] = \text{0.0222 g CO2}$$

The mass of water in the original sample can be determined by subtracting the amount of PZ and CO2 in the original sample. First, the mass of PZ is calculated by assuming all the alkalinity is PZ.

$$\text{8.4 mL H2SO4} * \frac{\text{0.2 mole H2SO4}}{\text{1000 mL}} * \frac{\text{1 mole Alk}}{\text{1 mole H2SO4}} * \frac{\text{1 mole PZ}}{\text{2 mole Alk}} * \frac{\text{86.14 g PZ}}{\text{1 mole PZ}} = \text{0.0724g PZ}$$

$$(\text{0.2 g sample}) - (\text{0.0222 g CO2}) - (\text{0.0724 g PZ}) = \text{0.1052 g H2O}$$

Finally, the CO2-free molality of PZ can be calculated:

$$\frac{\text{0.00084 mole PZ}}{\text{0.1054 g H2O}} * \frac{\text{1000 g H2O}}{\text{kg H2O}} = \text{7.969 m PZ}$$

Using this calculation procedure, the concentration of a single amine can be determined in terms of molality directly from a simple and quick titration procedure.

Appendix D

Appendix D provides the Fortran User Subroutine for the diffusivity model *'dlou'* after adjusting the modeled diffusivity of PZ to match values predicted by Stokes-Einstein.

'dlou' Fortran Code

```
C Log keyword added
C
C$ #1 BY: SUPHAT WATANASIRI 09-SET-2007 USER ROUTINE FOR LIQUID BINARY
C                                DIFFUSION COEFFICIENTS
C
C ==========================cvs revision history=========================
      SUBROUTINE DL0U ( T, P, X, N, IDX, IRW, IIW, KCALC, KOP,
     *                  NDS, KDIAG, QBIN, KER )
C*********************************************************************
C     Template for DL0U routine for binary liquid diffusion coefficients
C     STUB ROUTINE
C
C     T = temperature
C     P = pressure (system)
C     X(N) = mole fraction
C     N = number of components present in X
C     IDX(N) = index of component present
C     IRW = real work area index
```

```
C     IIW = integer work area index

C     KCALC = calculation code (0=do not calculate, 1 = calculate)

C     KOP(10) = model option code

C     NDS = data set number

C     KDIAG = diagnostic message level

C     QBIN(N,N) = results. Binary diffusion coeffcients.

C     QBIN(i,j) is binary diffusion coefficient of component i in component j

C     KER = error return code (0 = no error)

C     All input and output in this user routine are in SI Units

C     with Gas constant = 8314.33

C***********************************************************************

C

      IMPLICIT NONE

C

C     DECLARE VARIABLES USED IN DIMENSIONING

C

      INTEGER N

#include "dms_global.cmn"

#include "dms_errout.cmn"

#include "ppexec_user.cmn"

#include "dms_maxwrt.cmn"

C

C     DECLARE ARGUMENTS

C
```

```
      INTEGER IDX(N), IRW, IIW, KCALC, KOP, NDS, KDIAG, KER
            INTEGER IWATER, IPZCOO, ICO2, IPZCOO2, IHPZCOO, IHCO3
            INTEGER IPZH, IPZ, ICO3, IMDEA, IMDEAH, IN2, IO2
            INTEGER DMS_KCCIDC
      REAL*8 X(N), QBIN(N,N), T, P
            REAL*8 WATER, PZCOO, CO2, PZCOO2, HPZCOO, HCO3, PZH, PZ
            REAL*8 CO3, MDEA, MDEAH
            REAL*8 LDG, XPZCOO2, XCO2T, XPZT, XMDEAT
            REAL*8 MWPZ, MWCO2, MWH2O, MWMDEA, XH2O, MWT, XWPZ, XWMDEA
            REAL*8 XWAMINE
            REAL*8 IOND, CO2D, MDEAD, PZD, XMOLT, CO2DW
            REAL*8 MA, MB, MC, MD, ME, MUMX, MUMX1
            REAL*8 A, E, B, THET, C, MU0, MUW, R, HG
            Real*8 VISC, LVISC, VM
            integer nbopst(6), name(2)
            CHARACTER*256 BUFFER(1)
C
C     DECLARE LOCAL VARIABLES
C
      INTEGER IPROG(2), I, J, K
C
C      DATA STATEMENTS
C
      DATA IPROG /4HDL0U, 4H    /
```

```
C
C     BEGIN EXECUTABLE CODE
C             DIFFUSIVITIES CALCULATED BY (...) METHOD
C             VALUES OBTAINED FROM THE DIFFUSIVITY REGRESSION
              KER = 0
              IF (KCALC .EQ. 0) RETURN
c
C             INDEX VALUES FOR COMPONENTS IN SIMULATION
C
      IWATER = DMS_KCCIDC('H2O')
      IPZCOO = DMS_KCCIDC('PZCOO-')
      ICO2 = DMS_KCCIDC('CO2')
      IPZCOO2 = DMS_KCCIDC('PZCOO-2')
      IHPZCOO = DMS_KCCIDC('HPZCOO')
      IHCO3  = DMS_KCCIDC('HCO3-')
      IPZH = DMS_KCCIDC('PZH+')
      IPZ = DMS_KCCIDC('PZ')
              ICO3 = DMS_KCCIDC('CO3--')
              IMDEA = DMS_KCCIDC('C5H13-01')
              IMDEAH = DMS_KCCIDC('C5H14-01')
              IN2 = DMS_KCCIDC('N2')
              IO2 = DMS_KCCIDC('O2')
C
C
```

```
C          ASSIGNMENT OF INDEX NUMBERS FOR SPECIES PRESENT
C
           DO 50 I = 1, N
           IF (IDX(I). EQ. IWATER) IWATER = I
           IF (IDX(I). EQ. IPZCOO) IPZCOO = I
           IF (IDX(I). EQ. ICO2) ICO2 = I
           IF (IDX(I). EQ. IPZCOO2) IPZCOO2 = I
           IF (IDX(I). EQ. IHPZCOO) IHPZCOO = I
           IF (IDX(I). EQ. IHCO3) IHCO3 = I
           IF (IDX(I). EQ. IPZH) IPZH = I
           IF (IDX(I). EQ. IPZ) IPZ = I
           IF (IDX(I). EQ. ICO3) ICO3 = I
           IF (IDX(I). EQ. IMDEA) IMDEA = I
           IF (IDX(I). EQ. IMDEAH) IMDEAH = I
           IF (IDX(I). EQ. IN2) IN2 = I
           IF (IDX(I). EQ. IO2) IO2 = I
  50 CONTINUE
C
C          LOADING CALCULATION
           XPZCOO2 = 2D0*X(IPZCOO2)
           XCO2T = X(IPZCOO)+X(ICO2)+XPZCOO2+X(IHPZCOO)+X(IHCO3)
           XPZT = X(IPZCOO)+X(IPZCOO2)+X(IHPZCOO)+X(IPZH)+X(IPZ)
           XMDEAT = X(IMDEA)+X(IMDEAH)
           LDG = XCO2T/(2D0*XPZT + XMDEAT)
```

```
C
C
C           AMINE MASS FRACTION CALCULATION
C
            MWPZ = 86.14D0
            MWCO2 = 44.01D0
            MWH2O = 18D0
            MWMDEA = 119.163D0
            XH2O = X(IWATER)
            MWT = XCO2T*MWCO2 + XPZT*MWPZ + XH2O*MWH2O + XMDEAT*MWMDEA
            XWPZ = (XPZT*MWPZ)/MWT
            XWMDEA = (XMDEAT*MWMDEA)/MWT
            XWAMINE = XWPZ + XWMDEA

c           Viscosity of solution from Aspen
            call PPUTL_GOPSET ( NBOPST , NAME )
c
            CALL PPMON_VISCL (T, P, X, N, IDX, NBOPST, KDIAG, VISC, KER)
            LVISC = VISC
            MUMX = LVISC
C
C    Viscosity of water according to Likhachev E.R. Technical Physics, Vol. 48 N0.4 2003 pp. 514-515
C    Viscosity in Pa-s
     E = 4.753D0
```

```
      MU0 = 0.000024055D0
      THET = 139.7D0
            A = 0.000442D0
            B = 0.0009565D0
            C = 0.0124D0
            R = 0.008314D0
            P = P / 100000D0
            HG = A * P +((E - B * P)/(R * (T - THET - C * P)))
            MUW = MU0 * EXP(HG)
C
C     DIFFUSIVITY OF CO2 IN WATER
      CO2DW = 0.00000235D0 * EXP(-2119D0 / T)
C
C     DIFFUSIVITY OF CO2 IN SOLUTION BASED ON VERSTEEG, 2003
      CO2D = CO2DW * (MUW / MUMX)**(0.8D0)
C
C     DIFFUSIVITY OF AMINE IN WATER, FROM Frailie's dissertation, 2014
C     Second line does a temperature correction, third line applies viscosity correction on top of temperature
C           Last line applies 0.2384 correction factor directly to diffusivity instead of area, Suresh Babu, 2023
      VM = 129.371D0
      PZD = 0.00000000005404192D0*((T/313.15D0)**-2.5819D0)
      PZD = PZD*((MUMX/0.0155D0)**-1.449118D0)
C
C
```

```
C     ASSIGNING VALUES IN THE DIFFUSIVITY MATRIX
C
C
      DO 200 I = 1, N
        DO 100 J = 1, N
          IF (I.EQ.J) THEN
            QBIN(I,J) = 0D0
          ELSE
            QBIN(I,J) = PZD
            IF (I.EQ.ICO2)QBIN(I,J) = CO2D
            IF (J.EQ.ICO2)QBIN(I,J) = CO2D
            IF (I.EQ.IN2)QBIN(I,J) = CO2D
            IF (J.EQ.IN2)QBIN(I,J) = CO2D
            IF (I.EQ.IO2)QBIN(I,J) = CO2D
            IF (J.EQ.IO2)QBIN(I,J) = CO2D
          END IF
  100   CONTINUE
  200 CONTINUE


c
C               WRITE VARIABLES TO HISTORY FILE
C
C                THE WRITE TO UNIT USER_NHSTRY WRITES TO THE HISTORY FILE
                WRITE (BUFFER, *) 'Executed fortran subroutine'
```

```
      CALL DMS_WRTALN(USER_NHSTRY, BUFFER(1))
      WRITE (BUFFER, *) 'Pressure ', P
      CALL DMS_WRTALN(USER_NHSTRY, BUFFER(1))
      WRITE (BUFFER, *) 'Temperature ', T
      CALL DMS_WRTALN(USER_NHSTRY, BUFFER(1))
      WRITE (BUFFER, *) 'LVISC ', LVISC
      CALL DMS_WRTALN(USER_NHSTRY, BUFFER(1))
      WRITE (BUFFER, *) ' '
      CALL DMS_WRTALN(USER_NHSTRY, BUFFER(1))
C 999 RETURN
    END
```

Appendix E

Appendix E shows photos from surface temperature measurements taken during the SRP 2021-22 campaign and the NCCC 2023 campaign in some key locations relevant for heat loss in the advanced stripper system.

Appendix E.1

Appendix E.1 shows the photos taken from the UT SRP 2021-22 campaign.

E.1.1 Stripper Sump

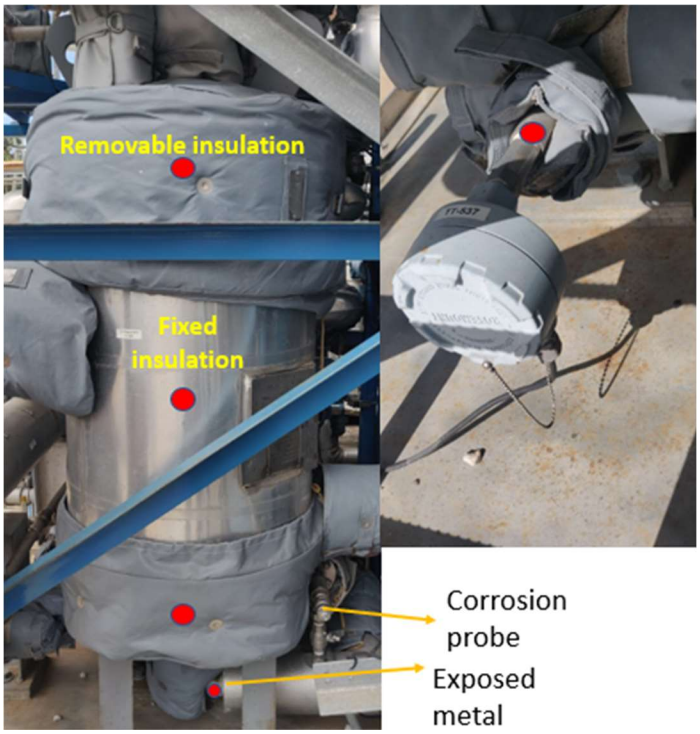

E.1.2 Stripper Column

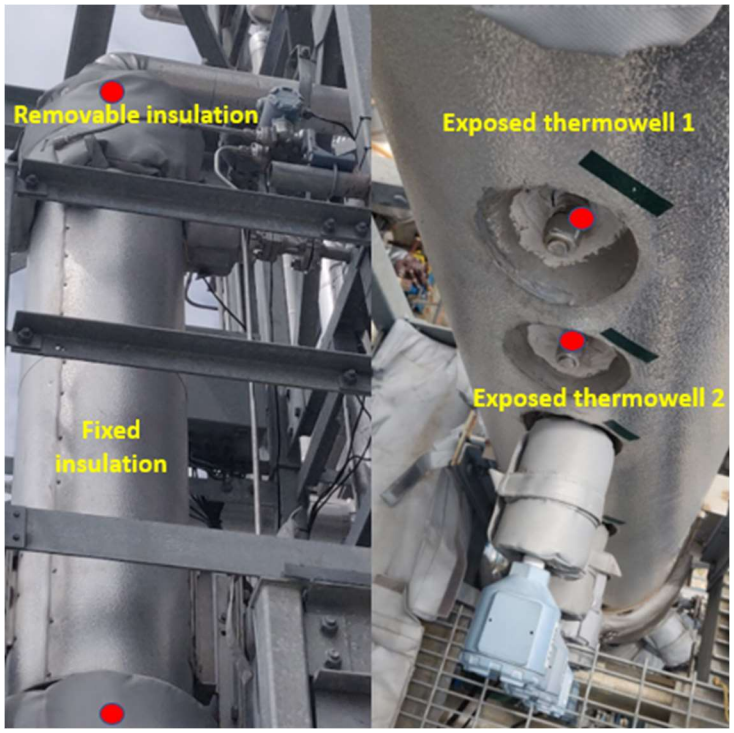
Removable insulation
Exposed thermowell 1
Exposed thermowell 2
Fixed insulation

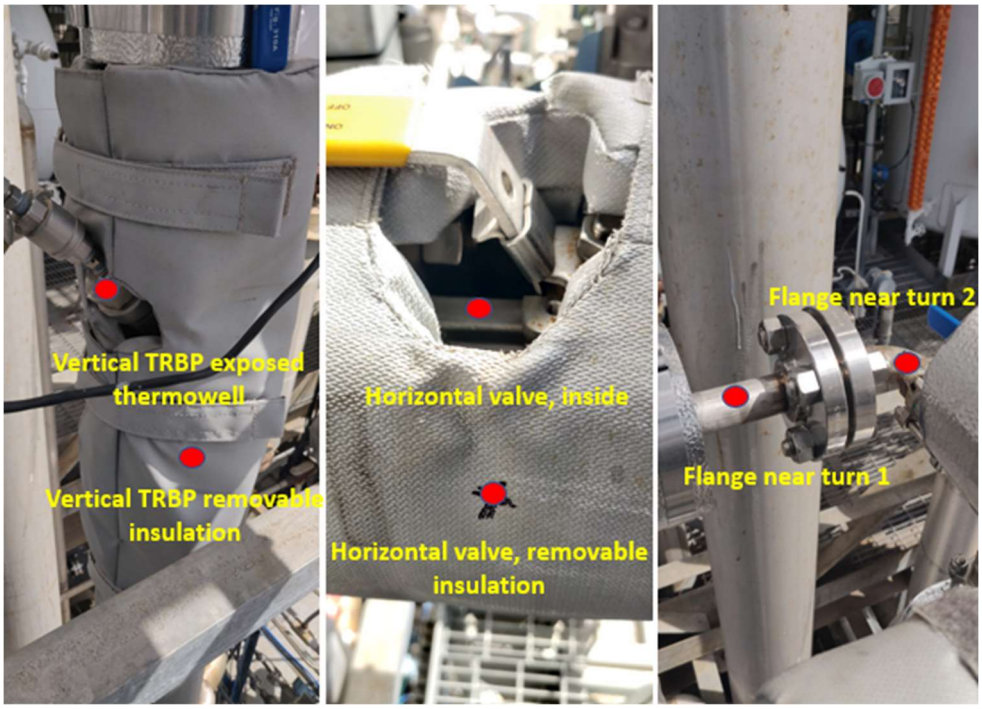
Vertical TRBP exposed thermowell
Vertical TRBP removable insulation
Horizontal valve, inside
Horizontal valve, removable insulation
Flange near turn 2
Flange near turn 1

E.1.3 Oxidation Tank for Residence Time Increase

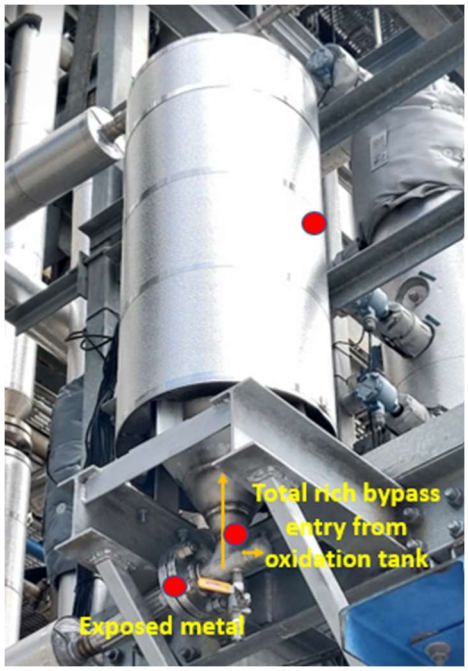

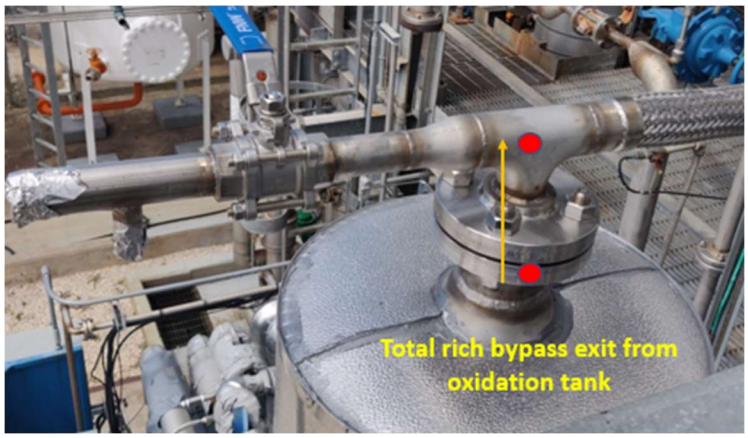

E.1.4 Low Pressure Steam Heater Area

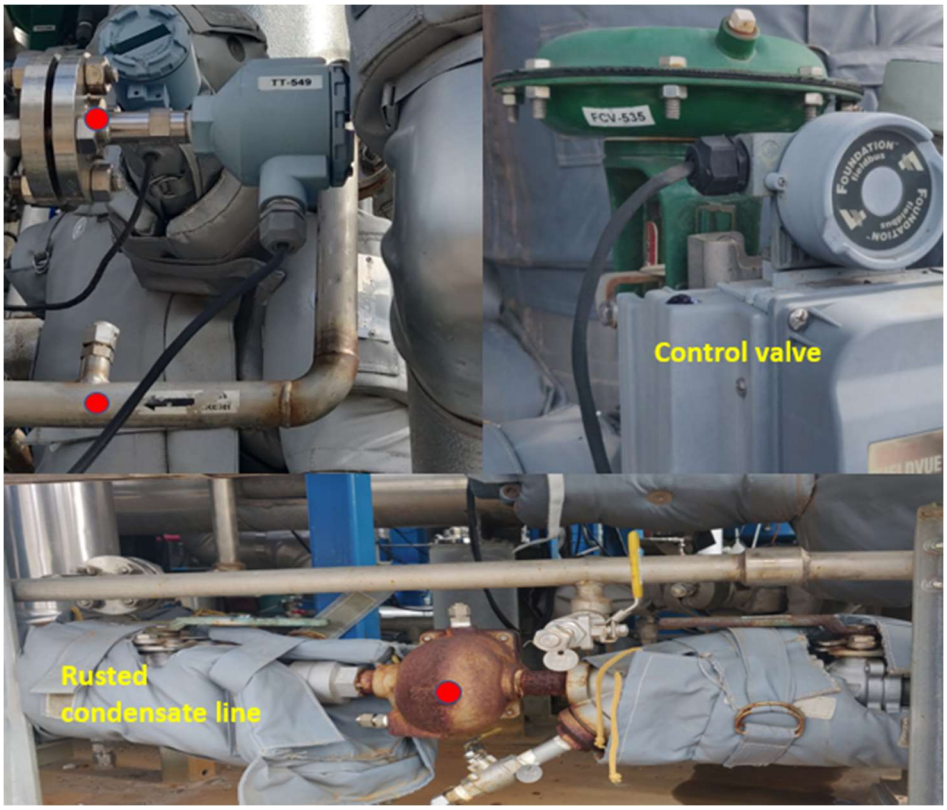

E.1.5 High Pressure Steam Heater Area

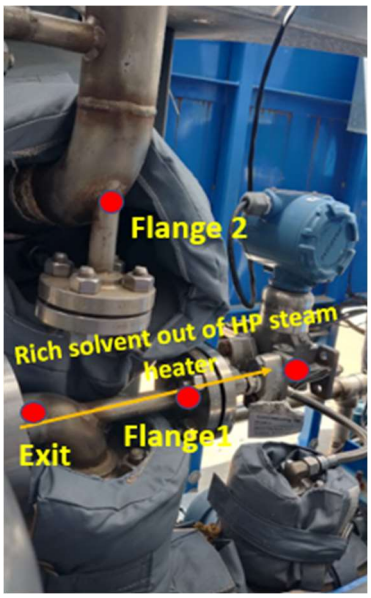
Flange 2
Rich solvent out of HP steam heater
Exit
Flange1

Condensate out rusted line

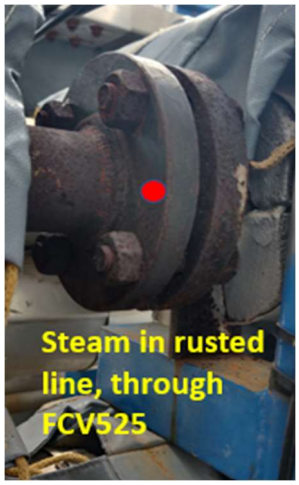
Steam in rusted line, through FCV525

E.1.6 Hot Heat Exchanger Area

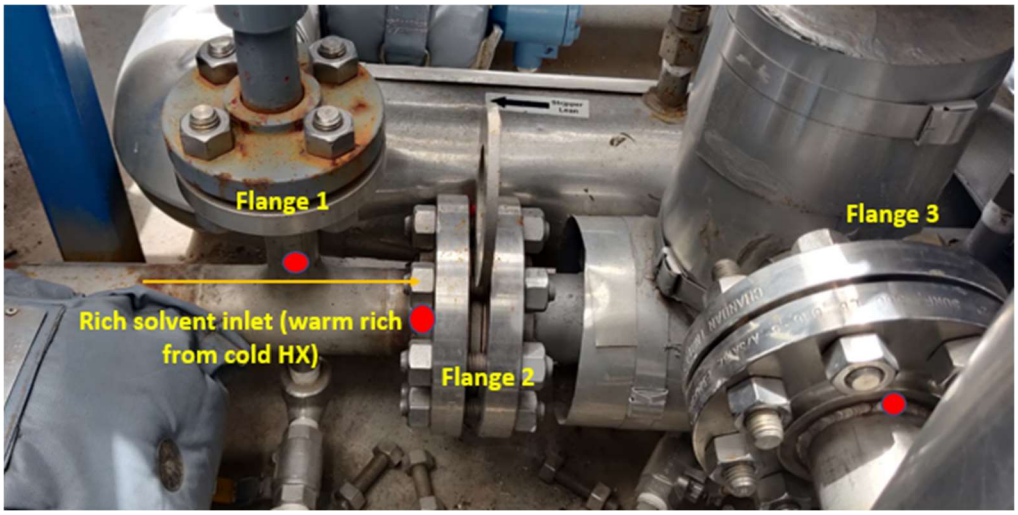

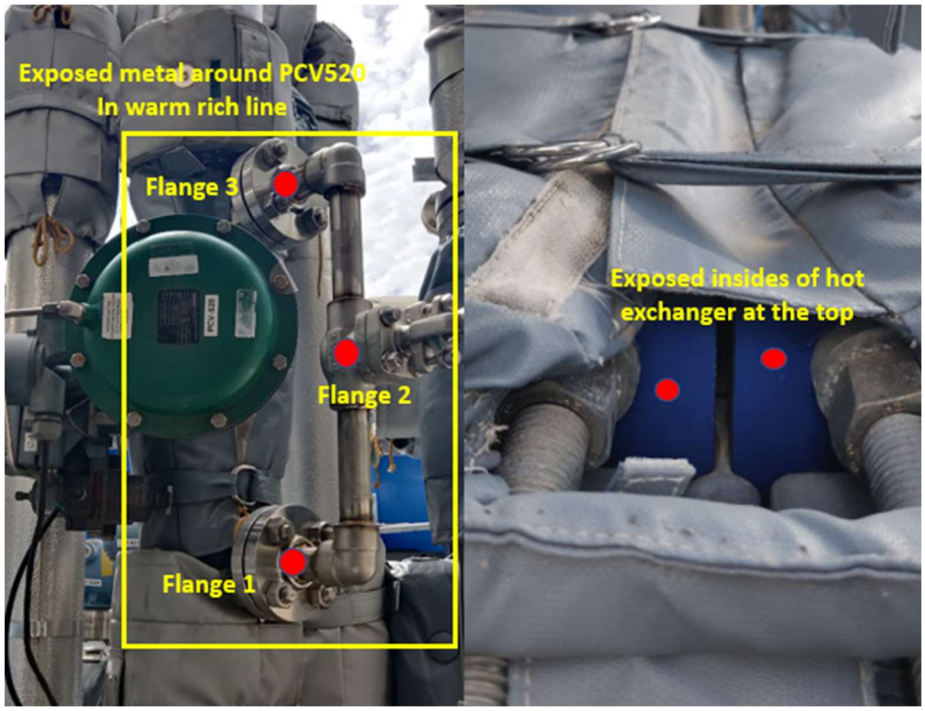
Exposed metal around PCV520
In warm rich line
Flange 3
Flange 2
Flange 1
Exposed insides of hot
exchanger at the top

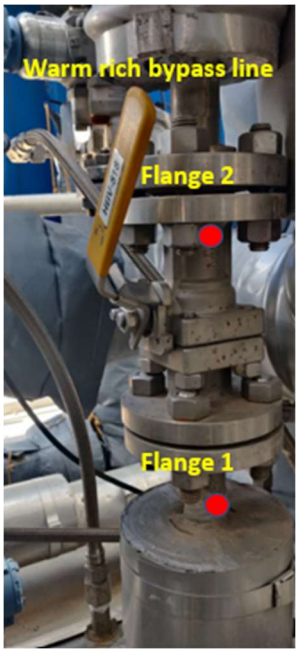
Warm rich bypass line
Flange 2
Flange 1

E.1.7 Lean Startup Pump Area (Hot Lean Line)

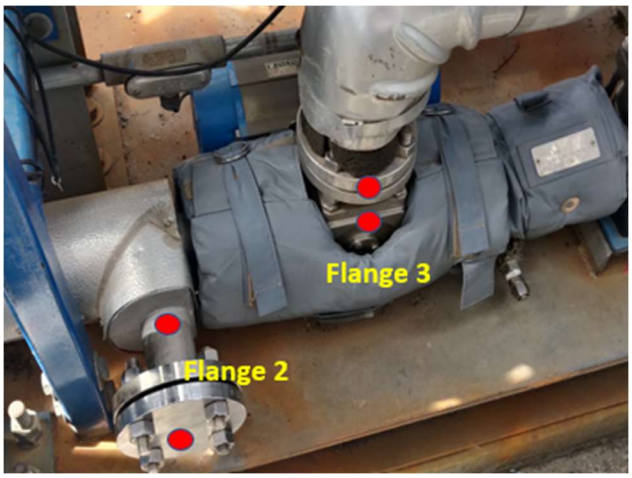

Appendix E.2

Appendix E.2 shows the photos from the NCCC 2023 campaign.

E.2.1 Stripper Sump

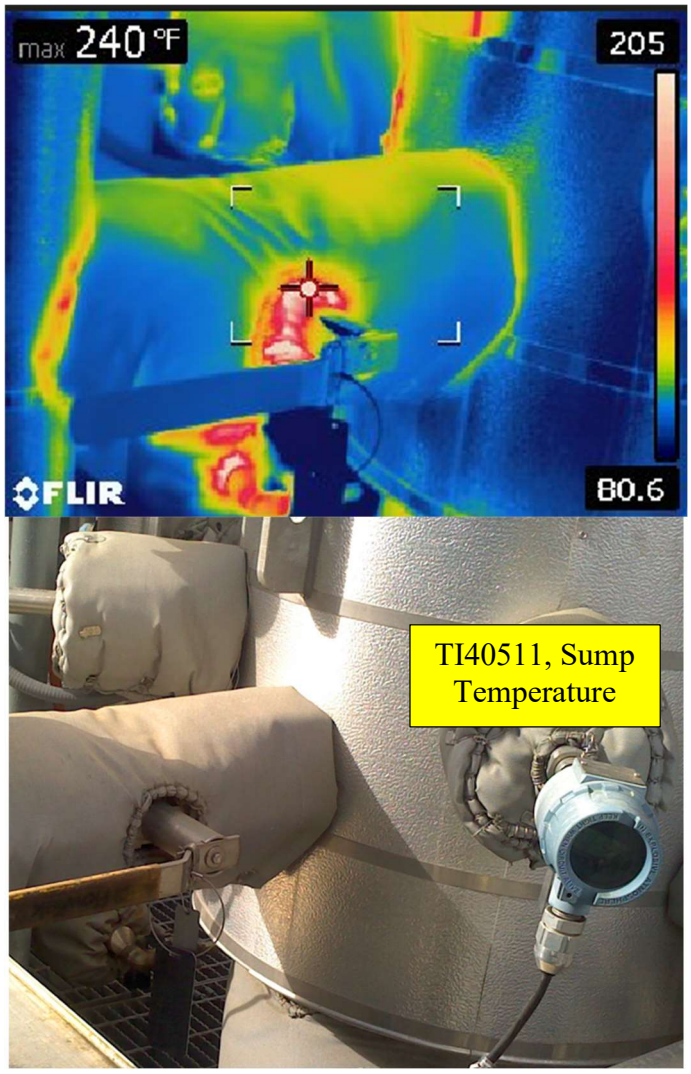

max 171 °F
198
27.9
FLIR

TI40517, Upper
Sump Temperature

E.2.2 Stripper Column

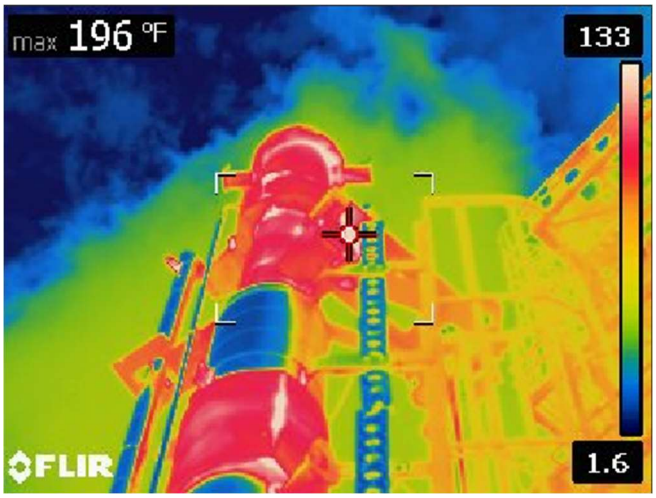

max *263 °F
213
54.0
FLIR

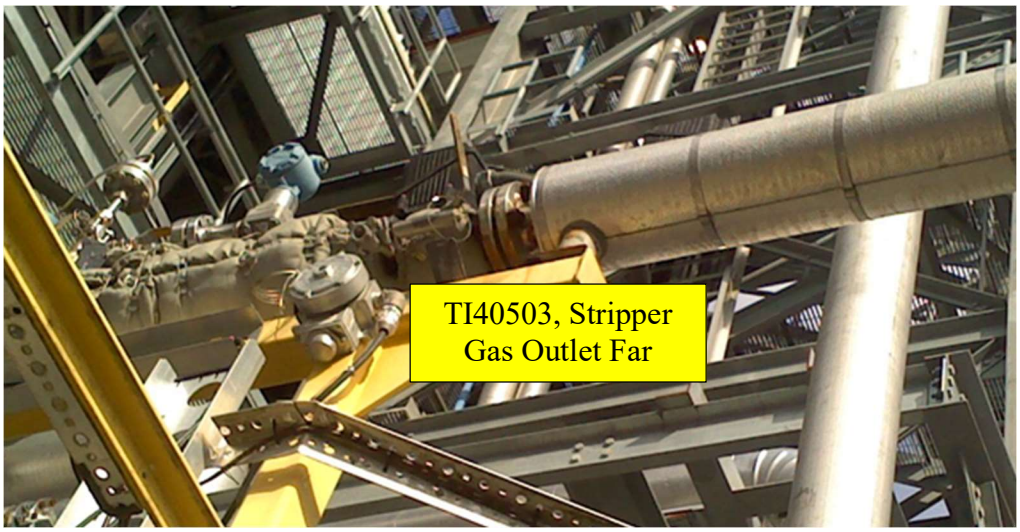
TI40503, Stripper
Gas Outlet Far

max 199 °F
153
-0.2
FLIR

TI40513, Stripper
Gas Outlet Near

E.2.3 Steam and Condensate Lines

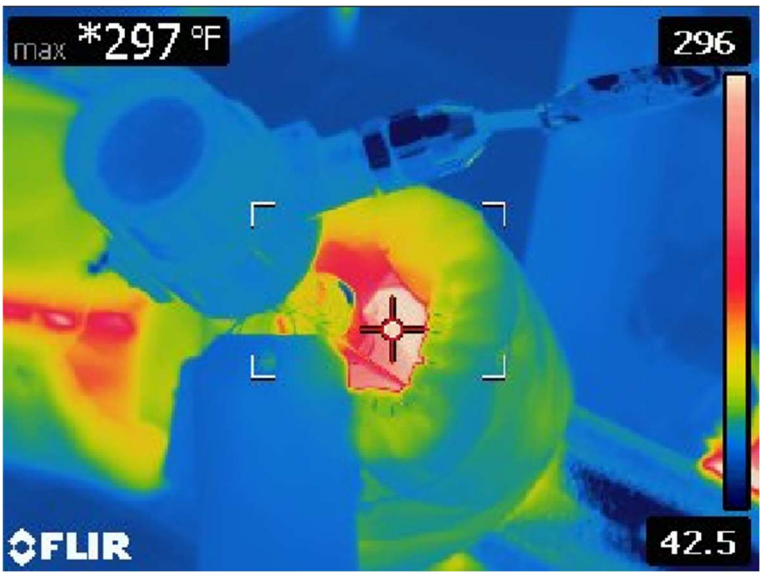

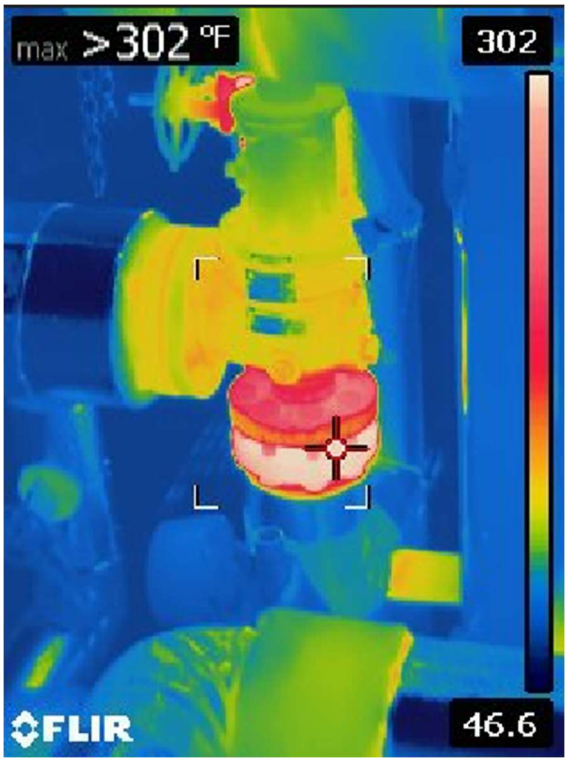
max >302 °F
302
FLIR
46.6

max >302 °F
290
71.1
FLIR

Steam Heater

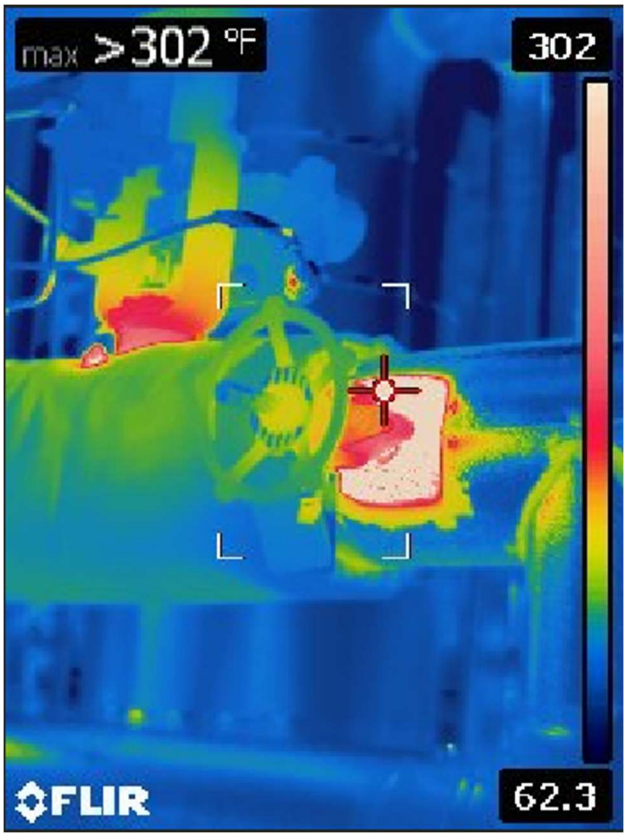
max >302 °F
302
FLIR
62.3

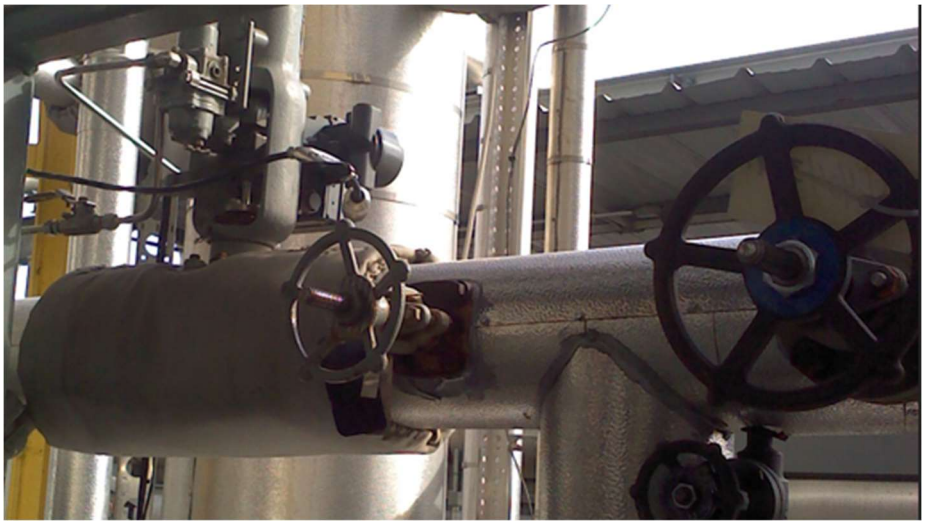

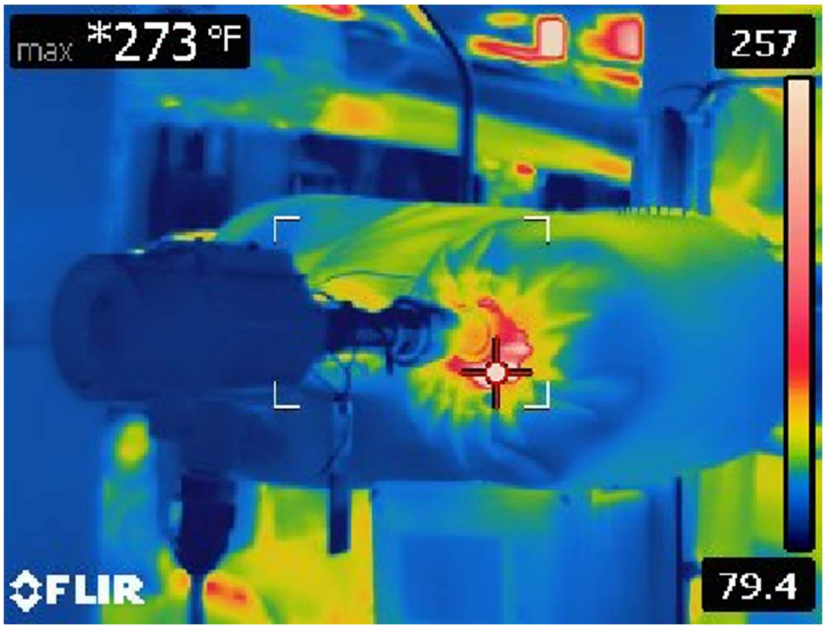
max *273 °F
257
FLIR
79.4

TI40510, Hot Rich T
out of Steam Heater

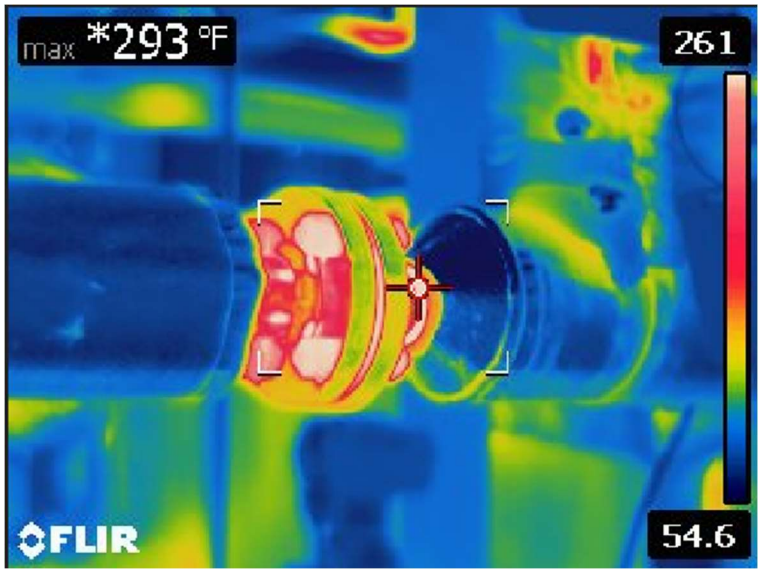
max *293 °F
261
FLIR
54.6

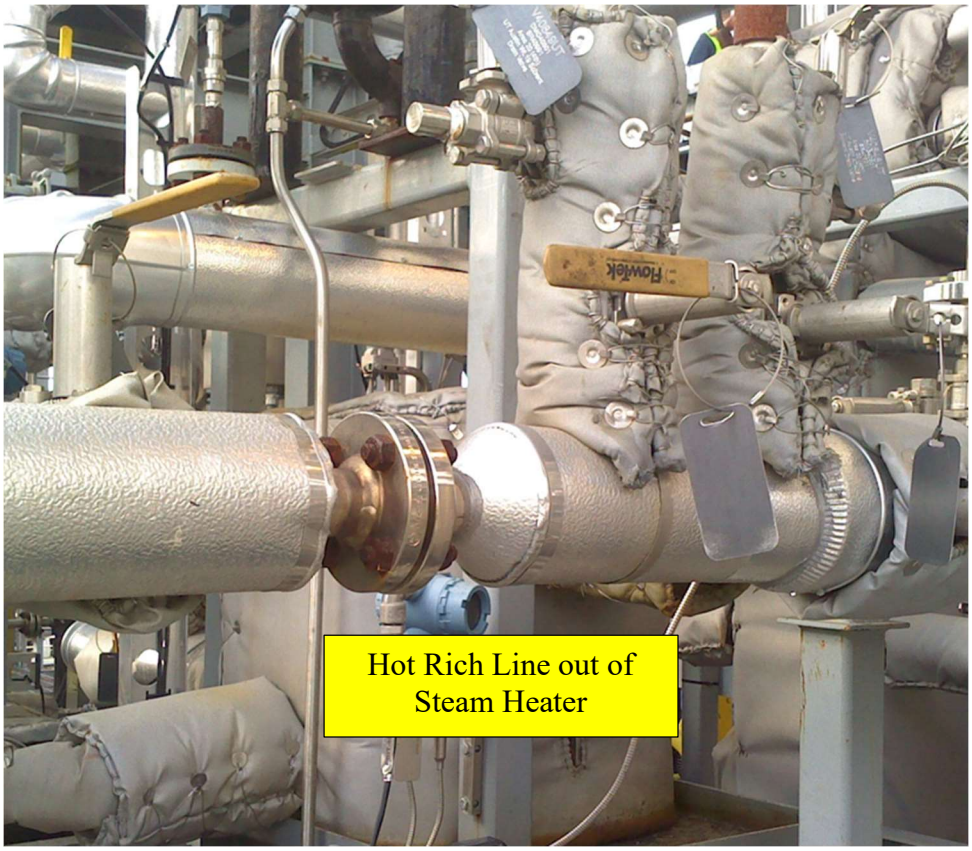
Hot Rich Line out of
Steam Heater

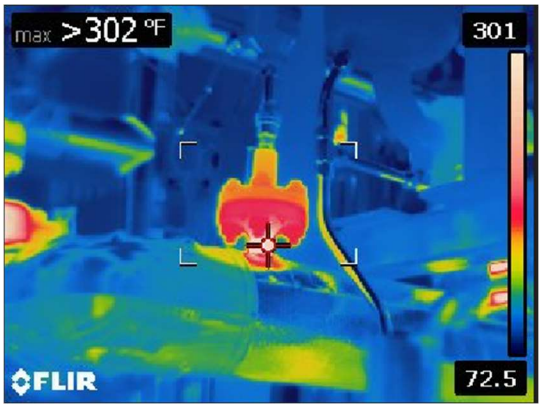
max >302 °F
301
FLIR
72.5

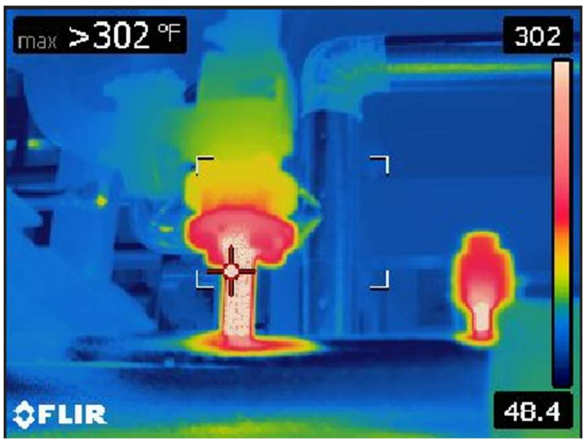
max >302 °F
302
FLIR
48.4

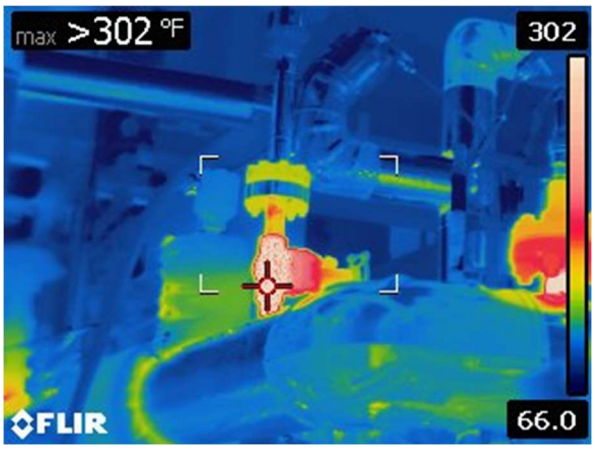
max >302 °F
302
FLIR
66.0

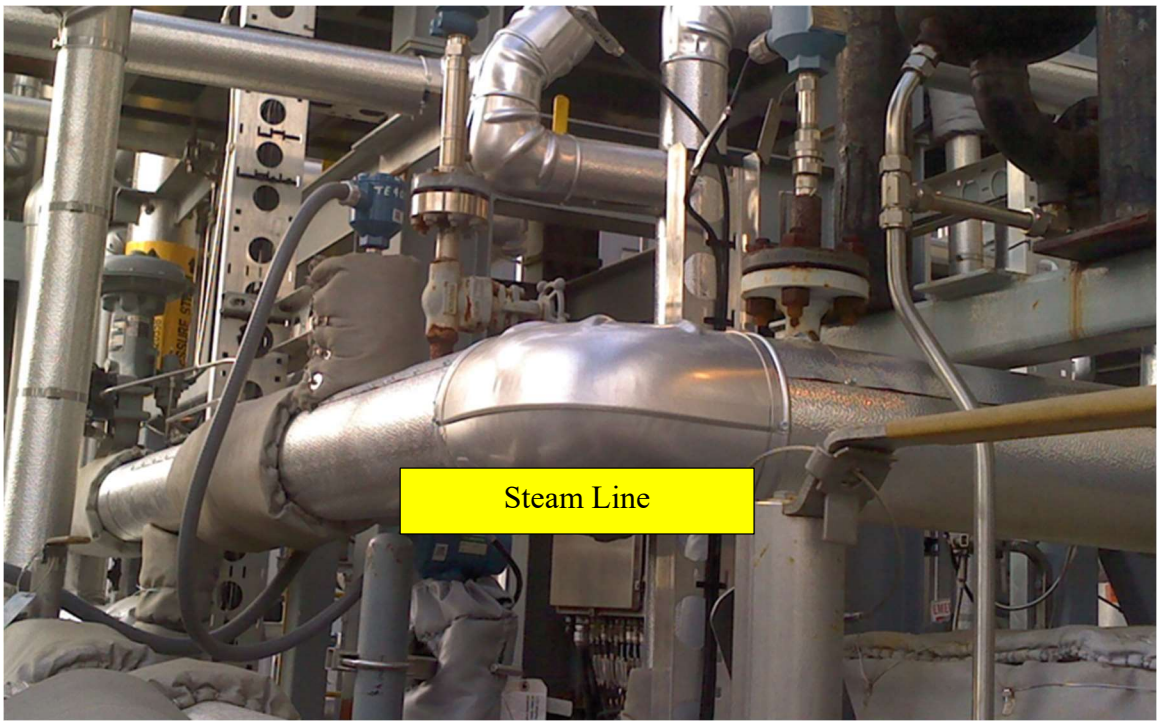
Steam Line

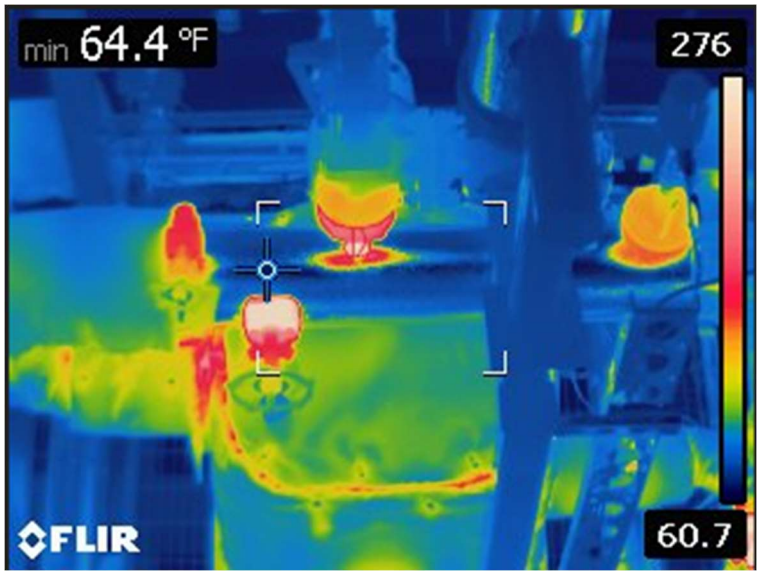
min 64.4 °F
276
FLIR
60.7

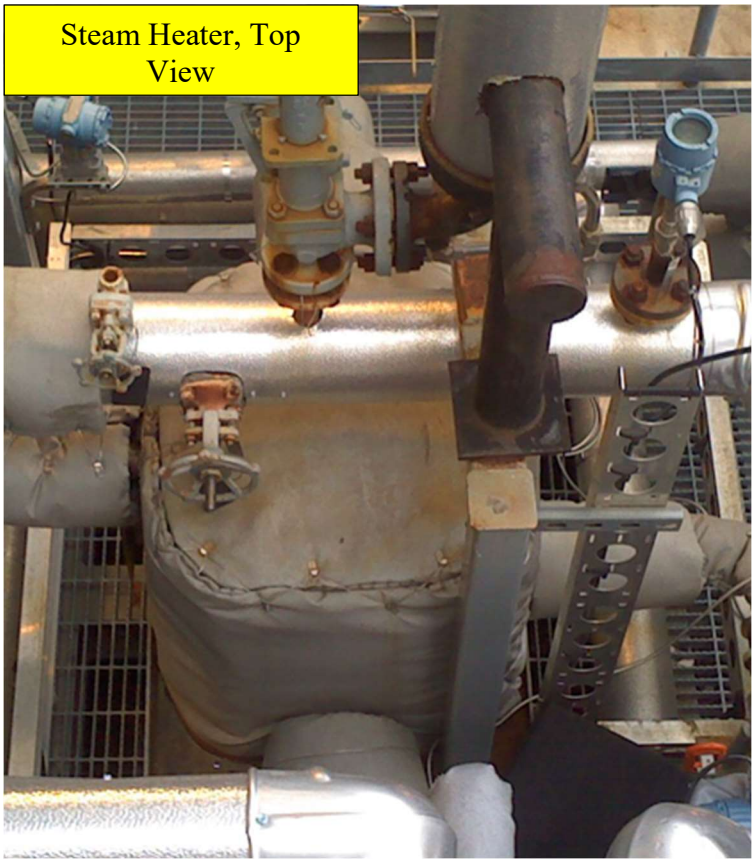
Steam Heater, Top View

E.2.4 Hot Cross Exchanger

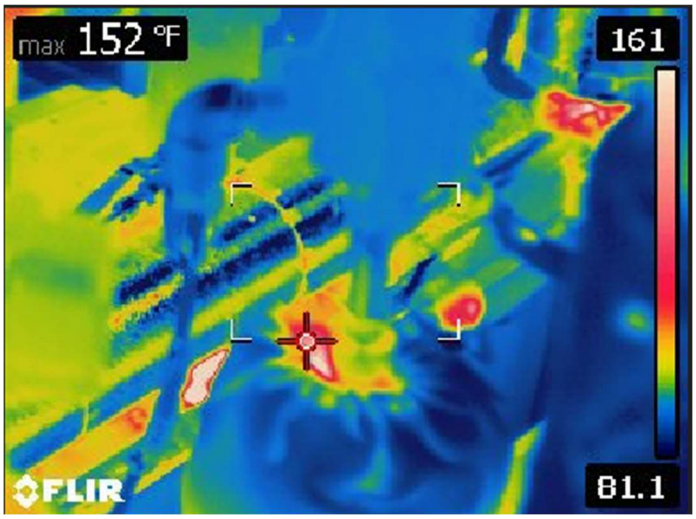

FIT-4050S

max 217 °F
201
76.5
FLIR

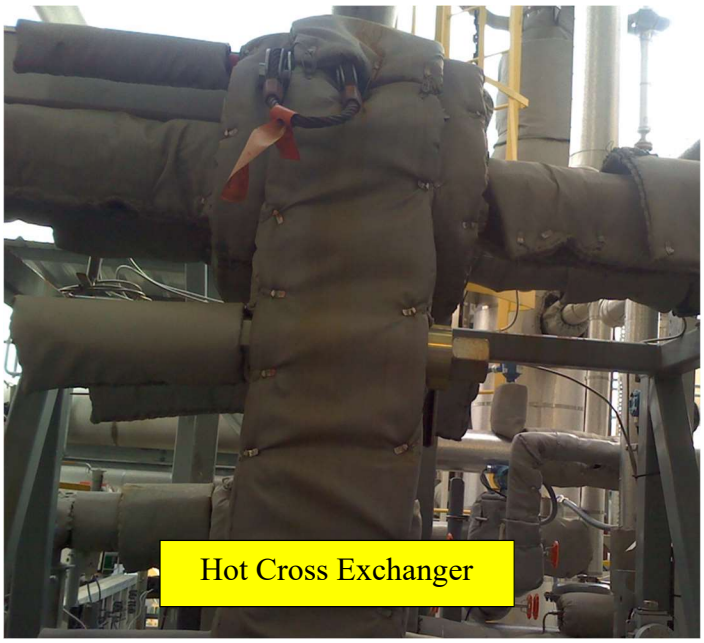
Hot Cross Exchanger

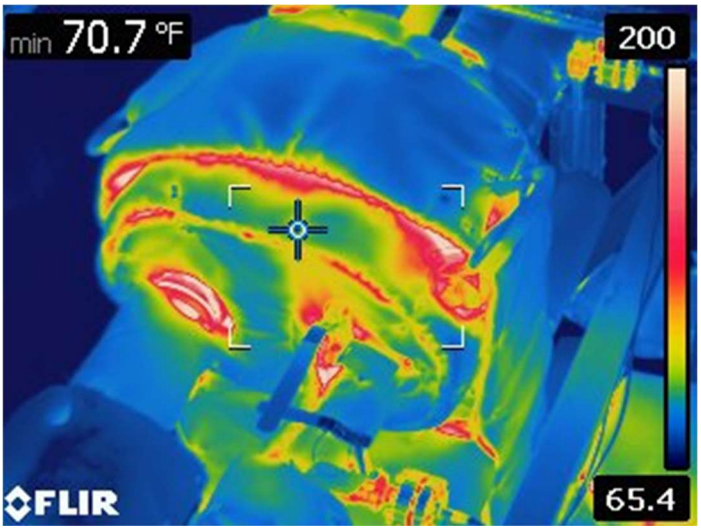
min 70.7 °F
200
65.4
FLIR

E.2.5 CO_2 Exchanger

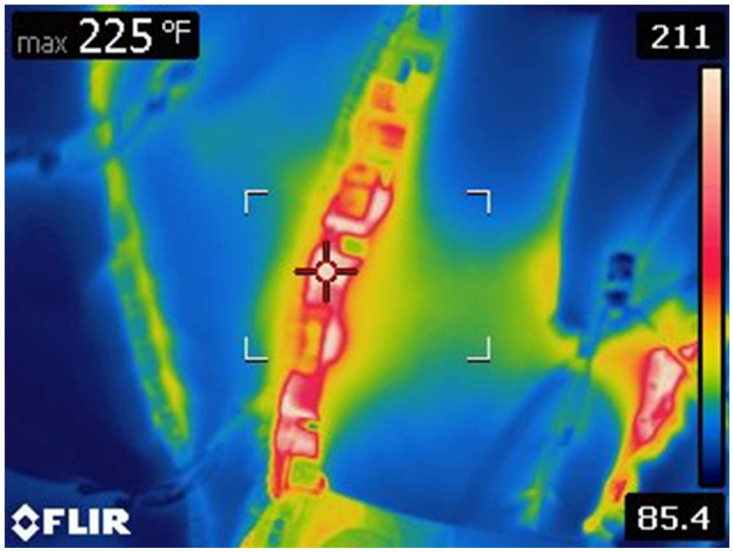

Heated CRBP line,
TI40502

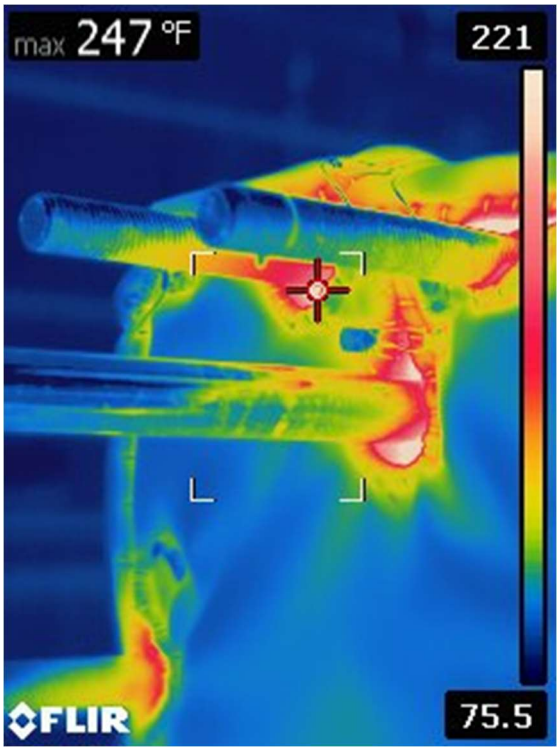
max 247 °F
221
FLIR
75.5

CO_2 Exchanger, Side View

E.2.6 Cold Cross Exchanger

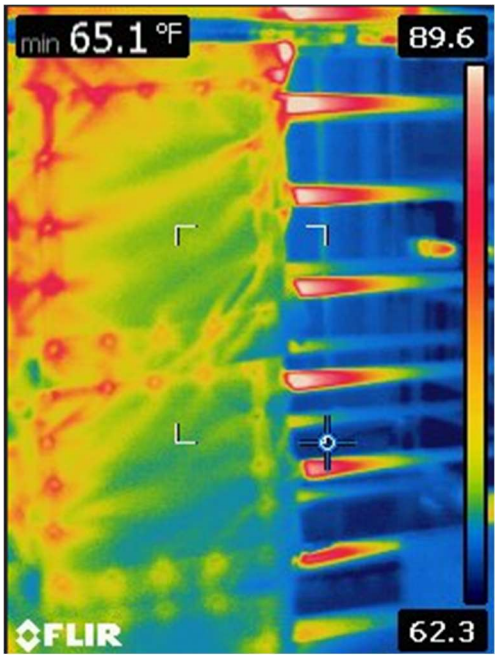

Appendix F

Appendix F shows the stripper-side surrogate models and tabulates the R^2 values of these models used in process optimization (Chapters 5-6).

F. 1 Stripper Section Surrogate Models

Flooding - Top Section

Flood 1 = 7145.1634319051636339282 * RichLDG - 0.78592777273752176259158E-001 * RichFPZAS + 0.21598549403577921822206E-002 * LCRBP + 0.27360276563073156023964E-002 * LWRBP + 0.41509530626651630624835 * CO2Flow - 27806.766836658240208635 * RichLDG^2 + 0.71017333156276195196659E-004 * RichFPZAS^2 + 0.25617475724341690101245E-004 * LCRBP^2 - 0.21425884571776486286045E-005 * LWRBP^2 - 0.28544647877208399050497E-001 * CO2Flow^2 + 47599.293079851457150653 * RichLDG^3 - 0.34547777794137080834781E-007 * RichFPZAS^3 + 0.69479607776637268036490E-003 * CO2Flow^3 - 30354.192167873996368144 * RichLDG^4 -

0.48326180742010977245773E-005 * CO2Flow^4 + 0.17085955351601431195796 * RichLDG*RichFPZAS - 0.60548119570512995424316E-002 * RichLDG*LCRBP - 0.78109101958257522169138E-002 * RichLDG*LWRBP + 0.13628675029104039828631 * RichLDG*CO2Flow - 0.21524246175413098812338E-004 * RichFPZAS*LCRBP + 0.10349825698104271700414E-005 * RichFPZAS*LWRBP + 0.29286548289996047929329E-003 * RichFPZAS*CO2Flow + 0.29443420182644238614457E-005 * LCRBP*LWRBP - 0.13997290301915728759873E-003 * LCRBP*CO2Flow - 0.26480366949924985433412E-003 * (RichLDG*RichFPZAS)^2 - 0.12138942664301899517984E-003 * (RichLDG*LCRBP)^2 - 0.21790860984386904025678E-001 * (RichLDG*CO2Flow)^2 + 0.11958405237111713351795E-006 * (RichLDG*LWRBP)^3 + 0.67686284992484786618774E-004 * RichLDG*RichFPZAS*LCRBP - 679.56285962994309102214

Flooding - Bottom Section

Flood 2 = 1542.8667352995037163055 * RichLDG + 0.16045842923689848658064 * RichFPZAS + 0.56965982458608032702740E-003 * LCRBP + 0.83221243352686966737730E-002 * LWRBP - 0.75949938348055223702460 * CO2Flow - 6135.0165344911274587503 * RichLDG^2 - 0.39265130734603598304869E-003 * RichFPZAS^2 + 0.46095007635371459345924E-004 * LCRBP^2 - 0.25478442867449732612238E-004 * LWRBP^2 - 0.81831495071281790121276E-001 * CO2Flow^2 + 11222.920458015945769148 * RichLDG^3 + 0.17692788211175541270754E-006 * RichFPZAS^3 + 0.78972175939839809705764E-008 * LWRBP^3 + 0.12814984514035268094168E-002 * CO2Flow^3 - 7874.8059874121563552762 * RichLDG^4 - 0.59567948776980638085177E-005 * CO2Flow^4 - 0.51374995040456317152433 * RichLDG*RichFPZAS + 0.31356773975652757480148E-002 * RichLDG*LCRBP - 0.20233542101616767278083E-001 * RichLDG*LWRBP + 3.77606181667530771406 40 * RichLDG*CO2Flow - 0.35266219166360797767669E-004 * RichFPZAS*LCRBP + 0.74343632928953917104006E-006 * RichFPZAS*LWRBP + 0.12272988677706347937502E-001 * RichFPZAS*CO2Flow + 0.29536220188067086887048E-005 * LCRBP*LWRBP - 0.55033143907962198560641E-003 * LCRBP*CO2Flow + 0.35479337066784332951896E-002 * (RichLDG*RichFPZAS)^2 - 0.21917488862762974505261E-003 * (RichLDG*LCRBP)^2 + 0.11737362238352198754235E-003 * (RichLDG*LWRBP)^2 + 0.35151788118461652077329 * (RichLDG*CO2Flow)^2 - 0.76119960601171320865830E-007 * (RichFPZAS*CO2Flow)^2 - 0.18027628173943131760957E-009 * (LCRBP*LWRBP)^2 - 0.12221534430250976697431E-007 * (LWRBP*CO2Flow)^2 - 0.51533935847648683050088E-005 *

(RichLDG*RichFPZAS)^3 - 0.9747968458934441748908 7E-002 * (RichLDG*CO2Flow)^3 + 0.1201659482079961557485 2E-003 * RichLDG*RichFPZAS*LCRBP - 0.3407361967449587525358 4E-001 * RichLDG*RichFPZAS*CO2Flow + 0.1490953895681636654641 0E-003 * RichLDG*LCRBP*CO2Flow + 0.2475180835906548312025 3E-006 * RichFPZAS*LCRBP*CO2Flow + 0.3405968277253286252856 8E-009 * (RichLDG*RichFPZAS*LWRBP)^2 + 0.6494119271809772102753 1E-006 * (RichLDG*RichFPZAS*CO2Flow)^2 + 0.1126830287574837319537 8E-008 * (RichLDG*LCRBP*LWRBP)^2 - 151.77221351091432666180

Lean Solvent Temperature

Lean T = 585.05442823447879163723 * RichLDG - 0.2982185261308696877513 6 * RichFPZAS + 0.2239792415797451918813 0 * RichT + 0.4174892084764719180078 9 * LCRBP - 0.2123011827062125725373 9E-001 * LWRBP - 1542.4965514378091029357 * RichLDG^2 + 0.8382953726896178511113 2E-003 * RichFPZAS^2 + 0.7207927661290278002759 2E-002 * RichT^2 + 0.2316813970244002360288 1E-002 * LCRBP^2 - 0.1459145561383130265589 0E-003 * LWRBP^2 + 1387.1778251957705379027 * RichLDG^3 - 0.6076324984008505644987 2E-006 * RichFPZAS^3 - 0.6950783201952296225234 7E-005 * LCRBP^3 + 0.3015745101478477164655 6E-006 * LWRBP^3 - 0.1144911486146356210946 7 * RichLDG*RichFPZAS - 0.4697632637278167933025 9E-001 * RichLDG*LCRBP + 0.1308106615371242564815 9 * RichLDG*LWRBP - 0.1148224974867861772689 9E-002 * RichFPZAS*LCRBP - 0.1534421386397059969969 3E-002 * RichT*LCRBP + 0.1538129641543771087435 8E-004 * LCRBP*LWRBP + 0.3694132369879714240965 7E-008 * (RichFPZAS*LCRBP)^2 - 0.3661693169833215638351 9E-006 * (RichLDG*LCRBP)^4

CO_2 Flow Rate

CO_2 Flow = - 55.19533888432678736535 3 * RichLDG - 0.1870476958852205773276 0 * RichFPZAS + 0.9530653979973664480240 8 * WRBP + 306.60572912929302447083 * RichLDG^2 - 429.41131428929656976834 * RichLDG^3

Heat Duty

HD = - 57.36144456428422699900 7 * RichLDG + 0.5352280258460393309828 3E-004 * RichFPZAS - 84.02674263276634292196 8 * CRBP - 10.74047983782050508239 1 * WRBP - 0.6873750828476937746458 5E-001 * RichT + 48.14570639287812525708 4 * RichLDG^2 + 214.58950034988740185327 * CRBP^2 + 4.4854211695217376387745 * WRBP^2 -

224.86948672325809184258 * CRBP^3 + 115.77402997015356334032 * RichLDG*CRBP + 6.7925269224453463934310 * RichLDG*WRBP + 0.15466105629425852541203 * RichLDG*RichT + 0.19632379543067188807162E-003 * RichFPZAS*CRBP + 0.27759684027382235983750E-002 * RichFPZAS*WRBP + 75.85284534511083620600 4 * CRBP*WRBP - 389.11318529534088384025 * (RichLDG*CRBP)^2 - 1.3414542646777622980636 * (RichLDG*WRBP)^2 + 77.051089792319174875956 * (CRBP*WRBP)^2 - 888.64643262942058754561 * (CRBP*WRBP)^3 - 179.01957523894307655610 * RichLDG*CRBP*WRBP + 785.84733631467406667070 * (RichLDG*CRBP*WRBP)^2 - 0.18970457711050276307201E-003 * (RichFPZAS*CRBP*WRBP)^2 + 22.956947495688041271933

Appendix F. 2 R^2 values

Surrogate Model		R-Squared
Stripper	Flooding – Top Section	0.977
	Flooding – Bottom Section	0.983
	Lean Solvent Temperature	0.963
	CO_2 Flowrate	1.0
	Heat Duty	0.993
	Average of cold lean and cold rich temperature	0.995

Appendix G

Appendix G provides the results on model validation of the UT-SRP NGCC 2021 campaign. Methods used for modeling, pilot measurements, and data reconciliation are included in Chapter 3.

Model Reconciliation in the UT-SRP NGCC 2021-22 Campaign

Aspen Plus® Data Fit™ ensured that the predicted lean solvent rate almost perfectly matched the average lean solvent rate measured at the plant by manipulating the rich solvent rate and rich loading. Figure G1 plots the ratio of the estimated lean solvent flow rate to the measured lean solvent flow rate after manipulation of input variables by Data Fit™. The ratio is 1 in almost all cases barring few instances where there is a deviation of 2–4%. Any error in the model after Data Fit™ could now be interpreted to be purely a function of thermodynamics or mass transfer and is not linked to differences in solvent flow between the measurement and the model.

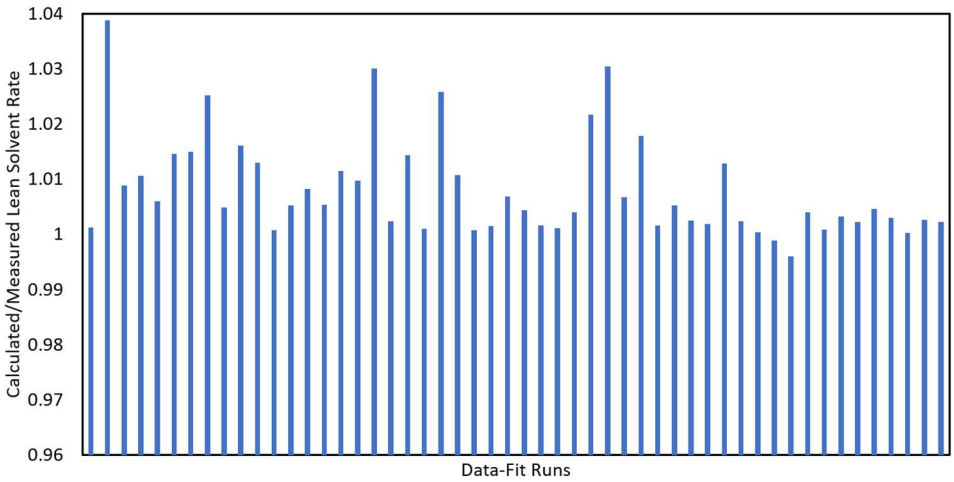

Figure G1: Model reconciliation of lean solvent flowrate using Aspen Plus® Data Fit™

Figure G2 shows the extent of change in the variables selected for Data Fit™ to reconcile the model with measurements. In the 16 independent variables chosen, the average change across multiple Data Fit™ runs did not exceed 1% on the positive or negative side. This was an acceptable and reasonable change that accounts for fluctuations in sensor-measured data at the pilot plant. The most important changes were applied to rich solvent flow rate, rich loading, and the temperature of the heated cold rich bypass. Overall, it appears that measurements made at the pilot plant in the lab did not significantly affect the performance of the model.

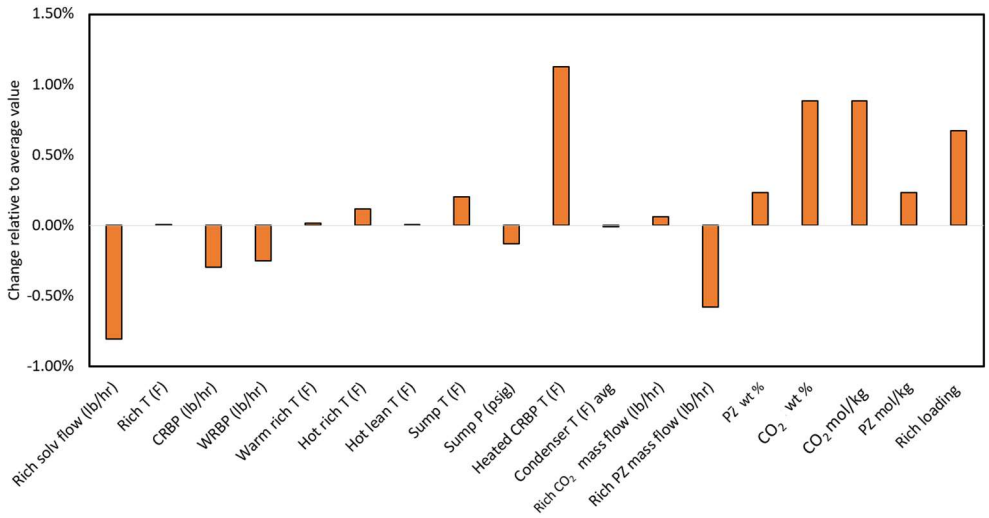

Figure G2: Percentage change in variables manipulated by Aspen Plus® Data Fit™ relative to time-averaged pilot plant values

The reconciled value of lean loading after Data Fit™ is compared to the calculated value of CO_2 flow rate by the model in Figure G3. In all the Data Fit™ runs, there exists a clear correlation between the reconciled value of lean loading and the calculated value of CO_2 flow. Due to the overprediction of lean loading by the thermodynamic model in Aspen Plus® (with an average error of 13%), the CO_2 flow rate is consistently underpredicted by

the model (with an average error of 20%). This is clearly linked to the thermodynamic model parameters, and therefore the heats of formation of species relevant to low lean loading conditions in the stripper.

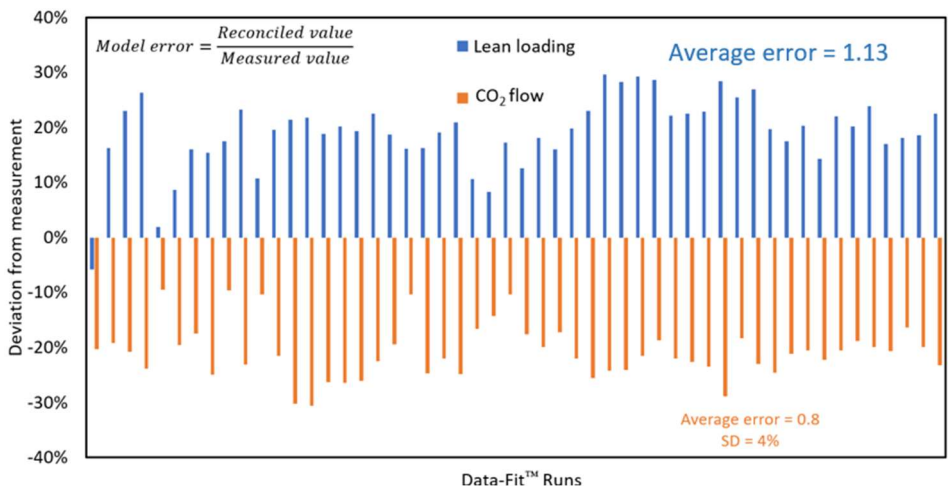

Figure G3: Model consistently over-predicts lean loading which causes an underprediction in CO_2 flowrate indicating issues with thermodynamics at low lean loading

Figure G4 shows that the error in heat rate is lower on average than those of lean loading and CO_2 flow. The model can reconcile heat rate with the measured heat rate better with a lower error of 5%. The combined effect of this error in heat rate and CO_2 flow results in a large deviation between the measured and modeled heat duty for this campaign, also shown in Figure G4. On average this error is 33%, and most of this error comes from incorrect prediction of CO_2 flow (due to an incorrect prediction of lean loading). It is also possible that the CO_2 flowmeter in this pilot plant requires calibration.

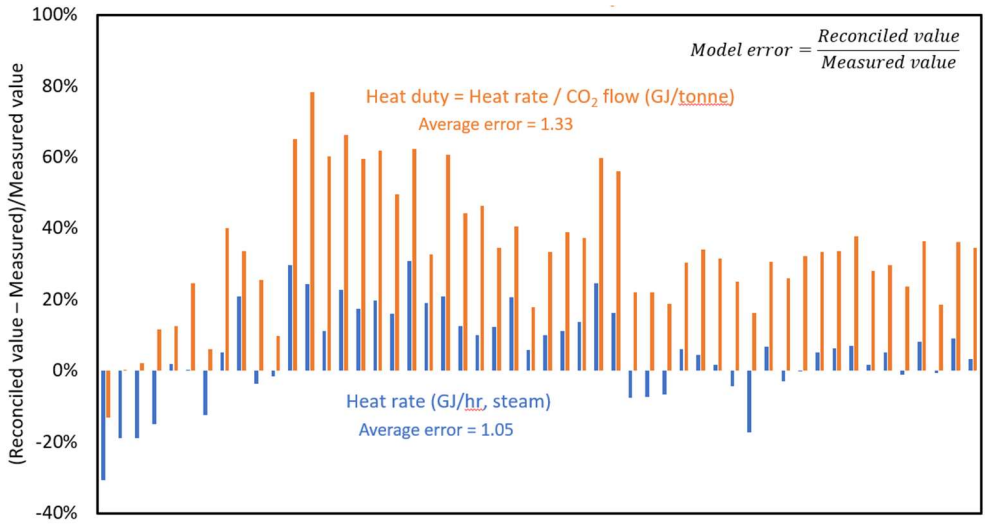

Figure G4: Error in model reconciled heat rate and heat duty versus measurements

The error in CO_2 flowrate or thermodynamics of the model propagates into model validation of temperature profiles. Run 62 at steady state was used to compare the temperature profile in the stripper column between the model and the measurements. Figures G5 to G7 compare the temperature measurements in the column with the model predictions. The measured flowrate of CO_2 for this run was 114.3 lb/hr and the measured lean loading from manual titrations was 0.2 mol/mol. Figure G5 shows that at a sump temperature of 297.6 °F, the measured temperature profile shows a bottom-side pinch in the column while the model tends towards a top-side pinch.

Most of the temperature measurements do not agree with the model in this case. The lean loading predicted by the model was higher at 0.233 mol/mol (+16.5%) giving rise to a lower modeled CO_2 flow rate of 78.6 lb/hr (-31.2%). This low vapor rate in the modeled column gives rise to the top-side pinch (low L/G) at the same total rich bypass flow rate (specified as input). Due to the lower CO_2 flowrate, the heat duty predicted by the model is 3.25 GJ/tonne compared to a measured net heat duty of 2.9 GJ/tonne.

The low CO_2 flowrate predicted by the model also caused issues in the modeling of the CO_2 exchanger in the campaign. The low gas flowrate in the gas-side of the exchanger compared to the cold rich bypass flowrate in the model caused this exchanger to have a temperature cross over at the cold end, therefore predicting an incorrect gas temperature leaving the CO_2 exchanger. However, this was inconsequential to the prediction of the heat duty and lean loading as the temperature of the cold rich bypass leaving the CO_2 exchanger was directly specified as an input to the model.

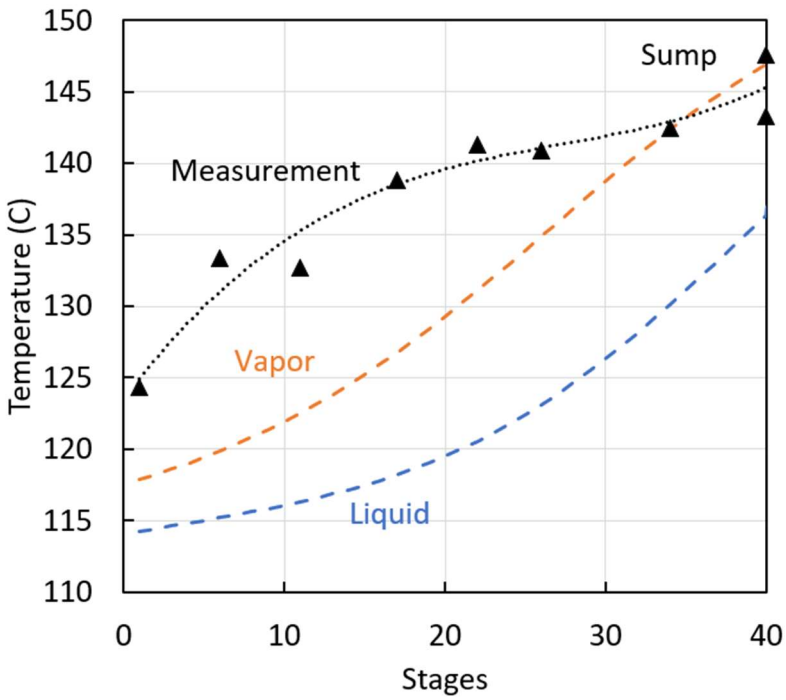

Figure G5: Model predicts a top-side pinch while temperatures indicate a bottom-side pinch, stage 1 is top, stage 40 is bottom; wetted area correction factor of 0.16; measured sump temperature = 297.6 °F; measured lean loading = 0.2 mol/mol; stages represent computational segments

To better reconcile the stripper temperature profiles, the lean loading in the model was forced to match the measured value of 0.2 mol/mol by adjusting the stripper sump

temperature at constant pressure. The calculated value of sump temperature was 302.5 °F (2% above measured value) and the modeled CO_2 flowrate increased to 92.9 lb/hr but was still lower than the measured value of CO_2 flow by 23%. In this case, the temperature measurements agreed more with the modeled values with almost all measurements agreeing better with the vapor temperature profile. This is shown in Figure G6. The general temperature profile in the model and the measurements agree in this case.

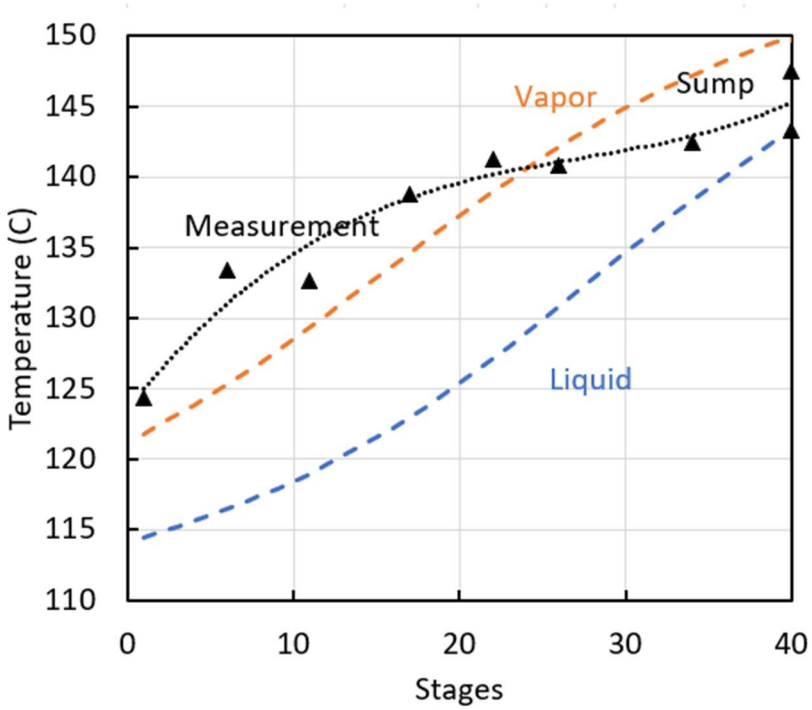

Figure G6: Model predictions are closer to measured values of temperature profile when lean loading is forced to match measurements by manipulating stripper temperature, stage 1 is top, stage 40 is bottom; wetted area correction factor of 0.16; measured sump temperature = 297.6 °F; measured lean loading = 0.2 mol/mol; stages represent computational segments

A third adjustment was made by matching the CO_2 flow rate instead of the lean loading between the model and measurement. This was done by adjusting the sump

temperature in the model. A sump temperature (308.4 °F) about 4% higher than the measurement was predicted in this case which also made the lean loading lower at 0.16 mol/mol compared to 0.2 mol/mol from measurement. This correction in sump temperature does not agree with that made by Aspen Plus® Data Fit™. Data Fit only manipulated stripper sump temperature by less than 0.5% indicating that the stripper temperature measurements are reliable. It is therefore likely that the measured CO_2 is incorrect, and the model-predicted CO_2 to a lesser extent.

However, in this case, due to the perfect agreement of CO_2 flowrate between the measurement and model and consequently the L/G in the column, the bottom-side pinch was predicted by the model more accurately. The temperature measurements appeared to lie closer to the liquid profile towards the bottom of the column and in between the vapor and liquid profile towards the top. This is shown in Figure G7. The L/G and gas flowrate prediction in the column appeared to significantly affect the temperature profile in the column.

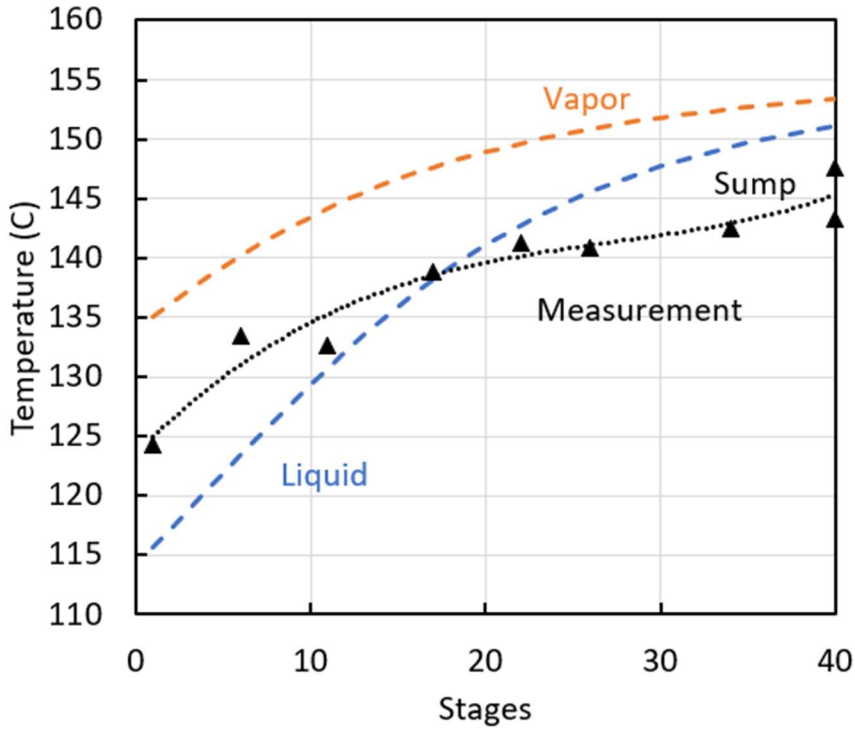

Figure G7: Model predictions when CO_2 flowrate is forced to match measurements by manipulating stripper temperature, stage 1 is top, stage 40 is bottom; wetted area correction factor of 0.16; measured sump temperature = 297.6 °F; measured lean loading = 0.2 mol/mol; stages represent computational segments

Appendix H

Appendix H provides the data for change in variable profit and equipment capacity with a decrease in number of constraints on the optimization problem for 0.18 lean loading for which the most change in profit and equipment capacity is observed. This data is discussed in Figure 6.1 of Chapter 6.

95% HRSG flue gas is processed by the absorber. Three ambient temperatures, 40, 65, and 105 °F are considered.

CASE: 0.18 lean loading, 40 °F

Constraint removed (cumulative)	Boiler capacity (%, heat rate/max. heat rate)	Boiler fan capacity (%, RPM/max. RPM)	Compressor capacity (%, CO_2 mass flow/max. CO_2 mass flow)	Profit Change (%, respective to most constrained base case)
None, base	60	85	100	0
Precipitation	60	85	100	0
Compressor	73	92	120	20.9
Absorber flood	73	92	120	20.9
Boiler fan speed	96	108	124	21.1
Stripper flood	96	108	124	21.1
Boiler	133	134	130	21.45
Lean pump	133	134	130	21.45
Rich pump	133	134	130	21.45
Bypasses	133	134	130	21.45

CASE: 0.18 lean loading, 65 °F

Constraint removed	Boiler capacity (%, heat rate/max. heat rate)	Boiler fan capacity (%, RPM/max. RPM)	Compressor capacity (%, CO_2 mass flow/max. CO_2 mass flow)	Profit Change (%, respective to most constrained base case)
None, base	57	78	100	0
Precipitation	57	78	100	0
Compressor	91	98	115	11
Absorber flood	91	98	115	11
Boiler fan speed	95	102	116	11.03
Stripper flood	95	102	116	11.03
Boiler	130	126	121	11.62
Lean pump	130	126	121	11.62
Rich pump	130	126	121	11.62
Bypasses	130	126	121	11.62

CASE: 0.18 lean loading, 105 °F

Constraint removed	Boiler capacity (%, heat rate/max. heat rate)	Boiler fan capacity (%, RPM/max. RPM)	Compressor capacity (%, CO_2 mass flow/max. CO_2 mass flow)	Profit Change (%, respective to most constrained base case)
None, base	55	75	100	0
Precipitation	55	75	100	0
Compressor	90	98	111	5.9
Absorber flood	90	98	111	5.9
Boiler fan speed	96	102	112	6.1
Stripper flood	96	102	112	6.1
Boiler	116	116	115	6.2
Lean pump	116	116	115	6.2
Rich pump	116	116	115	6.2
Bypasses	116	116	115	6.2

References

Abreu, M., & Rochelle, G. (2021). Heat Exchanger Performance in Pilot Plant Testing of Piperazine with the Advanced Stripper™. In Proceedings of the 15th Greenhouse Gas Control Technologies Conference (pp. 15-18).

Abreu, M., & Rochelle, G. (2022). CO_2 absorber intensification by high liquid flux operation. Available at SSRN 4282100.

Aburime, E. I., Omoregbe, O., Amenaghawon, N. A., Aziaka, D. S., & Tashie-Lewis, B. C. (2022). Amino-2-methyl-1-propanol-based Post-combustion Capture Process with Solvent Storage for Decarbonisation of Natural Gas Combined Cycle Power Plant. Carbon Capture Science & Technology, 2, 100024.

Adu, E., Zhang, Y. D., Liu, D., & Tontiwachwuthikul, P. (2020). Parametric process design and economic analysis of post-combustion CO_2 capture and compression for coal- and natural gas-fired power plants. Energies, 13(10), 2519.

Akula, P., Eslick, J., Bhattacharyya, D., & Miller, D. C. (2021). Model development, validation, and optimization of an MEA-based post-combustion CO_2 capture process under part-load and variable capture operations. Industrial & Engineering Chemistry Research, 60(14), 5176-5193.

Artanto, Y., Jansen, J., Pearson, P., Puxty, G., Cottrell, A., Meuleman, E., & Feron, P. (2014). Pilot-scale evaluation of AMP/PZ to capture CO_2 from flue gas of an Australian brown coal–fired power station. International journal of Greenhouse Gas control, 20, 189-195.

Aspen Exchanger Design & Rating (EDR) (2013), Aspen Technology, Inc., Cambridge, MA.

Babu, A. S., & Rochelle, G. T. (2022). Energy use of piperazine with the advanced stripper from pilot plant testing. International Journal of Greenhouse Gas Control, 113, 103531.

Babu, A. S., & Rochelle, G. T. (2022). Process design of the piperazine advanced stripper for a 460 MW NGCC. International Journal of Greenhouse Gas Control, 115, 103631.

Babu, A. S., & Rochelle, G. T. (2023). High Temperature Solvent Separation With Advanced Stripper and Direct Contact Condenser. U.S. Patent Application.

Bhattacharyya, D., Turton, R., & Zitney, S. E. (2011). Steady-state simulation and optimization of an integrated gasification combined cycle power plant with CO_2 capture. Industrial & Engineering Chemistry Research, 50(3), 1674-1690.

Billet, R., & Schultes, M. (1993). Predicting mass transfer in packed columns. Chemical Engineering & Technology: Industrial Chemistry-Plant Equipment-Process Engineering-Biotechnology, 16(1), 1-9.

Borhani, T. N., Oko, E., & Wang, M. (2019). Process modelling, validation and analysis of rotating packed bed stripper in the context of intensified CO_2 capture with MEA. Journal of Industrial and Engineering Chemistry, 75, 285-295.

Bottoms, R. (1930). Process for separating acidic gases. US Patent, 1783901.

Bravo, J. L. (1985). Mass transfer in gauze packings. Hydrocarbon processing, 64(1), 91-95.

Bravo, J., Drapanauskaite, D., Sarunac, N., Romero, C., Jesikiewicz, T., & Baltrusaitis, J. (2021). Optimization of energy requirements for CO_2 post-combustion capture process through advanced thermal integration. Fuel, 283, 118940.

Brown, A., Meuleman, E., Heller, G., Silverman, T., Staab, G., Kupfer, R., Brown, R., Atcheson, J., Brown, N. (2017) ION Engineering Final Project Report National Carbon Capture Center Pilot Testing. ION Engineering, USA.

Brúder, P., Owrang, F., & Svendsen, H. F. (2012). Pilot study—CO_2 capture into aqueous solutions of 3-methylaminopropylamine (MAPA) activated dimethyl-monoethanolamine (DMMEA). International Journal of Greenhouse Gas Control, 11, 98-109.

Bui, M., Gunawan, I., Verheyen, V., Feron, P., & Meuleman, E. (2016). Flexible operation of CSIRO's post-combustion CO_2 capture pilot plant at the AGL Loy Yang power station. International Journal of Greenhouse Gas Control, 48, 188-203.

Bumb, P., Kumar, R., Khakharia, P., & Goetheer, E. (2014). Demonstration of advanced APBS solvent at TNO's CO_2 capture pilot plant. Energy Procedia, 63, 1657-1666.

Bumb, P., Patkar, P. A., Mather, R., Kumar, R., Hall, J., Morton, F., & Anthony, J. (2017). Field Demonstration of Advanced CDRMax Solvent at the US-DOE's National Carbon Capture Centre and the CO_2 Technology Centre Mongstad DA, Norway. Energy Procedia, 114, 1087-1099.

Campbell, M. (2014). Technology innovation & advancements for shell cansolv CO_2 capture solvents. Energy Procedia, 63, 801-807.

Chen, E. (2007). Carbon dioxide absorption into piperazine promoted potassium carbonate using structured packing. PhD dissertation. The University of Texas at Austin.

Chen, E., Eseyin, A., Gao, T., & Rochelle, G. T. (2018). Advanced Flash Stripper with Concentrated Piperazine and Absorber Intercooling at NGCC Conditions: Report for October 2018 Pilot Campaign Prepared by CO_2 Capture Pilot Plant Project (C2P3), The University of Texas at Austin For Osaka Gas Co., LTD. (2018)

Chen, E., Fulk, S., Beaudry, M., Lin, Y. J., Sachde, D., Zhang, Y., ... & Bernau, M. (2019). Evaluation of Concentrated Piperazine for CO_2 Capture from Coal-Fired Flue Gas (Final Report, REV0) (No. DOE-URS-5654-1). URS Group, Inc., Austin, TX (United States).

Chen, E., Fulk, S., Sache, D., Lin, Y., & Rochelle, G. T. (2014). Pilot plant activities with concentrated piperazine. Energy Procedia, 63, 1376-1391.

Chinen, A. S., Morgan, J. C., Omell, B. P., Bhattacharyya, D., & Miller, D. C. (2016). Dynamic data reconciliation and model validation of a MEA-based CO_2 capture system using pilot plant data. IFAC-PapersOnLine, 49(7), 639-644.

Chiyoda's Testing of T-3 Solvent at the National Carbon Capture Center. 2014. https://www.nationalcarboncapturecenter.com/wp-content/uploads/2021/01/Chiyoda-Testing-of-T-3-Solvent-2014.pdf

Closmann, F., Rochelle, G., Gao, T., Suresh Babu, A., Abreu, M., & Drewry, B. (2021, March). FEED for Piperazine with the Advanced Stripperr™ on NGCC at Denver City, Texas. In Proceedings of the 15th Greenhouse Gas Control Technologies Conference (pp. 15-18).

Closmann, F.B., (2011). Oxidation and thermal degradation of methyldithanolamine/piperazine in CO_2 capture. PhD dissertation. The University of Texas at Austin.

Cousins, A., Cottrell, A., Lawson, A., Huang, S., & Feron, P. H. (2012). Model verification and evaluation of the rich-split process modification at an Australian-based post combustion CO_2 capture pilot plant. Greenhouse Gases: Science and Technology, 2(5), 329-345.

Cozad, A., Sahinidis, N. V., & Miller, D. C. (2014). Learning surrogate models for simulation-based optimization. AIChE Journal, 60(6), 2211-2227.

Du, Y. (2016). Amine solvent development for carbon dioxide capture. PhD dissertation. The University of Texas at Austin.

Du, Y., Gao, T., Rochelle, G. T., & Bhown, A. S. (2021). Zero-and negative-emissions fossil-fired power plants using CO_2 capture by conventional aqueous amines. International Journal of Greenhouse Gas Control, 111, 103473.

Dubois, L., & Thomas, D. (2018). Comparison of various configurations of the absorption-regeneration process using different solvents for the post-combustion CO_2 capture applied to cement plant flue gases. International Journal of Greenhouse Gas Control, 69, 20-35.

Final Report NCCC (Simulated Natural Gas): Cansolv Technologies Inc. 2017. https://www.nationalcarboncapturecenter.com/wp-

content/uploads/2021/01/Cansolv-Testing-of-Cansolv-DC-201-CO_2-Capture-System-with-Simulated-Natural-Gas-Testing-2015.pdf

Fine, N., Kupfer, R., Staab, G., Silverman, T., Awtry, A., Dinsdale, B., ... & Meuleman, E. (2022). Demonstration of ION's Novel CO_2 Capture Solvent (ICE-31) with High Performance and Exceptional Stability through Field Testing at NCCC's PSTU with Coal and NGCC Gas. Available at SSRN 4274368.

Frailie, P. T. (2014). Modeling of carbon dioxide absorption/stripping by aqueous methyldiethanolamine/piperazine (Doctoral dissertation). PhD dissertation. The University of Texas at Austin.

Freeman, S. A. (2011). Thermal degradation and oxidation of aqueous piperazine for carbon dioxide capture (Doctoral dissertation). PhD dissertation. The University of Texas at Austin.

Frimpong, R. A., Nikolic, H., Bahr, D., Kiran, G., & Liu, K. (2021). Pilot scale testing of an advanced solvent in a 0.7 MWe post-combustion CO_2 capture unit. International Journal of Greenhouse Gas Control, 106, 103290.

Gao, J., Yin, J., Zhu, F., Chen, X., Tong, M., Kang, W., ... & Lu, J. (2017). Experimental study of regeneration performance for CO_2 desorption from a hybrid solvent MEA-methanol in a stripper column packed with three different packing: Sulzer BX500, mellapale Y500 and pall rings 16× 16. Environmental Progress & Sustainable Energy, 36(3), 838-844.

Gao, T. (2021). Absorber modeling and design in amine scrubbing for carbon capture (Doctoral dissertation). PhD dissertation. The University of Texas at Austin.

Gao, T., & Rochelle, G. T. (2022). Creative absorber design and optimization for CO_2 capture with aqueous piperazine. International Journal of Greenhouse Gas Control, 113, 103534.

Gao, T., Selinger, J. L., & Rochelle, G. T. (2019). Demonstration of 99% CO_2 removal from coal flue gas by amine scrubbing. International Journal of Greenhouse Gas Control, 83, 236-244.

Gayheart, J. W., Moorman, S. A., Parsons, T. R., & Poling, C. W. (2013). Babcock & Wilcox Power Generation Group, Inc.'s RSAT™ Process and Field Demonstration of the OptiCap™ Advanced Solvent at the US-DOE's National Carbon Capture Center. Energy Procedia, 37, 1951-1967.

Heberle, J. R., Nikolic, H., Thompson, J., Liu, K., Pinkerton, L. L., Brubaker, D., ... & Bhown, A. S. (2017). Techno-Economic Analysis of a Secondary Air Stripper Process. Energy Procedia, 114, 1069-1074.

Jiang, K., Li, K., Yu, H., & Feron, P. H. (2018). Piperazine-promoted aqueous-ammonia-based CO_2 capture: Process optimizsation and modification. Chemical Engineering Journal, 347, 334-342.

Jiang, K., Li, K., Yu, H., Chen, Z., Wardhaugh, L., & Feron, P. (2017). Advancement of ammonia based post-combustion CO_2 capture using the advanced flash stripper process. Applied Energy, 202, 496-506.

Jin, H., Liu, P., & Li, Z. (2018). Energy-efficient process intensification for post-combustion CO_2 capture: A modeling approach. Energy, 158, 471-483.

Jovnovic, S., Rigby, S., Sieder, G., Stoffregen, T., Perez, E., England, M., ... & Jones, A. P. (2012). Slipstream Pilot-Scale Demonstration of a Novel Amine-Based Post-Combustion Technology for Carbon Dioxide Capture from Coal-Fired Power Plant Flue Gas. Topical Report: Techno-Economic Analysis of 550 MWe subcritical PC power plant with CO_2 capture.

Jung, J., Jeong, Y. S., Lee, U., Lim, Y., & Han, C. (2015). New configuration of the CO_2 capture process using aqueous monoethanolamine for coal-fired power plants. Industrial & Engineering Chemistry Research, 54(15), 3865-3878.

Jung, J., Jeong, Y. S., Lim, Y., Lee, C. S., & Han, C. (2013). Advanced CO_2 capture process using MEA scrubbing: Configuration of a split flow and phase separation heat exchanger. Energy Procedia, 37, 1778-1784.

Karimi, M., Hillestad, M., & Svendsen, H. F. (2011). Capital costs and energy considerations of different alternative stripper configurations for post combustion CO_2 capture. Chemical engineering research and design, 89(8), 1229-1236.

Karimi, M., Hillestad, M., & Svendsen, H. F. (2012). Investigation of the dynamic behavior of different stripper configurations for post-combustion CO_2 capture. International journal of greenhouse gas control, 7, 230-239.

Knudsen, J. N., Andersen, J., Jensen, J. N., & Biede, O. (2011). Evaluation of process upgrades and novel solvents for the post combustion CO_2 capture process in pilot-scale. Energy Procedia, 4, 1558-1565.

Knudsen, J. N., Jensen, J. N., Vilhelmsen, P. J., & Biede, O. (2007, September). First year operation experience with a 1 t/h CO_2 absorption pilot plant at Esbjerg coal-fired power plant. In Proceedings of European Congress of Chemical Engineering (ECCE-6) (Vol. 3, pp. 57-61).

Krishnamurthy, K. R. (2017). Slipstream pilot-scale demonstration of a novel amine-based post-combustion technology for carbon dioxide capture from coal-fired power plant flue gas. Linde LLC, Murray Hill, NJ (United States).

Kwak, N. S., Lee, J. H., Lee, I. Y., Jang, K. R., & Shim, J. G. (2012). A study of the CO_2 capture pilot plant by amine absorption. Energy, 47(1), 41-46.

Li, K., Cousins, A., Yu, H., Feron, P., Tade, M., Luo, W., & Chen, J. (2016). Systematic study of aqueous monoethanolamine-based CO_2 capture process: model development and process improvement. Energy Science & Engineering, 4(1), 23-39.

Li, K., Yu, H., Feron, P., Wardhaugh, L., & Tade, M. (2016). Techno-economic assessment of stripping modifications in an ammonia-based post-combustion capture process. International Journal of Greenhouse Gas Control, 53, 319-327.

Li, L. (2015). Carbon dioxide solubility and mass transfer in aqueous amines for carbon capture.

Lin, Y. J. (2016). Modeling advanced flash stripper for carbon dioxide capture using aqueous amines (Doctoral dissertation). PhD dissertation. The University of Texas at Austin.

Lin, Y. J., & Rochelle, G. T. (2016). Approaching a reversible stripping process for CO_2 capture. Chemical Engineering Journal, 283, 1033-1043.

Liu, C. T. (2022). Corrosion of stainless and carbon steel in aqueous piperazine for CO_2 capture (Doctoral dissertation). PhD dissertation. The University of Texas at Austin.

Liu, J., Wong, D. S. H., & Chen, D. S. (2020). Energy-saving performance of advanced stripper configurations for CO_2 capture by ammonia-based solvents. Journal of the Taiwan Institute of Chemical Engineers, 113, 273-284.

Madan, T. (2013). Modeling of stripper configurations for CO_2 capture using aqueous piperazine. MS Thesis. The University of Texas at Austin.

Madan, T., Van Wagener, D. H., Chen, E., & Rochelle, G. T. (2013). Modeling pilot plant results for CO_2 stripping using piperazine in two stage flash. Energy Procedia, 37, 386-399.

Mangalapally, H. P., & Hasse, H. (2011). Pilot plant experiments for post combustion carbon dioxide capture by reactive absorption with novel solvents. Energy Procedia, 4, 1-8.

Mangalapally, H. P., Notz, R., Asprion, N., Sieder, G., Garcia, H., & Hasse, H. (2012). Pilot plant study of four new solvents for post combustion carbon dioxide capture by reactive absorption and comparison to MEA. International Journal of Greenhouse Gas Control, 8, 205-216.

Merkin, J. H. (1994). Natural-convection boundary-layer flow on a vertical surface with Newtonian heating. International Journal of Heat and Fluid Flow, 15(5), 392-398.

Meuleman, E., Artanto, Y., Jansen, J., Osborn, M., Pearson, P., Cottrell, A., & Feron, P. (2010, June). CO_2 capture performance of MEA and blended amine solvents in

CSIRO's pilot plant with flue gas from a brown coal-fired power station. In 6th International Technical Conference on Clean Coal & Fuel Systems (Vol. 3).

Moser, P., Schmidt, S., Sieder, G., Garcia, H., & Stoffregen, T. (2011). Performance of MEA in a long-term test at the post-combustion capture pilot plant in Niederaussem. International Journal of Greenhouse Gas Control, 5(4), 620-627.

Nguyen, H. L. Q., & Wong, D. S. H. (2021). Integration of rich and lean vapor recompression configurations for aqueous ammonia-based CO_2 capture process. Chemical Engineering Research and Design, 169, 86-96.

Oh, H. T., Ju, Y., Chung, K., & Lee, C. H. (2020). Techno-economic analysis of advanced stripper configurations for post-combustion CO_2 capture amine processes. Energy, 206, 118164.

Owrang, F., & Svendsen, H. F. (2010, November). Estimating the heat losses from a laboratory pilot plant for CO_2 absorption. In 2010 2nd International Conference on Chemical, Biological and Environmental Engineering (pp. 180-183). IEEE.

Oyenekan, B. A. (2007). Modeling of strippers for carbon dioxide capture by aqueous amines (Doctoral dissertation, The University of Texas at Austin).

Peters, M. S., Timmerhaus, K. D., & West, R. E. (2003). Plant design and economics for chemical engineers (Vol. 4). New York: McGraw-Hill.

Plaza, J. M., & Rochelle, G. T. (2011). Modeling pilot plant results for CO_2 capture by aqueous piperazine. Energy Procedia, 4, 1593-1600.

Putta, K. R., Campbell, M., & Shah, M. I. (2022). Development of CO_2 Capture Process Cost Baseline for 555 MWe NGCC Power Plant Using Standard MEA Solution. Muhammad Ismail, Development of CO_2 Capture Process Cost Baseline for, 555.

Rocha, J. A., Bravo, J. L., & Fair, J. R. (1996). Distillation columns containing structured packings: a comprehensive model for their performance. 2. Mass-transfer model. Industrial & engineering chemistry research, 35(5), 1660-1667.

Rochelle, G. T., Akinpelumi, K., Gao, T., Liu, C. T., Babu, A. S., & Wu, Y. (2022). Pilot plant results with the piperazine advanced stripper at NGCC conditions. International Journal of Greenhouse Gas Control, 113, 103551.

Rochelle, G., Chen, E., Freeman, S., Van Wagener, D., Xu, Q., & Voice, A. (2011). Aqueous piperazine as the new standard for CO_2 capture technology. Chemical engineering journal, 171(3), 725-733.

Rochelle, G., Closmann, F., Abreu, M., Suresh Babu, A., Drewry, B., Gao, T.,T., ... & Piggott, B. (2022). Cost details from Front-End Engineering Design of Piperazine with the advanced stripper. Karen, F., Karen and Bryan, Sscott Rr., and Bbernau, M.,max and Sexton, A.,ndrew and Dombrowski, K.,atherine and Jjones, Rr.,osalind

Mand marsh, M.,michael and Piggott, B.,rad &and Mmyers, Dduane., Cost details from Front-End Engineering Design of piperazine with the advanced stripper (August 29, 2022).

Rochelle, G.T. (2009). Amine Scrubbing for CO_2 Capture. Science, 325(5948), 1652-1654. doi: 10.1126/science.1176731.

Rochelle, G.T., Closmann, F., Suresh Babu, A., Drewry, B., Gao, T., Martorell, J., Abreu, M., Steen, W. A., Farmer, K., Bryan, S., Bernau, M., Sexton, A., Dombrowski, K., Myers, D., Marsh, M., Piggott, B., Jones, R., & Lee, J. (2022) Front-End Engineering Design for Piperazine with the Advanced Stripper, Final report for DE-FE0031844.

Seibert, F., Chen, E., Perry, M., Briggs, S., Montgomery, R., & Rochelle, G. (2011). UT/SRP CO_2 capture pilot plant—Operating experience and procedures. Energy Procedia, 4, 1616-1623.

Seo, K., Tsay, C., Hong, B., Edgar, T. F., Stadtherr, M. A., & Baldea, M. (2020). Rate-based process optimization and sensitivity analysis for ionic-liquid-based post-combustion carbon capture. ACS Sustainable Chemistry & Engineering, 8(27), 10242-10258.

Simon, L. L., Elias, Y., Puxty, G., Artanto, Y., & Hungerbuhler, K. (2011). Rate based modeling and validation of a carbon-dioxide pilot plant absorbtion column operating on monoethanolamine. Chemical Engineering Research and Design, 89(9), 1684-1692.

Sipöcz, N., Tobiesen, A., & Assadi, M. (2011). Integrated modelling and simulation of a 400 MW NGCC power plant with CO_2 capture. Energy Procedia, 4, 1941-1948.

Snijder, E. D., te Riele, M. J., Versteeg, G. F., & Van Swaaij, W. P. M. (1993). Diffusion coefficients of several aqueous alkanolamine solutions. Journal of Chemical and Engineering data, 38(3), 475-480.

Song, D. (2017). Effect of liquid viscosity on liquid film mass transfer for packings (Doctoral dissertation). PhD dissertation. The University of Texas at Austin.

Stec, M., Tatarczuk, A., Więcław-Solny, L., Krótki, A., Ściążko, M., & Tokarski, S. (2015). Pilot plant results for advanced CO_2 capture process using amine scrubbing at the Jaworzno II Power Plant in Poland. Fuel, 151, 50-56.

Stec, M., Tatarczuk, A., Więcław-Solny, L., Krótki, A., Spietz, T., Wilk, A., & Śpiewak, D. (2016). Demonstration of a post-combustion carbon capture pilot plant using amine-based solvents at the Łaziska Power Plant in Poland. Clean Technologies and Environmental Policy, 18, 151-160.

Suresh Babu, A., & Rochelle, G. (2022). Heat Loss Characteristics and Energy Use of Piperazine with the Advanced Stripper (PZAS) at the UT-SRP Pilot Plant. Gary, Heat Loss Characteristics and Energy Use of Piperazine with the Advanced Stripper (PZAS) at the UT-SRP Pilot Plant (October 24, 2022).

Suresh Babu, A., Abreu, M., Drewry, B., Chen, Y. L., & Rochelle, G. T. (2023). Optimization of Operating Profit for the FEED of the PZAS process for CO_2 Capture on a 460 MW NGCC. Submitted to Industrial and Engineering Chemistry Research.

Testing of Hitachi H3-1 Solvent at the National Carbon Capture Center: Final Report.2012.https://www.nationalcarboncapturecenter.com/wp-content/uploads/2021/01/Hitachi-Power-Systems-America-Testing-of-Hitachi-H3-1-Solvent-2012.pdf.

Teymourtash, A. R., & Ebrahimi Warkiani, M. (2009). Natural convection over a non-isothermal vertical flat plate in supercritical fluids. Scientia Iranica, 16(6).

Tobiesen, F. A., Juliussen, O., & Svendsen, H. F. (2008). Experimental validation of a rigorous desorber model for CO_2 post-combustion capture. Chemical Engineering Science, 63(10), 2641-2656.

U.S. Energy Information Administration. (2021). Homepage. Retrieved from https://www.eia.gov/.

Van Wagener, D. H. (2011). Stripper modeling for CO_2 removal using monoethanolamine and piperazine solvents (Doctoral dissertation). PhD dissertation. The University of Texas at Austin.

Van Wagener, D. H., & Rochelle, G. T. (2011). Stripper configurations for CO_2 capture by aqueous monoethanolamine. Chemical engineering research and design, 89(9), 1639-1646.

Versteeg, G. F., & Van Swaaij, W. P. (1988). Solubility and diffusivity of acid gases (carbon dioxide, nitrous oxide) in aqueous alkanolamine solutions. Journal of Chemical & Engineering Data, 33(1), 29-34.

Wang, C. (2015). Mass transfer coefficients and effective area of packing (Doctoral dissertation). PhD dissertation. The University of Texas at Austin.

Wu, Y. (2022). Mitigation methods for piperazine oxidation in post-combustion carbon capture (Doctoral dissertation). PhD dissertation. The University of Texas at Austin.

Zhao, B., Liu, F., Cui, Z., Liu, C., Yue, H., Tang, S., ... & Liang, B. (2017). Enhancing the energetic efficiency of MDEA/PZ-based CO_2 capture technology for a 650 MW power plant: Process improvement. Applied energy, 185, 362-375.

Vita

Athreya was born in the coastal city of Chennai, Tamil Nadu, India in 1996. He completed his bachelor's degree in Chemical Engineering at Anna University, Chennai, during which time he conducted research in chemical reaction engineering for water treatment technologies under Dr. Jagannathan Krishnan. Following undergraduate studies, he earned a master's degree in Environmental and Water Resources Engineering (EWRE) at The University of Texas at Austin. During this time, he conducted experimental research for reaction kinetics in flue gas desulfurization, a project co-advised by Dr. Gary T. Rochelle and Dr. Desmond Lawler. He continued his doctoral studies in stripper modeling with Dr. Gary T. Rochelle in the Texas Carbon Management Program of the McKetta Department of Chemical Engineering at UT Austin. During his PhD, the author completed two research internships: one in economics for Direct Air Capture at the start-up Electric Tree (subsidiary of Global Thermostat) and one in modeling amine scrubbing processes at ExxonMobil Research Engineering in Annandale, New Jersey. Following the completion of his PhD in the summer of 2023, the author will continue working on amine scrubbing with ExxonMobil Technology and Engineering Company in Houston, Texas.

Permanent email: athreya96@utexas.edu

This dissertation was typed by Athreya Suresh Babu.